

19980311 172

**DISTRIBUTION STATEMENT A**

Approved for public release;  
Distribution Unlimited

DEPARTMENT OF THE AIR FORCE  
AIR UNIVERSITY  
**AIR FORCE INSTITUTE OF TECHNOLOGY**

Wright-Patterson Air Force Base, Ohio

DTIC QUALITY INSPECTED 4

AFIT/DS/ENY/98M-01

**ANALYSIS OF TURBULENCE MODELS AS  
APPLIED TO TWO- AND  
THREE-DIMENSIONAL INJECTION FLOWS**

**DISSERTATION**

**Clarence F. Chenault B.S., M.S.  
Captain, USAF**

**AFIT/DS/ENY/98M-01**

Approved for public release; distribution unlimited

## **Disclaimer**

The views expressed in this dissertation are those of the author and do not reflect the official policy or position of the United States Air Force, the Department of Defense, or the United States Government.

AFIT/DS/ENY/98M-01

***ANALYSIS OF TURBULENCE MODELS AS  
APPLIED TO TWO- AND THREE-DIMENSIONAL  
INJECTION FLOWS***

**DISSERTATION**

Presented to the Faculty of the School of Engineering  
of the Air Force Institute of Technology  
Air University  
in Partial Fulfillment of the  
Requirements for the Degree of  
**Doctor of Philosophy**

**Clarence F. Chenault B.S., M.S.**  
**Captain, USAF**

March, 1998

Sponsored by the Air Force Research Laboratory

Approved for public release; distribution unlimited



**ANALYSIS OF TURBULENCE MODELS AS  
APPLIED TO TWO- AND THREE-DIMENSIONAL  
INJECTION FLOWS**

**Clarence F. Chenault B.S., M.S.**

**Captain, USAF**

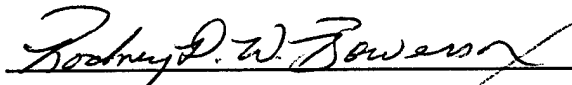
Approved:



Dr. Philip S. Beran  
Committee Chairman

2 Feb 98

Date



Dr. Rodney D. W. Bowersox  
Committee member

20 Jan '98

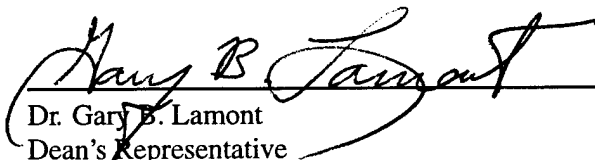
Date



Dr. David E. Weeks  
Committee member

20 Jan 98

Date



Dr. Gary B. Lamont  
Dean's Representative

20 JAN 98

Date

Accepted:



Dr. Robert A. Calico  
Dean, School of Engineering

## **Dedication**

This work is dedicated to the people who gave me the strength to persevere when life got tough.

To my father William Thomas Chenault. Dad, we only had eleven years together, but your example of how I should meet life's challenges has never left me with any doubt about the path I should follow.

To my grandparents Nunclee Harmon and Katie Estell Chenault. Papa and Grandmother, you picked up where Dad left off. Your absence is only tempered by the knowledge that you and your son have been reunited.

To my wife Barbara, and children Brianna, Kellie and Thomas. Thank you so much for your love and support over the years. I could never survive without your faith in me.

## Acknowledgments

My time at AFIT has been extremely rewarding. I have worked in a field of study that I sincerely enjoy and find a constant challenge and I have had the pleasure of working with many people that I truly respect. In the forefront of these people is my advisor, Dr. Philip Beran, who from the very beginning of our association has been accessible and helpful. He is one of my strongest advocates and I will always be grateful for his guidance and efforts with my work.

I would also like to thank my co-advisor Dr. Rodney Bowersox. Dr. Bowersox had a huge impact on the quality and significance of this work and his knowledge of turbulence and turbulence modeling helped me get past many stumbling blocks to the successful completion of this work.

I would also like to thank the members of my doctoral committee: Dr. David Weeks and Dr. Gary Lamont, and my sponsor Dr. Miguel Visbal. Their enthusiasm for this research has always been a comfort.

An enormous debt of gratitude and thanks goes to Mr. Joseph Morrison of Analytical Services & Materials, Inc. I am indebted to Mr. Morrison on two counts, first he wrote the majority of the software I used to conduct my research and second for providing invaluable tutelage on its operation.

I would also like to thank Kristen Larson for her ceaseless efforts to keep the computer systems up and running.

Finally, I must thank Bob Latin for being my sounding board and helping me stay focused on the task at hand.

# Table Of Contents

	Page
Dedication .....	iv
Acknowledgments .....	v
List of Figures .....	xiv
List of Tables .....	xxvi
List of Symbols .....	xxviii
Abstract .....	xxxiv
Chapter 1. INTRODUCTION .....	1
1.1 Background .....	1
1.2 Primary Research Issues .....	3
1.3 Objectives .....	6
1.4 Document overview .....	7
Chapter 2. METHODOLOGY .....	8
2.1 Basis for Methodology .....	8
2.1.1 Computational Data Base .....	8
2.1.2 Experimental Data Base .....	9
2.1.3 Algorithm Performance Issues .....	12
2.1.4 Secondary Research Issues .....	15
2.2 Approach to Meeting the Objectives .....	15

	Page
2.2.1 Solver and Turbulence Model Selection .....	16
2.2.2 Two-dimensional validation and evaluation .....	16
2.2.3 Three-dimensional validation and evaluation .....	18
2.2.4 Validation Criteria .....	19
Chapter 3. GOVERNING EQUATIONS .....	21
3.1 Introduction .....	21
3.2 Navier-Stokes Equations .....	21
3.3 Favré-Averaged Navier-Stokes Equations .....	23
Chapter 4. TURBULENCE MODELS .....	26
4.1 Introduction .....	26
4.2 Two-Equation Models .....	26
4.2.1 The K- $\epsilon$ Model .....	27
4.2.2 The Boussinesq Approximation and Secondary Flowfields .....	33
4.3 Second-Order Reynolds Stress Turbulence Models .....	35
4.3.1 Reynolds-Stress and Dissipation-Rate Transport Equations .....	35
4.3.2 Higher-Order Correlation Models for the Reynolds-Stress Transport Equation and the Dissipation-Rate Transport Equation .....	38
4.3.2.1 Launder, Reece, and Rodi (LRR) RSTM Closure .....	38
4.3.2.2 Shima RSTM Closure .....	40
4.3.2.3 Lai and So RSTM Closure .....	42
4.3.2.4 Lai, So, Zhang, and Speziale (LSZS) RSTM Closure .....	44

	Page
4.3.2.5 Zhang, So, Gatski, and Speziale (ZSGS) RSTM Closure . . . . .	45
4.3.2.6 Turbulent Diffusion, Viscous Diffusion and Mass Flux Variations . . . . .	46
4.4 Navier-Stokes Equations in a Second-Order Model . . . . .	47
Chapter 5. ALGORITHM FORMULATION . . . . .	49
5.1 Introduction . . . . .	49
5.2 Governing Equation Formulation . . . . .	49
5.2.1 Integral Formulation . . . . .	49
5.2.2 Finite-Volume Formulation . . . . .	51
5.2.3 Implicit Time-Difference Formulation . . . . .	55
5.3 Discretization . . . . .	56
5.3.1 Linearization . . . . .	56
5.3.2 Factorization . . . . .	58
5.3.3 Diagonalization . . . . .	58
5.3.4 Spatial Discretization . . . . .	60
5.3.5 Roe Flux-Differencing . . . . .	60
5.3.6 Variable Extrapolation . . . . .	64
5.3.7 Gradient Theorem . . . . .	64
5.4 Non-Dimensionalization . . . . .	65
Chapter 6. TWO-DIMENSIONAL ANALYSIS AND RESULTS . . . . .	67
6.1 Introduction . . . . .	67

	Page
6.1.1 General Flowfield Description .....	67
6.1.2 Overexpansion, Underexpansion and the Concept of Effective Back Pressure .....	69
6.2 Sonic Injection Configurations .....	70
6.2.1 Boundary Conditions and Computational Grid .....	72
6.2.2 Pressure Profile Data .....	73
6.2.3 Turbulence Data .....	78
6.2.3.1 Flat-Plate Validation .....	79
6.2.3.2 Reynolds Stress Profiles .....	80
6.2.3.3 Flowfield Contours .....	84
6.2.3.4 Vorticity .....	86
6.2.3.5 Total Energy .....	87
6.2.4 Summary of Sonic Injection Results .....	87
6.3 Supersonic Injection Configuration .....	89
6.3.1 Boundary Conditions and Computational Grid .....	90
6.3.2 Shock Structure and Mean Flow Analysis .....	92
6.3.3 Plume Structure .....	93
6.3.4 Turbulence Data .....	95
6.3.4.1 Reynolds Stress Profiles .....	95
6.3.4.2 Flowfield Contours .....	97
6.3.4.3 Total Energy .....	101

	Page
6.3.5 Summary of Supersonic Injection Results . . . . .	101
Chapter 7. THREE-DIMENSIONAL RESULTS AND ANALYSIS . . . . .	104
7.1 Introduction . . . . .	104
7.1.1 Generalized Three-Dimensional Flowfield Description and Terminology . . . . .	105
7.2 Supersonic Oblique Injection: McCann and Bowersox Configuration . . . . .	107
7.2.1 Boundary Conditions and Grid Configurations . . . . .	109
7.2.2 Non-Dimensionalization . . . . .	111
7.3 Evaluation of Results at Station 20 . . . . .	112
7.3.1 Comparison of Experimental Data to Computational Results at Station 20 . . . . .	112
7.3.2 Evaluation of Computational Results for Variables Without Experimental Data at Station 20 . . . . .	119
7.3.3 Boundary-layer Analysis . . . . .	127
7.3.4 Summary of Results at Station 20 . . . . .	131
7.4 Evaluation of Results at Station 40 . . . . .	133
7.4.1 Symmetry Boundary Condition Evaluation . . . . .	134
7.4.2 Comparison of Experimental Results to Computational Results at Station 40 . . . . .	136
7.4.3 Summary of Results at Station 40 . . . . .	143
7.5 Flowfield Investigation . . . . .	144
7.5.1 Identification of Relevant Flow Features . . . . .	146



	Page
7.5.2 Streamwise Description . . . . .	153
7.5.3 Further Descriptions with the $x - z$ Plane . . . . .	168
7.5.4 Surface Temperature and Friction . . . . .	171
7.5.5 Summary of Flowfield Investigation and Conclusions . . . . .	173
Chapter 8. CONCLUSIONS AND RECOMMENDATIONS . . . . .	176
8.1 Conclusions and Contributions . . . . .	176
8.2 Recommendations For Further Research . . . . .	181
Bibliography . . . . .	184
Appendix A. TIME-AVERAGED NAVIER-STOKES EQUATIONS AND THE FAVRÉ-AVERAGED REYNOLDS-STRESS EQUATION . . . . .	351
A.1 Navier-Stokes Equations . . . . .	351
A.2 Reynolds Averaged Navier-Stokes Equations . . . . .	352
A.2.1 Reynolds Averaged Navier-Stokes Equation Summary . . . . .	354
A.3 Favré Averaged Navier-Stokes Equations . . . . .	355
A.3.1 Favré Averaged Navier-Stokes Equation Summary . . . . .	360
A.4 Favré-Averaged Reynolds-Stress Equation . . . . .	361
Appendix B. SUMMARY OF REYNOLDS STRESS TURBULENCE MODEL CLOSURES . . . . .	365
B.1 Navier-Stokes Equations in a Second-Order Model . . . . .	365
B.2 Second-Order Models . . . . .	365
B.2.1 Launder, Reece, and Rodi Closure Summary . . . . .	366

	Page
B.2.2 Shima Closure Summary .....	368
B.2.3 Lai and So Closure Summary .....	370
B.2.4 Lai, So, Zhang, and Speziale Closure Summary .....	372
B.2.5 Zhang, So, Gatski, and Speziale Closure Summary .....	374
Appendix C. METRIC DEVELOPMENT .....	377
Appendix D. DIAGONALIZATION MATRICES .....	382
Appendix E. BOUNDARY CONDITIONS .....	385
E.1 Inflow Boundary Conditions .....	385
E.2 Wall, Tangency, Symmetry and Extrapolation Boundary Conditions .....	385
E.3 Jet Boundary Conditions .....	386
E.3.1 Two-Dimensional Jet .....	387
E.3.2 Three-Dimensional Jet .....	389
Appendix F. CONVERGENCE CRITERIA .....	394
F.1 Temporal Convergence Criteria .....	394
F.2 Spatial Convergence Studies .....	395
F.2.1 Aso et al./Spaid and Zukoski Configuration .....	395
F.2.2 Tucker Configuration .....	396
F.2.3 McCann and Bowersox Configuration .....	397
F.2.3.1 Two-Dimensional Grid .....	398
F.2.3.2 Three-Dimensional Grid .....	399

	Page
F2.3.3 Half-Plane Grid . . . . .	400
F2.3.4 Full-Plane Grid . . . . .	401
Appendix G. HIGHER PRESSURE RATIO SIMULATION RESULTS . . . . .	423
Appendix H. RUN TIME SUMMARY . . . . .	429
Vita . . . . .	433

## List of Figures

	Page
Figure 1. Schematic of a flowfield generated by normal injection of a sonic fluid through a two-dimensional slot into a supersonic flow . . . . .	191
Figure 2. Schematic of a three-dimensional flowfield generated by normal injection of a sonic fluid through a circular nozzle into a supersonic flow [70] . . . . .	191
Figure 3. McCann and Bowersox windtunnel configuration [52] . . . . .	192
Figure 4. Full-plane grid location with respect to test section . . . . .	193
Figure 5. Half-plane grid location with respect to test section . . . . .	193
Figure 6. Transformation from Physical Space to Computational Space [37] . . . . .	194
Figure 7. Schematic of slot injection flowfield . . . . .	195
Figure 8. Schematic of surface static pressure regions . . . . .	196
Figure 9. Spaid and Zukoski experimental configuration [88] . . . . .	197
Figure 10. Aso et al. experimental configuration [6] . . . . .	198
Figure 11. Comparison of surface pressure profiles for Aso et al. configuration for a static pressure ratio of 4.86 . . . . .	199
Figure 12. Comparison of surface pressure profiles for Aso et al. configuration for a static pressure ratio of 10.29 . . . . .	200
Figure 13. Comparison of surface pressure profiles for Aso et al. configuration for a static pressure ratio of 17.72 . . . . .	201
Figure 14. Comparison of surface pressure profiles for Aso et al. configuration for a static pressure ratio of 25.15 . . . . .	202
Figure 15. Separation length and plume height as a function of static pressure ratio for the Aso et al. configuration . . . . .	203

	Page
Figure 16. Comparison of Mach disk generated at two different pressure ratios and definition of Mach disk height (Aso et al. configuration) . . . . .	204
Figure 17. Comparison of surface pressure profiles for Spaid and Zukoski configuration for a static pressure ratio of 8.743 . . . . .	205
Figure 18. Comparison of surface pressure profiles for Spaid and Zukoski configuration for a static pressure ratio of 17.117 . . . . .	206
Figure 19. Comparison of surface pressure profiles for Spaid and Zukoski configuration for a static pressure ratio of 42.79 . . . . .	207
Figure 20. Comparison of surface pressure profiles for Spaid and Zukoski configuration for a static pressure ratio of 63.5 . . . . .	208
Figure 21. Separation length and plume height as a function of static pressure ratio for the Spaid and Zukoski configuration . . . . .	209
Figure 22. Separation length as a function of plume height for the Aso et al. and Spaid and Zukoski configurations . . . . .	210
Figure 23. Location of cross sectional data samples relative to particle paths for Spaid and Zukoski configuration . . . . .	211
Figure 24. Comparison of $\tau_{xy}$ profiles at $x/l = 0.9000$ for Spaid and Zukoski configuration . . . . .	212
Figure 25. Comparison of $\tau_{xx}$ profiles at $x/l = 0.9000$ for Spaid and Zukoski configuration . . . . .	213
Figure 26. Comparison of $\tau_{yy}$ profiles at $x/l = 0.9000$ for Spaid and Zukoski configuration . . . . .	214
Figure 27. Comparison of $\tau_{xy}$ profiles at $x/l = 0.9700$ for Spaid and Zukoski configuration . . . . .	215
Figure 28. Comparison of $\tau_{xx}$ profiles at $x/l = 0.9700$ for Spaid and Zukoski configuration . . . . .	216
Figure 29. Comparison of $\tau_{yy}$ profiles at $x/l = 0.9700$ for Spaid and Zukoski configuration . . . . .	217

	Page
Figure 30. Comparison of $\tau_{xy}$ profiles at $x/l = 0.9950$ for Spaid and Zukoski configuration . . . . .	218
Figure 31. Comparison of $\tau_{xx}$ profiles at $x/l = 0.9950$ for Spaid and Zukoski configuration . . . . .	219
Figure 32. Comparison of $\tau_{yy}$ profiles at $x/l = 0.9950$ for Spaid and Zukoski configuration . . . . .	220
Figure 33. Comparison of $\tau_{xy}$ profiles at $x/l = 1.0125$ for Spaid and Zukoski configuration . . . . .	221
Figure 34. Comparison of $\tau_{xx}$ profiles at $x/l = 1.0125$ for Spaid and Zukoski configuration . . . . .	222
Figure 35. Comparison of $\tau_{yy}$ profiles at $x/l = 1.0125$ for Spaid and Zukoski configuration . . . . .	223
Figure 36. Contours for anisotropic wall function, $f_{w_1}$ , used in the RSTM . . . . .	224
Figure 37. Comparison of $\tau_{xy}$ contours for Spaid and Zukoski configuration . . . . .	225
Figure 38. Range of near zero $\partial \tilde{u} / \partial y$ at the wall and grids spacing around the jet . . . . .	226
Figure 39. Comparison of $\tau_{yy}$ contours for Spaid and Zukoski configuration . . . . .	227
Figure 40. Comparison of $\tau_{xx}$ contour for Spaid and Zukoski configuration . . . . .	228
Figure 41. Comparison of $\omega_z$ contours for Spaid and Zukoski configuration . . . . .	229
Figure 42. Fraction of $E$ comprised by $K$ for Spaid and Zukoski configuration . . . . .	230
Figure 43. Tucker's injection model schematic [100] . . . . .	231
Figure 44. Schematic of slot coordinates used in numerical simulations . . . . .	232
Figure 45. Tucker's two-dimensional injector nozzle [100] . . . . .	233
Figure 46. Experimental flowfield sketch for supersonic injection [100] . . . . .	234

	Page
Figure 47. Computational flowfield predictions for supersonic injection . . . . .	235
Figure 48. Comparison of Mach contours for Tucker's [100] heated injection configuration . . . . .	236
Figure 49. Comparison of pressure contours for Tucker's [100] heated injection configuration . . . . .	237
Figure 50. Schlieren of injection flowfield for heated injection [100] . . . . .	238
Figure 51. Comparison of Mach contours for pressure ratios ( $p_{inj}/p_{\infty}$ ) of 5 and 10. . . . .	239
Figure 52. Comparison of $\tau_{xy}$ profiles for cooled injection at $x/l = 11.4$ . . . . .	240
Figure 53. Comparison of $\tau_{xy}$ profiles for heated injection at $x/l = 11.4$ . . . . .	241
Figure 54. Comparison of $\tau_{xy}$ contours for supersonic cooled injection . . . . .	242
Figure 55. Visualization of boundary layer separation and reattachment locations by comparison of $y^+$ contours for supersonic cooled injection . . . . .	243
Figure 56. Comparison of computational grids used for sonic and supersonic injection simulations . . . . .	244
Figure 57. Comparison of $\tau_{yy}$ contours for supersonic cooled injection . . . . .	245
Figure 58. Comparison of $\tau_{xx}$ contours for supersonic cooled injection . . . . .	246
Figure 59. Comparison of anisotropic wall damping function, $f_{w1}$ , with and without $y^+$ clipping . . . . .	247
Figure 60. Comparison of fraction of $E$ comprised by $K$ for supersonic cooled injection . . . . .	248
Figure 61. Schematic of a three-dimensional flowfield generated by normal injection of a sonic fluid through a circular nozzle into a supersonic flow [70] . . . . .	249
Figure 62. RSTM predictions of $\omega_x$ for McCann and Bowersox configuration . . . . .	249
Figure 63. Tunnel coordinate system . . . . .	250

	Page
Figure 64. Comparison of $y - z$ domains of the computational and experimental data grids .....	251
Figure 65. Experimental data for the $U$ component of velocity at station 20 [52] .....	252
Figure 66. Comparison of turbulence model predictions of the $U$ component of velocity at station 20 .....	253
Figure 67. Experimental data for the $V$ component of velocity at station 20 [52] .....	254
Figure 68. Comparison of turbulence model predictions of the $V$ component of velocity at station 20 .....	255
Figure 69. Experimental data for $\tau_{xy}$ at station 20 [52] .....	256
Figure 70. Comparison of turbulence model predictions of $\tau_{xy}$ at station 20 .....	257
Figure 71. Comparison of turbulence model predictions for Mach number at station 20 .....	258
Figure 72. Comparison of predictions of $\tau_{xy}$ with Mach number overlay at station 20 .....	259
Figure 73. Experimental data for $K$ at station 20 [52] .....	260
Figure 74. Comparison of turbulence model predictions of $K$ at station 20 .....	261
Figure 75. Comparison of turbulence model predictions of $K$ at station 20 (rescaled) .....	262
Figure 76. Comparison of turbulence model predictions of $\tau_{xx}$ at station 20 .....	263
Figure 77. Comparison of turbulence model predictions of $\tau_{yy}$ at station 20 .....	264
Figure 78. Comparison of turbulence model predictions of $\tau_{zz}$ at station 20 .....	265
Figure 79. Homogenization effects on axial Reynolds stresses at station 20 .....	266
Figure 80. Comparison of turbulence model predictions of $\omega_x$ at station 20 .....	267
Figure 81. Comparison of turbulence model predictions of the $W$ component of	



	Page
velocity at station 20 . . . . .	268
Figure 82. Comparison of turbulence model predictions of temperature at station 20 . . . . .	269
Figure 83. Comparison of turbulence model predictions for fraction of $E$ comprised by $K$ at station 20 . . . . .	270
Figure 84. Comparison of turbulence model predictions of $\tau_{xz}$ at station 20 . . . . .	271
Figure 85. Comparison of turbulence model predictions of $\tau_{yz}$ at station 20 . . . . .	272
Figure 86. Comparison of turbulence model predictions of $\omega_y$ at station 20 . . . . .	273
Figure 87. Comparison of turbulence model predictions of $\omega_z$ at station 20 . . . . .	274
Figure 88. Comparison of turbulence model predictions of $K$ in the boundary layer at station 20 . . . . .	275
Figure 89. Comparison of turbulence model predictions of $\tau_{xx}$ in the boundary layer at station 20 . . . . .	276
Figure 90. Comparison of turbulence model predictions of $\tau_{yy}$ in the boundary layer at station 20 . . . . .	277
Figure 91. Comparison of turbulence model predictions of $\tau_{zz}$ in the boundary layer at station 20 . . . . .	278
Figure 92. Comparison of turbulence model predictions of streamwise vorticity in the boundary layer at station 20 . . . . .	279
Figure 93. Homogenization of the axial Reynolds stresses in the boundary-layer . . . . .	280
Figure 94. Comparison of turbulence model predictions of $K/E$ in the boundary layer at station 20 . . . . .	281
Figure 95. Comparison of turbulence model predictions of mean flow temperature in the boundary layer at station 20 . . . . .	282
Figure 96. Comparison of turbulence model predictions of $\tau_{xy}$ in the boundary layer at station 20 . . . . .	283

	Page
Figure 97. Comparison of turbulence model predictions of $\tau_{xz}$ in the boundary layer at station 20 . . . . .	284
Figure 98. Comparison of turbulence model predictions of $\tau_{yz}$ in the boundary layer at station 20 . . . . .	285
Figure 99. Magnitude of anisotropic wall damping function $f_{w1}$ in the boundary layer . . . . .	286
Figure 100. Comparison of turbulence model predictions of $U$ component of velocity in the boundary layer at station 20 . . . . .	287
Figure 101. Comparison of turbulence model predictions of $V$ component of velocity in the boundary layer at station 20 . . . . .	288
Figure 102. Comparison of turbulence model predictions of $W$ component of velocity in the boundary layer at station 20 . . . . .	289
Figure 103. Comparison of cross-plane grid spacing . . . . .	290
Figure 104. Symmetry boundary condition evaluation for the $V$ component of velocity . . . . .	291
Figure 105. Symmetry boundary condition evaluation for the $W$ component of velocity . . . . .	292
Figure 106. Symmetry boundary condition evaluation for the $U$ component of velocity . . . . .	293
Figure 107. Symmetry boundary condition evaluation for $\omega_x$ . . . . .	294
Figure 108. Symmetry boundary condition evaluation for $K$ . . . . .	295
Figure 109. Symmetry boundary condition evaluation for $\tau_{xy}$ . . . . .	296
Figure 110. Symmetry boundary condition evaluation for $\tau_{xz}$ . . . . .	297
Figure 111. Comparison of experimental data and computational results of Mach number at station 40 . . . . .	298
Figure 112. Comparison of experimental data and computational results of the $U$	

	Page
component of velocity at station 40 . . . . .	299
Figure 113. Comparison of experimental data and computational results of the $V$ component of velocity at station 40 . . . . .	300
Figure 114. Comparison of experimental data and computational results of the $W$ component of velocity at station 40 . . . . .	301
Figure 115. Comparison of experimental data and computational results for $\omega_x$ at station 40 . . . . .	302
Figure 116. Comparison of experimental data and computational results for $K$ at station 40 . . . . .	303
Figure 117. Comparison of experimental data and computational results for $\tau_{xy}$ at station 40 . . . . .	304
Figure 118. Comparison of experimental data and computational results for $\tau_{xz}$ at station 40 . . . . .	305
Figure 119. Mach contours at test section centerline . . . . .	306
Figure 120. Near field numerical oil smear . . . . .	307
Figure 121. Far field numerical oil smear . . . . .	308
Figure 122. $\omega_x$ contours at test section surface . . . . .	309
Figure 123. Expansion and shock structure in $x - y$ plane ( $z/d = 0.0$ ) . . . . .	310
Figure 124. Expansion and shock structure in $y - z$ plane ( $x/d = 2.00$ ) . . . . .	311
Figure 125. Expansion and shock structure in $x - z$ plane ( $y/d = 0.91$ ) . . . . .	312
Figure 126. Expansion and shock structure in $x - z$ plane ( $y/d = 1.45$ ) . . . . .	313
Figure 127. Mach and $\omega_x$ contours at $x/d = -1.50$ . . . . .	314
Figure 128. Mach and $\omega_x$ contours at $x/d = -1.25$ . . . . .	315

	Page
Figure 129. Mach and $\omega_x$ contours at $x/d = -1.00$ . . . . .	316
Figure 130. Mach and $\omega_x$ contours at $x/d = -0.50$ . . . . .	317
Figure 131. Mach and $\omega_x$ contours at $x/d = -0.25$ . . . . .	318
Figure 132. Mach and $\omega_x$ contours at $x/d = 0.50$ . . . . .	319
Figure 133. Mach and $\omega_x$ contours at $x/d = 1.00$ . . . . .	320
Figure 134. Mach and $\omega_x$ contours at $x/d = 1.25$ . . . . .	321
Figure 135. Mach and $\omega_x$ contours at $x/d = 1.50$ . . . . .	322
Figure 136. Mach and $\omega_x$ contours at $x/d = 2.00$ . . . . .	323
Figure 137. JI vortex sustainment mechanism at $x/d = 2.00$ . . . . .	324
Figure 138. Mach and $\omega_x$ contours at $x/d = 3.00$ . . . . .	325
Figure 139. JI vortex sustainment mechanism at $x/d = 3.00$ . . . . .	326
Figure 140. Mach and $\omega_x$ contours at $x/d = 4.00$ . . . . .	327
Figure 141. Mach and $\omega_x$ contours at $x/d = 4.50$ . . . . .	328
Figure 142. Mach and $\omega_x$ contours at $x/d = 5.00$ . . . . .	329
Figure 143. Enlarged view of $\omega_x$ contours at $x/d = 5.00$ . . . . .	330
Figure 144. Mach and $\omega_x$ contours at $x/d = 6.00$ . . . . .	331
Figure 145. Mach and $\omega_x$ contours at $x/d = 7.00$ . . . . .	332
Figure 146. RSI vortex . . . . .	333
Figure 147. Plume boundary definition at $x/d = 6.00$ . . . . .	334
Figure 148. Plume boundary definition at $x/d = 6.50$ . . . . .	334

	Page
Figure 149. Plume boundary definition at $x/d = 7.00$ . . . . .	335
Figure 150. Plume boundary definition at $x/d = 7.50$ . . . . .	335
Figure 151. Plume boundary definition at $x/d = 8.00$ . . . . .	336
Figure 152. Mach and $\omega_x$ contours at $x/d = 8.00$ . . . . .	337
Figure 153. Mach and $\omega_x$ contours at $x/d = 9.50$ . . . . .	338
Figure 154. Mach and $\omega_x$ contours at $x/d = 10.50$ . . . . .	339
Figure 155. Mach and $\omega_x$ contours at $x/d = 12.50$ . . . . .	340
Figure 156. Mach and $\omega_x$ contours at $x/d = 14.50$ . . . . .	341
Figure 157. Mach and $\omega_x$ contours at $x/d = 16.50$ . . . . .	342
Figure 158. Mach and $\omega_x$ contours at $x/d = 20.00$ . . . . .	343
Figure 159. Mach and $\omega_x$ contours at $y/d = 0.022$ . . . . .	344
Figure 160. Mach and $\omega_x$ contours at $y/d = 0.100$ . . . . .	345
Figure 161. $\omega_x$ contours at $y/d = 0.910$ . . . . .	346
Figure 162. $\omega_x$ contours at $y/d = 1.49$ . . . . .	347
Figure 163. Surface temperature contours: $K - \epsilon$ model . . . . .	348
Figure 164. Surface temperature contours: RSTM . . . . .	348
Figure 165. $c_f$ contours: $K - \epsilon$ model . . . . .	349
Figure 166. $c_f$ contours: RSTM . . . . .	349
Figure 167. Upwash amplification device . . . . .	350
Figure 168. Transformation from Physical Space to Computational Space . . . . .	381

	Page
Figure 169. Typical computational box .....	393
Figure 170. Three-dimensional conic jet boundary condition .....	393
Figure 171. Residual results for Aso et al. configuration ( $p_{inj}/p_{\infty} = 10.29$ ) .....	403
Figure 172. Surface static pressure ratio results for various iteration levels (Aso et al. configuration with $p_{inj}/p_{\infty} = 10.29$ ) .....	403
Figure 173. Sonic injection configuration normal direction grid refinement results .....	404
Figure 174. Sonic injection configuration streamwise direction grid refinement results .....	404
Figure 175. Two-dimensional computational grid used for Aso et al. and Spaid and Zukoski configurations .....	405
Figure 176. Supersonic injection configuration normal direction grid refinement results .....	406
Figure 177. Supersonic injection configuration streamwise direction grid refinement results .....	406
Figure 178. Tucker configuration computational grid .....	407
Figure 179. Two-dimensional mesh study results for $\rho$ .....	408
Figure 180. Two-dimensional mesh study results for the $U$ component of velocity .....	409
Figure 181. Two-dimensional mesh study results for the $V$ component of velocity .....	410
Figure 182. Two-dimensional mesh study results for $p$ .....	411
Figure 183. Two-dimensional mesh study results for $T$ .....	412
Figure 184. Two-dimensional mesh study results for $K$ .....	413
Figure 185. Three-dimensional mesh study results for $\rho$ at $x/d = 8.0$ .....	414
Figure 186. Three-dimensional mesh study results for the $U$ component of	

	Page
velocity at $x/d = 8.0$ .....	415
Figure 187. Three-dimensional mesh study results for the $V$ component of velocity at $x/d = 8.0$ .....	416
Figure 188. Three-dimensional mesh study results for the $W$ component of velocity at $x/d = 8.0$ .....	417
Figure 189. Three-dimensional mesh study results for $p$ at $x/d = 8.0$ .....	418
Figure 190. Three-dimensional mesh study results for $T$ at $x/d = 8.0$ .....	419
Figure 191. Three-dimensional mesh study results for $K$ at $x/d = 8.0$ .....	420
Figure 192. Half-plane grid (339 x 121 x 61) .....	421
Figure 193. Full-plane grid (275 x 105 x 101) .....	422
Figure 194. Comparison of $\rho$ at higher pressure ratio ( $x/d = 10.0$ ) .....	424
Figure 195. Comparison of the $U$ component of velocity at higher pressure ratio ( $x/d = 10.0$ ) .....	424
Figure 196. Comparison of the $V$ component of velocity at higher pressure ratio ( $x/d = 10.0$ ) .....	425
Figure 197. Comparison of the $W$ component of velocity at higher pressure ratio ( $x/d = 10.0$ ) .....	425
Figure 198. Comparison of $T$ at higher pressure ratio ( $x/d = 10.0$ ) .....	426
Figure 199. Comparison of $K$ at higher pressure ratio ( $x/d = 10.0$ ) .....	426
Figure 200. Comparison of $\tau_{xy}$ at higher pressure ratio ( $x/d = 10.0$ ) .....	427
Figure 201. Comparison of $\tau_{xz}$ at higher pressure ratio ( $x/d = 10.0$ ) .....	427
Figure 202. Comparison of $\tau_{yz}$ at higher pressure ratio ( $x/d = 10.0$ ) .....	428
Figure 203. Comparison of $\omega_x$ at higher pressure ratio ( $x/d = 10.0$ ) .....	428

## List of Tables

	Page
Table 1. Two-dimensional sonic injection boundary conditions . . . . .	72
Table 2. Two-dimensional sonic injection mean flow parameters . . . . .	73
Table 3. Slope of $x_{sep}/h$ linear fit . . . . .	78
Table 4. Two-dimensional supersonic injection boundary conditions . . . . .	91
Table 5. Two-dimensional supersonic injection freestream mean flow conditions [100] . . . . .	91
Table 6. Two-dimensional supersonic injector mean flow conditions [100] . . . . .	91
Table 7. Freestream mean flow conditions for McCann and Bowersox configuration [52] . . . . .	108
Table 8. Injector mean flow conditions for McCann and Bowersox configuration [52] . . . . .	109
Table 9. Uncertainty analysis results [52] . . . . .	109
Table 10. Three-dimensional supersonic oblique injection boundary conditions for the full-plane grid . . . . .	111
Table 11. Three-dimensional supersonic oblique injection boundary conditions for the half-plane grid . . . . .	111
Table 12. Half-plane grid mesh spacing . . . . .	400
Table 13. Full-plane grid mesh spacing . . . . .	402
Table 14. System performance data . . . . .	429
Table 15. Aso et al. run time data . . . . .	430
Table 16. Aso et al. CFL data . . . . .	431



	Page
Table 17. Spaid and Zukoski run time data . . . . .	431
Table 18. Spaid and Zukoski CFL data . . . . .	431
Table 19. Tucker run time data . . . . .	432
Table 20. Tucker CFL data . . . . .	432
Table 21. McCann and Bowersox run time data . . . . .	432
Table 22. McCann and Bowersox CFL data and memory requirements . . . . .	432

## List of Symbols

### English Symbols

Symbol	Definition
$A$	Flux Jacobian
$A_v$	Viscous flux Jacobian
$a$	Speed of sound
$B$	Flux Jacobian
$B_v$	Viscous flux Jacobian
$C$	Generic constant of proportionality
$C$	Flux Jacobian
$C_v$	Viscous flux Jacobian
$C_\mu, C_{\omega_1}, C_{\omega_2}$	Turbulence model closure coefficients
$C_\epsilon, C_{\epsilon_1}, C_{\epsilon_2}$	Turbulence model closure coefficients
$C_1, C_2, C_s$	Turbulence model closure coefficients
$C_v$	Specific heat at constant volume
$D$	Source vector flux Jacobian
$D^t$	Turbulent diffusion
$D_\epsilon, D_\omega$	Dissipation destruction
$D_{\epsilon_s}$	Solenoidal dissipation destruction
$D_\epsilon^t, D_\omega^t$	Dissipation diffusion
$D_{\epsilon_s}^t$	Diffusion of solenoidal dissipation
$D_{ij}^t$	Turbulent diffusion
$D_{ij}^v$	Viscous diffusion
$d$	Diameter

$E$	Non-dimensional specific total energy
$e$	Specific internal energy
$\mathbf{f}$	Inviscid flux vector in the $x$ coordinate direction
$\mathbf{f}_v$	Viscous flux vector in the $x$ coordinate direction
$f_1, f_2, f_\mu$	Turbulence model closure coefficients
$\mathbf{g}$	Inviscid flux vector in the $y$ coordinate direction
$\mathbf{g}_v$	Viscous flux vector in the $y$ coordinate direction
$H$	Specific total enthalpy
$h$	Specific internal enthalpy; inviscid flux vector in the $y$ coordinate direction; injectant penetration height
$\mathbf{h}_v$	Viscous flux vector in the $z$ coordinate direction
$J$	Jacobian of transformation
$\hat{i}, \hat{j}, \hat{k}$	Unit vectors in the $x, y$ , and $z$ directions
$K$	Turbulence kinetic energy
$\mathbf{M}$	Mach number
$M_{ij}$	Mass flux variation
$M_t$	Turbulent Mach number
$n$	Turbulence model closure coefficient; iteration time level
$\vec{n}$	Unit normal vector
$p_b$	Back pressure
$p_{eff}$	Effective back pressure
$p_{ex}$	Exhaust pressure
$P_\epsilon, P_\omega$	Dissipation production
$P_{\epsilon_s}$	Production of solenoidal dissipation

$P_{ij}$	Turbulent production
$Pr$	Prandtl number
$Pr_t$	Turbulent Prandtl number
$P$	non-dimensional pressure
<b>Q</b>	Vector of conserved quantities
<b>R</b>	Residual vector
$q_i$	Heat transfer rate per unit area in index notation
$q_i^t$	Turbulence heat transfer rate per unit area in index notation
$Re_t$	Turbulent Reynolds number
<b>S</b>	Source term vector
$\vec{S}^\epsilon, \vec{S}^\eta, \vec{S}^\zeta$	Surface area vectors
$S_{ij}$	Strain-rate tensor component
$T$	Non-dimensional temperature
$T_i$	Similarity transformation matrix
$T_i^{-1}$	Inverse similarity transformation matrix
$t$	time
$U, V, W$	Non-dimensional velocities
$\tilde{U}, \tilde{V}, \tilde{W}$	Contravariant velocities
$u_i$	Velocity in index notation
$u_\tau$	Friction velocity
$x, y, z$	Rectangular Cartesian coordinates
$x_i$	Position vector in tensor notation
$y^+$	Dimensionless, sublayer-scaled distance

## Greek Symbols

Symbol	Definition
$\alpha, \alpha_1, \alpha_2$	Turbulence model closure coefficients
$\delta$	Boundary-layer thickness
$\delta_{ij}$	Kronecker delta
$\delta_i$	Difference operator
$\epsilon$	Turbulence dissipation rate per unit mass
$\epsilon_c$	Compressible part of the turbulence dissipation rate per unit mass
$\epsilon_s$	Solenoidal part of the turbulence dissipation rate per unit mass
$\gamma$	Ratio of specific heats
$\kappa$	Thermal conductivity coefficient
$\Lambda_i$	Eigenvalues of the inviscid flux Jacobians
$\lambda$	Second bulk viscosity coefficient
$\mu$	First bulk viscosity coefficient, molecular viscosity
$\mu_t$	Turbulent eddy viscosity
$\nu$	Kinematic viscosity
$\nu_t$	Turbulent kinematic eddy viscosity
$\xi, \eta, \zeta$	Dimensionless coordinates
$\xi_i, \eta_i, \zeta_i$	Transformation metrics
$\rho$	Density
$\Pi_{ij}$	Pressure-velocity-gradient correlation
$\sigma_{ij}$	Stress tensor component
$\sigma_\epsilon, \sigma_\kappa, \sigma_\rho, \sigma_\omega$	Turbulence model closure coefficients

$\tau$	Turbulent time scale; dummy variable of integration
$\tau_{ij}$	Favre-averaged Reynolds stress tensor component
$\tau_w$	Shear stress at the wall
$\omega$	Turbulence specific dissipation rate

### Subscripts

Symbol	Definition
$i, j, k$	Tensor indices
$jet$	Property of the injectant
$t$	Stagnation value
$v$	Viscous quantity
$wall$	Magnitude of a quantity at the viscous wall
$\infty$	Freestream or undisturbed value

### Superscripts

Symbol	Definition
$t$	Turbulent value
$(\tilde{*})$	Mean value of Favre-averaged variable
$(*'' )$	Fluctuating value of Favre-averaged variable
$(\overline{*})$	Mean value of Reynolds-averaged variable, time average of any variable or group of variables
$(*')$	Fluctuating value of Reynolds-averaged variable
$(\hat{*})$	Denotes unit vector, direction cosine or division by $J$
$(\check{*})$	Denotes Roe-averaged variable

## Abbreviations

Abbreviation	Definition
AFIT	Air Force Institute of Technology
DPP	Downwash Pivot Point
JI	Jet Induced
LE OB	Leading Edge Oblique Shock
MTE OB	Mirrored Trailing Edge Oblique Shock
NMG	Negative Mach Gradient
OB	Oblique Shock
PDV	Primary Downstream Vortex
PMG	Positive Mach Gradient
PUV	Primary Upstream Vortex
RSI	Recompression Shock Induced
SDV	Secondary Downstream Vortex
SUV	Secondary Upstream Vortex
TE OB	Trailing Edge Oblique Shock
TJISF	Transverse Jet Injection into Supersonic Flow
TUV	Tertiary Upstream Vortex
UPP	Upwash Pivot Point
UR	Upwash Recompression
US	Upwash Slip

The full, three-dimensional Favré-averaged Navier Stokes equations, coupled with the second-order Zhang, So, Gatski and Speziale (ZSGS) Reynolds stress turbulence model (RSTM) and the ZSGS  $K - \epsilon$  model were used to numerically simulate injection into supersonic flow. The solution was computed with an implicit second-order accurate algorithm based on a diagonalized, Beam and Warming approximate factorization scheme with second-order Roe flux differencing.

A multi-phase study evaluated the validity of the turbulence models and the algorithm for normal injection of air with two-dimensional slot nozzles and oblique injection at a  $25^\circ$  angle with a three-dimensional elliptic nozzle into the primary flow. Numerical results were compared to experimental data and the turbulence models were evaluated qualitatively and quantitatively for accurate prediction of thermo-mechanical mean flow variables, Reynolds stresses, flowfield shock structure and boundary-layer phenomena.

Comparison of the RSTM simulation results to experimental data for two- and three-dimensional configurations revealed physically consistent and accurate predictions for the mean flow and turbulent quantities. Simulations with the  $K - \epsilon$  model for the same configurations resulted in non-physical and inconsistent turbulence predictions which make the  $K - \epsilon$  formulation inappropriate for detailed numerical simulations of this flowfield when physically correct turbulent quantities are needed from the simulation.

Simulations of the three-dimensional flowfield with the RSTM showed that the vortical motion in the jet plume was caused by the recompression shock induced (RSI) vortices. These vortices were generated through the combined effects of the inflow air upwash behind the plume and the mirrored trailing-edge oblique-barrel (MTE OB) shock, which was mirrored across a reflection point downstream of the plume. Furthermore, it was shown that lateral expansion of the plume was impeded by the upwash recompression (UR) shock and the inflow air sidewash. The combined



effects of the UR shock, the inflow sidewash and the boundary of the jet plume acted to sustain the jet induced (JI) vortices. The JI vortices were initially formed at the sides of the nozzle orifice and extended back along the sides of the jet plume. The mechanisms sustaining the JI vortices retarded plume expansion by directing inflow sidewash back towards the center of the test section and into the plume. The mechanisms which generated the RSI vortices accelerated plume expansion by creating an outflow sidewash forcing the injectant to move out and away from the center of the test section. It was seen that once the MTE OB shock and the UR shock intersected, the mechanisms sustaining the JI vortices were disrupted and lateral expansion of the plume accelerated.

It was also observed that the skin friction predictions from the two models were nearly identical for the entire flowfield.

# ***ANALYSIS OF TURBULENCE MODELS AS APPLIED TO TWO- AND THREE-DIMENSIONAL INJECTION FLOWS***

## **Chapter 1 - Introduction**

### **1.1 Background**

Resurgent interest in supersonic/hypersonic vehicles and highly maneuverable aircraft employing thrust vector control has prompted a flurry of experimental and numerical investigations attempting to describe the flowfield generated by transverse jet injection into supersonic flow (TJISF) [5, 6, 20, 50, 52, 70, 88, 112]. Comprehensive descriptions and accurate predictions of the shock structure generated by this flowfield are critical to the design of SCRAMjet combustors [60], film cooled turbine fans [49], rocket motor thrust vector regulation systems [65] and high speed flight vehicle reaction control jets [65]. However, incomplete data describing the physics of the flowfield and the accompanying turbulent stresses generated by TJISF continues to hinder advances in many areas of the aerospace industry.

The driving thrust of research into TJISF is enhanced mixing of fuel and air in SCRAMjet combustors. Mixing efficiency is critical because the time available to mix the fuel and inflow air, combust the mixture and exhaust the products in SCRAMjets is on the order of milliseconds [20,50]. Mixing efficiency, hence, thrust efficiency, is dependent on the injection angle, fuel-to-air pressure ratio, total pressure and shock losses, fuel penetration depth and many other variables too numerous to list [60].

Injection angle is critical to fuel penetration depth. Tangential injection is one of two extremes for the injection angle. When tangential injection is used, penetration is nonexistent and if the fuel-to-air pressure ratio is unity, mixing is slow. However, tangential injection has the advantage of

lower airstream total pressure losses and all of the momentum gained from fuel injection contributes to thrust production. Normal injection is at the other extreme for injection angle and this angle maximizes fuel penetration, however, the large total pressure losses and the minimal momentum contribution of the injected fuel are counter productive to the advantages gained from the rapid initial mixing [50].

An optimized oblique injection configuration has the potential of deep injectant penetration and a significant momentum contribution to the streamwise wise. The potential advantages of oblique injection has lead to many studies trying to characterize this injection concept [50,51].

Underexpanding the injectant also promotes rapid initial mixing by quickly increasing the frontal area of the plume thus, providing a larger area for fuel and air interaction. However, excessive underexpansion of the fuel causes shocks to form within the plume and reduces total pressure.

Figures 1 and 2 illustrate typical two- and three-dimensional TJISF generated by normal injection of an underexpanded fluid. The two-dimensional flowfield illustrated in Figure 1 is generated by sonic injection through a two-dimensional slot normal to the supersonic freestream. In the two-dimensional flowfield, the underexpanded gas penetrates the turbulent boundary layer and sets up a system of shock and recirculation regions fore and aft of the slot. The flowfield obstruction of the injectant plume induces a bow shock and boundary-layer separation results from the subsequent adverse pressure gradient upstream of the slot. Between the separation point and the slot, a recirculation region forms consisting of counter-rotating primary and secondary upstream vortices (PUV and SUV respectively). A separation shock also forms as a result of the boundary-layer displacement caused by the vortices in the upstream recirculation region and a sonic surface resembling a compression ramp forms between the recirculating region and the separation shock.

Upon exiting the nozzle, expansion waves from the expanding injectant, reflect off of the boundary between the jet plume and the inflow air as compression waves. The reflected

compression waves form a barrel shock at the boundary of the plume and the inflow air. At the point where the reflected compression waves converge inside the plume, a Mach disk is formed.

Downstream of the jet, the flow is turned parallel to the surface, producing a recompression shock and a corresponding separated, recirculation region behind the nozzle. This region consists of counter-rotating primary and secondary downstream vortices (PDV and SDV respectively). These structures collectively act as an expansion ramp over which downstream turning of the fluid occurs.

The three-dimensional flowfield illustrated in Figure 2 is generated by underexpanded injection through a circular nozzle normal to the supersonic freestream. As discussed by Santiago and Dutton [70], this figure depicts the supersonic freestream flowfield with injection through the bottom of the wall. The obstruction caused by the jet generates a bow shock in the freestream (not shown). After leaving the orifice, the jet expands through a Prandtl-Meyer fan and then recompresses through the barrel shock which ends in a Mach disk. Beyond the Mach disk, the jet plume is quickly turned downstream and from the outset of the injection, a pair of counter-rotating crossflow vortices are shown in the jet plume. This vortical or rotational *secondary flow* is the primary source of injectant entrainment into the surrounding inflow and according to Santiago and Dutton [70], these structures dominate the jet's downstream velocity field [116]. Other vortical structures present in the TJISF are the horseshoe vortex (a secondary flow), which wraps around the upstream side of the jet and trails downstream, shear layer vortices that form around the circumference of the jet (not shown), and wake vortices periodically shed near the base of the inner jet core [70].

## 1.2 Primary Research Issues

Now, more than ever before, the high cost associated with full-scale wind tunnel testing dictates that potential engine designs be dry tested prior to wind tunnel testing and test stand firing. One of the most effective cost cutting tools available for dry testing is computational fluid dynamics (CFD).

Unfortunately, the full potential of CFD is still far from being realized because of a lack of robust turbulence models capable of accurately describing the complex turbulent flowfield generated by TJISE.

Efforts to numerically simulate flowfields similar to those shown in Figures 1 and 2 have historically been confined to algebraic mixing-length models and eddy viscosity models [7, 23, 53, 67, 112]. While these simulations have provided the engineering community with gross estimates of the flowfield structure, the turbulence models employed are incapable of correctly modeling the secondary flow structures or the turbulent stresses found in injection flowfields [90, 109].

The overriding deficiency of mixing length models is the absence of a second turbulent microscale [109]. Mixing length models only account for the length microscale and completely ignores the turbulent velocity and time microscales. Therefore, they “will work well only for the flows for which they have been fine tuned . . . [and] . . . there is very little hope of extrapolating beyond the established data base for which an algebraic model is calibrated [109].”

Eddy viscosity models compensate for many of the deficiencies of the algebraic models by incorporating two additional transport equations which model two of the three turbulent microscales. However, these models are still limited to flowfields where the Boussinesq approximation is valid [109].

The Boussinesq approximation provides closure for the components of the Reynolds stress tensor,  $\tau_{ij}$ . This tensor, henceforth referred to as the Favré-averaged Reynolds stress tensor (FARST), is defined in component form as

$$\tau_{ij} \equiv \overline{w_i'' w_j''} \quad (1)$$

As described in Chapter 3, the double primed velocities represent the Favré-averaged fluctuating portion of the instantaneous velocities and the over bar represents time averaging. This tensor is an integral component of the Favré-averaged Navier-Stokes (FANS) equations and the turbulent

transport equations (see Chapters 3 and 4 for the forms of these equations).

The fundamental assumption of the Boussinesq approximation is “. . . that the principal axes of the [components of the] Reynolds stress tensor,  $\tau_{ij}$ , are coincident with those of the mean strain-rate tensor,  $S_{ij}$ , at all points in a turbulent flow, . . . [where] . . . the constant of proportionality between  $\tau_{ij}$  and  $S_{ij}$  is the eddy viscosity,  $\mu_t$  [109].” This approximation provides adequate results for a limited number of flow fields, but often provides poor turbulence predictions for many other flowfields, including three-dimensional flows, flows in ducts with secondary motions, and rotating flows [109].

Second-order Reynolds stress turbulent models (RSTM) can predict the secondary flow structures and the Reynolds stresses found in the aforementioned flowfields, but these models are much more complex than the eddy viscosity models. In addition to the five thermo-mechanical equations, RSTM's use six additional transport equations derived from the Reynolds stress equation (RSE) to describe the behavior of  $\tau_{ij}$  (a derivation of the RSE is presented in Appendix A). According to Wilcox [109], an RSTM corrects many of the Boussinesq approximation's shortcomings because an RSTM automatically accounts for the convection and diffusion of  $\tau_{ij}$  and the effects of flow history. These models also include convection and production terms that automatically respond to effects such as streamline curvature and system rotation [109]. Finally, the RSTM “ . . . gives no a priori reason for the normal stresses to be equal when the mean strain rate vanishes. Rather their values will depend upon initial conditions and other flow process, so that the model should behave properly for flows with sudden changes in strain rate [109].”

Despite the many apparent advantages of RSTMs, limited computational resources has confined numerical simulations with second-order RSTMs to very simple geometries with flowfields only slightly more complex than flow past a shallow compression ramp [59]. However, improved computational resources<sup>1</sup> (computational speed, memory, and archival resources) have

---

<sup>1</sup>Aeronautical Systems Command Major Shared Resource Center, Wright-Patterson AFB, OH.

made it possible to apply RSTMs to more complex flowfields. In light of the current resources available and the mathematical evidence that **second-order RSTMs can more accurately capture the secondary flow structures and the turbulent stresses found in three-dimensional rotating flowfields than lower order models**, two questions immediately present themselves:

1. *How accurate are RSTMs in the modeling of complex secondary flows associated with TJISF?*
2. *Are the differences provided by RSTM and  $K - \epsilon$  models different enough to warrant the added complexity needed to implement an RSTM?*

These questions and many others are addressed by the objectives stated in the next section.

### 1.3 Objectives

In light of the apparent superiority of the RSTM and the availability of improved computational resources, the primary objectives of this research are 1) numerical simulation of the three-dimensional flowfield generated by oblique injection into a supersonic inflow; 2) validation of a second-order RSTM for turbulence closure, and 3) investigation of the flowfield near the nozzle. Upon meeting these objectives, the following contributions to the current state-of-the-art for turbulence modeling and mixing enhancement are anticipated:

1. Physically correct simulation of the Reynolds stresses in secondary flowfields
2. Qualitative and quantitative comparison of a second-order RSTM and  $K - \epsilon$  model to experimental data for two-dimensional and three-dimensional flowfields resulting in a greater understanding of the strengths and weaknesses of these two classes of turbulence models
3. Examination the physical flowfield predicted by the RSTM resulting in greater understanding of the behavior of the Reynolds stresses, thermo-mechanical mean flow quantities and the vorticity in the region immediately surrounding the jet orifice

4. Visualization of the effects the secondary flow system in the boundary layer has on temperature and skin friction beyond current experimental capabilities
5. Enhanced description of the vortical mixing mechanism generated by oblique injection

## 1.4 Document overview

This document is divided into chapters, which are intended to provide a logical progression of the steps taken to achieve the stated objectives. In the chapter immediately following this one, the methodology used to meet the stated research objectives is outlined. Following the discussion of the methodology, the significance of the Favré-averaged form of the governing equations is presented in Chapter 3. Chapter 3 is followed by a detailed review of the theory behind eddy viscosity models and some of the limitations of the Boussinesq approximation. After presentation of the  $K - \epsilon$  model theory, a discussion of the second-order Reynolds stress turbulence model is provided. This discussion details the evolution of RSTMs beginning with the fundamental assumptions made by Rotta [69] and Kolmogorov [36] about the velocity-pressure-gradient correlation tensor and the dissipation-rate tensor, and progresses through the work of Launder, Reece, and Rodi's [40] up to the current RSTM model of Zhang, So, Gatski and Speziale (ZSGS) [113] used for this research. Chapter 5 presents a comprehensive description of the underlying theory upon which the algorithm ISAAC is based. The material presented in Chapter 5 discusses the discretization and solution of the governing equations, including linearization, diagonalization, and the Roe flux differencing method.

Presentation and discussion of the results is divided into two chapters. Chapter 6 contains the results of the two-dimensional analyses and is followed by the three-dimensional model validation and flowfield analysis in Chapter 7. The final chapter is a summary of the conclusions and contributions, and a discussion of recommended areas for continued research.



## **Chapter 2 - Methodology**

Prior to discussing how the objectives will be met, a review of some past experimental and computational research results as well as some relevant algorithm performance issues will be helpful in establishing some of the obstacles to accurate modeling of TJISF. Once a basis for the methodology is established, the individual steps that will be taken over the course of this research is presented.

### **2.1 Basis for Methodology**

This section begins with a review of some computational results from previous numerical simulations of TJISF using eddy viscosity models. Then, experimental results available for model validation are presented and evaluated. Next, a discussion of several algorithm performance issues that must be considered prior to defining an approach to the numerical simulation of three-dimensional turbulent flowfields is provided. Finally, some secondary research issues are addressed.

#### **2.1.1 Computational Data Base**

There have been many numerical simulations for two- and three-dimensional TJISF [7, 23, 53, 65, 110, 112]. However, the major thrust of these simulations was prediction of the mean flow properties and the species concentration [7, 110]. The modeling of Reynolds stresses and the assessment of turbulence model accuracy were only given cursory treatment in the majority of these simulations, most of which used the simple Baldwin-Lomax mixing length model for turbulence closure of the Navier-Stokes equations [7, 53, 110]. Attempts that more correctly account for the effects of the Reynolds stresses were made by Rizzetta [65] and Gerlinger, Algermissen, and Bruggenmann [23] for two-dimensional flows, and by McClure and Ervin [53] and Yokota and Kaji [112] for three-dimensional flows. Each of the aforementioned authors used an eddy viscosity model to simulate the effects of turbulence in their numerical simulations.

While each of these studies have points of merit, only the RSTM, which none of these studies

used, has the potential to accurately predict the Reynolds stresses and the secondary flow structures.

### **2.1.2 Experimental Data Base**

There is an abundance of experimental studies focusing on two- and three-dimensional TJISF. Some of the more recent of these studies include the works of Aso, Okuyama, Ando and Fujimori [5]; Aso, Okuyama, Kawai and Ando [6] and Aso, Tannou, Maekawa, Okuyama, Ando, Yamane and Fukuda [7]. Some less current, but still valuable studies are those of Schetz and Billig [76]; Schetz, Hawkins and Lehman [77] and Spaid and Zukoski [88]. Unfortunately, many of these studies only measured mean flow quantities and species distributions and do not include any turbulence data.

Of the reports listed here, only those by Spaid and Zukoski [88] and Aso, Okuyama, Kawai, and Ando [6] report mean flow data for a two-dimensional flowfield in a readable format with sufficient fidelity to allow turbulence model validation of the mean flow quantities. In their experiments, both Spaid and Zukoski [88] and Aso et al. [6] injected a sonic fluid normal to the inflow through a two-dimensional slot. Both of these reports provide data describing the shock structure and Mach contours of the flowfield at various jet-to-freestream pressure ratios and surface static-pressure data for the different pressure ratios along with the boundary-layer separation points.

Reports for the three-dimensional injection experiments by Mays, Thomas and Schetz [50] and Aso, Okuyama, Ando and Fujimori [5] also lack turbulence data. However, each of these experiments has added to the overall understanding of the mean flow characteristics of three-dimensional TJISF. Experiments conducted by Mays et al. [50] for oblique, sonic injection through a circular nozzle at injection angles of  $15^\circ$  and  $30^\circ$  found that bow shocks exist very close to the jet, indicating that reversed flow is limited to a small region or is altogether absent upstream of the jet [50]. This is in contrast to the substantial separation zones reported by Aso et al. [5] ahead of the jet for normal injection through a circular nozzle. Aso et al. also conducted three-dimensional normal injection experiments with sonic jet conditions at three different jet-to-freestream pressure

ratios using circular nozzles with diameters of  $3\text{mm}$  and  $5\text{mm}$ . Many of the flow structures found in the oil smears presented in their report are similar to those shown in Figure 2. Based on the oil smears, Aso et al. reported primary and secondary separation lines upstream of the nozzle. These structures imply that a horseshoe vortex is generated in front of the nozzle and extends downstream of the jet. Behind the nozzle, flow attachment lines between the horseshoe vortex and the centerline are observed. Aso et al. [5] also observed that as the pressure ratio is increased, the primary and secondary separation points move forward of the jet and the attachments lines behind the jet become wider.

The data presented in the aforementioned documents have identified many important flow structures arising from two-dimensional TJISF and many of the surface characteristics of three-dimensional TJISF. However, turbulence model development and validation depends on experimental data; if the data is poor, so is any model based on that data. According to Settles and Dodson [79, 80], experimental data suitable for compressible turbulence model development and validation should adhere to the following standards:

1. be for turbulent flows with a Mach number greater than or equal to Mach 3.0
2. have a geometry simple enough that it may be modeled by CFD methods
3. provide meaningful data at flowfield locations other than the surface
4. have well-defined experimental boundary conditions
5. have well-defined experimental error bounds
6. provide consistent results
7. provide machine readable data
8. provide adequate spatial resolution of data.

Unfortunately, when Settles and Dodson compiled their databases [79, 80], they did not find any experimental data for TJISF that satisfied their criteria. Thus, analysis of TJISF must use data published since Settles and Dodson's list was compiled or use data satisfying most, but not all the aforementioned criteria. The dearth of quality data has recently been remedied by two-dimensional experiments conducted by Tucker [100] and three-dimensional experiments conducted by McCann and Bowersox [52]. Tucker conducted experiments with a normally injected, supersonic TJISF for both heated and cooled injectants. Experimental values for the mean flow properties,  $\tau_{xy}$  and  $K$  were measured at a single station  $11.4\text{cm}$  ( $x/d = 72$ ,  $d = 0.15875\text{cm}$ ) downstream of the nozzle. Additional data available from Tucker's experiment are shadow graphs describing the flowfield shock structure, upstream boundary layer separation point, downstream boundary layer reattachment point, and jet penetration height.

McCann and Bowersox [52] specifically set out to conduct an experimental investigation of TJISF that satisfied all of criteria for inclusion in Settles and Dotson's database. The data collected during their experiment provides the clearest view to date of the three-dimensional oblique supersonic TJISF. Experimental values for the mean flow and turbulence data for  $\tau_{xy}$ ,  $\tau_{xz}$  and  $K$  were measured at two stations,  $7.72\text{cm}$  ( $x/d = 20$ ,  $d = 0.3861\text{cm}$ ) and  $15.44\text{cm}$  ( $x/d = 40$ ), downstream of the jet [51, 52]. Shadow graphs were also reported which described the flowfield shock structure and oil smears describing the surface flow conditions. McCann and Bowersox stated that the recompression shock behind the jet was somewhat unsteady and based this statement on changes observed in the shape and location of the shock in the shadow graphs [51]. This unsteady flow situation was not noted in the reports cited above for three-dimensional normal sonic TJISF. Another unexpected feature reported by McCann and Bowersox were prominent asymmetries in the flowfield. While the asymmetries were present in all of the flow variables reported by McCann, they were especially evident in variables whose signs reverse when the test section centerline was

crossed, i.e.  $w, \tau_{xz}$  and  $\tau_{yz}$ . Minor asymmetries in flow variables were also reported by Williams and Hartfield [110] and by Wilson [111]. However, these asymmetries were significantly smaller than those reported by McCann and Bowersox.

### 2.1.3 Algorithm Performance Issues

The major emphasis of this research is turbulence model validation and investigation of the TJISF structure. Therefore, an existing algorithm requiring minimal modifications was an absolute requirement for this study. This prerequisite required the author to consider several algorithm characteristics prior to selection of the final algorithm used to model TJISF. Of particular interest were 1) turbulence models incorporated into the software; 2) discretization method; 3) flux differencing method; 4) total energy expression; 5) computational efficiency and effectiveness; and 6) temporal accuracy.

The turbulence models available in a particular program was of vital importance. Since the present research is based upon the assumption that the Boussinesq approximation is inappropriate for the flowfield under investigation, a solver that incorporates second-order RSTMs must be used.

The domain discretization strategy was also considered when selecting the solver. The greater flexibility for grid development provided by finite-volume methods are usually preferred over finite-difference methods when modeling complex three-dimensional domains [30].

A flux differencing scheme which automatically captures shock structures was mandatory. Two commonly used schemes satisfying this requirement are the van Leer [103] and Roe [68] flux differencing methods. An algorithm with a second-order accurate implementation of either one of these schemes was acceptable.

Another issue of concern during the comparison turbulent flow solvers was the expression used for the Favré-averaged total energy,  $\tilde{E}$ . The complete form of the total energy expression for the FANS equations is given by Vandromme and HaMinh [102] as

$$\tilde{E} = \tilde{e} + \frac{\tilde{u}_i^2}{2} + K \quad (2)$$

where

$$K = \frac{\tau_{ii}}{2} \quad (3)$$

$\tilde{e}$  is the Favré-averaged specific internal energy and  $\tilde{u}_i$  are the Favré-averaged velocity vector components.

It is not uncommon for algorithm developers to add turbulence models to laminar flow solvers and omit  $K$  from the calculation of  $\tilde{E}$ . For subsonic and supersonic flows near Mach one, this omission may not have much effect on the outcome of the solution, however, for high speed flows and TJISF, this omission may have a significant impact. Huang and Coakley [32] reported that excluding  $K$  from  $\tilde{E}$  in their two-dimensional  $K-\omega$  model computations resulted in a 50% increase in size of the separation bubble created by a hypersonic flow encountering a compression shock. They did not report the effect excluding  $K$  had on three-dimensional, rotational flows or the effect it had on their  $K-\epsilon$  model computations. Thus, the relevance of omitting  $K$  from the computation of  $\tilde{E}$  has on more complicated flowfields is left open to speculation.

It is not unreasonable to expect  $K$  to be at a maximum in regions containing strong shocks, boundary layer separation points, strong vortical motion or combusting gases. Therefore, it is likely that  $K$  comprises a significant fraction of the total energy in these regions. Thus, these regions of the flowfield are where the omission of  $K$  from the computation of  $\tilde{E}$  may have a significant impact on the flowfield solution [32].

The bandwidths of the matrices solved at each time step greatly influences the computational requirements necessary to reach a converged solution. The large bandwidth of matrices arising from the discretization of the nonlinear fluid and turbulence closure equations can be lessened by splitting large systems of equation into smaller subsets of equations. In this split-equation approach,

an iterative solution of the five FANS equations is obtained and the updated values of the mean flow variables are then used in the solution of the turbulence model equations. This approach is often taken by programmers who have added a turbulence model to a laminar flow solver [21].

A significant draw back to splitting the governing equations is a decrease in temporal fidelity and the loss of equation coupling. Lagging the turbulence model introduces an  $O(\Delta t)$  error to the solution since the time step used to solve the mean flow equations may differ from the time step used to solve the turbulence equations. Temporal fidelity is not an issue when evaluating a predominately steady flowfield, as in the case of TJISE. However, the loss of equation coupling may cause a reduced rate of convergence since some of the information about the solution is not available to the algorithm.

Temporal fidelity is preserved when the system of equations are simultaneously solved at equivalent time levels. However, large computational time requirements can result from simultaneous integration of the discrete equations even when approximately factored matrices are used. *Diagonalization* of the discrete equations is a technique which reduces computation time and memory requirements by reducing the block tri-diagonal inversion of the approximately factored matrices to simple matrix multiplication and scalar tri-diagonal inversions [63]. According to Steger and Pulliam [63], this can result in a 40% savings in computation time for two-dimensional inviscid flow and results in an almost linear change in computation time when equations are added or subtracted from a system [57]. The near linear change in computational time is a significant improvement over the quadratics change seen in undiagonalized schemes [63].

It would appear that diagonalization of the approximately factored equations would be the preferred method for solution of steady flows, since significant savings in computational time and memory requirements can be realized.

#### 2.1.4 Secondary Research Issues

The discussions in the previous sections have given rise to some additional research issues that warrant investigation:

1. *What is the source of the asymmetries reported by McCann and Bowersox [52]?*
2. *What impact does the form of  $\tilde{E}$  have on the flowfield solution?*

The approach to resolving these issues and the primary research issues raised in Section 1.2 are addressed in Section 2.2.

### 2.2 Approach to Meeting the Objectives

It is clear from the review of the computational database that significant efforts to validate an RSTM suitable for modeling the two- and three-dimensional flowfields remain. Equally clear from the review of the experimental database is that aspects of the three-dimensional flowfield remain uncharacterized. Aside from profile and surface data extracted from shadow graphs and oil smears, the region immediately surrounding the nozzle is largely uncharacterized. Additionally, characterization of the boundary layer and the flowfield surrounding the jet itself have been difficult due to mechanical and thermodynamic limitations of physical probes and flowfield seeding limitations of LASER Doppler velocimetry (LDV). The lower limit of McCann and Bowersox's and Tucker's experiments was approximately  $0.16\text{cm}$  above the surface [52, 100]. Crossflow planes examined with hot wire probes have been limited to planes 20 nozzle diameters or more downstream from the jet [20, 50, 51]. The LDV measurements of Santiago and Dutton [70] were at station 3 and 5 nozzle diameters ( $d$ ), where  $d = 4\text{mm}$ , downstream of the jet. Data upstream of the jet was not reported. Thus, aside from data inferred from shadow graphs and a few crossflow data planes, the flow structure, Reynolds stresses, and vorticity evolution of the TJISF is largely unknown.

Clearly, a better understanding of how the flowfield changes from the upstream boundary layer



separation point to the downstream cross flow data planes requires a validated second-order RSTM capable of modeling a TJISF. Once a suitable model has been validated, numerical simulations to investigate TJISFs are possible and the objectives of the study satisfied. Thus, the approach taken to meet the objectives are outlined in the ensuing discussion.

### **2.2.1 Solver and Turbulence Model Selection**

The numerical solver selected for use in this study was version 3.7 of NASA Langley's Integrated Solution Algorithm for Arbitrary Configurations (ISAAC) [56]. ISAAC is a three-dimensional finite-volume program that uses time integration of the governing equations to compute a steady-state solution of the Favré-Averaged Navier-Stokes equations [56]. This software package satisfied all of the selection criteria discussed in Section 2.1.3. ISAAC is a maturing code which has undergone extensive testing and validation [58]. A detailed discussion of the algorithm is presented in Chapter 5.

Several two-equation and second-order RSTMs suitable for modeling a variety of flow conditions are incorporated into ISAAC. However, for supersonic, wall-bounded flows, only the ZSGS  $K - \epsilon$  model [113] and ZSGS RSTM [113] are fully operational in the current version of ISAAC. The ZSGS RSTM has been validated for fully turbulent, flat-plate flowfields by Zhang et al. [113] and Morrison [56], and for flow past a compression ramp by Morrison, Gatski, Sommer, Zhang, and So [59]. Morrison et al. reported favorable comparisons between predictions made by ISAAC with a two-dimensional grid and experimental findings of Settles and Dodson [79] for ramp angles of  $8^\circ$  and  $16^\circ$ . However, at a ramp angle of  $20^\circ$ , the comparison was poor. Morrison et al. attribute the failure at  $20^\circ$  to three-dimensional effects not accounted for by the two-dimensional grid [59].

### **2.2.2 Two-dimensional validation and evaluation**

The second phase of this investigation extended the validation of the ZSGS RSTM to sonic and

supersonic two-dimensional slot injection flowfields. After the initial code familiarization process, the two-dimensional data reported by Aso et al. [6] and Spaid and Zukoski [88] were selected for model validation. Prior to simulation of the two configurations, appropriate jet boundary condition subroutines were developed/modified (see Appendix E for details of the jet boundary condition implementation). Once the jet boundary conditions were established, temporal and grid convergence criteria were established (see Appendix F for details). The Aso et al. [6] and Spaid and Zukoski [88] experimental conditions were simulated numerically with the ZSGS  $K - \epsilon$  turbulence model and the ZSGS RSTM. The predictions from these two models for mean flow structures and surface static pressure were compared to each other and to experimental data. Furthermore, contour plots of vorticity and two-dimensional Reynolds stress predictions and profiles of the Reynolds stress predictions at selected streamwise locations were used to evaluate the differences between the two models. However, comparison of the model predictions for the turbulent quantities was not possible, since neither Aso et al. nor Spaid and Zukoski reported any turbulence data.

Turbulence data for two-dimensional supersonic TJISF were reported by Tucker [100]. Therefore, Tucker's configuration was simulated numerically with both ZSGS models to better establish the accuracy of each model's predictions of the Reynolds stresses. As with the previous configuration, a grid convergence study was performed for this configuration and the results are summarized in Appendix F. Profiles of the experimental turbulence data and the predictions from the two models were compared to each other to establish the validity of the turbulence predictions. Mean flow data, contour plots and shock structure predictions were also evaluated to establish the validity of the RSTM for this class of injection flowfields.

The significance of including  $K$  in the definition of  $\tilde{E}$  is evaluated for each of the two-dimensional experimental configurations simulated. The relevance of  $K$  is evaluated by examining contour plots of  $K/\tilde{E}$ .

### 2.2.3 Three-dimensional validation and evaluation

The third phase of this investigation extended the validation of the ZSGS RSTM to the three-dimensional oblique supersonic injection flowfield generated by McCann and Bowersox's [52] experimental configuration and characterized the flowfield generated by the oblique injection. Prior to performing any analyses of this flowfield, a subroutine to model the three-dimensional elliptic nozzle boundary conditions was developed and a grid convergence study performed (see Appendices E and F for details of the boundary condition implementation and the grid study).

In their experiments, McCann and Bowersox injected supersonic air from an elliptic nozzle angled  $25^\circ$  downstream into a supersonic primary flow. A sketch of the configuration used by McCann and Bowersox is shown in Figure 3 [52], along with the relative location of the nozzle orifice ( $x/d = 0.0$ , where  $d = 0.3861\text{cm}$ ) and the two downstream locations ( $x/d = 20$  and  $x/d = 40$ ) where the turbulence data was collected.

The large computational domain required to capture both data locations, both sides of the jet and the upstream shock structures naturally lead to segmentation of the research into three parts. The first part examined a reduced domain that encompassed the region shown in Figure 4. The associated grid is referred to as the "full-plane" grid because the grid is wide enough to capture the majority of the flow structure on both sides of the nozzle orifice. This grid extends far enough upstream of the nozzle to capture the undisturbed inflow conditions and far enough downstream of the nozzle to encompass the experimental data collection point at  $x/d = 20$ . The grid also extended far enough in the  $y$  direction to capture the majority of the flow structures normal to the wall.

Contour plots of the numerical results at  $x/d = 20$  from both turbulence models are compared to each other and to the experimental data collected at this location. These comparisons are used to establish the validity of the RSTM for this flowfield and to establish the symmetry of the computed flowfield. Contour plots of the RSTM predictions at other locations within this grid's domain are

also used to examine the flowfield in and around the jet plume and to describe the development of the vortical structures as the injected fluid moves downstream and interacts with the surrounding fluid.

The computational domain shown in Figure 5 is used in the second part of the three-dimensional phase of this study. The associated grid is referred to as the “half-plane” grid since it models only half of the wind tunnel. The domain of this grid extends to the walls at the top, bottom and right-hand-sides of the test section. A symmetry boundary condition is applied at  $z/d = 0$  to simulate the test section centerline. This grid also extends far enough upstream of the nozzle to capture the undisturbed inflow air and far enough downstream to encompass the experimental data collection point at  $x/d = 40$ .

The second part of the three-dimensional phase evaluated the validity of the symmetry boundary condition. This was carried out by comparing contours of the RSTM predictions at  $x/d = 20$  from the full-plane grid to the RSTM predictions at  $x/d = 20$  from the half-plane grid. After validation of the half-plane grid, the three-dimensional analysis was performed, in which RSTM predictions are compared to experimental data at  $x/d = 40$ .

The third part of the three-dimensional phase evaluated the flowfield near the nozzle orifice. This phase of the research used the results obtained from the simulations with the full-plane grid.

#### **2.2.4 Validation Criteria**

The following criteria are used to determine a turbulence model’s validity for simulating a particular flowfield:

1. correct prediction of the magnitude of the quantity under investigation
2. correct prediction of the profile or contour shape of the quantity under investigation
3. absence of non-physical predictions for the quantity under investigation

4. consistent behavior in the predictions of the quantity under investigation from one evaluation station to another
5. consistent behavior when boundary conditions change

A turbulence model does not need to satisfy all of these criteria to be a valid and useful model. However, the more criteria each of the mean flow and turbulence variables satisfy, the greater the confidence in the model's ability to correctly simulate flowfields other than the one currently under investigation.

## Chapter 3 - Governing Equations

### 3.1 Introduction

The equations of fluid mechanics fundamental to the present research are presented in this chapter. In the first part of this chapter, conservation of mass, momentum and energy are expressed through the fully three-dimensional Navier-Stokes equations. In the second part of this chapter, these mathematical relationships are placed in a form more suitable for turbulence modeling by separating the conserved variables into mean flow and fluctuating parts through the Favré averaging process.

### 3.2 Navier-Stokes Equations

In the strictest sense, the complete three-dimensional Navier-Stokes equations are comprised of only the three momentum equations, one for each of the independent coordinate directions. However, for purposes of compactness, the continuity and energy equations are often lumped together with the momentum equations and are collectively called the Navier-Stokes equations. When taken together the five aforementioned equations are more correctly called the *conservation laws of fluid motion*, however, when simulating complex fluid flows, equations other than the Navier-Stokes equations are often included in the system, i.e., turbulence models. Thus, it has become common practice to refer to the Navier-Stokes equations and any other equations being discretized as the *conservation laws* or the *conservation equations* when discussing discretization. Thus, compressible Navier-Stokes equations in conservative, differential form for a rectilinear coordinate system are given as follows:

$$\frac{\partial \rho}{\partial t} + \frac{\partial (\rho u_k)}{\partial x_k} = 0 \quad (4)$$

$$\frac{\partial (\rho u_i)}{\partial t} + \frac{\partial (\rho u_i u_k + p \delta_{ik})}{\partial x_k} - \frac{\partial \sigma_{ik}}{\partial x_k} = 0 \quad (5)$$

$$\frac{\partial (\rho E)}{\partial t} + \frac{\partial (\rho u_k H)}{\partial x_k} - \frac{\partial (u_i \sigma_{ij} - q_k)}{\partial x_k} = 0 \quad (6)$$

where

$$\sigma_{ik} = 2\mu S_{ik} + \lambda S_{jj} \delta_{ik} \quad (7)$$

$$S_{ik} = \frac{1}{2} \left( \frac{\partial u_i}{\partial x_k} + \frac{\partial u_k}{\partial x_i} \right) \quad (8)$$

$$E = e + \frac{1}{2} u_i u_i \quad (9)$$

$$H = E + \frac{p}{\rho} \quad (10)$$

$$q_k = -\kappa \frac{\partial T}{\partial x_k} \quad (11)$$

and by Stokes hypothesis, the second viscosity constant is given as

$$\lambda = -\frac{2}{3} \mu \quad (12)$$

In Eqs. 4, 5 and 6 the first terms on the left-hand side are the unsteady flow terms and the second terms are the convection terms. The terms on the right-hand-side are the diffusion, or viscous terms. The symbols used in the above equations are defined as follows:  $\rho$  is density,  $u_i$  are velocity vector components,  $p$  is pressure,  $t$  is time, and  $T$  is temperature. Also,  $\sigma_{ik}$  are the components of the stress tensor,  $S_{ik}$  are the components of the strain-rate tensor,  $\mu$  is the molecular viscosity,  $E$  is the specific total energy,  $e$  is the specific energy,  $H$  is the specific total enthalpy,  $q_k$  are the components of the heat transfer rate vector per unit area,  $\kappa$  is the convective heat transfer coefficient, and  $\delta_{ik}$  is the Kronecker delta. The subscripts  $i$ ,  $j$  and  $k$  are indices that represent the three Cartesian coordinate directions.

Much of current state-of-the-art CFD research is aimed at simulating turbulent flow. The small length scales associated with turbulent flow necessitates the use of statistical correlations to predict flow characteristics [97]. Proper modeling of the statistical correlations is a major challenge to the aerospace engineer.

Typical methods used within the engineering community for turbulence modeling is to statistically separate instantaneous flow variables into a mean flow values and a fluctuating flow values. These statistical formulations are then substituted into the Navier-Stokes equations, resulting in a number of higher order statistical correlations. These correlations are then modeled as terms that are numerically calculated or experimentally measured. The two most prevalent statistical methods used are Reynolds time-averaging and Favré mass-averaging. Since Favré averaging is the more suitable of the two methods for the compressible flowfield examined here, it will be discussed in greater detail in the next section. See Appendix A for additional details on Reynolds averaging.

### 3.3 Favré-Averaged Navier-Stokes Equations

Favré-averaging is the preferred method of decomposing the flow variables in high speed flows because the resultant system of equations has many similarities to the laminar Navier-Stokes equations [19]. Introduced in 1965, Favré decomposed the flow variables into mean flow and fluctuating parts as follows:

$$\phi_i = \tilde{\phi}_i + \phi_i'' \quad (13)$$

where “ $\sim$ ” denotes the mean flow part of a Favré-averaged variable and “ $''$ ” denotes the fluctuating part of a Favré-averaged variable. In Favré’s decomposition the mean flow part is defined as

$$\tilde{\phi}_i \equiv \frac{\int_t^{t+T} \rho(\mathbf{x}_k, \tau) \phi_i(\mathbf{x}_k, \tau) d\tau}{\int_t^{t+T} \rho(\mathbf{x}_k, \tau) d\tau} \quad (14)$$

and after some algebraic manipulations (see Appendix A) the time average of the Favré-averaged fluctuating part can be expressed as

$$\overline{\phi_i''} = -\frac{\overline{\rho' \phi_i'}}{\bar{\rho}} \neq 0 \quad (15)$$

where the “ $'$ ” indicates a fluctuating part of a Reynolds-averaged variable. Furthermore, it can be shown that  $\overline{\rho \phi_i''} = 0$  (see Appendix A).



The Navier-Stokes equations are mass averaged using a combination of Favré- and Reynolds-averaged flow properties, which are decomposed as follows:

$$u_i = \tilde{u}_i + u_i'' \quad e = \tilde{e} + e'' \quad (16)$$

$$\rho = \bar{\rho} + \rho' \quad p = \bar{p} + p' \quad (17)$$

$$\sigma_{ik} = \bar{\sigma}_{ik} + \sigma'_{ik} \quad q_i = \bar{q}_i + q'_i \quad (18)$$

$$h = \tilde{h} + h'' \quad (19)$$

where  $h$  is the specific enthalpy. Substitution of the above decompositions into the Navier-Stokes equations yields a set of equations commonly referred to as the Favré-averaged Navier-Stokes equations. These equations can be found in many sources including the works of Speziale [91] and Morrison [56] and are derived in Appendix A. They are given here as:

$$\frac{\partial \bar{\rho}}{\partial t} + \frac{\partial (\bar{\rho} \tilde{u}_k)}{\partial x_k} = 0 \quad (20)$$

$$\frac{\partial (\bar{\rho} \tilde{u}_i)}{\partial t} + \frac{\partial (\bar{\rho} \tilde{u}_i \tilde{u}_k + \bar{p} \delta_{ik})}{\partial x_k} - \frac{\partial (\bar{\sigma}_{ik} - \bar{\rho} \tau_{ik})}{\partial x_k} = 0 \quad (21)$$

$$\frac{\partial (\bar{\rho} \tilde{E})}{\partial t} + \frac{\partial (\bar{\rho} \tilde{u}_k \tilde{H})}{\partial x_k} - \frac{\partial (\tilde{u}_i \bar{\sigma}_{ik} - \bar{\rho} \tilde{u}_i \tau_{ik} - \bar{q}_k + \overline{u_i'' \sigma_{ik}} + \bar{\rho} \overline{E'' u_k''})}{\partial x_k} = 0 \quad (22)$$

where

$$\tau_{ik} \equiv \overline{u_i'' u_k''} \quad (23)$$

$$\tilde{E} \equiv \tilde{e} + \frac{1}{2} \tilde{u}_i \tilde{u}_i + K \quad (24)$$

$$\tilde{H} \equiv \tilde{h} + \frac{1}{2} \tilde{u}_i \tilde{u}_i + K \quad (25)$$

$$K = \frac{\tau_{ii}}{2} \quad (26)$$

$$\overline{\rho E'' u_k''} = \overline{u_k' \sigma_{ik}'} - \frac{1}{2} \overline{\rho u_k'' u_i'' u_i''} - C_p \overline{\rho u_k'' T''} \quad (27)$$

The term,  $\tau_{ik}$  represents the components of the kinematic, or specific, Favré-averaged Reynolds-stress tensor and hereafter are referred to as the Reynolds stress tensor components. Note that while the more common definition for the components of the Favré-averaged Reynolds-stress tensor is  $\tau_{ik} = -\overline{\rho u_i'' u_k''}$ , the notation used in Eq. 23 is adopted to maintain consistency with sources and software cited from the NASA Langley Research Center. As in Section 2.1.3,  $\tilde{E}$  is the Favré-averaged total energy. Furthermore,  $\tilde{H}$  is the Favré-averaged specific total enthalpy and  $C_p$  is the specific heat at constant pressure. Finally, it should be understood that henceforth  $K$  refers to the Favré-averaged turbulent kinetic energy.

The Favré-averaged transformation of the Navier-Stokes equations is extremely advantageous to turbulence model developers. After Favré-averaging, the resultant form of the turbulent flow continuity equation is identical to the laminar flow continuity equation, the Favré-averaged momentum equations are equivalent to the laminar flow momentum equations plus one additional term to model, and the apparent unsteady energy term found in the Reynolds-averaged Navier-Stokes (see Appendix A) does not appear in the Favré-averaged energy equation. Furthermore, all of the additional turbulent terms in the Favré-averaged Navier-Stokes equations have analogous laminar expressions that can be employed to simplify the solution of the equations.

In addition to the turbulent closure models which are discussed in the Chapter 4, an equation-of-state must be specified. The perfect gas equation-of-state is used for this study and defined as [102]

$$\bar{p} = \bar{\rho}(\gamma - 1) \left( \tilde{E} - \frac{1}{2} \tilde{u}_i \tilde{u}_i - K \right) \quad (28)$$

where  $\gamma$  is the ratio of specific heats. The presence of  $K$  in Eq. 28 is a result of the Favré-averaging process. It will be seen in Section 4.2.1 that this term creates a strong coupling between the Favré-averaged Navier-Stokes equations and the turbulence transport equations.

## Chapter 4 - Turbulence Models

### 4.1 Introduction

All fluid models must have appropriate characteristic scales to capture properly the fluid motion. Magnitudes of the independent variables at some specified location or time are often used as characteristic scales. While characteristic scales for mean flow equations can be quite large, characteristic scales for turbulence equations can be quite small [97]. Therefore, caution must be exercised when selecting characteristic scales for the fluid model, otherwise pertinent information about the flowfield may be masked.

Consider flow over something as simple as a flat plate. The appropriate length scale for the mean flow equations outside of the boundary layer might be the length of the plate, while in the boundary layer the appropriate length scale is the boundary layer thickness [108]. Neither of these lengths is small enough to capture the turbulent flow characteristics. To capture the turbulent fluctuations, the turbulent microscales of length, time, and/or velocity must be used [97] and a turbulence model is said to be complete if it contains two of the three characteristic microscales [109].

As noted in Section 1.2, turbulence models are generally classified as either zero-equation, one-equation, two-equation, or second-order. The zero- and one-equation models are examples of incomplete turbulence models. These models are easy to implement because they only use one of the microscales, or some term derived from a combination of microscales, e.g., the eddy viscosity,  $\mu_t$ . These model's relative ease of implementation makes them very attractive engineering tools and are frequently employed when modeling simple flowfields. Unfortunately, the lack of two independent microscales limits their usefulness when modeling complex flowfields [109].

### 4.2 Two-Equation Models

The simplest complete turbulence model is the two-equation model. Most two equation models

have characteristics that are advantageous in certain flow situations, but may be unsuitable in others. The most popular two-equation model currently in use is the  $K - \epsilon$  model. This model uses the turbulence kinetic energy,  $K$ , as the velocity microscale, the turbulence dissipation rate,  $\epsilon$ , as the second independent turbulence variable and the Boussinesq approximation to model the RSTC [93].

#### 4.2.1 The $K - \epsilon$ Model

Most of the  $K - \epsilon$  models currently in use are based on the Launder-Spalding model [44] or one of its many modified forms. First introduced in 1972, the Launder-Spalding  $K - \epsilon$  model is reasonably well behaved away from a solid boundary and has achieved moderate success when applied to a variety of engineering problems. Some variations of the original Launder-Spalding  $K - \epsilon$  model currently in use are the models of Jones and Launder [33], Launder and Sharma [42], Lam and Bremhorst [39], Chien [12], Coakley and Huang [14], Zhang, So, Speziale and Lai [114] and many others. Each of these models have either provided a correction to an earlier model or is tailored for a specific type of flowfield.

The exact transport equation for  $K$  is given by Speziale and Sarkar [94] as

$$\frac{D(\bar{\rho}K)}{Dt} - \frac{\partial D^t}{\partial x_k} - \frac{\partial D^\nu}{\partial x_k} = P_{ik} + \Pi_i - \bar{\rho}\epsilon \quad (29)$$

where

$$\frac{D(\cdot)}{Dt} = \frac{\partial(\cdot)}{\partial t} + \bar{u}_k \frac{\partial(\cdot)}{\partial x_k} \quad (30)$$

and the turbulence production, pressure-velocity-gradient correlation, turbulent diffusion, and viscous diffusion are respectively defined as

$$P_{ik} = \bar{\rho} \tau_{ik} \frac{\partial \bar{u}_i}{\partial x_k} \quad (31)$$

$$\Pi_i = -\overline{p' u_i'} \quad (32)$$

$$D^t = -\frac{1}{2} \overline{\rho u_i' u_j' u_k'} \quad (33)$$

$$D^\nu = \bar{\mu} \frac{\partial K}{\partial x_k} \quad (34)$$

As stated by Wilcox [109]: “Morkovin hypothesized that the effects of density fluctuations on the turbulence is small provided they remain small relative to the mean density.” Thus, by Morkovin’s hypothesis [54] and the equation-of-state, the pressure-velocity-gradient correlation, Eq. 32, is assumed to be negligible. The turbulent diffusion term is modeled using the gradient transport hypothesis such that [93]

$$D^t = -\frac{\mu_t}{\sigma_K} \frac{\partial K}{\partial x_k} \quad (35)$$

The gradient transport hypothesis assumes a term,  $F$ , can be modeled by the gradient of a characteristic variable,  $\kappa$ , and a constant of proportionality,  $\varrho$ , such that [75]

$$F = \varrho \frac{\partial \kappa}{\partial x_k} \quad (36)$$

In Eq. 35 the constant of proportionality is the turbulent eddy viscosity which is given as

$$\mu_t = C_\mu f_\mu \bar{\rho} \frac{K^2}{\epsilon} \quad (37)$$

The damping function  $f_\mu$  and values for constants  $C_\mu$  and  $\sigma_K$  are dependent on the particular model being used.

The exact transport equation for the dissipation rate is given as [29]

$$\frac{D(\rho\epsilon)}{Dt} - \frac{\partial D_\epsilon^t}{\partial x_k} - \frac{\partial D_\epsilon^\nu}{\partial x_k} = P_\epsilon - D_\epsilon \quad (38)$$

where  $P_\epsilon$ ,  $D_\epsilon$ ,  $D_\epsilon^t$ , and  $D_\epsilon^\nu$  are, respectively, the dissipation production, destruction, and viscous diffusion. The reader is referred to Speziale, Abid and Anderson [93] for the exact expressions for these terms, however, the modeled forms are given here as follows: [93]

$$P_\epsilon = C_{\epsilon_1} f_1 \frac{\epsilon}{K} \bar{\rho} \tau_{ik} \frac{\partial \bar{u}_i}{\partial x_k} \quad (39)$$

$$D_\epsilon = C_{\epsilon_2} f_2 \bar{\rho} \frac{\epsilon^2}{K} \quad (40)$$

$$D_\epsilon^\nu = \frac{\mu_t}{\sigma_\epsilon} \frac{\partial \epsilon}{\partial x_k} \quad (41)$$

$$D_\epsilon^\nu = \bar{\mu} \frac{\partial \epsilon}{\partial x_k} \quad (42)$$

where  $\sigma_\epsilon$ ,  $C_{\epsilon_1}$  and  $C_{\epsilon_2}$  are constants particular to the model and  $f_1$  and  $f_2$  are wall damping functions also particular to the model.

The  $K - \epsilon$  model is best suited to high-Reynolds number situations where the flow is not constrained by a solid surface. However, many engineering problems are constrained by solid surfaces and require integration directly to the surface (a low-Reynolds number condition). This requirement causes the  $K - \epsilon$  model to lose much of its robustness [93]. This is brought about by stiffness problems that arise from asymptotic inconsistencies and a lack of natural boundary conditions at the wall for the dissipation rate equation. The problem is further exacerbated by the appearance of higher order correlations in the dissipation rate equation [93].

A perturbation analysis of the  $K - \epsilon$  model as the wall boundary is approached reveals the source of the numerical stiffness within this model [93]. By performing a Taylor series expansion for the components, Hinze [29] showed that near the wall

$$\begin{array}{lll} K = O(y^2) & \mu_t = O(y^3) & \epsilon = O(1) \\ \frac{\partial \bar{u}}{\partial y} = O(1) & \overline{u'^2} = O(y^2) & \overline{u'v'} = O(y^3) \\ \overline{v'^2} = O(y^4) & \overline{w'^2} = O(y^2) & \tau_{ij} \bar{u}_{i,j} = O(y^3) \\ D^t = O(y) & P_\epsilon = O(y) & D_\epsilon^t = O(1) \\ D_\epsilon = O(1) & \nabla^2 K = O(1) & \nabla^2 \epsilon = O(1) \end{array}$$

Substituting the asymptotic relations given above into the  $K$  and  $\epsilon$  equations, reveals that since

$\mu_t$  must be of  $O(y^3)$  near the wall for asymptotic consistency,  $f_\mu$  must be of  $O(1/y)$  in this region. Furthermore, for asymptotic consistency of the dissipation production and dissipation destruction,  $f_1$  must be  $O(1)$  and  $f_2$  must be  $O(y^2)$  near the wall. All three of these damping functions must approach unity away from the wall. *“It thus follows that the  $K - \epsilon$  model will generate solutions for  $K$ ,  $\epsilon$ , and  $\overline{u'v'}$  that are asymptotically consistent if the damping functions  $f_\mu = O(1/y)$  and  $f_2 = O(y^2)$  near a wall with  $f_1 = 1$ . [29]”*

Although the  $K - \epsilon$  model can be made asymptotically consistent near the wall, the problem of appropriate boundary conditions is still unresolved. An absence of turbulent kinetic energy at the wall,  $K = 0$ , is the natural boundary condition for  $K$ . However, natural boundary conditions do not exist for the dissipation-rate equation. Therefore, several derived boundary conditions have been used to complete the closure of the model. One commonly used boundary condition is

$$\mu \frac{\partial^2 K}{\partial y^2} = \rho \epsilon \quad (43)$$

which is derived from Eq. 29 as the wall is approached. However, this boundary condition requires information about  $K$  at cells away from the wall in order to achieve second-order accuracy for the second derivative of  $K$ , a requirement which can lead to considerable numerical stiffness [61]. The Neumann boundary condition

$$\frac{\partial \epsilon}{\partial y} = 0 \quad (44)$$

has been shown to be a more robust boundary condition than Eq. 43, but it is completely *ad hoc* with no real theoretical or experimental justification [39].

The final difficulty with the  $K - \epsilon$  model lies in the balance of terms for Eq. 38 at the wall. At the wall, Eq. 38 reduces to

$$\bar{\mu} \frac{\partial^2 \epsilon}{\partial y^2} = D_\epsilon \quad (45)$$

The above expression involves higher-order correlations and second-order derivatives which is more difficult to compute since information about  $\epsilon$  at cells away from the wall is required to achieve second-order accuracy of the second derivative of  $\epsilon$ . Also, extreme accuracy is required for the near wall modeling of the destruction of dissipation,  $D_\epsilon$ , which can further exasperate the already stiff system of equations [93].

The preceding analysis was based on a model formulated for incompressible flow conditions. However, the observations made are still valid for the compressible flow regime provided asymptotic consistency of the equations is maintained.

There are many flowfields of interest (including the flowfield to be studied here) which experience compressibility effects which are not accounted for by incompressible models. Several methods have been developed to account for flowfield compressibility and one such method is Sarkar, Erlebacher, Hussaini, and Kreiss's compressibility correction [74]. This is the compressibility correction model used by Rizzetta [65] when he model the sonic injection experiment conducted by Aso et al. [6] with the Jones-Launder  $K - \epsilon$  model.

Sarkar et al.'s compressibility correction provides a means by which the incompressible dissipation-rate correlations and equations can be applied to compressible flows [74, 94]. Sarkar et al.'s compressibility correction is based on the premise that the dissipation rate can be separated into solenoidal, or incompressible, and compressible components such that the dissipation rate can be expressed as  $\epsilon = \epsilon_s + \epsilon_c$ . In this model  $\epsilon_s$  is the solenoidal component and  $\epsilon_c$  is the compressible component. Sarkar et al. proposed that the compressible component can be modeled as

$$\epsilon_c = \epsilon_s \alpha M_t^2 \quad (46)$$

where  $\alpha = 0.5$  is a numerical constant based upon direct simulation data and  $M_t = \sqrt{\tau_{ii}}/\bar{a}_\infty$  is the turbulent Mach number [73]. Thus,  $\epsilon$  is now expressed as [74]

$$\epsilon \cong \epsilon_s (1 + \alpha M_t^2) \quad (47)$$



The solenoidal dissipation rate,  $\epsilon_s$ , is computed with the high Reynolds number isotropic dissipation-rate equation where  $\epsilon_s$  is used in place of  $\epsilon$ . Complete closure of the Jones-Launder  $K - \epsilon$  model with Sarkar et al.'s correction is found in Rizzetta's AIAA paper *Numerical Simulation of Slot Injection into a Turbulent Supersonic Stream* [65].

Another method to account for compressibility is to develop a model specifically designed to account for compressibility effects. The Zhang, So, Gatski and Speziale (ZSGS)  $K - \epsilon$  model used in this study is a contraction of the ZSGS Reynolds-stress turbulence model for compressible flow (discussed in detail in Section 4.3.2.5) [113]. Closure for the ZSGS  $K - \epsilon$  model, as given by Zhang et al. is [114]

$$D_{ik}^v = \bar{\mu} \frac{\partial K}{\partial x_k} \quad (48)$$

$$D_{ik}^t = \left( \frac{\mu_t}{\sigma_K} \right) \frac{\partial K}{\partial x_k} \quad (49)$$

$$P_{ik} = -\bar{\rho} \tau_{ik} \frac{\partial \tilde{u}_i}{\partial x_k} \quad (50)$$

$$\Pi_i = 0 \quad (51)$$

$$M_{ik} = 0 \quad (52)$$

where  $\sigma_K$  is a constant taken to be 0.75 and the RSTC in the turbulent production term are modeled using the standard eddy viscosity formulation. Zhang et al. [113] gives the RSTC as

$$\tau_{ik} = -2 \frac{\mu_t}{\bar{\rho}} \left( \tilde{S}_{ik} - \frac{1}{3} \tilde{S}_{jj} \delta_{ik} \right) + \frac{2}{3} K \delta_{ik} \quad (53)$$

where  $\mu_t$  is the eddy viscosity defined in Eq. 37 in the eddy-viscosity formulation,  $C_\mu = 0.096$  and the damping function is given as [113]

$$f_\mu = \left( 1 + 3.45 / \sqrt{Re_t} \right) \tanh(y^+ / 115) \quad (54)$$

where

$$Re_t = \frac{K^2}{\bar{\nu}\epsilon} \quad (55)$$

$$y^+ \equiv \frac{y}{\bar{\nu}} \sqrt{\frac{\tau_w}{\bar{\rho}_w}} \quad (56)$$

$$\tau_w = \mu \left. \frac{\partial u}{\partial y} \right|_{y=0} \quad (57)$$

is the shear stress at the wall [11]. The pressure-velocity-gradient correlation and mass flux terms are assumed to be negligible by Morkovin's hypothesis [54]. The dissipation-rate transport equation developed for the ZSGS RSTM is also used for the  $K - \epsilon$  model. However, for the two-equation model,  $D_\epsilon^t$  is modeled as  $(\mu_t/\sigma_\epsilon) \partial\epsilon/\partial x_k$  and  $\sigma_\epsilon = 1.45$  [113].

#### 4.2.2 The Boussinesq Approximation and Secondary Flowfields

The fundamental assumption of the Boussinesq approximation is “. . . that the principal axes of the Reynolds stress tensor,  $\tau_{ij}$ , are coincident with those of the mean strain-rate tensor,  $S_{ij}$ , at all points in a turbulent flow . . . [where] . . . the constant of proportionality between  $\tau_{ij}$  and  $S_{ij}$  is the eddy viscosity,  $\mu_t$  [109].” The Boussinesq approximation provides adequate results for a limited number of flowfields, but completely breaks down for many other flowfields, including three-dimensional flows, flow in ducts with secondary motions, and rotating flows [109].

The contribution of the normal Reynolds stresses on vorticity and secondary flow is shown with the following summary of an analysis given by Speziale [90]. From Speziale, the transport equation for the  $x$  component of vorticity,  $\omega_x$ , is

$$\rho \frac{D(\omega_x)}{Dt} = \frac{\partial^2 (\tau_{zz} - \tau_{yy})}{\partial y \partial z} + \frac{\partial^2 \tau_{yz}}{\partial y^2} - \frac{\partial^2 \tau_{yz}}{\partial z^2} \quad (58)$$

where

$$\frac{D(\cdot)}{Dt} \equiv \frac{\partial(\cdot)}{\partial t} + \bar{u}_k \frac{\partial(\cdot)}{\partial x_k} \quad (59)$$

and

$$\omega_x \equiv \frac{\partial w}{\partial y} - \frac{\partial v}{\partial z} \quad (60)$$

As a result of Eq. 60, Speziale states that the development of secondary flow is directly tied to the presence of a nonzero axial mean vorticity  $\omega_x$  and it is clear that the streamwise vorticity source term

$$\frac{\partial^2 (\tau_{zz} - \tau_{yy})}{\partial y \partial z} + \frac{\partial^2 \tau_{yz}}{\partial y^2} - \frac{\partial^2 \tau_{yz}}{\partial z^2} \quad (61)$$

is the cause of secondary flow. Speziale goes on to make the point that a unidirectional mean turbulent flow exists (i.e. an absence of secondary flow) in a pipe unless

$$\tau_{yz} = 0 \quad (62)$$

Hence, secondary flow will develop if the condition

$$\frac{\partial^2 (\tau_{zz} - \tau_{yy})}{\partial y \partial z} = 0 \quad (63)$$

is violated.

A simple integration of Eq. 63 yields

$$\tau_{zz} - \tau_{yy} = \text{constant} \quad (64)$$

However, since Reynolds stresses vanish at the wall, the constant must be zero, i.e.

$$\tau_{zz} - \tau_{yy} = 0 \quad (65)$$

Consequently, if the streamwise mean velocity gives rise to a nonzero normal Reynolds stress difference

$$\tau_{zz} - \tau_{yy} \neq 0 \quad (66)$$

secondary flow will occur.

The limitations of the Boussinesq approximation with respect to Speziale's analysis are dramatically illustrated by Speziale for the special case of incompressible, fully turbulent flow in a square duct [90, 91]. Under these flow conditions, Speziale has shown that the Boussinesq approximation used to model the Reynolds stresses in the standard  $K - \epsilon$  model, predicts  $\tau_{zz} = \tau_{yy}$  and  $\tau_{yz} = 0$ . Thus, the  $K - \epsilon$  predictions imply that secondary flows do not form in a square duct [90]. This is known to be incorrect since Brundrett and Bains [10] have shown experimentally that there are secondary flows in the planes perpendicular to the axial flow direction.

Speziale has also shown that for a separated turbulent flow over a backward-facing step, the standard  $K - \epsilon$  model yields inaccurate values for the separation length and for the Reynolds stresses [91]. These inaccuracies arise because the Reynolds stresses are not properly related to each other by the Boussinesq approximation. This improper relationship becomes clear after Speziale shows that the standard  $K - \epsilon$  model predicts  $\tau_{xx} + \tau_{yy} = 2\tau_{zz}$  for all locations in the flowfield. Obviously an impossibility in a recirculating flowfield [91]. Clearly, a turbulence model which does not depend upon the Boussinesq approximation to model the Reynolds stresses is required to correctly model flowfields with secondary flows or recirculation. One such model is the second-order RSTM.

### 4.3 Second-Order Reynolds Stress Turbulence Models

The next step up in turbulence model complexity is the second-order model. These models are often referred to as RSTM because they treat the individual components of the Reynolds-stress tensor as independent variables to be solved along with the mean flow variables. Thus, these models are significantly more complex than the two-equation models, but they are not limited by the Boussinesq approximation. Development of Reynolds-stress equation modeling and the higher-order correlations necessary to close the models are presented in the following sections.

#### 4.3.1 Reynolds-Stress and Dissipation-Rate Transport Equations

The foundation upon which second-order turbulence models are built is the Reynolds-stress

tensor. This tensor and its trace are fundamental components of the FANS equations and the equation-of-state. Thus, expressions for the computation of the tensor are required before a solution to the system of equations can be obtained. When turbulent flow conditions are encountered, the RSTCs can be interpreted as transport properties; therefore, a transport equation can be derived for  $\tau_{ij}$ . Expressions for the Favré-averaged Reynolds-stress (FARS) transport equation are found in several sources, including Gatski, Sarkar, Speziale, Balakrishnan, Abid and Anderson [22], Zhang et al. [113] and Morrison [56]. A derivation of this equation is found in Appendix A, and the results are presented here:

$$\frac{\partial (\bar{\rho} \tau_{ij})}{\partial t} + \frac{\partial (\bar{\rho} \tilde{u}_k \tau_{ij})}{\partial x_k} - \frac{\partial D_{ij}^t}{\partial x_k} - \frac{\partial D_{ij}^v}{\partial x_k} = P_{ij} + M_{ij} - \epsilon_{ij} + \Pi_{ij} \quad (67)$$

In Eq. 67, the terms on the left-hand side represents the unsteady transport, convection, turbulent diffusion,  $D_{ij}^t$ , and viscous diffusion,  $D_{ij}^v$ , of the turbulent stresses. While, the terms on the right-hand side represents the turbulent stress transport produced by the turbulent production,  $P_{ij}$ , the mass flux variation,  $M_{ij}$ , the viscous dissipation-rate tensor,  $\epsilon_{ij}$ , and the velocity-pressure-gradient correlation tensor,  $\Pi_{ij}$  [22]. The expressions in Eq. 67 are given as

$$D_{ij}^t = -\overline{\rho u_i'' u_j'' u_k''} \quad (68)$$

$$D_{ij}^v = \overline{\sigma'_{ik} u'_j} + \overline{\sigma'_{jk} u'_i} \quad (69)$$

$$P_{ij} = -\bar{\rho} \tau_{ik} \frac{\partial \tilde{u}_j}{\partial x_k} - \bar{\rho} \tau_{jk} \frac{\partial \tilde{u}_i}{\partial x_k} \quad (70)$$

$$M_{ij} = \overline{u_i''} \left( \frac{\partial \bar{\sigma}_{jk}}{\partial x_k} - \frac{\partial \bar{p}}{\partial x_j} \right) + \overline{u_j''} \left( \frac{\partial \bar{\sigma}_{ik}}{\partial x_k} - \frac{\partial \bar{p}}{\partial x_i} \right) \quad (71)$$

$$\epsilon_{ij} = \overline{\sigma'_{ik} \frac{\partial u'_j}{\partial x_k}} + \overline{\sigma'_{jk} \frac{\partial u'_i}{\partial x_k}} \quad (72)$$

and

$$\Pi_{ij} = \left( \overline{u'_i \frac{\partial p'}{\partial x_j}} + \overline{u'_j \frac{\partial p'}{\partial x_i}} \right) \quad (73)$$

The velocity-pressure-gradient correlation tensor is often expressed as

$$\Pi_{ij} = \left( \overline{p' \frac{\partial u'_i}{\partial x_j}} + \overline{p' \frac{\partial u'_j}{\partial x_i}} \right) - \frac{\partial \left( \overline{p' u'_i \delta_{jk}} + \overline{p' u'_j \delta_{ik}} \right)}{\partial x_k} \quad (74)$$

where the first grouping is the pressure-strain-rate and the second grouping is the pressure diffusion.

As with two-equation models, an additional equation is needed in conjunction with the FARS equations to model the transport of the turbulence dissipation-rate. Referring to the defining relationship for the dissipation-rate tensor given in Eq. 72, one can see that the dissipation-rate transport equation can be derived by taking moments of the Reynolds-averaged fluctuating momentum equation. Thus, a general form of the dissipation-rate transport equation, as found in So, Lai, Zhang and Hwang [85] and Wilcox [109], is

$$\frac{\partial (\bar{\rho} \epsilon)}{\partial t} + \frac{\partial (\bar{\rho} \tilde{u}_k \epsilon)}{\partial x_k} - \frac{\partial D_\epsilon^\nu}{\partial x_k} - \frac{\partial D_\epsilon^t}{\partial x_k} = +P_\epsilon - D_\epsilon + \Psi + \xi \quad (75)$$

The terms on the right-hand side of Eq. 75 are the molecular diffusion,  $D_\epsilon^\nu$ , turbulent diffusion,  $D_\epsilon^t$ , dissipation turbulent production,  $P_\epsilon$ , viscous dissipation of the dissipation-rate,  $D_\epsilon$ , extra production,  $\Psi$ , and near-wall corrections,  $\xi$ . The first four terms on the right-hand side are traditionally modeled as

$$D_\epsilon^\nu = \bar{\mu} \frac{\partial \epsilon}{\partial x_k} \quad (76)$$

$$D_\epsilon^t = C_\epsilon \bar{\rho} \frac{K}{\epsilon} \tau_{ik} \frac{\partial \epsilon}{\partial x_k} \quad (77)$$

$$P_\epsilon = C_{\epsilon_1} \frac{\epsilon}{K} \tilde{P} \quad (78)$$

$$D_\epsilon = C_{\epsilon_2} \bar{\rho} \frac{\epsilon^2}{K} \quad (79)$$

where  $\tilde{P} = \frac{1}{2}P_{ii}$ . The remaining two terms,  $\Psi$  and  $\xi$ , and the constants  $C_\epsilon$ ,  $C_{\epsilon_1}$ , and  $C_{\epsilon_2}$ , are closure model dependent.

#### 4.3.2 Higher-Order Correlation Models for the Reynolds-Stress Transport Equation and the Dissipation-Rate Transport Equation

Developing higher-order correlations is one of the fundamental challenges in turbulence modeling. While in the incompressible regime “. . . several well established models have been tested and proven in a variety of flow situations. [However,] the modeling of the unknown correlations in the compressible case is not as mature . . . [56]” With this statement in mind, two of the most challenging terms to model are the velocity-pressure-gradient correlation tensor,  $\Pi_{ij}$ , and the dissipation-rate tensor,  $\epsilon_{ij}$ .

##### 4.3.2.1 Launder, Reece, and Rodi (LRR) RSTM Closure

Ground breaking work on the modeling of the velocity-pressure-gradient correlation tensor and the dissipation-rate tensor was performed by Rotta [69] and Kolmogorov [36] respectively. Kolmogorov had developed an isotropic model for the dissipation-rate tensor in 1941 and Rotta had assumed that for a high Reynolds number flow the pressure diffusion can be neglected because the pressure-strain rate correlation dominates the velocity-pressure-gradient correlation tensor. Thus, the isotropic assumption was extended to the velocity-pressure-gradient correlation tensor and was put forth by Rotta as the return-to-isotropy model in 1951 [69].

Rotta's work was extended by LRR in their landmark paper *Progress in the Development of a Reynolds-Stress Turbulence Closure* [40]. In this paper, LRR put forth a high Reynolds number model with near wall corrections. LRR recognized the importance of the pressure-diffusion term in the near-wall region and accounted for it with a near-wall correction. The general form of the LRR velocity-pressure-gradient correlation tensor model is

$$\Pi_{ij} \cong \phi_{ij,1} + \phi_{ij,2} + \phi_{ij}^w \quad (80)$$

where  $\phi_{ij,1}$  is Rotta's [69] return-to-isotropy model

$$\phi_{ij,1} = -C_1 \bar{\rho} \frac{\epsilon}{2K} \left( \tau_{ij} - \frac{2}{3} K \delta_{ij} \right) \quad (81)$$

$\phi_{ij,2}$  is LRR's [40] pressure redistribution model

$$\begin{aligned} \phi_{ij,2} = & -\alpha_1 \left( P_{ij} - \frac{1}{3} P_{kk} \delta_{ij} \right) - \beta_1 \left( D_{ij} - \frac{1}{3} P_{kk} \delta_{ij} \right) \\ & - 2\gamma_1 \bar{\rho} K \left( \tilde{S}_{ij} - \frac{1}{3} \tilde{S}_{kk} \delta_{ij} \right) \end{aligned} \quad (82)$$

and  $\phi_{ij}^w$  is LRR's near-wall correction to the high-Reynolds number model [40].

$$\phi_{ij}^w = \left[ 0.125 \frac{\epsilon}{K} \left( \tau_{ij} - \frac{2}{3} K \delta_{ij} \right) + 0.015 (P_{ij} - D_{ij}) \right] \left( \frac{K^{\frac{3}{2}}}{\epsilon x_2} \right) \quad (83)$$

In the above expressions

$$P_{ij} = -\bar{\rho} \tau_{ik} \frac{\partial \tilde{u}_j}{\partial x_k} - \bar{\rho} \tau_{jk} \frac{\partial \tilde{u}_i}{\partial x_k} \quad (84)$$

$$D_{ij} = -\bar{\rho} \tau_{ik} \frac{\partial \tilde{u}_k}{\partial x_j} - \bar{\rho} \tau_{jk} \frac{\partial \tilde{u}_k}{\partial x_i} \quad (85)$$

$$\tilde{S}_{ij} = \frac{1}{2} \left( \frac{\partial \tilde{u}_i}{\partial x_j} + \frac{\partial \tilde{u}_j}{\partial x_i} \right) \quad (86)$$

$$\alpha_1 \equiv \frac{C_2 + 8}{11} \quad (87)$$

$$\beta_1 \equiv \frac{8C_2 - 2}{11} \quad (88)$$

$$\gamma_1 \equiv \frac{30C_2 - 2}{55} \quad (89)$$

where  $C_1 = 3.0$  and  $C_2 = 4.0$ .

To complete the closure of their model, LRR modeled the dissipation-rate tensor,  $\epsilon_{ij}$ , after Kolmogorov [36]. The Kolmogorov model is simply

$$\epsilon_{ij} = \frac{2}{3} \bar{\rho} \epsilon \delta_{ij} \quad (90)$$



where  $\epsilon$  is computed with an additional dissipation-rate transport equation. The LRR model computes  $\epsilon$  with the dissipation-rate transport equation given in Section 4.3.1 with  $C_\epsilon = 0.11$ ,  $C_{\epsilon_1} = 1.44$ , and  $C_{\epsilon_2} = 1.90$ .

Since its publication in 1975, the LRR model has become the standard starting point for virtually every second-order model put forth since. However, since the LRR model's introduction, research has found that for any modern Reynolds-stress model to be of practical use, it must satisfy two constraints [92]. The first is *realizability*. Realizability, as stated by Schumann [78], requires that the component energies of a Reynolds-stress model have positive values, i.e.,  $\tau_{\alpha\alpha} \geq 0$ , with no summation on  $\alpha$ , for any turbulent flow. The second constraint is frame invariance. Frame invariance was first advocated by Donaldson and Rosenbaum [16] in 1968 as a necessity if Reynolds-stress models were ever to be extended to more complex flows, particularly to flows involving curvilinear coordinates. To insure frame invariance, the Reynolds-stress transport equation and all modeled terms must be cast in tensor form.

There have been numerous attempts to improve upon the LRR model and an excellent review of many of these models is found in *A Review of Near-Wall Reynolds Closures* by So et al. [85]. Of the models examined by So et al., they state that only the Shima [83], Launder and Shima [43], and Lai and So [38] give reasonable predictions of the turbulence statistics in a fully-developed channel flow. The models of Shima, and Lai and So are summarized below along with two models that are proposed improvements to the models discussed in So et al. [85].

#### 4.3.2.2 Shima RSTM Closure

Noting several deficiencies in the near-wall term of the LRR model, Shima [83] modified the return-to isotropy term and the near-wall correction term to improve near-wall behavior. Shima retained LRR's pressure redistribution term,  $\phi_{ij,2}$ , but replaced  $\phi_{ij,1}$  with [83]

$$\phi_{ij,1} = -C_1^* \bar{\rho} \frac{\epsilon}{2K} \left( \tau_{ij} - \frac{2}{3} K \delta_{ij} \right) \quad (91)$$

where

$$C_1^* = C_1 \left[ 1 - \left( 1 - \frac{1}{C_1} \right) f_{w_1} \right] \quad (92)$$

$$f_{w_1} = \exp \left[ - \left( \frac{0.015 x_2 \sqrt{K}}{\bar{\nu}} \right)^4 \right] \quad (93)$$

Citing that the term  $K^{\frac{3}{2}}/\epsilon x_2$  in Eq. 83 vanishes at the wall and  $\phi_{ij}^w$  has little effect in the immediate vicinity of the wall, Shima replaced  $\phi_{ij}^w$  with [83]

$$\phi_{ij}^w = f_{w_1} \left[ \alpha \left( P_{ij} - \frac{2}{3} P_{kk} \delta_{ij} \right) + \beta \left( D_{ij} - \frac{2}{3} P_{kk} \delta_{ij} \right) + \gamma K S_{ij} \right] \quad (94)$$

In an attempt to prevent excessive non-physical coupling between the turbulent kinetic energy and the dissipation-rate brought about by the coincidence of  $\partial\epsilon/\partial t$  and  $\partial(\nu\partial^2 K/\partial x_i \partial x_i)/\partial t$  at the wall, Shima made two modifications to the dissipation-rate transport equation. First, following Hanjalic and Launder [26], Shima replaced  $D_\epsilon$  as defined in Eq. 79 with

$$D_\epsilon = C_{\epsilon_2} \bar{\rho} \frac{\epsilon \tilde{\epsilon}}{K} \quad (95)$$

where

$$\tilde{\epsilon} = \epsilon - 2\bar{\nu} \left( \frac{\partial \sqrt{K}}{\partial x_i} \right)^2 \quad (96)$$

and introduced the additional near-wall term

$$\xi = \bar{\rho} f_{w_1} \left[ \left( \frac{7}{9} C_{\epsilon_2} - 2 \right) \frac{\epsilon \bar{\epsilon}}{K} - \frac{\bar{\epsilon}^2}{2K} \right] \quad (97)$$

where

$$\bar{\epsilon} = \epsilon - \bar{\nu} \frac{\partial^2 K}{\partial x_i^2} \quad (98)$$

Second, Shima grouped the turbulent production and extra production terms together to form

$$P_\epsilon + \Psi = C_{\epsilon_1} (1 + \sigma f_{w_1}) \frac{\epsilon_s}{K} \tilde{P} \quad (99)$$

The closure constants, damping functions and wall boundary conditions used by Shima are given in Appendix B.

#### 4.3.2.3 Lai and So RSTM Closure

Using an asymptotic analysis of the near-wall behavior, Lai and So [38] sought to balance the modeled terms of the Reynolds-stress and dissipation-rate transport equations to the lowest order. Specifically, they sought to develop an asymptotically correct velocity-pressure-gradient correlation (not just the pressure strain-rate correlation tensor) and dissipation-rate tensor models, and a dissipation-rate transport equation that ensured correct behavior in the near-wall region. Upon performing asymptotic expansions of the terms in the Reynolds-stress equation, Lai and So found that the dissipation-rate tensor and the viscous diffusion terms exhibit  $O(y^2)$  behavior near the wall while the convection, production and turbulent diffusion terms exhibit  $O(y^3)$  behavior near the wall. Consequently, the velocity-pressure-gradient correlation tensor must balance the difference of the dissipation-rate tensor and the viscous diffusion terms, or

$$\Pi_{ij} = \epsilon_{ij} - \frac{\partial D_{ij}^\nu}{\partial x_k} \quad (100)$$

of which the difference is  $O(y^2)$ .

For high Reynolds number flows, the viscous diffusion is often neglected since it is frequently overshadowed by turbulent diffusion effects [56]. However, Lai and So's asymptotic analysis [38] showed for near-wall flows, the opposite is true and the viscous diffusion dominates the turbulent diffusion. Thus, using the gradient transport hypothesis, the viscous diffusion was modeled as

$$D_{ij}^\nu = \bar{\mu} \left( \frac{\partial \tau_{ij}}{\partial x_k} + \frac{\partial \tau_{jk}}{\partial x_i} + \frac{\partial \tau_{ik}}{\partial x_j} \right) \quad (101)$$

Recall that the general expression for the velocity-pressure-gradient correlation tensor is

$$\Pi_{ij} \cong \phi_{ij,1} + \phi_{ij,2} + \phi_{ij}^w \quad (102)$$

Lai and So proposed to use the expressions developed by Rotta [69] and LRR [40] to model  $\phi_{ij,1}$  and  $\phi_{ij,2}$ . However, according to Lai and So [38],  $\phi_{ij}^w$  should “compensate” for the incorrect asymptotic

behavior of  $\phi_{ij,1}$  while providing additional terms to balance  $(\epsilon_{ij} - D_{ij}^\nu)$ . "Furthermore, according to Shima (1988) and Launder et al. (1975),  $\phi_{ij}^w$  should also provide additional terms to account for wall reflection effects in the not-too-near-wall region. [38]" Thus, Lai and So modeled  $\phi_{ij}^w$  as

$$\phi_{ij}^w = f_{w_1} \left[ C_1 \bar{\rho} \frac{\epsilon}{K} \left( \tau_{ij} - \frac{2}{3} K \delta_{ij} \right) - \bar{\rho} \frac{\epsilon}{K} (\tau_{ik} n_k n_j + \tau_{jk} n_k n_i) + \alpha^* \left( P_{ij} - \frac{1}{3} P_{kk} \delta_{ij} \right) \right] \quad (103)$$

where  $\alpha^* = 0.45$ . According to Lai and So [38], this model for the velocity-pressure-gradient correlation tensor,  $\Pi_{ij}$ , is asymptotically correct to at least  $O(y^2)$  for all components.

Based on the suggestions of Hanjalic and Launder [26], Launder and Reynolds [41] and Launder and Tselepidakis [45]; Lai and So proposed a model for the dissipation-rate tensor that provides  $O(y^2)$  near-wall behavior and asymptotes to Kolmogorov's [36] model far away from the wall. Thus, the proposed dissipation-rate tensor model is given as

$$\epsilon_{ij} = \frac{2}{3} \bar{\rho} \epsilon \delta_{ij} + \epsilon_{ij}^w \quad (104)$$

where

$$\epsilon_{ij}^w = f_{w_1} \left[ -\frac{2}{3} \bar{\rho} \epsilon \delta_{ij} + \bar{\rho} \frac{\epsilon}{K} \frac{(\tau_{ij} + \tau_{ik} n_k n_j + \tau_{jk} n_k n_i + n_i n_j \tau_{kl} n_k n_l)}{(1 + \frac{3}{2} \frac{\tau_{kl} n_k n_l}{K})} \right] \quad (105)$$

In their model for the dissipation-rate transport equation, Lai and So retained Shima's form for  $\Psi + P_\epsilon$  (see Eq. 99), but put forth a functional form for  $\sigma$ . Based on data of Kim et al. [34] and Mansour et al. [48], Lai and So proposed

$$\sigma = 1.0 - 0.6 \exp \left[ - \left( \frac{Re}{10^4} \right) \right] \quad (106)$$

Citing convenience and numerical stability, Lai and So expressed  $\xi$  as

$$\xi = \bar{\rho} f_{w_2} \left[ \left( \frac{7}{9} C_{\epsilon_2} - 2 \right) \frac{\epsilon \tilde{\epsilon}}{K} - \frac{\epsilon^{*2}}{2K} \right] \quad (107)$$

where

$$\tilde{\epsilon} = \epsilon - 2\bar{\nu} \left( \frac{\partial \sqrt{K}}{\partial x_2} \right)^2 \quad (108)$$

and

$$\epsilon^* = \epsilon - \frac{\bar{\nu}K}{x_2^2} \quad (109)$$

Lai and So claim that their expression for  $\epsilon^*$  is more robust than Shima's expression for  $\bar{\epsilon}$ .

The closure constants, damping functions and wall boundary conditions proposed by Lai and So are listed in Appendix B.

#### 4.3.2.4 Lai, So, Zhang, and Speziale (LSZS) RSTM Closure

In *A Review of Second-Order Near-Wall Closures* by So et al. [85] it was observed that none of the models evaluated could reproduce the distributions of  $\epsilon_{11}$  and  $\epsilon$  correctly beyond  $y^+ \approx 20$ . Lai and So [38] claim that the inability to predict these near-wall distributions “. . . lies in the incorrect modeling of the near-wall production and dissipation terms proposed for the  $\epsilon$  equation as well as the velocity-pressure-gradient correlation [tensor] [85].”

Since modeling in the  $\epsilon$  transport equation is rather ad hoc anyway, Lai and So suggested that attempts to improve this equation should be given priority. To this end, So et al. [86] proposed an alternative  $\xi$  function based on the studies of Shima [83] and Mansour et al. [48] The altered form of  $\xi$  is given as

$$\xi = \bar{\rho}f_{w_2} \left[ -2\frac{\epsilon\tilde{\epsilon}}{K} + 3\frac{\epsilon^{*2}}{2K} \right] \quad (110)$$

where  $\tilde{\epsilon}$ , and  $\epsilon^*$  are defined by Eqs. 108 and 109 in Section 4.3.2.3. In this updated model, So et al. [85] has retained most of the model constant values specified by Lai and So, but found they had better agreement with the experimental data by defining  $\sigma$  as

$$\sigma = 1.0 - 1.5\exp \left[ - \left( \frac{Re}{10^4} \right) \right] \quad (111)$$

In conjunction with the velocity-pressure-gradient correlation tensor model given by Lai and So [38], So et al. [85] applied this modified form of the  $\epsilon$  transport equation (henceforth referred

to as LSZS) to the flow conditions given by Mansour et al. [48]. Comparison of the distributions of the turbulent flow quantities show that LSZS gives better predictions of the overall profiles of all quantities, including the near-wall behavior of  $\epsilon$  and  $\epsilon_{11}$  (see So et al. [85] for plots of the data). However, there are still deficiencies in the near-wall predictions for  $\tau_{xy}$ ,  $\epsilon_{12}$ ,  $\epsilon_{22}$ ,  $\epsilon_{33}$  and the mean velocity values in the buffer region.

As with previous models, the closure constants, damping functions and wall boundary conditions proposed by So et al. are listed in Appendix B.

#### 4.3.2.5 Zhang, So, Gatski, and Speziale (ZSGS) RSTM Closure

So et al. [85] attributed the inability of previous second-order models to correctly predict the mean velocity values in the buffer region and the dissipation-rate profile at the wall to poor modeling of the velocity-pressure-gradient correlation tensor in the near-wall region, specifically the pressure diffusion term. Zhang et al. [115] expanded on this line of thought and went on to point out that in previous models the effects of pressure diffusion had been lumped together with the near-wall correction term  $\phi_{ij}^w$  [115]. To correct this deficiency, Zhang et al. [115] proposed a pressure diffusion model be added to Lai and So's [38] velocity-pressure-gradient correlation tensor model and modifications made to the LSZS [85] dissipation-rate transport equation to account for the reflection of the pressure in the near-wall region brought about by pressure diffusion. Thus, Zhang et al. proposed the velocity-pressure-gradient correlation tensor be written as

$$\Pi_{ij} \cong \phi_{ij,1} + \phi_{ij,2} + \phi_{ij}^w + \phi_{ij}^R \quad (112)$$

where  $\phi_{ij,1}$  and  $\phi_{ij,2}$  are as given by LRR in Section 4.3.2.1 and  $\phi_{ij}^w$  is taken from Eq. 103 in Section 4.3.2.3. The pressure reflection,  $\phi_{ij}^R$ , is given by Zhang et al. [113] as

$$\phi_{ij}^R = 2C_w \bar{\rho} K \left( S_{ij} - \frac{1}{3} S_{kk} \delta_{ij} \right) \frac{K^{\frac{2}{3}}}{\epsilon x_2} \quad (113)$$

where

$$\begin{aligned} C_w &= (C_w)_{in} - (5.8 \times 10^{-4}) M_\infty & \text{for } M_\infty > 2.5 \\ C_w &= (C_w)_{in} & \text{for } M_\infty < 2.5 \end{aligned} \quad (114)$$

In the expression above,  $M_\infty$  is the freestream Mach number. Since  $(C_w)_{in}$  is dependent on the momentum thickness Reynolds number,  $Re_\theta$ , appropriate expressions for  $(C_w)_{in}$  must be specified.

These are found in Zhang et al. [113] and given as

$$\begin{aligned} (C_w)_{in} &= 4.14 \times 10^{-3} + 3 \times 10^{-3} (\log Re_\theta) & \text{for } Re_\theta \leq 5.500 \\ (C_w)_{in} &= 0.0153 & \text{for } Re_\theta > 5.500 \end{aligned} \quad (115)$$

The ZSGS model uses the LSZS model for the dissipation-rate tensor.

Near-wall modifications by Zhang et al. [113] to the dissipation-rate transport equation consist of a new form for  $\xi$ . The new form is given as

$$\xi = f_{w_2} \bar{\rho} \left( -2 \frac{\epsilon \tilde{\epsilon}}{K} + 1.5 \frac{\bar{\epsilon}}{K} \right) \quad (116)$$

where

$$\tilde{\epsilon} = \epsilon - 2\bar{\nu} \left( \frac{\partial \sqrt{K}}{\partial x_2} \right)^2 \quad (117)$$

$$\bar{\epsilon} = \epsilon - 2\bar{\nu} \frac{K}{x_2^2} \quad (118)$$

$$f_{w_2} = \exp \left[ - \left( \frac{Re_t}{40} \right)^2 \right] \quad (119)$$

Any additional closure constants and damping functions as well as the wall boundary conditions proposed by Zhang et al. are listed in Appendix B.

#### 4.3.2.6 Turbulent Diffusion, Viscous Diffusion and Mass Flux Variations

Many different models have been proposed to compute the triple velocity correlation found in the turbulent diffusion term, Eq. 68. Some of these models are the isotropic model of Shir [84] and the gradient diffusion models of Daly and Harlow [15] and Hanjalic and Launder [25]. These models and several others were evaluated in a comparative study by Amano and Goel [2] and the results of

their study indicated that the gradient diffusion model of Hanjalic and Launder [25] produced the best results of the models evaluated. The Hanjalic and Launder model is given as

$$\overline{\rho u_i'' u_j'' u_k''} = -\bar{\rho} C_s \frac{K}{\epsilon} \left( \frac{\partial \tau_{ij}}{\partial x_k} + \frac{\partial \tau_{jk}}{\partial x_i} + \frac{\partial \tau_{ik}}{\partial x_j} \right) \quad (120)$$

where  $C_s = 0.18$ . Thus

$$D_{ij}^t = \bar{\rho} C_s \frac{K}{\epsilon} \left( \frac{\partial \tau_{ij}}{\partial x_k} + \frac{\partial \tau_{jk}}{\partial x_i} + \frac{\partial \tau_{ik}}{\partial x_j} \right) \quad (121)$$

A model for the viscous diffusion, Eq. 69, is obtained from an asymptotic near wall analysis and by neglecting fluctuations in the viscosity as well as some higher-order correlations, particularly those involving dilatational effects [94]. These assumptions are possible because in a high-Reynolds number flow, the viscous diffusion effects would only be significant extremely close to the wall where the turbulence Mach number is small and Morkovin's hypothesis may be invoked [94]. Thus, the viscous diffusion is modeled as

$$D_{ij}^v \cong \bar{\mu} \left( \frac{\partial \tau_{ij}}{\partial x_k} + \frac{\partial \tau_{jk}}{\partial x_i} + \frac{\partial \tau_{ik}}{\partial x_j} \right) \quad (122)$$

If Morkovin's hypothesis is invoked, the mass flux variation,  $M_{ij}$ , may be assumed negligible [54]. For the situations where this is not true, standard gradient transport hypotheses are generally used to model this term [113].

#### 4.4 Navier-Stokes Equations in a Second-Order Model

Since there are several higher-order correlations to be modeled in the Favré-averaged total energy equation, Eq. 22 it is shown here for convenience:

$$\frac{\partial (\bar{\rho} \tilde{E})}{\partial t} + \frac{\partial (\bar{\rho} \tilde{u}_j \tilde{H})}{\partial x_j} - \frac{\partial \left( -\bar{\rho} \tilde{u}_j \tau_{ij} + \tilde{u}_i \bar{\sigma}_{ij} + \kappa \frac{\partial \tilde{T}}{\partial x_j} + \bar{\rho} \overline{E'' u_j''} + \overline{u_i'' \sigma_{ij}} \right)}{\partial x_j} = 0$$

where

$$\tilde{E} \equiv \tilde{e} + \frac{1}{2} \tilde{u}_i \tilde{u}_i + K$$

$$\tilde{H} \equiv \tilde{h} + \frac{1}{2} \tilde{u}_i \tilde{u}_i + K$$



$$\bar{\rho} \overline{E'' u_j''} \equiv \overline{u_j' \sigma_{ij}'} - \frac{1}{2} \bar{\rho} \overline{u_j'' u_i'' u_i''} - C_p \bar{\rho} \overline{u_j'' T''}$$

The energy flux is given by standard gradient transport hypotheses as

$$\overline{u_j'' T''} \cong - \frac{C_\mu f_\mu}{Pr_t} \frac{K^2}{\epsilon} \frac{\partial \tilde{T}}{\partial x_j} \quad (123)$$

where  $Pr_t$  is the turbulent Prandtl number, which is assumed to be 0.9 for air [94].

Contractions of Eqs. 120 and 122 are also used in the total energy equation. Specifically Eq.

122 contracts to

$$\overline{\sigma_{ij}' u_j'} \cong \bar{\mu} \left( \frac{\partial K}{\partial x_i} + \frac{\partial \tau_{ij}}{\partial x_j} \right) \quad (124)$$

and Eq. 120 contracts to

$$\frac{1}{2} \bar{\rho} \overline{u_j'' u_i'' u_i''} \cong - \bar{\rho} C_s \frac{K}{\epsilon} \left( \frac{\partial K}{\partial x_j} + \frac{\partial \tau_{ij}}{\partial x_i} \right) \quad (125)$$

where  $C_s$  is model dependent. The  $\partial \tau_{ij} / \partial x_i$  terms in the two contracted equations above are often ignored [57] and  $C_s$  is optimized to account for these missing terms.

## Chapter 5 - Algorithm Formulation

### 5.1 Introduction

The algorithm used to solve the governing equations is described in this chapter. ISAAC uses an integral formulation of the governing equations and these equations are discretized over a structured grid of finite-volume cells. This algorithm uses implicit time differencing for added robustness and uses time linearization, approximate factorization and matrix diagonalization for computational efficiency. Second-order accurate upwinding is employed to evaluate the implicit terms in the discretized governing equations and second-order accurate Roe flux differencing is used to evaluate the fluxes in the residual. Greater detail on each of these topics is provided in this chapter. In this chapter, the only subscripts which imply partial differentiation are  $x, y, z, \xi, \eta$  and  $\varsigma$ .

### 5.2 Governing Equation Formulation

#### 5.2.1 Integral Formulation

ISAAC is based on the integral formulation of the governing equations for flow of a single-species, perfect gas. If one considers a volume,  $Vol$ , inclosed by a surface,  $S$ , these equations can be written as [30]

$$\frac{\partial}{\partial t} \left( \int_{Vol} \mathbf{Q} dVol \right) + \oint_S (\vec{\mathbf{F}} - \vec{\mathbf{F}}_v) \cdot \vec{n} dS = \int_{Vol} \mathbf{S} dVol \quad (126)$$

where

$$\oint_S \vec{n} dS = 0 \quad (127)$$

$$\int_{Vol} dVol = Vol \quad (128)$$

$$\vec{\mathbf{F}} = f\hat{\mathbf{i}} + g\hat{\mathbf{j}} + h\hat{\mathbf{k}} \quad (129)$$

$$\vec{F}_v = f_v \hat{i} + g_v \hat{j} + h_v \hat{k} \quad (130)$$

and  $Q$  is the solution vector;  $f$ ,  $g$  and  $h$ ; and  $f_v$ ,  $g_v$  and  $h_v$  are respectively; the inviscid and viscous flux vectors in the  $x$ ,  $y$  and  $z$  coordinate direction and  $S$  is the vector of source terms.

In this formulation, the Favré-averaged Navier-Stokes equations presented in Chapter 3 are used to describe the mean flow behavior of the fluid and the Favré-averaged Reynolds stress and dissipation-rate equations detailed in Chapter 4 are used to describe the turbulent behavior of the fluid. Therefore,  $Q$  is given as

$$Q = [\bar{\rho}, \bar{\rho}\tilde{u}, \bar{\rho}\tilde{v}, \bar{\rho}\tilde{w}, \bar{\rho}\tilde{E}, \bar{\rho}\tau_{11}, \bar{\rho}\tau_{22}, \bar{\rho}\tau_{33}, \bar{\rho}\tau_{12}, \bar{\rho}\tau_{13}, \bar{\rho}\tau_{23}, \bar{\rho}\epsilon]^T \quad (131)$$

and the individual components of the flux vectors are

$$f = \begin{bmatrix} \bar{\rho}\tilde{u} \\ \bar{\rho}\tilde{u}^2 + \bar{p} \\ \bar{\rho}\tilde{u}\tilde{v} \\ \bar{\rho}\tilde{u}\tilde{w} \\ \bar{\rho}\tilde{u}\tilde{H} \\ \bar{\rho}\tilde{u}\tau_{11} \\ \bar{\rho}\tilde{u}\tau_{22} \\ \bar{\rho}\tilde{u}\tau_{33} \\ \bar{\rho}\tilde{u}\tau_{12} \\ \bar{\rho}\tilde{u}\tau_{13} \\ \bar{\rho}\tilde{u}\tau_{23} \\ \bar{\rho}\tilde{u}\epsilon \end{bmatrix} \quad g = \begin{bmatrix} \bar{\rho}\tilde{v} \\ \bar{\rho}\tilde{v}^2 + \bar{p} \\ \bar{\rho}\tilde{v}\tilde{u} \\ \bar{\rho}\tilde{v}\tilde{w} \\ \bar{\rho}\tilde{v}\tilde{H} \\ \bar{\rho}\tilde{v}\tau_{11} \\ \bar{\rho}\tilde{v}\tau_{22} \\ \bar{\rho}\tilde{v}\tau_{33} \\ \bar{\rho}\tilde{v}\tau_{12} \\ \bar{\rho}\tilde{v}\tau_{13} \\ \bar{\rho}\tilde{v}\tau_{23} \\ \bar{\rho}\tilde{v}\epsilon \end{bmatrix} \quad h = \begin{bmatrix} \bar{\rho}\tilde{w} \\ \bar{\rho}\tilde{w}^2 + \bar{p} \\ \bar{\rho}\tilde{w}\tilde{u} \\ \bar{\rho}\tilde{w}\tilde{v} \\ \bar{\rho}\tilde{w}\tilde{H} \\ \bar{\rho}\tilde{w}\tau_{11} \\ \bar{\rho}\tilde{w}\tau_{22} \\ \bar{\rho}\tilde{w}\tau_{33} \\ \bar{\rho}\tilde{w}\tau_{12} \\ \bar{\rho}\tilde{w}\tau_{13} \\ \bar{\rho}\tilde{w}\tau_{23} \\ \bar{\rho}\tilde{w}\epsilon \end{bmatrix} \quad (132)$$

$$f_v = \begin{bmatrix} 0 \\ \hat{\tau}_{11} \\ \hat{\tau}_{12} \\ \hat{\tau}_{13} \\ b_1 \\ \tau_{11}^D \\ \tau_{22}^D \\ \tau_{33}^D \\ \tau_{12}^D \\ \tau_{13}^D \\ \tau_{23}^D \\ \epsilon_1 \end{bmatrix} \quad g_v = \begin{bmatrix} 0 \\ \hat{\tau}_{12} \\ \hat{\tau}_{22} \\ \hat{\tau}_{23} \\ b_2 \\ \tau_{11}^D \\ \tau_{22}^D \\ \tau_{33}^D \\ \tau_{12}^D \\ \tau_{13}^D \\ \tau_{23}^D \\ \epsilon_2 \end{bmatrix} \quad h_v = \begin{bmatrix} 0 \\ \hat{\tau}_{13} \\ \hat{\tau}_{23} \\ \hat{\tau}_{33} \\ b_3 \\ \tau_{11}^D \\ \tau_{22}^D \\ \tau_{33}^D \\ \tau_{12}^D \\ \tau_{13}^D \\ \tau_{23}^D \\ \epsilon_3 \end{bmatrix} \quad (133)$$

and the components of the source vector are

$$\mathbf{S} = \begin{bmatrix} 0 \\ 0 \\ 0 \\ 0 \\ 0 \\ P_{11} + \bar{\rho}\epsilon_{11} + \Pi_{11} + M_{11} \\ P_{22} + \bar{\rho}\epsilon_{22} + \Pi_{22} + M_{22} \\ P_{33} + \bar{\rho}\epsilon_{33} + \Pi_{33} + M_{33} \\ P_{12} + \bar{\rho}\epsilon_{12} + \Pi_{12} + M_{12} \\ P_{13} + \bar{\rho}\epsilon_{13} + \Pi_{13} + M_{13} \\ P_{23} + \bar{\rho}\epsilon_{23} + \Pi_{23} + M_{23} \\ P_\epsilon - D_\epsilon + \Psi + \xi \end{bmatrix} \quad (134)$$

where

$$\hat{\tau}_{ik} = \bar{\sigma}_{ik} - \bar{\rho}\tau_{ik} \quad (135)$$

$$\tau_{ij}^D = D_{ij}^t + D_{ij}^v \quad (136)$$

$$\epsilon_k^D = D_\epsilon^t + D_\epsilon^v \quad (137)$$

$$b_k = \tilde{u}_i \hat{\tau}_{ik} - \bar{q}_k + \overline{u_i'' \sigma_{ik}} + \bar{\rho} \overline{E'' u_k''} \quad (138)$$

The expressions for  $P_{ik}$ ,  $\epsilon_{ik}$ ,  $\Pi_{ik}$ ,  $M_{ik}$ ,  $D_{ij}^t$ ,  $D_{ij}^v$ ,  $D_\epsilon^t$ ,  $D_\epsilon^v$ ,  $\overline{u_i''}$  and  $\overline{E'' u_k''}$  are model dependent. The expressions for these terms from the RSTM's discussed in Chapter 4 are given in Appendix B.

### 5.2.2 Finite-Volume Formulation

Discretization of the domain into a structured grid of finite-volume cells with constant fluid properties over the cell volume, permits application of Eq. 126 to the individual cells. Upon performing the volume integration for an individual cell, Eq. 126 is expressed as:

$$\frac{\partial}{\partial t} [(\mathbf{QVol})_{i,j,k}] + \oint_{S_{i,j,k}} (\vec{\mathbf{F}} - \vec{\mathbf{F}}_v) \cdot \vec{n} dS = (\mathbf{SVol})_{i,j,k} \quad (139)$$

where the  $i$ ,  $j$ , and  $k$  subscripts are coordinate indices for the cell centers. Since a structured grid approach is used for this formulation, the indices range from 1 to the maximum cell index;  $I_{max}$ ,  $J_{max}$  or  $K_{max}$ , in each coordinate direction.

Applying the geometric constraints given by Eqs. 127 - 128 to individual cells results in

$$\oint_{S_{i,j,k}} \vec{n} dS = 0 \quad (140)$$

$$\int_{Vol_{i,j,k}} dVol = Vol_{i,j,k} \quad (141)$$

where

$$\sum_{i=1}^{Imax} \sum_{j=1}^{Jmax} \sum_{k=1}^{Kmax} Vol_{i,j,k} = Vol \quad (142)$$

Equations 140 and 141 require the volume of any cell identified by its  $i, j, k$  index, be finite and have a closed surface area. Additionally, Eq. 142 requires the sum of the individual cell volumes given by Eq. 141, equal the volume of the domain given by Eq. 128. These conditions are easily satisfied in finite-volume discretization schemes when the surface area and cell volume calculation methods described in Vinokur [106], and Kordulla and Vinokur [37] are used. These methods allow a great deal of flexibility in cell dimensions since they do not require planar cell faces.

Consider a six-sided cell with eight arbitrary corners as shown in Figure 6a, for which the surface area vectors and cell volume must be evaluated. This figure represents the transformation of a cell in physical space into a cell in computational space. The cell centroid is located at node  $i, j, k$  with vertices at points 1, 2, 3, 4, 5, 6, 7 and 8. The sides of the cell are not necessarily planar and they represent a potential source of geometric error in the following analysis. However, this error need not be incurred, since Kordulla and Vinokur [37] have devised a method for which a cell with non-planar sides is easily and accurately evaluated by dividing each cell face into two planar triangles and the volume into six tetrahedra.

Expressions for the cell surface area and cell volume are derived in Appendix C [37]; however, some key results of the derivation are provided here. Let the surface area vectors in the positive  $\xi, \eta$  and  $\zeta$  directions be denoted by  $\vec{S}^\xi, \vec{S}^\eta$  and  $\vec{S}^\zeta$  respectively and define the Jacobian of transformation

as  $J$ , where the cell volume is  $J^{-1} = 1/J$  [3]. The components of these vectors are projections of the surface area of the side of a cell in the positive  $\xi$ ,  $\eta$  and  $\zeta$  coordinate directions. The surface area vectors and the cell volume are given as [106]:

$$\vec{S}^\xi = \vec{S}_{1234} = \frac{\xi_x}{J} \hat{\mathbf{i}} + \frac{\xi_y}{J} \hat{\mathbf{j}} + \frac{\xi_z}{J} \hat{\mathbf{k}} \quad (143)$$

$$\vec{S}^\eta = \vec{S}_{1265} = \frac{\eta_x}{J} \hat{\mathbf{i}} + \frac{\eta_y}{J} \hat{\mathbf{j}} + \frac{\eta_z}{J} \hat{\mathbf{k}} \quad (144)$$

$$\vec{S}^\zeta = \vec{S}_{1584} = \frac{\zeta_x}{J} \hat{\mathbf{i}} + \frac{\zeta_y}{J} \hat{\mathbf{j}} + \frac{\zeta_z}{J} \hat{\mathbf{k}} \quad (145)$$

$$Vol_{i,j,k} = J^{-1} = \frac{1}{3} (\vec{r}_{71}) \cdot (\vec{S}_{1265} + \vec{S}_{1584} + \vec{S}_{1234}) \quad (146)$$

where  $\xi_x, \xi_y, \xi_z, \eta_x, \eta_y, \eta_z, \zeta_x, \zeta_y$  and  $\zeta_z$  are transformation metrics and  $\vec{r}_{71}$  is the vector defining the diagonal distance between vertices 7 and 1 (see Figure 6). The numeric subscripts on  $\vec{S}$  indicate the vertices in Figure 6 which describe the cell side represented by the surface area vector.

Utilizing the relationships given in Eqs. 143 - 146, the surface integral in Eq. 139 can be placed in the following form

$$\begin{aligned} \frac{\partial}{\partial t} (\hat{\mathbf{Q}}_{i,j,k}) = & - \left[ (\hat{\mathbf{F}} - \hat{\mathbf{F}}_v)_{i+\frac{1}{2},j,k} - (\hat{\mathbf{F}} - \hat{\mathbf{F}}_v)_{i-\frac{1}{2},j,k} \right] \\ & - \left[ (\hat{\mathbf{G}} - \hat{\mathbf{G}}_v)_{i,j+\frac{1}{2},k} - (\hat{\mathbf{G}} - \hat{\mathbf{G}}_v)_{i,j-\frac{1}{2},k} \right] \\ & - \left[ (\hat{\mathbf{H}} - \hat{\mathbf{H}}_v)_{i,j,k+\frac{1}{2}} - (\hat{\mathbf{H}} - \hat{\mathbf{H}}_v)_{i,j,k-\frac{1}{2}} \right] + \hat{\mathbf{S}}_{i,j,k} \end{aligned} \quad (147)$$

where “ $\hat{\phantom{x}}$ ” denotes division by  $J$  and the  $1/2$  on the indices denotes evaluation of the flux terms at a cell interface. The inviscid flux vectors in the  $\xi$ ,  $\eta$  and  $\zeta$  directions are given as

$$\begin{aligned}
\hat{\mathbf{F}} &= \frac{|\nabla\xi|}{J} \begin{bmatrix} \bar{\rho}U \\ \bar{\rho}\tilde{u}\tilde{U} + \hat{\xi}_x\bar{p} \\ \bar{\rho}\tilde{v}\tilde{U} + \hat{\xi}_y\bar{p} \\ \bar{\rho}\tilde{w}\tilde{U} + \hat{\xi}_z\bar{p} \\ \bar{\rho}\tilde{U}\tilde{H} \\ \bar{\rho}\tilde{U}\tau_{11} \\ \bar{\rho}\tilde{U}\tau_{22} \\ \bar{\rho}\tilde{U}\tau_{33} \\ \bar{\rho}\tilde{U}\tau_{12} \\ \bar{\rho}\tilde{U}\tau_{13} \\ \bar{\rho}\tilde{U}\tau_{23} \\ \bar{\rho}\tilde{U}\epsilon \end{bmatrix} & \hat{\mathbf{G}} &= \frac{|\nabla\eta|}{J} \begin{bmatrix} \bar{\rho}\tilde{V} \\ \bar{\rho}\tilde{u}\tilde{V} + \hat{\eta}_x\bar{p} \\ \bar{\rho}\tilde{v}\tilde{V} + \hat{\eta}_y\bar{p} \\ \bar{\rho}\tilde{w}\tilde{V} + \hat{\eta}_z\bar{p} \\ \bar{\rho}\tilde{V}\tilde{H} \\ \bar{\rho}\tilde{V}\tau_{11} \\ \bar{\rho}\tilde{V}\tau_{22} \\ \bar{\rho}\tilde{V}\tau_{33} \\ \bar{\rho}\tilde{V}\tau_{12} \\ \bar{\rho}\tilde{V}\tau_{13} \\ \bar{\rho}\tilde{V}\tau_{23} \\ \bar{\rho}\tilde{V}\epsilon \end{bmatrix} \\
\hat{\mathbf{H}} &= \frac{|\nabla\zeta|}{J} \begin{bmatrix} \bar{\rho}\tilde{W} \\ \bar{\rho}\tilde{u}\tilde{W} + \hat{\zeta}_x\bar{p} \\ \bar{\rho}\tilde{v}\tilde{W} + \hat{\zeta}_y\bar{p} \\ \bar{\rho}\tilde{w}\tilde{W} + \hat{\zeta}_z\bar{p} \\ \bar{\rho}\tilde{W}\tilde{H} \\ \bar{\rho}\tilde{W}\tau_{11} \\ \bar{\rho}\tilde{W}\tau_{22} \\ \bar{\rho}\tilde{W}\tau_{33} \\ \bar{\rho}\tilde{W}\tau_{12} \\ \bar{\rho}\tilde{W}\tau_{13} \\ \bar{\rho}\tilde{W}\tau_{23} \\ \bar{\rho}\tilde{W}\epsilon \end{bmatrix}
\end{aligned} \tag{148}$$

where the contravariant velocities  $\tilde{U}$ ,  $\tilde{V}$  and  $\tilde{W}$  are defined as

$$\tilde{U} = \hat{\xi}_x\tilde{u} + \hat{\xi}_y\tilde{v} + \hat{\xi}_z\tilde{w} \tag{149}$$

$$\tilde{V} = \hat{\eta}_x\tilde{u} + \hat{\eta}_y\tilde{v} + \hat{\eta}_z\tilde{w} \tag{150}$$

$$\tilde{W} = \hat{\zeta}_x\tilde{u} + \hat{\zeta}_y\tilde{v} + \hat{\zeta}_z\tilde{w} \tag{151}$$

and the direction cosines are given as

$$\hat{m}_i = \frac{m_i}{|\nabla m|} \tag{152}$$

where  $m = \xi, \eta$  or  $\zeta$  and  $i = x, y$  or  $z$ ; and

$$\nabla m = m_x\hat{\mathbf{i}} + m_y\hat{\mathbf{j}} + m_z\hat{\mathbf{k}} \tag{153}$$

The viscous flux vectors in the  $\xi, \eta$  and  $\zeta$  directions are given as

$$\hat{\mathbf{M}}_v = \frac{|\nabla m|}{J} \begin{bmatrix} 0 \\ \hat{m}_x \hat{\tau}_{11} + \hat{m}_y \hat{\tau}_{12} + \hat{m}_z \hat{\tau}_{13} \\ \hat{m}_x \hat{\tau}_{12} + \hat{m}_y \hat{\tau}_{22} + \hat{m}_z \hat{\tau}_{23} \\ \hat{m}_x \hat{\tau}_{13} + \hat{m}_y \hat{\tau}_{23} + \hat{m}_z \hat{\tau}_{33} \\ \hat{m}_x b_1 + \hat{m}_y b_2 + \hat{m}_z b_3 \\ \hat{m}_x \tau_{11}^D + \hat{m}_y \tau_{11}^D + \hat{m}_z \tau_{11}^D \\ \hat{m}_x \tau_{22}^D + \hat{m}_y \tau_{22}^D + \hat{m}_z \tau_{22}^D \\ \hat{m}_x \tau_{33}^D + \hat{m}_y \tau_{33}^D + \hat{m}_z \tau_{33}^D \\ \hat{m}_x \tau_{12}^D + \hat{m}_y \tau_{12}^D + \hat{m}_z \tau_{12}^D \\ \hat{m}_x \tau_{13}^D + \hat{m}_y \tau_{13}^D + \hat{m}_z \tau_{13}^D \\ \hat{m}_x \tau_{23}^D + \hat{m}_y \tau_{23}^D + \hat{m}_z \tau_{23}^D \\ \hat{m}_x \epsilon_1^D + \hat{m}_y \epsilon_2^D + \hat{m}_z \epsilon_3^D \end{bmatrix} \quad (154)$$

where  $\mathbf{M}_v = \mathbf{F}_v, \mathbf{G}_v$  or  $\mathbf{H}_v$ .

The semi-discrete form of the governing equations given in Eq. 147 is not efficiently solved which numerical methods in its current form. However, if a  $\delta$  operator, defined as

$$\delta_m(\cdot) \equiv (\cdot)_{i+\frac{1}{2}} - (\cdot)_{i-\frac{1}{2}} \quad (155)$$

is applied to Eq. 147, a compact discrete form emerges which can be further manipulated into a format which is efficiently solved with numerical methods. This  $\delta$  operator is a second-order accurate spatial representation of  $\partial(\cdot)/\partial m$  at the cell centroid when  $\Delta m = 1$ . After application to Eq. 147, the compact discrete form of the governing equations is

$$\frac{\partial \hat{\mathbf{Q}}}{\partial t} + \delta_\xi (\hat{\mathbf{F}} - \hat{\mathbf{F}}_v) + \delta_\eta (\hat{\mathbf{G}} - \hat{\mathbf{G}}_v) + \delta_\zeta (\hat{\mathbf{H}} - \hat{\mathbf{H}}_v) - \hat{\mathbf{S}} = 0 \quad (156)$$

### 5.2.3 Implicit Time-Difference Formulation

Numerous sources have demonstrated that implicit time-difference formulations are significantly more robust than explicit formulations for a much wider range of flow situations [46, 47, 63, 98, 99]. This is especially true for steady-state situations where some schemes allow CFL numbers as large as 1 billion [47].

Using a backward-difference form that is first-order accurate in time, the unsteady term in Eq. 156 is expressed as



$$\frac{\Delta \hat{\mathbf{Q}}^n}{\Delta t} + \delta_\xi (\hat{\mathbf{F}} - \hat{\mathbf{F}}_v)^{n+1} + \delta_\eta (\hat{\mathbf{G}} - \hat{\mathbf{G}}_v)^{n+1} + \delta_\zeta (\hat{\mathbf{H}} - \hat{\mathbf{H}}_v)^{n+1} - \hat{\mathbf{S}}^{n+1} = 0 \quad (157)$$

where

$$\Delta \hat{\mathbf{Q}}^n \equiv \hat{\mathbf{Q}}^{n+1} - \hat{\mathbf{Q}}^n \quad (158)$$

and the superscript “ $n$ ” denotes the current time level. The introduction of this backward-difference formulation reduces the time accuracy of the ISAAC algorithm to first-order at best.

### 5.3 Discretization

The information presented in this section is a review of the algorithm development as described by Morrison [55–58] with additional details taken from works of Beam and Warming [8], Pulliam and Steger [63], Coakley [13], Hoffman and Chiang [31], Walters and Thomas [107] and Venkatakrishnan [104].

#### 5.3.1 Linearization

In order to solve Eq. 157 for  $\Delta \hat{\mathbf{Q}}^n$ , the flux vectors must be linearized in time, i.e. express Eq. 157 in terms of the original unknown  $\Delta \hat{\mathbf{Q}}^n$ . Linearization is accomplished by expanding the fluxes with a Taylor series centered about time level  $n$ . For example, the inviscid flux vector in the  $\xi$  direction is linearized as follows:

$$\hat{\mathbf{F}}^{n+1} = \hat{\mathbf{F}}^n + \frac{\partial \hat{\mathbf{F}}^n}{\partial t} \Delta t + O(\Delta t^2) \quad (159)$$

$$\hat{\mathbf{F}}^{n+1} = \hat{\mathbf{F}}^n + \frac{\partial \hat{\mathbf{F}}}{\partial \hat{\mathbf{Q}}} \frac{\partial \hat{\mathbf{Q}}}{\partial t} \Delta t + O(\Delta t^2) \quad (160)$$

$$\hat{\mathbf{F}}^{n+1} = \hat{\mathbf{F}}^n + \frac{\partial \hat{\mathbf{F}}}{\partial \hat{\mathbf{Q}}} \frac{\Delta \hat{\mathbf{Q}}}{\Delta t} \Delta t + O(\Delta t^2) \quad (161)$$

$$\hat{\mathbf{F}}^{n+1} = \hat{\mathbf{F}}^n + \mathbf{A}^n \Delta \hat{\mathbf{Q}}^n + O(\Delta t^2) \quad (162)$$

where the flux Jacobian,  $\mathbf{A}$ , is defined as  $\frac{\partial \hat{\mathbf{F}}}{\partial \hat{\mathbf{Q}}}$ . An identical process is used to linearize the remaining

flux vectors:

$$\hat{\mathbf{F}}_v^{n+1} = \hat{\mathbf{F}}_v^n + \mathbf{A}_v^n \Delta \hat{\mathbf{Q}}^n + O(\Delta t^2) \quad (163)$$

$$\hat{\mathbf{G}}^{n+1} = \hat{\mathbf{G}}^n + \mathbf{B}^n \Delta \hat{\mathbf{Q}}^n + O(\Delta t^2) \quad (164)$$

$$\hat{\mathbf{G}}_v^{n+1} = \hat{\mathbf{G}}_v^n + \mathbf{B}_v^n \Delta \hat{\mathbf{Q}}^n + O(\Delta t^2) \quad (165)$$

$$\hat{\mathbf{H}}^{n+1} = \hat{\mathbf{H}}^n + \mathbf{C}^n \Delta \hat{\mathbf{Q}}^n + O(\Delta t^2) \quad (166)$$

$$\hat{\mathbf{H}}_v^{n+1} = \hat{\mathbf{H}}_v^n + \mathbf{C}_v^n \Delta \hat{\mathbf{Q}}^n + O(\Delta t^2) \quad (167)$$

$$\hat{\mathbf{S}}^{n+1} = \hat{\mathbf{S}}^n + \mathbf{D}^n \Delta \hat{\mathbf{Q}}^n + O(\Delta t^2) \quad (168)$$

The remaining inviscid flux Jacobians are defined as

$$\mathbf{B} = \frac{\partial \hat{\mathbf{G}}}{\partial \hat{\mathbf{Q}}} \quad \mathbf{C} = \frac{\partial \hat{\mathbf{H}}}{\partial \hat{\mathbf{Q}}} \quad (169)$$

and the viscous flux Jacobians are defined as

$$\mathbf{A}_v = \frac{\partial \hat{\mathbf{F}}_v}{\partial \hat{\mathbf{Q}}} \quad \mathbf{B}_v = \frac{\partial \hat{\mathbf{G}}_v}{\partial \hat{\mathbf{Q}}} \quad \mathbf{C}_v = \frac{\partial \hat{\mathbf{H}}_v}{\partial \hat{\mathbf{Q}}} \quad (170)$$

Finally

$$\mathbf{D} = \frac{\partial \hat{\mathbf{S}}}{\partial \hat{\mathbf{Q}}} \quad (171)$$

is the flux Jacobian for the source terms. Expressions for the inviscid and viscous flux Jacobians are available in Knight [35]. The flux Jacobian for the source terms is model dependent and must be derived on an individual basis. After substitution of the linearized expressions into Eq. 157 and after some rearrangement, the governing equations are given as

$$[\mathbf{I} + \Delta t (\delta_\xi (\mathbf{A}^n - \mathbf{A}_v^n) + \delta_\eta (\mathbf{B}^n - \mathbf{B}_v^n) + \delta_\zeta (\mathbf{C}^n - \mathbf{C}_v^n) - \mathbf{D}^n)] \Delta \hat{\mathbf{Q}}^n = -\mathbf{R}^n \quad (172)$$

where  $\mathbf{I}$  is the identity matrix. The residual,  $\mathbf{R}^n$ , of the solution is defined as

$$\mathbf{R}^n \equiv \left\{ \left[ \delta_\xi (\hat{\mathbf{F}}^n - \hat{\mathbf{F}}_v^n) + \delta_\eta (\hat{\mathbf{G}}^n - \hat{\mathbf{G}}_v^n) + \delta_\zeta (\hat{\mathbf{H}}^n - \hat{\mathbf{H}}_v^n) + \hat{\mathbf{S}}^n \right] \right\} \Delta t \quad (173)$$

The residual will vanish once a steady-state solution is achieved and  $\Delta\hat{\mathbf{Q}}^n$  will equal zero.

The methods used for spatial discretization of the flux Jacobians and the evaluation of the flux terms in the residual are presented in Sections 5.3.4 and 5.3.5.

### 5.3.2 Factorization

The storage requirements needed to solve Eq. 172 for a large three-dimensional problem are prohibitive. However, by using the approximate-factorization methods of Beam and Warming [8], Morrison significantly reduced the bandwidth and rank of the matrices. The reduction is realized, because storage of an approximate solution for only one coordinate direction is required at any point in the solution process. The approximately factored form of Eq. 172 is given by Morrison as [56]:

$$\begin{aligned} & [\mathbf{I} - \Delta t \mathbf{D}] [\mathbf{I} + \Delta t \delta_\xi \mathbf{A} - \Delta t \delta_\xi \mathbf{A}_v] [\mathbf{I} + \Delta t \delta_\eta \mathbf{B} - \Delta t \delta_\eta \mathbf{B}_v] \\ & [\mathbf{I} + \Delta t \delta_\zeta \mathbf{C} - \Delta t \delta_\zeta \mathbf{C}_v] \Delta\hat{\mathbf{Q}}^n = -\mathbf{R} \end{aligned} \quad (174)$$

This equation is now split into four relatively easy to solve matrix problems. The superscript  $n$  is dropped on all terms except  $\Delta\hat{\mathbf{Q}}$  and it should be understood that all terms are evaluated at time level  $n$ .

### 5.3.3 Diagonalization

Pulliam and Steger have shown that for steady state applications, the diagonalization of approximately factored equations dramatically decreases the computational work required to solve such equations [63]. However, diagonalization of the implicit side of Eq. 174 further reduces the time accuracy of the algorithm [63].

Diagonalization of the inviscid flux Jacobians is possible because each Jacobian has real eigenvalues. Through similarity transformations, the inviscid flux Jacobians can be written as follows:

$$\mathbf{A} = \mathbf{T}_\xi \mathbf{\Lambda}_\xi \mathbf{T}_\xi^{-1} \quad \mathbf{B} = \mathbf{T}_\eta \mathbf{\Lambda}_\eta \mathbf{T}_\eta^{-1} \quad \mathbf{C} = \mathbf{T}_\zeta \mathbf{\Lambda}_\zeta \mathbf{T}_\zeta^{-1} \quad (175)$$

and the subscripts  $\xi$ ,  $\eta$  and  $\zeta$  indicate the coordinate direction the transformation matrices are associated with. The components of the similarity matrices;  $\mathbf{T}_\xi$ ,  $\mathbf{T}_\eta$  and  $\mathbf{T}_\zeta$  and the inverse of the similarity matrices;  $\mathbf{T}_\xi^{-1}$ ,  $\mathbf{T}_\eta^{-1}$  and  $\mathbf{T}_\zeta^{-1}$  are given in Appendix D.

The diagonal eigenvalue matrix is denoted by  $\Lambda$  and the elements of this matrix are the eigenvalues  $\lambda_i$ , are given by Morrison [56] as

$$\lambda_1 = \lambda_2 = \lambda_3 = \lambda_6 = \lambda_7 = \lambda_8 = \lambda_9 = \lambda_{10} = \lambda_{11} = \lambda_{12} = \tilde{U} |\nabla m| \quad (176)$$

and

$$\lambda_4 = \left[ (\tilde{U} + a) |\nabla m| \right] \quad \lambda_5 = \left[ (\tilde{U} - a) |\nabla m| \right] \quad (177)$$

In viscous calculations the diagonalization algorithm cannot be rigorously applied. However, Coakley [13] has shown that the viscous flux Jacobians can be approximated by replacing them with the matrix  $\nu_{\mathbf{M}} \mathbf{I} \delta_m$ , where  $\nu_{\mathbf{M}}$  is the largest eigenvalue of the viscous Jacobian  $\mathbf{M}_v$ ,  $\delta_m$  is the difference operator and  $m$  is the coordinate direction of the difference.

Substitution of the above expressions into Eq. 174 results in the following diagonalized, approximately factored system of equations

$$\begin{aligned} & [\mathbf{I} - \Delta t \mathbf{D}] \mathbf{T}_\xi [\mathbf{I} + \Delta t \delta_\xi (\Lambda_\xi - \nu_{\mathbf{A}_v} \mathbf{I} \delta_\xi)] \mathbf{T}_\xi^{-1} \mathbf{T}_\eta [\mathbf{I} + \Delta t \delta_\eta (\Lambda_\eta - \nu_{\mathbf{B}_v} \mathbf{I} \delta_\eta)] \quad (178) \\ & \mathbf{T}_\eta^{-1} \mathbf{T}_\zeta [\mathbf{I} + \Delta t \delta_\zeta (\Lambda_\zeta - \nu_{\mathbf{C}_v} \mathbf{I} \delta_\zeta)] \mathbf{T}_\zeta^{-1} \Delta \hat{\mathbf{Q}}^n = -\mathbf{R} \end{aligned}$$

This system of equations can be solved with a series of four sweeps of the domain as follows:

$$[\mathbf{I} - \Delta t \mathbf{D}] \Delta \hat{\mathbf{Q}}' = -\mathbf{R} \quad (179)$$

$$[\mathbf{I} + \Delta t \delta_\xi (\Lambda_\xi - \nu_{\mathbf{A}_v} \mathbf{I} \delta_\xi)] \Delta \hat{\mathbf{Q}}'' = \mathbf{T}_\xi^{-1} \Delta \hat{\mathbf{Q}}' \quad (180)$$

$$[\mathbf{I} + \Delta t \delta_\eta (\Lambda_\eta - \nu_{\mathbf{B}_v} \mathbf{I} \delta_\eta)] \Delta \hat{\mathbf{Q}}''' = \mathbf{T}_\eta^{-1} \mathbf{T}_\xi \Delta \hat{\mathbf{Q}}'' \quad (181)$$

$$[\mathbf{I} + \Delta t \delta_\zeta (\Lambda_\zeta - \nu_{\mathbf{C}_v} \mathbf{I} \delta_\zeta)] \Delta \hat{\mathbf{Q}}^{iv} = \mathbf{T}_\zeta^{-1} \mathbf{T}_\eta \Delta \hat{\mathbf{Q}}''' \quad (182)$$

$$\Delta \hat{\mathbf{Q}}^n = \mathbf{T}_\zeta \Delta \hat{\mathbf{Q}}^{iv} \quad (183)$$

$$\hat{\mathbf{Q}}^{n+1} = \hat{\mathbf{Q}}^n + \Delta \hat{\mathbf{Q}}^n \quad (184)$$

The source terms can be treated in a point implicit manner; thus, the first sweep of the

domain requires only a block inversion at each point in the flowfield. Morrison justified his implicit treatment of the source terms with a recent work by Shih and Chyu [82]. Shih and Chyu recommend including the source terms in the spatial factors rather than as a separate inversion to reduce factorization error. Evaluation of the right-hand-side of Eqs. 180 - 183 is a simple matter of matrix-vector multiplication, since analytic expressions for the transformation matrices and their inverses are available.

### 5.3.4 Spatial Discretization

Spatial discretization of the implicit side of Eq. 178 and of the residual term is performed differently. Spatial discretization of the implicit side is performed by replacing the delta operator given in Eq. 155 with a first-order accurate upwind difference operator where the upwind direction is dependent on the sign of the eigenvalue. Based upon the methods outlined in Hirsch [30], the new implicit operator is

$$\bar{\delta}_m(\cdot) \equiv \frac{1}{2\Delta m} \left[ (\cdot)_{l+1} - (\cdot)_{l-1} + \frac{|\Lambda_m|}{\Lambda_m} (2(\cdot)_l - (\cdot)_{l+1} - (\cdot)_{l-1}) \right] \quad (185)$$

where  $m$  is the coordinate direction of interest,  $l$  is the index of the cell centroid in the  $m$  direction and  $\Lambda_m$  is the largest eigenvalue of the inviscid flux Jacobian in the  $m$  direction. This operator automatically upwinds in the proper direction regardless of the sign of the eigenvalue and results in a block tri-diagonal system.

Discretization of the residual term is performed with the second-order-accurate central-difference operator defined in Eq. 155. To use this operator, the fluxes at the cell interfaces must be evaluated. The fluxes are evaluated with the Roe flux-differencing method which is presented in the next section.

### 5.3.5 Roe Flux-Differencing

Second-order accurate Roe flux-differencing is used to evaluate the fluxes at each cell

interface. This method treats the interface in each of the three coordinate directions as a locally one-dimensional Riemann problem normal to the cell interface such that the governing equation is reduced to:

$$\frac{\partial \check{\mathbf{Q}}}{\partial t} + \frac{\partial \hat{\mathbf{F}}}{\partial m} = 0 \quad (186)$$

with initial conditions of the left,  $L$ , and right,  $R$ , states given as

$$\check{\mathbf{Q}} = \begin{cases} \check{\mathbf{Q}}_L & m < 0 \\ \check{\mathbf{Q}}_R & m > 0 \end{cases} \quad (187)$$

where  $m$  is the coordinate normal to the cell interface ( $\xi$ ,  $\eta$  or  $\zeta$ ); " $\check{\cdot}$ " denotes a Roe-averaged variable (to be defined later);  $\hat{\mathbf{F}}$  is either  $\hat{\mathbf{F}}$ ,  $\hat{\mathbf{G}}$  or  $\hat{\mathbf{H}}$ ; and  $U$  is either  $U$ ,  $V$  or  $W$  depending on the coordinate direction of  $m$ . The form of the flux vectors and contravariant velocities was previously defined in Eqs. 148 - 151.

The exact solution of the Riemann problem is nonlinear, requiring an iterative process for computation. A more computationally effective procedure developed by Roe [68] was to construct the solution to the approximate, linearized problem as

$$\frac{\partial \check{\mathbf{Q}}}{\partial t} + \check{\mathbf{A}} \frac{\partial \check{\mathbf{Q}}}{\partial m} = 0 \quad (188)$$

where  $\check{\mathbf{A}}$  is the Roe averaged flux Jacobian  $\frac{\partial \hat{\mathbf{F}}}{\partial \check{\mathbf{Q}}}$  and is evaluated at an averaged state about the cell interface which satisfies the jump condition

$$\hat{\mathbf{F}}_R - \hat{\mathbf{F}}_L = \check{\mathbf{A}} (\check{\mathbf{Q}}_R - \check{\mathbf{Q}}_L) \quad (189)$$

at the cell interface. Here,  $\hat{\mathbf{F}}_R$  and  $\hat{\mathbf{F}}_L$  are the fluxes at a cell interface when the interface is approached from the left or the right. These fluxes are evaluated with variable extrapolation methods described in Section 5.3.6.

Walters and Thomas [107] have shown that the interface flux can be written as the average of the interface fluxes calculated from the left state crossing negative running waves and the right state

crossing positive running waves, as

$$\hat{\mathbf{F}}_{i+\frac{1}{2}} = \frac{1}{2} \left[ \hat{\mathbf{F}}_R + \hat{\mathbf{F}}_L - \left| \check{\mathbf{A}} \right| \left( \check{\mathbf{Q}}_R - \check{\mathbf{Q}}_L \right) \right] \quad (190)$$

This may be written in a more computationally efficient manner as

$$\hat{\mathbf{F}}_{i+\frac{1}{2}} = \frac{1}{2} \left[ \hat{\mathbf{F}}_R + \hat{\mathbf{F}}_L - \sum \left| \check{\Delta} \mathbf{F} \right| \right] \quad (191)$$

where  $\check{\Delta}(\cdot) = (\cdot)_R - (\cdot)_L$ . The flux differences,  $\check{\Delta} \mathbf{F}$ , are written as [56]

$$\left| \check{\Delta} \mathbf{F}_{\tilde{U}} \right| = \frac{\left| \check{\Lambda}_{\tilde{U}} \right|}{J} \left[ \left( \check{\Delta} \bar{\rho} - \frac{\check{\Delta} \bar{p}}{\check{a}^2} \right) \begin{pmatrix} 1 \\ \check{u} \\ \check{v} \\ \check{w} \\ \frac{\check{q}^2}{2} + \check{K} \\ \check{\tau}_{11} \\ \check{\tau}_{22} \\ \check{\tau}_{33} \\ \check{\tau}_{12} \\ \check{\tau}_{13} \\ \check{\tau}_{23} \\ \check{\epsilon} \end{pmatrix} + \bar{\rho} \begin{pmatrix} 0 \\ \check{\Delta} \check{u} - \hat{m}_x \check{\Delta} \check{U} \\ \check{\Delta} \check{v} - \hat{m}_y \check{\Delta} \check{U} \\ \check{\Delta} \check{w} - \hat{m}_z \check{\Delta} \check{U} \\ \check{u} \check{\Delta} \check{u} + \check{v} \check{\Delta} \check{v} + \check{w} \check{\Delta} \check{w} \\ - \check{U} \check{\Delta} \check{U} + \check{\Delta} \check{K} \\ \check{\Delta} \tau_{11} \\ \check{\Delta} \tau_{22} \\ \check{\Delta} \tau_{33} \\ \check{\Delta} \tau_{12} \\ \check{\Delta} \tau_{13} \\ \check{\Delta} \tau_{23} \\ \check{\Delta} \epsilon \end{pmatrix} \right] \quad (192)$$

$$\left| \check{\Delta} \mathbf{F}_{\tilde{U} \pm a} \right| = \frac{\left| \check{\Lambda}_{\tilde{U} \pm a} \right|}{J} \left( \frac{\check{\Delta} \bar{p} \pm \rho \check{a} \check{\Delta} \check{U}}{2 \check{a}^2} \right) \begin{pmatrix} 1 \\ \check{u} \pm \hat{m}_x \check{a} \\ \check{v} \pm \hat{m}_y \check{a} \\ \check{w} \pm \hat{m}_z \check{a} \\ \check{H} \pm \check{U} \check{a} \\ \check{\tau}_{11} \\ \check{\tau}_{22} \\ \check{\tau}_{33} \\ \check{\tau}_{12} \\ \check{\tau}_{13} \\ \check{\tau}_{23} \\ \check{\epsilon} \end{pmatrix} \quad (193)$$

The Roe averaged variables that satisfy Eq. 189 and used in Eqs. 192 and 193 are given in

Walters and Thomas [107] and Morrison [56] as

$$\check{\rho} = \sqrt{\bar{\rho}_L \bar{\rho}_R} \quad (194)$$

$$\check{H} = \frac{\sqrt{\bar{\rho}_L} \check{H}_L + \sqrt{\bar{\rho}_R} \check{H}_R}{\sqrt{\bar{\rho}_L} + \sqrt{\bar{\rho}_R}} \quad (195)$$

$$\check{u} = \frac{\sqrt{\bar{\rho}_L} \check{u}_L + \sqrt{\bar{\rho}_R} \check{u}_R}{\sqrt{\bar{\rho}_L} + \sqrt{\bar{\rho}_R}} \quad (196)$$

$$\check{v} = \frac{\sqrt{\bar{\rho}_L} \check{v}_L + \sqrt{\bar{\rho}_R} \check{v}_R}{\sqrt{\bar{\rho}_L} + \sqrt{\bar{\rho}_R}} \quad (197)$$

$$\check{w} = \frac{\sqrt{\bar{\rho}_L} \check{w}_L + \sqrt{\bar{\rho}_R} \check{w}_R}{\sqrt{\bar{\rho}_L} + \sqrt{\bar{\rho}_R}} \quad (198)$$

$$\check{\tau}_{11} = \frac{\sqrt{\bar{\rho}_L} \tau_{11_L} + \sqrt{\bar{\rho}_R} \tau_{11_R}}{\sqrt{\bar{\rho}_L} + \sqrt{\bar{\rho}_R}} \quad (199)$$

$$\check{\tau}_{22} = \frac{\sqrt{\bar{\rho}_L} \tau_{22_L} + \sqrt{\bar{\rho}_R} \tau_{22_R}}{\sqrt{\bar{\rho}_L} + \sqrt{\bar{\rho}_R}} \quad (200)$$

$$\check{\tau}_{33} = \frac{\sqrt{\bar{\rho}_L} \tau_{33_L} + \sqrt{\bar{\rho}_R} \tau_{33_R}}{\sqrt{\bar{\rho}_L} + \sqrt{\bar{\rho}_R}} \quad (201)$$

$$\check{\tau}_{12} = \frac{\sqrt{\bar{\rho}_L} \tau_{12_L} + \sqrt{\bar{\rho}_R} \tau_{12_R}}{\sqrt{\bar{\rho}_L} + \sqrt{\bar{\rho}_R}} \quad (202)$$

$$\check{\tau}_{13} = \frac{\sqrt{\bar{\rho}_L} \tau_{13_L} + \sqrt{\bar{\rho}_R} \tau_{13_R}}{\sqrt{\bar{\rho}_L} + \sqrt{\bar{\rho}_R}} \quad (203)$$

$$\check{\tau}_{23} = \frac{\sqrt{\bar{\rho}_L} \tau_{23_L} + \sqrt{\bar{\rho}_R} \tau_{23_R}}{\sqrt{\bar{\rho}_L} + \sqrt{\bar{\rho}_R}} \quad (204)$$

$$\check{\epsilon} = \frac{\sqrt{\bar{\rho}_L} \epsilon_L + \sqrt{\bar{\rho}_R} \epsilon_R}{\sqrt{\bar{\rho}_L} + \sqrt{\bar{\rho}_R}} \quad (205)$$

$$\check{q}^2 = \check{u}^2 + \check{v}^2 + \check{w}^2 \quad (206)$$



$$\check{a}^2 = (\gamma - 1) \left( \check{H} - \frac{\check{q}^2}{2} - \check{K} \right) \quad (207)$$

$$\tilde{U} = \hat{m}_x \check{u} + \hat{m}_y \check{v} + \hat{m}_z \check{w} \quad (208)$$

where the subscripts  $L$  and  $R$  denote interface values of variables extrapolated from the left and right of the interface.

### 5.3.6 Variable Extrapolation

Morrison used Venkatakrishnan's [104] flux limiter for variable extrapolation and oscillation suppression at discontinuities. This limiter is based on the  $\kappa = 1/3$  scheme which results in a third order-accurate, upwind biased scheme. Venkatakrishnan states this limiter is differentiable and does not react to very small oscillations in smooth regions [104]. Rather, this limiter has a limiting effect only in non-smooth regions which give it the added advantage of not clipping smooth extrema in the solution.

For any variable  $B$ , the Venkatakrishnan limiter is given as

$$B_{L_{i+1/2}} = B_i + 1/2 \delta_{1/3} \quad (209)$$

$$\delta_{1/3} = \frac{(2a^2 + \varepsilon^2) b + (b^2 + 2\varepsilon^2) a}{2a^2 - ab + 2b^2 + 3\varepsilon^2} \quad (210)$$

where

$$a = B_{i+1} - B_i \quad b = B_i - B_{i-1} \quad (211)$$

and  $\varepsilon^2$  is a small value used to prevent division by zero and is set to  $1 \times 10^{-8}$  in this algorithm. For  $B_{R_{i-1/2}}$  the forms of  $a$  and  $b$  are reversed such that

$$a = B_i - B_{i-1} \quad b = B_{i+1} - B_i \quad (212)$$

### 5.3.7 Gradient Theorem

The viscous flux terms and the source terms each contain spatial derivatives which must be

evaluated at the cell interfaces. These derivative can be approximated with the gradient theorem by integrating around an auxiliary cell centered at the computational cell interfaces [62]. If  $\varphi$  represents a scalar field, then a vector relationship is given by the gradient theorem as [4]

$$\oint_S \varphi d\vec{S} \equiv \int_{Vol} \nabla \varphi dVol \quad (213)$$

where  $\vec{S} = (S_x^\xi + S_x^\eta + S_x^\zeta) \hat{\mathbf{i}} + (S_y^\xi + S_y^\eta + S_y^\zeta) \hat{\mathbf{j}} + (S_z^\xi + S_z^\eta + S_z^\zeta) \hat{\mathbf{k}}$ , and  $\nabla$  is the gradient operator. Thus for a closed volume element, this equation can be written as

$$\begin{aligned} \frac{\partial \varphi}{\partial \xi} \hat{\mathbf{i}} + \frac{\partial \varphi}{\partial \eta} \hat{\mathbf{j}} + \frac{\partial \varphi}{\partial \zeta} \hat{\mathbf{k}} = \\ \frac{1}{Vol} \sum_{s=1}^6 \left[ \varphi (S_x^\xi + S_x^\eta + S_x^\zeta) \hat{\mathbf{i}} + \varphi (S_y^\xi + S_y^\eta + S_y^\zeta) \hat{\mathbf{j}} + \varphi (S_z^\xi + S_z^\eta + S_z^\zeta) \hat{\mathbf{k}} \right] \end{aligned} \quad (214)$$

where the summation indicates summation over the six sides,  $s$ , of the cell. Setting the vector components equal to each other results in

$$\frac{\partial \varphi}{\partial \xi} = \frac{1}{Vol} \sum_{s=1}^6 \varphi (S_x^\xi + S_x^\eta + S_x^\zeta) \quad (215)$$

$$\frac{\partial \varphi}{\partial \eta} = \frac{1}{Vol} \sum_{s=1}^6 \varphi (S_y^\xi + S_y^\eta + S_y^\zeta) \quad (216)$$

$$\frac{\partial \varphi}{\partial \zeta} = \frac{1}{Vol} \sum_{s=1}^6 \varphi (S_z^\xi + S_z^\eta + S_z^\zeta) \quad (217)$$

Flow variable values required at these interfaces are obtained from arithmetic averages of neighboring cell averages.

## 5.4 Non-Dimensionalization

Non-dimensional quantities are used throughout the remainder of this document. Unless otherwise stated, the following non-dimensionalizations are used:

$$U = \frac{\tilde{u}}{a_\infty} \quad V = \frac{\tilde{v}}{a_\infty} \quad W = \frac{\tilde{w}}{a_\infty}$$

$$\begin{aligned}
E &= \frac{\tilde{E}}{a_\infty^2} & K &= \frac{K_d}{a_\infty^2} & \tau_{ij} &= \frac{\tau_{ijd}}{a_\infty^2} \\
P &= \frac{\bar{p}_d}{p_\infty} & \rho &= \frac{\bar{\rho}_d}{\rho_\infty} & T &= \frac{T_d}{T_\infty} \\
x/l &= \frac{x_d}{l} & y/l &= \frac{y_d}{l} & z/l &= \frac{z_d}{l} \\
\bar{\mu} &= \frac{\bar{\mu}_d}{\mu_\infty} & \epsilon &= \frac{\epsilon_d}{\mu_\infty a_\infty^2}
\end{aligned} \tag{218}$$

where  $a$  is speed of sound,  $\infty$  denotes a freestream quantity, the subscript  $d$  denotes a dimensional quantity and  $l$  is the reference length. Note, the energy and turbulence quantities are specific, meaning the density is not included in the quantity.

## Chapter 6 - Two-Dimensional Analysis and Results

### 6.1 Introduction

In this chapter, a two part process for the validation of the ZSGS RSTM in two-dimensions is presented. The first part of the investigation attempts to validate the ZSGS RSTM for a flowfield with sonic injection into a supersonic inflow. This is accomplished by comparing numerical results from three turbulence models; the ZSGS RSTM, the ZSGS  $K - \epsilon$  model and the Jones-Launder  $K - \epsilon$  model [65]; to experimental data from the slot injection experiments of Spaid and Zukoski [88] and Aso et al. [6]. The second part of this investigation validates the ZSGS RSTM for the supersonic injection configuration used by Tucker [100]. This is accomplished by numerically simulating Tucker's configuration with the ZSGS RSTM and ZSGS  $K - \epsilon$  model and then comparing the numerical predictions from the two turbulence models to each other and to experimental data.

#### 6.1.1 General Flowfield Description

A typical two-dimensional flowfield generated by sonic injection is characterized in Figure 7. As discussed in Section 1.1, when an underexpanded fluid is injected normal to the freestream inflow, the injectant penetrates the turbulent boundary-layer and causes a system of shock/boundary-layer interactions and recirculation regions to form fore and aft of the nozzle. In the inviscid region upstream of the nozzle, a jet induced shock forms due to blockage of the flow and the subsequent adverse pressure gradient causes boundary-layer separation. In the region immediately upstream of the nozzle, a recirculation region consisting of counter-rotating primary and secondary upstream vortices (PUV and SUV respectively) are present. For some cases examined, a tertiary upstream vortex (TUV) is predicted between the surface of the plate and the PUV. Slightly upstream of the boundary-layer separation point, the boundary-layer displacement of the vortices causes a separation shock to form. Between the PUV and the separation shock is a sonic surface which has flow displacement characteristics similar to a compression ramp in a supersonic flow [88]. Upon exiting

the nozzle, expansion of the jet is followed by a rapid decrease in the local pressure. This results in a normal shock within the plume, and thus a sonic surface and a Mach disk forms around the jet plume. Downstream of the jet, the flow is turned parallel to the inflow resulting in a recompression shock and a corresponding separated, recirculation region behind the nozzle. This region consists of counter-rotating primary and secondary downstream vortices (PDV and SDV respectively).

The effects the primary and secondary vortices upstream and downstream of the jet have on the surface pressure distribution are shown in Figure 8. The pressure profile shown in this figure was computed with the ZSGS RSTM for the Spaid and Zukoski configuration with  $p_{inj}/p_{\infty} = 63.50$ . The details of how these results were obtained are discussed in Section 6.2.2. Depicted in this figure are five distinct regions within the surface static-pressure profile. Spaid and Zukoski [88] report a steep rise in pressure (region 1) as a result of the boundary-layer separation and the separation shock formation. This pressure rise is followed by a reduction in the pressure gradient upstream of the jet (region 2). The behavior of the pressure in region 2 is a result of the relatively constant flow conditions on the lower side of the PUV. The reduction of the pressure gradient is followed by a pressure spike (region 3) which is associated with the SUV. Immediately downstream of the jet is a large pressure well (region 4) with two subregions contained therein. These subregions are not identified by Spaid and Zukoski, but are present in the results of the numerical simulations. The first subregion is a slight pressure rise associated with the leading edge of the PDV. The second subregion is a pressure drop associated with the SDV. The pressure well is followed by a pressure hump (region 5) associated with the trailing edge of the PDV where boundary-layer reattachment occurs.

The two-dimensional flowfield described above has many similarities to flow past a forward facing step and to flow over a compression ramp. Data presented by Sterrett and Holloway [96] indicate that if the step height and jet penetration distance is adjusted so that the separation lengths

of the two flowfields are approximately the same, the flowfield produced by a forward-facing step is the same as the upstream flowfield produced by a jet. Spaid and Zukoski [88] reported that shock boundary-layer structures seen upstream of the jet induced separation region are similar to those seen in compression ramps. Furthermore, for the cases they examined, they found that the inclination angle of the sonic surface is approximately  $13^\circ$  and that the pressure rise near the separation point was approximately equivalent to the pressure rise obtained by turning an inviscid flow through the same angle. Thus, the sonic surface is analogous to the surface of a compression ramp.

### **6.1.2 Overexpansion, Underexpansion and the Concept of Effective Back Pressure**

The effects of overexpansion and underexpansion on the structure of the plume are discussed extensively in this chapter. Overexpansion and underexpansion are best defined with respect to the supersonic exhaust of a nozzle and a surrounding flowfield of stagnant air. The pressure of the surrounding air is defined as the back pressure,  $p_b$  [4]. When the pressure of the exhaust,  $p_{ex}$ , and  $p_b$  are equal, neither shocks nor expansion waves form in the plume and streamlines of the exhaust are normal to the exit plane of the nozzle, thus, the plume is said to be structureless [76]. When  $p_b < p_{ex}$ , the jet is underexpanded and expansion waves form at the jet exit. Streamlines of the underexpanded exhaust move away from the centerline of the nozzle, but further downstream, they turn back in towards the centerline as the expansion waves reflect off the jet boundary forming compression waves. These compression waves may converge to form a shock in the exhaust plume [28]. When  $p_b > p_{ex}$ , the jet is overexpanded and a pressure adjustment in the plume is made through a series of oblique shocks, expansion waves and compression waves. This series of compression and expansion of the exhaust forms a distinctive diamond pattern in the plume. Streamlines of the overexpanded exhaust move in towards the nozzle centerline until they are turned back out by the expansion waves [28].

In TJISF applications, the total pressure loss of the injectant and the surrounding flow is

determined by the severity of the shocks caused by pressure equalization of the injectant [76]. Thus, the structureless plume associated with “matched” exhaust and back pressures is the optimum condition. However, matching  $p_{ex}$  to  $p_b$  is not possible in TJISE, since  $p_b$  upstream of the jet is different than  $p_b$  downstream of the jet. Schetz and Billig [76] state that there is some combination of the two pressures, or an effective back pressure,  $p_{b_{eff}}$ , such that the structure in the plume is a minimum. An analysis of the effects different inject-to-inflow pressure ratios have on the plume structure is conducted in Section 6.3.2.

## 6.2 Sonic Injection Configurations

A schematic of Spaid and Zukoski's [88] experimental apparatus is shown in Figure 9. The apparatus consisted of a flat-plate with a sharp leading edge located a distance  $l = 22.86cm$  upstream of the center line of the nozzle. This plate was placed in a wind tunnel test section  $51cm$  long and  $45cm$  wide. A sonic jet of gas was injected, normal to the inflow through the throat of a converging nozzle  $0.02667cm$  wide and  $15.24cm$  long in the transverse direction. A  $14.6cm$  gap was left between the edges of the slot and the tunnel wall. End plates with glass inserts were mounted on either side of the slot to insure two-dimensionality of the flowfield. The experiments were conducted with a test section Mach number of 3.50. Measured quantities consisted of test-section mean flow parameters, jet-reservoir mean flow parameters, and static-pressure distributions at the surface of the plate around the jet. Shadow graphs and surface static-pressure profiles indicated the flow was fully turbulent upstream of the jet and free of shocks between the plate leading edge and the separation shock. Spaid and Zukoski also reported that without the plates at the edges of the slot (see Figure 9) there were measurable three-dimensional effects. The three-dimensional relaxation of the flow resulted in reduced maximum values of the surface static-pressure and caused the upstream separation point to move closer to the slot.

This data set is useful for turbulence model validation as Spaid and Zukoski [88] reported very

smooth and consistent pressure profile data and used a sufficient number of pressure taps to capture the pressure spike upstream of the jet and the pressure well downstream of the jet. Furthermore, two-dimensionality of the flow was enhanced by the addition of end plates on both sides of the jet slot.

Aso et al. [6] used a similar experimental configuration to conduct their experiments. Their configuration, shown in Figure 10, consisted of a flat-plate with a sharp leading edge located  $l = 33.0\text{cm}$  upstream of the centerline of the slot in a  $15 \times 15\text{cm}$  test section operating at Mach 3.75. They also injected a sonic jet of gas normal to the external flow through the surface of the model. A converging nozzle with a throat measuring  $1.0\text{mm}$  with a transverse length of  $13.0\text{cm}$  was used in this configuration. This transverse length left a gap of  $1.0\text{cm}$  between the edges of the slot and the test section wall. Measured quantities consisted of test-section mean flow parameters, jet-reservoir mean flow parameters, static-pressure distributions at the surface of the plate around the jet, jet penetration height,  $h$ , and boundary-layer separation distance from the jet,  $x_{sep}$  (see Figure 7).

The Aso et al. configuration was simulated numerically by Rizzetta [65] with the Jones-Launder  $K - \epsilon$  model [33]. In this simulation, Rizzetta used the Sarkar et al. [74] compressibility correction [72] to model the compressible turbulent dissipation rate in the kinetic energy equation, but did not include  $K$  in the total energy equation. Rizzetta reported relatively good agreement with the experimental surface pressure in regions 1 and 2, but the Jones-Launder model consistently over predicted the peak pressure in region 3.

Observations about the quality of simulations conducted with the Jones-Launder  $K - \epsilon$  model may be misleading since there are a number of deficiencies in the data reported by Aso et al. [6]. These deficiencies are evident from the choppy nature of the static-pressure distributions upstream of the separation point and suggests that the flow leading up to the jet is unstable or that there are shock/boundary-layer interactions elsewhere on the plate. Furthermore, the number of pressure



taps used to collect the data was insufficient to capture the pressure spike upstream of the jet or the pressure well downstream of the jet. These deficiencies combined with the lack of end plates to ensure two-dimensionality of the flow renders this data set less than ideal for turbulence model validation.

### 6.2.1 Boundary Conditions and Computational Grid

The dimensions of the computational grid used for both of these configurations was determined through a grid resolution study. The results of this study and a schematic of the grid are found in Section E2.1.

Although the grid used from this study is two-dimensional, the formulation of the finite-volume algorithm requires that every grid have a finite width as well as a length and height. Thus, side wall boundary conditions must also be specified.

All of the numerical simulation results discussed in Section 6.2 are based on the boundary conditions listed in Table 1. The methods used to implement each of these boundary conditions are presented in Section E.3.1. Table 2 is a summary of the mean flow parameters and slot widths used during this study.

Table 1. Two-dimensional sonic injection boundary conditions

Plane	Boundary Condition
Inflow	Listed in Table 2
Outflow	Extrapolation
Left side	Extrapolation
Right side	Extrapolation
Top	Tangency
Bottom	Viscous wall
Jet	Two-dimensional jet, 3 cells

Table 2. Two-dimensional sonic injection mean flow parameters

	Aso et al.	Spaid and Zukoski
$M_\infty$	3.75	3.5
$p_{t_\infty}$	$12 \times 10^5$ Pa	$2.4 \times 10^5$ Pa
$p_\infty$	11090 Pa	3145 Pa
$T_\infty$	78.43 K	86.5 K
$a_\infty$	177.5 m/s	186.4 m/s
$Re/m$	$62.73 \times 10^6$	$13.4 \times 10^6$
$M_{inj}$	1.0	1.0
$p_{inj}/p_\infty$	4.86, 10.29, 17.72, 25.15	8.74, 17.12, 42.79, 63.50
$T_{inj}$	249 K	298 K
$u_{inj}$	0 m/s	0 m/s
$v_{inj}$	316.3 m/s	346.0 m/s
$w_{inj}$	0 m/s	0 m/s
Slot width	1.0mm	0.2667mm

### 6.2.2 Pressure Profile Data

In this section the experimentally measured values of the surface static pressure for Aso et al.'s configuration is compared to numerical predictions from the two ZSGS models and to predictions reported by Rizzetta [65] for the Jones-Launder  $K - \epsilon$  model.

It was noted in Section 6.2, that the number of pressure taps used by Aso et al. was insufficient to capture all of the characteristics of the surface pressure profile. The experimental pressure data shown in Figures 11 - 14, reveal that only the measurements made at the largest static pressure ratio (Figure 14) captured the pressure rise just upstream of the jet. Also, the pressure measurements for the smallest static pressure ratio did not capture the pressure well downstream of the jet (Figure 11). Furthermore, the surface static pressure ratio ( $p_{wall}/p_\infty$ ) upstream of the separation point is greater than unity for all of the pressure ratios investigated. This suggests that the shock off of the tip of the plate increased the downstream static pressure and was not counted for in the scaling of the data.

Despite the shortcomings of this data set, flowfield simulations of the four static pressure ratios listed in Table 2 were computed using the ZSGS RSTM and ZSGS  $K - \epsilon$  models. Resultant

surface static pressure distributions for these simulations were compared to experimental data and to Rizzetta's [65] computations with the Jones-Launder  $K - \epsilon$  model in Figures 11 - 14. The Jones-Launder model had good agreement with the pressure profiles in region 1 at the two higher pressure ratios, while simulations with the two ZSGS models had good agreement with the pressure profiles in region 1 at the two lower pressure ratios. All of the models over predicted the maximum pressure in region 2 and the peak pressure in region 3. However, the ZSGS RSTM model predicted pressure values much closer to the experimental data than either of the  $K - \epsilon$  models. None of the predicted values from the models were in good agreement with the experimental data in regions 4 and 5. However, in this region, the predicted values of the Jones-Launder  $K - \epsilon$  model were in better agreement with experimental values than the results of either ZSGS model.

The predictions of the ZSGS models for  $x_{sep}$  and  $h$  were in better agreement with the experimental data at the lower pressure ratios than they were at the higher pressure ratios, however, the opposite trend was seen for the Jones-Launder  $K - \epsilon$  model. The trends exhibited by the models are summarized in Figure 15 and in this figure the trends indicate that the ZSGS models predictions were more accurate than those of the Jones-Launder  $K - \epsilon$  model at lower pressure ratios. Furthermore, it was seen that the Jones-Launder  $K - \epsilon$  model predictions were more accurate than either of the ZSGS models at the higher pressure ratios. In Figure 15, the boundary-layer separation distance from the jet,  $x_{sep}$ , was plotted against  $p_{inj}/p_{\infty}$ . Consistent with the methodology used by Aso et al., the location of  $x_{sep}$  was approximated by the intersection of a line drawn tangent to the data defining region 1 with the line  $p_{wall}/p_{\infty} = 1$ . At the two lower pressure ratios, the ZSGS models accurately predicted the experimentally observed separation point: within 5% for the ZSGS RSTM and within 10% for the ZSGS  $K - \epsilon$  model. The predictions by the Jones-Launder  $K - \epsilon$  model at these two pressure ratios had differences from the experimental data of 18% or more. At the two higher pressure ratios, the results of both ZSGS models became progressively poorer, while

the results of the Jones-Launder model improved.

The jet plume height,  $h$ , with respect to  $p_{inj}/p_{\infty}$  is of vital interest to designers of SCRAMjet combustors and it has a direct impact on mixing efficiency [60]. Thus, a comparison of  $h$  and  $p_{inj}/p_{\infty}$  was also included in Figure 15. The Jones-Launder model results were nearly identical to the experimental data, while the differences from the experimental results for the two ZSGS model ranged from a low of 21% at the highest pressure ratio to a high of 83% at the lowest pressure ratio.

The large discrepancies of the ZSGS models may be a result of the ambiguity of how the plume height was measured. Although not explicitly stated, Aso et al. [6] implied, through their Figure 5, that  $h$  was defined as the point where the sonic surface upstream of the jet intersected the Mach disk. On the other hand, the data Rizzetta reported, implied he measured the height from a flat point on the sonic disk.

The RSTM predictions shown in Figure 16 show that the maximum height of the Mach disk was not necessarily a well defined point, contrary to the implications of References [5, 6, 65, 88]. There are at least three possible places in the plume which can be taken as the maximum plume height. The height denoted by  $h_1$  in Figure 16 is the height apparently used by Rizzetta and this height provided the best match of the ZSGS simulation results to the experimental data reported by Aso et al. The contour plots show this point corresponds to a flat point in the Mach disk for  $p_{inj}/p_{\infty} = 4.86$  and to the lower limit of the Mach disk for  $p_{inj}/p_{\infty} = 25.15$ . Another point where the plume height can be measured from is the height defined by  $h_2$ . This height is measured from the upper most flat part of the Mach disk. The third location where the plume height may be measured from is defined by  $h_3$ . This is the point that Aso et al. indicated they used in their measurements. Using this point as a reference creates problems at higher pressure ratios, since the Mach disk does not necessarily completely cross the top of the plume. Thus, the point where the barrel shock and Mach disk intersect is not defined. All of these definitions for the plume height can be argued as the

right one. However,  $h_1$  is used in this study because its values have the agreement with the data reported by Aso et al.

For the most part, all three models had poor agreement with the experimental data and much of the disagreement is attributed to deficiencies in the experimental configuration, which likely led to three-dimensional effects in the flowfield and strong leading edge shocks. The supposition of three-dimensional effects is consistent with the results shown by Spaid and Zukoski [88], when the end plates were removed. Specifically, the boundary-layer separation point moves closer to the nozzle and peak pressure in region 3 decreases.

Spaid and Zukoski's data provided a better representation of the surface conditions than the data reported by Aso et al. By using 92 pressure taps, Spaid and Zukoski captured the pressure spike in region 3 for all but the lowest pressure ratio (8.743) and captured the pressure-well in region 4 at all four pressure ratios. As evidenced by the smooth transition from the undisturbed freestream flow to the boundary-layer separation point, the upstream flowfield appeared to be fully turbulent and free of shock/boundary-layer interactions.

Numerical simulations with the mean flow conditions listed in Table 2 for Spaid and Zukoski's [88] configuration were performed with both ZSGS turbulence model and numerical results of the surface static pressure distributions and experimental data are compared in Figures 17 - 20.

The computational results of the two ZSGS models compare very well to the experimental data at the three lower pressure ratios. At pressure ratios of 8.743 and 17.117 (Figures 17 and 18 respectively) the RSTM results are nearly identical to experimental results while the  $K - \epsilon$  results are within 10% of experimental data at any given location on the pressure curve. However, as with Aso et al.'s configuration, differences between the numerical results and experimental data increase as the pressure ratio increases. At a pressure ratio of 42.79 (Figure 19), both models begin to over predict the pressure in regions 2 and 3. At the pressure peak, computed results are in excess of

experimental data by 9% for RSTM and 18% for  $K - \epsilon$ . However, both models continue to have good agreement with experimental data in regions 4 and 5. At a pressure ratio of 63.5 (Figure 20), the accuracy of the predicted location for  $x_{sep}$  begins to deteriorate and both models significantly over predict the pressure in regions 2 and 3. Furthermore, the numerical predictions downstream of the jet (regions 4 and 5) begin to differ from the experimental results. As with the lower pressure ratios, the RSTM predictions are in better agreement upstream of the jet with experimental values than the  $K - \epsilon$  predictions. However, in the flowfield regions downstream of the jet,  $K - \epsilon$  predictions are in better agreement with experimental values than are the RSTM predictions for both of the higher pressure ratios.

As with the Aso et al. configuration, the ZSGS models predictions for  $x_{sep}$  and  $h$  are in better agreement with the experimental data at the lower pressure ratios than they are at the higher pressure ratios and the trends exhibited by the models are summarized in Figure 21. At the three lower pressure ratios, the predicted and experimentally measured values for  $x_{sep}$  are in good agreement, within 15% for both models. However, at the pressure ratio of 63.5, computed values of  $x_{sep}$  are relatively poor; differences are within 24% for RSTM and 28% for  $K - \epsilon$ . Also reported in Figure 21 are the plume heights predicted by the two models. The predictions are nearly identical; however, these results cannot be compared with experimental data, since Spaid and Zukoski do not report values for this parameter.

Over the course of their experiments, Spaid and Zukoski [88] made the observation that boundary separation point occurs about four plume heights upstream of the slot. This phenomenon is also predicted by both ZSGS models for both the Spaid and Zukoski, and the Aso et al. configurations (Figure 22). Figure 22 is a plot of  $x_{sep}$  versus  $h$  for the two ZSGS models for both configurations examined. Also shown in this figure are linear fits of the computational data at each of the four pressure ratios. Table 3 summarizes the slopes of these linear fits and shows that the

computational results are consistent with Spaid and Zukoski's observation. These results show that regardless of the configuration, the slopes predicted by RSTM were closer to four than the slopes predicted by the  $K - \epsilon$  model.

Table 3. Slope of  $x_{sep}/h$  linear fit

Model	Spaid and Zukoski	Aso et al.
ZSGS RSTM	4.13	3.73
ZSGS $K - \epsilon$	4.41	3.55

### 6.2.3 Turbulence Data

It is seen above that  $K - \epsilon$  models are generally satisfactory for the computation of surface pressure values. However, turbulent quantities are also of significant interest since they directly affect heat transfer rates and shear forces. Therefore, predicted values of selected flow variables and derived quantities from the ZSGS  $K - \epsilon$  model are now compared to those predicted by the ZSGS RSTM. Of the simulations discussed in the previous section, the best agreement with experimental data is obtained for the Spaid and Zukoski configuration with  $p_{inj}/p_{\infty} = 17.117$ ; therefore, this configuration is used as a basis for comparison between the ZSGS  $K - \epsilon$  model and the ZSGS RSTM.

The analysis of the turbulence quantities begins with an evaluation of the law-of-the-wall predictions from the two models. In this analysis, predicted values of  $u^+$  and  $y^+$  are compared to theoretical values for the law-of-the-wall. This is followed by a discussion of cross-sectional Reynolds stress profiles in terms of characteristic flowfield structures. The streamwise stations shown in Figure 23 encompass flat-plate turbulent flow conditions upstream of the jet, vortex and shock/boundary-layer interactions upstream of the slot, and vortex/jet wake interactions downstream of the slot. Finally, a global characterization of the flowfield surrounding the slot is presented with

contour plots of the Reynolds stresses,  $z$  component of vorticity,  $\omega_z$ , and the ratio of  $K$  to  $E$ .

### 6.2.3.1 Flat-Plate Validation

All turbulence models simulating wall bounded flows must adhere to the law-of-the-wall when modeling a fully turbulent flow past a flat-plate [109]. The law-of-the-wall requires the nondimensional inner variables  $u^+$  and  $y^+$  equal each other in the linear sublayer. These nondimensional inner variables terms are defined in White [108] as

$$u^+ = \frac{\bar{u}}{v^*} \quad y^+ = \frac{yv^*}{\nu_w} \quad v^* = \left( \frac{\mu_w}{\rho_w} \frac{\partial \bar{u}}{\partial y} \Big|_w \right)^{1/2} \quad (219)$$

Between the laminar sublayer and the turbulent boundary-layer is the overlap region where transition between the inner and outer regions occurs. For low speed flows, the overlap region is modeled as

$$u^+ = \frac{1}{\kappa} \ln y^+ + B \quad (220)$$

where  $\kappa$  and  $B$  are near-universal constants for turbulent flow past smooth, impermeable walls. The currently accepted values for these terms are  $\kappa = 0.41$  and  $B = 5.0$  [108].

Compressibility effects in the overlap region are accounted for with one of two methods. The first method, is the van Driest II coordinate transformation [101]. This transformation maps compressible flow data to the incompressible domain. The second method is White's compressibility correction formula [108]. This method performs the opposite transformation of van Driest II, i.e., it modifies the incompressible relations for compressibility effects.

Law-of-the-wall validation of the ZSGS models are extensively documented by Zhang et al. [113] and Zhang, So, Speziale and Lai [114]. Additional validations of the ZSGS models, as implemented in the ISAAC algorithm, are reported by Morrison [55,56] and Morrison et al. [59]. Morrison performed his validations by comparing predicted values of  $u^+$  and  $y^+$  to theoretical values using van Driest II coordinate transformations.

Morrison's findings are confirmed in this study by comparing the predicted values of  $u^+$  and



$y^+$  to theoretical values using Spalding's buffer layer formula [89] and White's compressibility correction formula [108] for values of  $\kappa = 0.41$  and  $B = 5.0$ . In this comparison, data at a station upstream of the slot and prior to boundary-layer separation ( $x/l = 0.9000$ ) are used. Predictions from both ZSGS models are within 6% of theory, thus both ZSGS models are considered valid for the limited range of flow conditions that correspond to flat-plate flowfields.

### 6.2.3.2 Reynolds Stress Profiles

Profiles of the two-dimensional Favré-averaged Reynolds stresses are presented in this section. These profiles show that the RSTM is generally more responsive than the  $K - \epsilon$  model to the rapid changes in velocity and pressure that occur at the interfaces of various flow structures.

The first set of profile data examined is taken from station  $x/l = 0.9000$ . The flowfield at this station is fully turbulent flow past a flat-plate and the predicted values of  $\tau_{xy}$ , shown in Figure 24, are nearly identical for both of the turbulence models. This is not surprising, since most turbulence models are designed to match  $\tau_{xy}$  data in the flat-plate region of a flowfield. However, predicted values for  $\tau_{xx}$  (Figure 25) and  $\tau_{yy}$  (Figure 26) from the two models differ by more than 100% near the wall. In particular, the maximum predicted by RSTM for  $\tau_{xx}$  has a greater magnitude than the maximum predicted by the  $K - \epsilon$  model, while the opposite is true of  $\tau_{yy}$  at this station. While there is no particular significance as to which of the axial stresses is larger, it is significant to note that the values of  $\tau_{xx}$  and  $\tau_{yy}$  predicted by the RSTM differ by an order of magnitude from each other, whereas the values predicted by  $K - \epsilon$  are nearly identical. It is easily shown with Eq. 53 that the reason the axial Reynolds stresses computed with the  $K - \epsilon$  model are nearly identical is because the equations for each component differs only by  $\partial u/\partial x$  and  $\partial v/\partial y$ , and in the flat-plate region, these derivatives are negligible. Contrary to the  $K - \epsilon$  model, the axial Reynolds stresses in the RSTM are based on the flow physics and not on any predefined relationships. The predicted values of the Reynolds stresses from the RSTM seen here are consistent with the results reported

by Morrison [56] and Morrison et al. [59] for flat-plate flows.

The Reynolds stress profiles examined at  $x/l = 0.9700$  differ significantly from those seen at the previous station. The profiles at this station are associated with the PUV (Figures 27 - 29) and the peaks in these stress profiles correspond to the interface between the PUV and the freestream flow. At this interface there is a sonic surface where the flow changes from supersonic to subsonic conditions as the wall is approached. While the Reynolds stress profiles predicted by the two models are qualitatively similar, there are significant quantitative differences within the vortices. The maximum predicted by RSTM for  $\tau_{xx}$  is 18% greater than that predicted by the  $K - \epsilon$  model (Figure 28), while the maxima of  $\tau_{xy}$  (Figure 27) and  $\tau_{yy}$  (Figure 29) from  $K - \epsilon$  are 62% and 83% greater in magnitude, respectively, than those predicted by the RSTM.

Additional complexities in the structure of the flowfield at station  $x/l = 0.9950$  result in further changes in the stress profiles. The multiple extrema in the Reynolds stress profiles reported in Figures 30 - 32 are caused by changes in the velocity and pressure fields associated with the different flow structures. For example, the local maximum predicted by RSTM for  $\tau_{xy}$  at  $y/l = 0.008$  (Figure 30) occurs at the interface of the SUV and the upper edge of the PUV (see Figure 7), while the minimum at  $y/l = 0.014$  corresponds to the interface between the vortices and the freestream flow. The  $K - \epsilon$  model predicted minimal changes in the magnitude of the Reynolds stresses at the interface of the two vortices, while the RSTM predicted small, but noticeable, differences in  $\tau_{xy}$  and  $\tau_{yy}$  (Figure 32) at this interface. As with the  $K - \epsilon$  model, the RSTM predicted only minimal changes in  $\tau_{xx}$  (Figure 31) at the vortex interface and across the sonic surface interface, the Reynolds stress profiles exhibited behavior similar to that seen at the sonic surface at station  $x/l = 0.9700$ .

The final set of profile data examined,  $x/l = 1.0125$ , shows there are significant differences between the behavior of the Reynolds stresses in the upstream vortices and the downstream vortices.

At this station the data sample crosses three flow structure interfaces. These interfaces are between the upper portion of the jet wake and the freestream flow at  $y/l = 0.018$ , between the PDV the lower portion of the jet wake (downstream sonic surface) at  $y/l = 0.01$  and between the PDV and SDV at  $y/l = 0.002$ . Data at the interface of the upper portion of the jet wake and the freestream flow is similar to the data seen in the previous figures of the stress profiles. That is, the stresses smoothly asymptote to zero. However, at the interface of the PDV and the lower portion of the jet wake, differences between the models are significant. There is a large extrema in the RSTM predictions for  $\tau_{xy}$  (Figure 33) and  $\tau_{xx}$  (Figure 34) near  $y/l = 0.01$ , while the  $K - \epsilon$  prediction for  $\tau_{xy}$  is negligible and the  $K - \epsilon$  prediction for  $\tau_{xx}$  is nearly 600% smaller than the RSTM prediction. Both models predict similar magnitudes for the extrema of  $\tau_{yy}$  (Figure 35) near  $y/l = 0.01$ . However, the vertical distance over which the changes take place are significantly different. The magnitude of the RSTM prediction for  $\tau_{yy}$ , quickly increases from approximately 0.02 to 0.16 between  $y/l$  station 0.07 to 0.10 and then returns to 0.02 by  $y/l = 0.13$ . On the other hand, the  $K - \epsilon$  predictions start with  $\tau_{yy} = 0.10$  at  $y/l = 0.06$  and increase to  $\tau_{yy} = 0.13$  at  $y/l = 0.10$ . This is only a 116% increase over a distance of 0.04, as compared to the 700% increase in  $\tau_{yy}$  in the RSTM over a distance of 0.3. All of the differences start to occur past the interface between the PDV and SDV at  $y/l = 0.002$ . Prior to crossing this location the predictions from both models are nearly identical.

The cause of the large defences between the two models for the Reynolds stresses at the interface of the jet and the PDV is illustrated with Figure 36. The contour plot in this figure is the wall damping function,  $f_{w_1}$ . This damping function is used to determine when the anisotropic dissipation-rate model at the wall, Eq. 432, and the anisotropic velocity-pressure-gradient correlation model at the wall, Eq. 103, is active in the RSTM. When  $f_{w_1}$  is greater than zero, the models are active and the closer  $f_{w_1}$  is to unity, the stronger the effect of the models. In the current version of ISAAC,  $f_{w_1}$  is forced to zero when  $y^+ > 250$ . This accounts for the choppy

edges of the contours as the freestream is approached. Also shown in this figure are streamtraces which roughly define the interfaces and a vertical line indicating the location of station 1.0125.

The implications that anisotropic wall effects cause the large differences in magnitude of the Reynolds stresses and the response rate to flow changes should be clear. At the interface between the jet and the freestream,  $f_{w_1}$  is near zero and the stress profiles for both models should be, and are, similar to the profiles seen at previous stations when the freestream is entered. However, at every other point at this station,  $f_{w_1} \geq 0.5$ . Therefore, the anisotropic wall models are active in the RSTM model. These anisotropic models, along with the fact that the Reynolds stresses do not any predefined relationships to each other, are the most likely cause of the differences in the predictions from the two models.

It is emphasized again that the velocity-pressure-gradient correlation,  $\Pi_{ij}$ , is not modeled at all in the  $K - \epsilon$  formulation and that isotropic turbulence dissipation rates are assumed in the  $K - \epsilon$  model. As a result, the turbulence dissipation-rate tensor is modeled as  $\epsilon_{ij} = \frac{2}{3}\epsilon\delta_{ij}$  in the  $K - \epsilon$  formulation. These two limitations cause the  $K - \epsilon$  model to respond slowly or not at all to flow conditions that excite the velocity pressure-gradient correlation tensor and the anisotropic behavior of  $\epsilon_{ij}$ .

Based on the data provided in the turbulence profiles several observations can be made. First, outside the recirculation zones and in regions of the flow where the velocity and pressure gradients are small, the two models predict similar values for the Reynolds stresses. However, in regions where the velocity and pressure gradients are not small, i.e., across shocks and wake/freestream interfaces, the models predict significantly different values for the Reynolds stresses. The large disparities in peak values of the Reynolds stresses at  $y/l = 0.010$  at station 1.0125 are attributed to isotropic turbulence assumptions and the lack of the second-order term  $\Pi_{ij}$  in the turbulent kinetic energy equation of the  $K - \epsilon$  model.

### 6.2.3.3 Flowfield Contours

The profiles presented in the previous section reflect many important details of injection flowfields, but they are only localized descriptions of isolated points. The contour plots seen in Figures 37 - 40 provide a global characterization of how the Reynolds stresses are effected by flowfield changes around the slot. These contour plots encompass a region around the slot extending upstream to a station near the boundary-layer separation point and downstream to a station near the boundary-layer reattachment point. In these contour plots the slot is centered about  $x/l = 1.0$  and particle streamtraces are superimposed on the contour plots and provide visual references for the location of the recirculation zones and the injectant plume.

Immediately seen in the results for  $\tau_{xy}$  (Figure 37) are the different magnitudes in the two model's predictions for the Reynolds stress downstream of the slot and the discontinuous distribution in the  $K - \epsilon$  model predictions at  $x/l = 0.994$  for the Reynolds stress.

The differences in the magnitudes are readily attributed to the anisotropic behavior of  $\Pi_{ij}$  and  $\epsilon_{ij}$ . In the previous section, it was seen in Figure 36 that the anisotropic models were active over most of the flowfield immediately behind the slot. Furthermore, comparison of the contours of  $f_{w_1}$  in Figure 36 to the RSTM contours for  $\tau_{xy}$ , show the changes in Reynolds stress follow the changes in  $f_{w_1}$ . Whereas, the Reynolds stresses in the  $K - \epsilon$  results are computed from the Boussinesq approximation and does not account for anisotropic behavior.

The discontinuity in the Reynolds stresses is a non-physical phenomena and is caused by the eddy viscosity model used in the Boussinesq approximation. The discontinuity can be traced through the Boussinesq approximation to the wall damping function,  $f_\mu$  (Eq. 54), which is part of Eq. 37 and is used to compute the turbulent eddy viscosity,  $\mu_t$ . For wall-bounded flows,  $f_\mu$  is required to maintain asymptotic consistency of the  $K$  and  $\epsilon$  equations as the solid surface is approached. For flat-plate, attached boundary-layer flows,  $f_\mu$  is formulated such that it approaches unity as

$y \rightarrow \delta$ , where  $\delta$  is the boundary-layer thickness. The rate at which  $f_\mu \rightarrow 1$  is largely governed by the magnitude of the viscous shear stress at the wall which is defined as,  $\tau_w = \bar{\mu} \partial \tilde{u} / \partial y|_{y=0}$ . The nondimensional form of  $\tau_w$  is normally somewhat larger than unity at the plate surface and generally, the larger  $\partial \tilde{u} / \partial y|_{y=0}$  is, the faster  $f_\mu \rightarrow 1$  as  $y \rightarrow \delta$ . However, for recirculating flows and stagnation fields, there are points on the plate surface where  $\partial \tilde{u} / \partial y|_{y=0} \approx 0$ . In the neighborhood of these points,  $\partial \tilde{u} / \partial y|_{y=0} \ll 1$ , implying locally that  $\tau_w \ll 1$  and causing  $f_\mu$  to approach unity much slower than it would for a flat-plate boundary-layer. Thus, the damping needed to preserve asymptotic consistency of the  $K$  and  $\epsilon$  equations, adversely affects computations far away from the wall. The effect is felt away from the wall because the value computed for  $\tau_w$  at any axial station is used to compute  $f_\mu$  at every node normal to the axial station. In this flowfield, the result is a discontinuous distribution of the Reynolds stress at  $x/l = 0.994$  in the  $K - \epsilon$  model.

The severity of the discontinuous behavior is determined by the proximity of the separation and stagnation point to a grid node and the size of the region where  $\partial \tilde{u} / \partial y|_{y=0} \approx 0$ . As an example, consider the differences shown in Figure 38 for grid spacing near  $x/l = 0.915$  and  $x/l = 0.994$  and the size of the region where  $\partial \tilde{u} / \partial y|_{y=0} \approx 0$ . At both of these axial stations  $\partial \tilde{u} / \partial y|_{y=0} \approx 0$ . However, the likelihood of the zero condition being coincident with one or more of the nodes is much greater at  $x/l = 0.994$  than it is at  $x/l = 0.915$ . This is because the spacing is finer at  $x/l = 0.994$  than it is at  $x/l = 0.915$  and the region where  $\partial \tilde{u} / \partial y|_{y=0} \approx 0$  is larger at  $x/l = 0.994$  than it is at  $x/l = 0.915$ .

Similar stagnation conditions are present in the flowfield predicted by the RSTM, however, the discontinuity in the  $\tau_{xy}$  is not seen since the RSTM does not use the eddy viscosity model to compute the Reynolds stress. In the RSTM the Reynolds stresses are treated as conserved variables and their predicted values are arrived at just like any other mean flow variable.

The same discontinuity seen in the  $K - \epsilon$  results for  $\tau_{xy}$  is also present in the contour plots for

$\tau_{yy}$  and  $\tau_{xx}$  (Figures 39 and 40 respectively). However, in the plots of  $\tau_{yy}$  and  $\tau_{xx}$ , the discontinuity it is not as prominent a feature. The reason for the difference in the severity is clear when the expanded forms of Eq. 53 are examined. For  $\tau_{xx}$ ,  $\tau_{yy}$  and  $\tau_{xy}$ , the expanded forms are

$$\tau_{xy} = -\frac{\mu_t}{\rho} \left( \frac{\partial u}{\partial y} + \frac{\partial v}{\partial x} \right) \quad (221)$$

$$\tau_{xx} = \frac{2}{3}K - \frac{\mu_t}{\rho} \left[ 2\frac{\partial u}{\partial x} - \frac{2}{3} \left( \frac{\partial u}{\partial x} + \frac{\partial v}{\partial y} + \frac{\partial w}{\partial z} \right) \right] \quad (222)$$

$$\tau_{yy} = \frac{2}{3}K - \frac{\mu_t}{\rho} \left[ 2\frac{\partial v}{\partial y} - \frac{2}{3} \left( \frac{\partial u}{\partial x} + \frac{\partial v}{\partial y} + \frac{\partial w}{\partial z} \right) \right] \quad (223)$$

It was seen in Section 4.2.1 that  $K$  is of  $O(y^2)$ , whereas  $(\mu_t/\rho)(\partial u_i/\partial x_i)$  is of  $O(y^3)$ . Thus, the  $K - \epsilon$  predictions for  $\tau_{yy}$  and  $\tau_{xx}$  are dominated by  $K$  and  $\mu_t$  has only a higher order influence on the results. Of course, none of this has any bearing on the RSTM predictions for  $\tau_{yy}$  and  $\tau_{xx}$  since, these terms are also modeled as conserved variables and are not subject to the Boussinesq approximation.

The effects of anisotropic behavior are also seen in the contour plots for  $\tau_{yy}$  and  $\tau_{xx}$ . In Figure 40, the RSTM predictions for the stress behind the jet is significantly larger than the  $K - \epsilon$  predictions. Again comparison to Figure 36 shows that this region of increased Reynolds stress coincides with changes in the contours of  $f_{w_1}$ .

#### 6.2.3.4 Vorticity

It is reasonable to expect the discontinuity seen in the Reynolds stress contours to have an influence on other flow variables since the turbulence model equations and the mean flow equations are strongly coupled through the equation-of-state. This conjecture is verified in Figure 41, which shows a contour plot of  $\omega_z$ , where  $\omega_z \equiv \partial u/\partial y - \partial v/\partial x$ . From this plot, it is clear that the eddy viscosity model degrades the smoothness of the mean flow variables as well as the Reynolds stresses. Although not shown here, the vortical anomaly at  $x/l = 0.994$  is also found for each of

the conserved mean flow variables computed with the  $K - \epsilon$  model.

#### **6.2.3.5 Total Energy**

Often when a laminar Navier-Stokes solver is modified to include a turbulence model, the contribution of  $K$  to the total energy term,  $E$ , is neglected. Huang and Coakley [32] did a comparative study with a hypersonic cylinder flare to determine the effects of neglecting  $K$  in the expression for  $E$ . Their results showed a decrease of 9% in peak surface pressure when  $K$  is accounted for in the total energy term.

Results from the current study of a TJISF are similar to Huang and Coakley's. Rizzetta's numerical simulation of Aso et al.'s configuration with the Jones-Launder  $K - \epsilon$  model, was performed without  $K$  contributing to  $E$  [65], whereas the current simulation with the ZSGS  $K - \epsilon$  model accounts for  $K$ 's contribution. Returning to the pressure profiles reported in Figures 11 - 14, it is seen that the ZSGS  $K - \epsilon$  model predicts a lower peak surface pressure than that predicted with the Jones-Launder  $K - \epsilon$  model. Some insight as to why the peak surface pressure is different for the two sets of computational results is provided by Figure 42. This figure shows that in the regions just upstream and downstream of the jet,  $K$  accounts for as much as 12% of  $E$ .

#### **6.2.4 Summary of Sonic Injection Results**

A comparative study was completed in order to evaluate the relative performance of the ZSGS second-order RSTM, the ZSGS  $K - \epsilon$  model and the Jones-Launder  $K - \epsilon$  models for shock/boundary-layer interactions resulting from TJISF at the surface of a flat-plate. A mesh step-size study summarized in Appendix F indicated the adequacy of numerical resolution for the present application. Eight cases were examined, comprising two different experimental configurations and four different pressure ratios for each configuration.

Surface static pressure distributions computed with the ZSGS RSTM and the ZSGS  $K - \epsilon$  model for the Spaid and Zukoski [88] configuration compared very well for the three lowest pressure



ratios examined. Furthermore, good agreement was observed between the computed separation length and the experimentally obtained values. Only at the largest pressure ratio did the ZSGS models predict results significantly different from the experimental data.

This disparity may have been caused by poor modeling of the turbulent properties at the slot exit or as a result of turbulence model limitations for the overall flowfield at higher pressure ratios. Furthermore, the simple boundary conditions presented in Section E.3.1 may remain physically realistic only when conditions at the slot exit impact a small domain in the immediate vicinity of the nozzle. For sufficiently large pressure ratios, this situation does not exist.

Taken as a whole, the surface static pressure distributions computed with all three of the turbulence models for the Aso et al. [6] configuration were of marginal quality. In light of the excellent agreement seen with the Spaid and Zukoski configuration, the poor agreement with the Aso et al. data, was likely due to three-dimensional effects and leading-edge bluntness, devaluing this data set for turbulence model validation.

Additional evaluation of the turbulence profiles computed for the Spaid and Zukoski configuration indicated that both ZSGS models satisfied the law-of-the-wall for flat-plate flows. Furthermore, it was seen that away from flow structure interfaces the two models predicted similar values for the Reynolds stresses. However, the models predicted significantly different values for the Reynolds stresses in the vicinity of shocks and flow structure interfaces, particularly at interfaces where there were rapid changes in pressure and flow direction. The latter disparity was a result of the  $K - \epsilon$  formulation not modeling the second-order pressure-velocity-gradient term and the restriction to isotropic turbulence dissipation rates.

The non-physical behavior seen in the contour plots of  $\tau_{ij}$  and  $\omega_z$  highlight the deficiencies of the eddy viscosity model used in the  $K - \epsilon$  formulation. This non-physical behavior in the presence of recirculating flows and at stagnation zones discredits this model's validity for TJISF simulation.

On the other hand, the continuous physically consistent results of the RSTM warrant continued research to determine the validity of the ZSGS RSTM.

Finally, it was shown that  $K$  accounts for as much as 12% of  $E$  in regions with significant shock/boundary-layer interaction.

### 6.3 Supersonic Injection Configuration

The second part of the two-dimensional investigation validates the ZSGS RSTM for the supersonic TJISF configuration used by Tucker [100]. This is accomplished by simulating numerically Tucker's experiments with the ZSGS RSTM and ZSGS  $K - \epsilon$  models and then comparing the numerically predicted values to experimental data. As an ongoing part of the validation, analyses of the effects the boundary layer thickness,  $\delta$ , has on  $x_{sep}$  and the effect  $\delta$  has on the 4:1 ratio of  $x_{sep}$   $h$  are performed. An analysis of the shock structure within the plume with respect to the effective back pressure,  $p_{beff}$ , is also presented in Section 6.3.3. Comparisons of numerical predictions of  $\tau_{xy}$  for heated and cooled injection to experimental data are discussed in Section 6.3.4 along with an analysis of the numerical predictions for the near-field Reynolds stress and  $K$  from both turbulence models.

Tucker experimentally investigated the mean flow and turbulent flow structure associated with normal injection of a supersonic fluid into a supersonic core flow. The mean flow conditions of the tunnel and injector are listed in Tables 5 and 6. In the cooled injection experiments, Tucker used an adiabatic wall and in the heated injection experiments, the wall temperature,  $T_w$ , was held constant at 328 K.

Tucker's experiments were conducted in the AFIT Mach 3.0 wind tunnel, which consists of a rectangular, 33cm long test section with cross sectional dimensions of  $6.35 \times 6.35$ cm (see Figure 43). A schematic of the converging-diverging injection nozzle used by Tucker is shown in Figure 45 [100]. The nozzle had a slot length of 4.45cm; a throat width,  $A^*$ , of 0.159cm and an exit width,

AE, of  $0.198\text{cm}$ . The ratio of exit area to throat area,  $AE/A^*$ , was 1.25 and resulted in injection at Mach 1.6. This nozzle was centered in the upper surface of the test section creating a gap of  $0.95\text{cm}$  on either side of the nozzle between it and the wall. Tucker verified the two dimensionality of the flowfield by examining Mach contours for the cooled injectant case at locations  $5.09\text{cm}$  and  $13.04\text{cm}$  downstream of the nozzle [100] (all distances are measured from the centerline of the slot, see Figure 44).

Experimental data was collected at  $x/l = 11.4$  ( $l = 1\text{cm}$ ) with multiple overheat cross-film anemometry for the turbulence variables and Pitot static probes for the mean flow variables. Shadow graph and schlieren photography was also used to visualize the two-dimensional shock structure of the flowfield.

### 6.3.1 Boundary Conditions and Computational Grid

All simulation results discussed in this section satisfy the boundary conditions listed in Table 4. A velocity profile with  $\delta = 0.5\text{cm}$  was used for the inflow plane. The  $\delta$  used for this simulation was the  $\delta$  on the wind tunnel wall opposite the nozzle (see Figure 43). The inflow profile was generated by performing a flat-plate simulation with the inflow conditions given in Table 5. Mean flow and turbulent data at the outflow plane of the simulation at the station where  $\delta = 0.5\text{cm}$  was used as the inflow profile for the injection simulations. The parameters listed in Table 6 were used as the inflow conditions for the injectant. The implementation method of the other boundary conditions are presented in Section E.3.1.

The computational grid used in this part of the two-dimensional analysis, its dimensions and the grid resolution study performed to arrive at the current grid configuration, are presented in Section F.2.2. The grid used in this simulation has the cells swept back to provide better definition of the jet induced shocks.

Table 4. Two-dimensional supersonic injection boundary conditions

Plane	Condition
Inflow	Inflow profile
Outflow	Extrapolation
Left side	Extrapolation
Right side	Extrapolation
Top	Tangency
Bottom	Wall
Jet	Two-dimensional jet, 3 cells

Table 5. Two-dimensional supersonic injection freestream mean flow conditions [100]

Parameter	Cooled injection	Heated injection
M	$2.9 \pm 0.03$	$2.9 \pm 0.03$
$p_{t\infty}$	$203.9 \pm 2.8$ kPa	$201.8 \pm 2.8$ kPa
$T_{t\infty}$	$295.0 \pm 0.25$ K	$293.0 \pm 0.25$ K
$\rho_{t\infty}$	$2.41 \pm 0.03$ kg/m <sup>3</sup>	$2.40 \pm 0.03$ kg/m <sup>3</sup>
$p_{\infty}$	$6.45 \pm 0.09$ kPa	$6.39 \pm 0.09$ kPa
$T_{\infty}$	$110.3 \pm 0.08$ K	$109.3 \pm 0.08$ K
$\rho_{\infty}$	$0.204 \pm 0.003$ kg/m <sup>3</sup>	$0.204 \pm 0.003$ kg/m <sup>3</sup>
$U_{\infty}$	$610 \pm 5.0$ m/s	$608 \pm 5.0$ m/s
$a_{\infty}$	$210$ m/s	$209$ m/s
$Re/m$	$16.2 \times 10^6$	$16.2 \times 10^6$
$T_w$	adiabatic	328 K

Table 6. Two-dimensional supersonic injector mean flow conditions [100]

Parameter	Cooled injection	Heated injection
M	1.6	1.6
$p_{t_{inj}}$	$61 \pm 0.7$ kPa	$64.9 \pm 1.38$ kPa
$T_{t_{inj}}$	$273 \pm 0.5$ K	$329 \pm 2.0$ K
$\rho_{t_{inj}}$	$0.78 \pm 0.01$ kg/m <sup>3</sup>	$0.69 \pm 0.019$ kg/m <sup>3</sup>
$p_{inj}$	$14.4 \pm 0.11$ kPa	$15.3 \pm 0.29$ kPa
$T_{inj}$	$181 \pm 0.25$ K	$217 \pm 1.9$ K
$u_{inj}$	$0$ m/s	$0$ m/s
$v_{inj}$	$161$ m/s	$176$ m/s
$w_{inj}$	$0$ m/s	$0$ m/s
$\rho_{inj}$	$0.277 \pm 0.002$ kg/m <sup>3</sup>	$0.245 \pm 0.007$ kg/m <sup>3</sup>

### 6.3.2 Shock Structure and Mean Flow Analysis

The experimentally measured shock structure of Tucker's supersonic TJISF for heated injection is shown in Figure 46 [100]. In this figure, Tucker reports the angles of the separation and recompression shocks, and the location of the hot-film data collection region relative to the slot. By extending the lines of the separation and recompression shocks, Tucker also identified the location of the boundary-layer separation point as  $2.0\text{cm}$  upstream of the slot and the reattachment point as  $0.7\text{cm}$  downstream of the slot. Visualizations of the numerically predicted shock structure from the  $K - \epsilon$  model and the RSTM are seen in Figure 47. In these contour plots the separation and recompression shock locations are identified and the angle of the shocks given.

The predictions from both turbulence models for the location of the recompression shock and its angle are nearly identical to Tucker's measurements. Furthermore, predictions from both models for the separation shock angle are similar ( $31.2^\circ$  for RSTM,  $30.7^\circ$  for  $K - \epsilon$ ), each of which are within 16% of Tucker's value of  $27.5^\circ$ . However, the prediction for  $x_{sep}$  is significantly different from that seen in the experimental data. Predictions for  $x_{sep}$  from both models occur at  $x/l = -3.2$ , or 60% further upstream of  $x/l = -2.0$  as reported by Tucker. The discrepancy in  $x_{sep}$  is caused by improper inflow boundary-layer matching. Subsequent simulations of this configuration without an initial  $\delta$ , predicts  $x_{sep}$  at  $x/l = -1.7$ , which is 15% further downstream of the experimentally measured value. Clearly, implying the cause and effect inflow  $\delta$  profiles have on  $x_{sep}$ .

This discrepancy indicates that using the  $\delta$  from the lower wall is not a proper method for inflow boundary-layer modeling if a half-angle nozzle (Figure 43) is used to accelerate the inflow air. The asymmetric surface curvature of the half-angle nozzle has a more favorable pressure gradient on the upper surface than on the lower surface [4]. This results in a thinner  $\delta$  on the upper surface than the lower surface [75].

The discrepancy in  $x_{sep}$  and  $\delta$  does not have an impact on  $h$  for this configuration. Tucker

reported  $h = 0.4$  for his heated injection case; the predicted value of  $h$  from the models is 0.42 for  $K - \epsilon$  and 0.45 for RSTM (Figure 48). However, the  $\delta$  discrepancy does impact the 4:1 correlation between  $x_{sep}$  and  $h$  reported by Spaid and Zukoski [88] and corroborated in Section 6.3. Based on the values of  $x_{sep}$  and  $h$  reported from the models, the ratio is 7.6 for  $K - \epsilon$  and 7.1 for RSTM. The ratio of the experimentally measured values of  $x_{sep}$  and  $h$ , is 5.0 This is only a 25% larger than the expected 4:1 ratio as compared to 90% for  $K - \epsilon$  and 77.5% for RSTM.

Based on the numerical and experimental data discussed above, it is concluded that the inflow  $\delta$  only has a significant impact on the recirculation zone upstream of the jet. It does not affect the value for  $h$  or the shocks and reattachment points downstream of the slot. Furthermore, it is concluded that Spaid and Zukoski's 4:1 correlation for  $x_{sep}$  and  $h$  is not valid for an arbitrary  $\delta$ .

### 6.3.3 Plume Structure

An analysis of the plume shock structure for Tucker's heated injection configuration and the effects the shocks have on total pressure,  $p_t$ , loss for three different pressure ratios are discussed in this section. Minimal  $p_t$  losses are associated with efficient combustion and thrust development in SCRAMjet engines [60] and as noted in Section 6.1.2, a structureless plume minimizes  $p_t$  losses. However, a structureless plume in a TJISF is not possible, since the back pressure,  $p_b$ , on either side of the plume is different. Therefore, the best that can be achieved is a plume with minimal shock structure [76].

The pressure contours in the plume for Tucker's heated injection configuration (Figure 49) clearly show the distinctive diamond shock pattern associated with an overexpanded jet [28]. The diamond shock pattern is also easily seen in the Mach contours (Figure 48) and corroborates the observation from the pressure contours that the jet is overexpanded. Further evidence of overexpansion is found in the schlieren photograph shown in Figure 50 [100]. Close examination of the injectant plume in the schlieren also reveals the diamond shock pattern in the experimental

results. Further examination of the shock pattern surrounding the plume in Figure 50, indicates the absence of a Mach disk at the end of the plume. This observation is also seen in the numerical results in Figure 48. Although the Mach disk does not form, there is a concentration of the Mach contours near the top of the plume in Figure 48. This structure is henceforth denoted as the *shock disk*.

In the absence of a Mach disk, the  $p_t$  loss of the injectant should be small. For the pressure ratio,  $p_{inj}/p_\infty = 2.25$ ,  $p_t$  within the plume, just prior to the shock disk, is 58kPa and  $p_t$  across the shock disk is 53kPa (an 8% loss in  $p_t$ ).

It should be clear from the Mach contours in Figure 16, which was discussed in Section 6.2.2, that the larger the pressure ratio, the larger the Mach disk and the deeper the penetration of the injectant into the core flow. Thus, it should be expected that a trade off between injectant penetration and  $p_t$  losses is required with larger pressure ratios. This supposition is verified by numerical simulation with the RSTM for  $p_{inj}/p_\infty = 5$  and  $p_{inj}/p_\infty = 10$  and the results of these computations are shown in Figure 51. The results for  $p_{inj}/p_\infty = 5$  are shown in upper set of contours and  $p_{inj}/p_\infty = 10$  are seen in the lower set. In these contours, subsonic flow is masked to emphasize the region where the Mach disk forms.

An underexpanded jet results when  $p_{inj}/p_\infty = 5$  and all other inflow properties are held constant. Underexpansion is indicated by an absence of the diamond shock pattern in the plume and the upstream turning of the injectant leaving the upstream side of the nozzle. Although the jet is underexpanded, this pressure ratio is not sufficiently large to form a Mach disk. Deeper penetration of the fluid into the core does result from the higher initial pressure of the jet, 0.7cm as compared to 0.4cm for  $p_{inj}/p_\infty = 2.25$  (a 75% increase in fluid penetration into the core flow). However, the larger pressure ratio results in much larger  $p_t$  losses. Total pressure within the plume prior to the shock is 134kPa, but  $p_t$  across the shock is 40kPa (a 70% loss in  $p_t$ ).

Even deeper injectant penetration is realized when  $p_{inj}/p_\infty = 10$ . Jet penetration at this

pressure ratio is  $1.2cm$  as compared to  $0.4cm$  for  $p_{inj}/p_{\infty} = 2.25$  (a 200% increase in injectant penetration). A Mach disk does form at this pressure ratio and  $p_t$  losses are even larger. Prior to the shock, the total pressure within the plume is 268kPa but across the shock,  $p_t$  has decrease to 27kPa (a 90% loss in  $p_t$ ).

Clearly in terms of  $p_t$  loss, an underexpanded jet is undesirable and one that is underexpanded so much that a Mach disk forms is even less desirable. However, the increase in mixing and combustion efficiency gained by the deeper penetration of the injectant into the inflow may outweigh the  $p_t$  losses.

#### 6.3.4 Turbulence Data

In Section 6.2.3 the lack of experimental turbulence data limited the analysis of the Reynolds stresses to a comparison of numerical results from the two models. However, validation with experimental data, as well as a qualitative and quantitative analysis is possible for Tucker's configuration, because  $\tau_{xy}$  data was collected for cooled and heated injection at  $x/l = 11.4$ .

A comparison of  $\tau_{xy}$  profiles from the numerical results to the experimental data at  $x/l = 11.4$  is the first part of the overall analysis of the turbulence predictions. The profile analysis is followed by an evaluation of the Reynolds stress contours in the recirculation zones surrounding the slot injector. The analysis of two-dimensional injection is concluded with an evaluation of the contribution  $K$  has to  $E$  in Tucker's configuration.

The data presented in Sections 6.3.2 and 6.3.3 have the  $y/l$  axis inverted to allow easy visual comparisons with Tucker's experimental data and schlieren photographs. However, the conventional plotting of the  $y/l$  axis is resumed in this section to facilitate contrast and comparison with the contours from Section 6.2.3.

##### 6.3.4.1 Reynolds Stress Profiles

Profiles from both models for  $\tau_{xy}$  are qualitatively similar in shape to the experimentally



measured data for both of the injection configurations. These comparisons are shown in Figures 52 and 53 along with a ninth-order polynomial fit of the experimental data. The numerical data in each of these figures is shifted by  $1.3mm$  in the  $y$  direction and  $2.5mm$  in the  $x$  direction to account for the positioning error of the probe as detailed by Tucker [100].

The similarity of the RSTM and  $K - \epsilon$  model profiles to each other is consistent with observations made in Section 6.2.3. In that section it was seen that predictions from both models were similar in flow regions where velocity and pressure gradients were small. A similar flow situation is seen at  $x/l = 11.4$  in the Mach contours shown in Figure 47. At  $x/l = 11.4$ , the change in the velocity proceeds through a smooth transition from the turbulent boundary-layer to local freestream conditions.

The similarity of the numerical results to the experimental data for cooled injection is easily seen in the plots. Quantitative evaluation of the data, between  $y/l = 0.4$  and  $y/l = 0.6$  in Figure 52, show that the RSTM correctly predicted the experimentally measured values of  $\tau_{xy}$  to within 1% of the experimental data, while predictions from  $K - \epsilon$  are in error by at least 19% in this region. Predictions from both models are significantly less accurate in the range between  $y/l = 0.6$  and  $y/l = 1.2$ . Over this part of the boundary-layer, predictions from RSTM are in error from 16% to 36% of the experimentally measured values, while predictions from  $K - \epsilon$  have errors between 25% to 38% of the experimentally measured values. Beyond  $y/l = 1.2$ , predictions from both models asymptote to zero. In general, the RSTM predictions for cooled injection are closer to the experimental data than the  $K - \epsilon$  prediction.

While not as obvious as it is for cooled injection, the similarity of the numerical results and the experimental data is present in the simulations for  $y/l > 0.6$ . Above  $y/l = 0.6$ , the general shape of the experimental data and numerical results compare well but, the magnitudes are significantly less accurate than they are for cooled injection. Between  $y/l = 0.4$  and  $y/l = 1.0$ , the error in

the predictions for the RSTM ranged from 36% to 68%, while predictions from  $K - \epsilon$  have errors ranging from 71% to 85%. As with the cooled injection case, predictions from both models beyond  $y/l = 1.0$  asymptote to zero.

The cause of the poor comparison below  $y/l = 0.6$  is not readily apparent, however, it is likely that any one or combinations of the following factors account for the poor agreement with the data: 1) inflow conditions were at the extremes of the mean values reported in Tables 5 and 6; 2) inaccurate modeling of inflow  $\delta$ ; 3) three-dimensional effects unaccounted for in the simulations; 4) inaccurate initial conditions for the turbulence variables over the slot exit; or 5) the model is not valid for a non-adiabatic wall.

#### **6.3.4.2 Flowfield Contours**

As in Section 6.2.3.3, a global characterization of the behavior of the Reynolds stresses around the nozzle is presented here. The contour plots of the Reynolds stresses discussed in this section encompass most of the recirculation region around the slot for Tucker's cooled injection case. The cooled injection results are used for this analysis because the turbulence models had better agreement with the data for this configuration. Particle streamtraces defining the upper and lower limits of the injectant penetration are superimposed over the contour plots. A particle path of the injectant leaving from the center of the slot is also shown. As with the contours seen in Section 6.2.3.3, there are two significant differences between the model results of this simulation. First is the non-physical discontinuities in the  $K - \epsilon$  predictions for  $\tau_{xy}$ . Second is the difference in magnitude between the two models for  $\tau_{xx}$  and  $\tau_{yy}$ .

The discontinuities seen in Figure 54 are more frequent in the current simulation than they are in the sonic injection simulations. Also, in the current simulation, the discontinuities are swept back, downstream of their initial location at the test section surface. Both of these differences are tied more directly to differences in the grid spacing rather than differences in the flowfield structure.

A comparison of the grids used for the sonic simulations and the supersonic simulations is shown in Figure 56. Shown in these figures is a  $2.0\text{cm}$  length of the grid around the slot. Both grids are scaled so that the dimensional distances shown are identical. The cells in the grid used for the sonic injection simulations are at right angles to each other. In contrast, the cells of grid used for the supersonic simulations are not at right angles, but they are orthogonal to each other. Furthermore, the spacing of the cells behind the slot is finer in the grid used for the supersonic simulations than the spacing in the grid used for the sonic simulations.

The increased frequency of the discontinuities in the current simulation is a result of the finer spacing behind the slot. It was seen in Section 6.2.3.3 that the discontinuous behavior of the Reynolds stresses in the  $K - \epsilon$  model predictions were a result of the Boussinesq approximation and the eddy viscosity,  $\mu_t$ . It was also shown that the discontinuities occurred when  $\partial u / \partial y|_{y=0} \approx 0$ , thus  $y^+ \approx 0$  in the neighborhood of more than one cell.

The increased number of locations where spikes in  $y^+$  occur is seen in Figure 55. Here again, both models exhibit these spikes, however, the non-physical behavior in  $\tau_{xy}$  is only seen in the  $K - \epsilon$  model results. This is because the Reynolds stresses are modeled as conservative variables in the RSTM and does not rely upon the Boussinesq approximation and eddy viscosity formulations.

The swept back appearance of the discontinuities and the spikes in  $y^+$  are caused by the method used to evaluate  $y^+$  away from the surface. The definition of  $y^+$  is given in Eq. 56 as

$$y^+ \equiv \frac{y}{\bar{\nu}} \sqrt{\frac{\tau_w}{\bar{\rho}_w}} \quad (224)$$

and every value of  $y^+$  evaluated at a given location of  $y$  should be computed with the  $\tau_w$  evaluated at the surface normal to  $y$ . Thus, the spikes in  $y^+$  seen in Figure 55 should be vertical, not swept back. However, in ISAAC,  $y^+$  is evaluated along lines of constant indices. In other words, whatever value of  $\tau_w / \bar{\rho}_w$  computed at a streamwise index, is the value used along the line of constant index, regardless of how its streamwise coordinate changes. Thus, a value computed for  $\tau_w / \bar{\rho}_w$  at

$x/l = 0.20$  might be used to compute  $y^+$  for a  $y/l$  location which is not normal to  $x/l = 0.20$ .

In addition to the discontinuities, the turbulence models predicted different magnitudes for  $\tau_{yy}$  and  $\tau_{xx}$  in the recirculation region downstream of the slot and upstream of the slot where the jet plume is turned by the inflow. The predicted differences in magnitude of  $\tau_{yy}$  (Figure 57) downstream of the slot is consistent with the predictions from the underexpanded sonic injection simulation (Figure 39). That is  $K - \epsilon$  predicted larger magnitudes for  $\tau_{yy}$  than RSTM. However, there is an absence of  $\tau_{yy}$  in the RSTM predictions just downstream of the slot which is inconsistent with the underexpanded sonic injection predictions. Further discussion of this inconsistency is presented later in this section.

Upstream of the slot, where the plume is turning downstream, the RSTM predictions for  $\tau_{yy}$  in the current overexpanded simulation are reversed from those seen in Figure 39 for the underexpanded injection. In Figure 57 the RSTM predictions are larger than the  $K - \epsilon$  predictions. The reversal in magnitude is likely a result of the models responding differently to overexpanded and underexpanded flowfields. The underexpanded flowfield requires more turning of the upstream side of the plume than the overexpanded jet in the current simulation. The added turning results in larger values of  $K$ , thus larger values of  $\tau_{yy}$  in the  $K - \epsilon$  predictions (see Eq. 53).

As with  $\tau_{yy}$ ,  $\tau_{xx}$  predictions from the models are consistent with the sonic simulations in part of the flowfield and inconsistent in other parts. Consistent predictions are observed between the two models and the configurations where the inflow turns the jet plume (Figures 40 and 58). In both configurations, the predictions from RSTM are larger than the  $K - \epsilon$  predictions. Downstream of the slot, the predictions from the  $K - \epsilon$  model are also consistent with the predictions from the underexpanded simulation. However, the RSTM predictions are not consistent with the predictions from the underexpanded simulation.

A significant difference between the RSTM predictions for  $\tau_{xx}$  is seen in the figures for the two

configurations. In Figure 58, the RSTM predicted values for  $\tau_{xx}$  are negligible immediately behind the jet. In Figure 40,  $\tau_{xx}$  is at a maximum in the region behind the jet. Although underexpanded injection does not cause as much initial turning of the plume on the downstream side of the jet, there is significant turning at the top of the plume. This downstream turning should result in a marked increase of turbulent stress in one of the axial Reynolds stresses, but both  $\tau_{xx}$  and  $\tau_{yy}$  are near zero at these locations.

Inspection of contours for the anisotropic wall damping function,  $f_{w_1}$ , reveals the cause of the inconsistency and once again, it is  $y^+$  and the sweep of the grid. In the ISAAC algorithm,  $f_{w_1}$  for the ZSGS RSTM is implemented as shown here

$$f_{w_1} = \begin{cases} \exp \left[ - \left( \frac{Re_t}{150} \right)^2 \right] & \text{if } y^+ < 250 \\ 0 & \text{if } y^+ \geq 250 \end{cases} \quad (225)$$

where

$$Re_t = \frac{K^2}{\bar{\nu}\epsilon}$$

The computed values of  $f_{w_1}$  as it is currently implemented are shown in the upper set of contours in Figure 59. The lower set of contours show the values of  $f_{w_1}$  without  $y^+$  clipping. Clearly, a significant part of the recirculation region where  $f_{w_1}$  is non-zero is truncated by the step function in Eq. 225. The inappropriate truncation of  $f_{w_1}$  is caused by evaluating  $y^+$  with  $\tau_w$  values which are not at the streamwise location normal to the current  $y/l$  location.

There are several methods by which the current discrepancy caused by the truncation can be corrected. The first is to use a grid with cells at right angles to each other. While this is not difficult to implement in this application, more complex geometries may not lend themselves to this luxury. A second method is to raise the threshold where truncation occurs. This also limits the flexibility of the algorithm and the model. For this particular simulation,  $y^+ \geq 1000$  would have sufficed to limit truncation to most of the flow outside of the recirculation zone, but this value may be inappropriate

for other applications or other parts of this flowfield. Also, increasing the threshold will not correct the problem at locations normal to the nozzle exit. Over the exit,  $y^+$  is infinite because there is not a solid surface where  $\tau_w$  can be computed. Thus, all of the flowfield above the slot is treated as isotropic regardless of the flow conditions in the flowfield. It is clearly seen in the farfield data of the lower set of contours that some form of truncation is needed. In the farfield,  $f_{w_1}$  asymptotes to unity, thus, clipping can not be turned off altogether. The best solution is development of a damping function which does not depend upon  $y^+$  and asymptotes to zero outside the boundary-layer. Until such a function is developed, the ISAAC algorithm should be modified so that  $y^+$  is evaluated correctly.

#### **6.3.4.3 Total Energy**

The fraction of  $E$  comprised by  $K$  is also evaluated for the current underexpanded configuration. As with the overexpanded injection cases, the largest ratios of  $K/E$  are in the recirculation zone behind the slot and upstream of the slot where the plume is turning (Figure 60). In these regions,  $K$  accounts for as much as 8% of  $E$ . In both models, the largest fraction is coincident with the recompression shock behind the jet and the lambda shock formed above the jet plume where the boundary-layer separation and jet induced shocks intersect.

#### **6.3.5 Summary of Supersonic Injection Results**

A comparative study was conducted in order to evaluate the relative performance of the ZSGS second-order Reynolds stress and the ZSGS  $K - \epsilon$  turbulence models for shock/boundary-layer interactions resulting from supersonic TJISF through the surface of a flat-plate. A mesh sensitivity study summarized in Appendix F indicated the adequacy of grid resolution for the present application. Two different injectant temperatures were simulated numerically and compared to experimental data collected by Tucker [100]. Two additional pressure ratios for the heated injection configuration were also examined to assess the effects different values of  $p_{inj}/p_\infty$  had

on the formation of the Mach disk and  $p_t$  losses in the jet plume.

Mach contours and shock structure predictions from both turbulence models were generally found to compare well with experimental results. The only significant discrepancy was the predicted location of  $x_{sep}$ . This discrepancy was shown to be the result of incorrect modeling of the inflow boundary-layer thickness.

It was found through variation of the injectant pressure that a Mach disk formed at a pressure ratio between  $p_{inj}/p_\infty = 5$  and  $p_{inj}/p_\infty = 10$ . Corresponding to the increase of injectant pressure, the shock structure of the plume became more defined and when  $p_{inj}/p_\infty = 10$ , the total pressure loss across the shock was 90% of  $p_t$  prior to crossing the shock. This was a significant increase in  $p_t$  losses from the 8% loss seen when  $p_{inj}/p_\infty = 2.25$  and the plume had a less defined shock structure. While pressure losses were large for  $p_{inj}/p_\infty = 10$ , at this pressure ratio injectant penetration into the inflow was 200% deeper than the penetration was for  $p_{inj}/p_\infty = 2.25$ . Clearly, in terms of  $p_t$  losses, the higher pressure ratio was less desirable than the lower pressure ratio. However, the increase in mixing and combustion efficiency gained by the deeper penetration of the injectant into the inflow may outweigh the total pressure losses.

Profiles of  $\tau_{xy}$  predicted by the two turbulence models compared well to the experimental data available. The general shape of the computed profiles for  $\tau_{xy}$  agreed with the experimental data for both injectant temperature configurations. Errors in magnitude were noted for both models, however the predictions of the RSTM were significantly better than those predicted by the  $K - \epsilon$  model.

Non-physical predictions by the  $K - \epsilon$  model and some inconsistencies in the RSTM were identified in the comparisons of contour plots for the Reynolds stress,  $y^+$  and  $f_{w_1}$ . It was shown that the  $K - \epsilon$  model predicted non-physical discontinuities in the Reynolds stresses when  $\tau_w$  was approximately zero over more than one cell. This caused  $y^+$  to remain inappropriately small outside

the boundary-layer. The inconsistencies seen in the RSTM were caused by incorrect computation of  $y^+$ . The current computational method for  $y^+$  in the ISAAC algorithm did not insure the value used for  $\tau_w$  was at the streamwise location normal to the vertical location of  $y$  for which  $y^+$  was being computed. This oversight resulted in incorrect values for of the anisotropic wall damping function,  $f_{w_1}$ , which caused incorrect application of the anisotropic dissipation rate and pressure-velocity-gradient correlation models in the recirculation region behind the slot.

Finally, it was shown that  $K$  accounts for as much as 8% of  $E$  in regions with significant shock/boundary-layer interaction.



## Chapter 7 - Three-Dimensional Results and Analysis

### 7.1 Introduction

The primary objective of the second phase of research is validation of the second-order ZSGS RSTM for three-dimensional supersonic injection at a  $25^\circ$  angle. Once the model is validated, numerical simulations with the RSTM are used to investigate aspects of the flowfield not readily visible with conventional data collection methods.

This chapter is divided into four sections in which the results of this investigation are presented. Section 7.2 provides an overview of the McCann and Bowersox experimental configuration and associated test conditions (see Figure 3) [52]. In Section 7.3 arguments are presented attesting to the suitability of the RSTM and  $K - \epsilon$  models for simulating the aforementioned flowfield. The discussion is based on results from three analyses. The first is a comparison of experimental data and computational results from the two turbulence models at a station approximately 20 effective nozzle diameters,  $d$ , downstream of the nozzle ( $d = 0.3861\text{cm}$ ). At this station, experimental data and computational results are compared for correctness of magnitude and flowfield distribution. The second analysis is a comparison of computational results of mean flow and turbulent variables from the two turbulence models for which experimental data is not available. The model predictions are evaluated for differences in magnitude, flowfield distribution and non-physical behavior. The final analysis presented in Section 7.3 is for the boundary-layer predictions from the two models. The main conclusion of these analyses is that the  $K - \epsilon$  formulation is unacceptable for modeling transverse jet injection into a supersonic flow (TJISF) because of non-physical behavior of the computed Reynolds stresses arising from the Boussinesq approximation. The analyses also show that the RSTM is a physically consistent formulation, however, the RSTM should be evaluated further for flowfield validity.

The topic of Section 7.4 is validation of the computational procedure for implementation of

the RSTM. Section 7.4 begins with a discussion of flowfield symmetry and how it can be used to reduce the number of grid points required to simulate the flowfield at downstream locations beyond station 20. Numerical simulations from two different computational grids at station 20 ( $x/d = 19.81$ ) are used to assess the suitability of a symmetry boundary condition at the test section centerline. These simulations are performed with the RSTM. The *full-plane* grid modeled both sides of a symmetric flowfield, while the *half-plane* grid only modeled half of the flowfield and used a symmetry boundary condition at the test section centerline. An analysis of the results shows that the computed flowfield solutions are essentially the same. The second part of this section is a comparison of the computational results from the RSTM and the experimental data collected at station 40 ( $x/d = 39.65$ ). As at station 20, the experimental data available and the computational results are compared for correctness of magnitude and flowfield structure, leading to the conclusion that the RSTM is a reasonably valid model for simulation of oblique TJISE.

Finally, Section 7.5 presents a detailed description of the evolution of the flowfield simulated with the RSTM from a streamwise station  $1.5d$  upstream of the nozzle center, to a station  $20d$  downstream of the nozzle center. This description is performed with visualizations of Mach contours,  $\omega_x$  contours and velocity vectors. The flowfield description identifies many flow features not readily visible with conventional LDV or hot-wire techniques. Of particular interest are the mechanisms that induce the rotation of the heretofore unidentified recompression-shock-induced vortices and the locations where the jet induced vortices develop in the flowfield and where they dissipate from the flowfield.

### **7.1.1 Generalized Three-Dimensional Flowfield Description and Terminology**

Prior to beginning the analysis of the flowfield and the turbulence models, a brief description of some differences and similarities between normal injection flowfields and the oblique injection flowfield under investigation is given. During this discussion, much of the terminology used

throughout the rest of this chapter is introduced.

Many of the flow structures found in the oblique TJISF generated by McCann and Bowersox's experiments are similar to the features identified by Santiago and Dutton [70] in Figure 61 for normal TJISF. Some of the flow structures common to both types of injection and some previously unidentified structures are shown in Figure 62. Each of these features are discussed in greater detail in Section 7.5. This figure is a visualization of the RSTM predictions for  $\omega_x$  at the surface of the test section and at selected cross sectional planes. Like the normal TJISF, the obstruction caused by oblique TJISF, results in jet induced and boundary-layer separation shocks upstream of the nozzle, these shocks are collectively referred to as the bow shock. The surface location of the bow shock and boundary-layer separation line is visible near the leading edge of the test section surface in Figure 62. Also common to both types of injection is the horseshoe vortex which forms just upstream of the nozzle orifice. However, the lower injection angle of this configuration results in a weaker, less defined horseshoe vortex than those seen in normal TJISF [5, 70].

In Figure 61, Santiago and Dutton [70] depict the crossflow vortices as continuous structures forming at the nozzle orifice with a barrel shock and Mach disk imbedded within the vortex structure. The analysis presented in Section 7.5 indicates that this depiction is incorrect for oblique injection at a  $25^\circ$  angle. In Section 7.5, it is shown that vortical fluid rotation begins at the sides of the nozzle orifice and is outside of the injectant plume, not within it. This rotation is induced by the interaction of the expanding injectant and the inflow air which has moved up and over the horseshoe vortex. These jet induced (JI) vortices then follow along the sides of the plume until they are consolidated with the vortices inside the expanding plume near  $x/d = 8.0$ .

The analysis in Section 7.5 also shows that the crossflow vortices identified by Santiago and Dutton in Figure 61 are actually recompression shock induced (RSI) vortices. The RSI vortices form near  $x/d = 6.5$  and are caused by the combined effects of the upwash and the mirrored shock

structure of the oblique barrel (OB) shock. Shortly after the RSI vortices appear in the flowfield, the mechanisms which sustain the rotation of the JI vortices are disrupted and the rotating fluid in the JI vortices is incorporated into the RSI vortices near  $x/d = 8.0$ . It is shown that the RSI vortices are not simply a translation of the JI vortices to another location within the flowfield since both of these vortices are present between  $x/d = 6.5$  and  $x/d = 7.5$ .

A fourth vortex pair forms in the wake of the plume near the test section surface. These wake vortices, shown in Figure 62, trail behind the plume on either side of the line defined by  $z/d = 0.0$ .

Throughout this chapter the terms core flow and inflow air are used interchangeably and they both refer to the supersonic inflow air which originates upstream of the bow shock. The terms jet and plume are also used interchangeably to refer to the mass of fluid entering the flowfield through the nozzle orifice.

## 7.2 Supersonic Oblique Injection: McCann and Bowersox Configuration

McCann and Bowersox experimentally investigated the mean flow and turbulence structure associated with oblique TJISF for the tunnel and injector mean flow conditions listed in Tables 7 and 8. The experiments were conducted in the AFIT Mach 3.0 wind tunnel, which consists of a rectangular test section, 33cm long with cross sectional dimensions of  $6.35 \times 6.35\text{cm}$  (see Figure 3). A conical nozzle was designed to inject pressurized air at a  $25^\circ$  angle downstream into the inflow air and was set in the center of the test section. The nozzle throat and exit diameters were 3.264mm and 3.861mm respectively. The exit of the conical nozzle at the surface of the test section floor was an ellipse. The elliptical exit had major and minor axes measuring 9.5mm and 4mm. The exit diameter of the conical nozzle,  $d = 3.861\text{mm}$ , is used as the reference length throughout this chapter. At  $x/d = 20$ , McCann and Bowersox reported experimental data obtained with single overheat hot-wire probes for mean flow variables  $U$  and  $V$ , and turbulence data for  $\tau_{xy}$  and  $K$ . Data was also collected at  $x/d = 40$  for mean flow variables  $U$ ,  $V$  and  $W$ , and turbulence variables  $\tau_{xy}$ ,

$\tau_{xz}$  and  $K$ . Schlieren photography was also used to visualize streamwise shocks in the flowfield and oil smears were used to describe surface flow conditions [52].

McCann and Bowersox's data collection grid consisted of 13 streamwise planes between  $z/d = -3$  and  $z/d = 3$  at half diameter intervals and 85 vertical stations between  $y/d = 0.4$  and  $y/d = 10.0$  at  $0.11429d$  intervals. A stepper-motor drive assembly was used to move the probes through the grid points normal to the test section surface at each  $z/d$  station. Lateral translation between the streamwise planes was performed manually by a mechanical screw/slide assembly which held the stepper motor.

Numerical uncertainty estimates provided by McCann and Bowersox [52] are summarized in Table 9. According to McCann and Bowersox, these uncertainty estimates account for the propagation of Pitot and cone static probe transducer calibration, probe location, and tunnel condition repeatability [52].

McCann and Bowersox's data collection grid is superimposed over the contour plots of all quantities in this chapter for which experimental data is available. This was done to facilitate comparison of the numerical results and the experimental data.

Table 7. Freestream mean flow conditions for McCann and Bowersox configuration [52]

Parameter	Tunnel Conditions
$M_\infty$	2.9
$p_{t_\infty}$	204 kPa
$T_{t_\infty}$	294 K
$\rho_{t_\infty}$	$2.41 \text{ kg/m}^3$
$p_\infty$	6.45 kPa
$T_\infty$	110.0 K
$\rho_\infty$	$0.204 \text{ kg/m}^3$
$u_\infty$	$610 \text{ m/s}$
$a_\infty$	$210 \text{ m/s}$
$Re/m$	$16.2 \times 10^6$

Table 8. Injector mean flow conditions for McCann and Bowersox configuration [52]

Parameter	Injector Conditions
$M_{inj}$	1.8
$p_{t_{inj}}$	391.1 kPa
$T_{t_{inj}}$	294.0 K
$\rho_{t_{inj}}$	4.64 kg/m <sup>3</sup>
$p_{inj}$	67.34 kPa
$T_{inj}$	178.4 K
$\rho_{inj}$	1.32 kg/m <sup>3</sup>
$u_{inj}$	436 m/s
$v_{inj}$	203 m/s
$w_{inj}$	0 m/s
$Re/m$	$52.6 \times 10^6$

Table 9. Uncertainty analysis results [52]

Measurement	Error, %
$p_t/p_{t_\infty}$	11.0
$\overline{\rho u_i}/(\rho u)_\infty$	6.0
Reynolds stresses	20.0

### 7.2.1 Boundary Conditions and Grid Configurations

All numerical simulation results for the full-plane and half-plane grids discussed in this chapter use the boundary conditions listed in Tables 10 and 11. The implementation of these boundary conditions for turbulence and mean flow variables is presented in Section E.3.2. The mean flow parameters listed in Tables 7 and 8 are used as inflow and jet boundary conditions for all numerical simulation results discussed in this chapter.

An inflow boundary layer was not simulated for these computations since reliable boundary-layer data upstream of the jet was unavailable at the time the simulations were performed.

The full-plane grid used in Sections 7.3 and 7.5 had  $i, j, k$  dimensions of  $275 \times 101 \times 105$  and physical dimensions of  $x/d = -5$  to  $x/d = 21$ ,  $y/d = 0$  to  $y/d = 5.2$  and  $z/d = -3.25$

to  $z/d = 3.25$ . The domain of this grid was not required to extend to the upper and side walls of the test section because the reflected shocks from these wall did not interact with the injection flowfield prior to station 20. The dimensions of this grid encompass all relevant flow structures needed to model the flowfield at  $x/d = 20$ . The half-plane grid used to obtain the simulation results presented in Section 7.4 had  $i, j, k$  dimensions of  $339 \times 121 \times 61$  and a physical domain ranging from  $x/d = -7.0$  to  $x/d = 41.5$ ,  $y/d = 0$  to  $y/d = 16.4$  and  $z/d = 0$  to  $z/d = 8.22$ . Modeling of the upper and side walls was needed to properly simulate the flowfield past station 20, because the reflected shocks from these walls interacted with the injection flowfield prior to station 40.

The grid sensitivity studies conducted to arrive at these two grid configurations are presented in Section F2.3. The coordinate system originates at the center of the nozzle orifice for both grids and is shown in Figure 63.

Comparison and contrasts of the  $y-z$  domains of the two computational grids and the McCann and Bowersox data collection grid are shown in Figure 64. As seen in Figure 64, the full-plane grid extends beyond the  $z/d$  domain of the experimental data collection grid, but covers only half of the  $y/d$  domain. In contrast to the full-plane grid, the half-plane grid extends beyond the  $y/d$  domain, up to the upper wall of the test section, but covers only half of the  $z/d$  domain. However, on one side of the test section, the half-plane grid extends beyond the  $z/d$  domain and out to the side wall of the test section. Complete schematics of these grids and their associated cell spacings are given in Figures 193 and 192 in Section F2.3.

Table 10. Three-dimensional supersonic oblique injection boundary conditions for the full-plane grid

Plane	Condition
Inflow	Tunnel conditions listed in 7
Outflow	Extrapolation
Left side	Extrapolation
Right side	Extrapolation
Top	Extrapolation
Bottom	Wall
Jet	Jet conditions listed in 8
Nozzle dimensions	semimajor axis=0.475 semiminor axis=0.200

Table 11. Three-dimensional supersonic oblique injection boundary conditions for the half-plane grid

Plane	Condition
Inflow	Tunnel conditions listed in 7
Outflow	Extrapolation
Left side	Tangency
Right side	Tangency
Top	Tangency
Bottom	Wall
Jet	Jet conditions listed in 8
Nozzle dimensions	semimajor axis=0.475 semiminor axis=0.200

### 7.2.2 Non-Dimensionalization

Contour plots of the numerical results and experimental data are all non-dimensionalized as specified in Section 5.4 with the exception of vorticity. The contour plots of the vorticity components have dimensional units of  $rad/s$ . Vorticity is reported in dimensional units to allow direct comparison to the experimental data. Also, unless otherwise stated, all turbulence terms are scaled by  $U^2$ . This scaling retains consistency with the traditional reporting methods of experimental turbulence data. For example,  $\tau_{xy}/U^2 = (\tau_{xy_d}/a_\infty^2) (a_\infty^2/\tilde{u}^2) = \tau_{xy_d}/\tilde{u}^2$ , where  $\tau_{xy_d}$  and  $\tilde{u}$  are



both dimensional quantities.

### 7.3 Evaluation of Results at Station 20

In this section, numerical predictions of the  $U$  and  $V$  components of velocity, the turbulent shear stress  $\tau_{xy}$  and the turbulent kinetic energy  $K$  are compared to experimental data obtained at station 20 (Subsection 7.3.1). Also evaluated are the numerical predictions of the thermo-mechanical and Reynolds stress variables for which experimental data is unavailable (Subsection 7.3.2). Finally, a boundary-layer analysis of the two turbulence model predictions is presented (Subsection 7.3.3).

#### 7.3.1 Comparison of Experimental Data to Computational Results at Station 20

In this subsection, an analysis of the experimental data and the corresponding numerical results from station 20 is presented. The contour intervals used to plot the experimental data are also used to plot the numerical results. While these contour intervals may mask some of the finer flowfield details of the computational results, especially in the boundary layer, it allows direct comparison of the computational results to the experimental data. The limits of the contour intervals for the computational results are rescaled for boundary-layer analysis in Section 7.3.3.

Two distinct flow regions are identified in the contour plots of the experimental data for the mean flow and turbulence variables. In the middle part of each contour plot is the injectant plume and in the lower part of the plot is the boundary layer. The separation of the plume and boundary-layer is clearly seen in the experimental data for the  $U$  component of velocity (Figure 65). In this figure, there is a distinct region where the velocity of the plume is markedly different from the surrounding flowfield. At this station the axial velocity in the plume has increased from the initial streamwise velocity of 2.2 at the nozzle exit to about 2.6. This is still lower than the surrounding flowfield's streamwise velocity of 2.8. The lateral extent of the jet plume has increased from the initial value of  $1.036d$  at the nozzle exit to approximately  $3.75d$  and exhibits some minor asymmetric

behavior about  $z/d = 0.0$ . The “bottle” neck of the contours on the lower side of the plume rising further above the boundary layer as it moves farther downstream of the nozzle. The indentations along the bottom of the plot at  $z/d = 0.0$  and  $z/d = 2.0$  represent the upper limits of the boundary layer.

Only minor differences are seen in the predictions from the two turbulence models for the  $U$  component of velocity (Figure 66). The only appreciable differences occur near the centerline in the boundary layer, as discussed later in Section 7.3.3. The height of the plume at the centerline is measured with the predictions of the  $U$  component of velocity and predictions from both models agree well with the experimental data. The predicted height of  $4.0d$  from the RSTM is only 1% less than the experimentally measured value of  $4.03d$ , while the value of  $4.2d$  from the  $K - \epsilon$  model is only 4% greater than the experimental value. The numerical predictions for the vertical extent of the plume is  $2.6d$  from RSTM and  $2.7d$  from  $K - \epsilon$ . Both of these predictions are in good agreement with the experimentally measured value of  $2.62d$  (1.5% for RSTM and 3% for  $K - \epsilon$ ). The numerical predictions for the lateral extent of the plume are in poorer agreement with the experimentally measured value of  $3.7d$ . Both models predicted lateral extents of  $2.90d$ , or a 21% difference. Generally, the predicted magnitude of  $U$  from both models is slightly larger than the experimentally measured magnitudes over most of the domain.

Contours of the experimental data for the  $V$  component of velocity are shown in Figure 67. These data exhibit an asymmetric behavior about  $z/d = 0.0$  that is somewhat stronger than that seen in  $U$ . The maximum upwash velocity at this station has decreased from the initial upwash velocity of 0.97 at the nozzle exit, to a maximum of about 0.8 at  $z/d = 0.0$ . The maximum downwash velocities near  $z/d = -1.5$  and  $z/d = 2.0$  correspond to the outer edges of the RSI vortices discussed in Section 7.5. The downwash is helpful in identifying the lateral extent of the vortices at this station.

Only minor differences for the  $V$  component of velocity (Figure 68) are seen in the predictions of the two turbulence models. Predictions from both models for the magnitude and location of maximum upwash are nearly identical to the experimentally measured values. However, at  $z/d = -1.5$  the predictions from both models for the magnitude of the maximum downwash are 0.3 less than the experimentally measured value. In contrast to, the predicted values from both models for the downwash are in complete agreement with the measured values at  $z/d = 1.5$ .

The experimental data seen in Figure 69 for the  $\tau_{xy}$  component of the Reynolds stress tensor shows a central core of positive shear stress slightly offset to the right of the centerline. However, the extent of positive shear stress is symmetric about the centerline. This central core is surrounded by a horseshoe shaped region of negative shear stress which is basically centered about the centerline. However, the shear stress is more negative to the left of the centerline.

The predicted structure of  $\tau_{xy}$  is not consistent between the two turbulence models. The horseshoe shaped region and the central core identified in Figure 69 is predicted by both turbulence models. However, as seen in Figure 70, only the RSTM correctly predicted the relative location of the horseshoe structure with respect to the central core. The  $K - \epsilon$  model incorrectly predicted the location of the horseshoe structure, placing it well above the central core of positive stress.

In general, the RSTM predictions for  $\tau_{xy}$  are consistent with the experimental data in that they smoothly progress from the large positive values in the central core to the negative values away from the centerline. In contrast to this, the  $K - \epsilon$  predictions simply reflect a change in the flow direction: positive shear stress when the flow turns in towards the center of the test section and a negative shear stress when it turns away from the center.

A physical phenomenon can be attached to these regions of positive and negative stresses through an evaluation of the Mach contours and shear stresses as shown in Figures 71 and 72. The analysis in Section 7.5 and the work of Hartfield and Bayley [27] and Williams and Hartfield

[110] show that in the plume, much of the fluid between  $z/d = -0.25$  and  $z/d = 0.25$  is inflow air. Furthermore, the analysis shows that the injectant is concentrated in the regions between  $z/d = -1.25$  and  $z/d = -0.75$  and between  $z/d = 0.75$  and  $z/d = 1.25$ . The majority of the mixing occurs in the transition zone between the regions of inflow concentration and injectant concentration. These regions are identified in the Mach contours shown in Figure 71. The interfaces between the zones are defined by sharp gradients in the Mach contour levels and are also marked in Figure 71. In Figure 72, the Mach lines are superimposed over a magnified area of  $\tau_{xy}$ . The  $\tau_{xy}$  contours from the  $K - \epsilon$  model respond to steep Mach gradients in the vertical direction. On the other hand, the  $\tau_{xy}$  contours from the RSTM respond to Mach gradients in all directions and for all magnitudes of the gradient.

The sign of the  $\tau_{xy}$  results from the  $K - \epsilon$  model are characterized by the direction of the Mach gradient with respect to origin of the Cartesian coordinate system superimposed over the contours in Figure 72. In the  $K - \epsilon$  model,  $\tau_{xy}$  is computed from Eq. 53 and is of the form

$$\tau_{xy} = -\frac{\mu_t}{\rho} \left( \frac{\partial \tilde{u}}{\partial y} + \frac{\partial \tilde{v}}{\partial x} \right) \quad (226)$$

It should be clear from the results shown in Figures 66 and 68 that in the plume,  $\partial \tilde{u}/\partial y$  is dominate over  $\partial \tilde{v}/\partial x$ . Thus, in quadrants I and II,  $\tau_{xy}$  is negative because  $\partial \tilde{u}/\partial y$  is positive and in quadrants III and IV,  $\tau_{xy}$  is positive because  $\partial \tilde{u}/\partial y$  is negative. The gradients of  $\tilde{u}$  with respect to  $z$  are not accounted for in Eq. 226; thus values of  $\tau_{xy}$  at the sides of the interfaces have either the wrong sign or the predicted value is negligible.

In the contours for the RSTM, the sign of  $\tau_{xy}$  correspond to radial changes in the Mach gradients. As a radial line from the plume origin passes through negative Mach gradients,  $\tau_{xy}$  becomes more positive and when positive gradients are encountered,  $\tau_{xy}$  becomes more negative. Despite this analysis, the validity of one model over the other is determined by the experimental data in Figure 69 and the experimental data clearly shows that only the RSTM predictions are physically

consistent.

Predictions for the vertical and lateral extent of the stresses are also inconsistent between the two models. The RSTM correctly predicts the range of the vertical extent of the positive shear stress, placing it between  $y/d = 2.4$  and  $3.3$ , while the  $K - \epsilon$  model incorrectly places the range between  $y/d = 2.3$  and  $2.7$ . The experimentally determined range is between  $y/d = 2.2$  and  $3.4$ . The RSTM prediction for the lateral extent of the shear stresses is also more accurate than those of the  $K - \epsilon$  model. The RSTM placed the range of the lateral extent ( $3.08d$  wide) between  $z/d = -1.54$  and  $1.54$ , while the extent predicted by the  $K - \epsilon$  model is between  $z/d = -0.74$  and  $0.74$  ( $1.48d$  wide). The experimental data showed the lateral extent of the plume is actually located between  $z/d = -1.99$  and  $2.0$  ( $3.99d$  wide). Thus, the range predicted by the RSTM is 22% smaller than the experimental range, while the range predicted by the  $K - \epsilon$  is 63% smaller than the experimental range.

The higher resolution of the computational grid used for the RSTM predictions reveal details about the structure of  $\tau_{xy}$  distribution not visible in the experimental data ( $K - \epsilon$  predictions are not discussed here since they are physically inconsistent). A definite partitioning of the central core and the horseshoe structure is seen in the RSTM predictions (Figure 70). Furthermore, these partitioned structures are symmetric about the test section centerline. The predictions for the positive central core show it is comprised of five subregions. There are the two prominent positive stress structures on either side of  $z/d = 0.0$ . There is also a very thin region of positive stress running vertically up the  $z/d = 0.0$  line. This region is approximately  $0.06d$  wide. Between the pockets of positive stress is a band of negative stress which connects the upper and lower sections of the horseshoe structure. The horseshoe structure is also partitioned at  $z/d = 0.0$  by a band of lower magnitude negative stresses. Also seen in the predictions by the RSTM is a region out beyond the horseshoe structure where positive stresses reappear.

As with  $\tau_{xy}$ , the experimental data for  $K$  has a central core of turbulent kinetic energy concentrated about the centerline (Figure 73). The structure of the contours suggest there are two separate maxima for  $K$ , one on either side of the centerline. Along the bottom of Figure 73 are two distinct regions of increased activity centered about  $z/d = -1$  and  $z/d = 1$  which are representative of the upper extent of the boundary layer.

The partitioning of the  $K$  distribution is clearly seen in the numerical predictions of  $K$  (Figure 74). The RSTM captures the general upside-down cardioid shape of the experimentally measured cross-sectional area, whereas the  $K - \epsilon$  model does not. The cross-sectional area of the plume is implied by the vertical and lateral extent of  $K$  [9]. Both models predict cross-sectional areas for  $K$  that are significantly smaller than the experimentally measured area (Figure 73). A lateral extent of  $2.74d$  and a vertical extent of  $3.0d$  is predicted by the RSTM, whereas the predictions by  $K - \epsilon$  have dimensions of  $1.75d$  and  $2.6d$  respectively. Thus, the RSTM predicts a significantly larger area than the  $K - \epsilon$  model, but the RSTM prediction is still smaller than the experimentally measured dimensions of  $3.8d$  and  $4.05d$ . Both turbulence models give similar predictions for the vertical extent of the maximum turbulence. Using only the contour with the greatest magnitude, the RSTM and  $K - \epsilon$  predictions are  $1.8d$  and  $1.6d$  respectively, which are significantly larger than the experimentally measured length of approximately  $0.6d$ .

Based on this analysis, several general observations about the accuracy of the turbulence models and the resolution of the experimental data are appropriate. The choice of turbulence model does not have a significant effect on the predicted values of the  $U$  and  $V$  velocity components outside of the boundary layer. To within 7%, both turbulence models correctly predict the values of  $U$  and  $V$  at station 20. In contrast to the velocity components, model selection has a significant effect on the distribution and magnitude of  $\tau_{xy}$ , and to a lesser degree on  $K$ . Generally, correct predictions of the shape and magnitude of  $\tau_{xy}$  contours by the RSTM contribute to the validation of this model

for TJISF. The incorrect prediction of the distribution of  $\tau_{xy}$  with the  $K - \epsilon$  formulation indicates that this model is not appropriate for accurate simulation of TJISF.

The adequacy of the lateral resolution of the experimental data is questionable and could contribute to some of the discrepancies already noted. Of the variables examined thus far, contour plots of the numerical results indicate that maxima and minima of quantities being measured do not consistently correspond to the experimental data collection grid points. The small width of the negative turbulent shear stress between the positive turbulent shear stresses in Figure 70 could have been missed during experimental data collection. This lack of resolution could also have exaggerated the apparent asymmetry of the experimental flowfield, especially if a maximum or minimum is captured on one side of the centerline, but not on the other. Considering that the computed gradients of the turbulence variables are very large and that the probes were repositioned by hand, the asymmetry observed in the experimental data could have been exaggerated by poor grid resolution and systemic errors in probe positioning. Additional data supporting this conjecture is provided in subsequent sections.

It should be noted that the initial condition for the  $W$  component of velocity exiting the nozzle was assumed to be zero. Subsequent evaluation of the injector-nozzle used by McCann and Bowersox revealed that this device had a divergence angle of  $0.83^\circ$ . This increase to outward velocity of the injectant could account for some of the error seen in the numerical results for the width of the plume.

Correct modeling of the flowfield physics is crucial to supersonic combustion simulations [9, 24]. Of the two models evaluated, only the RSTM correctly predicted the distribution of  $\tau_{xy}$  seen in the experimental data. The Reynolds stresses at the interface of the injectant and inflow air are critical to mixing. These terms influence the rate of convection and diffusion of the two fluids through the momentum and energy equations, Eqs. 21 and 22 respectively [9]. If the stresses at

the interfaces are physically incorrect representations of the flowfield, the mixing rates will also be incorrect. Gruber has stated that injectors which create large magnitudes of Reynolds stresses, generally have better mixing characteristics than those with smaller magnitudes of the Reynolds stresses [24].

### 7.3.2 Evaluation of Computational Results for Variables Without Experimental Data at Station 20

One of the most significant advantages CFD has over other forms of analysis is the ability to examine aspects of the flowfield that cannot be measured experimentally, or if they can, there is an unacceptable degree of error in the measurements. This advantage is used here to further assess the suitability of the turbulence models by examination of the predicted behavior of the five other Reynolds stresses, the three components of vorticity, the  $W$  component of velocity and the mean flow temperature.

The individual axial Reynolds stresses are often not reported in experimental data. Frequently, these terms are lumped together and collectively reported as  $K$ . The following discussion presents an analysis of the effects the individual axial stresses have on the structure of  $K$  and their contribution to vorticity. Also addressed are the inconsistencies between the two models for enforcement of the realizability constraint placed on the axial stresses and  $K$ .

In Section 7.3.1 the contour intervals for  $K$  are scaled to maximize visualization of the experimental data. However, this masked many of the details present in the numerical results. Therefore, the contour intervals for  $K$  are rescaled in Figure 75 to maximize visualization of the structure of  $K$  outside of the boundary layer. The contour intervals are rescaled again to maximize visualization of the boundary layer in Section 7.3.3.

The axial Reynolds stresses and  $K$  are related through the expression

$$K = \frac{\tau_{xx} + \tau_{yy} + \tau_{zz}}{2} \quad (227)$$



Easy evaluation of each axial stress component's contribution to  $K$  is possible if the limits of the contour intervals of the stresses are based on the above relationship. If each axial stress component is assumed to contribute equally to the total magnitude of  $K$  (this is the assumption made in the  $K - \epsilon$  model to  $O(y^2)$  [29]), then the appropriate maximum contour level for the axial stresses should be 2/3 maximum contour level of  $K$ . The minimum contour level is determined by Schumann's *realizability* constraint ( see Section 4.3.2.1) [78]. Realizability requires  $K$  and the axial Reynolds stresses be greater than zero at all locations in the flowfield.

Despite the realizability constraint, predictions for the axial Reynolds stresses with the  $K - \epsilon$  model often result in non-physical values. The colorless regions shown in the  $K - \epsilon$  contours for  $\tau_{yy}$  and  $\tau_{zz}$  (Figures 77 and 78), are areas where negative values are predicted. Negative axial Reynolds stresses are a violation of Schumann's requirement of realizability [78] and imply negative turbulent energy. In the  $K - \epsilon$  model, realizability is only applied to the conserved variable  $K$  and not on the axial Reynolds stresses which are derived variables in the  $K - \epsilon$  model and are computed with the constituent relationship given by Eq. 53. The axial stress form of Eq. 53 is

$$\tau_{ii} = \frac{2}{3}K - \frac{2\mu_t}{\rho} \left( \frac{\partial \tilde{u}_i}{\partial x_i} - \frac{1}{3} \frac{\partial \tilde{u}_l}{\partial x_l} \right) \quad (228)$$

and relates the axial stresses to  $K$  and to the axial velocity gradients through the Boussinesq approximation. It is easily seen that if  $K$  is negligible and the velocity gradients are sufficiently large, a negative value for  $\tau_{ii}$  will result.

In contrast to the  $K - \epsilon$  model, in the RSTM realizability is enforced on each of the individual axial Reynolds stresses and because they are the conserved variables in this model,  $K$  is the derived term [56]. This not only assures a physically consistent solution for the axial Reynolds stresses, but since  $K$  is computed from Eq. 227, it has a physically consistent solution as well. As seen in the RSTM results shown in Figures 76 - 78, all of the axial Reynolds stress predictions are greater than zero.

The contour plots of  $K$  in Figure 75 graphically illustrate the dependence on  $K$  of the axial Reynolds stresses in the  $K - \epsilon$  model. Comparison of the contours in Figure 75 to the contours of the Reynolds stresses in Figures 76 - 78 for the  $K - \epsilon$  model show that each of the components are nearly identical. In contrast to this, the axial Reynolds stresses and  $K$  from the RSTM have the same general shape, but the magnitudes of the individual components are significantly different.

The root cause of the patterns seen in these figures is again found in the method used to arrive at the individual shear stresses. In Section 4.2 it is shown that in Eq. 228,  $K$  is  $O(y^2)$  and that  $(\mu_t/\rho)(\partial \tilde{u}_i/\partial x_i)$  is at most  $O(y^3)$ . Thus, the magnitude of the axial stresses, computed in the  $K - \epsilon$  model, are dominated by  $K$  and the velocity gradients only have a lower order contribution. Since axial Reynolds stresses are conserved variables in the RSTM, they are determined by the flow physics.

Computing the axial Reynolds stresses with Eq. 228 also has a homogenizing effect on these terms and removes the anisotropic turbulent behavior from the flowfield solution. Anisotropic turbulence is defined in Hinze [29] as turbulent flow where the axial Reynolds stresses are not equal. The homogenization of the axial stresses is seen in Figure 79. Shown in this figure are contours of  $\tau_{zz} - \tau_{yy}$ . These contour clearly show that outside of the boundary layer the predicted difference of these terms computed with the  $K - \epsilon$  model is an order of magnitude less than the predictions from the RSTM. It is easily shown with Eq. 228 that the difference between the  $K - \epsilon$  predictions for  $\tau_{zz}$  and  $\tau_{yy}$  is simply  $\partial \tilde{w}/\partial z - \partial \tilde{v}/\partial y$ .

Homogenization of the axial stresses also has an impact on secondary flow development and vorticity generation. It was shown in Section 4.2.2, for the special case of incompressible, fully developed turbulent flow in a rectangular duct, that secondary flows only occur when  $\tau_{zz} - \tau_{yy} \neq 0$  [90, 91]. While secondary flow development in an injection flowfield is not solely dependent on  $\tau_{zz} - \tau_{yy} \neq 0$ , this term's contribution to  $\omega_x$  is seen mathematically in Eq. 58 and graphically in

Figure 80. In Figure 79 the difference between  $\tau_{zz}$  and  $\tau_{yy}$  outside the boundary layer is as much as an order of magnitude larger for RSTM than it is for  $K - \epsilon$ . This implies that predictions from the RSTM for  $\omega_x$  should be larger than the prediction from  $K - \epsilon$ . As seen in Figure 80, this is exactly what occurs. In this figure the maximum magnitude of vorticity outside of the boundary layer is approximately  $10,000 \text{ rad/s}$  (12.5%) greater in the RSTM predictions than it is in the  $K - \epsilon$  model and the RSTM prediction for vorticity strength in the boundary layer is almost an order of magnitude larger than the vorticity predicted by the  $K - \epsilon$  model. The boundary-layer vorticity is discussed further in Section 7.3.3.

It is noted here, that aside from the differences in magnitude, the distribution of  $\omega_x$  (Figure 80) is nearly identical for both models. The relevance of this observation will be made clear later in this section.

The vorticity component,  $\omega_x$ , is a measure of the rate of rotation of a fluid particle. Thus, the vorticity should be largest at points in the flow where the highest rates of rotation occur. This observation is illustrated in Figure 80, where the RSI vortex centers of rotation are seen at  $y/d = 2.88$  and  $z/d = \pm 0.64$ . Accordingly, the largest magnitudes of vorticity are seen near these points in Figure 80.

The relative velocity vectors in Figure 80 show why the largest magnitudes do not coincide with the centers of rotation. The  $x$  component of vorticity was defined in Eq. 60 as

$$\omega_x \equiv \frac{\partial \tilde{w}}{\partial y} - \frac{\partial \tilde{v}}{\partial z}$$

Thus, maximum values of  $\omega_x$  occur where velocity gradient differences are largest. As seen in the relative velocity vectors, the maximum velocity gradient for  $\partial \tilde{v} / \partial z$  occurs normal to  $z/d = 0$  as the centers of rotation are approached and  $\partial \tilde{w} / \partial y$  is relatively small compared to  $\partial \tilde{v} / \partial z$  over most of the flowfield outside of the boundary layer.

The sign of  $\omega_x$  indicates the direction of rotation. In Figure 80, positive  $\omega_x$  corresponds to

clockwise rotation and negative  $\omega_x$  to counter-clockwise rotation. This is also verified with the relative velocity vectors in Figure 80.

The vertical extent of the RSI and wake vortices can be estimated with the contours of the  $W$  component of velocity (Figure 81). It is reasonable to expect maxima of  $W$  to correspond to upper and lower extrema of a vortex. The extrema of the vortices are labeled in Figure 81. Extrema 1 and 2 correspond to the upper and lower bounds of the RSI vortices, while Extrema 3 and 4 to the wake vortices.

The local rate of rotation and the frequency of contact between the interfaces of the injectant and the inflow can be inferred from the magnitude of  $W$  at the extrema. The larger  $W$  is, the faster the local rate of rotation, thus the more frequent the contact. Northam and Anderson have shown that mixing rates increase as the frequency of contact between the injectant and inflow increases [60]. In the RSTM predictions, the magnitude of  $W$  at the bottom of the RSI vortices and at the top of the wake vortices are approximately equal to each other. However, in the  $K - \epsilon$  contours, the magnitudes of  $W$  at these same extrema differ by approximately 15%. Thus the frequency of contact between these two interfaces is less frequent in the  $K - \epsilon$  model than it is in the RSTM.

Accurate temperature predictions are critical to combustion processes and thrust production in SCRAMjets [49, 60] and proper predictions of the magnitude of the axial Reynolds stresses impact the temperature at every location in the flowfield. The temperature in the flowfield is computed from the nondimensional form of the total energy expression (Eq. 2)

$$E = e + \frac{U_i^2}{2} + K \quad (229)$$

and the perfect gas relation  $T = c_v E$ , where  $c_v$  is the specific heat at constant volume. Thus the axial Reynolds stresses influence flowfield temperature through  $K$  and algorithms which omit  $K$  from the computation of  $E$  may have an adverse effect on temperature predictions.

Outside of the boundary layer, the choice of turbulence model has its most significant effects

on temperature in the transition zone of the plume (Figure 82). It is seen in this figure that the RSTM predictions for temperature in the transition zone is slightly higher than the predictions of the  $K - \epsilon$  model. The reason for the differences are seen in Figure 83. Clearly,  $K$  comprises a larger fraction of  $E$  in the transition zone of the RSTM predictions than it does in the  $K - \epsilon$  model predictions. Comparison of Figures 82 and 83 show the region where  $K/E$  is larger in the RSTM corresponds to the same location where the temperature is higher in Figure 82. As discussed earlier, the reason for the difference in the magnitude of  $K$  is found in how  $K$  and the axial Reynolds stresses are computed.

The predictions for  $\tau_{xz}$  from the RSTM are significantly more complex than the predictions from the  $K - \epsilon$  model (Figure 84). The RSTM predicts several small flow features not obtained with the latter model. The  $K - \epsilon$  model predicted a weaker band of shear stress, near the centerline and surrounding the larger turbulent structure than the RSTM. Furthermore, the  $K - \epsilon$  model did not predict the crescent shaped bands of turbulence seen in the RSTM results which bracket the outer limits of the larger turbulent structures.

In the absence of experimental data, the correctness of one set of results over the other can not be asserted with absolute certainty. However, if the analysis applied to the  $\tau_{xy}$  contours is applied here for  $\tau_{xz}$ , the Mach gradients indicate the RSTM results are the correct representation of  $\tau_{xz}$ . The contours of the RSTM results reflect changes in the shear stress at all of the Mach gradient interfaces. However, the  $K - \epsilon$  results only reflect gradient changes in the  $z$  coordinate direction. The reason for this is obvious from the equation below

$$\tau_{xz} = -\frac{\mu_t}{\rho} \left( \frac{\partial u}{\partial z} + \frac{\partial w}{\partial x} \right) \quad (230)$$

In this region of the flow field, values of  $\tau_{xz}$  are dominated by  $\partial u / \partial z$  as changes in  $w$  with respect to  $x$  are negligible.

The sign of  $\tau_{xz}$  in the RSTM predictions reflects a dependence on Mach number gradient with

respect to the radial distance from the apparent center of the plume similar to that seen for  $\tau_{xy}$  with one exception. The sign of  $\tau_{xz}$  reverses when  $z/d = 0$  is crossed. Thus, for  $z/d > 0$ ,  $\tau_{xz}$  is positive if the Mach gradient is negative and negative if the Mach gradient is positive. Conversely when  $z/d < 0$ ,  $\tau_{xz}$  is negative if the Mach gradient is negative and positive if the Mach gradient is positive.

Outside the boundary layer, differences in the predictions of  $\tau_{yz}$  by the two models are visible in Figure 85, but they are relatively small. The differences are small because  $\tau_{yz}$  is modeled by gradients of  $V$  and  $W$  and at this station the velocity gradients for these terms are small. However, the cause of the differences is apparent from the following equation which is used in the  $K - \epsilon$  model to compute  $\tau_{yz}$

$$\tau_{yz} = -\frac{\mu_t}{\rho} \left( \frac{\partial v}{\partial z} + \frac{\partial w}{\partial y} \right) \quad (231)$$

It is seen in this equation that only changes in one coordinate direction is considered for each velocity component. However, **velocity gradients are not unidirectional in rotating flowfields**. This is the primary reason models based on the Boussinesq approximation fail to predict physically consistent distributions for the shear stresses in a rotating flowfield. The RSTM predictions are physically consistent because they are not constrained to unidirectional changes in the velocity gradients.

It may be possible to modify the  $K - \epsilon$  formulation to consistently predict shear stresses in a rotating fluid. It was noted earlier in this section that the only significant difference between the predictions from the two model for  $\omega_x$  is the magnitude of the vorticity. Outside of the boundary layer, this same observation is true for  $\omega_y$  (Figure 86) and  $\omega_z$  (Figure 87). A remarkable similarity is now observed between the distribution of the  $\tau_{yz}$  contours from RSTM (Figure 85) and the distribution of the  $\omega_x$  contours from  $K - \epsilon$  (Figure 80). Aside from a difference in magnitude, outside of the boundary layer the distribution of these two sets of contours are nearly identical. This observation (with an additional change in sign) is also true of the  $\tau_{xz}$  contours from the RSTM

(Figure 84) and the  $\omega_y$  contours from  $K - \epsilon$  (Figure 86). These two observations suggest that a more correct relationship of the shear stresses and the velocity gradients in a rotating flowfield, may be through the components of vorticity rather than the mean strain rate. The only limitation to this observation selection of the appropriate constant of proportionality and a suitable relationship for  $\tau_{xy}$ . Comparison of the RSTM predictions for  $\tau_{xy}$  in Figure 70 and the  $K - \epsilon$  predictions for  $\omega_z$  do not exhibit the similarities seen with the other two pairs of contours.

Now consider the specific expressions for the turbulent shear stresses given by Eq. 53 and the definition of the components of vorticity [3]. The equations are given below as:

$$\tau_{yz} = -\frac{\mu_t}{\rho} \left( \frac{\partial v}{\partial z} + \frac{\partial w}{\partial y} \right) \quad \tau_{xz} = -\frac{\mu_t}{\rho} \left( \frac{\partial u}{\partial z} + \frac{\partial w}{\partial x} \right) \quad \tau_{xy} = -\frac{\mu_t}{\rho} \left( \frac{\partial u}{\partial y} + \frac{\partial v}{\partial x} \right) \quad (232)$$

$$\omega_x = -\left( \frac{\partial v}{\partial z} - \frac{\partial w}{\partial y} \right) \quad \omega_y = -\left( \frac{\partial u}{\partial z} - \frac{\partial w}{\partial x} \right) \quad \omega_z = -\left( \frac{\partial u}{\partial y} - \frac{\partial v}{\partial x} \right) \quad (233)$$

Note the similarity in the form of these equations. The paired equations differ only by a proportionality constant and the sign of the second term. Thus, it is suggested that if an appropriate proportionality constant is developed, the expressions for the components of vorticity may provide better predictions for  $\tau_{xz}$  and  $\tau_{yz}$  than the traditional definition used in the standard  $K - \epsilon$  model. Therefore, a more correct form for the Boussinesq approximation for vortical flows may be  $\tau_{ij} \propto \epsilon_{ijk} \omega_k$ , where  $\epsilon_{ijk}$  is the alternating tensor, rather than  $\tau_{ij} \propto S_{ij}$ .

Based on the observations made in this section, the suitability of the  $K - \epsilon$  model for modeling this flowfield is questionable. The  $K - \epsilon$  model predicts non-physical solutions for the axial Reynolds stresses because the realizability constraint is enforced on  $K$  rather than the axial Reynolds stresses. This is caused by the improper relation of the axial Reynolds stresses to  $K$  and results in incorrect magnitudes for the axial Reynolds stresses and weaker vorticity and lower mean flow temperature predictions. It is also seen the Reynolds shear stresses are incorrectly modeled by the  $K - \epsilon$  formulation because the Boussinesq approximation does not properly account for multidirectional velocity gradients of the same velocity component. These incorrect predictions can

have a detrimental effect on mixing efficiency, combustion and, ultimately, thrust. To account for the multidirectional velocity gradients, it is proposed that a form for the Boussinesq approximation more consistent with vortical flow physics maybe  $\tau_{ij} \propto \epsilon_{ijk}\omega_k$  rather than traditional form of  $\tau_{ij} \propto S_{ij}$ .

### 7.3.3 Boundary-layer Analysis

Thermodynamic limitations of the hot wire probes used by McCann and Bowersox restricted their data collection grid to  $0.4d$  ( $1.6mm$ ) above the surface of the test section [51]. However, the versatility of numerical simulations permits visualization of the boundary-layer and in this section, further assessment of the differences observed in the predictions from the turbulence models are examined. Through a boundary layer analysis, a qualitative comparison of the mean flow thermo-mechanical variables and the turbulence variables discussed in the previous sections is presented.

To illustrate the lower bound of McCann and Bowersox's grid, the grid is superimposed over the numerical results in Figure 88. This plot, depicting the contours for  $K$  (Figure 88), shows the large region of the flowfield not captured by the intrusive methods used by McCann and Bowersox. It is clear that the indentations seen in previous contours of the experimental data are boundary-layer data. Note that in this figure and in all subsequent boundary-layer figures, the aspect ratio of the axes has been changed from 1 to 0.6. This was done to magnify the boundary-layer and still permit visualization of the entire  $z/d$  range shown in previous sections, however, this change may result in some boundary-layer phenomena being exaggerated. Also, in these figures, the turbulent quantities are no longer scaled by  $U^2$  but by  $a_\infty^2$ . This allows visual order of magnitude comparisons of the velocity components and the turbulence quantities without performing any conversions to the numerical results and it avoids division by zero at the test section surface.

The differences seen in the turbulence variables outside the boundary-layer, are just as pronounced inside the boundary-layer. This is especially true at the test section centerline. At the



centerline, the RSTM predictions for  $K$  (Figure 88) have their greatest magnitude. In contrast, the  $K - \epsilon$  predictions for  $K$  are almost constant across the surface. It is counter-intuitive for  $K$  to be nearly constant across the entire lower surface since the turbulent flow structure in the boundary layer must be affected by the wake vortices located on either side of the centerline.

Since the axial Reynolds stresses in the  $K - \epsilon$  model are essentially  $2/3K$ , it is reasonable to expect their contours to look just like the contours for  $K$  and this is exactly what is seen in the  $K - \epsilon$  model predictions shown in Figures 89 - 91. However, in RSTM,  $K$  is  $1/2$  the sum of the axial Reynolds stresses. Therefore, contours of the axial Reynolds stresses from the RSTM should look similar to  $K$ , but there is no reason for any two components to have the same values. As seen in Figures 89 - 91 the magnitudes predicted by the RSTM for the three components do vary greatly.

The RSTM predictions indicate that the relative magnitudes of the three axial Reynolds stresses to each other have changed from what they were outside the boundary-layer. Now  $\tau_{xx}$  has the largest magnitude of the three, followed by  $\tau_{zz}$  and then by  $\tau_{yy}$ . The reversal in the magnitudes of  $\tau_{zz}$  and  $\tau_{yy}$  in the boundary-layer implies that the direction of rotation of the wake vortices should be opposite that of the RSI vortices. This is verified by the vorticity contours seen in Figure 92.

The vorticity transport equation (Eq. 58) in Section 4.2.2, shows that vorticity strength is influenced by the magnitude of the difference between  $\tau_{zz}$  and  $\tau_{yy}$  [91]. This is seen by comparing the magnitude of  $\tau_{zz} - \tau_{yy}$  from the two models to the magnitude of  $\omega_x$ . At nearly every location below  $y/d = 0.4$  in Figure 93, the RSTM values for  $\tau_{zz} - \tau_{yy}$  are almost an order of magnitude larger than those from the  $K - \epsilon$  model. Comparison of the two models predictions for  $\omega_x$  shows that the RSTM values are also close to an order of magnitude larger than the  $K - \epsilon$  values for the vorticity in the wake vortex. In general, the RSTM values for  $\tau_{zz} - \tau_{yy}$  and  $\omega_x$  are larger throughout the boundary-layer. Thus, the opening statement about Eq. 58 holds true in the boundary-layer.

Since  $K$  has its greatest magnitude in the boundary-layer, it might be expected that the fraction

of  $E$  comprised by  $K$  would be more significant than it is outside the boundary-layer. The ratio of  $K/E$  is plotted in Figure 94, where it is seen that nowhere in the  $K - \epsilon$  model predictions does  $K$  comprise more than 1.4% of  $E$  or more than 1.9% in the RSTM predictions. The significance of these ratios on the flowfield are seen in the boundary-layer temperature contours (Figure 95). As seen in this figure, the  $K - \epsilon$  model predicts a constant temperature at all surface locations of station 20. In contrast, RSTM predicts a higher temperature than the  $K - \epsilon$  model over most of the surface, but in the region where  $K/E$  is a maximum, the temperature at the surface is a minimum. Clearly, the increased contribution of  $K$  to  $E$  at the centerline is insufficient to compensate for other factors which reduce  $E$ , and thus the temperature.

In addition to a higher temperature over most of the surface, the RSTM predicted a thicker thermal boundary-layer. This is seen as a thicker zone of higher temperatures at the surface. The thermal boundary-layer thickness and surface temperature are critical to accurate heat-transfer rate predictions and to the selection of materials used to construct combustors and other surfaces requiring heat resistant or heat conducting properties [87].

The contours of the turbulent shear stress predictions seen in Figures 96 - 98 show significant differences between model predictions for all three for these terms. These terms influence aerodynamic heating through the skin friction and drag and although the turbulent shear stresses go to zero at the wall, their magnitudes near the wall impact the laminar sublayer through the momentum and energy equations.

Using a two-dimensional flow analysis, it was shown in Sections 6.2.3 and 6.3.4 that because the  $K - \epsilon$  formulation does not model the second-order pressure-velocity-gradient tensor and is restricted to isotropic turbulence dissipation rates, the models predict significantly different values for the shear stresses in the vicinity of shocks and secondary flow structures. Figure 99 shows where anisotropic turbulence dissipation rates are modeled by the RSTM. The function  $f_{w1}$  is the

wall damping function used in Eq. 437 to determine where the anisotropic turbulence dissipation rate model is applied. In the RSTM, anisotropic turbulence dissipation rates are accounted for where  $f_{w_1}$  is non-zero. Since the  $K - \epsilon$  model does not model anisotropic turbulence dissipation rates of the shear stresses, its effect are unaccounted for in the predictions.

The lack of an anisotropic model in the  $K - \epsilon$  formulation does not account for the large differences seen in the shear stress contours in the boundary layer. Figure 99 shows that the region influenced by the wall models is small. The cause of the differences is identified in Section 7.3.2. The Boussinesq approximation in the  $K - \epsilon$  formulation only models unidirectional velocity gradients, and like the flow outside the boundary-layer, the presence of wake vortices clearly makes the boundary-layer a rotating flowfield.

In the previous two sections it is seen that outside of the boundary-layer the differences between the turbulence model predictions for the velocity components are not significant. However, within the boundary-layer the differences in the  $V$  and  $W$  components are more pronounced. The change in behavior is brought about by an increase in the magnitude of the axial Reynolds stresses in the boundary-layer. In the boundary-layer, the axial Reynolds stresses are only an order of magnitude less than the  $V$  and  $W$  components. This is seen in Figures 89 - 91 and Figures 101 and 102). In these figures, larger changes in the magnitude of  $V$  and  $W$  are predicted by the RSTM as the centerline is approached along the  $z/d$  axis and to a lesser degree, this trend is also seen in Figure 100 for  $U$ . These velocity differences are also a result of the RSTM model formulation which allows the Reynolds stresses to be solved as individual conserved variables without any presupposed relationships.

General observations of the numerical results in this section indicate that the  $K - \epsilon$  model provides less physically consistent predictions of the boundary-layer quantities than the RSTM. This is particularly true for the turbulent stresses and the surface temperature. The inconsistency in

the  $K - \epsilon$  predictions are linked to the model's inability to correctly account for non-unidirectional velocity gradients and anisotropic axial Reynolds stresses. Credibility of the RSTM predictions in the boundary-layer is reinforced by its consistency and accuracy outside the boundary-layer.

#### 7.3.4 Summary of Results at Station 20

A summary of the findings to this point is presented here. First, the  $K - \epsilon$  model has several inherent deficiencies which make it an inappropriate model for detailed numerical simulations of this flowfield when physically correct turbulent quantities are needed from the simulation. If mean flow values of the thermo-mechanical term are the desired quantities, the  $K - \epsilon$  model provides reasonably satisfactory results. This statement is based upon the following observations: 1) incorrect prediction of the distribution and magnitude of  $\tau_{xy}$  in the jet plume; 2) incorrect prediction of the distribution and magnitude of  $K$  in the jet plume; 3) prediction of non-physical solutions for the axial Reynolds stresses outside the boundary-layer; 4) incorrect relationships of the axial Reynolds stresses to  $K$  over the entire flowfield, and 5) correct prediction of the distribution and magnitude of  $U$  and  $V$ . Second, while not yet concluding that the RSTM is validated by this analysis, it is reasonable to conclude that this model is an improved choice for turbulence closure when conducting numerical simulations of this flowfield. This statement is based on the following observations made in the preceding analyses: 1) correct prediction of the distribution and magnitude of  $\tau_{xy}$  in the jet plume; 2) correct prediction of the distribution and magnitude of  $K$  in the jet plume; 3) prediction of physically possible solutions for the axial Reynolds stresses over the entire flowfield; 4) correct relationships of the axial Reynolds stresses to  $K$ , and 5) correct prediction of the distribution and magnitude of  $U$  and  $V$ .

Based on these observations, there is little reason to continue to evaluate flowfield simulation results from the  $K - \epsilon$  model, since a primary objective of this research is validation of the RSTM. Thus, further analysis of the flowfield is performed only with numerical results from the RSTM and

experimental data.

Separate regions where inflow air and injectant are concentrated is identified through an analysis of Mach contours and velocity gradients and it is shown that the interfaces between these regions are coincident with higher magnitudes of the Reynolds stresses. A correlation is noted between the sign of  $\tau_{xy}$  and the sign of the Mach number gradient with respect to radial distance from an apparent center of the plume. Furthermore, this correlation and numerical results from the RSTM and  $K - \epsilon$  model for  $\tau_{xz}$  and  $\tau_{yz}$ , is used to establish the unsuitability of the  $K - \epsilon$  model based upon the Boussinesq approximation for simulating Reynolds stresses in rotating flowfields. The Boussinesq approximation fails because its formulation assumes unidirectional changes in the velocity components used to compute the shear stresses.

It is also observed that the predicted distribution of vorticity of each component of vorticity from both models is nearly identical. It is also observed that the  $\tau_{xz}$  and  $\tau_{yz}$  predictions from the RSTM have distributions of shear stress very similar in shape to the distributions observed in the contour plots of  $\omega_x$  and  $\omega_y$ . Thus, it is postulated that more physically correct approximations of  $\tau_{xz}$  and  $\tau_{yz}$  may be given by  $\tau_{ij} \propto \epsilon_{ijk}\omega_k$  rather than traditional assumption that  $\tau_{ij} \propto S_{ij}$ .

Finally, it is suggested that a contributing factor to the asymmetry observed in the experimental data is the sparse number of streamwise data collection planes and systematic errors in probe positioning. The analysis conducted in Section 7.3.1 called into question the adequacy of the number of streamwise planes in which experimental data is reported. It is seen in the contour plots of variables for which experimental data is available, that the predicted maxima and minima of the variables do not consistently coincide with the data collection grid points. Since the spacing between each plane is almost  $2mm$ , a lack of resolution could easily exaggerate the apparent asymmetry of the experimental flowfield, especially if a maxima or minima is captured on one side of the centerline, but not on the other. The possibility of capturing a maxima or minima on one side of

the centerline and not capturing it on the other side is reasonable when one considers the predicted gradients of the turbulence variables are very large and that the lateral translation of the probes was performed by hand.

## 7.4 Evaluation of Results at Station 40

Two topics of discussion are presented in this section. The first topic is an evaluation of the symmetry boundary condition used with the half-plane grid and the second topic addressed in this section is the continued validation of the RSTM and its implementation in the ISAAC algorithm.

The primary experimental data station used by McCann and Bowersox is  $x/d = 40$ ; thus, the computational grid must extend beyond this station. Furthermore, the grid must extend to the upper and side walls of the test section so the reflection shocks are accounted for in the flowfield solution. A comparison of the cross-sectional domain of the full-plane grid and the test section (Figure 64) shows that a substantial increase in cross-sectional area needs to be modeled in order to capture the shocks.

Modeling the entire test section represents a significant increase in time and computational resources required to obtain a converged solution. A single converged solution with the full-plane grid requires approximately 250 CPU hours and 256 Megawords when the simulation was performed on the Cray J916 located at the Aeronautical Systems Command Major Shared Resource Center, Wright-Patterson AFB, OH. Thus, a strategy to reduce total CPU run time and the number of computational nodes is required so the test section from  $x/d = -5$  to 41 can be modeled. The reduction strategy employed is the symmetry boundary condition at the test section center line.

Since  $x/d = 40$  is the primary data collection point used by McCann and Bowersox [52], there is substantially more experimental data available for validation purposes at this location. At station 40, numerical predictions are compared to experimental data for the  $U$ ,  $V$  and  $W$  components of velocity,  $\tau_{xy}$ ,  $\tau_{xz}$  and  $K$ .

### 7.4.1 Symmetry Boundary Condition Evaluation

The symmetry condition reduces the computational resources required to model a symmetric flowfield by a factor of two. It is seen in Section 7.3 that the computational results for every variable in this flowfield is symmetric. Therefore, a properly implemented symmetry condition on the  $z/d = 0.0$  plane should be an acceptable alternative to modeling both sides of the test section. By using this boundary condition, the additional resources required to encompass station 40 are obtained from the redistribution of the resources used to model both sides of the flowfield with the full-plane grid. The grid resolution study, see Appendix F, resulted in the half-plane, which has  $i, j, k$  dimensions of  $339 \times 121 \times 61$ . After accounting for the ghost cells needed to enforce boundary conditions, this grid required 2,714,112 computational nodes. This is less than the number of nodes used in the full-plane. Approximately 8000 iterations (approximately 225 CPU hours and 256Megawords) are required to reach a converged solution with the RSTM. A visualization of the domain modeled by this grid is seen in Figure 192 and a summary of the cell spacing is also provided in Appendix F.

Validity of the symmetry boundary condition is investigated by comparing RSTM simulation results at station 20 from the full-plane grid to those of the half-plane grid. In Figures 103 - 110, displayed quantities for  $z/d > 0.0$  correspond to the half-plane grid and those for  $z/d < 0.0$  to the full-plane grid. The flow variables in these figures are selected for evaluation because these terms are compared to experimental data at station 40 in Section 7.4.2.

There are some minor differences in the grid spacing which are seen in Figure 103. In this figure, the region modeled by both grids is marked by the thick line.

Evaluation of the numerical data in Figures 104 - 110 indicate that the differences in the flowfield solution from the two grids are minor and do not constitute a significant change in the flowfield solution. The most significant changes are seen in the contour plots of the velocity

components. In each of the plots, the continued propagation of the bow shock is seen in the half-plane grid results and its presence contributes to the differences visible in the velocity components. These changes are minor and are only seen in the contours closest to zero in plots of the  $V$  and  $W$  components (Figures 104 and 105). The impact on  $U$  is also minor as is seen in Figure 106. In the full-plane grid, the extrapolated boundary condition predicted that the lower limit of the shock is slightly closer to the plume than it is in the half-plane grid. This may account for the slight differences between the two solutions in the central part of the plume as well. The changes in the velocity components are so small that vorticity is only affected in its contours closest to zero. There is a slight upward shift seen in Figure 107 of the location of the maxima. This shift is also seen in the contours for  $U$  and  $V$ .

The changes in the turbulence quantities are also minor. These differences are seen in Figures 108 - 110 and generally consist of a slight increase in the region where turbulent activity is predicted. There is also a slight elevation of the centers of activity in each of terms which is consistent with the trend seen in Figures 104 - 107.

In both the  $U$  and  $W$  contours from the full-plane grid predictions, there is a discontinuity in the contours at the uppermost plane. This is caused by the extrapolation of interior flowfield data to the boundary of the domain. This discontinuity only appears when there is a sudden change in flow conditions across the cells used for the extrapolation. This situation is seen at the top of the  $W$  contours in Figure 105. In Figure 105, there is a spot marked in the half-plane grid where the contour levels of  $W$  changes from one level to another. As seen in Figure 103, this change occurs between the cells defining the upper boundary in the full-plane grid. A similar phenomena is observed in the contours of variables in the half-plane grid along  $z/d = 0.0$ . This is because the symmetry boundary condition also uses extrapolated data from the interior of the domain to compensate for the lack of specific flowfield data at the boundary.



Overall, the symmetry and extrapolation boundary conditions give very similar results in the regions where they have common domains. The differences seen in the contours are attributed to the following deficiencies in the methods used to compute the solution. First, some fidelity of the solution is lost in the half-plane analysis at  $z/d = 0.0$  and in the full-plane analysis at the top of the domain, because extrapolated values from only the interior of the domain are used to establish the solution at these boundary locations. The impact of this limitation can be minimized with small grid spacing along these planes. Second, since the half-plane grid extends to the side and top walls of the test section, effects from the tangency boundary condition may be influencing the solution at the centerline. Third, there are minor differences in the grid spacing between the two grids.

It is seen in this section that the differences in the flow predictions from the two grids are minor and do not constitute a significant change in the flowfield solution. Therefore, it is assumed that the half-plane grid, with a symmetry condition at  $z/d = 0.0$ , will result in an acceptable discretization of the flowfield.

#### **7.4.2 Comparison of Experimental Results to Computational Results at Station 40**

Station 40 is the primary data collection point used by McCann and Bowersox [52], consequently there is substantially more experimental data at this station which can be used to further validate the RSTM for this flowfield. At this location, numerical predictions are compared to experimental data for the  $U$ ,  $V$  and  $W$  components of velocity,  $\tau_{xy}$ ,  $\tau_{xz}$  and  $K$ .

Contour plots of the experimental data collected by McCann and Bowersox at station 40 are shown in Figures 111 - 118. Visual comparisons of the data to the numerical results are enhanced by superimposing the experimental data grid over the contours in all of the figures presented in this analysis. For added ease of comparison between the data sets, the computational results from the half-plane grid are mirrored across the test section centerline.

Regions of higher concentrations of injectant and inflow air are identified at this station as

they are at station 20. In Figure 111 the inflow air forced up into the injectant plume (additional details in Section 7.5) has continued to rise further up into the test section. The region with the higher concentration of injectant has continued to rotate around the edges of inflow core and is now under it. The transition interface between the injectant and inflow is also shown in this figure. The relevance of the radial arrows labeled  $r_1$  and  $r_2$  in the experimental contours is addressed later during the discussion of the  $\tau_{xz}$  contours.

Good agreement is seen between the experimental data and the numerical results in Figure 111. The lower velocity inflow is easily identifiable in the experimental data, however, a concentrated zone of injectant can not be identified. This indicates that the injectant may have diffused faster than predicted by the RSTM. The remnants of the upwash is also identifiable in both sets of contours

The experimental data for the Mach number as well as the  $U$  component of velocity (Figure 112) indicates the jet plume is a single structure roughly centered about the test section centerline. Within the plume some asymmetric behavior is observed and this is indicated by the lower velocity region ( $U \approx 2.70$ ) offset from the centerline. There is also some asymmetric behavior in the boundary-layer, indicated by the low velocity indentations seen at  $z/d = -2.0$  and  $2.0$ . At  $z/d = 2.0$  the velocity is lower than it is at  $z/d = -2.0$ .

Overall, the numerical results for  $U$  and the experimental data are in good agreement for the range of velocities within the plume and at the upper edges of the boundary-layer. However, the RSTM predicted two separate low velocity zones on either side of the centerline, where as the experimental data only shows one. In Figure 66, discussed in Section 7.3.1, these regions are identified as zones containing a higher concentration of inflow air than injectant. It is also seen that the two regions identified as zones containing a higher concentration of injectant than inflow air, has rotated down and under the inflow zones.

Good agreement between the numerical results and data is also seen in the predicted plume

height. The experimentally measured height of the center of the plume was approximately  $4.25d$  and the height predicted by the RSTM was  $4.75d$ . The experimentally measured width of the plume at the center of the plume was approximately  $3d$  and the predicted plume width from the RSTM was  $2d$ . The RSTM prediction of a smaller plume width than the experimentally measured width is consistent with the trend seen at station 20.

Excellent agreement between the experimental data and the numerical results for  $V$  is seen in Figure 113. The only significant differences seen for the upwash is that the peak values of the experimental data are offset from the centerline by about  $0.25d$ . The experimentally measured width of the upwash is approximately  $2.25d$ , whereas the RSTM prediction is  $1.5d$ , thus continuing the trend of the RSTM predicting narrower structures than experimentally measured. The agreement for maximum downwash is not as good as the agreement for the upwash. The experimentally measured maximum downwash near  $z/d = -2.5$  is approximately  $-0.20$ , however, the RSTM predictions for the downwash are only  $-0.10$ . Furthermore, the location of maximum downwash differed by  $0.75d$  between the RSTM results and the data. There is also a significant difference in the measured maximum downwash from one side of the test section to the other. The peak downwash is 50% larger at  $z/d = -2.5$  than it is at  $z/d = -2.0$ . Furthermore, the measured value at  $z/d = -2.0$  is much closer to the numerical value.

The high degree of asymmetry seen in the experimental data for  $W$  conflicts strongly with the numerical results presented in Figure 114. The experimental data has the appearance of being shifted up for  $z/d > 0$  and down for  $z/d < 0$ . Also, the magnitudes of the measured sidewash are significantly larger for  $z/d > 0$  than the magnitudes for  $z/d < 0$ ; this is especially true for the positive sidewash. Its magnitude for  $z/d > 0$  is 78% larger than it is on the other side.

Since the RSTM predictions on one side of the test section are a reflection of the other, the numerical results can not be used to contradict the asymmetric behavior. However, examination of

the location of the extrema do suggest a possible cause for the asymmetry. The distances between the extrema seen in the numerical contours and the measured data suggest that the physical flowfield is indeed asymmetric and that there is a preferred state for the  $W$  component of velocity on opposite sides of the centerline. Labeled in the numerical results shown in Figure 114 are eight extrema for  $W$ , two for each vortex. In the experimental results there are only four extrema. Certainly, the limited range of the data collection grid accounts for the absence of extrema 4 and 8. However, the reason for the other two missing extrema is not apparent.

The vertical distances between the extrema in the numerical and experimental contours suggest that extrema 2 and 7 seen in the numerical results are the missing pair in the measured data. In the numerical results, the vertical distance between extrema 5 and 6 is  $2.2d$  and the distance between extrema 1 and 3 is  $3.73d$ . In the measured data, the vertical distance between extrema labeled 1 and 3 is  $4.05d$  and the distance between extrema 5 and 6 is  $2.4d$ . A comparison the separation distances between extrema 1 and 3 in the experimental data to the distance between these extrema in the numerical results, shows there is only an 8% difference in the separation distances. A comparison of the separation distances of extrema 5 and 6, also results in a 8% difference. These results indicate the labels assigned to the extrema of the measured data correctly correspond to the labels of the extrema in the numerical results. Thus, extrema 2 and 7 are absent from the experimentally measured data. Extrema 2, 3, 6 and 7 are small quantities and as seen in the numerical results, 2 and 3, and 6 and 7 are not directly below each other. Thus, extrema 2 and 7 may have not been detected through the combined effect of several factors. First, the small magnitude of the quantities; second, data grid resolution; and third, systematic errors in probe positioning.

The smallness of the quantities also lends support to the theory that the shocks off of the side walls may have perturbed to the flowfield enough to cause an asymmetric configuration. The perturbation caused by the shocks may not have been sufficient to cause the same reaction in the

numerical solution and the highly dissipative nature of the algorithm, coupled with the absence of time accuracy may have damped out any asymmetric behavior present in the flowfield.

Experimentally measured values and numerical predictions for  $\omega_x$  are seen in Figure 115. Reasonable agreement with the corresponding experimental data for maximum vorticity strength and location of the maximum is seen in these predictions. The wake vortex structures are also observed in the boundary-layer predictions from the RSTM.

Figure 116 shows poor agreement between the magnitude and distribution of the experimental data and the predicted results for  $K$  from the RSTM. The maximum magnitude of  $K$  predicted by the RSTM is significantly larger than the experimentally measured maximum. The experimental maximum is only 0.016, whereas the RSTM maximum is 0.05, (this value is too large to visually identify with the range of contours used to plot McCann and Bowersox's data, but it occurs at the vortex center of rotation located at  $z/d = 0.5, y/d = 4.5$ ). The magnitude of  $K$  predicted by RSTM in the boundary layer is also significantly larger than that reported experimentally. The maximum value reported in the experimental data for  $K$  in the boundary layer is 0.017, whereas the maximum predicted by RSTM in the boundary layer and in the domain of the data collection grid, is 0.6. This value is predicted along the line  $y/d = 0.4$  and is also too large for visual identification with the range of contours used. Despite the magnitude differences, there is good agreement for the vertical location of maximum  $K$  outside the boundary-layer. The average location of the two experimentally measured maxima is  $4.57d$ . The RSTM prediction for the location is  $4.8d$  or a difference of only  $0.23d$ . The average horizontal distance from the centerline of the experimentally measured maxima is  $0.90d$ . The RSTM prediction for the distance is  $0.50d$ .

The numerical predictions shown in Figure 117 for  $\tau_{xy}$  are in good agreement with the experimentally measured magnitudes of the shear stress. The contour shapes from the two sets of data also agree well and are similar to the distributions seen in Figures 69 and 70 at station 20. In

Figure 117, there is a central core of positive shear stress surrounded by a horseshoe shaped region of negative shear stress. Once again, some asymmetry is seen in the locations of  $\tau_{xy}$  extrema, but the overall distribution is relatively symmetric and the RSTM correctly predicted the formation of the horseshoe shaped region surrounding a core of positive shear stress. Here again, this structure corresponds to the interface between the upwash inflow air and the surrounding mixture of injectant and air. The vertical length of  $3.25d$  for the horseshoe structure predicted by the RSTM was only 5% less than the experimentally measured length of  $3.45d$ . Consistent with predictions of other flow structures, the lateral dimensions had poorer agreement with the experimentally measured values than it did in the vertical direction. The lateral dimensions of this structure were predicted by the RSTM as  $2.4d$  or 46% less than the experimentally measured value of  $4.5d$ .

As at station 40, the RSTM predicted two distinct regions of maximum positive shear stress that are symmetric about the centerline, whereas the experimental data reflects a single structure slightly elongated on one side. This region of shear stress corresponds the transition interface between the upwash inflow air and the injectant. The lateral width from the outer edges of these two structures is  $1.3d$ . This is only 7% less than the experimental value of  $1.4d$ . The vertical height of this region is  $1.5d$ , which also is 7% greater than the experimentally measured value of  $1.4d$  for the elongated side. The RSTM also predicted a second region of negative shear stress under the region of positive shear stress. This region corresponds to the interface between the injectant and mixture of inflow air and injectant under the plume.

The most significant differences between the RSTM predictions and the experimental data are for the measured values of  $\tau_{xz}$  as seen in Figure 118. The experimental data exhibited extreme asymmetric behavior in the region near the jet plume and in the boundary-layer. It is also seen in the experimental data, that every point in the flowfield has a positive value for the shear stress. The severe asymmetric behavior and the lack of negative shear stresses is completely contradicted by

the RSTM predictions.

The absence of negative shear stresses in the experimental data is inconsistent with other crossflow variables reported for the secondary flowfield and with the trend established in Section 7.3.2 for the sign of  $\tau_{xz}$ . In Section 7.3.2, it is shown that when  $z/d > 0$ ,  $\tau_{xz}$  is positive if the Mach gradient is negative and negative if the Mach gradient is positive; and when  $z/d < 0$ ,  $\tau_{xz}$  is negative if the Mach gradient is negative and positive if the Mach gradient is positive.

A possible explanation for the extreme asymmetry of  $\tau_{xz}$  is given once the correlation for the sign of the shear stress and the sign of the Mach number gradient is applied to Figure 111. First, consider the line  $r_1$  shown in Figure 111. This line passes through the positive Mach gradient (PMG) as its distance from the apparent center of radius increases. Since  $z/d < 0$  in this region and there is a PMG, values of  $\tau_{xz}$  should be positive, and this is what is seen in Figure 118. Now consider the line  $r_2$ , which is also shown in Figure 111. This line first passes through a negative Mach gradient (NMG) as it moves away from the center, and since  $z/d > 0$ , values of  $\tau_{xz}$  should be positive in this region. Again, this correlation is consistent with the experimental data as a very small region of increased positive shear stress is seen in the experimental data at  $z/d = 0.5, y/d = 4.9$ . Next  $r_2$  passes through a PMG, which appears to be as steep as the PMG  $r_1$  passed through. According to the correlation, this should result in negative values for  $\tau_{xz}$ . However, these negative values are not seen in the experimental data shown in Figure 118.

Consider the values for  $\tau_{xz}$  predicted by the RSTM in the lower set of contours in Figure 118. In these contours,  $\tau_{xz}$  has positive and negative values which are consistent with the correlation for sign and Mach gradients. However, the width of these structures is very small. The largest structures have widths less than  $0.3d$ . This is smaller than the lateral spacing along  $z/d$  in the experimental data collection grid. Thus, if experimental data collection grid is used to sample the numerical results, many of nonzero regions of these structures would be missed.

It is now suggested that the combination of an asymmetric flowfield with small  $\tau_{xz}$  structures and sparse lateral spacing in the data collection grid exaggerated the asymmetry in the flowfield. The trends between the experimental data and the numerical results indicate that the plume is wider than that predicted by the RSTM by a factor of 1.5. Thus, the predicted locations of the nonzero stresses are most likely to be about 1.5 times farther from the centerline than shown in the RSTM contours. If the flowfield is slightly asymmetric (as seen in the other experimental data) then it is possible that the large positive shear stress structure coincided with the data grid in one side of  $z/d = 0.0$ , but none of the negative shear stresses structures were close enough to a grid point to be detected, leading to the severe asymmetric behavior observed in the experimental data.

#### 7.4.3 Summary of Results at Station 40

In this section it is shown that there are only minor differences in the numerical flowfield solutions when a symmetry boundary condition is used at the test section centerline. The subsequent reduction in computational resources required to model only half of the test section made feasible the numerical simulation of the flowfield past the data collection point at station 20.

Comparison of numerical simulation results from the RSTM to experimental data at station 40 indicated that the RSTM is a reasonably valid turbulence model for simulating the oblique TJISF generated by the inflow conditions listed in Tables 7 and 8. Very good agreement is seen between the experimental data and the numerical results for  $U$ ,  $V$  and  $\tau_{xy}$ . Less consistency is seen between the experimental data and the numerical results for  $W$  and  $\tau_{xz}$ . The results of the numerical predictions for these two terms indicate that poor resolution of the data collection grid and systematic data collection errors may have exaggerated the asymmetries seen in the data.

Additional numerical simulations performed with a pressure ratio twice that specified in Table 8 also resulted in a symmetric solution for the flowfield. Contour plots of the thermo-mechanical and turbulence variable predictions at station 10 from the higher pressure simulation are given in



## Appendix G.

It is noted in Chapter 5 that the algorithm used for the numerical simulations uses local time stepping and a diagonalized approximate factorization scheme with second-order Roe flux differencing to solve the governing equations. These features result in a highly dissipative numerical algorithm. Furthermore, local time stepping is used, which means it is not time-accurate to any order of accuracy [63]. Thus, if the static asymmetric behavior seen in the experimental data is caused by the transient growth of an asymmetric mode, it could be filtered out during the computation. Therefore, even though it is suggested that the asymmetric behavior is amplified by poor grid resolution and systematic errors, inherent flow physics can not be completely discounted.

### 7.5 Flowfield Investigation

It is shown in this section that the principal agent responsible for enhanced vortical motion in the flowfield are the RSI vortices. These vortices are generated through the combined effects of the upwash behind the plume of the inflow air and the mirrored shock structure of the oblique barrel (OB) shock. This vortex pair forms downstream of the OB shock terminus and inside the jet plume. Additional analysis of this flowfield shows that the lateral expansion of the plume is impeded by the JI vortices. The rotation of the JI vortex pair is sustained by the combined effects of the upwash recompression (UR) shock, the inflow sidewash and deflection off of the boundary of the jet plume. The JI vortices, which are initially formed at the sides of the nozzle orifice, extend back along the sides of the plume following the path of the UR shock as it propagates through the test section. The mechanisms which sustain the JI vortices retard plume expansion by directing inflow sidewash back towards the center of the test section and into the plume. The mechanisms which generate the RSI vortices accelerate plume expansion, and therefore mixing, by forcing the injectant to move out away from the center of the test section. It will be seen that once the sustaining mechanism of the JI vortices are disrupted, lateral expansion of the plume accelerates.

It is put forth that the common near-field representation of the injection flowfield shown in Figure 61 is incorrect for oblique TJISF. This figure shows only a single pair of injection-induced counter-rotating vortices outside of the boundary layer. Based on the numerical simulations, a more correct representation of the near-field flow distinguishes between two pair of vortices: the JI vortex pair which forms at the sides of the nozzle and the RSI vortex pair which forms inside the jet plume, but downstream of the nozzle orifice. After the far-field consolidation of the RSI and JI vortices, the traditional representation of the wake structure depicted in Figure 61 is regained. Experimental data from Hartfield and Bayley [27] and [7] corroborates this near-field description and data from McCann and Bowersox [52] corroborates the far-field description.

The flowfield description given above is illustrated with a streamwise, station-by-station description of the evolution of the oblique TJISF. The discussion of the flowfield evolution is based on the RSTM numerical simulation results with the full-plane grid. The results of this simulation at  $x/d = 20$  are the RSTM results presented in Sections 7.3 and 7.4.1. Contour plots of Mach number and  $\omega_x$  at relevant cross-sectional planes are used to illustrate the flowfield evolution. Also included in many of these figures is the location of vortex centers of rotation present in the current cross-sectional plane.

The description of the flowfield begins in Section 7.5.1. In this section Mach contours from the plane defined by  $z/d = 0.0$  are used to identify some of the flowfield structures which will be discussed in Sections 7.5.2 and 7.5.3. Further identification of flowfield structures is provided with near-field and far-field numerical oil smears at the test section surface as well as surface contours of  $\omega_x$  and representative cross-sectional views of the  $x - z$  plane at  $y/d = 0.91$  and  $y/d = 1.49$ . In Section 7.5.2 the actual streamwise development of the flowfield is presented. This is followed by a discussion in Section 7.5.3 of the flowfield from the perspective of the  $x - z$  plane. As a final topic of discussion, in Section 7.5.4, contours plots of predictions from the RSTM and  $K - \epsilon$  models for

surface temperature and skin friction coefficient are compared.

### 7.5.1 Identification of Relevant Flow Features

The first flow features identified in this discussion are seen in the Mach number contours along the centerline of the test section. In the inset of Figure 119, the boundary-layer separation point is indicated at  $x/d = -1.48$ . Also identified in this figure are the boundary-layer separation and jet induced (JI) shocks. These two shocks are collectively referred to as the bow shock, which is shown in Figure 119 along with the centerline slip surface. The slip surface is the local, upper limit of the inflow upwash which is described in more detail in Section 7.5.2. Excellent agreement is seen in the RSTM results and the shadow graphs from McCann and Bowersox for the location of the bow shock. At  $x/d = 3.0$ , the experimental data shows the bow shock at  $y/d = 3.4$ , while the RSTM predict it at  $y/d = 3.7$ .

Also shown in Figure 119 are particle trajectories of injectant leaving the leading and trailing edges of the nozzle. It is seen from these paths that the injectant at the leading edge of the nozzle starts to turn parallel to the inflow air near  $x/d = 3.0$  and that it is almost completely parallel to the inflow air by  $x/d = 6.5$ . The streamtrace of the injectant leaving at the trailing edge of the nozzle closely follows the angle of the slip surface. This streamtrace also shows that the injectant at the trailing edge of the nozzle initially moves parallel to the test section surface before reaching a downstream separation point.

The near-field numerical oil smear (Figure 120) also shows several important surface structures of the flowfield and their approximate locations. This representation is generated with streamtraces of the  $U$  and  $W$  velocity components for the computational cells adjacent to the test section surface. These streamtraces are only two-dimensional representations of the particle paths and the apparent continuity of the path for a single particle in this plane is an illusion created by the absence of the  $V$  component of velocity. Thus, at any point in this flowfield, fluid from a plane above this one may

be replacing a fluid particle from this plane that has moved up to a higher elevation in the flowfield.

At the nozzle exit the high pressure injectant expands outward in all directions. This expansion causes boundary-layer separation upstream of the nozzle. The injectant expanding upstream of the nozzle forms a recirculation zone between the nozzle and the upstream extrema,  $x/d = -1.48$ , of the boundary-layer separation line. The experimentally measured extrema of the boundary-layer separation line is at  $x/d = -1.55$ ; thus, there is only a  $0.07d$  difference in the numerical and experimental data. Within this recirculating region, the fluid is almost exclusively injectant. At the leading edge of the recirculation zone, the inflow deflects the injectant up from the test section surface and back downstream. This results in a horseshoe vortex forming behind the line which defines the boundary-layer separation points. On the downstream side of this line, there is a thin layer of fluid containing injectant and inflow air. This layer is less than  $0.01d$  thick and the fluid above this layer is almost exclusively inflow air. However, because of the injectant's downstream deflection, it is possible for injectant to exist anywhere in the flowfield behind this line.

The outward expansion of the injectant leaving the nozzle between  $x/d = -1.23$  and  $x/d = 0.0$  is held in check by the inflow air which has moved up and over the horseshoe vortices. When the inflow air and the expanding injectant near the surface collide, part of the injectant is forced down to the surface and back in towards the nozzle. The impact points of the injectant with the test section surface is the attachment line seen in Figure 120. The JI vortices, which first appear near  $x/d = -0.25$  are a result of the injectant turning back in towards the nozzle. Consequently, the fluid in the region between the attachment line and the edge of the nozzle, to about  $x/d = 0.5$ , is almost exclusively injectant.

The line on either side of the nozzle between the JI vortices and the edges of the nozzle mark the point where the jet plume separates from the test section surface. These two separation lines converge as the plume rises above the surface, and near  $x/d = 2.0$ , the two lines merge into a single

secondary separation line. Between the plume separation lines the fluid is exclusively injectant. When the plume begins to rise above the test section surface near  $x/d = 0.5$ , inflow air is drawn down to the surface and turned back in towards the centerline to fill the void left by the plume. The turning of the inflow air causes an expansion fan to form and accelerate the air. As the plume begins to separate from the test section surface, the II vortices are carried along with it and near  $x/d = 0.5$  they also leave the vicinity of the surface. Near the point where the two plume separation lines merge, the inflow air streams from either side of the nozzle collide with each other. The line where they collide is the secondary separation line. It will be seen in Section 7.5 that the inflow air not only turns back out away from the centerline, but is pushed up into the bottom of the plume. This *upwash* turning causes an upwash recompression (UR) shock in the jet wake and an *upwash* slip (US) surface forms in the impact region between the upwash and the jet plume.

Not all of the upwash is deflected up into the plume. Some of it is directed back down to the test section surface and forms two wake vortices near  $x/d = 3.0$ . The lines trailing downstream of  $x/d = 3.0$  and away from the centerline can be interpreted as either wake vortex separation lines or as a continuation of the secondary separation line. Either way, this line defines the Mach angle (approximately  $10^\circ$ ) of the UR shock at the test section surface. In the far-field view of the numerical oil smear (Figure 121), it is seen that the wake vortex separation lines continue to move away from the centerline until about  $x/d = 16$ . At this station they are turned back in towards the centerline by inflow of core air. Finally, in Figure 120, a wake vortex attachment line is identified between the wake vortex separation lines.

A great deal of insight as to the structure of a flowfield is available through proper interpretation of  $\omega_x$ . The discussion in Section 7.5.2 relies heavily upon the fact that  $\omega_x$  represents turning of the fluid and that changes in the sign of  $\omega_x$  indicate changes in direction of the turning. As an illustration of the utility of  $\omega_x$ , the features identified in Figures 120 and 121 are correlated with the  $\omega_x$  contours

shown in Figure 122 and several additional flow phenomena not readily visible in the numerical oil smears are identified.

Flow features identified in Figure 120 and also clearly identifiable in Figure 122 by changes in the sign of  $\omega_x$  are the lines defining injectant attachment, jet boundary-layer separation and wake vortex separation. Some features which are not readily identifiable in the oil smear are the bow shock, the line defining the pivot points of the expansion fan and the UR shock and the leading edges of the JI and wake vortices. This figure clearly shows that the bow shock and the boundary-layer separation line are not coincident at any location in the flowfield. Even at the extrema of the shock and boundary-layer separation line, the bow shock is further upstream of the separation point. The line defining the UR shock shows the exact location of the point where the shock begins at the surface. Furthermore, these contours show that the initial angle of the shock in the  $x - z$  plane is approximately  $30^\circ$  and only after the formation of the wake vortices does it shallow to the  $10^\circ$  identified in the oil smear. The leading edges of the initial formation of the JI and wake vortices are also further upstream than indicated by the oil smear. Certainly, the utility of this parameter for identifying relevant flow structures has been demonstrated.

The OB shock is a highly three-dimensional structure, which has different shock characteristics in each of the three coordinate planes. The characteristics of each plane are presented in the following discussion, beginning with the  $x - y$  plane at  $z/d = 0.0$ .

The pressure ratio of the injectant and inflow air is not sufficient to form a sonic disk at the top of the plume or a sonic barrel shock around the plume. However, a *shock disk* and an OB shock do form at the end of the expansion process and are shown in Figure 123. The barrel shock is called oblique because outside of the boundary layer it does not cause a sonic condition around the plume. Like Figure 119, this figure is a contour plot of the Mach number at the test section centerline, but the range of contours has been changed to illustrate the shock and expansion structures in and around

the plume. As the injectant moves up into the core flow, expansion waves form. These expansion waves reflect off the boundary of the jet plume as compression waves and form a shock where they converge at the top of the plume [81]. These expansion and compression waves are manifested as the shock disk and OB shock and it should be noted that at this  $x - y$  plane ( $z/d = 0.0$ ) the OB shock is a slip surface, however in every other  $z/d$  plane it is a shock. The  $x - y$  reflection line roughly represents the vertical location in this plane where the expansion waves are reflected off the plume boundary as compression waves. It will be seen in subsequent discussions that the severity of the OB shock is delineated by this line. These expansion and compression waves, combined with the injection angle and the impact pressure created by the inflow air, give the OB shock a squashed over diamond shape in the  $x - y$  plane.

In the  $y - z$  plane and downstream of the nozzle at  $x/d = 2.0$  (Figure 124), the OB shock has less of a diamond shape. However, the formation of the expansion and compression waves is still evident. Again, below the  $y - z$  reflection line, the pressure equalization process is primarily expansion of the injectant. However, at the boundary of the plume, the expansion waves reflect off of the boundary as compression waves and turn the path of the fluid particles, thus, forming the lower part of the OB shock. The turning caused by the compression waves is illustrated by the streamtrace which exits below the reflection line. Above the reflection line the compression waves converge to form the shock disk and the upper part of the OB shock. The turning caused by the upper part of the OB shock is illustrated by the streamtrace which exits above the reflection line.

In Figure 125 the OB shock has the characteristic diamond pattern described by Hill and Peterson of an underexpanded fluid [28]. The lower part of the OB shock below the  $y - z$  plane reflection line is shown in this figure. In this figure, the OB shock is further categorized as leading edge (LE) and trailing edge (TE) OB shocks. Region I, which is bounded in this plane by the LE OB shock and the  $x - z$  plane reflection line, is composed almost exclusively of expansion waves

originating from the nozzle upstream of  $x/d = 0.0$  and by compression waves reflected from the upstream boundary of the plume. Region II, which is bounded in this plane by the TE OB shock and the  $x - z$  reflection line, is composed of expansion waves originating from the nozzle downstream of  $x/d = 0.0$  and by compression waves reflected from regions of the plume upstream of the  $x - z$  reflection line. The compression waves in region II are stronger than the compression waves in region I because it is downstream of the reflection line. The upper bound of regions I and II is the reflection line in Figure 123 and the lower bound is the lower part of the OB shock in Figure 124. The other labeled objects in Figure 125 will be discussed after the upper part of the OB shock in the  $x - z$  plane is discussed.

The shocks in the upper part of the OB shock are highly curved and form a tear-drop shape. This shape is characteristic of free falling fluids in an atmosphere [81] and the pressure of the inflow air has a similar effect on the shape of the injectant. The region bound by the LE OB shock and the  $x - z$  reflection line (region III) is composed of reflected compression waves from the lower parts of the plume and to a smaller degree, of expansion waves from the upstream part of the plume. Thus, the OB shock in region III should be stronger than the shock in either region I or II. Once again, injectant is leaving the plume through this upper surface in the vertical direction and is interacting with the inflow air, thus this is a shock and not a slip surface. Region IV is almost exclusively composed of reflected compression waves from the other three quadrants of the plume. Thus, the shocks bounding this region are the strongest shocks encountered by the injectant as it leaves the OB shock/shock disk structure.

In the preceding discussion, it is seen that the OB shock/shock disk structure surrounding the plume can be divided into one of four regions separated by three reflection lines, one in each coordinate plane. An expansion/mild-compression region (I), composed mostly of expanding injectant with a small degree of reflected compression waves; an expansion/compression region



(II), composed of a mixture of expanding injectant from the nozzle and reflected compression waves from the upstream regions of the plume; a compression/expansion region (III), composed of reflected compression waves from the lower regions of the plume, then reflected downstream as expansion waves; and finally, a compression/compression region (IV), composed almost entirely of compression waves from the other three regions of the plume.

Several additional shock structures critical to the downstream description of the flowfield form in the wake of the OB shock and are also introduced in Figures 125 and 126. Where the TE OB shocks cross in Figure 125, a type I interference shock pattern of the form identified by Edney [17] and described by Emanuel [18], is formed. As shown by the minimal turning of the particle stream paths crossing them, the mirrored trailing edge (MTE) OB shocks emanating from this region are very weak shocks. These are weak shocks because they are mirrors of the expansion/compression shocks in region II of the OB shock.

The UR shock and US surface formed by the upwash from the inflow air collision, is also identified in the figure. As seen by the significant turning of the particle stream paths, in this part of the flowfield the UR shocks are stronger than the MTE OB shocks. The upstream intersections of the UR and MTE OB shocks also form type I interference shock patterns. A fork at the trailing edge of the OB shock is formed where the upwash forms the US surface and at the downstream intersections of the UR and MTE OB shocks, a lambda shock or a type VI interference shock patterns forms [18].

The inflow air expansion fan is seen outside if the various shocks and the nozzle orifice is also visible in Figure 125.

It is seen in Figure 126 that the relative strength of the MTE OB shocks are significantly stronger above the  $y - z$  plane reflection line than they are below it. Above this reflection line the MTE OB shocks are mirrors of the region IV compression/compression shocks identified in the OB shock structure. The combined effects of these shocks and the UR shocks result in a dramatic

decrease in Mach number from  $\text{Mach} = 6.3$  in the plume to  $\text{Mach} = 1.7$  immediately downstream of the MTE crossover point. It is also seen in Figure 126 that the upstream edges of the UR shocks no longer intersect the OB shock in this plane. At the downstream intersection of these two shocks, a type VI interference shock pattern is formed and in the expansion region of the interference pattern, the upwash forms a slip surface.

### 7.5.2 Streamwise Description

A description of the streamwise evolution of the flowfield is given in the next series of figures. These figures are cross-sectional contour plots of Mach number and  $\omega_x$  in the  $y - z$  plane. The planes examined begin upstream at the bow shock at  $x/d = -1.5$  and continue downstream to  $x/d = 20.0$ . The edges of the nozzle are identified in each of the contour plots at  $x/d$  locations which cross the nozzle. In these figures, centers of rotation corresponding to the JI, RSI and wake vortices are indicated by either a circle or an ellipse. Also, two ranges for the axes are used in these figures. Contour plots at  $x/d$  locations upstream of the nozzle and those over the nozzle are displayed with an enlarged area of the near-field flow. Past the nozzle, the displayed area of the flowfield is increased so that all of the relevant flow activity is visible.

The flowfield description begins at  $x/d = -1.50$ . This location is at the leading edge of the boundary-layer separation shock. The Mach contours in Figure 127 give only the slightest indication of a flow disturbance and there is a slight increase in vorticity.

The correlation between the boundary-layer separation shock in Figure 119 and the shock seen in the Mach contours of Figure 128 is unmistakable. The contours shown in Figure 128 are at  $x/d = -1.25$ , which is just ahead of the nozzle, and as seen from Figures 119 and 120, this station is between the maxima of the line defined by the boundary-layer separation points and the trailing edge of the horseshoe vortices. The vorticity generated by the recirculation in the horseshoe vortices is clearly visible in the vorticity contours of Figure 128. Not all of this vorticity is generated by the

horseshoe vortices. The vorticity in the upper part of the contours is caused by the inflow air moving down towards the test section surface.

At  $x/d = -1.00$ , the leading edge of the nozzle has been crossed and the contours in Figure 129 show the injectant moving up into the flowfield. The recirculating fluid in the boundary layer is still clearly visible in the Mach contours and the sonic line of the OB shock is also seen. The height of the sonic line at this station,  $0.2d$ , is the maximum height attained in the simulation. The location of the injectant is clearly visible in the Mach contours under the recirculation region and a slight acceleration of the fluid caused by expansion is visible in these contours. The boundary-layer separation shock is spreading out and away from the plume and the JI shock is just beginning to move above the separation shock. The lambda shock created by the intersection of these two shocks is visible in the inset of Figure 119. The arms of vorticity overlapping the edges of the nozzle (lower contour plot) are caused by injectant and inflow air turning as the two fluids interact with each other. The majority of the vorticity in the arms is injectant expanding up into the inflow and out away from the nozzle, but some of the vorticity outside the edges of the nozzle is inflow air deflected off the plume boundary and directed up and outward into the test section. The vorticity labeled "up-and-over" is inflow air that is turning out, away from the plume, but is past the horseshoe vortices and is now moving down towards the test section. The vorticity generated by the separation and JI shocks is seen above the up-and-over vorticity. The absence of vorticity in the center of the jet plume indicates the core of the jet is an undisturbed fluid mass.

By  $x/d = -0.50$  (Figure 130), the inflow air has started to check the outward expansion of the injectant spilling over the sides of the nozzle. As indicated in Figure 120, at  $x/d = -0.50$ , the inflow air is forcing the injectant to turn back in on itself and downstream. This is also seen in the vorticity contours of Figure 122 near the point labeled "leading edge of jet induced vortices." In the Mach contours of Figure 130, the downturn in the sonic line near the nozzle edges is the inflow air

forcing the injectant down towards the surface. This turning is also seen in the vorticity contours. In these contours, there is a sign change in the vorticity where the injectant stops moving up-and-out and turns down-and-in.

As the fluids move downstream from  $x/d = -1.0$  to the current location at  $x/d = -0.50$  the jet plume and the JI shock have continued to propagate further up into the inflow air. At this station the JI shock has risen above the separation shock and at the point where they intersect, a lambda shock is formed. The vorticity caused by the inflow turning as it passes through these shocks is also labeled in Figure 130.

At  $x/d = -0.25$ , the JI vortex pair appears in the flowfield just above the sonic line of the OB shock. In the vorticity contours of Figure 131, a change in the sign of the vorticity is visible in small regions immediately under the circles, which mark the center of rotation of the JI vortices. These vortices are defined as the point in the flow where the head-to-tail connection of the  $V - W$  velocity vectors form a complete rotation in the  $y - z$  plane; see inset of the Mach contours in Figure 131. The continued increase in plume cross sectional area is shown by the increase in area where vorticity is negligible over the nozzle and the increase in area of vorticity surrounding the plume.

The nozzle orifice reaches its maximum width of  $1.036d$  at  $x/d = 0.00$ . Past this point, the trailing edge of the plume is attached to the test section surface. In this region the injectant moves parallel to the surface until separates from the surface along the plume separation lines shown in Figure 120. As the plume begins to separate from the test section surface, the curvature of the plume separation line begins to turn back in towards the test section centerline. This first occurs near  $x/d = 0.50$  and is coincident with the leading edge of the expansion fan (see Figure 120). The expansion fan forms when the inflow air turns in toward the centerline to fill the void left by the rising plume.

The effects of the preceding series of events are seen in Mach number and vorticity contours for

$x/d = 0.50$  (Figure 132). The elevation of the plume and the subsequent turning of the inflow air is indicated by a necking in of the vorticity contours near the base of the arms of vorticity. Furthermore, it is seen that the JI vortex centers of rotation are pulled up along with the plume and pushed up by the additional mass forced under the overhanging sides of the plume.

In this set of Mach contours, the OB shock is becoming more defined and the expansion waves and the compression waves defining it, are labeled in Figure 132. These waves form as the injectant expands into the lower pressure region of the inflow air. When the pressure of the two fluids balance, expansion stops and the expansion waves are reflected back into the plume as compression waves [81]. Where the compression waves converge, a shock is formed. Certainly, if the injectant is expanding, the inflow air in the vicinity of the expansion must be compressing. The inflow compression wave resulting from this interaction with the plume is also labeled in Figure 132. The plume overhang is also a manifestation of the balancing of the pressure and momentum of the two fluids.

The discontinuous contours in the interior of the arms of vorticity in Figure 132 show that the OB shock is not a slip surface and that the injectant is turned as it passes through the shock. At the previous station ( $x/d = -0.25$ ) the interior contours of the arms are relatively smooth. However, at this station, the contours have several discontinuous turns. The vorticity at the base of the region labeled “flames” is generated by injectant spilling over the sides of the nozzle. However, when the fluid encounters the lower portion of the OB shock, the injectant turns such that the velocity gradients defining  $\omega_x$  cancel, hence the absence of vorticity in the “pocket” of the flames. After the injectant has passed through the OB shock, it is entrained into the surrounding fluid and once again develops a dominant velocity gradient and generates vorticity. The vorticity labeled “islands” is generated by the injectant passing through the upper part of the OB shock. Note the similarity of the islands to the vorticity generated by the bow shock. It is seen during this analysis that these islands

of vorticity are characteristic of flow passing through a shock rather than a continuous turning of the fluid.

Downstream at  $x/d = 1.0$  (Figure 134), the flames have extended farther up into the plume as additional injectant enters the flowfield and encounters the OB shock after it starts to expand. In the pockets, the OB shock have become strong enough to reverse the sign of the vorticity of the injectant passing through it.

The downstream edge of the nozzle ends at  $x/d = 1.23$  and by this station the area of flow activity has substantially increased. Therefore, starting with Figure 134 ( $x/d = 1.25$ ), the range of the axes is rescaled to include more of the surrounding flowfield. This scale is used for all subsequent figures depicting the  $y - z$  plane.

Immediately behind the jet at  $x/d = 1.25$  (Figure 134) the lower edge of the plume is flat, indicating it is still attached to the test section surface. As indicated by the constant value of the Mach contours at the surface, injectant expansion in this part of the plume is being retarded by the wall. The vorticity in the pockets has extended further up along the arms and the islands are beginning to merge into a single band of vorticity on either side of the plume. Both of these changes are indications of increasing strength and definition of the OB shock structure in regions I and III defined in Section 7.5.1. The flames are still present at this station, but as less of the injectant is undergoing the rapid expansion seen at previous locations, they are becoming less defined. The vorticity at the wall where the flames originate, still has the same sign as the arms, a further indication that the plume is attached to the wall at this station.

When the plume first starts to separate from the surface near  $x/d = 0.5$ , an expansion fan is formed as the inflow air turns inward to fill the void left by the rising plume. As the plume continues to rise above the surface, the inflow air in the expansion fan accelerates as it turns to fill the void. The acceleration results in higher Mach number contours in the flowfield outside of the plume and

increases the vorticity in the boundary-layer.

The combination of plume separation and inflow acceleration around the plume continues as the fluid moves further downstream. At  $x/d = 1.50$  (Figure 135) the injectant core is high enough above the test section surface to allow expansion of the injectant on the underside of the plume. However, it is still attached to the wall as indicated by its flat lower surface.

The necking in of the vorticity contours identified at  $x/d = 0.50$  are now becoming prominent features in the Mach contours at  $x/d = 1.50$ . The necking in has caused the overall shape of the flowfield to resemble a mushroom, where the bow shock forms the mushroom's hat, the maximum downwash of the JI vortices form the stem, the upwash pivot points (UPP) form the connection between the hat and the stem, and the downwash pivot points (DPP) form the brim of the hat. The maximum downwash of the JI vortices defines the lateral extent of the JI vortex, i.e. fluid inside this point turns toward the plume and fluid outside of this point moves away from the plume. The UPP is the location where the fluid influenced by the rotation of the JI vortices and the plume, stops moving up and turns down towards the surface. The DPP is the location where this same fluid stops moving down and turns up away from the surface. The extent of the UPP and DPP can be seen in the vorticity contours of Figure 135

The rounding of the Mach contours on the underside of the plume at station  $x/d = 2.00$  (Figure 136) indicates that the plume has completely separated from the test section surface. Complete separation is also indicated by the convergence of the lines of vorticity at the wall and under the plume. The pockets and islands of vorticity almost form a complete ring within the arms of vorticity. This ring defines the boundary of the OB shock, thus, the extent of the still expanding injectant core. The initial formation of the shock disk is seen near the top of the ring. Also noted in this figure is that the center of rotation of the JI vortices have remained outside of the expanding part of the plume.

The rotation of the JI vortices is no longer sustained by the plume's upwash. As seen in Figure

137 a complex mechanism of inflow air deflection and injectant leaving through the OB shock is sustaining the rotation of these vortices. The sidewash of inflow air generated by the expansion fan is moving inward and under the plume. When the inflow sidewash reaches the bottom of the plume, it is deflected up and out either by the injectant leaving the plume or it simply reflects off of the OB shock. Thus, the opposing motion of the incoming sidewash and the outgoing sidewash of injectant and inflow air sustains the rotation started at  $x/d = -0.25$ .

It is seen in Figures 120 and 122 that between  $x/d = 2.00$  and  $x/d = 3.00$  the sidewash of inflow air on either side of the test section collides at the  $z/d = 0.0$ . In the wake of this collision, many critical changes in the flow structure occur and its initial effects are seen in Figure 138. When the inflow air collides, part of the air is deflected up into the bottom of the plume and creates an inflow upwash. The impact between the upwash and the injectant on the lower side of the plume results in an upwash slip (US) surface and an upwash recompression (UR) shock. This US surface is seen as the rounded indentation at the bottom of the plume and the UR shock is near the test section surface.

An enhanced view of the resultant flowfield created by the collision of the inflow sidewash is seen in the velocity vectors overlaid on the Mach contours in Figure 139. Here again, when the sidewash near the surface collides at the centerline, some of the fluid is immediately deflected up into the plume and forms the US surface, and some of it is deflected down to the test section floor creating the wake vortices. As more and more of the sidewash is turned up into the plume and down into the wake, a virtual compression ramp is formed, much like the virtual compression ramp formed by the sonic surface seen in the two-dimensional analysis in Chapter 6. In Figure 139, subsonic flow is masked, thus the virtual ramp is shown in white. The turning caused by this ramp results in the UR shock. As more of the sidewash is turned upward, the excess upwash is deflected off the lower part of the OB shock and off of the injectant leaving the plume through the lower sides of the OB



shock. It is seen in Figure 139 that this deflection/turning mechanism is still sustaining the rotation of the JI vortices. However, as the inflow sidewash gets thicker and the amount of deflected upwash increases, the JI vortex centers of rotation have begun to move up from the surface and out from the centerline.

Past this location, the OB shock begins to narrow as regions II and IV of the OB shock are entered (see Figures 125 and 126). At the current station of  $x/d = 3.00$ , the strongest part of the OB shock is above the  $y - z$  plane reflection line (region IV). As described in Section 7.5.1, the OB shock is stronger and generates stronger vorticity in this region because it is comprised of reflected compression waves from the other three regions of the plume. Since these waves crossover each other inside the plume, the injectant turns more than once before leaving the OB shock. Multiple turning results in more than one sign change in the vorticity; thus, two layers of vorticity are seen in some parts of the OB shock. One such region is marked in the vorticity contours of Figure 138. These multi-shock structures also cause sharp reductions in the Mach number. The result is an indentation of the contours in upper half of the injectant core, which is labeled in the Mach contours of Figure 138 as "reflected compression waves."

The figure inset in the vorticity contours (Figure 138), illustrates the crossover of the compression waves in the  $y - z$  plane and the formation of the shock disk. Two typical injectant paths are illustrated in this figure. One path moves through the expansion waves and passes through one of the compression waves and then out through the OB shock. The other path takes the injectant through the expansion waves and through both of the recompression waves. The extensions of the recompression waves above the cross-over point forms the shock disk.

It is seen in Figure 123 that the shock disk is fully formed at  $x/d = 4.00$ . The additional vorticity of the multiple shocks encountered during passage through the shock disk and the OB shock is clearly visible in the contours displayed in Figure 140. Increased vorticity from the US

surface is also seen near the bottom of the arms of vorticity. A diamond shaped object with an inverted tip at its bottom is seen in the vorticity contours outlining the OB shock. The relevance of this observation is seen in the contours for  $x/d = 6.00$ . The US surface has moved farther into the plume and the JI vortex centers of rotation have been carried farther up and out by the deflected upwash. The upwash indentation in the Mach contours has begun to form the fork at the end of the OB shock identified in Figure 125.

The  $V-W$  velocity vectors and the lines defining the UR shock show that the UR shock creates a type I interference pattern at its crossover point in the  $y-z$  plane. The extension of the shock is the mechanism which turns the sidewash up as it approaches the test section center line. The newly formed upwash then moves up until it is turned outward by the upwash deflected off of the lower side of the OB shock, thus, creating an outflow sidewash. The outflow sidewash is then turned down when it encounters the UR shock on the other side of the JI vortex. The resultant downwash completes the rotation mechanism of the JI vortices. Thus it is seen that the combination of the UR shock, the inflow sidewash and the upwash deflection off of the OB shock is the mechanism sustaining the JI vortices at  $x/d = 4.00$ . The downward turning of the fluid past the JI vortices stops where the UR shock leaves the current  $y-z$  plane. It is seen in Figures 138 and 140 that the location of the centers of rotation of the JI vortices has moved up from the test section surface and out away from the centerline as the UR shock propagates further out into the flowfield. The combined effect of the mechanisms which sustain the rotation of the JI vortices has caused a *waist* to form in the Mach contours near  $y/d = 0.6$ .

The trailing edge of the center part of the OB shock and shock disk/compression wave structure is encountered at  $x/d = 4.50$ . It is seen in Figure 123 that a pointed tip in the OB shock structure is formed along the centerline near  $x/d = 4.50$ . The part above the reflection line is in region IV and the part below it, is in region II. The effects of this tip in the  $y-z$  plane are seen in Figure 141

and the difference in the severity of the shock in these two regions is seen in the Mach and vorticity contours of this figure. The turning caused by the OB shock in region II is seen below the line drawn in the figure and the turning from the compression waves in region IV is above the line. This line is also drawn in the Mach contours of Figure 141, where it is seen that the compression waves in region IV cause the Mach number of the injectant to decrease from Mach 4.45 at  $x/d = 4.00$  to Mach 3.28 at  $x/d = 4.50$ .

After completely penetrating the OB shock, the upwash quickly moves further up into the plume and by  $x/d = 5.00$  (Figure 142) the US surface has moved from  $y/d = 1.0$  at  $x/d = 4.50$  to  $y/d = 1.75$  at  $x/d = 5.00$ . This is also the downstream plane where the crossover point of the TE and MTE OB shocks occurs (Figure 126). This crossover point is the convergence point of the two strong TE OB shocks from region IV. The crossover is seen in the Mach contours for this location (Figure 142) as the sharp reduction in Mach number at the center of the plume.

A visualization of the changes incurred by the upwash is seen in these Mach contours. As the upwash approaches the crossover point from below, its Mach number is decreasing. At the crossover point, there is a shock reduction in the Mach number of the upwash and then an increase in its Mach number as it expands to equalize its pressure with the surrounding pressure on the other side of the shock.

The vorticity contours in Figure 142 show three sharp changes in direction as the upwash moves through the crossover point. The region of increased turning is enlarged in Figure 143. In this figure, the velocity vectors show that the notch near the center of the arms of vorticity is caused by the upwash turning outward as it expands around the forks at the end of the OB shock. Above the notch, the upwash is turned back inward when it passes through the shock at the crossover point. Passage through the shock increases the pressure of the upwash, turning the upwash back outward as it expands. This fluid is then entrained into the upwash which went around the TE OB shock and

moves further up into the flowfield.

As the flow moves downstream from  $x/d = 5.00$  to  $x/d = 6.00$  the MTE OB shock begins to spread and a diamond shaped pattern with an inverted tip at its bottom the is seen in the Mach contours (Figure 144). This diamond pattern is the extension TE OB shock mirrored the across the crossover point near  $x/d = 5.00$ . The outline of this same pattern is visible upstream of the crossover point in the vorticity contours of Figure 140 at  $x/d = 4.00$ . It is also seen in Figure 144 that the UR shock has developed another change in direction. The cause of this change is becomes more apparent in Figure 145.

Between  $x/d = 6.00$  and  $x/d = 7.00$  a new vortex pair develops. These vortices are the result of the recompression suffered by the upwash as it passes through the MTE OB shock and the subsequent expansion needed to equalize its pressure with the surrounding fluid. This recompression shock induced (RSI) vortex pair is identified in Figure 145.

The shock/expansion mechanism which generates the RSI vortices is illustrated in Figure 146. In the upper diagram of this figure, the relative velocity vectors illustrate the location of the plume boundary. The boundary is taken to be the location where the inflow and outflow sidewash meet.

In the Mach number contours, the velocity vectors are also displayed along with the relevant flow features. When the sidewash passes through the UR shock, it is turned upward and is entrained with the already present upwash. The upwash then passes through the lower end of the MTE OB shock, compressing it and turning it out away from the test section centerline. As a result of the compression, the upwash expands to equalize its pressure with the surrounding fluid. The expansion causes additional turning which results in a localized outflow sidewash. This outflow sidewash then encounters the upper extreme of the MTE OB shock. Once again, the flow is turned, but this time it is turned down, creating a localized region of downwash. Next, this downwash is reflected off of the lower side of the plume boundary and back in towards to the center of the test section. Thus, a

rotation mechanism inside of the plume is established.

Outside of the plume, the rotation of the JI vortices is disrupted by the expansion of the plume and by  $x/d = 8.0$ , the JI vortices are engulfed by the expanding plume. An illustration of the process by which the JI vortices are engulfed is shown in Figures 147 - 151. In the velocity vectors for the flowfield at  $x/d = 6.0$  (Figure 147) the outline of the plume is marked and the JI vortex centers of rotation are denoted by the circles. At this station the upwash and inflow sidewash from the JI vortices are relatively unaffected by the almost nonexistent sidewash of the plume. Currently, both the injectant and JI vortex upwash reflect off of the plume's boundary. However, at  $x/d = 6.5$  (Figure 148) the MTE OB shock has started to turn the plume's upwash out to the sides toward the plume boundary, thereby, increasing the momentum of the plume's outflow sidewash. The increased outflow sidewash has started to decrease the amount of inflow sidewash deflected up and off of the plume's boundary, thereby, decreasing the amount of upwash recirculated by the JI vortices. By  $x/d = 7.0$  (Figure 149) the outflow sidewash has almost pushed the plume's boundary out to the JI vortex centers of rotation and the head on collisions between the inflow sidewash and the outflow sidewash is impeding the continued outward expansion of the plume. At  $x/d = 7.5$  (Figure 150), the ongoing expansion of the upwash after passing through the MTE OB shock, has continued to push the boundary of the plume out until it is now coincident with the JI vortex centers of rotation. At this point very little of the inflow sidewash is colliding head on with the outflow sidewash. Almost all of the collisions are glancing blows at oblique angles. Thus, less of the energy gained by the outflow during expansion is lost during the collision and the plume can continue to expand laterally. Finally, at  $x/d = 8.0$  (Figure 151), the outward expansion of the plume has extended beyond the JI vortices and the lateral expansion of the plume continues unimpeded from this point on at an accelerated rate. The accelerated rate of expansion is seen downstream of  $x/d = 8.0$  in Figure 125.

In Figure 125 and in Figure 126, the type VI interference shock pattern occurs near  $x/d = 8.0$  when the UR and MTE OB shocks intersect. It is also seen in these two figures that the UR shock is widening, while the plume is expanding between  $x/d = 6.0$  and  $x/d = 8.0$ . Thus, it is seen that the sequence of events described in the preceding discussion is a consequence of the shock interactions. This observation is also substantiated by the path of the UR shock in the figures for locations  $x/d = 4.0$  through  $x/d = 6.0$ . In each of these figures, the path of the UR shock intersects the JI vortex centers of rotation. Then when the UR shock and the MTE OB shock intersect near  $x/d = 8.0$ , the mechanism sustaining the rotation of the JI vortices is removed. Furthermore, the width of the plume's boundary at  $y/d = 1.45$  between  $x/d = 6.0$  and  $x/d = 8.0$  in Figures 147 - 151 is identical to width of the UR shock in Figure 126 over the same interval. Thus, the slow lateral expansion of the plume is not simply a result of the JI vortices, but of the mechanisms which sustain the rotation of these vortices.

Once the streamwise location of the plume is beyond the confinement of the UR shock, the plume rapidly begins to expand and the top of the US surface created by the inflow upwash quickly moves up through the remainder of the high Mach number contours, effectively bisecting the plume. Furthermore, with the consolidation of RSI and JI vortices, the traditional representation of the plume structure shown in Figure 61 is regained.

In Figure 151 ( $x/d = 8.0$ ) there is still a substantial difference between the relative velocity vectors from the plume and the remaining downwash from the JI vortices. This difference in the velocity vectors is seen in Figure 152 ( $x/d = 8.0$ ) as the extrema in the vorticity contours label the "wings." The vorticity labeled the "pockets" is the turning caused by the still present MTE OB shock and the large region of vorticity is generated by the RSI vortices and therefore, is labeled "RSI vorticity." Although they become smaller, the extrema in the wings are still visible as far downstream as  $x/d = 20.0$ . It is seen in Figure 115 from Section 7.4, that the extrema and the wing dissipate

between  $x/d = 20.0$  and  $x/d = 40.0$ .

The location of the MTE OB shocks at  $x/d = 8.0$  are still visible in the Mach contours as the lowest contour level outside of the boundary-layer (Figure 152) and the RSI vortex centers of rotation are slightly below these shocks. The mirrored image of the TE OB shock is losing its definition as it expands and becomes more rounded. The upper part of the reflection is still a slip surface as it will remain through  $x/d = 20.0$ .

The accelerated expansion of the plume is seen in the Mach contours at  $x/d = 9.5$  (Figure 153). The expansion is identified by the rapid changes in the bell shaped contours at  $x/d = 8.0$  to their current shape at  $x/d = 9.5$ . It is also seen that the top of the US surface has risen from a height of  $2d$  at  $x/d = 7.00$  to  $2.4d$  at the current location. In addition to the US surface rising, the RSI vortex centers of rotation are beginning to rise and spread out from the centerline. This is consistent with the propagation of the MTE OB shocks. At the centerline near a height of  $0.75d$ , there is a small zone of lower Mach number flow. This spot is seen in Figure 119 as a tail protruding from the US Surface. At the current  $x/d$  location, this protrusion is the point where the RSI vortices and the wake vortices share a common divergence point. Thus, the flow is completely axial at this location. This inflection point forms the divergence vorticity in the lower part of the RSI vortex structure. This divergence point is also the location where the lower part of the UR shocks crossover.

At  $x/d = 10.5$ , a shed vortex separates from the wake vortex in Figure 154. The shed vortex is released from the wake vortex because of the reduced inflow sidewash near the surface of the test section. As seen in Figure 121, at this downstream location, the inflow expansion fan is almost completely exhausted and is directing very little inflow sidewash towards the middle of the test section. Without the inwardly directed momentum from the sidewash, the force of the deflected downwash at  $z/d = 0.0$  is not sufficient to sustain the rotation of the entire mass of fluid in the wake vortices. Thus, a shed vortex is cast off and it quickly dissipates into the surrounding boundary-layer.

The remaining fluid near  $z/d = 0.0$  continues to rotate as the wake vortices.

The circles representing the RSI centers of rotation are replaced in this figure and at all remaining downstream locations with ellipses. The marker is changed to an ellipse because the circulation pattern is now more elliptical than circular.

At  $x/d = 12.5$  and beyond a specific structure which can be specified as the plume is difficult to identify. However, for purposes of discussion, the boxed region in Figure 155 is considered the plume. A similar region is assumed to be the plume in the remaining  $y - z$  plane contours. The Mach contours in Figures 155 - 158 show an ongoing reduction in Mach number of the fluid outside of the plume. This fluid will gradually asymptote to the Mach number of the inflow air far away from the plume and this fluid should eventually reach to a value near Mach 2.9. Within the plume the lateral spreading of the MTE OB shocks has ceased, but they continue to rise and carry the RSI vortex centers of rotation with them.

Extensive examination of three-dimensional particle stream paths has indicated that the region between the RSI vortex centers of rotation labeled "inflow core" is almost exclusively inflow air forced up into the plume by the upwash between this station and  $x/d = 3.0$ . These same three-dimensional stream paths indicate the regions labeled "injectant" is almost exclusively injectant. The fluid everywhere else in the flowfield is a mixture of the inflow air and the injectant and the majority of the rotating fluid is being recirculated between the plume and the freestream inflow.

As the mixture in the flowfield proceeds downstream through  $x/d = 14.5$  to  $x/d = 20.0$ , the inflow core moves up through the injectant and the injectant is seen to rotate around to the sides of the RSI vortex centers. At  $x/d = 20.0$ , the injectant has moved below the inflow core and is beginning to turn in towards the centerline. Figure 111 from Section 7.4.2 shows that the injectant has moved under the inflow core at  $x/d = 40.0$  and that the inflow core and the injectant are beginning to repeat this exchange of positions.



### 7.5.3 Further Descriptions with the $x - z$ Plane

Enhanced visualization of the shock and expansion patterns resulting from the interaction of the injectant and the inflow air is gained by viewing the flowfield from the perspective of the  $x - z$  cross sectional plane. From this vantage point the extent of the horseshoe vortices and the inflow expansion fan are visible in the contours of the Mach number and  $\omega_x$ . Viewing the numerical results in these planes also illustrates the angle of the UR shock as it propagates up into the test section and downstream of the nozzle. The vorticity generated at the edges of the OB shock is also visible as well as the vorticity generated by the fluid as it passes through the MTE OB shock and the crossover point.

In the following series of figures, the displayed particle streamtraces are computed with two of the three velocity components corresponding to the computational cells in the current plane. The reader is reminded that these streamtraces are only two-dimensional representations of three-dimensional motion and the apparent continuity of the path for a single particle in this plane is an illusion created by the absence of the third component of velocity. At any point in this flowfield, fluid from an plane may be replacing a fluid particle in the current plane and fluid particles in the current plane may be leaving this plane.

With regard to fluid turning, the region near the test section surface is one of the most active regions of the test section. The vorticity contours of the lower region of the boundary-layer are displayed in Figure 159 ( $y/d = 0.022$ ). The vorticity generated by the horseshoe vortex is visible at the leading edge of the vorticity contours. Unlike the horseshoe vortices generated by normal injection, this vortex pair does not retain its structure downstream in this flowfield much beyond  $x/d = 0.0$ . In normal injection flowfields, the horseshoe vortices retain their structure much farther downstream of the nozzle [7, 70]. Also seen in these contours is the vorticity generated by the expanding injectant as it leaves the nozzle orifice. In Figures 129 - 133 vorticity is seen both inside

and outside the nozzle edges near the test section surface. This same phenomena is seen in Figure 159. In Figure 159, the vorticity inside of the nozzle outline is caused by injectant expanding into the test section and the vorticity outside of the nozzle outline is also caused by expanding inject, but its is also the result of inflow air turning around the flowfield obstruction caused by the injectant plume. Many of the other flow features visible in the vorticity contours at  $y/d = 0.022$  are common to those seen at the test section surface. These are identified in the discussion of Figure 122 in Section 7.5.1.

About half of the flow at  $y/d = 0.022$  is subsonic. The regions of subsonic flow appear as white zones in the Mach contours. The large amount of subsonic flow is a natural consequence of the proximity to the test section surface. However, at  $y/d = 0.022$  there are equally large regions of supersonic flow. Regions of supersonic flow are visible over the nozzle orifice and immediately behind it. Obviously the flow over the nozzle is the supersonic injectant entering the flowfield and the flow behind the nozzle is the expanding injectant identified in Figures 134 and 135 as moving parallel to the test section surface. The plume boundary-layer separation line is also seen as a subsonic region in Figure 159. The flared out region on either side of the nozzle is the accelerating inflow air in the expansion fan moving around the plume.

Flow features in the upper part of the boundary-layer ( $y/d = 0.100$ ) are seen in Figure 160. In the Mach contours, the extent of the bow shock is clearly visible and its resultant turning of the inflow air is seen in the vorticity contours. Region II, identified as the expansion/compression region in Section 7.5.1, is visible behind the nozzle orifice. The thin bands of vorticity just downstream of the nozzle are generated by the injectant turning as it passes through the OB shock in region II. The downstream expansion angle ( $11^\circ$ ) of the UR shock is clearly visible in the Mach contours and the upper part of the virtual compression ramp, identified in Figure 139, is defined by the subsonic region. The turning caused by the UR shock and the wake vortices is labeled in the vorticity

contours. The vorticity generated by the inflow air turning within the expansion fan is also visible in this figure.

The discussion in Section 7.5.1 of the flowfield shock and expansion structures at  $y/d = 0.91$  and  $y/d = 1.49$  (Figures 125 and 126) does not address the vorticity generated as a result of fluid passing through these structures. Therefore, the vorticity generated by these structures is discussed in the following paragraphs.

Parts of regions I and II of the OB shock intersect the  $x - z$  plane at  $y/d = 0.91$ . In Figure 161, region I is upstream of the reflection line and region II is downstream of it. The thin bands of vorticity marked in this figure are generated by injectant passing through the OB shock. As is explained in Section 7.5.1, region I is comprised primarily of expansion waves with a smaller concentration of reflected compression waves. It is also shown in Section 7.5.1 that region II is comprised of expansion waves but has a larger concentration of reflected compression waves than region I. The larger concentration of compression waves, accounts for the slightly more extensive distribution of vorticity in region II.

A larger region of vorticity surrounds the broken ring of vorticity generated by the OB shock in Figure 161. The vorticity in this region upstream of the OB shock is generated by the inflow air turning to avoid the flow obstruction caused by the injection plume. The vorticity along the sides of the OB shock and downstream of the shock, is generated by inflow air turning in the expansion fan. Mixed in with the inflow air is the injectant entrained into the inflow air after it has passed through the OB shock. At the rear of this region of vorticity, is an upstream protrusion of vorticity which is caused by the upwash at the US slip surface turning downstream with the rest of the inflow air and injectant mixture.

The final regions of vorticity identified in this figure are generated by the UR shock when the upwash is deflected back out from the centerline and by the inflow air passing through the bow

shock.

The vorticity generated at  $y/d = 1.49$  (Figure 162) is caused by many different mechanisms. As in Figure 161, the vorticity farthest upstream is the inflow air turning after passing through the bow shock. Most of the vorticity in the region surrounding the OB shock is from inflow air turning around the plume and entrainment of the injectant into the inflow after passing through the OB shock.

The similarities between the previous  $x - z$  plane at  $y/d = 0.91$  and the current one at  $y/d = 1.49$ , ends with the beginning of the description of the OB shock vorticity. Parts of regions III and IV of the OB shock, intersect the  $x - z$  plane at  $y/d = 1.49$  (Figure 162), region III (upstream of the reflection line) is comprised of reflected compression waves and to a smaller degree, expansion waves (see Section 7.5.1) and region IV is comprised almost exclusively of compression waves. Therefore, the OB shock in these two regions are significantly stronger than the shock in regions I and II. The vorticity distribution between the two  $x - z$  planes is consistent with the shock strength.

The TE OB shock/MTE OB shock crossover point and the MTE OB shock also intersects this plane. The vorticity of the MTE OB shock is labeled in Figure 162 and it is immediately downstream of the crossover point. At the crossover point, the vorticity is negligible. Also seen on either side of the MTE OB shock vorticity is the deflected upwash vorticity. It is seen in Figures 147 - 151 in Section 7.5.2 that this vorticity is generated when the upwash is deflected off of the plume's boundary. The final region of vorticity seen in Figure 162 is generated by the RSI vortices.

#### **7.5.4 Surface Temperature and Friction**

Surface temperature and skin friction are critical to the design of combustors and surfaces within propulsion systems. Therefore, surface temperature profiles and contour plots are needed to identify regions where hot spots resulting from recirculation or stagnation points may form in a combustor. The figures presented in this section provide a comparison of the predictions from the

RSTM and the  $K - \epsilon$  models for surface temperature,  $T$ , and skin friction coefficient,  $c_f$  where [4]

$$c_f = \frac{\tau_w}{\frac{1}{2}u_\infty^2} \quad (234)$$

$$\tau_w = \mu \left. \frac{\partial u}{\partial y} \right|_{y=0}$$

Experimental data for these two quantities is not reported by McCann and Bowersox [52].

The differences between the surface temperature predictions from the two models is not significant over most of the test section surface. However, it is seen in Figures 164 and 163 that the RSTM generally predicts lower temperatures than the  $K - \epsilon$  model downstream of  $x/d = 9.0$ . In the regions upstream of the nozzle the RSTM and  $K - \epsilon$  model predict a similar value for the maximum temperature (2.87), but the RSTM predicts this higher temperature over a larger area upstream of the nozzle. The increased area is primarily the result of different predictions for upstream boundary-layer separation and the downstream sweep angle of the bow shock from the two models. The RSTM does predict higher temperatures behind the nozzle where the plume is attached to the surface, along the secondary separation line and along the wake vortex attachment line (see Figure 120). In the region where the expansion fan forms the RSTM predicts lower temperatures than the  $K - \epsilon$  model.

The predictions from the two models for  $c_f$  are very similar over most of the test section surface (Figures 166 and 165). Downstream of  $x/d = 11.0$  the predictions are nearly identical; therefore, only the area surrounding the jet and upstream of  $x/d = 11.0$  is presented. The most noticeable differences are between  $x/d = -0.25$  (JI vortex formation) and  $x/d = 0.50$  (expansion fan formation). It is seen in Figure 120 that the injectant attachment line is coincident with the area with dissimilar predictions from the models. In the predictions from the  $K - \epsilon$  model the contours along this line is not as smooth as they are in the RSTM predictions. It is seen in Sections 6.2.3.3 and 6.3.4.2 that the  $K - \epsilon$  formulation has poor performance characteristics at separation, stagnation and attachment points.

Differences in the  $c_f$  predictions are also seen in the recirculation region upstream of the nozzle. Here again, the differences are mostly a result of different model predictions for the upstream boundary-layer separation point.

The similarity in the two model's predictions for  $c_f$  and  $T$  is consistent with the surface results reported in Chapter 6. In Chapter 6, it is seen that the turbulence predictions from the two models are almost identical at the surface. The only notable exception is the boundary-layer separation point and without exception, the RSTM predicted boundary-layer separation earlier than the  $K - \epsilon$  model.

### **7.5.5 Summary of Flowfield Investigation and Conclusions**

It is shown in this section that the principal agents responsible for enhanced vortical motion of the flowfield are the RSI vortices. These vortices are generated through the combined effects of the upwash behind the injectant plume and the MTE OB shock. This vortex pair forms downstream of the OB shock terminus and inside the jet plume. Furthermore, it is shown that lateral expansion of the OB shock terminus and inside the jet plume. Furthermore, it is shown that lateral expansion of the plume is impeded by the JI vortices. The rotation of the JI vortex pair is sustained by the combined effects of the UR shock, the inflow sidewash and the boundary of the injectant plume. The JI vortices, which are initially formed at the sides of the nozzle orifice, extend back along the sides of the jet plume, following the path of the UR shock as it propagates through the test section. The mechanisms which sustain the JI vortices retard plume expansion by directing inflow sidewash back towards the center of the test section and into the plume. The mechanisms which generate the RSI vortices accelerate plume expansion by creating an outflow sidewash which forces the injectant to move out and away from the center of the test section. It is seen that once the MTE OB shock and the UR shock intersect with each other, the mechanisms sustaining the JI vortices are disrupted and lateral expansion of the plume accelerates.

It is also shown in this section that the OB shock can be separated into four regions of shock

intensity. The regions are labeled in Figures 125 and 126 and each of the region has distinct characteristics. Region I is designated an expansion/mild-compression zone because initially, the injectant is expanding in all directions and then the expansion waves are reflected off of the plume's boundary as compression waves. Region II is designated an expansion/compression zone because initially, the injectant is expanding, but the expansion process is slowed by reflected compression waves entering this region from other parts of the plume. Region III is designated a compression/expansion zone because initially reflected compression waves from other parts of the plume enter this zone which are then reflected out of this region as expansion waves. Finally, region IV is designated a compression/compression zone because the majority of the reflected compression waves from the other parts of the plume, converge in this region. The TE OB shock is formed by regions II and IV and these are the shocks which are mirrored across the crossover point.

It is also shown that the predictions for surface temperature from the RSTM and  $K - \epsilon$  models only have significant differences around the jet and in the region near the initial formation of the wake vortices. It is also seen that the skin friction predictions from the two models are nearly identical for the entire flowfield.

Finally, it is proposed here that mixing enhancement can be accomplished if three elements of the flowfield can be controlled. These are the location of the crossover point, amplification of the upwash deflected up into the plume and the location where the MTE OB shock intersects the UR shock and disrupts the sustainment mechanism of the JI vortices.

The first element to enhanced mixing is to have the crossover point form as close as possible to the terminus of the OB shock. This requires the angle of the TE OB shock in the  $x - z$  plane be as large as possible and OB shock elongation be as short as possible. Control of these two factors may be possible by changing the shape of the nozzle orifice and the angle of injection. The elliptic nozzle and the  $25^\circ$  injection angle simulated in this study resulted in a TE OB shock angle of approximately

20° and a crossover point about  $5d$  downstream of the nozzle center. The shallow injection angle certainly contributed to the downstream elongation of the OB shock and the elliptic shape of the nozzle may have contributed to the rather shallow angle of the TE OB shock. It seems reasonable that a circular nozzle with injection at a steeper angle would result in a crossover point closer to the nozzle exit. However, caution must be used in the selection of the injection angle, since steeper injection angles may result in greater flow blockage and stronger bow shocks, both of which cause higher total pressure losses and, ultimately, thrust reduction [60].

The second element for mixing enhancement is upwash amplification. The more fluid passing through the MTE OB shock, the more rotation will result. Amplification may be possible by placing a device similar to the one shown in Figure 167 along the centerline behind the nozzle. If properly designed, this device will turn the inflow sidewash near the surface of the test section up without the reduction in Mach number currently incurred by the collision of the inflow.

The upwash amplification device may also accomplish the third element to enhancement, control of the location where the MTE OB shock intersects the UR shock by increasing the angle of the UR shock in the  $y - z$  plane. If this intersection point is further upstream, the mechanism sustaining the II vortices will be disrupted quicker. It is seen in Figures 138 - 145 that the UR shock angle is approximately the angle of the virtual compression ramp formed by the wake vortices. Thus if this angle is increased by the amplification device, the UR shock angle will also increase.



## Chapter 8 - Conclusions and Recommendations

The important conclusions and contributions of this study are summarized in this chapter. Once these areas have been addressed, some recommendations for future study are presented.

### 8.1 Conclusions and Contributions

The primary objectives of this research were numerical simulation of the three-dimensional flowfield generated by oblique injection into a supersonic flow, validation of a second-order RSTM for turbulence closure and investigation of the resulting flowfield. Each of these objectives was achieved..

The impact of this study on the current state-of-the-art for turbulence modeling and mixing enhancement are summarized as follows:

- The qualitative and quantitative comparison of the second-order ZSGS RSTM and ZSGS  $K - \epsilon$  model to experimental data for two-dimensional and three-dimensional flowfields showed the superiority of ZSGS RSTM to the ZSGS  $K - \epsilon$  model in predicting physically correct behavior of the turbulent cross flow shear stresses. The RSTM prediction for the magnitude and distribution of  $\tau_{xy}$  and  $\tau_{xz}$  compared favorably with all available experimental data. In contrast, the  $K - \epsilon$  model predicted magnitudes well, but gave poor agreement with the distribution of the shear stresses. The improper distribution of the shear stresses was brought about by the unidirectional evaluation of the velocity gradients imposed by the Boussinesq approximation.
- The qualitative comparison of the second-order ZSGS RSTM to the ZSGS  $K - \epsilon$  model for two-dimensional and three-dimensional flowfields demonstrated the superiority of the RSTM to the ZSGS  $K - \epsilon$  model in predicting physically correct behavior of the Reynolds stresses and  $K$ . The inability to enforce the realizability constraint on the axial stresses in the  $K - \epsilon$  model and the improper relationship of the axial stresses to  $K$  and the mean strain-rate tensor, resulted in non-physical turbulence intensity in the three-dimensional flowfield. With the two-dimensional

flowfield, discontinuities in the Reynolds stresses were also identified above boundary-layer separation and stagnation points in regions with recirculating flow. The discontinuities were caused by the improper use of  $\tau_w$  in the relationship of the Reynolds stress tensor to the mean strain-rate tensor. The discontinuous behavior of the shear stresses were propagated to the momentum equations and caused discontinuous results in the velocity components as well.

- The RSTM predictions for the two-dimensional boundary-layer separation point and the magnitudes of the maximum static surface pressure were consistently more accurate than the  $K - \epsilon$  predictions. The  $K - \epsilon$  model consistently over predicted the maximum surface pressure and under predicted the distance from the upstream boundary-layer separation point to the center of the nozzle. The recirculation region behind the boundary-layer separation point is often considered an ideal location for a flame holder in a combustor flow [60]. Thus, the increased accuracy of the RSTM predictions increases the accuracy of initial combustor designs, which may lead to a reduced number of live fire testing.
- An examination the flowfield predicted by the RSTM has provided a better physical understanding of the behavior of the flowfield immediately surrounding the nozzle orifice and the mixing mechanisms of an injection flowfield. It was shown that the principal agent responsible for enhanced vortical motion of the flowfield was the recompression shock induced (RSI) vortices. These vortices were generated through the combined effects of the inflow air upwash behind the plume and the mirrored trailing-edge oblique shock (MTE OB) shock. These vortices formed downstream of the cross over point of the OB shock and the MTE OB shock and inside the jet plume. Furthermore, it was shown that lateral expansion of the plume was impeded by the JI vortices. The combined effects of the upwash recompression (UR) shock, the inflow sidewash and the jet plume boundary acted to sustain the jet induced (JI) vortices. The JI vortices, which were initially formed at the sides of the nozzle orifice, extended back along the sides

of the jet plume, following the path of the UR shock as it propagated through the test section. The mechanisms which sustained the JI vortices retarded plume expansion by directing inflow sidewash back towards the center of the test section and into the plume. The mechanisms which generated the RSI vortices accelerated plume expansion by creating an outflow sidewash, forcing the injectant to move out away from the center of the test section. It was seen that once the MTE OB shock and the UR shock intersected with each other, the mechanisms sustaining the JI vortices were disrupted and lateral expansion of the plume accelerated.

- The near field examination of the OB shock structure revealed that it could be separated into four regions of shock intensity. The regions were labeled in Figures 125 and 126 and each of the regions had distinct characteristics. Region I was designated an expansion/mild-compression zone because initially, the injectant was expanding in all directions and then the expansion waves were reflected off of the boundary of the plume as compression waves. Region II was designated an expansion/compression zone because initially, the injectant was expanding out from the nozzle, but the expansion process was slowed by reflected compression waves entering this region from other parts of the plume. Region III was designated a compression/expansion zone because initially this zone only contained reflected compression waves from other parts of the plume. These waves were then reflected out of this region as expansion waves. Finally, region IV was designated a compression/compression zone because the majority of the reflected compression waves from the other parts of the plume, converged in this region. It was seen that the TE OB shock was formed by regions II and IV and that this was the shock mirrored across the cross over point.
- Predictions for surface temperature from the two classes of turbulence models only had significant differences around the jet and in the region near the initial formation of the wake vortices. It was also seen that predictions for the skin friction coefficient were nearly identical

for the entire flowfield from both turbulence models. Knowing the location and magnitude of hot spots in a combustor will allow for more efficient cooling of the combustor surface and preheating of the fuel.

- Enhanced visualizations of the boundary layer, beyond current experimental capabilities showed that the  $K - \epsilon$  model provided less physically consistent predictions of the boundary-layer flow structure, Reynolds stresses and surface temperature than the RSTM. The inconsistencies of the  $K - \epsilon$  model were linked to the model's inability to correctly account for the anisotropic effects of the pressure-strain-rate tensor, the turbulence dissipation rate brought about by the wake vortices in the boundary-layer and the limitation of unidirectional velocity gradients in the Boussinesq approximation. Since the RSTM does account for these terms and its predictions outside of the boundary-layer were more accurate than the predictions from the  $K - \epsilon$  model, it is expected that the RSTM results were also more accurate in the boundary layer, as well as being physically consistent.

In Chapters 1 and 2 several questions and research issues were posed. In light of the study conducted, these questions and issues can be answered as follows:

- Are the differences in the predictions of the RSTM and  $K - \epsilon$  models sufficient to warrant the added complexity and computational effort needed to implement an RSTM?

The answer to this question is an unequivocal "yes" for analyses involving rotating fluids. For the extra computational effort needed to solve the twelve equations in the RSTM instead of the seven equations in the  $K - \epsilon$  model, the increased accuracy and physical consistency is an overriding factor. It should be noted that the computational run time required to reach a converged solution with the RSTM is approximately twice the run time required to reach a converged solution with the  $K - \epsilon$  model.

- How accurate are RSTMs in the modeling of complex secondary flows associated with TJISF?

Within the limitations of a single experimental data set available for comparison, the answer to this question is “very accurate” for the ZSGS RSTM. Comparison of the ZSGS RSTM predictions to experimental data showed very good agreement in secondary-flow regions for the  $U$  and  $V$  components of velocity,  $\omega_x$  and  $\tau_{xy}$ .

- What is the source of the asymmetries reported by McCann [52]?

A likely contributing factor to the severity of the asymmetry observed in the experimental data is the sparse number of streamwise data collection planes and systematic errors in probe positioning. The analysis conducted in Section 7.3.1 called into question the adequacy of the number of streamwise planes in which experimental data is reported. It is seen in the contour plots of variables for which experimental data is available, that the predicted maxima and minima of the variables do not consistently coincide with the data collection grid points. Since the location of each plane is almost  $1.93mm$  apart, a lack of resolution could exaggerate any asymmetries present in the experimental flowfield, especially if a maximum or minimum is captured on one side of the centerline, but not on the other. The possibility of capturing a maxima or minima on one side of the centerline and not capturing it on the other side is reasonable when one considers the predicted gradients of the turbulence variables are very large and that the lateral translation of the probes was performed by hand. It must also be noted that asymmetries have been noted in other experimental data for this type of flowfield [27]. However, insufficient information about the data collection methods by the investigators of these other configurations is available to ascertain the cause of the asymmetries reported.

It must be noted that there are several limitations of the algorithm and boundary conditions used, which may lead to the apparent contradiction between the numerical results and the experimental data. First, the algorithm uses local time stepping and a diagonalized approximate factorization scheme with second-order Roe flux differencing to solve the governing equations.

These features result in a highly dissipative numerical algorithm which is not time accurate [63]. Thus, if the static asymmetric behavior seen in the experimental data is caused by the transient growth of an asymmetric mode, it could be filtered out in the computation. Second, a zero thickness boundary-layer is used as the inflow condition. Third, the true conditions of the mean flow and turbulent quantities over the jet are unknown and therefore modeled with near constant values. Fourth, the flowfield is initialized as a symmetric flowfield. Finally, the turbulence model does not account for anisotropic dissipation rates in the far-wall region of the flow. However, there is no reason to believe the dissipation in the plume is isotropic. Therefore, even though there is sufficient cause to attribute exaggeration of the asymmetric behavior seen experimentally to grid resolution and systematic errors, no further conclusions can be made concerning the symmetry of three-dimensional injection flowfields.

- What impact does the form of  $E$  have on the flowfield solution?

Contour plots of  $K/E$  indicate that the omission of  $K$  from  $E$  would have a more significant impact on two-dimensional injection solution than it would for three-dimensional injection. With two-dimensional injection,  $K$  comprised as much as 12% of  $E$  in the region near the injector, whereas for three-dimensional injection,  $K$  comprised no more than 4% of  $E$  anywhere in the flowfield, and was confined to the recirculation region upstream of the injector. Since the primary location where omission of  $K$  may be significant is in the flame holding recirculation zone, its omission is likely to impact the accuracy of combustor flowfield solutions.

## 8.2 Recommendations For Further Research

Recommendations for future work are outlined in this section. These recommendations touch on ways to improve the algorithm, the turbulence models and the experimental configuration.

1. Foremost of the recommendations is further validation of the RSTM with another experimental data set. An all encompassing statement about the validity of the ZSGS RSTM cannot be made after evaluation of a single data set. The data set used in this study for the three-dimensional validation is limited to a single geometric configuration and pressure ratio. Furthermore, only the data for  $\tau_{xy}$  is sufficiently resolved to allow comparison to the numerical results. A suggested data set for future use is that of Santiago and Dutton [71]. This data set has 4000 data points for all six of the Reynolds stress terms. Unfortunately, this data is limited to only one side of the test section and only has data at two downstream locations ( $x/d = 3$  and  $x/d = 5$ )
2. Use a time accurate algorithm to model the flowfield. A solution with a time accurate algorithm will answer one of the lingering questions about the asymmetry of the experimental data. Do the asymmetries result from a growth of modes damped out by the current numerical procedure?
3. Perform a simulation which models the inflow boundary-layer thickness, and the flow variables over the nozzle orifice. The inflow boundary-layer thickness can be correctly modeled with the additional boundary layer data recently acquired for the wind tunnel used by McCann and Bowersox [52]. A more physically consistent profile of the mean flow and turbulence variables over the jet nozzle should also be used in future simulations. Since the shape of the injector and its flow properties are known, numerical simulations can be performed to generate an outflow profile over the nozzle exit.
4. Further investigate the effects of the RSI and JI vortices on mixing and plume expansion. This can be accomplished by collecting additional data with McCann and Bowersox's configuration to verify that the RSI and JI vortices do coexist between  $x/d = 6.5$  and  $7.5$ . Also perform numerical simulations of injection at different angles to see if the RSI and JI vortices are unique to this injection angle.

5. Perform numerical simulations and collect experimental data to assess the effect of the upwash amplification device described in Figure 167 on mixing efficiency and plume expansion. Of primary interest here is whether this device will accelerate the disruption of the mechanisms which sustain the rotation in the JI vortices.
6. Perform numerical simulations and collect experimental data to assess the effect different nozzle shapes and injection angles has on the location where the cross over point forms.
7. Perform numerical simulations with dissimilar species for the injectant and inflow. A comprehensive visualization of the mixing between the inflow air and the injectant could not be predicted from this study since the algorithm only models a single species. This type of simulation would also be useful in assessing the effectiveness of the upwash amplification device.
8. Further assessment of the supposition that a more correct form for the Boussinesq approximation for vortical flows may be  $\tau_{ij} \propto \epsilon_{ijk}\omega_k$ , rather than the traditional form of  $\tau_{ij} \propto S_{ij}$ . The RSTM is a very computationally intensive model. If a physically consistent  $K - \epsilon$  model is developed, it may be worthwhile to use it instead of the more expansive RSTM.



## Bibliography

- [1] Abbett, M. "Boundary Condition Calculation Procedures for Inviscid Supersonic Flow Fields." *Proceedings of the AIAA Computational Fluid Dynamics Conference* . pp. 153–172. Palm Springs California: AIAA, 1973.
- [2] Amano, R. and P. Goel. "Investigation of Third-Order Closure Models of Turbulence for the Computation of Incompressible Flows in a Channel with a Backward-Facing Step," *Journal of Fluids Engineering* , Vol. 109, pp. 424 – 428, 1987.
- [3] Anderson, D., J. Tannehill and R. Pletcher. *Computational Fluid Mechanics and Heat Transfer*. New York, NY: Hemisphere Publishing Corporation, 1984.
- [4] Anderson, J. *Fundamentals of Aerodynamics* . New York: McGraw-Hill, 1991.
- [5] Aso, S., S. Okuyama, Y. Ando and T. Fujimori. "Two-Dimensional and Three-Dimensional Mixing Flow Fields in Supersonic Flow Induced by Injected Secondary Flows Through Traverse Slot and Circular Nozzle," *31<sup>st</sup> Aerospace Sciences Meeting and Exhibit*, January, 1993. Reno, NV.
- [6] Aso, S., S. Okuyama, M. Kawai and Y. Ando. "Experimental Study on the Mixing Phenomena in Supersonic Flows with Slot Injection," *AIAA 29<sup>th</sup> Aerospace Sciences Meeting*, 1991. Reno, NV.
- [7] Aso, S., et al. "A Study on Mixing Phenomena in Three-Dimensional Supersonic Flow with Circular Injection," *32<sup>nd</sup> Aerospace Sciences Meeting and Exhibit*, January, 1994. Reno, NV.
- [8] Beam, R. and R. Warming. "An Implicit Factored Scheme for the Compressible Navier-Stokes Equations," *AIAA Journal* , Vol. 16, No. 4, pp. 393–402, April, 1978.
- [9] Bowersox, R., "Assistant Professor of Aerospace Engineering, University of Alabama." Private conversation, October 1997.
- [10] Brundrett, E. and W. Baines. "The Production and Diffusion of Vorticity in Duct Flow," *Journal of Fluid Mechanics* , Vol. 19, pp. 375 – 395, 1964.
- [11] Cebeci, T. and A. Smith. *Analysis of Turbulent Boundary Layers* . New York, NY: Academic Press, 1974.
- [12] Chien, K. "Predictions of Channel and Boundary-Layer Flows with a Low-Reynolds-Number Turbulence Model," *AIAA Journal* , Vol. 20, No. 1, pp. 33–38, January, 1982.
- [13] Coakley, T. "Implicit Upwind Methods for the Compressible Navier-Stokes Equations," *AIAA Journal* , Vol. 23, No. 3, pp. 374 – 380 March, 1985.
- [14] Coakley, T. and P. Huang. "Turbulence Modeling for High Speed Flows," *AIAA 30<sup>th</sup> Aerospace Sciences Meeting and Exhibit*, January, 1992. Reno, NV.
- [15] Daly, B. and F. Harlow. "Transport Equations in Turbulence," *The Physics of Fluids* , Vol. 13, pp. 2634 – 2649, 1970.
- [16] Donaldson, C. and H. Rosenbaum. *Calculation of the Turbulent Shear Flows Through Closure of the Reynolds Equations by Invariant Modeling* . Technical Report Report number 127, Princeton, New Jersey: Aeronautical Research Association, Princeton, 1968.

- [17] Edney, B. "Effects of Shock Impingement on the Heat Transfer Around Blunt Bodies," *AIAA Journal*, Vol. 6, No. 1, pp. 15 – 2, January, 1968.
- [18] Emanuel, G. *Gas Dynamics: Theory and Applications*. AIAA Education Series, New York, New York: American Institute of Aeronautics and Astronautics, Inc., 1986.
- [19] Favre, A. "Equations des Gaz Turbulents Compressibles," *Journal de Mechanique*, Vol. 4, No. 3, pp. 361–390, 1965.
- [20] Fuller, E., R. Thomas and J. Schetz. "Effects of Yaw on Low Angle Injection Into a Supersonic Flow," *AIAA 29<sup>th</sup> Aerospace Sciences Meeting*, January, 1991. Reno, NV.
- [21] Gaitonde, D. Private conversation, October 1995.
- [22] Gatski, T., S. Sarkar, C. Speziale, L. Balakrishnan, R. Abid and E. Anderson. "Assessment and Application of Reynolds Stress Closure Models to High-Speed Compressible Flows," *AIAA 2<sup>nd</sup> International Aerospace Planes Conference*, October, 1990. Orlando, FL.
- [23] Gerlinger, P., J. Algermissen and D. Bruggemann. "Simulation of Turbulent Slot Injection of Different Gases Into a Supersonic Air Stream," *25<sup>th</sup> AIAA Fluid Dynamics Conference*, June, 1994.
- [24] Gruber, M., "Research Engineer-High Speed Systems Development Branch, Air Force Research Laboratory." Private conversation, November 1997.
- [25] Hanjalic, K. and B. Launder. "A Reynolds-Stress Model of Turbulence and Its Application to Thin Shear Flows," *Journal of Fluid Mechanics*, Vol. 52, pp. 609 – 638, 1972.
- [26] Hanjalic, K. and B. Launder. "Contribution Towards a Reynolds-Stress Closure for Low-Reynolds-Number Turbulence," *Journal of Fluid Mechanics*, Vol. 74, pp. 593 – 610, 1976.
- [27] Hartfield, R. and D. Bayley. "Experimental Investigation of Angled Injection in a Compressible Flow," *Journal of Propulsion and Power*, Vol. 12, No. 2, pp. 442 – 445 March - April, 1996.
- [28] Hill, P and C. Peterson. *Mechanics and Thermodynamics of Propulsion* (Second Edition). Reading, Massachusetts: Addison-Wesley Publishing Company, 1992.
- [29] Hinze, J. *Turbulence*. New York, NY: McGraw-Hill, 1975.
- [30] Hirsch, C. *Numerical Computation of Internal and External Flows: Computational Methods for Inviscid and Viscous Flows*, Volume 2. New York, NY: John Wiley and Son, 1990.
- [31] Hoffmann, K. and S. Chiang. *Computational Fluid Dynamics for Engineers: Volume I*. Wichita, KS: Engineering Education System, 1993.
- [32] Huang, P. and T. Coakley. "An Implicit Navier-Stokes Code for Turbulent Flow Modeling," *AIAA 30<sup>th</sup> Aerospace Sciences Meeting and Exhibit*, January, 1992. Reno, NV.
- [33] Jones, W. and B. Launder. "The Prediction of Laminarization with a Two-Equation Model of Turbulence," *International Journal of Heat and Mass Transfer*, Vol. 15, pp. 301–314, January, 1972.
- [34] Kim, J., P. Moin and R. Moser. "Turbulence Statistics in Fully Developed Channel Flows at Low Reynolds Number," *Journal of Fluid Mechanics*, Vol. 177, pp. 133 – 186, 1987.
- [35] Knight, D. "A Fully Implicit Navier-Stokes Algorithm Using an Unstructured Grid and

Flux Difference Splitting," *AIAA 31<sup>st</sup> Aerospace Sciences Meeting and Exhibit*, January, 1993. Reno, NV.

- [36] Kolmogorov, A. "Local Structure of Turbulence in Incompressible Viscous Fluids for Very Large Reynolds Number," *Doklady AN SSSR*, Vol. 30, pp. 299 – 303, 1941.
- [37] Kordulla, W. and M. Vinokur. "Efficient Computation of Volume in Flow Predictions," *AIAA Journal*, Vol. 21, No. 6, pp. 917–918, June, 1983.
- [38] Lai, Y. and R. So. "On Near-Wall Turbulent Flow Modeling," *Journal of Fluid Mechanics*, Vol. 221, pp. 641–673, January, 1990.
- [39] Lam, C. and K. Bremhorst. "Modified Form of K- $\epsilon$  Model for Predicting Wall Turbulence," *ASME Journal of Fluids Engineering*, Vol. 103, pp. 456–460, September, 1981.
- [40] Launder, B., G. Reece and W. Rodi. "Progress in the Development of a Reynolds-Stress Turbulence Closure," *Journal of Fluid Mechanics*, Vol. 68, pp. 537 – 566, January, 1975.
- [41] Launder, B. and W. Reynolds. "Asymptotic Near-Wall Stress and Dissipation Rates in a Turbulent Flow," *Physics of Fluids*, Vol. 26, pp. 1157 – 1158, 1983.
- [42] Launder, B. and B. Sharma. "Application of the Energy Dissipation Model of Turbulence to the Calculation of Flow Near a Spinning Disc." *Letters in Heat and Mass Transfer*, Vol. 1. No. 2. pp. 131–138. 1974.
- [43] Launder, B. and N. Shima. "Second-Moment Closure for the Near-Wall Sublayer: Development and Application," *AIAA Journal*, Vol. 27, No. 10, pp. 1319 – 1325, October, 1989.
- [44] Launder, B. and D. Spalding. *Mathematical Models of Turbulence*. London: Academic Press, 1972.
- [45] Launder, B. and D. Tselepidakis. "Contribution to the Second-Moment Modeling of Sublayer Turbulent Transport," *Zaric Memorial International Seminar on Near-Wall Turbulence*, May, 1988.
- [46] MacCormack, R. "Current Status of Numerical Solutions of the Navier-Stokes Equations," *AIAA 23<sup>rd</sup> Aerospace Sciences Meeting*, January, 1985. Reno, NV.
- [47] MacCormack, R. "Solution of the Navier-Stokes Equations in Three Dimensions," *AIAA 21<sup>st</sup> Fluid Dynamics, Plasma Dynamics and Lasers Conference*, June, 1990. Seattle, WA.
- [48] Mansour, N., J. Kim and P. Moin. "Near-Wall  $K - \epsilon$  Turbulence Modeling," *AIAA Journal*, Vol. 27, pp. 1068 – 1073, 1989.
- [49] Mattingly, J., W. Heiser and D. Daley. *Aircraft Engine Design*. Education Series, New York: AIAA, 1987.
- [50] Mays, R., R. Thomas and J. Schetz. "Low Angle Injection Into a Supersonic Flow," *AIAA/ASME/SAE/ASEE 25<sup>th</sup> Joint Propulsion Conference*, July, 1989. Monterey, CA.
- [51] McCann, G. *Compressible Turbulence Measurement in Low-Angle Injection into a Supersonic Flow*. Master's Thesis, Graduate School of Engineering, Air Force Institute of Technology (AETC), Wright-Patterson AFB, OH, March 1995. AFIT/GAE/ENY/95M-03.
- [52] McCann, G. and R. Bowersox. "Experimental Investigation of Supersonic Gaseous Injection Into a Supersonic Freestream," *AIAA Journal*, Vol. 35, No. 2, pp. 317 – 323,

February, 1996.

- [53] McClure, T. and E. Ervin. "CFD Analysis of Circular Transverse Injector for a Scramjet Combustor," *AIAA 34<sup>th</sup> Aerospace Sciences Meeting and Exhibit*, January, 1996. Reno, NV.
- [54] Morkovin, M. "Effect of Compressibility on Turbulent Flow." *The Mechanics of Turbulence* edited by A. Favre, New York: Gordon and Beach, 1964.
- [55] Morrison, J. "Flux Difference Split Scheme for Turbulent Transport Equations," *AIAA 2<sup>nd</sup> International Aerospace Planes Conference*, October, 1990. Orlando, FL.
- [56] Morrison, J. *A Compressible Navier-Stokes Solver with Two-Equation and Reynolds Stress Turbulence Closure Models*. NASA Contractor Report NASA CR-4440, 1992.
- [57] Morrison, J. Private conversation, December 1995.
- [58] Morrison, J. Private conversation, October 1995.
- [59] Morrison, J., T. Gatski, T. Sommer, H. Zhang and R. So. "Evaluation of a Near-Wall Turbulent Closure Model in Predicting Compressible Ramp Flows." *Near-Wall Turbulent Flows* edited by R. So, et al., pp. 239–250, New York, NY: Elsevier, January 1993.
- [60] Northam, G. and G. Anderson. "Supersonic Combustion Ramjet Research at Langley," *AIAA 24<sup>th</sup> Aerospace Sciences Meeting*, January, 1986. Reno, NV.
- [61] Patel, V., W. Rodi and G. Scheuerer. "Turbulence Models for Near-Wall and Low Reynolds Number Flows: A Review," *AIAA Journal*, Vol. 23, No. 9, pp. 1308–1319, September, 1985.
- [62] Peyret, R. and T. Taylor. *Computational Methods for Fluid Flow*. New York, NY: Springer-Verlag, 1983.
- [63] Pulliam, T. and J. Steger. "Recent Improvements in Efficiency, Accuracy, and Convergence for Implicit Approximate Factorization Algorithms," *AIAA 23<sup>rd</sup> Aerospace Sciences Meeting*, January, 1985. Reno, NV.
- [64] Reynolds, O. "On the Dynamical Theory of Incompressible Viscous Fluids and the Determination of the Criterion." *Philosophical Transactions of the Royal Society of London*, Vol. 186. Series A, pp. 123–164, 1895.
- [65] Rizzetta, D. "Numerical Simulation of Slot Injection into a Turbulent Supersonic Stream," *AIAA 30<sup>th</sup> Aerospace Sciences Meeting and Exhibit*, January, 1992. Reno, NV.
- [66] Rizzetta, D. Private Conversation, December 1994.
- [67] Rizzetta, D. "Numerical Investigation of Supersonic Wing-Tip Vortices," *AIAA 26<sup>th</sup> Fluid Dynamics Conference*, June, 1995. San Diego, CA.
- [68] Roe, P. "Approximate Riemann Solvers, Parameter Vectors, and Difference Schemes," *Journal of Computational Physics*, Vol. 43, pp. 357–372, 1981.
- [69] Rotta, J. "Statistische Theorie Nichthomogener Turbulenz," *Zeitschrift fur Physik*, Vol. 131, pp. 547 – 572, 1951.
- [70] Santiago, J. and J. Dutton. "Crossflow Vortices of a Jet Injected Into a Supersonic Crossflow," *AIAA Journal*, Vol. 35, No. 5, pp. 915 – 917, May, 1997.
- [71] Santiago, J. and J. Dutton. "Velocity Measurements of a Jet Injected Into a Supersonic

Crossflow," *Journal of Propulsion and Power*, Vol. 13, No. 2, pp. 264 – 273, March - April, 1997.

- [72] Sarkar, S. *Modeling the Pressure-Dilatation Correlation*. ICASE Report No. 91-42, 1991. NASA Langley Research Center.
- [73] Sarkar, S., G. Erlebacher and M. Hussaini. *Direct Simulation of Compressible Turbulence in a shear Flow*. ICASE Report No. 91-29, 1991. NASA Langley Research Center.
- [74] Sarkar, S., G. Erlebacher, M. Hussaini and H. Kreiss. "The Analysis and Modeling of Dilatational Terms in Compressible Turbulence," *Journal of Fluid Mechanics*, Vol. 227, pp. 473–493, 1991.
- [75] Schetz, J. *Boundary Layer Analysis*. Englewood Cliffs, New Jersey: Prentice-Hall, Inc., 1993.
- [76] Schetz, J. and F. Billig. "Penetration of Gases Jets Injected into a Supersonic Stream," *Journal of Spacecraft*, Vol. 3, pp. 1658–1665, November, 1966.
- [77] Schetz, J., P. Hawkins and H. Lehman. "Structure of Highly Underexpanded Transverse Jets in a Supersonic Stream," *AIAA Journal*, Vol. 5, pp. 882–884, May, 1967.
- [78] Schumann, U. "Realizability of Reynolds Stress Turbulence Models," *Physics of Fluids*, Vol. 20, pp. 721 – 725, 1977.
- [79] Settles, G. and L. Dodson. *Hypersonic Turbulent Boundary-Layer Interaction Database*. Technical Report NASA CR-177577, April 1991.
- [80] Settles, G. and L. Dodson. *Hypersonic Turbulent Boundary-Layer and Free Shear Database*. Technical Report NASA CR 177610, April 1993.
- [81] Shapiro, A. *The Dynamics and Thermodynamics of Compressible Fluid Flow*, Vol. 1. New York: John Wiley and Sons, 1953.
- [82] Shih, T. and W. Chyu. "Approximate Factorization with Source Terms," *AIAA Journal*, Vol. 29, No. 10, pp. 1759–1760, October, 1991.
- [83] Shima, N. "A Reynolds-Stress Model for Near-Wall and Low-Reynolds Number Regions," *Journal of Fluids Engineering*, Vol. 110, pp. 38–44, March, 1988.
- [84] Shir, C. "A Preliminary Numerical Study of Atmospheric Turbulent Flows in the Idealized Planetary Boundary Layer," *Journal of Atmospheric Sciences*, Vol. 30, pp. 1327 – 1339, 1973.
- [85] So, R., Y. Lai, H. Zhang and B. Hwang. *A Review of Near-Wall Reynolds-Stress Closures*. Technical Report NASA CR-4369, January 1991.
- [86] So, R., H. Zhang and C. Speziale. "Near-Wall Modeling of the Dissipation Rate Equation," *AIAA Journal*, Vol. 29, No. 12, pp. 2069–2076, December, 1991.
- [87] Soares, C. and M. Rasmussen. "Integration of Scramjets with Waverider Configuration," *AIAA/ASME/SAE/ASEE 25<sup>th</sup> Joint Propulsion Conference*, July, 1989. Monterey, CA.
- [88] Spaid, F. and E. Zukoski. "A Study of the Interaction of Gases Jets from Transverse Slots with Supersonic External Flows," *AIAA Journal*, Vol. 6, No. 2, pp. 205–212, February, 1968.
- [89] Spalding, D. "A Single Formula for the Law of the Wall," *Journal of Applied Mechanics*,

Vol. 28, pp. 455–457, 1961.

- [90] Speziale, C. “On Turbulent Secondary Flows in Pipes of Noncircular Cross-Section,” *International Journal of Engineering Science*, Vol. 20, No. 7, pp. 863 – 872, July, 1982.
- [91] Speziale, C. “On Nonlinear  $K - l$  and  $K - \epsilon$  Models of Turbulence,” *Journal of Fluid Mechanics*, Vol. 178, pp. 459 – 475, 1987.
- [92] Speziale, C. “Analytical Methods for the Development of Reynolds-Stress Closures in Turbulence,” *Annual Review of Fluid Mechanics*, Vol. 23, pp. 107–157, 1991.
- [93] Speziale, C., R. Abid and E. Anderson. “A Critical Evaluation of Two-Equation Models for Near Wall Turbulence,” *AIAA 21<sup>st</sup> Fluid Dynamics, Plasma Dynamics and Lasers Conference*, June, 1990. Seattle, WA.
- [94] Speziale, C. and S. Sarkar. “Second-Order Closure Models for Supersonic Turbulent Flows,” *AIAA 29<sup>th</sup> Aerospace Sciences Meeting*, 1991. Reno, NV.
- [95] Steinbrenner, J. and J. Chawner. *The GRIDGEN Version 9: Multiple Block Grid Generation Software*. Technical Report MDA Engineering Report 94-01, Arlington, Texas: MDA Engineering, Inc., August 1994.
- [96] Sterett, J. and P. Holloway. “On the Effect of Transition on Parameters Within a Separated Region at Hypersonic Speeds—with Emphasis on Heat Transfer.” *Symposium on Fully Separated Flows, American Society of Mechanical Engineers*. pp. 15–26. May 1964.
- [97] Tennekes, H. and L. Lumley. *A First Course in Turbulence*. Cambridge, MA: MIT Press, 1972.
- [98] Thomas, J., B. VanLeer and R. Walters. “Implicit Flux-Split Schemes for the Euler Equations,” *AIAA 18<sup>th</sup> Fluid Dynamics and Plasma Dynamics and Lasers Conference*, 1985. Cincinnati, OH.
- [99] Thomas, J. and R. Walters. “Upwind Relaxation Algorithms for the Navier-Stokes Equations,” *AIAA Journal*, Vol. 25, No. 4, pp. 527–534, April, 1987.
- [100] Tucker, K. *Experimental Investigation of Non-Adiabatic Supersonic Slot Injection Into a Supersonic Cross-Flow*. MS thesis, Air Force Institute of Technology, Wright-Patterson AFB, OH, December 1995.
- [101] VanDriest, E. “The Problem of Aerodynamic Heating,” *Journal of Aeronautical Sciences*, Vol. 23, pp. 1007 – 1011 1956.
- [102] Vandromme, D. and H. HaMinh. “About the Coupling of Turbulence Closure Models with Averaged Navier-Stokes Equations,” *Journal of Computational Physics*, Vol. 65, pp. 386–409, 1986.
- [103] VanLeer, B. “Toward the Ultimate Conservative Difference Schemes V. A Second Order Sequel to Godunov’s Method,” *Journal of Computational Physics*, Vol. 32, pp. 101–136, 1979.
- [104] Venkatakrishnan, V. “Preconditioned Conjugate Gradient Methods for the Compressible Navier-Stokes Equations,” *AIAA Journal*, Vol. 29, No. 7, pp. 1092–1100, July, 1991.
- [105] Vinokur, M. “On One-Dimensional Stretching Functions for Finite-Difference Calculations,” *Journal of Computational Physics*, Vol. 50, pp. 215 – 234, 1983.

- [106] Vinokur, M. *An Analysis of Finite-Difference and Finite-Volume Formulations of Conservation Laws*. Technical Report NASA CR-177416, June 1986.
- [107] Walters, R. and J. Thomas. "Advances in Upwind Relaxation Methods." *State-of-the-Art Surveys on Computational Mechanics* Chapter 4, pp. 145–183, January 1989.
- [108] White, F. *Viscous Fluid Flow* (2<sup>nd</sup> Edition). New York: McGraw-Hill, 1991.
- [109] Wilcox, D. *Turbulence Modeling for CFD*. La Canada, CA: DCW Industries, Inc., 1993.
- [110] Williams, S. and R. Hartfield. "An Analytical Investigation of Angled Injection Into a Compressible Flow," 32<sup>nd</sup> AIAA/ASME/SAE/ASEE Joint Propulsion Conference, July, 1996. Lake Buena Vista, FL.
- [111] Wilson, M. MS thesis, Air Force Institute of Technology, Wright-Patterson AFB, OH, 1995.
- [112] Yokota, K. and S. Kaji. "Two and Three Dimensional Study on Supersonic Flow and Mixing Fields with Hydrogen Injection," AIAA Sixth International Aerospace Planes and Hypersonics Technologies Conference, April, 1995. Chattanooga, TN.
- [113] Zhang, H., R. So, T. Gatski and C. Speziale. "A Near-Wall Second-Order Closure for Compressible Turbulent Flows." *Near-Wall Turbulent Flows* edited by R. So, et al., pp. 209–218, New York, NY: Elsevier, January 1993.
- [114] Zhang, H., R. So, C. Speziale and Y. Lai. "A Near-Wall Two-Equation Model for Compressible Turbulent Flows," AIAA 30<sup>th</sup> Aerospace Sciences Meeting,, AIAA 92-0442, January, 1992. Reno, NV.
- [115] Zhang, H., R. So and M. Zhu. "A Near-Wall Second-Order Turbulence Model for Wall-Bounded Flows." *Ninth Symposium on "Turbulent Shear Flows"* Chapter 8, pp. 2.1 – 2.6, August 1993.
- [116] Zukoski, E. and F. Spaid. "Secondary injection of Gases into a Supersonic Flow," *AIAA Journal*, Vol. 2, No. 10, pp. 1689–1696, October, 1964.

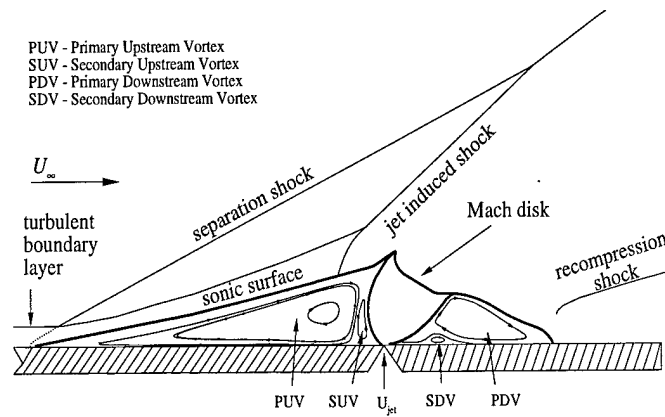


Figure 1. Schematic of a flowfield generated by normal injection of a sonic fluid through a two-dimensional slot into a supersonic flow

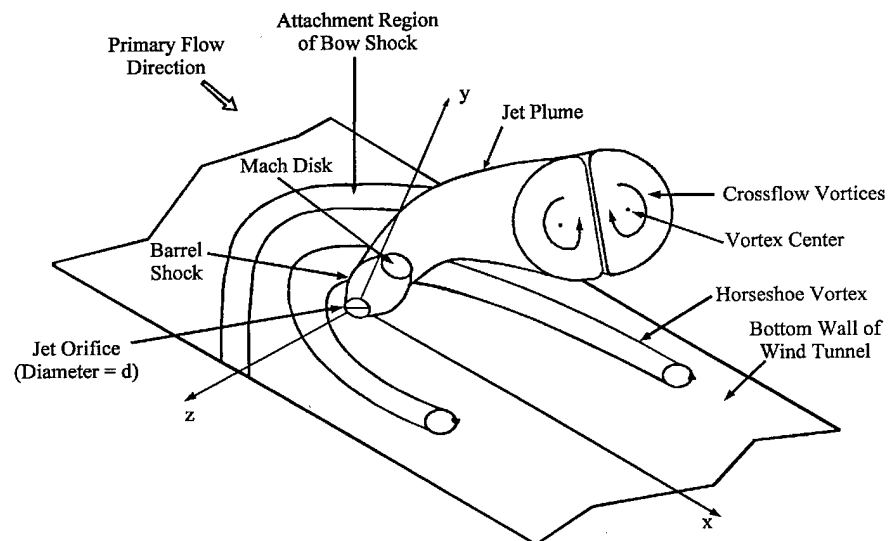


Figure 2. Schematic of a three-dimensional flowfield generated by normal injection of a sonic fluid through a circular nozzle into a supersonic flow [70]



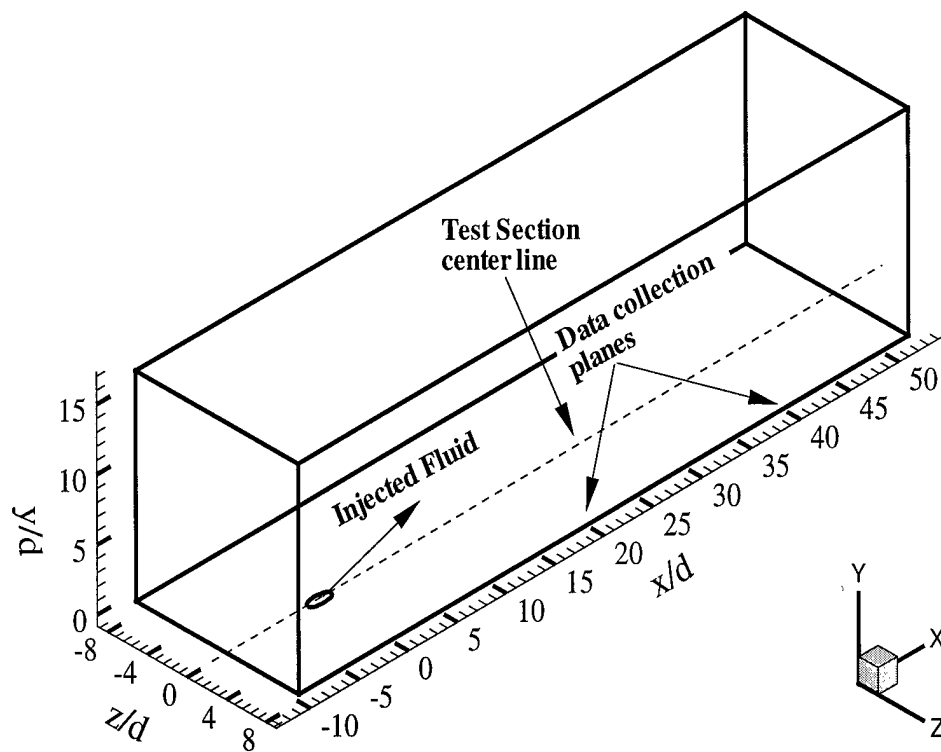


Figure 3. McCann and Bowersox windtunnel configuration [52]

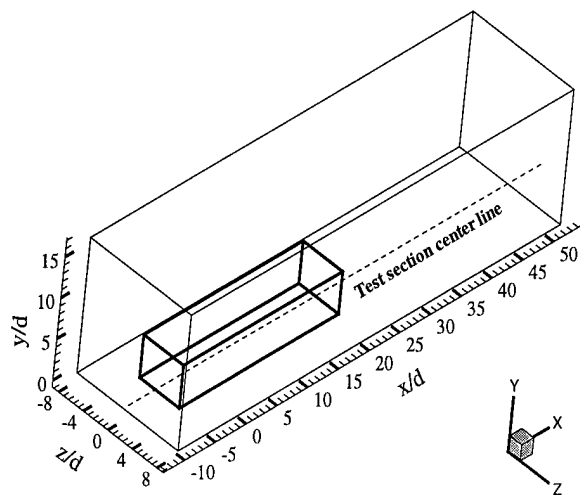


Figure 4. Full-plane grid location with respect to test section

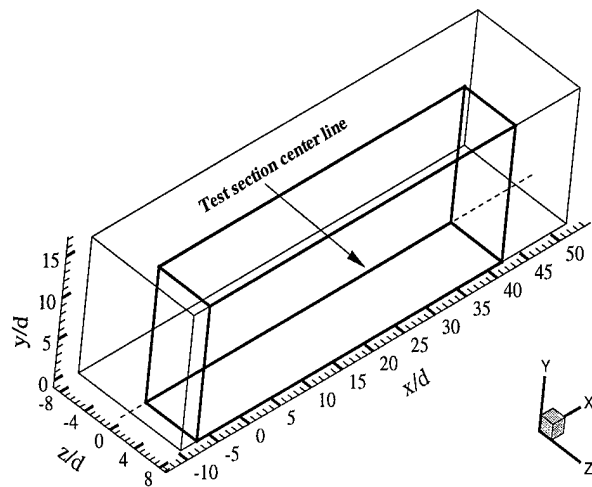


Figure 5. Half-plane grid location with respect to test section

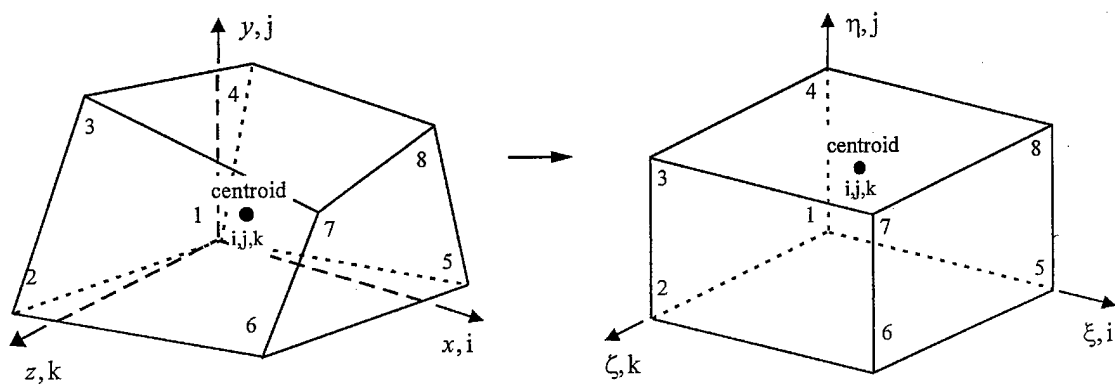


Figure 6. Transformation from Physical Space to Computational Space [37]

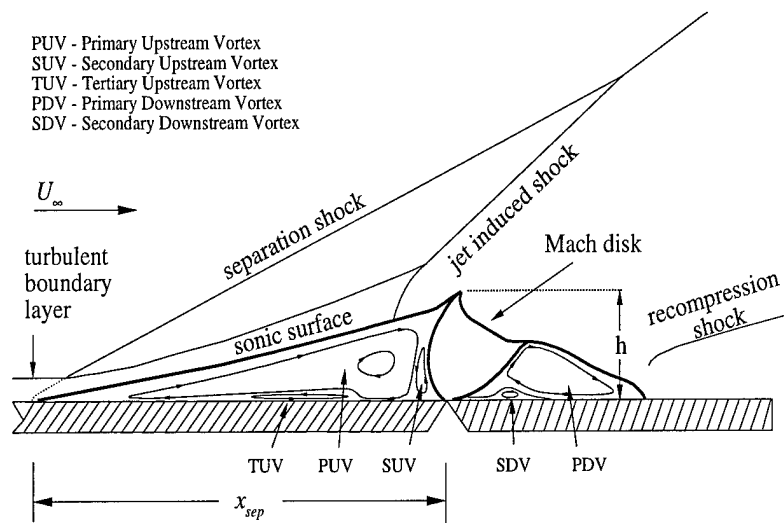


Figure 7. Schematic of slot injection flowfield

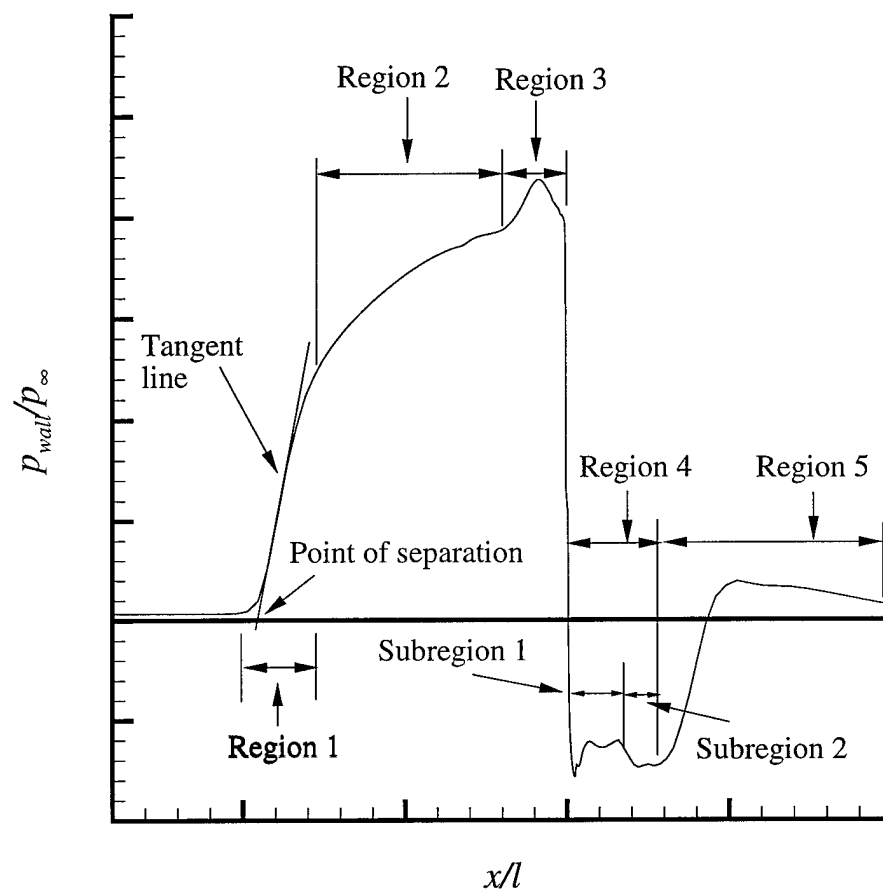


Figure 8. Schematic of surface static pressure regions

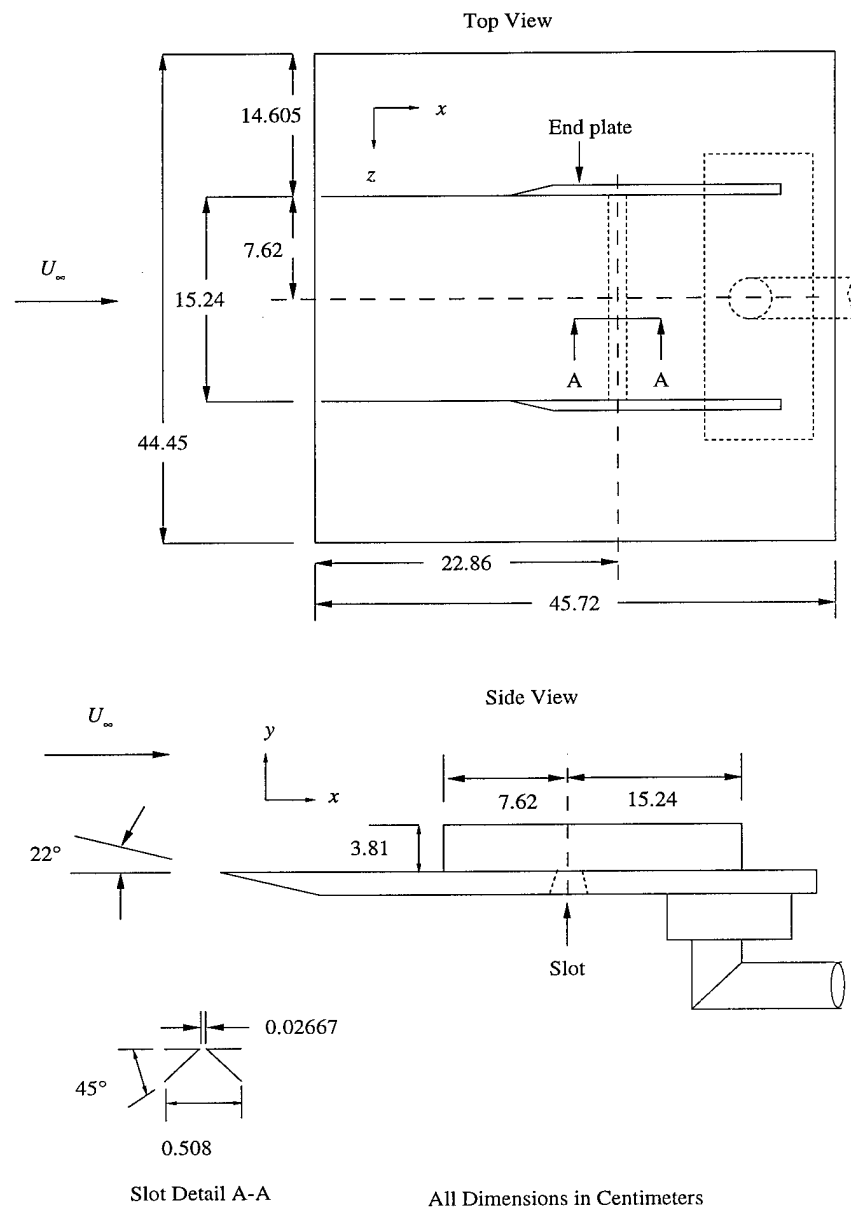
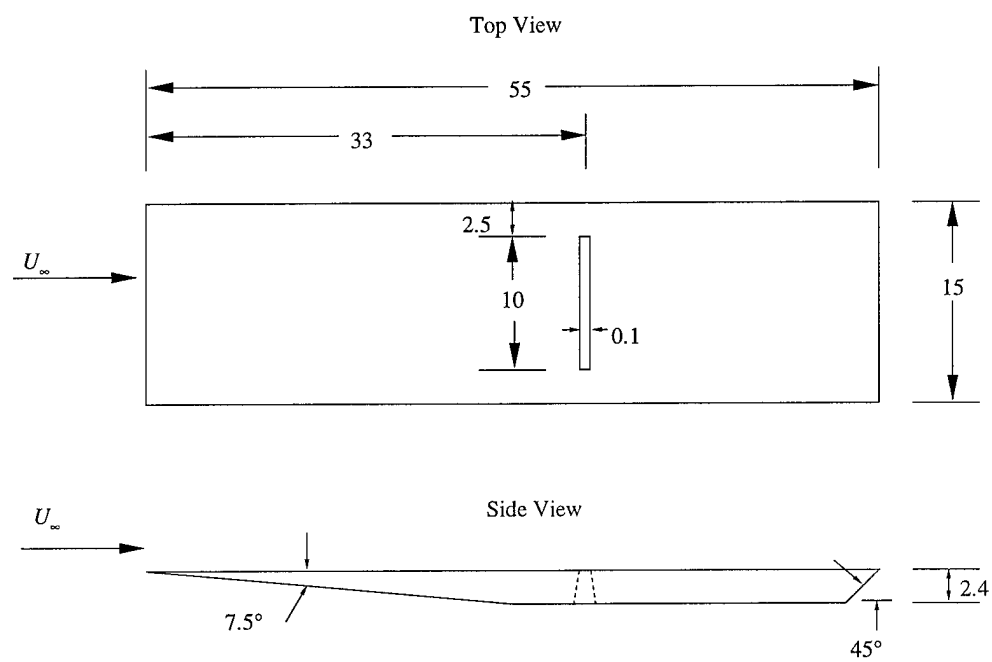


Figure 9. Spaid and Zukoski experimental configuration [88]



All Dimensions in Centimeters

Figure 10. Aso et al. experimental configuration [6]

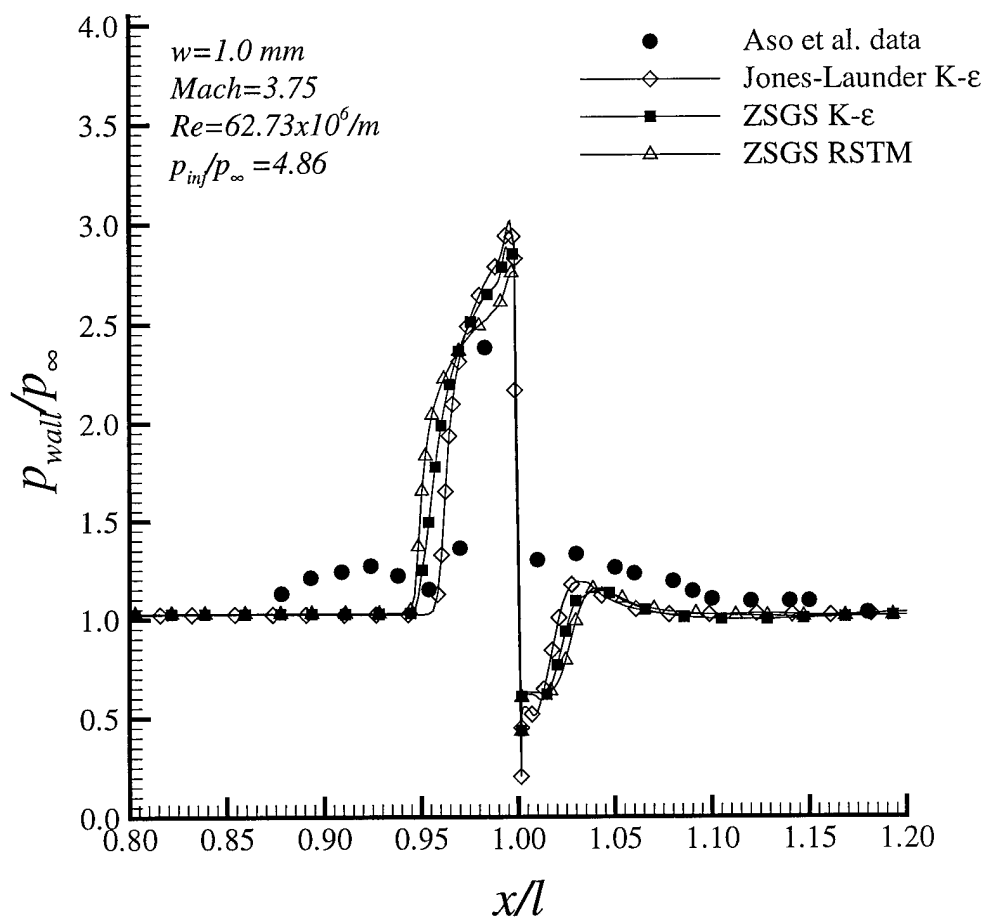


Figure 11. Comparison of surface pressure profiles for Aso et al. configuration for a static pressure ratio of 4.86



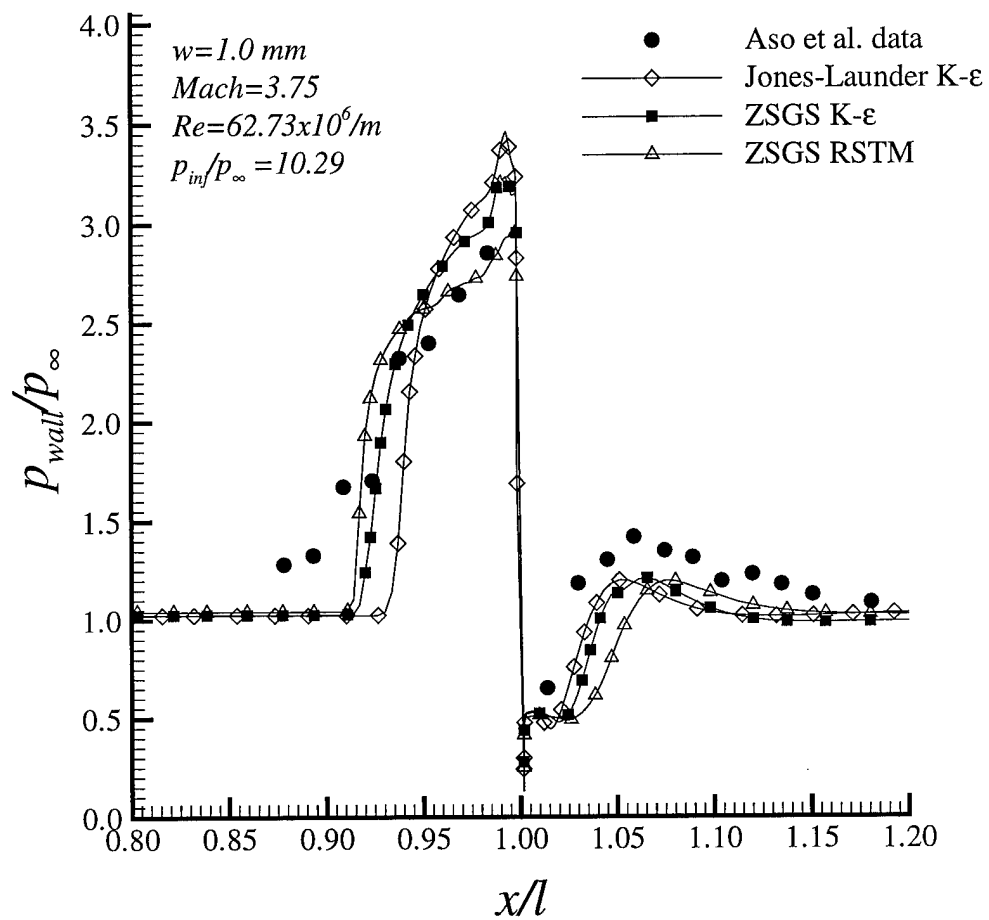


Figure 12. Comparison of surface pressure profiles for Aso et al. configuration for a static pressure ratio of 10.29

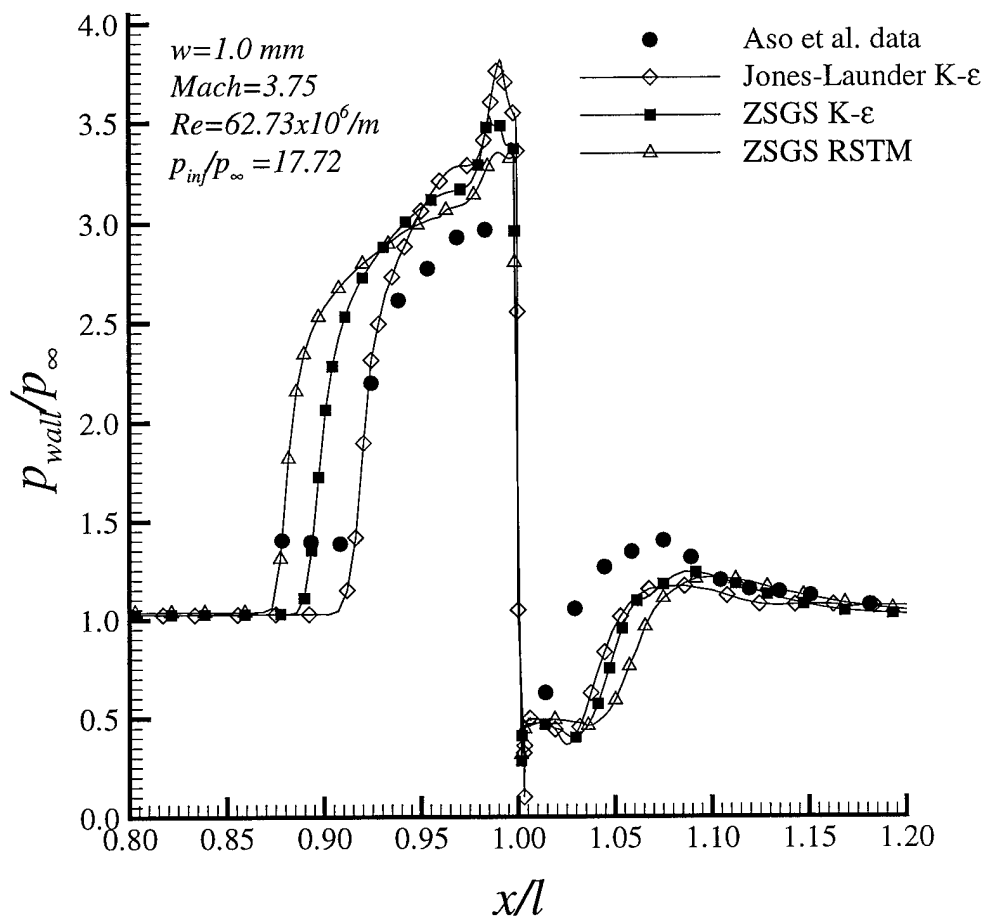


Figure 13. Comparison of surface pressure profiles for Aso et al. configuration for a static pressure ratio of 17.72

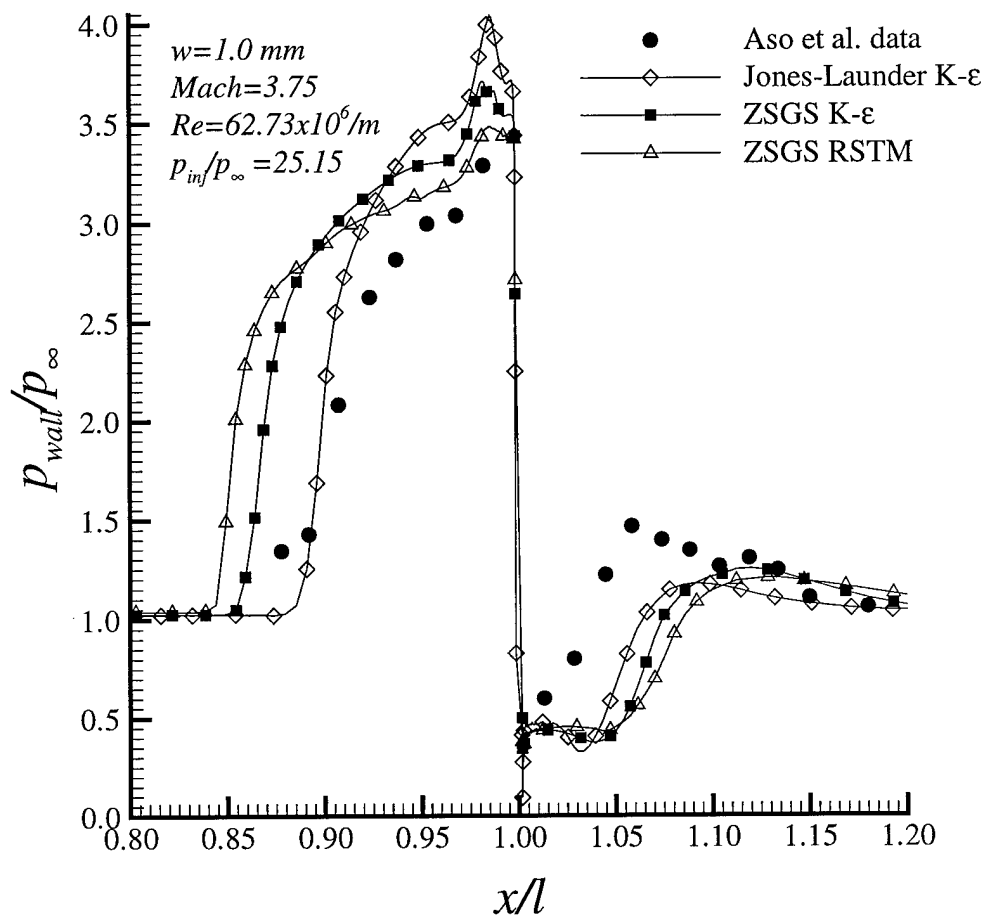


Figure 14. Comparison of surface pressure profiles for Aso et al. configuration for a static pressure ratio of 25.15

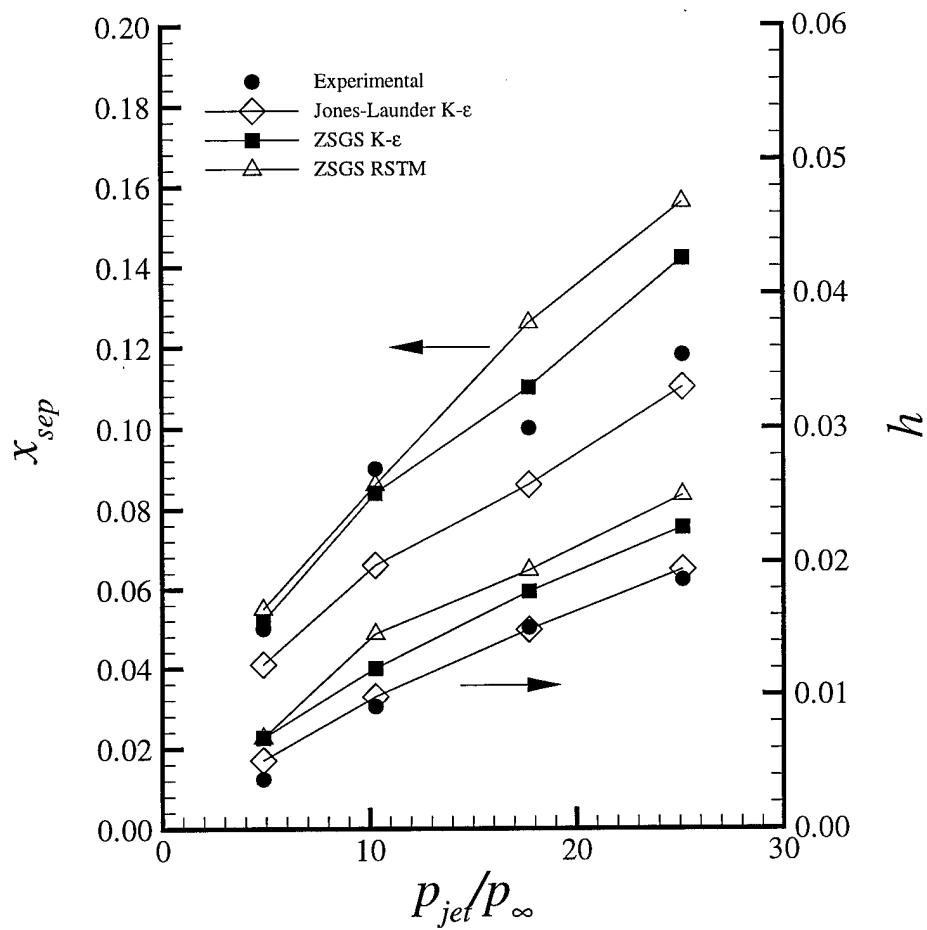


Figure 15. Separation length and plume height as a function of static pressure ratio for the Aso et al. configuration

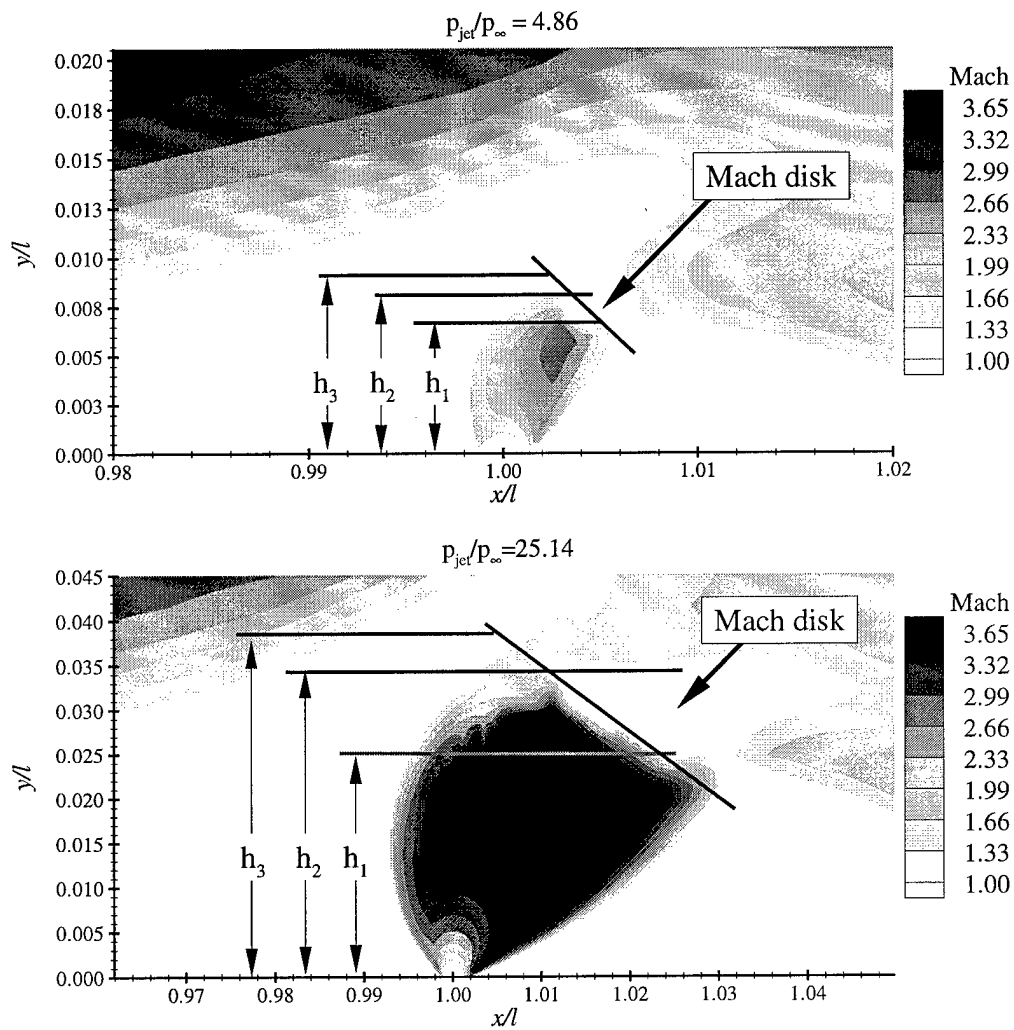


Figure 16. Comparison of Mach disk generated at two different pressure ratios and definition of Mach disk height (Aso et al. configuration)

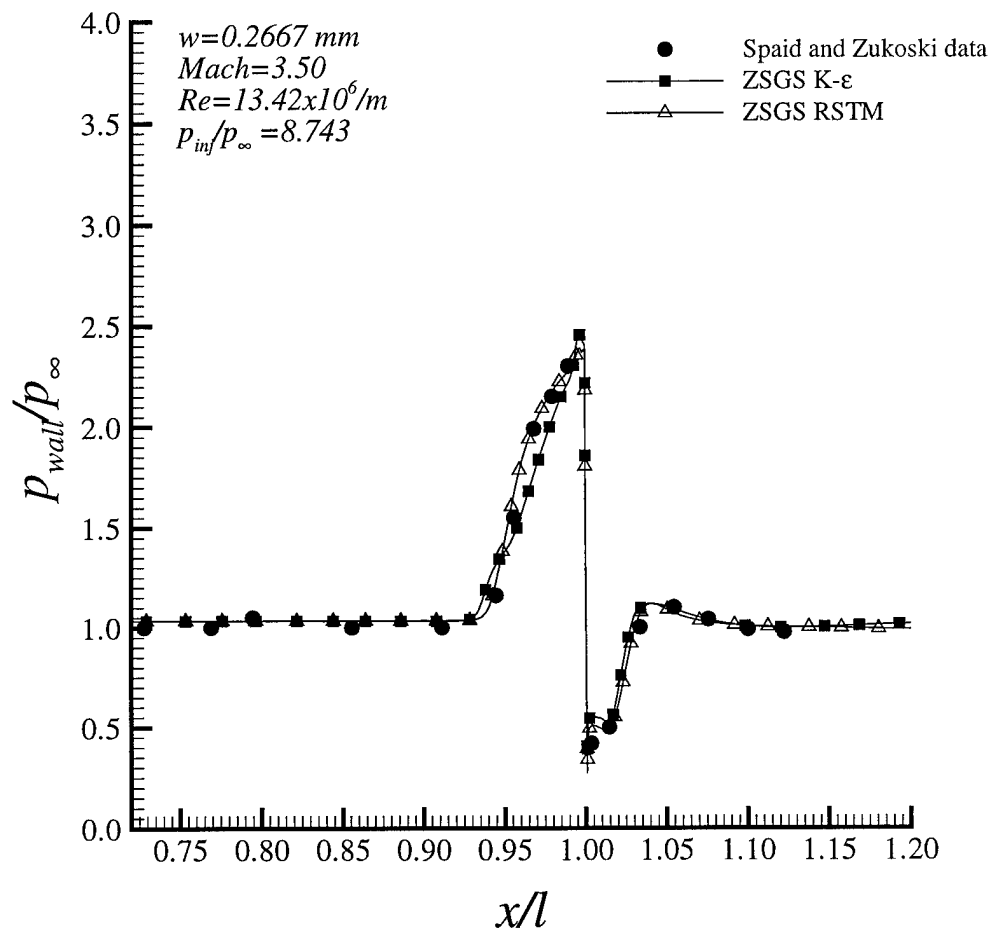


Figure 17. Comparison of surface pressure profiles for Spaid and Zukoski configuration for a static pressure ratio of 8.743

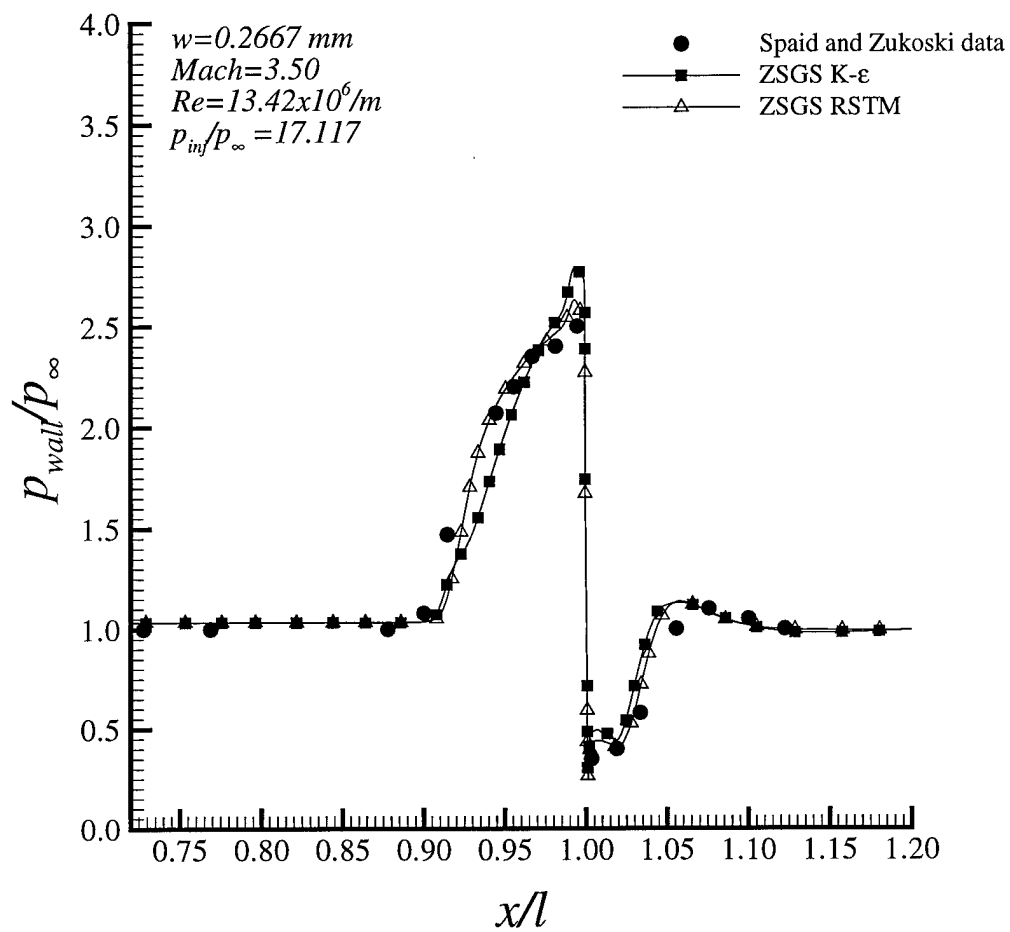


Figure 18. Comparison of surface pressure profiles for Spaid and Zukoski configuration for a static pressure ratio of 17.117

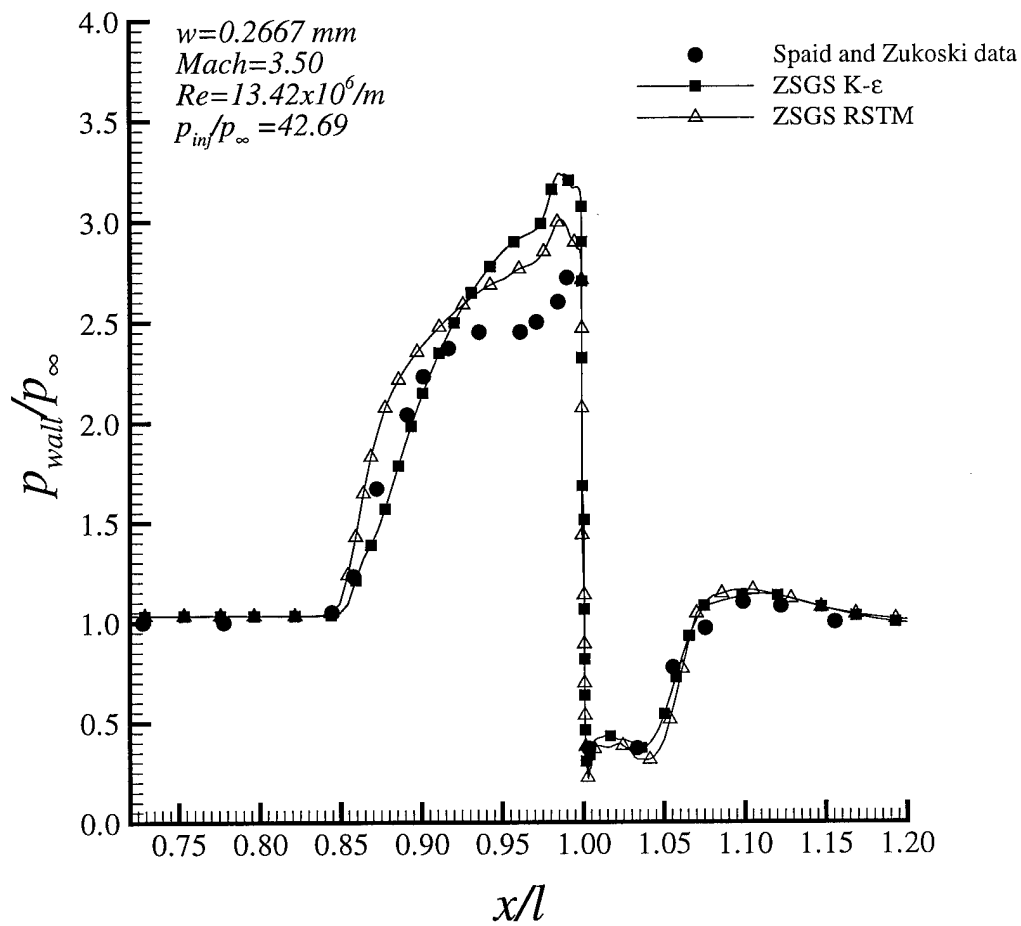


Figure 19. Comparison of surface pressure profiles for Spaid and Zukoski configuration for a static pressure ratio of 42.79



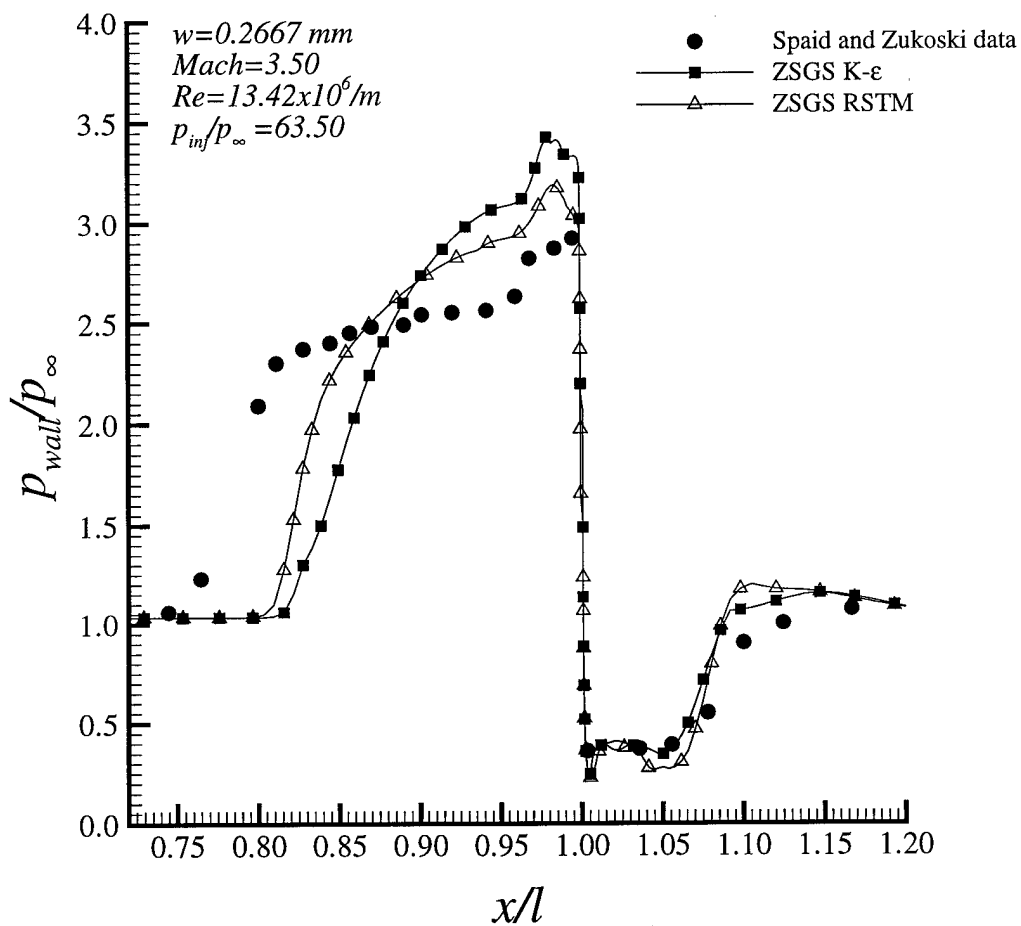


Figure 20. Comparison of surface pressure profiles for Spaid and Zukoski configuration for a static pressure ratio of 63.5

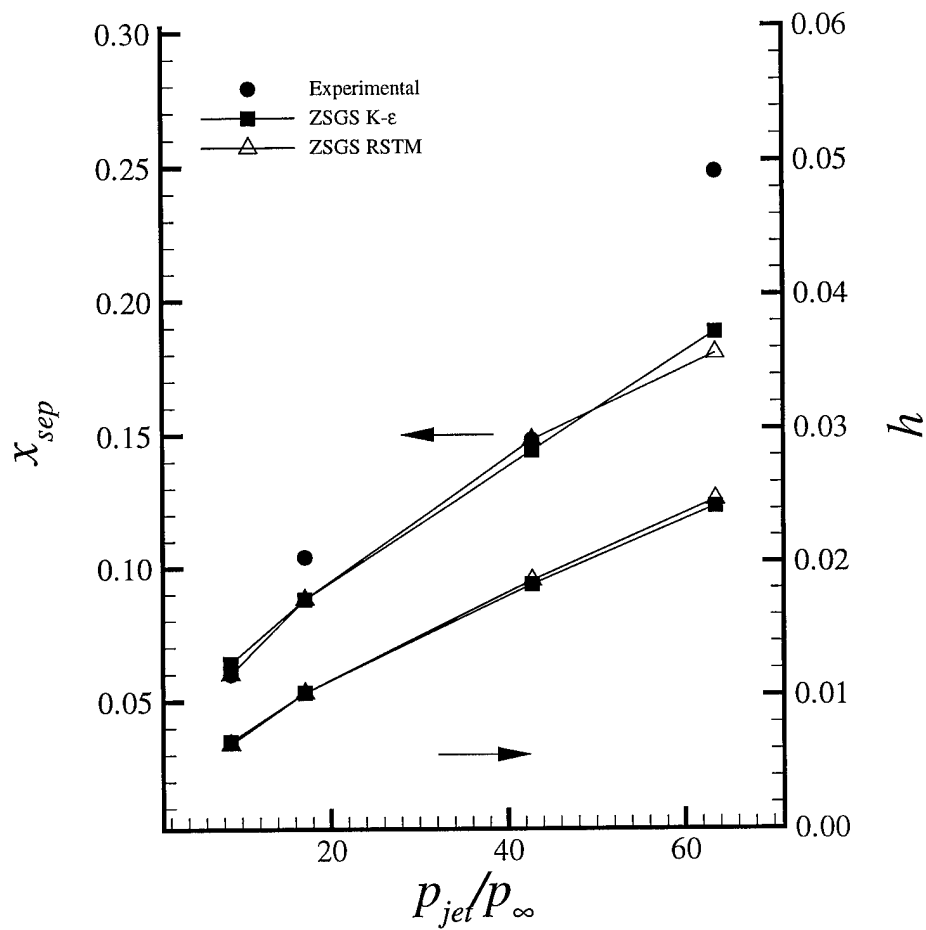


Figure 21. Separation length and plume height as a function of static pressure ratio for the Spaid and Zukoski configuration

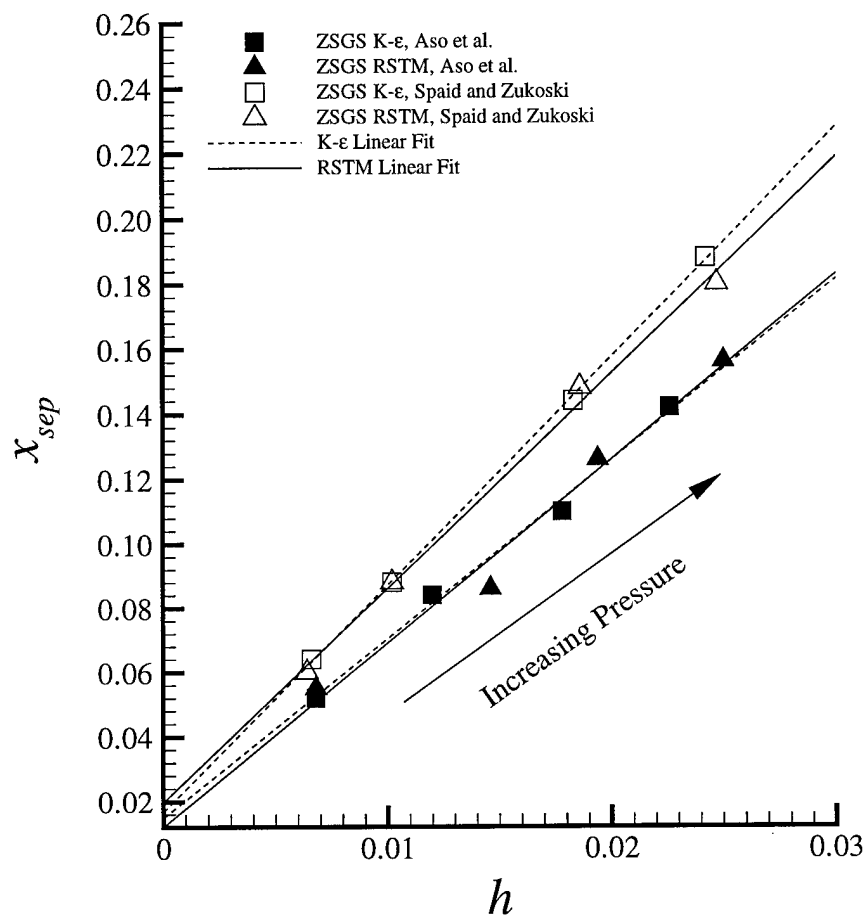


Figure 22. Separation length as a function of plume height for the Aso et al. and Spaid and Zukoski configurations

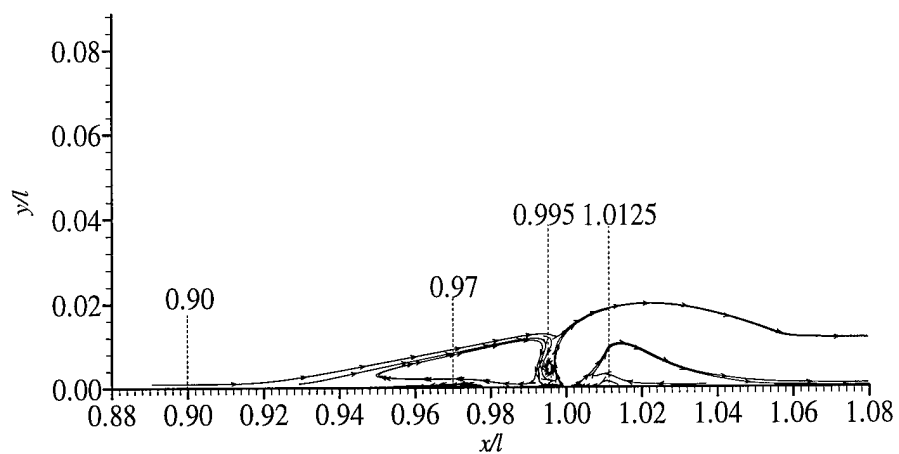


Figure 23. Location of cross sectional data samples relative to particle paths for Spaid and Zukoski configuration

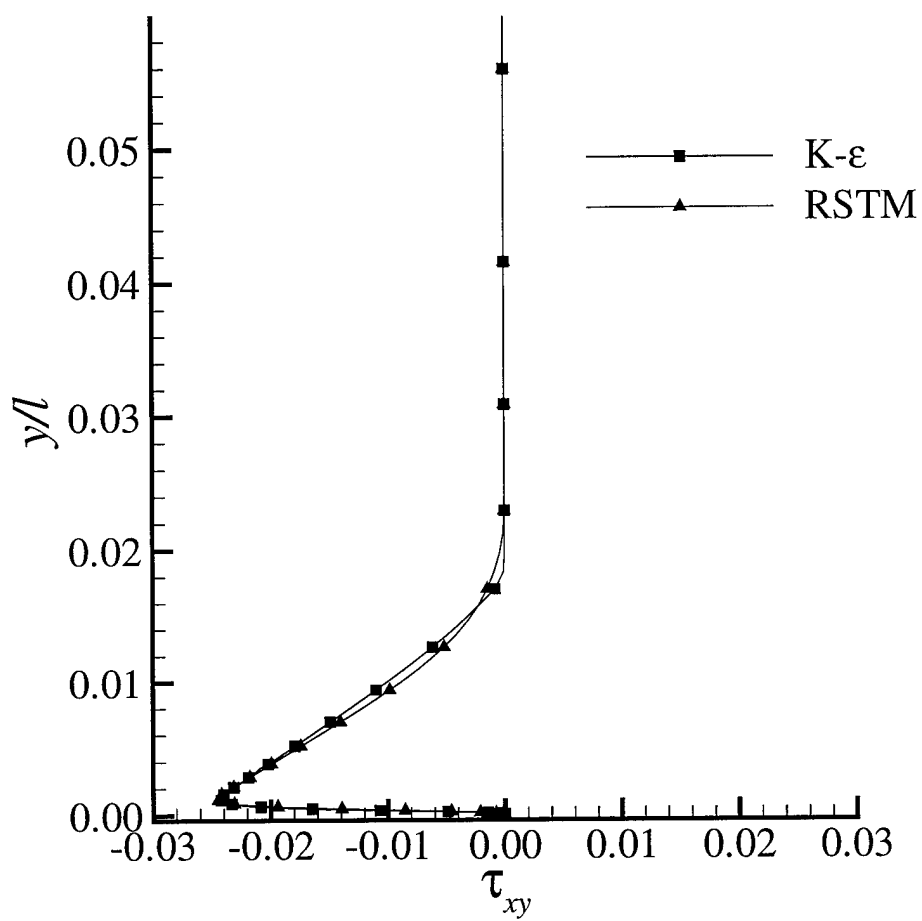


Figure 24. Comparison of  $\tau_{xy}$  profiles at  $x/l = 0.9000$  for Spaid and Zukoski configuration

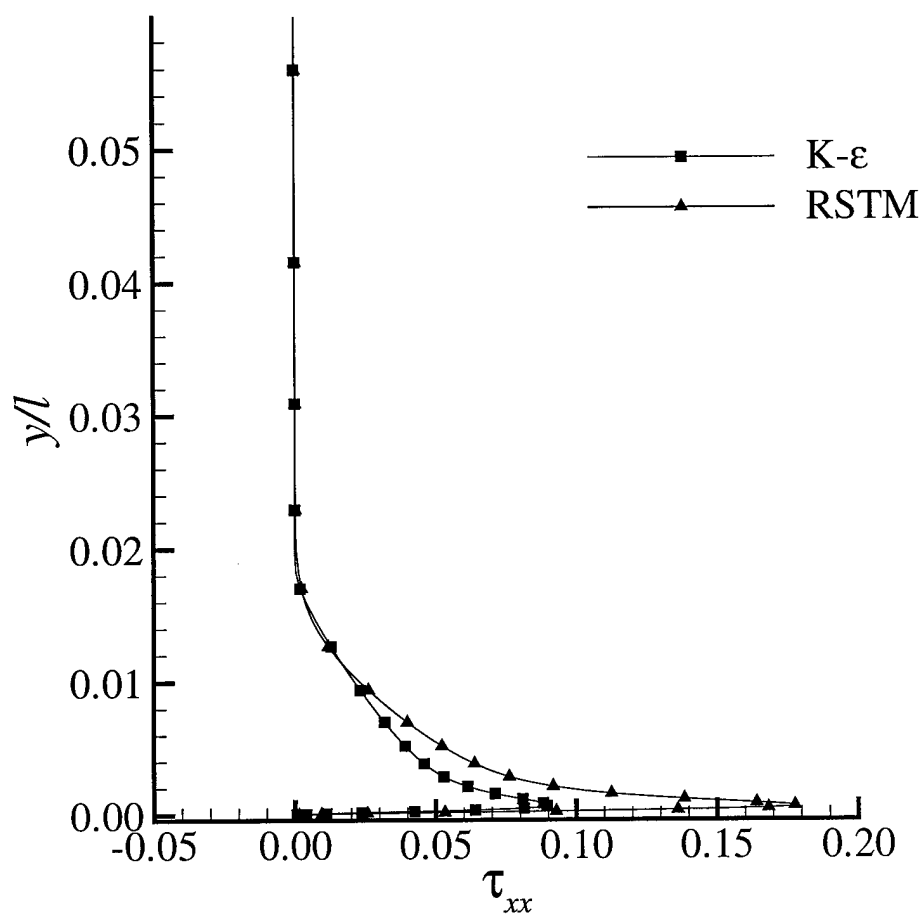


Figure 25. Comparison of  $\tau_{xx}$  profiles at  $x/l = 0.9000$  for Spaid and Zukoski configuration

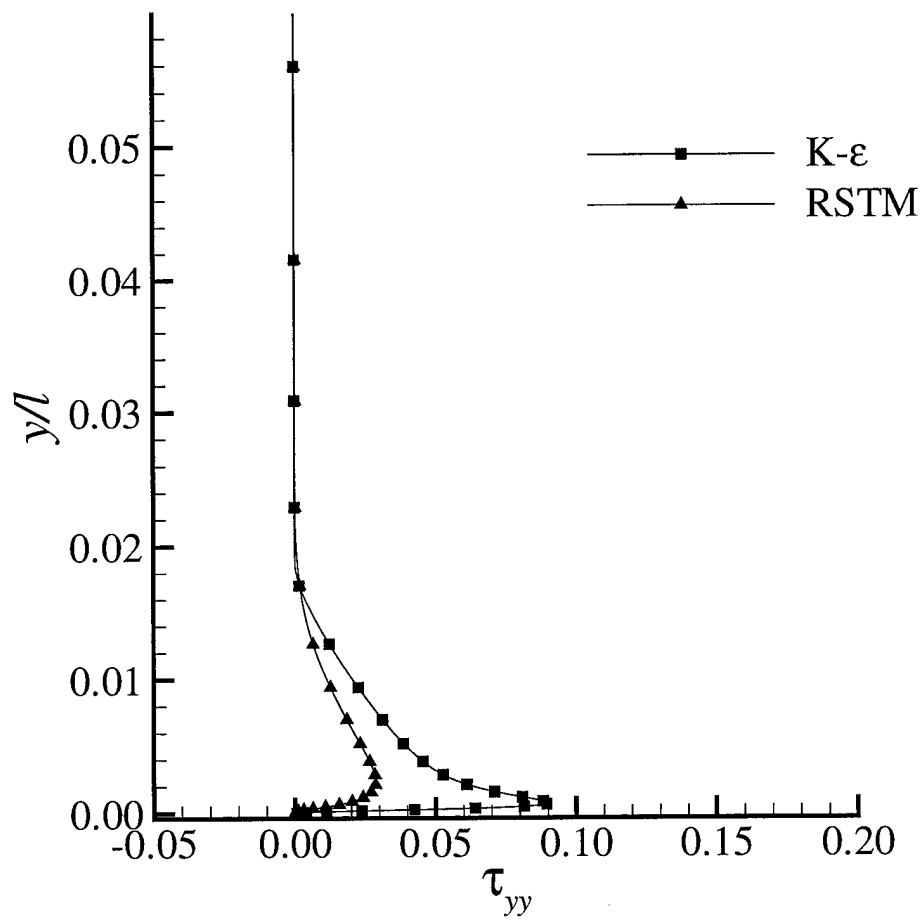


Figure 26. Comparison of  $\tau_{yy}$  profiles at  $x/l = 0.9000$  for Spaid and Zukoski configuration

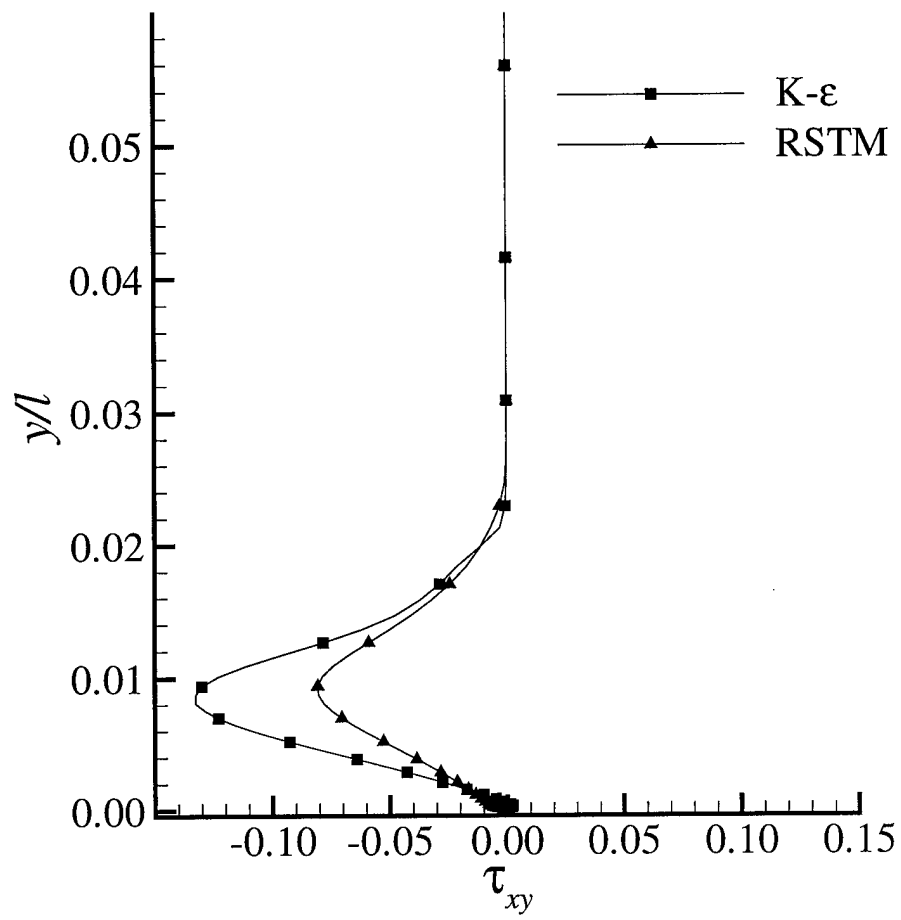


Figure 27. Comparison of  $\tau_{xy}$  profiles at  $x/l = 0.9700$  for Spaid and Zukoski configuration



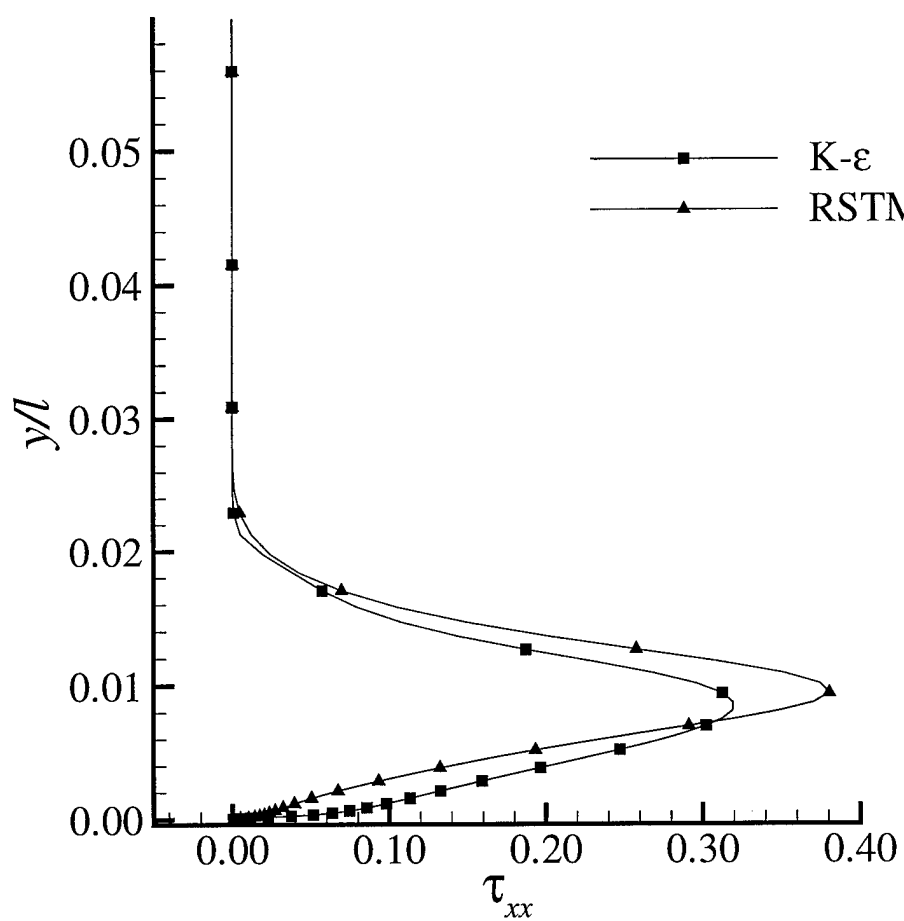


Figure 28. Comparison of  $\tau_{xx}$  profiles at  $x/l = 0.9700$  for Spaid and Zukoski configuration

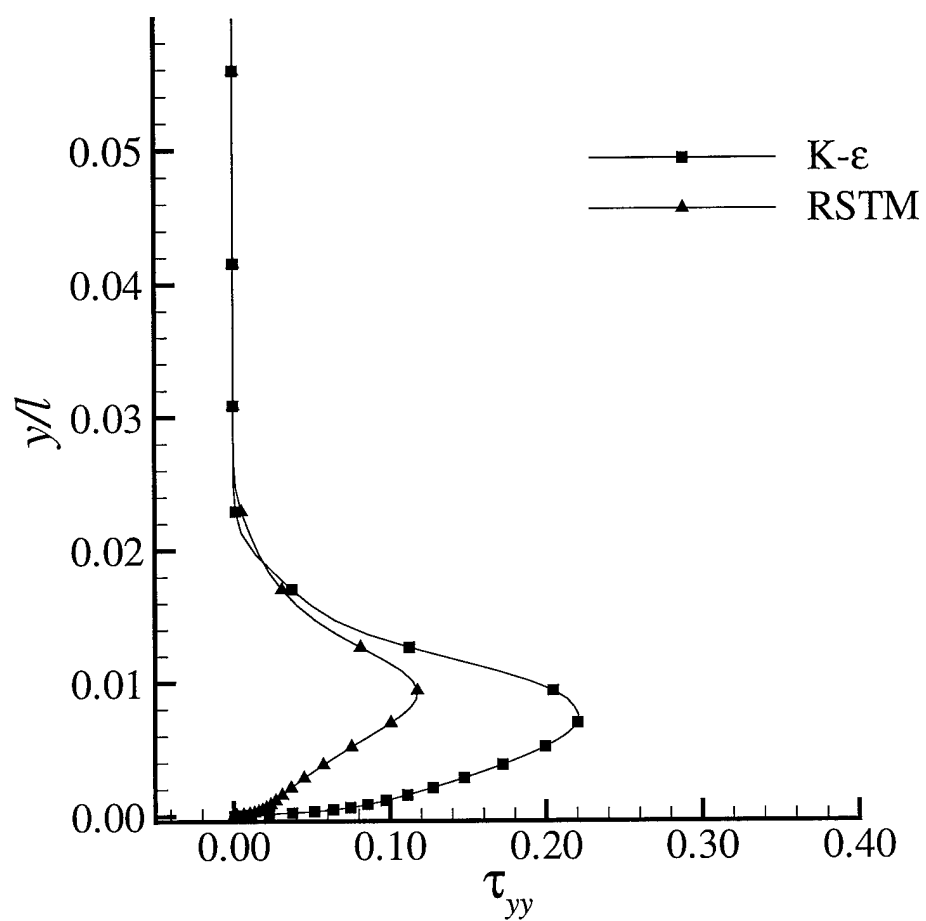


Figure 29. Comparison of  $\tau_{yy}$  profiles at  $x/l = 0.9700$  for Spaid and Zukoski configuration

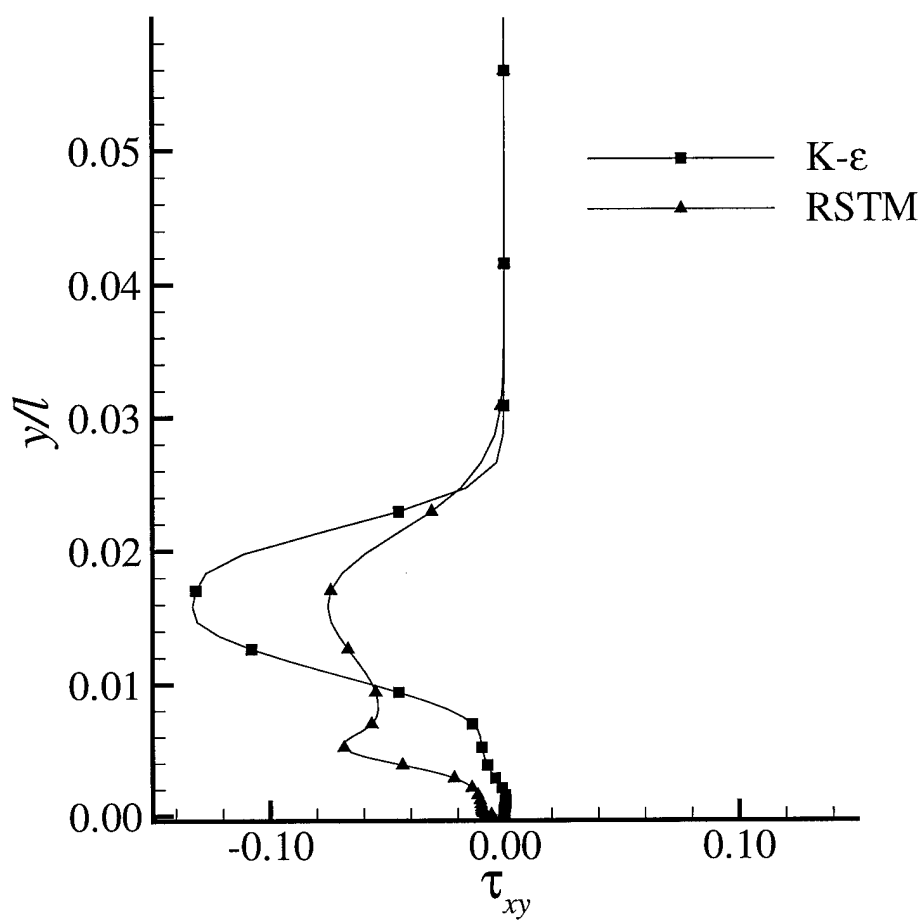


Figure 30. Comparison of  $\tau_{xy}$  profiles at  $x/l = 0.9950$  for Spaid and Zukoski configuration

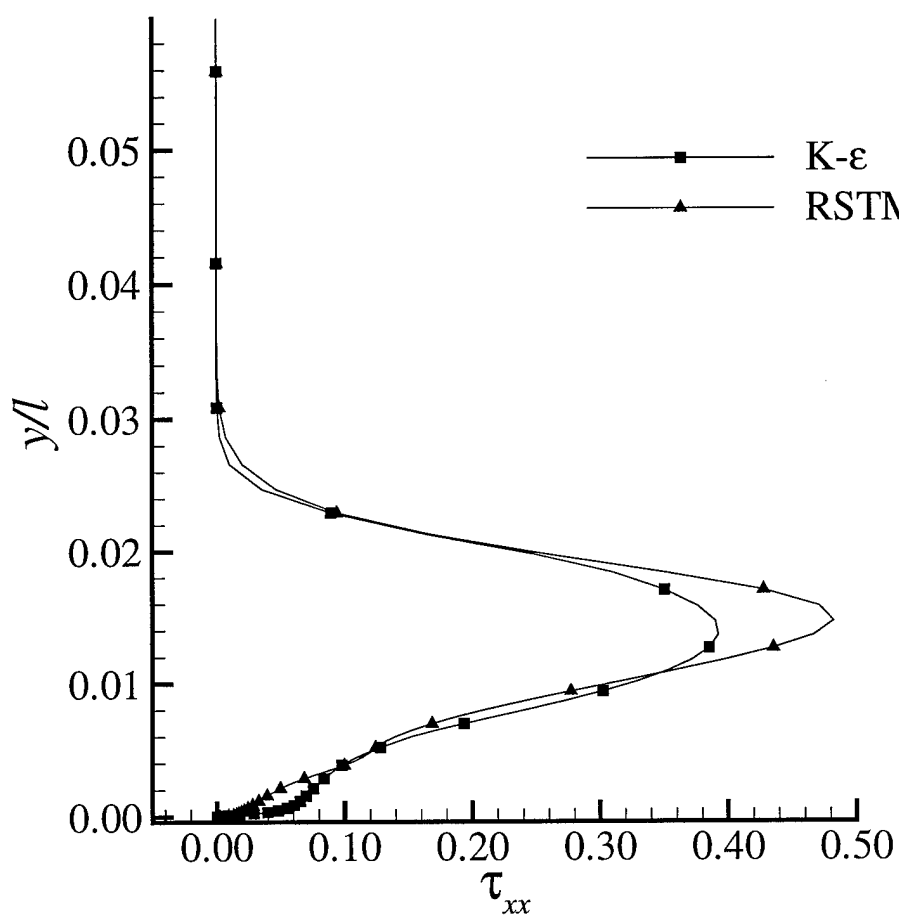


Figure 31. Comparison of  $\tau_{xx}$  profiles at  $x/l = 0.9950$  for Spaid and Zukoski configuration

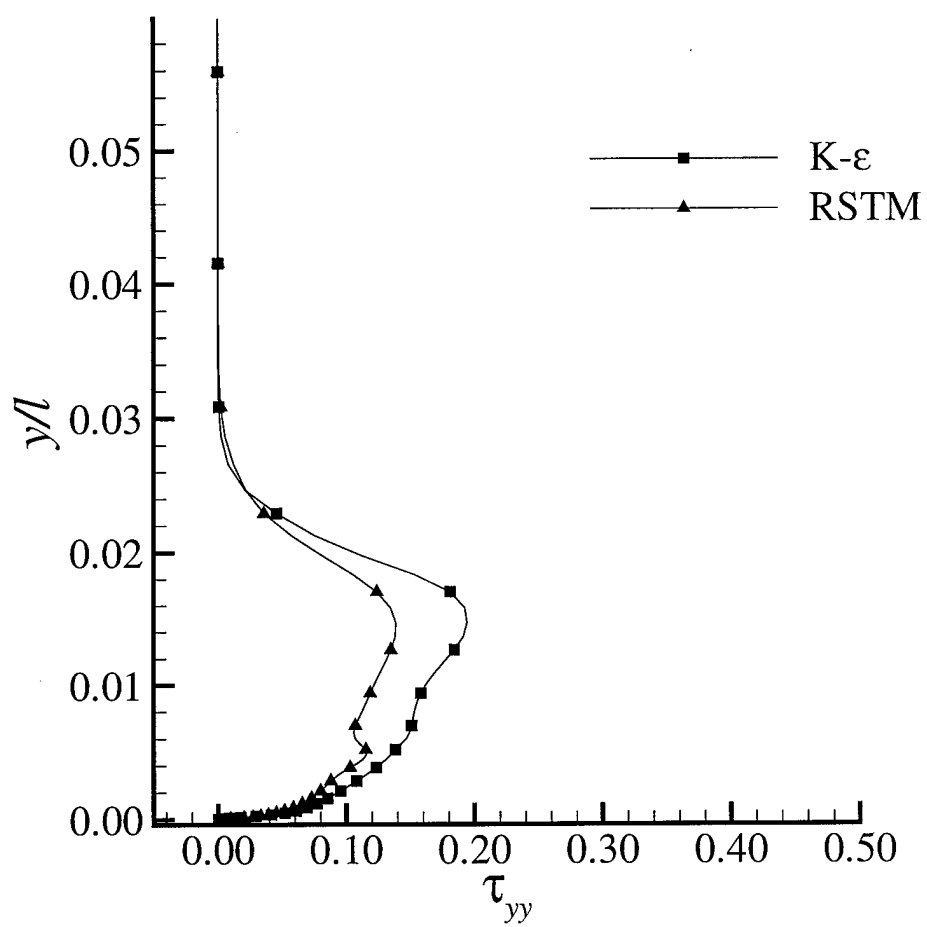


Figure 32. Comparison of  $\tau_{yy}$  profiles at  $x/l = 0.9950$  for Spaid and Zukoski configuration

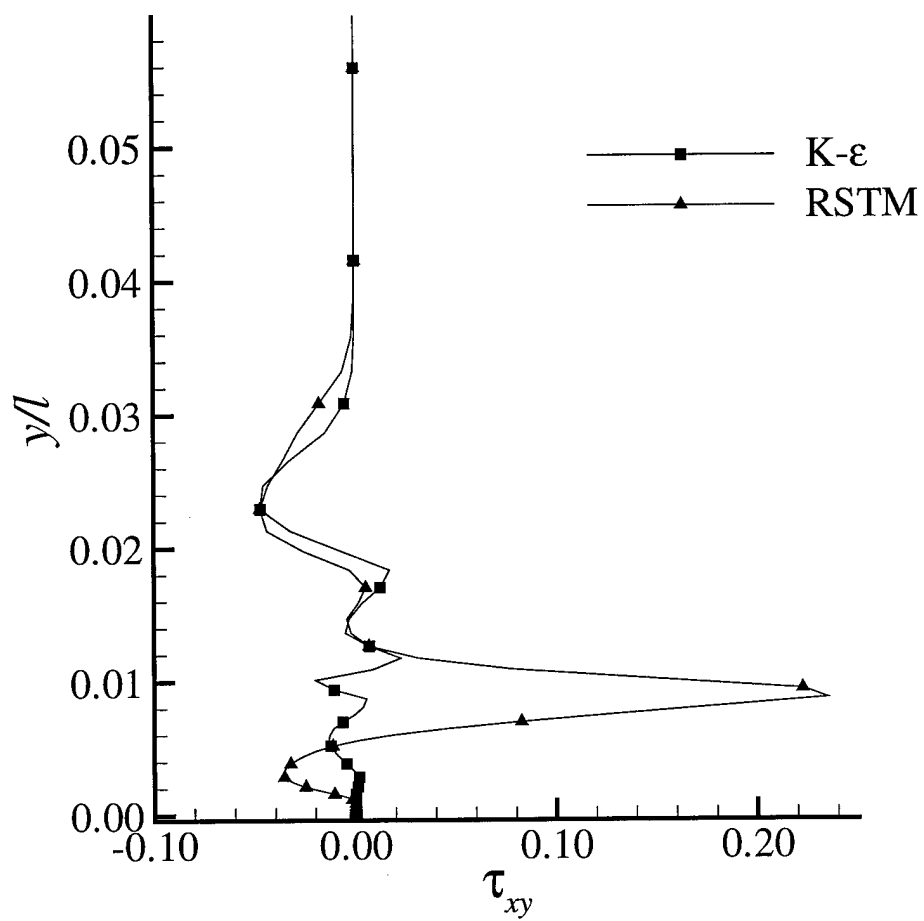


Figure 33. Comparison of  $\tau_{xy}$  profiles at  $x/l = 1.0125$  for Spaid and Zukoski configuration

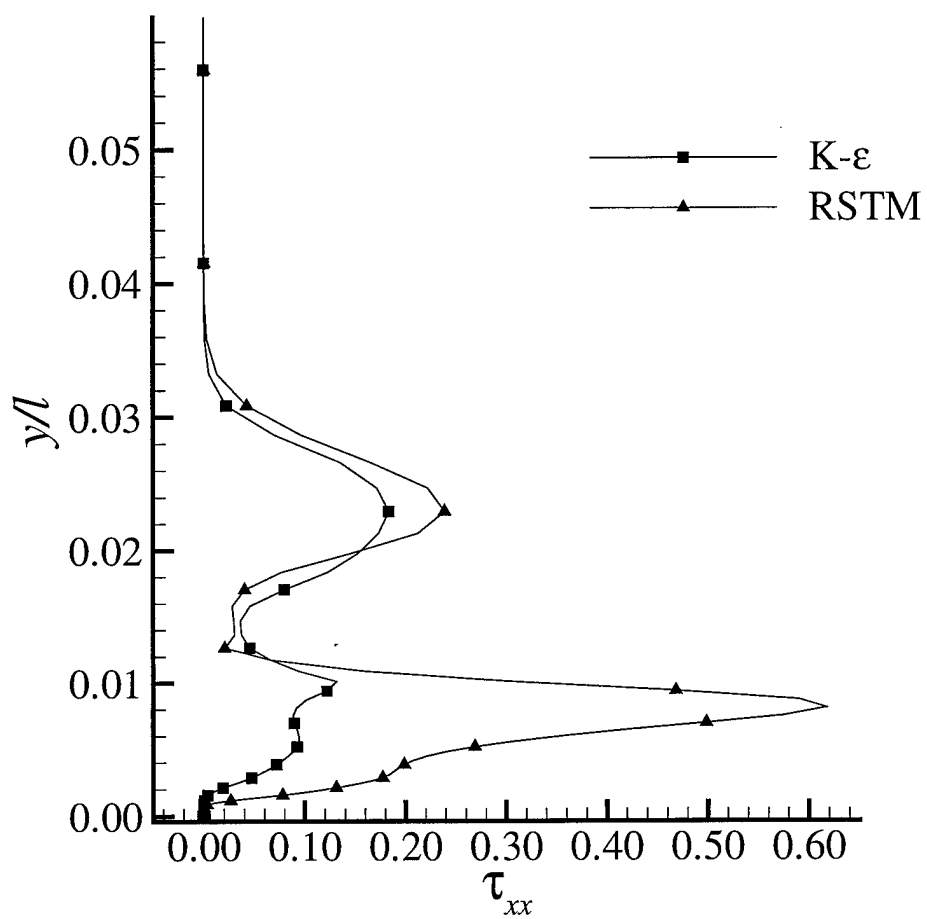


Figure 34. Comparison of  $\tau_{xx}$  profiles at  $x/l = 1.0125$  for Spaid and Zukoski configuration

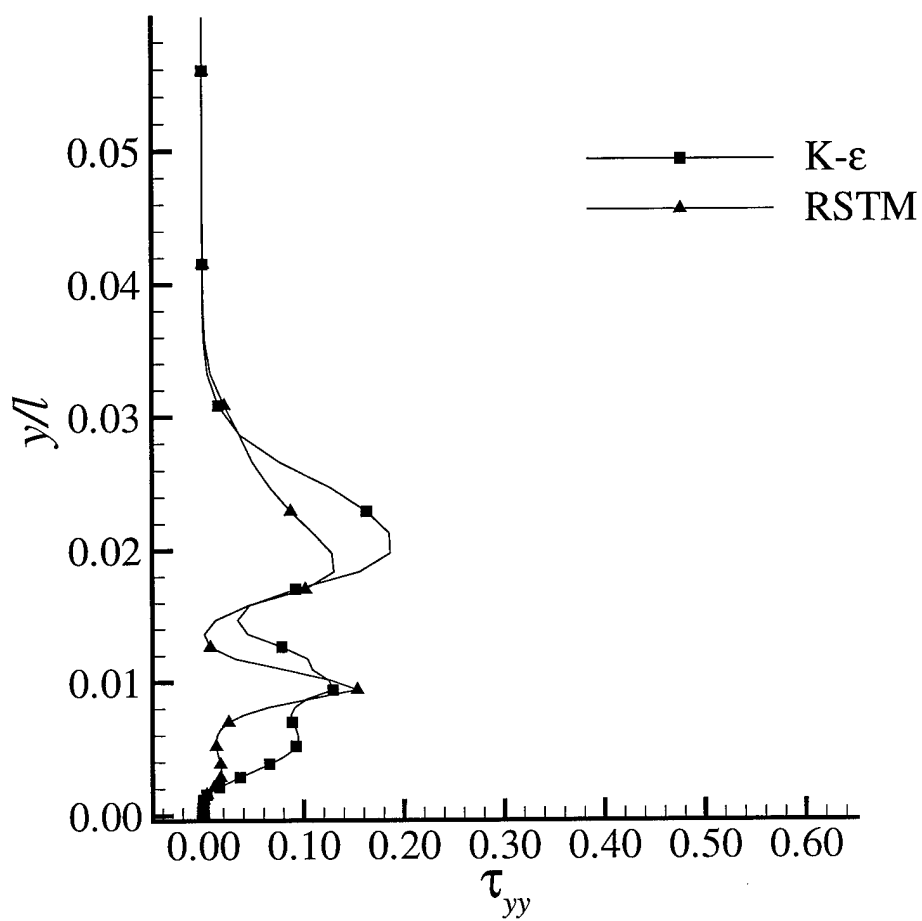


Figure 35. Comparison of  $\tau_{yy}$  profiles at  $x/l = 1.0125$  for Spaid and Zukoski configuration



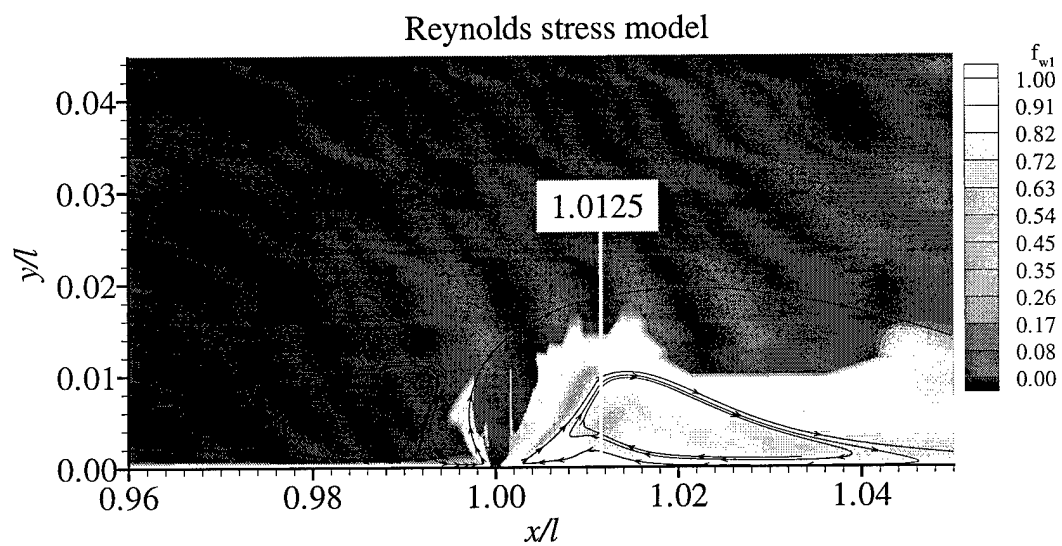


Figure 36. Contours for anisotropic wall function,  $f_{w1}$ , used in the RSTM

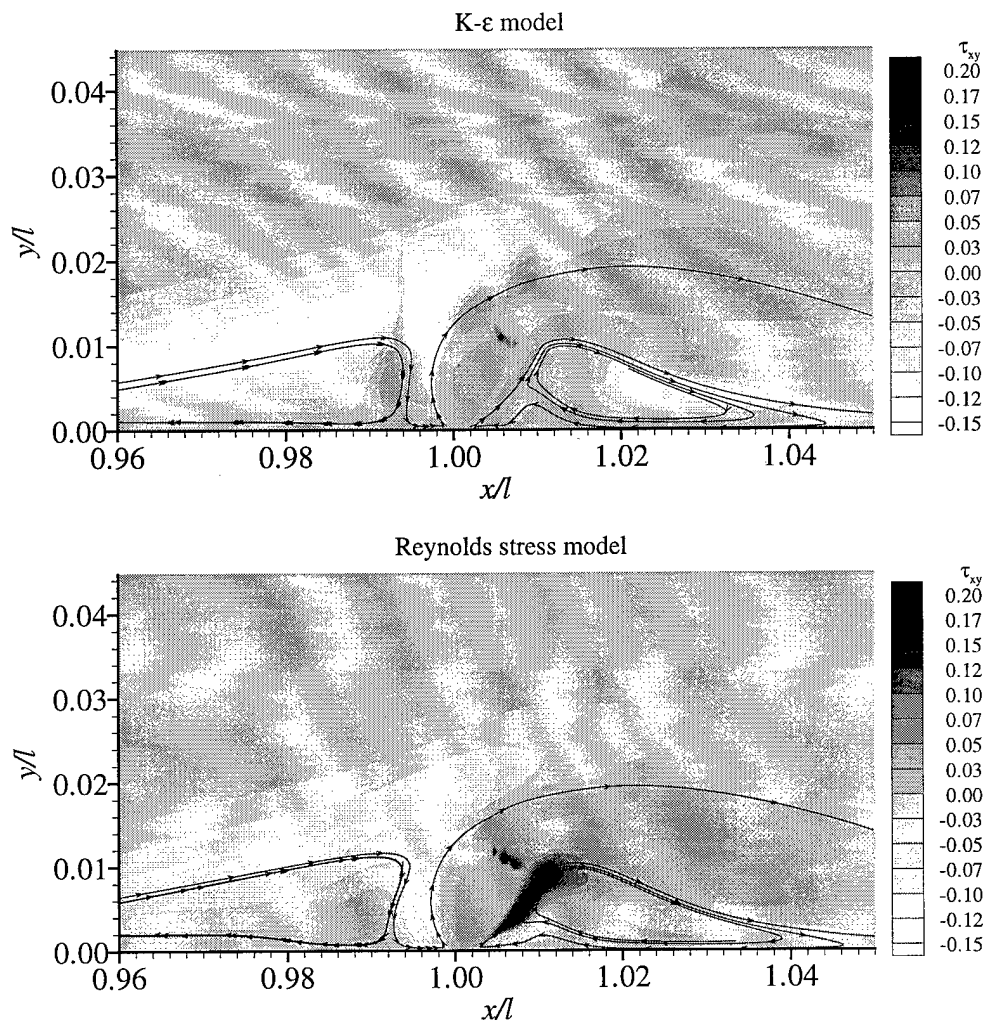


Figure 37. Comparison of  $\tau_{xy}$  contours for Spaid and Zukoski configuration

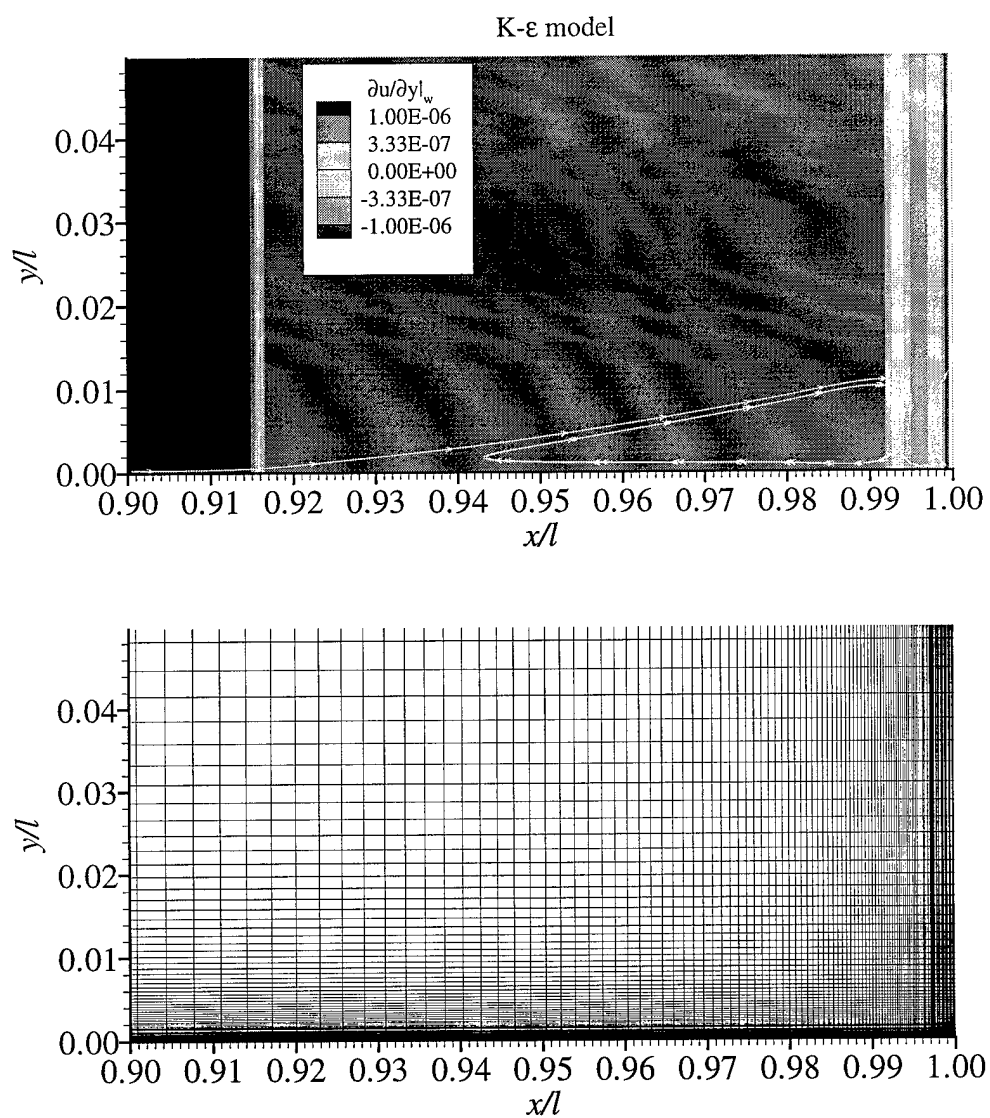


Figure 38. Range of near zero  $\partial \tilde{u} / \partial y$  at the wall and grids spacing around the jet

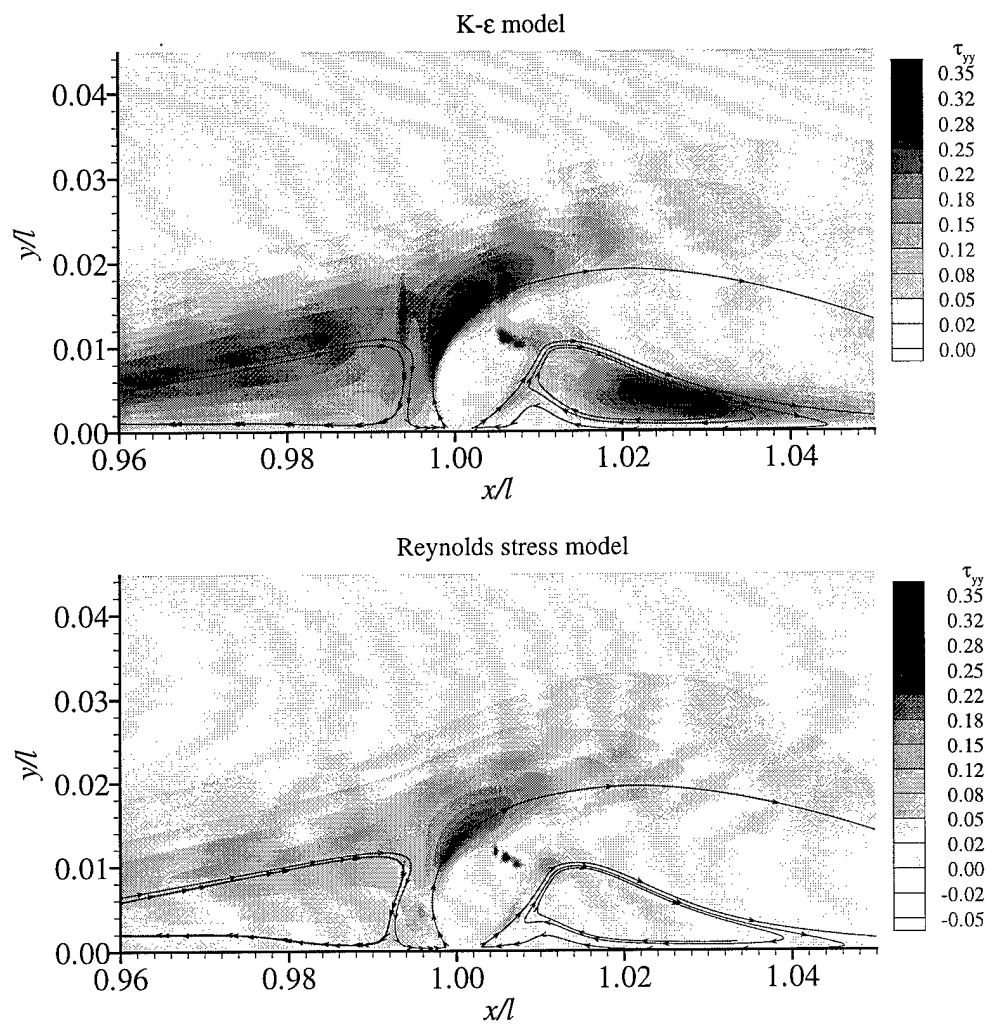


Figure 39. Comparison of  $\tau_{yy}$  contours for Spaid and Zukoski configuration

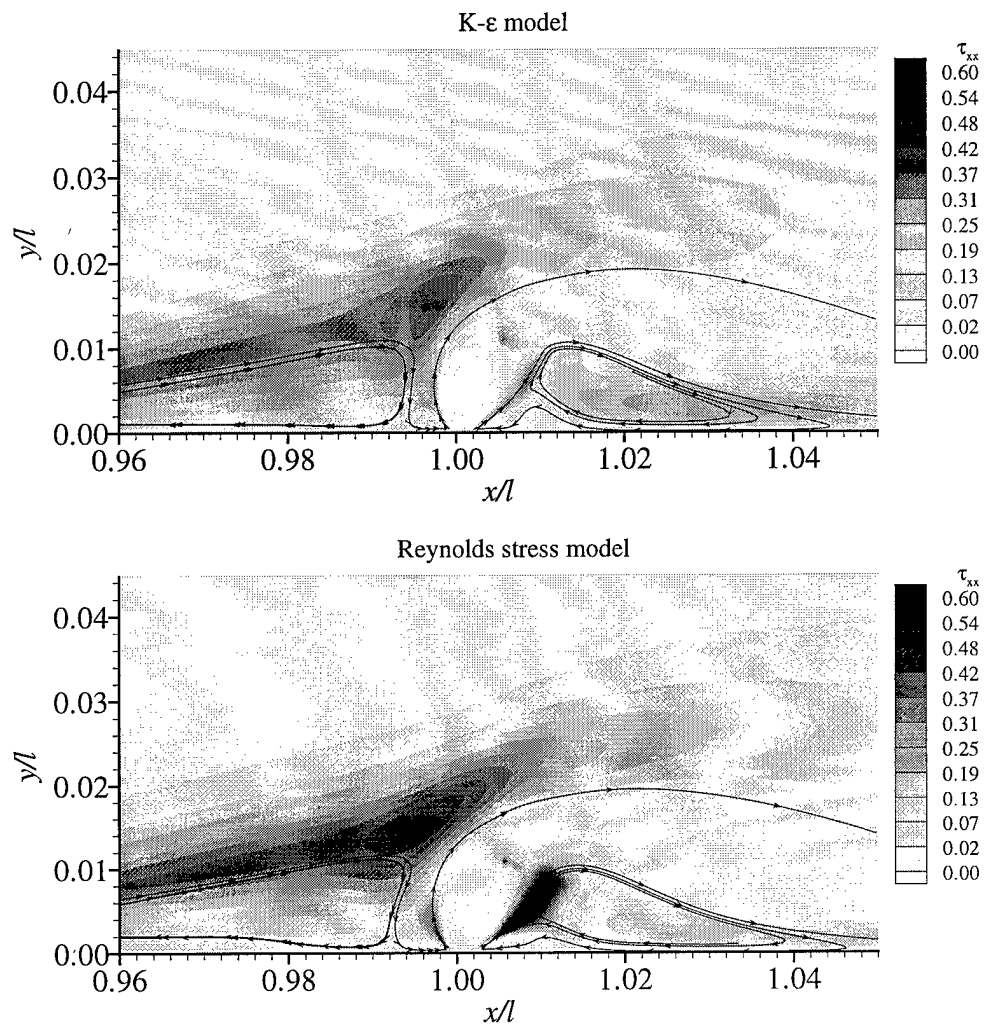


Figure 40. Comparison of  $\tau_{xx}$  contour for Spaid and Zukoski configuration

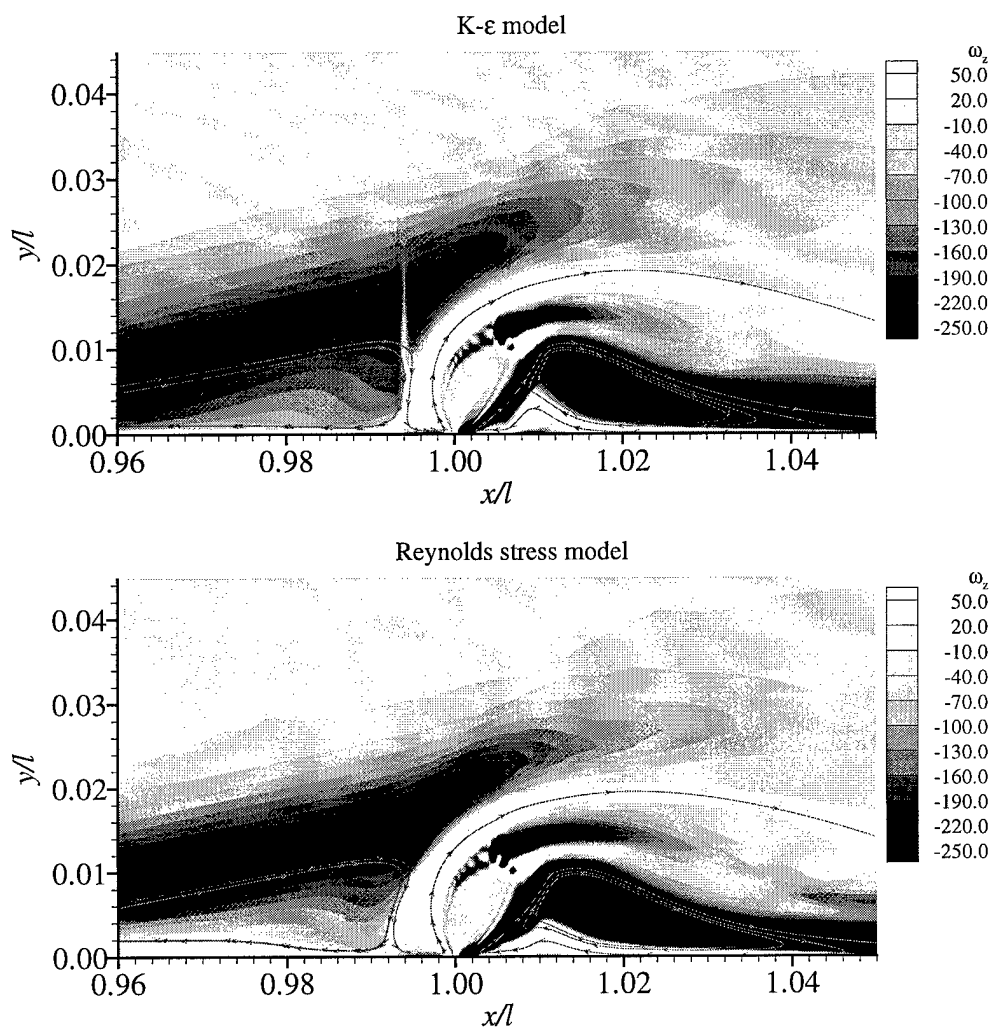


Figure 41. Comparison of  $\omega_z$  contours for Spaid and Zukoski configuration

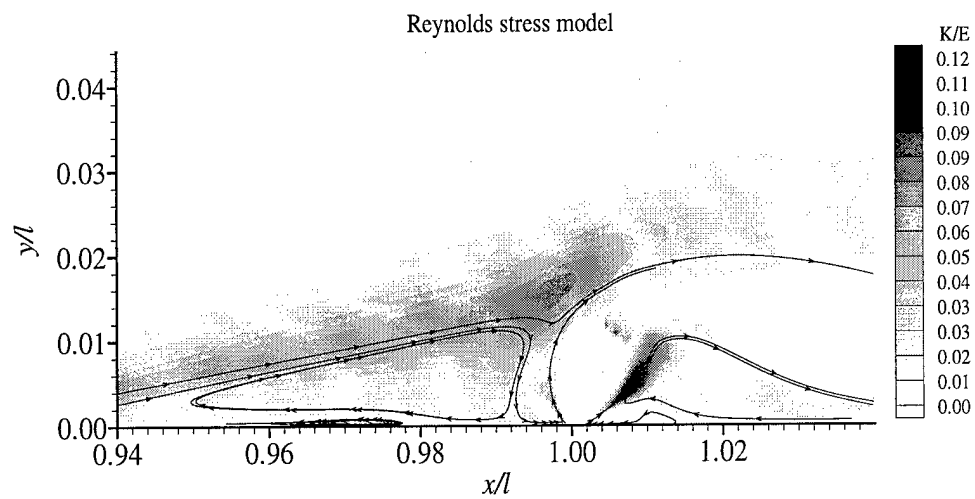


Figure 42. Fraction of  $E$  comprised by  $K$  for Spaid and Zukoski configuration

# 2D INJECTION MODEL SCHEMATIC

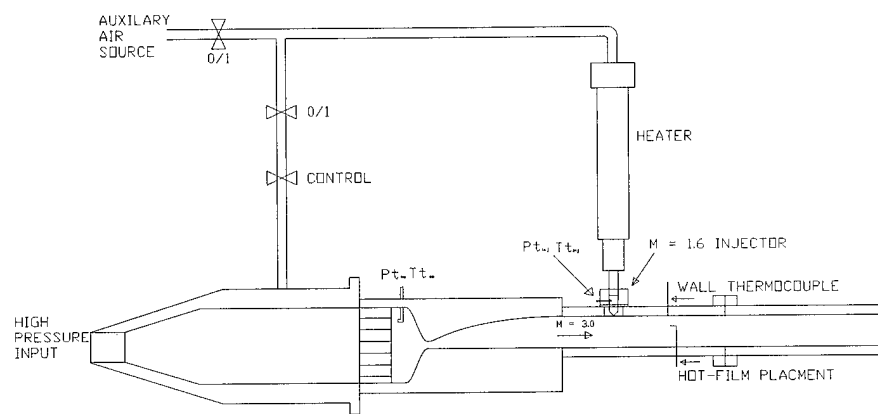


Figure 43. Tucker's injection model schematic [100]



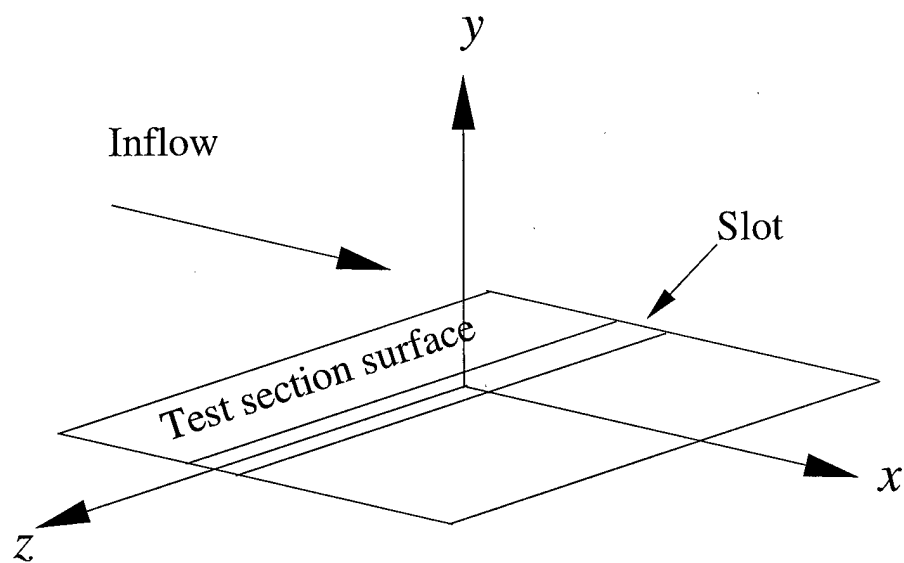


Figure 44. Schematic of slot coordinates used in numerical simulations

$$M=1.6 \quad AE/A^*=1.25$$

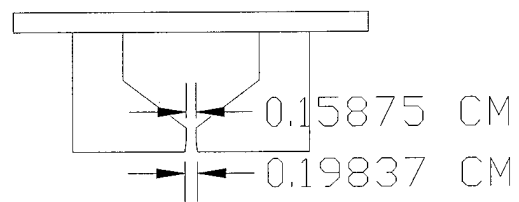


Figure 45. Tucker's two-dimensional injector nozzle [100]

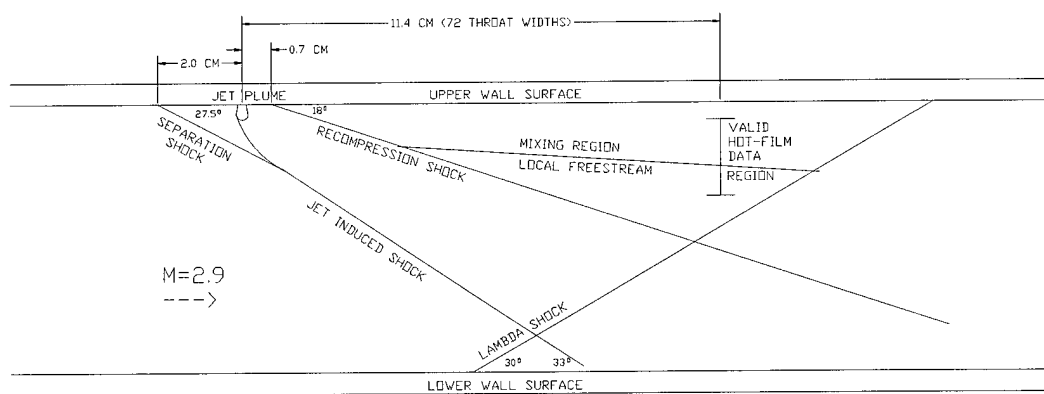


Figure 46. Experimental flowfield sketch for supersonic injection [100]

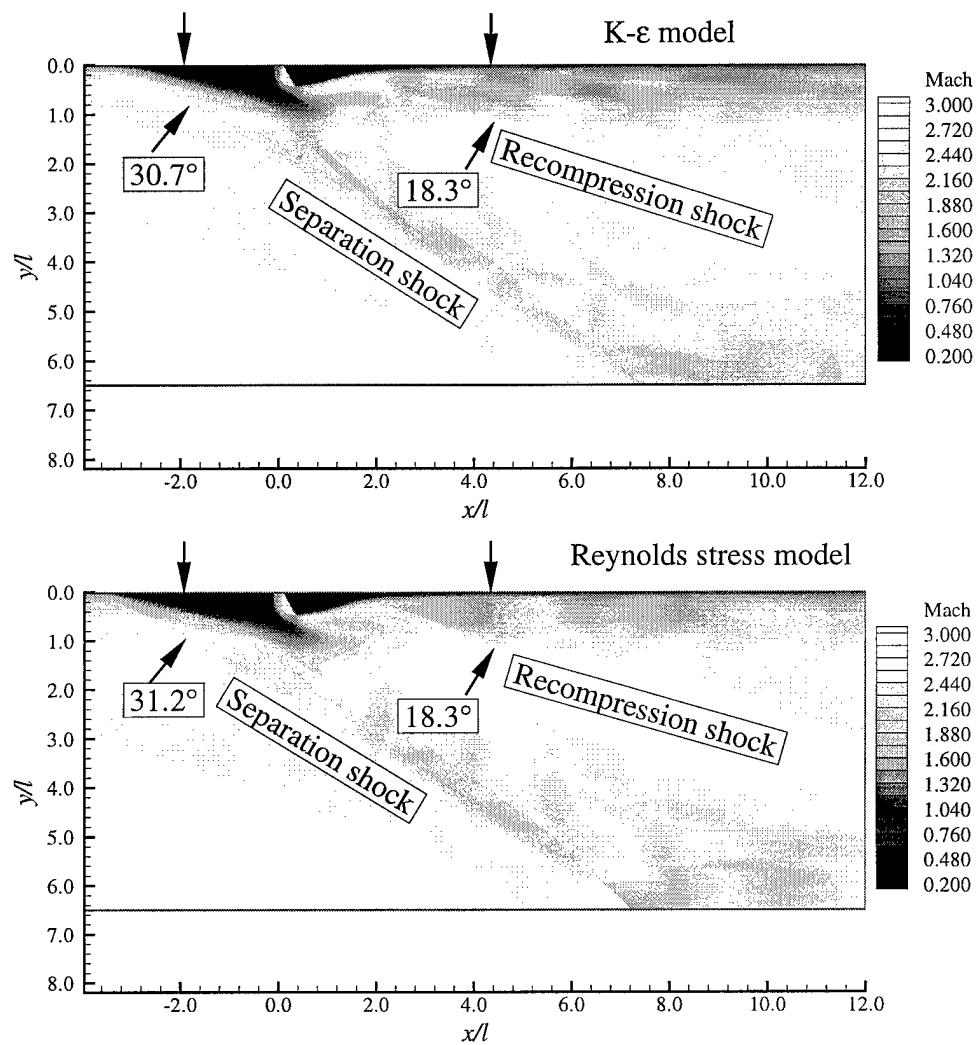


Figure 47. Computational flowfield predictions for supersonic injection

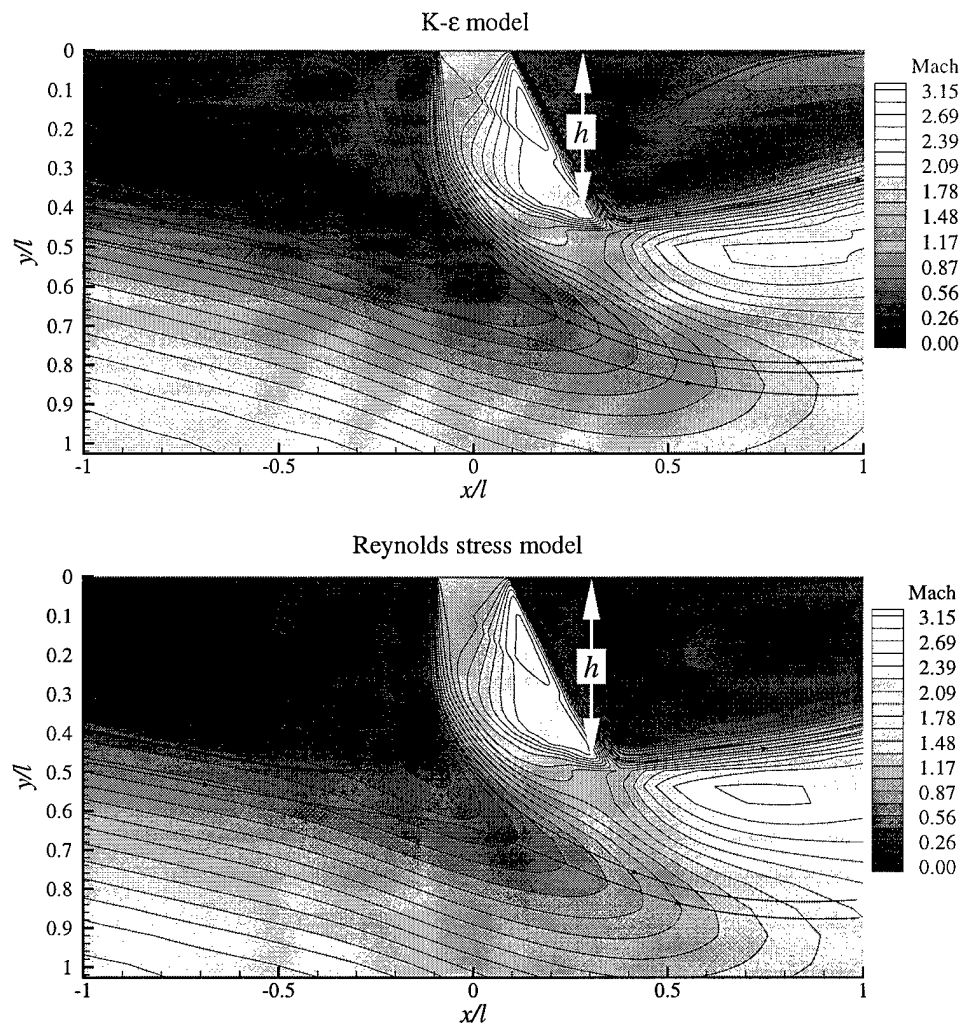


Figure 48. Comparison of Mach contours for Tucker's [100] heated injection configuration

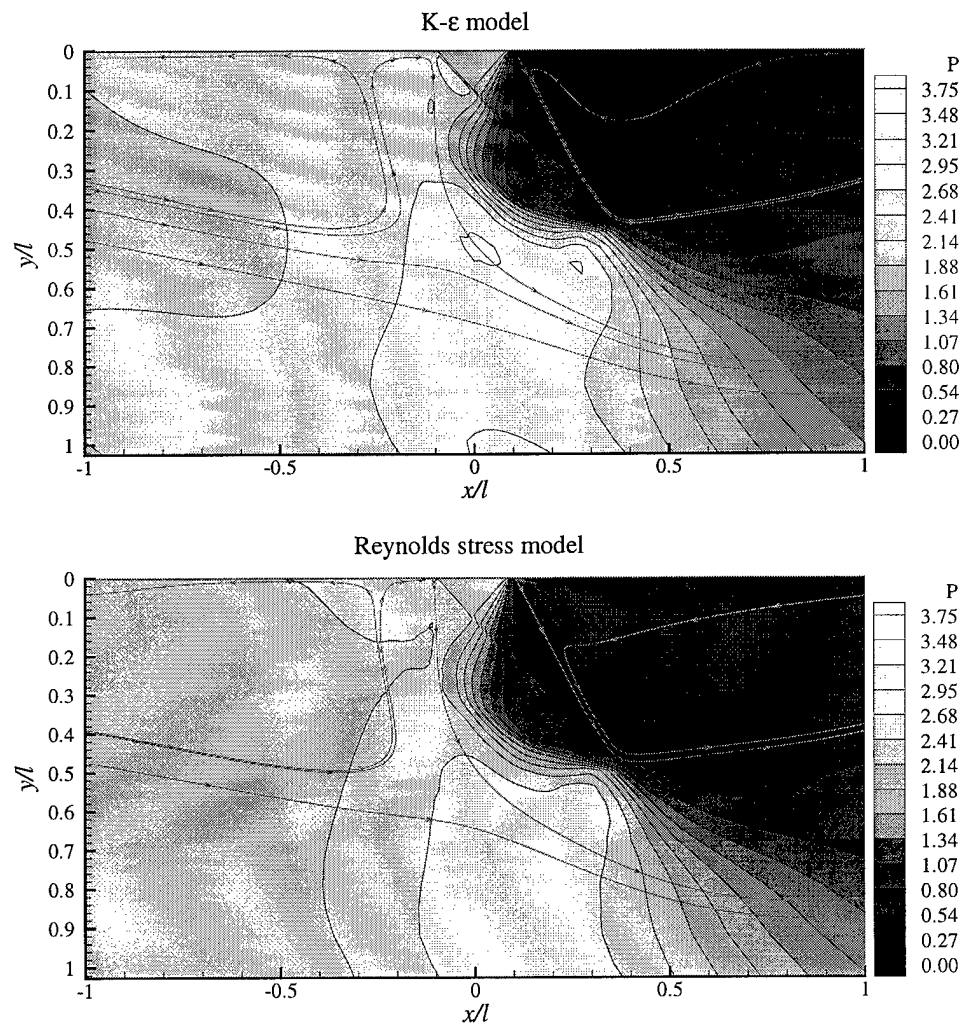


Figure 49. Comparison of pressure contours for Tucker's [100] heated injection configuration

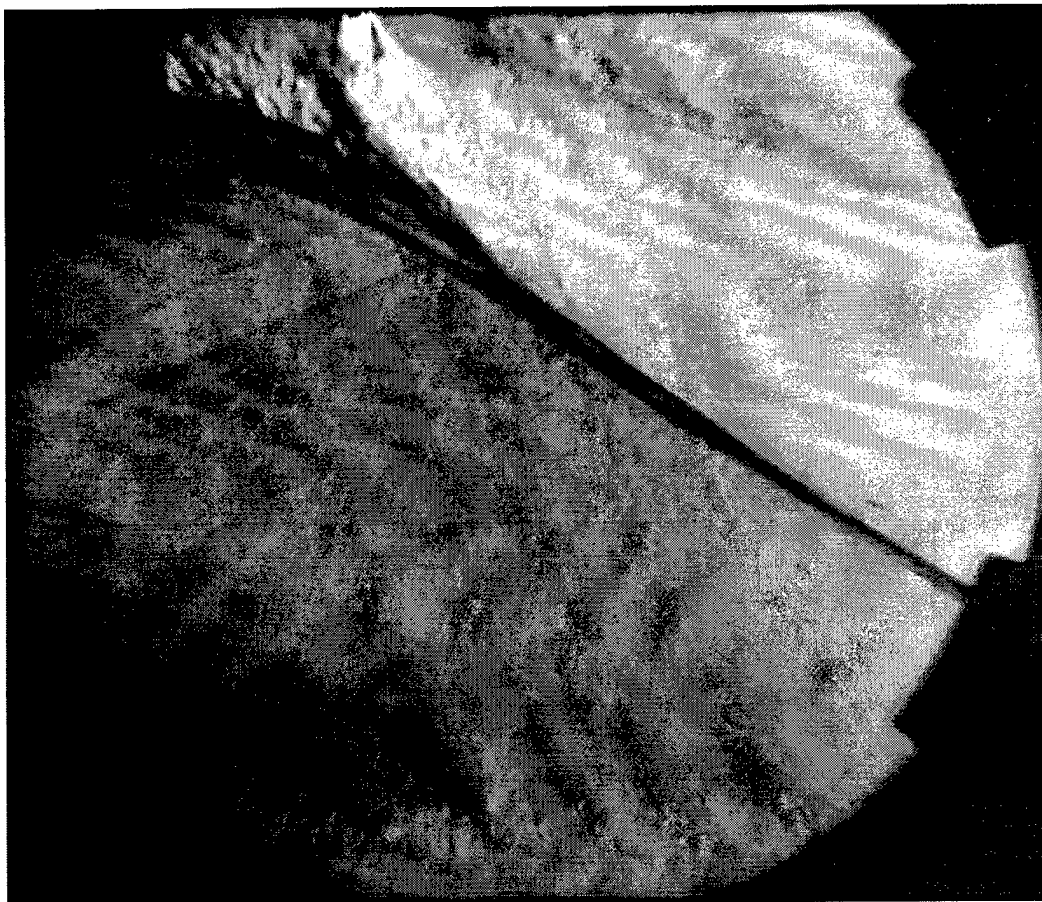


Figure 50. Schlieren of injection flowfield for heated injection [100]

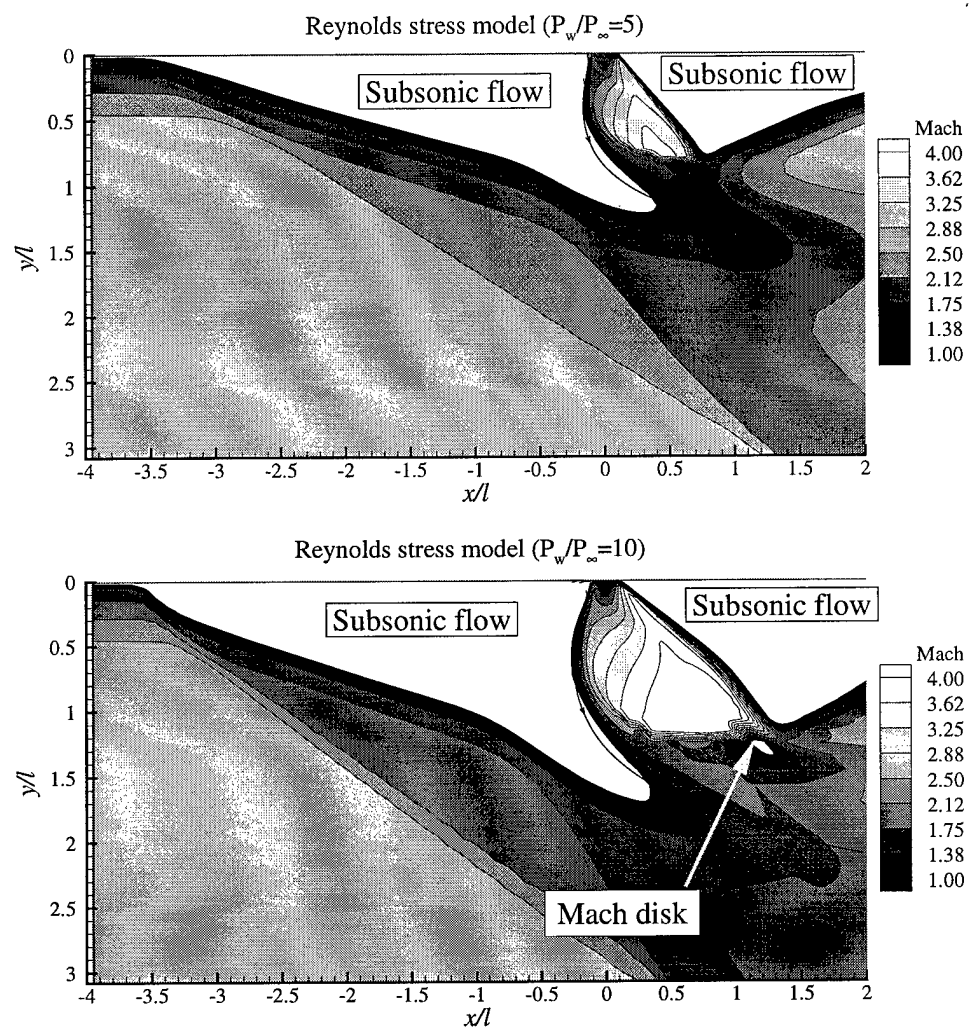


Figure 51. Comparison of Mach contours for pressure ratios ( $p_{inj}/p_\infty$ ) of 5 and 10



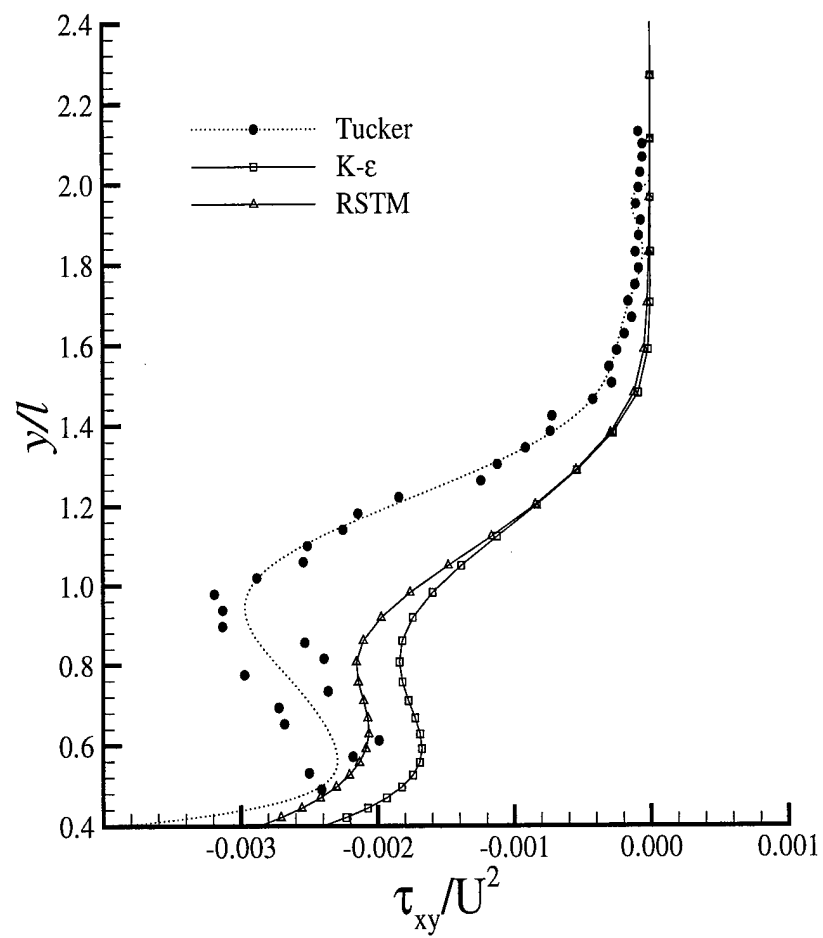


Figure 52. Comparison of  $\tau_{xy}$  profiles for cooled injection at  $x/l = 11.4$

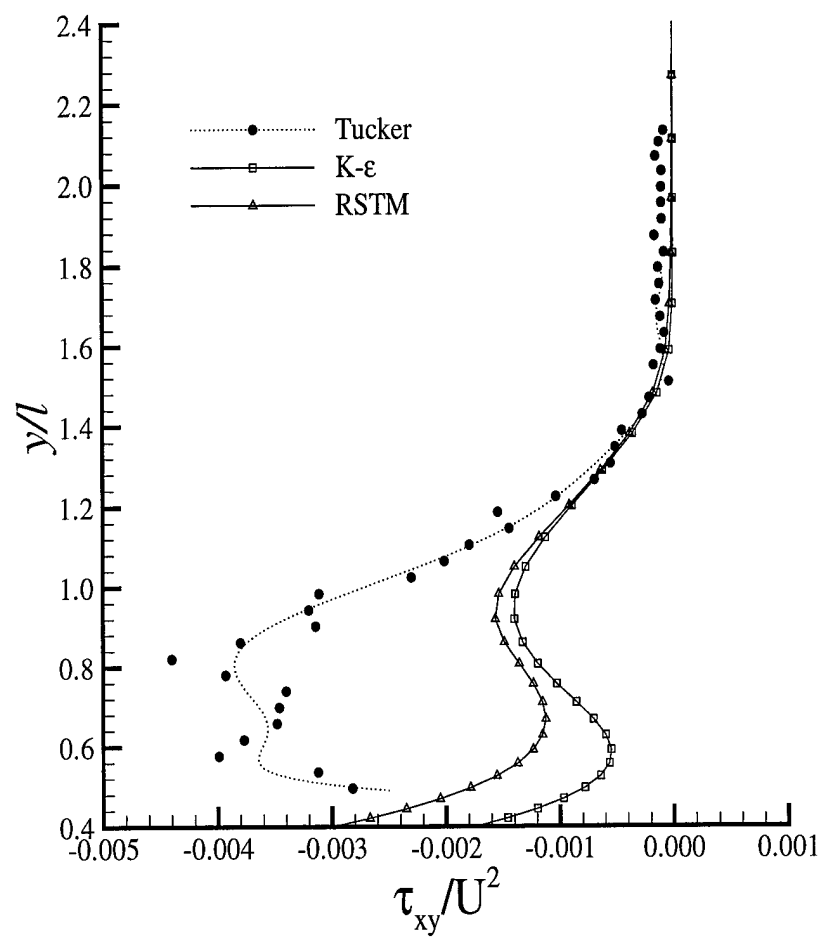


Figure 53. Comparison of  $\tau_{xy}$  profiles for heated injection at  $x/l = 11.4$

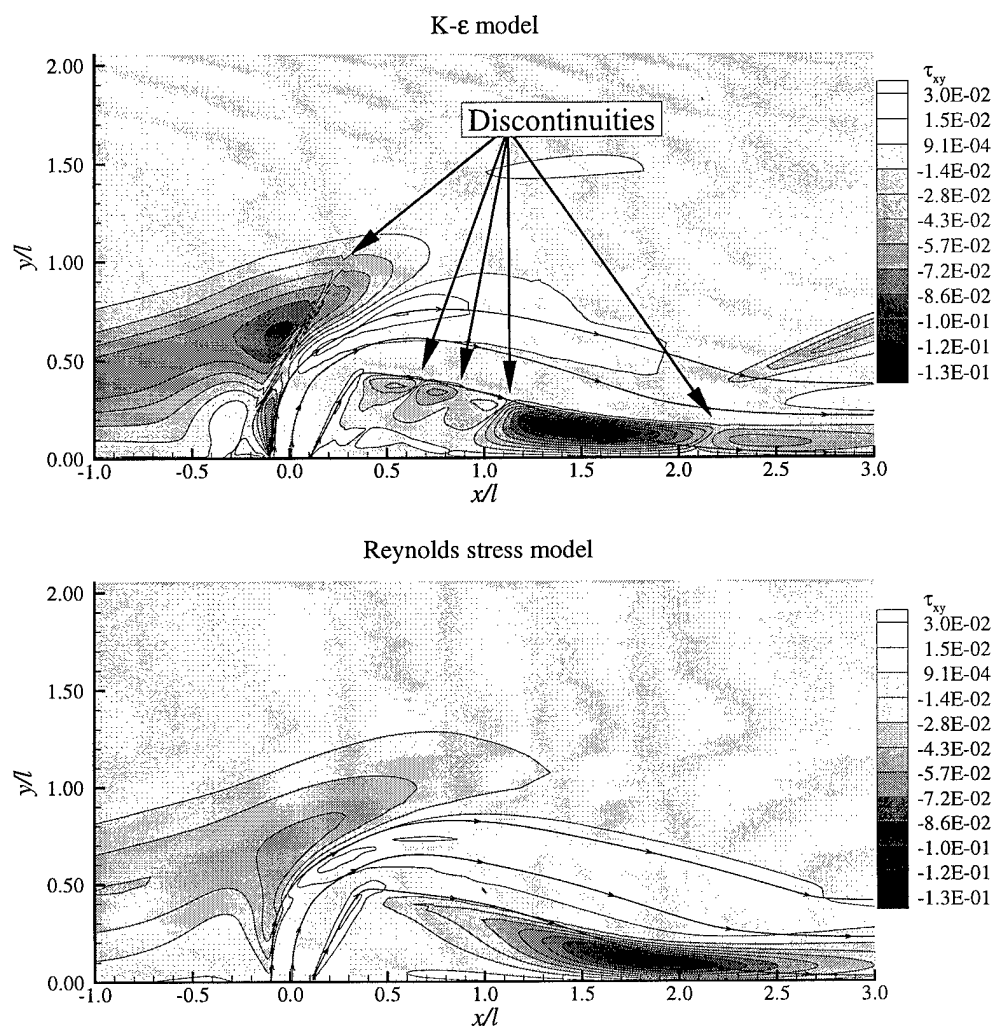


Figure 54. Comparison of  $\tau_{xy}$  contours for supersonic cooled injection

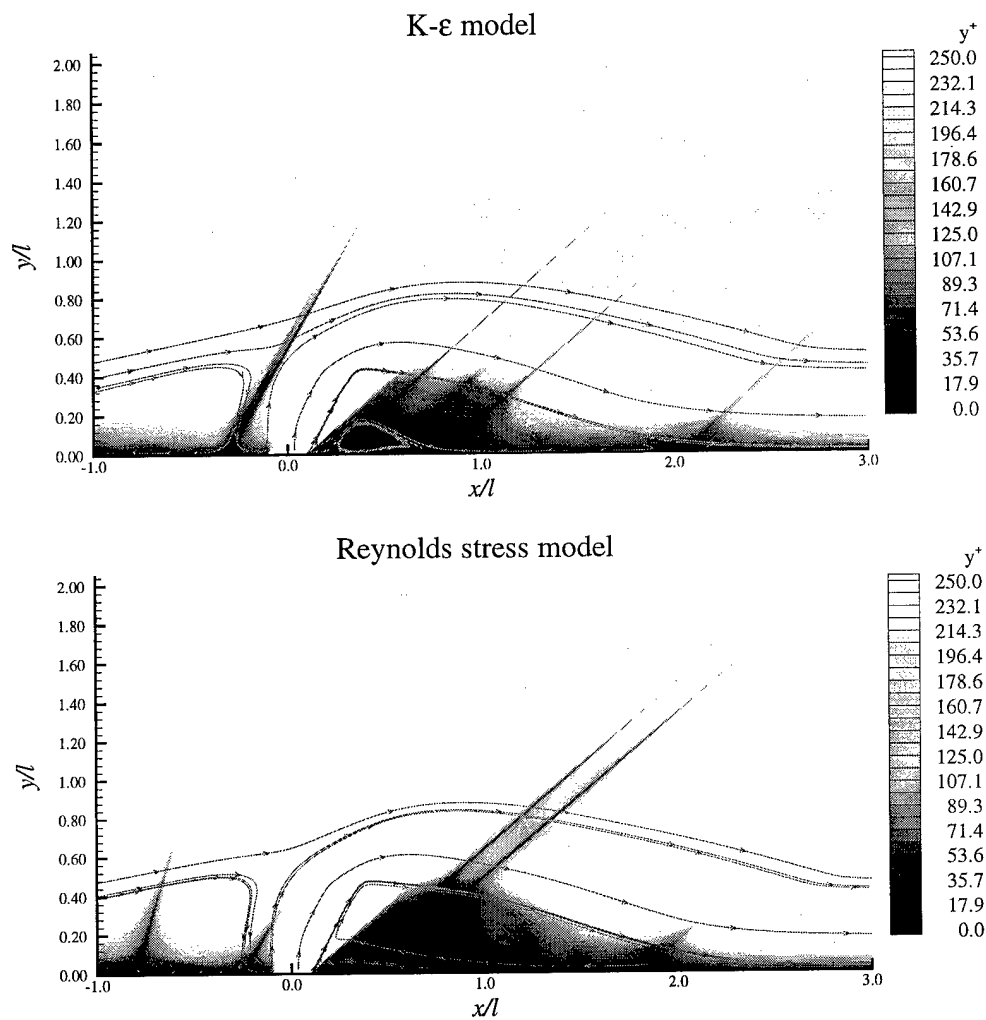


Figure 55. Visualization of boundary layer separation and reattachment locations by comparison of  $y^+$  contours for supersonic cooled injection

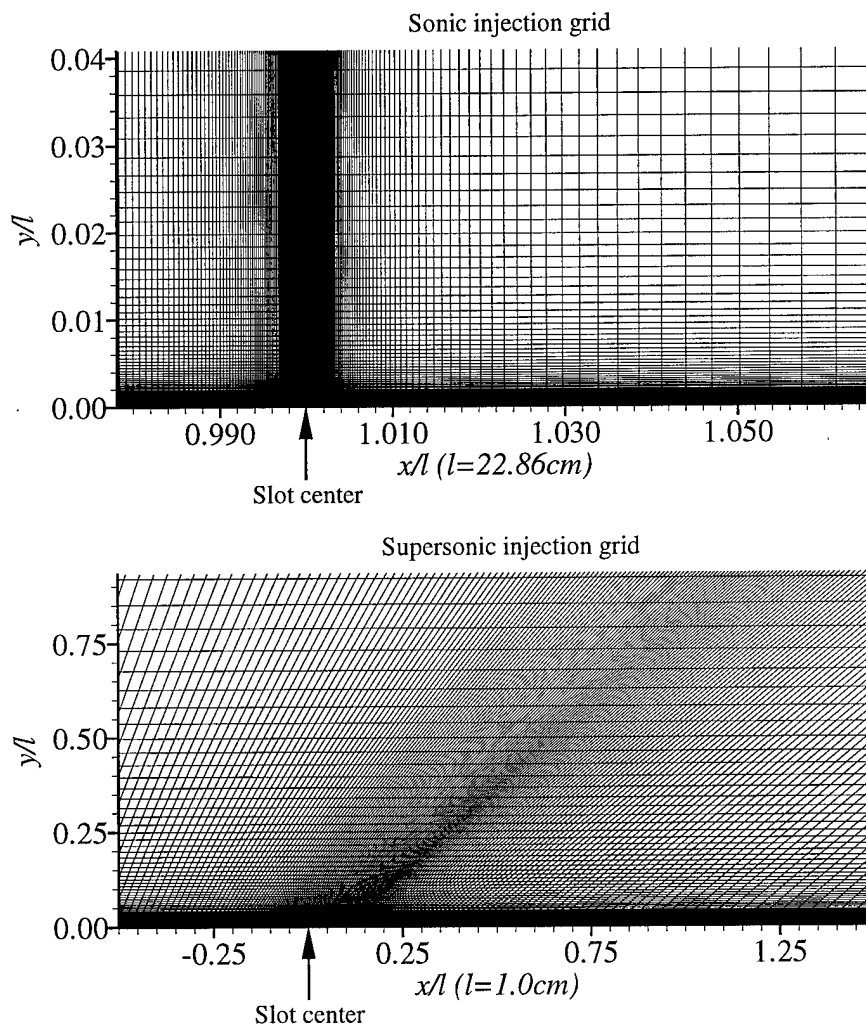


Figure 56. Comparison of computational grids used for sonic and supersonic injection simulations

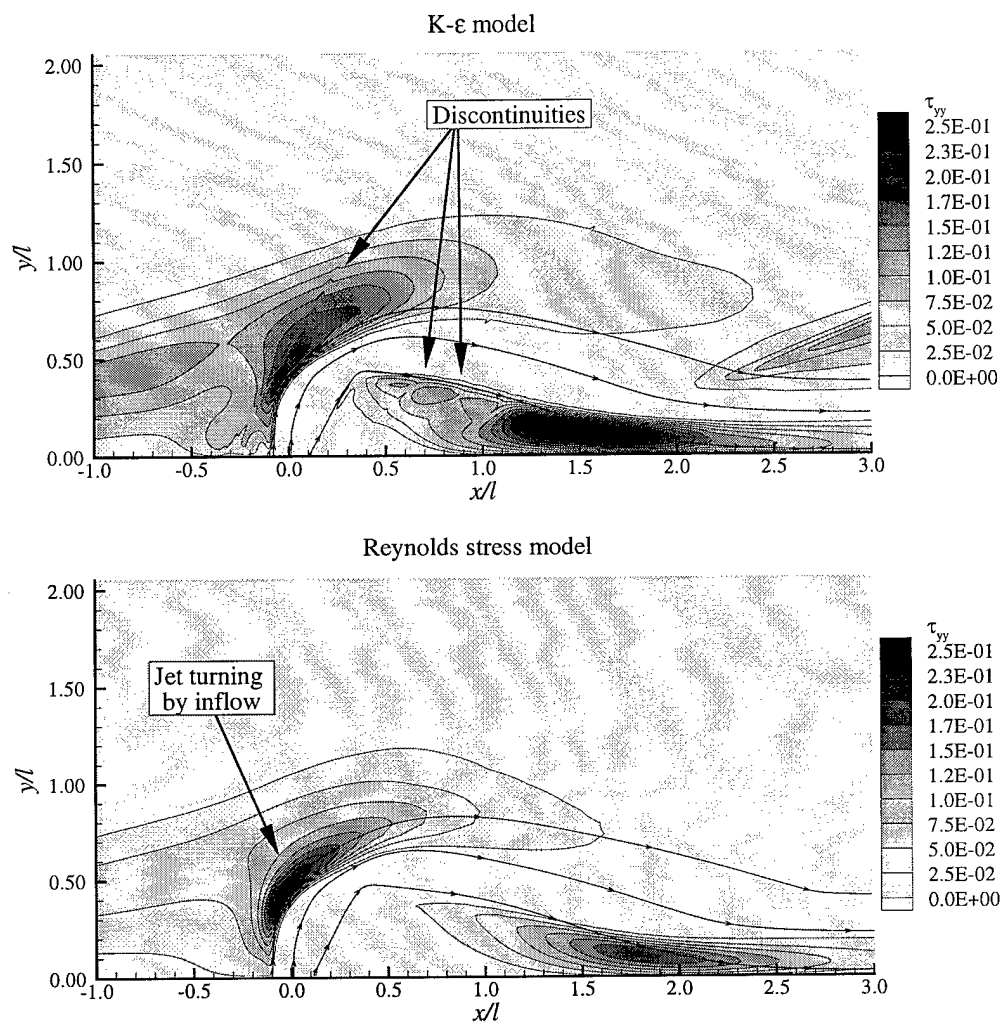


Figure 57. Comparison of  $\tau_{yy}$  contours for supersonic cooled injection

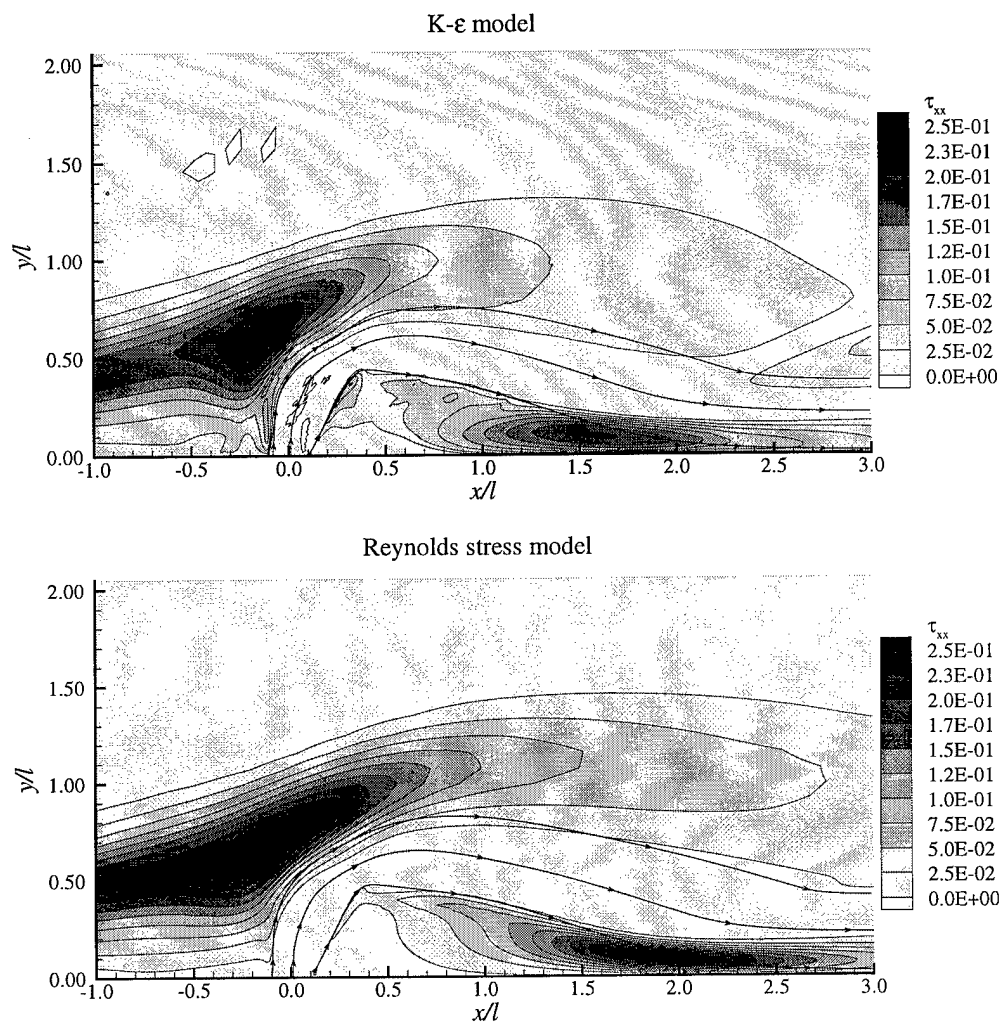


Figure 58. Comparison of  $\tau_{xx}$  contours for supersonic cooled injection

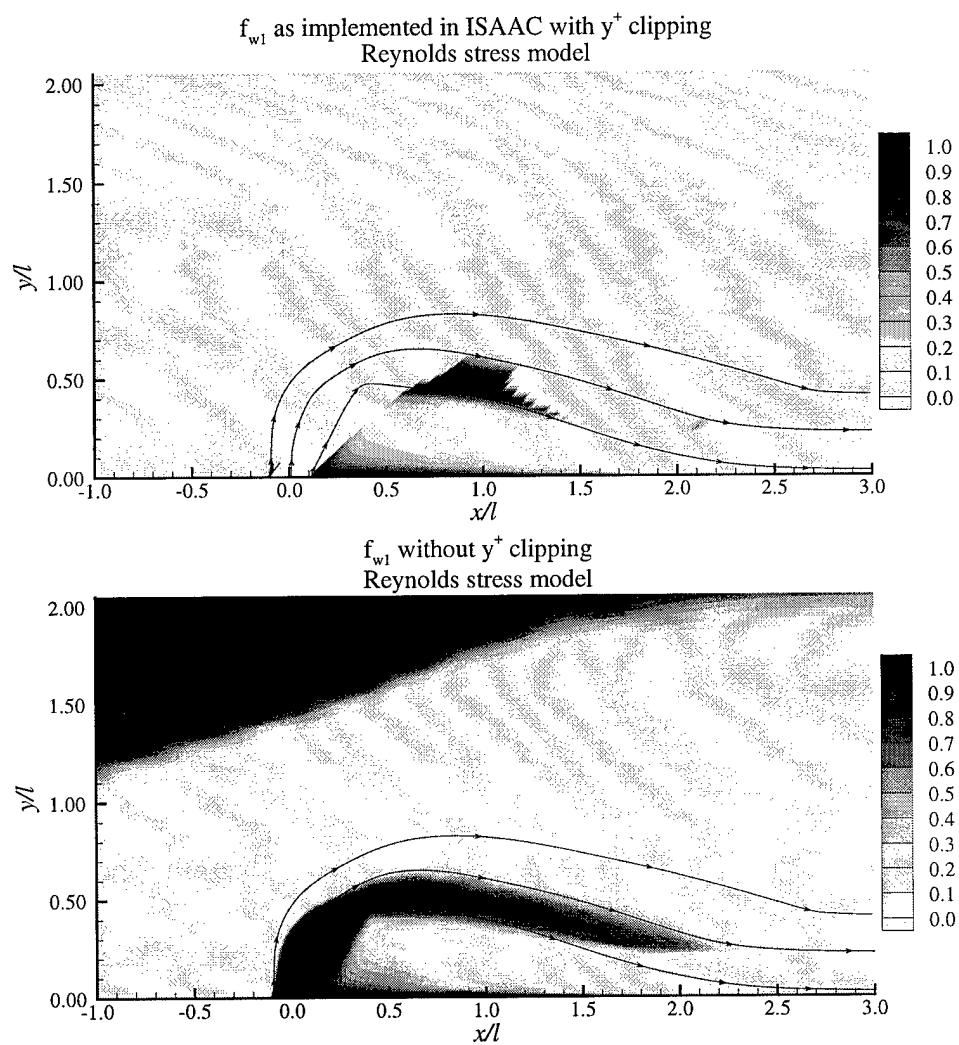


Figure 59. Comparison of anisotropic wall damping function,  $f_{w1}$ , with and without  $y^+$  clipping



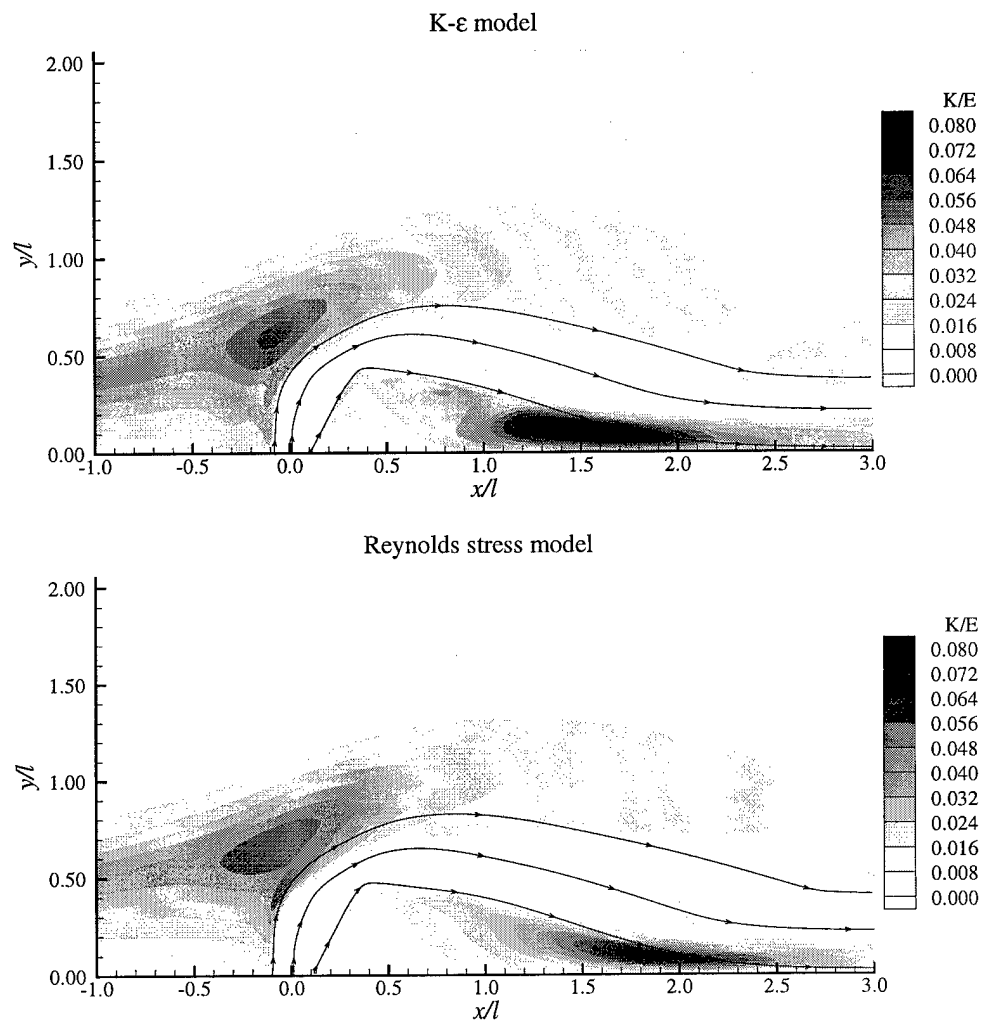


Figure 60. Comparison of fraction of  $E$  comprised by  $K$  for supersonic cooled injection

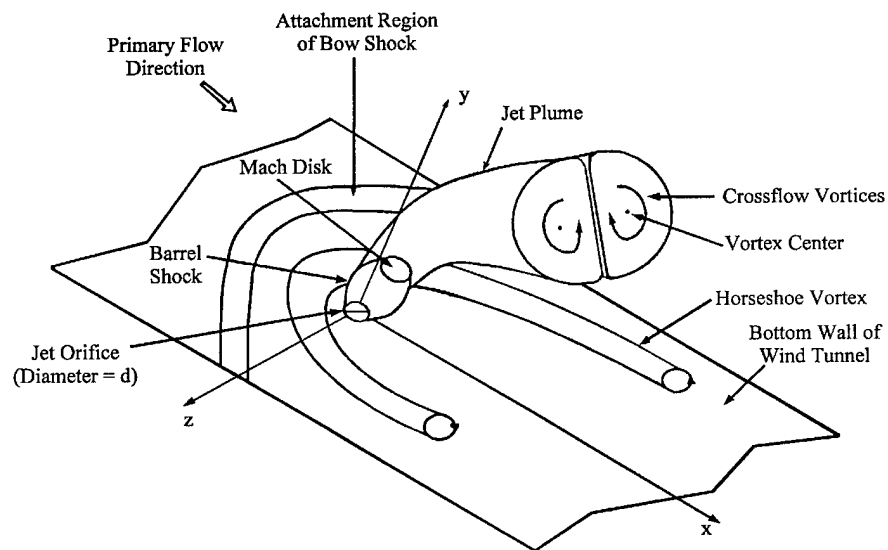


Figure 61. Schematic of a three-dimensional flowfield generated by normal injection of a sonic fluid through a circular nozzle into a supersonic flow [70]

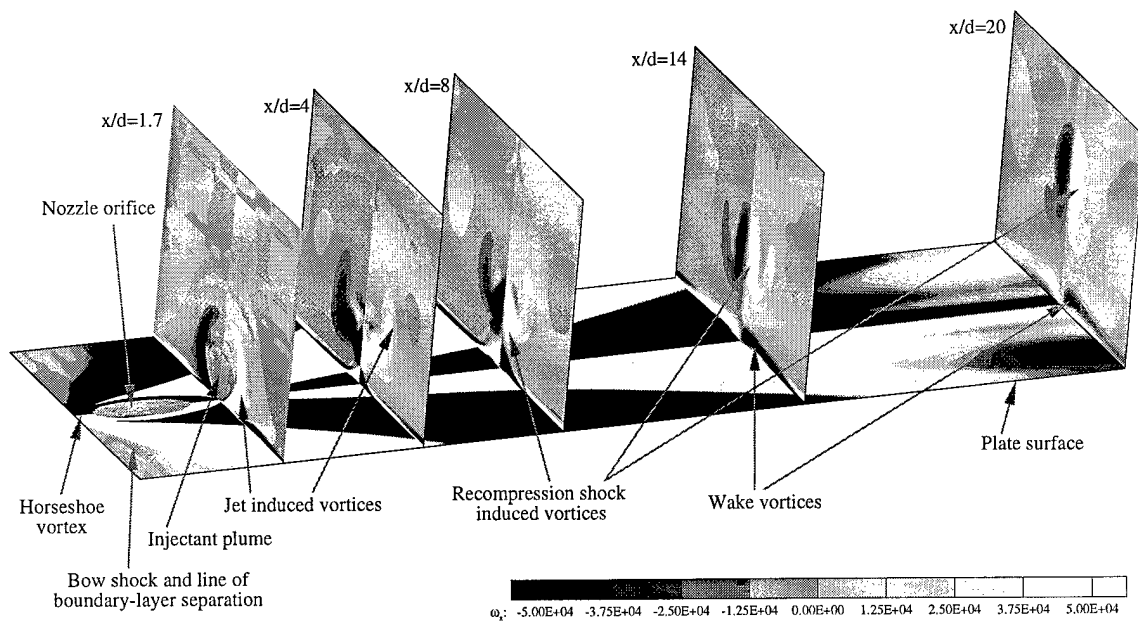


Figure 62. RSTM predictions of  $\omega_x$  for McCann and Bowersox configuration

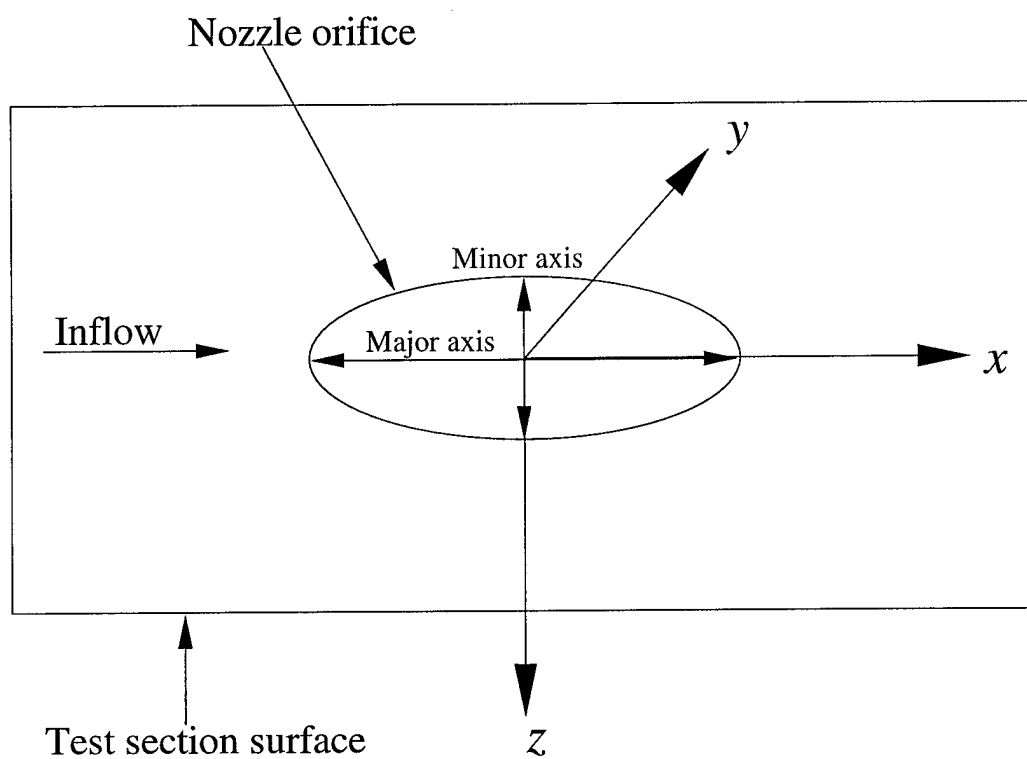


Figure 63. Tunnel coordinate system

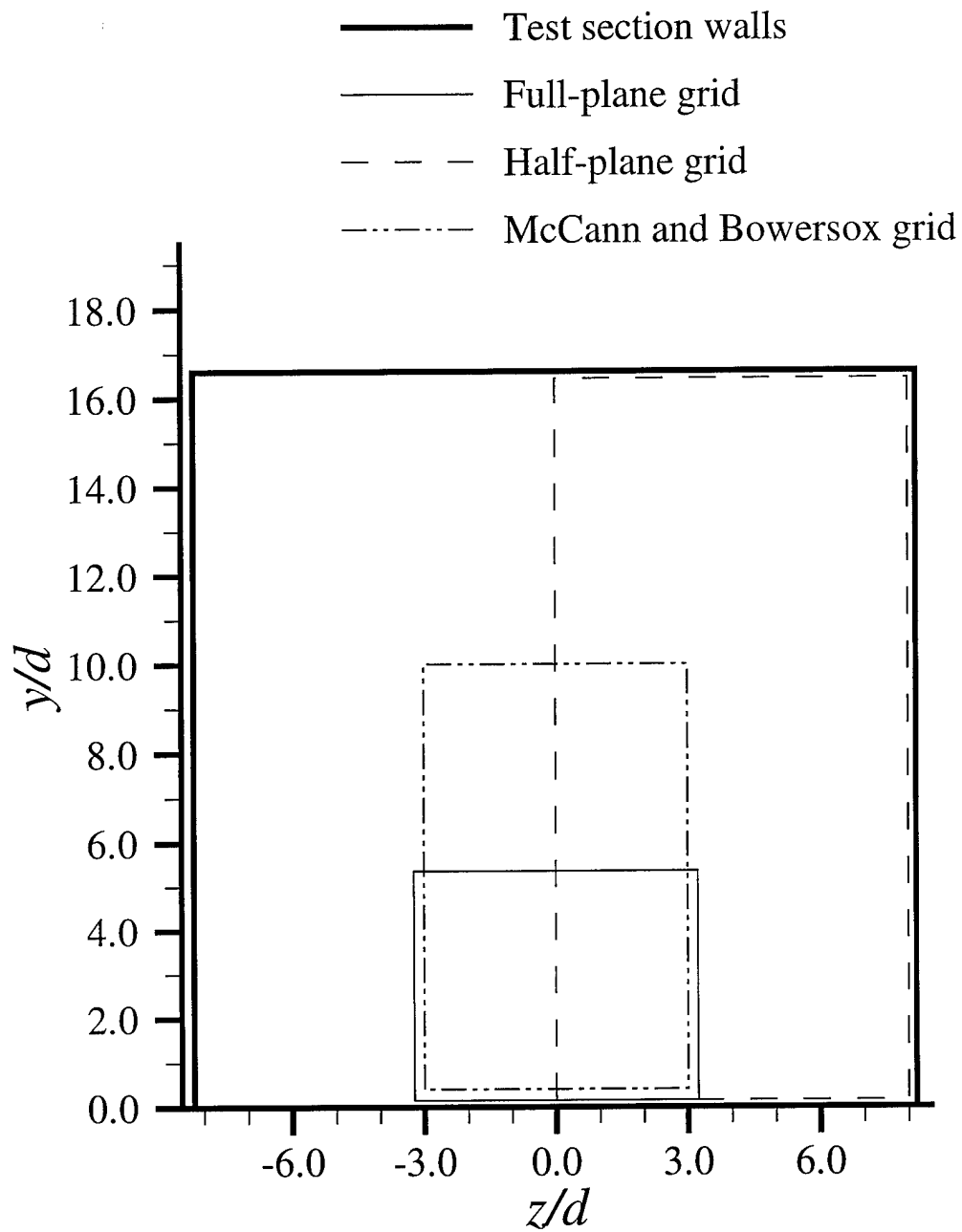


Figure 64. Comparison of  $y - z$  domains of the computational and experimental data grids

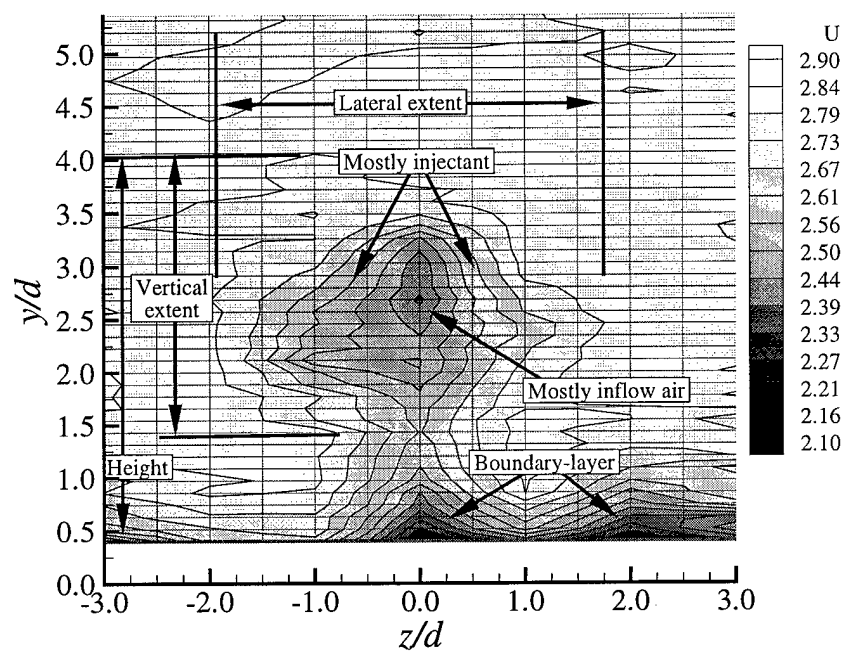


Figure 65. Experimental data for the  $U$  component of velocity at station 20 [52]

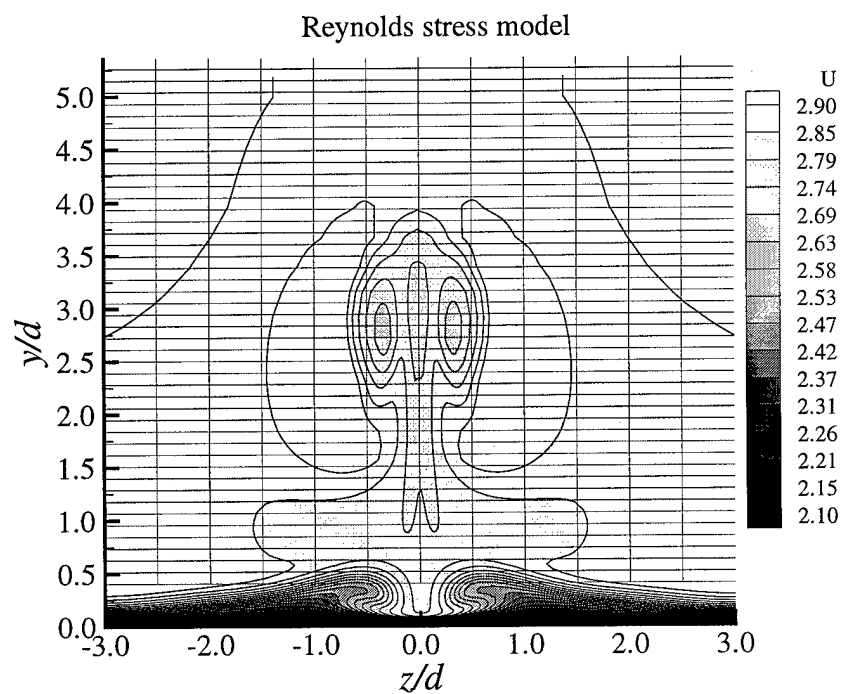
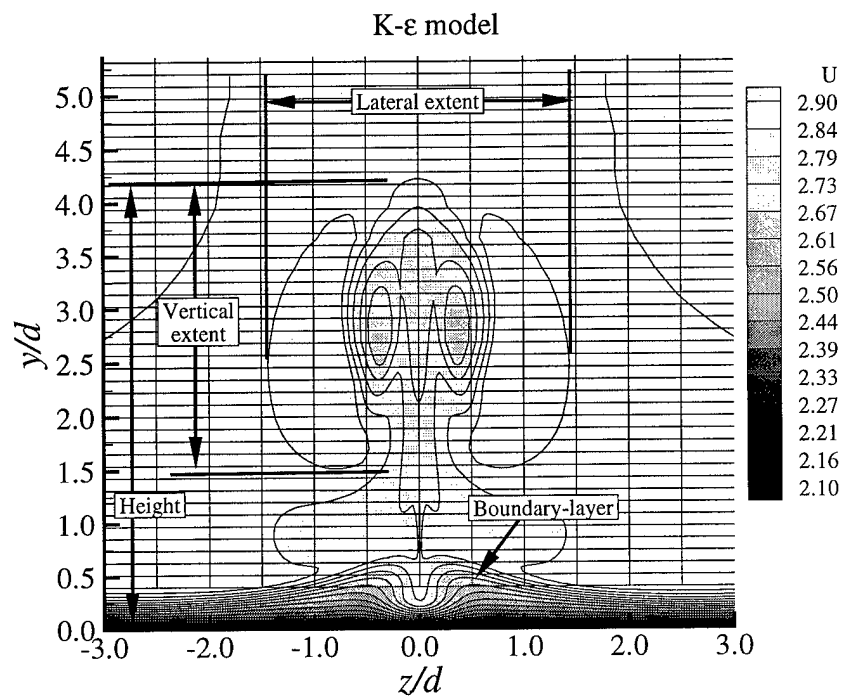


Figure 66. Comparison of turbulence model predictions of the  $U$  component of velocity at station 20

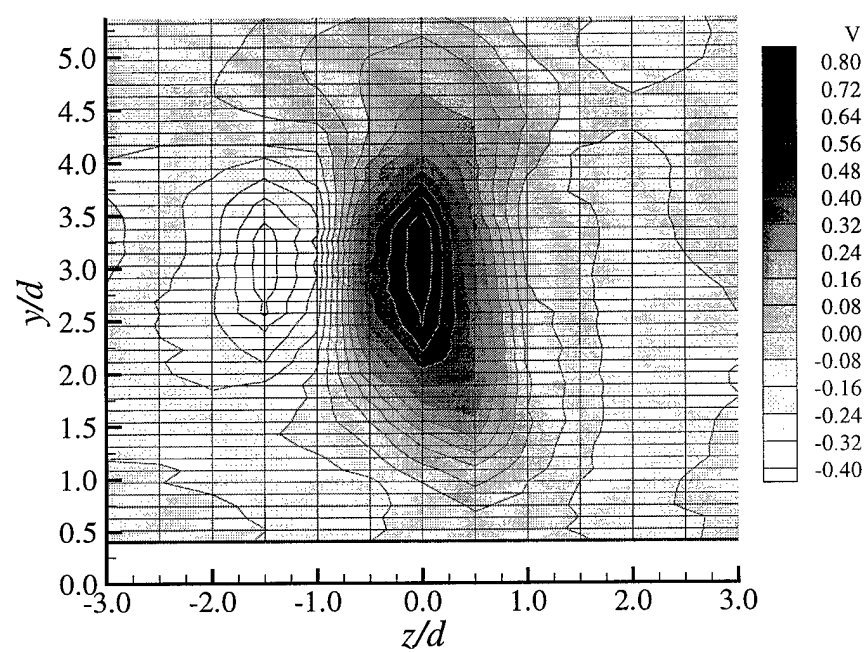


Figure 67. Experimental data for the  $V$  component of velocity at station 20 [52]

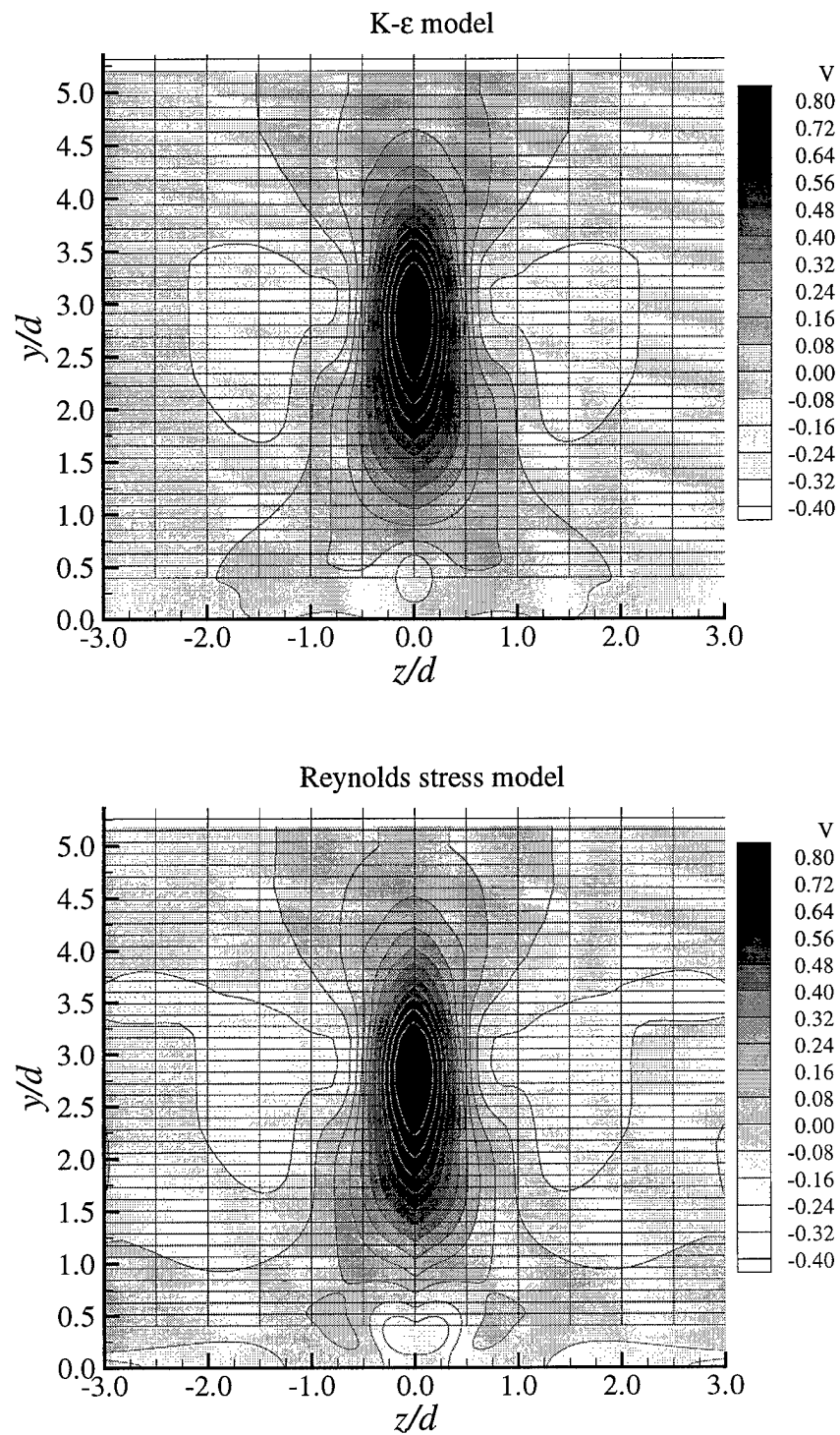


Figure 68. Comparison of turbulence model predictions of the  $V$  component of velocity at station 20



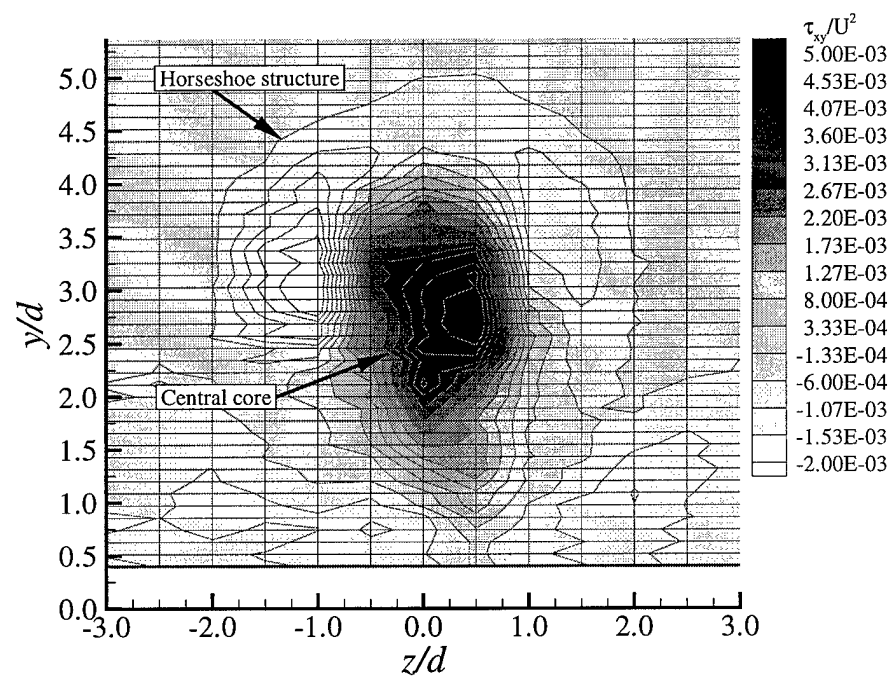


Figure 69. Experimental data for  $\tau_{xy}$  at station 20 [52]

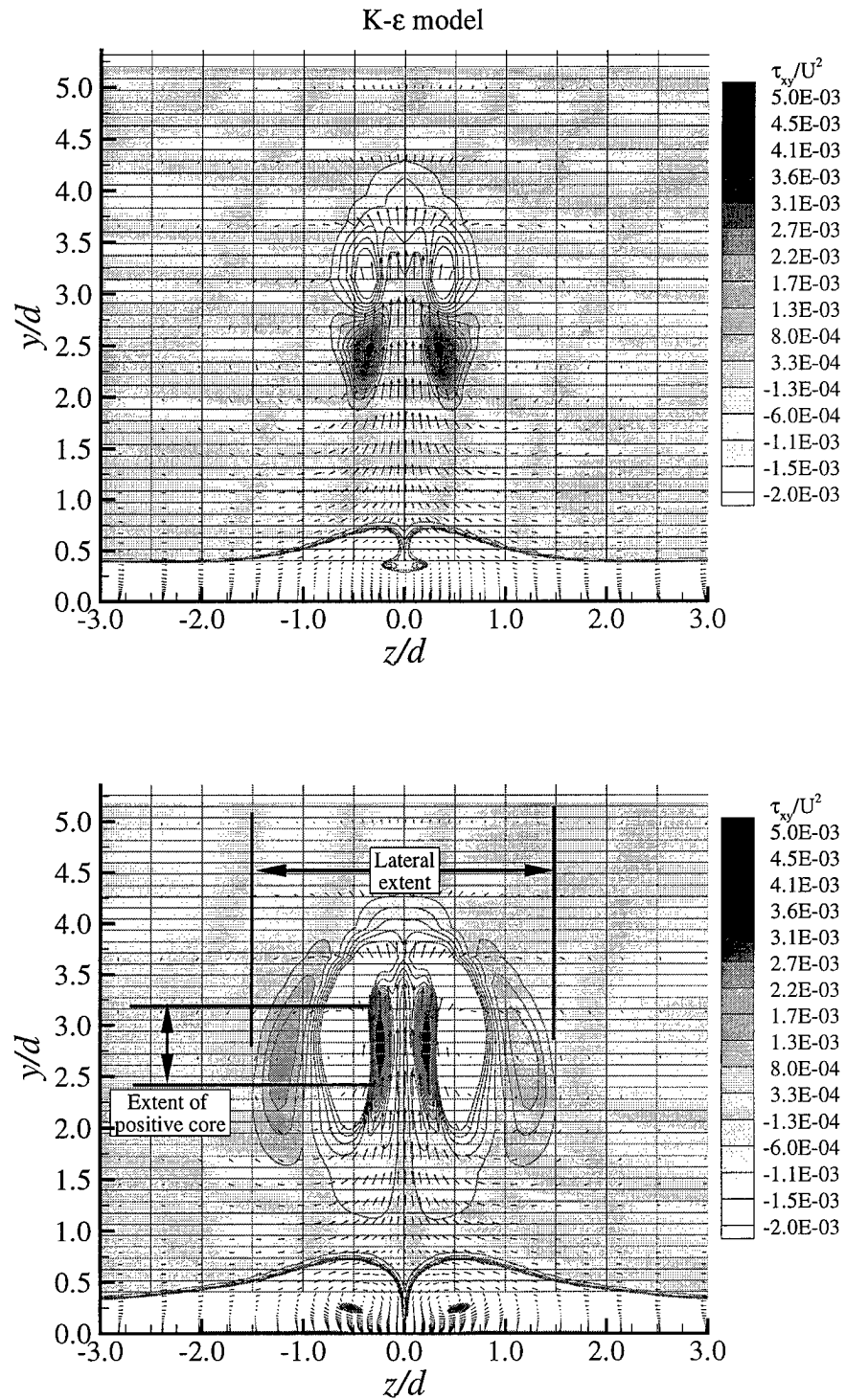


Figure 70. Comparison of turbulence model predictions of  $\tau_{xy}$  at station 20

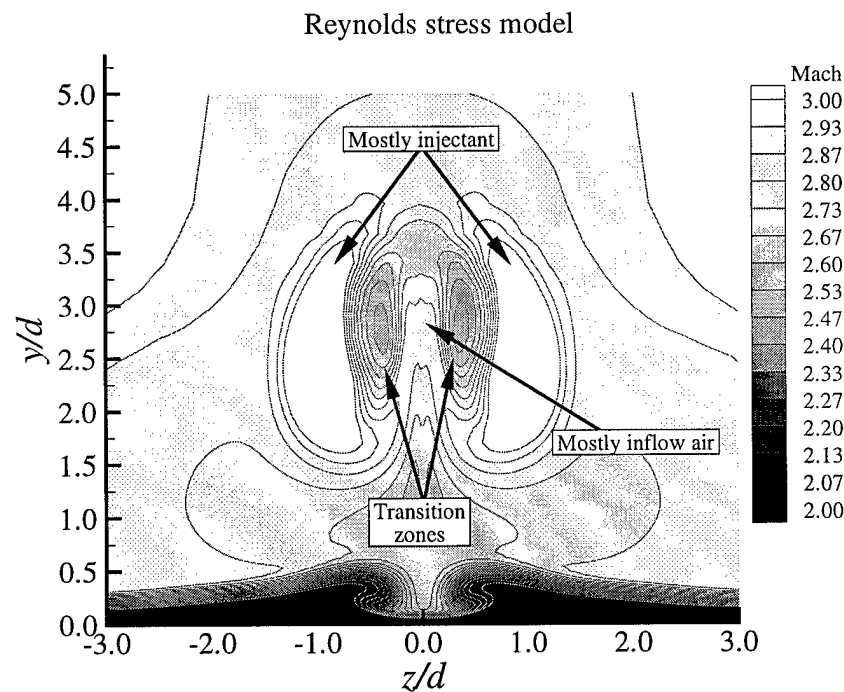
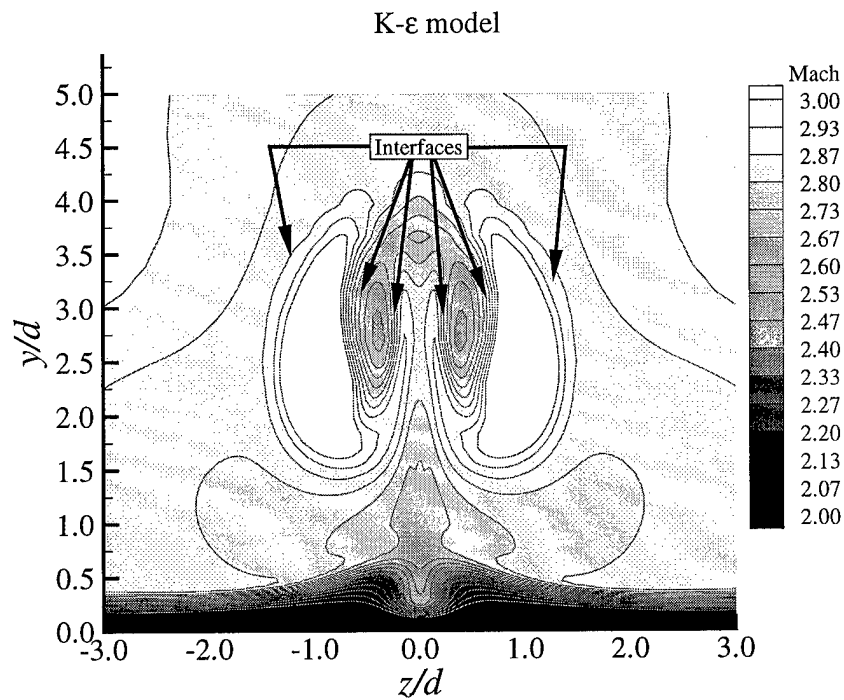


Figure 71. Comparison of turbulence model predictions for Mach number at station 20

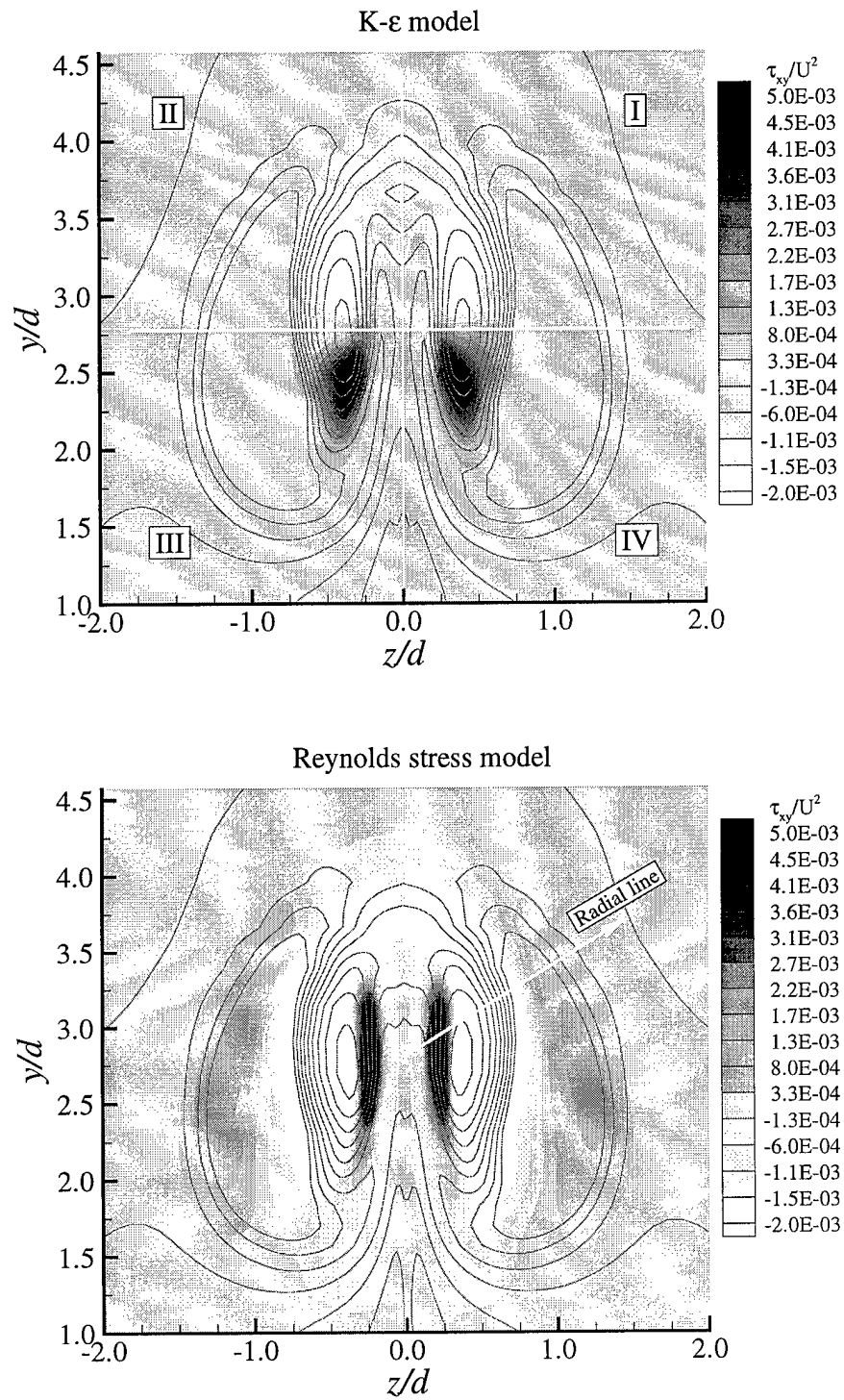


Figure 72. Comparison of predictions of  $\tau_{xy}$  with Mach number overlay at station 20

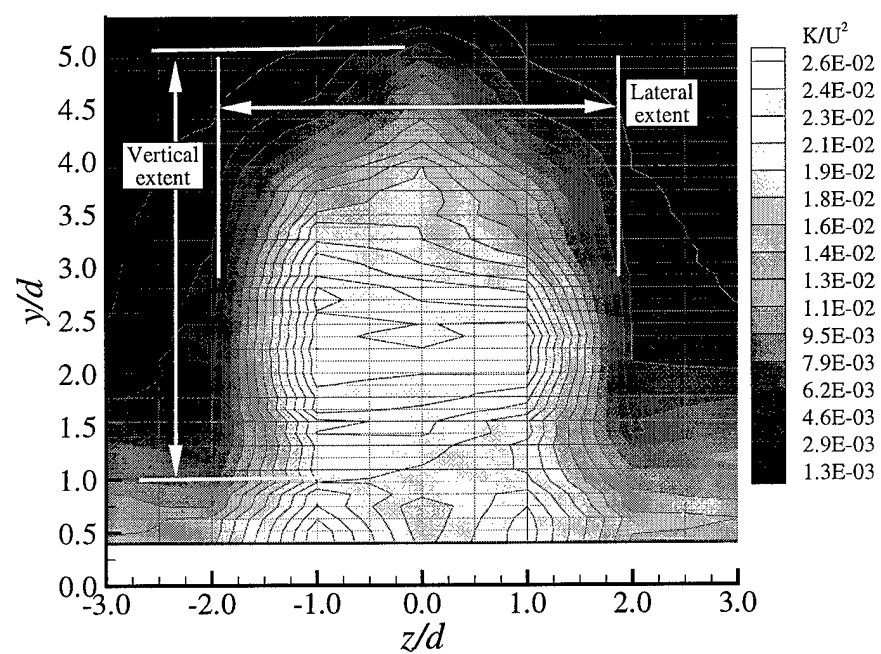


Figure 73. Experimental data for  $K$  at station 20 [52]

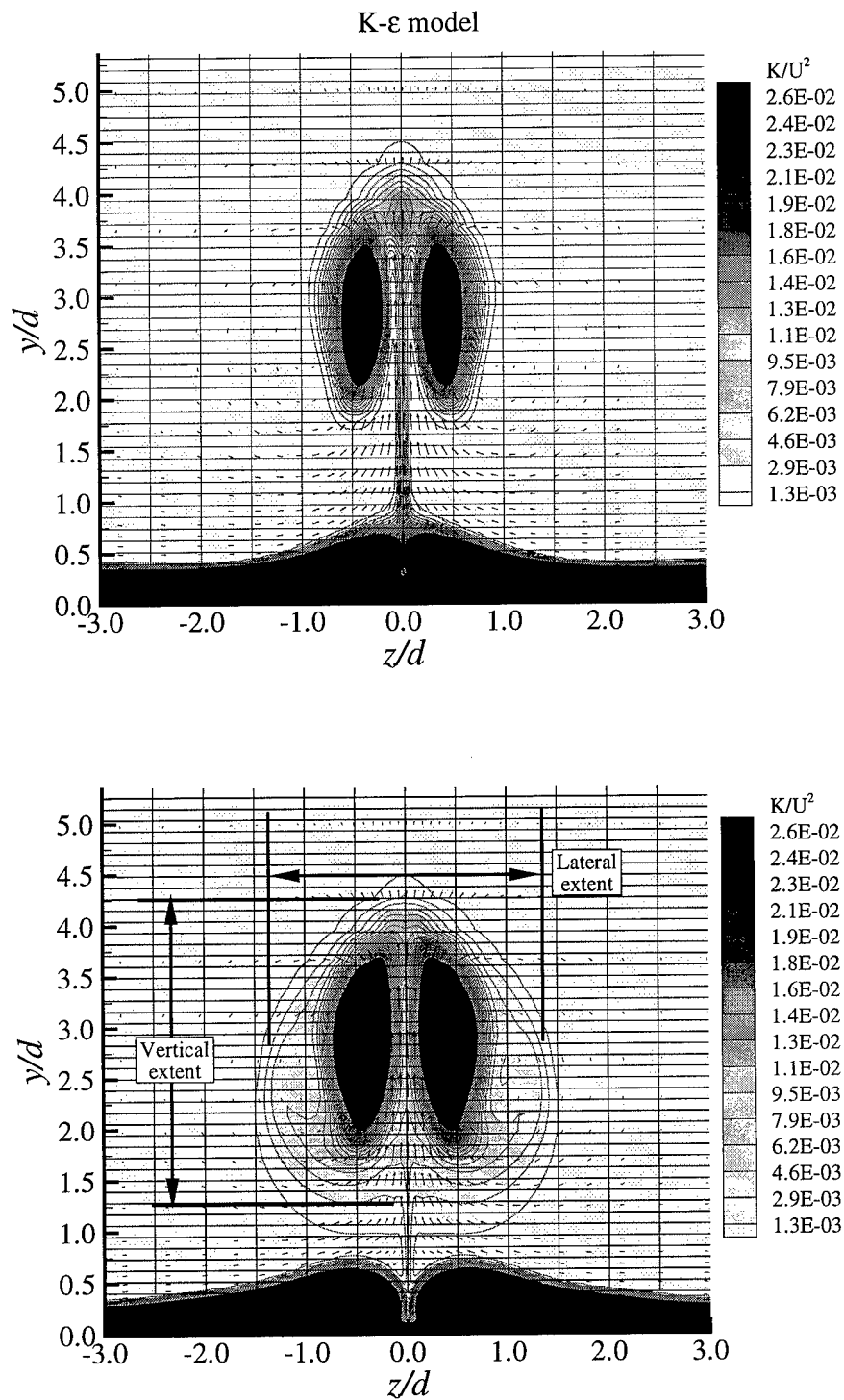


Figure 74. Comparison of turbulence model predictions of  $K$  at station 20

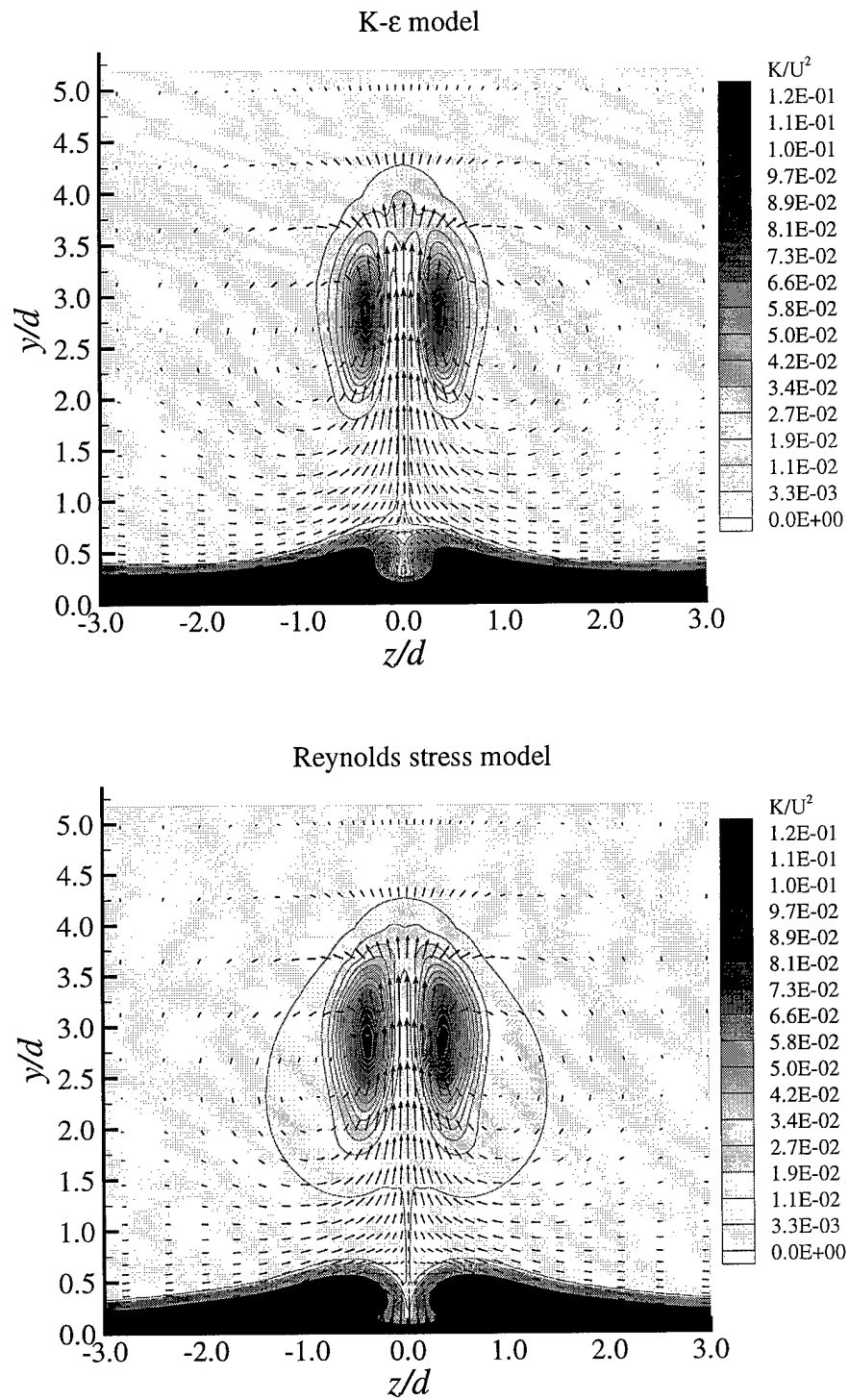


Figure 75. Comparison of turbulence model predictions of  $K$  at station 20 (rescaled)

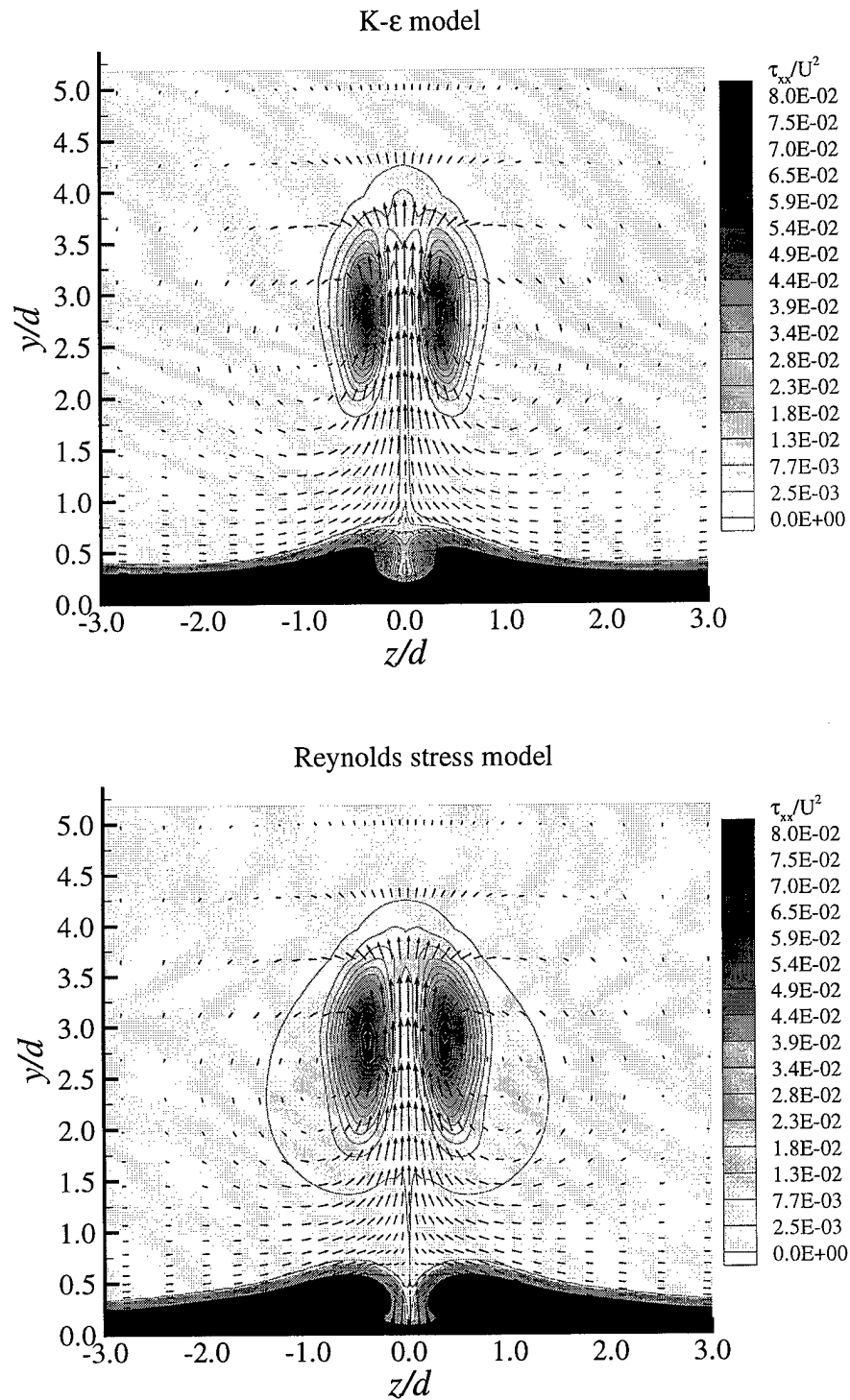


Figure 76. Comparison of turbulence model predictions of  $\tau_{xx}$  at station 20



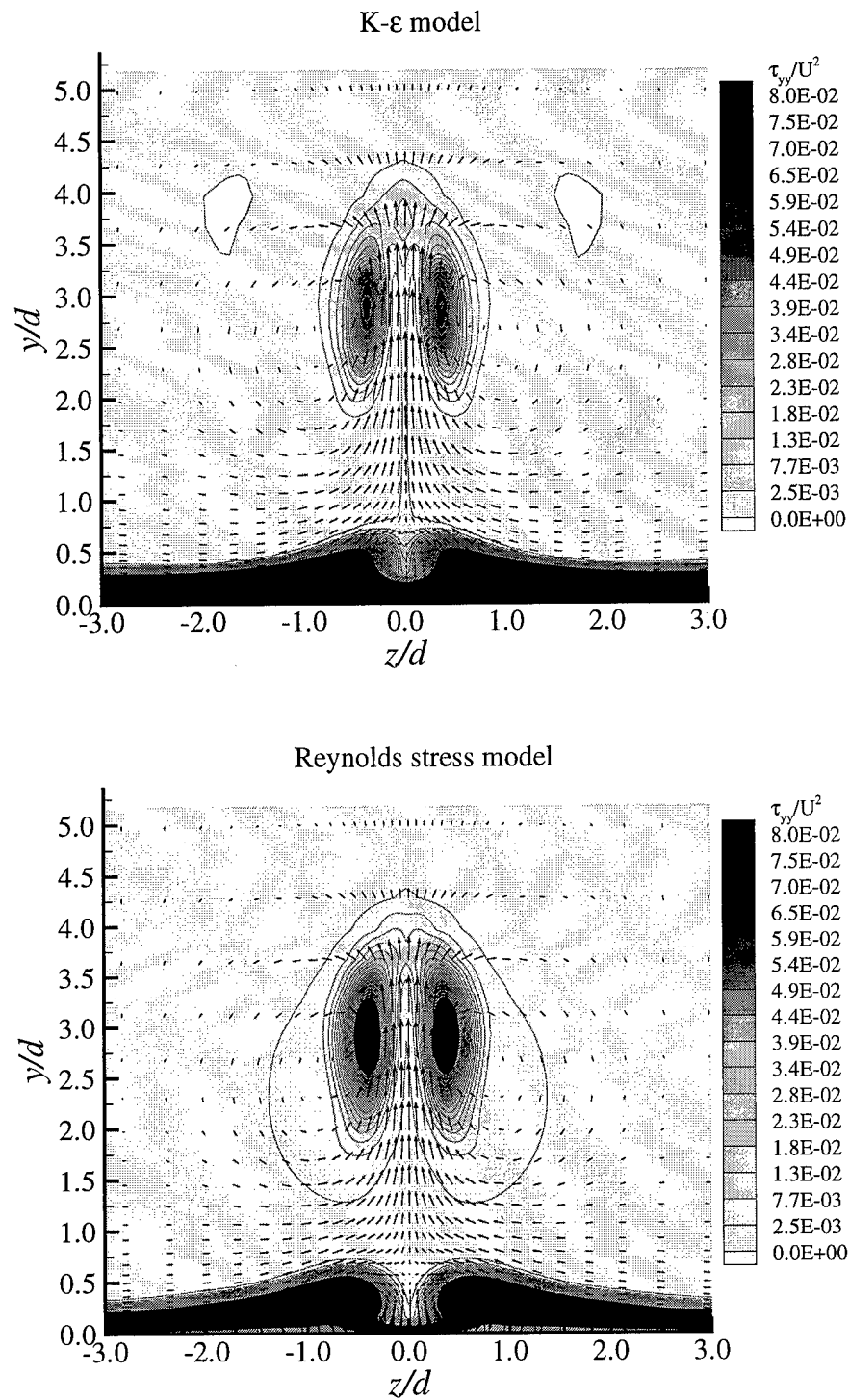


Figure 77. Comparison of turbulence model predictions of  $\tau_{yy}$  at station 20

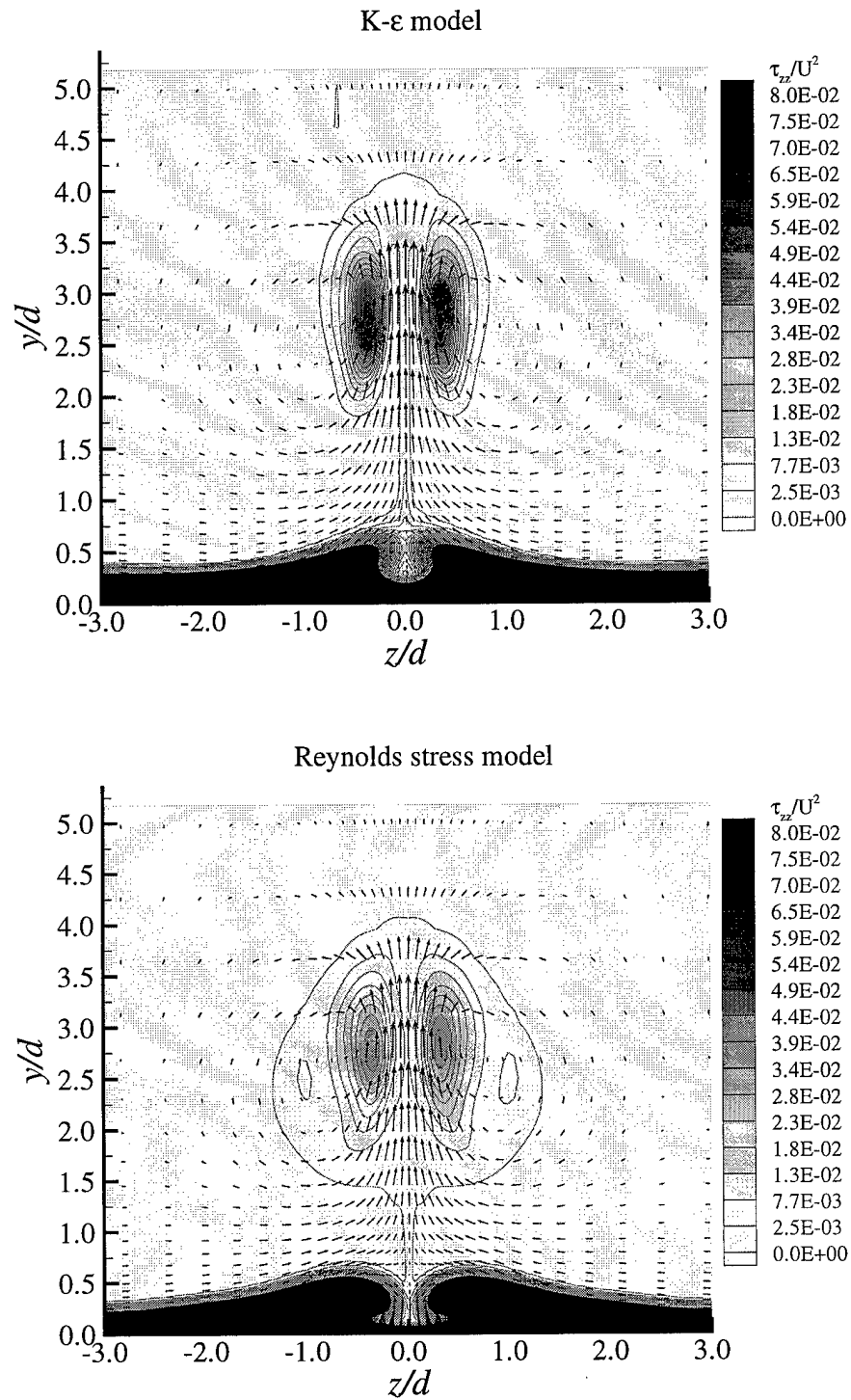


Figure 78. Comparison of turbulence model predictions of  $\tau_{zz}$  at station 20

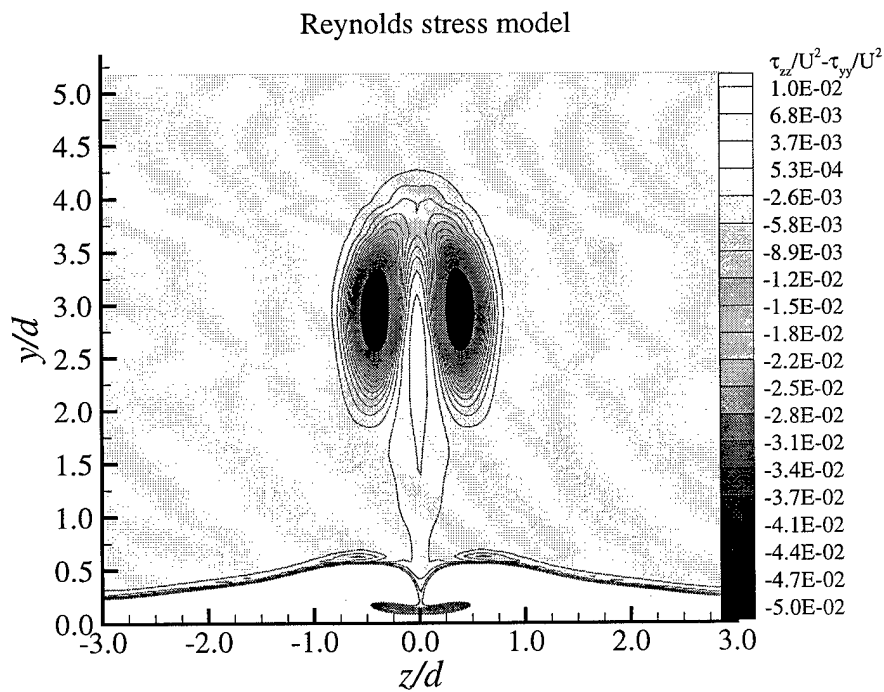
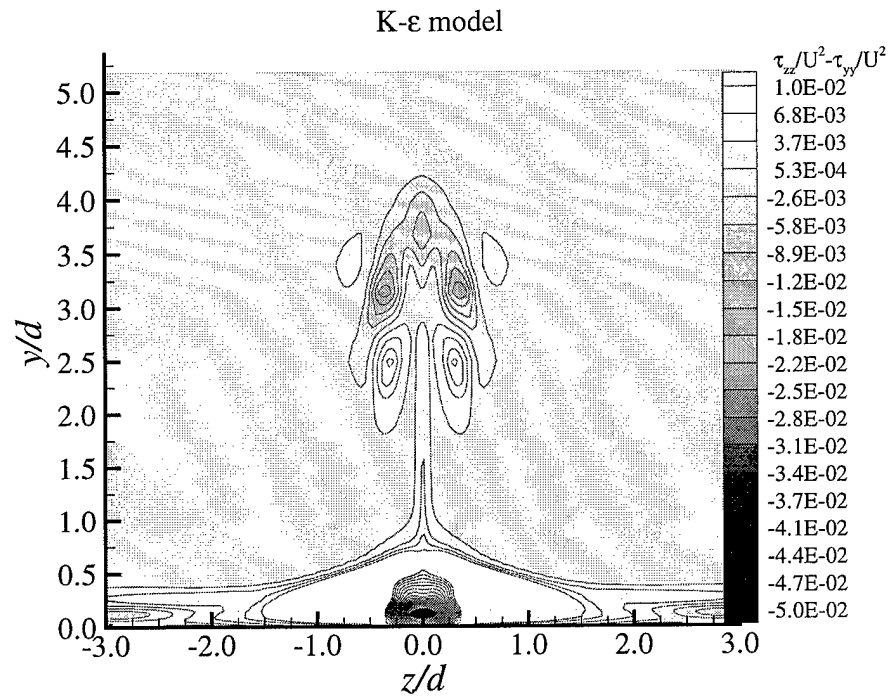


Figure 79. Homogenization effects on axial Reynolds stresses at station 20

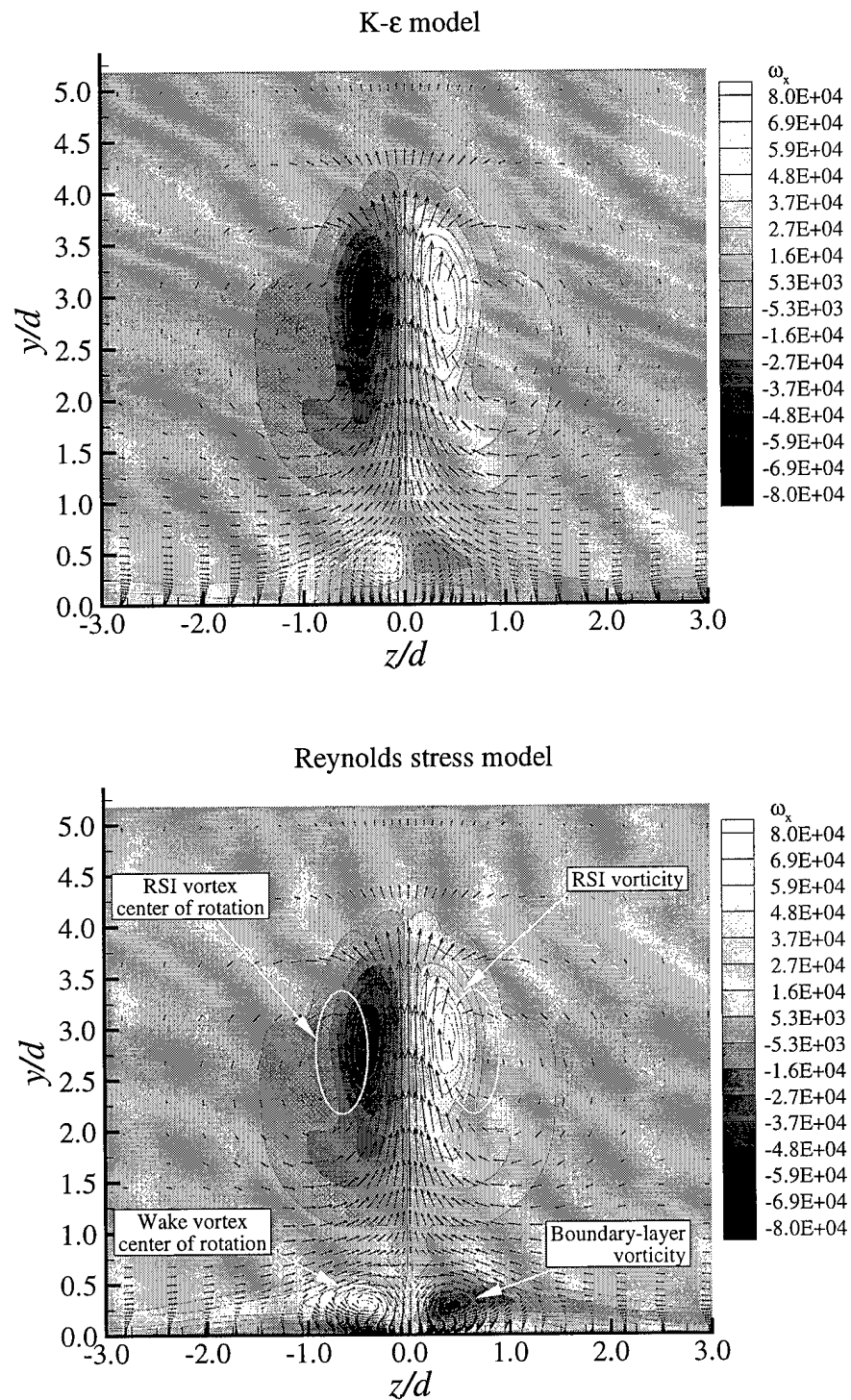


Figure 80. Comparison of turbulence model predictions of  $\omega_x$  at station 20

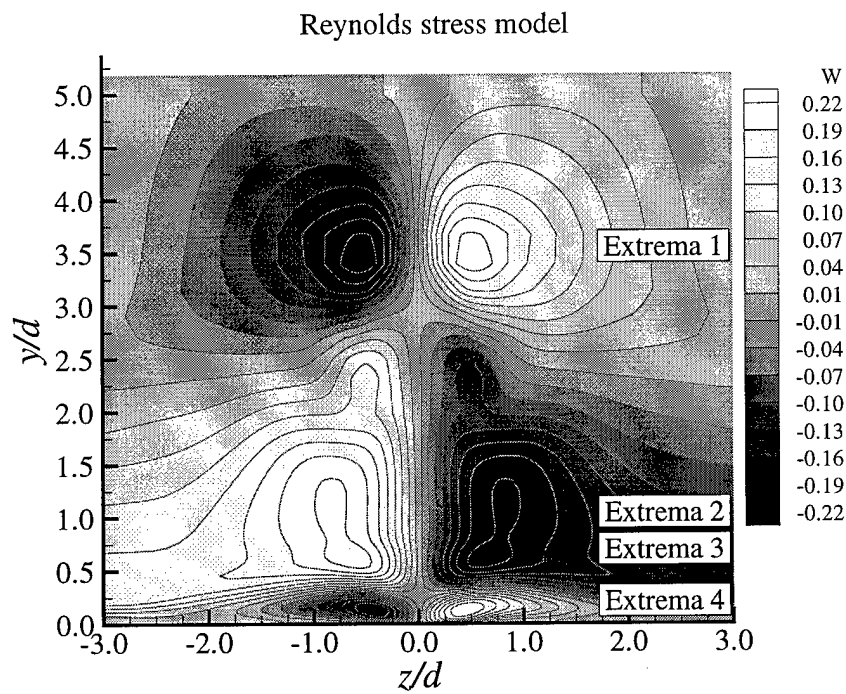
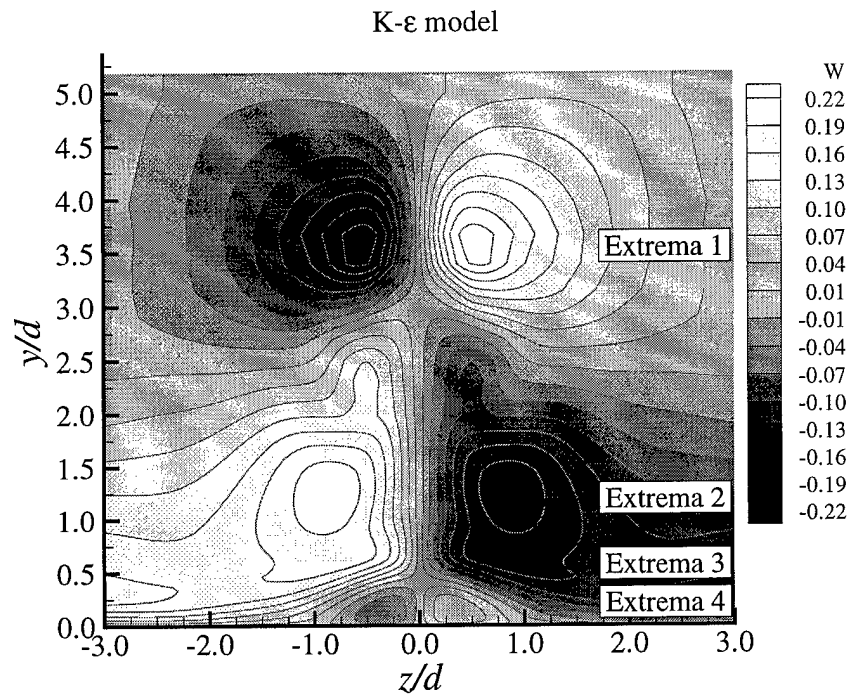


Figure 81. Comparison of turbulence model predictions of the  $W$  component of velocity at station 20

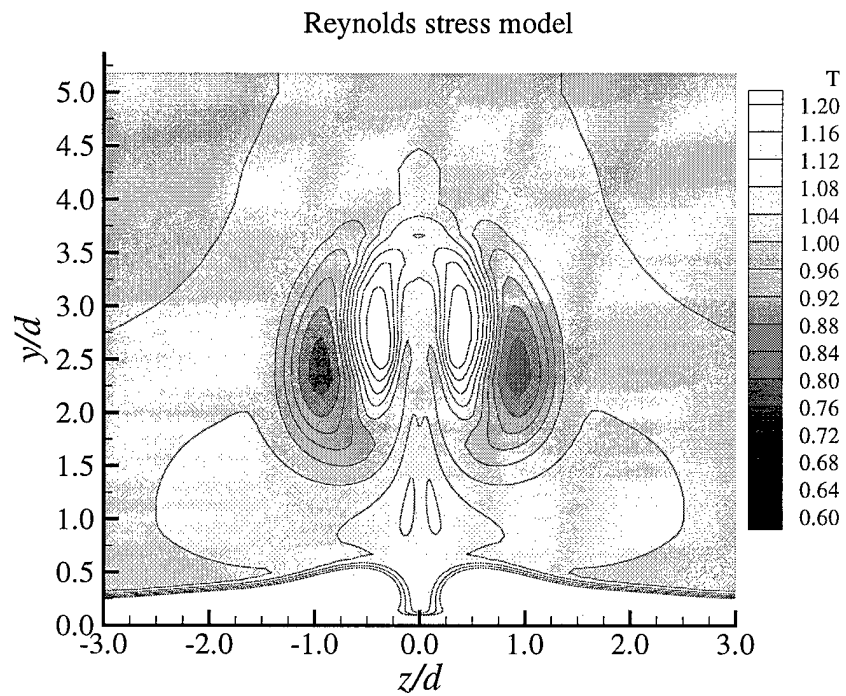
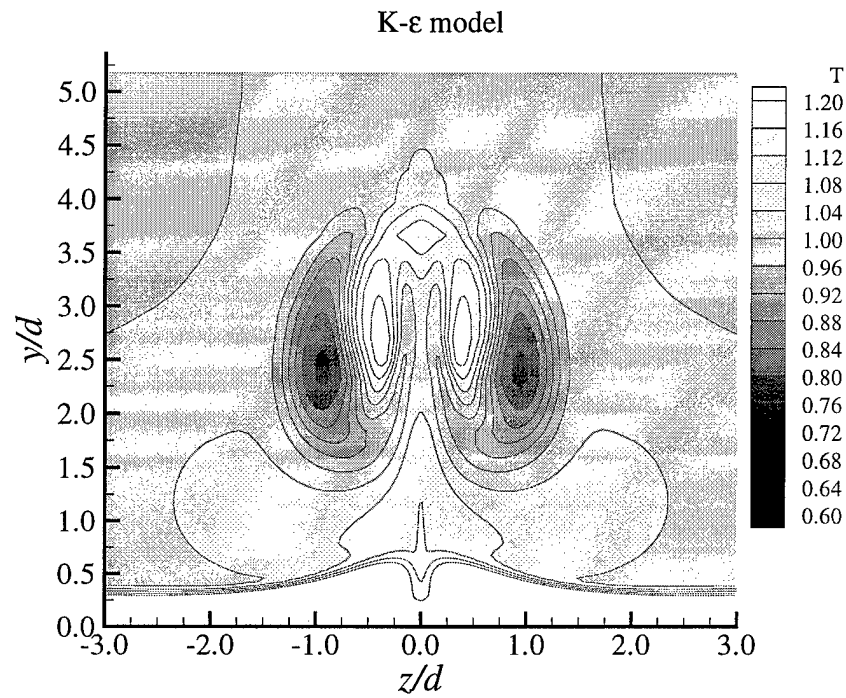


Figure 82. Comparison of turbulence model predictions of temperature at station 20

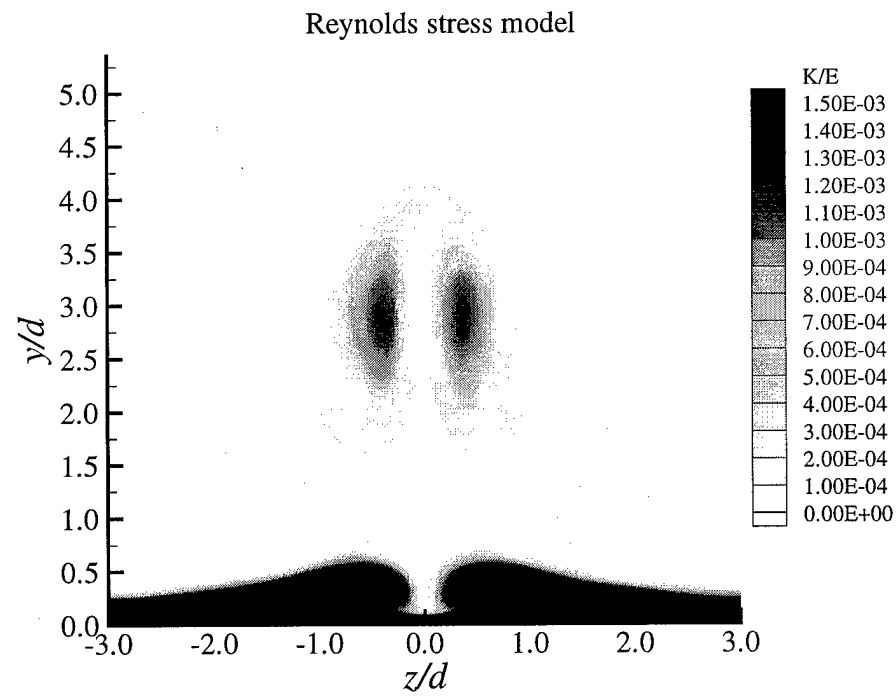
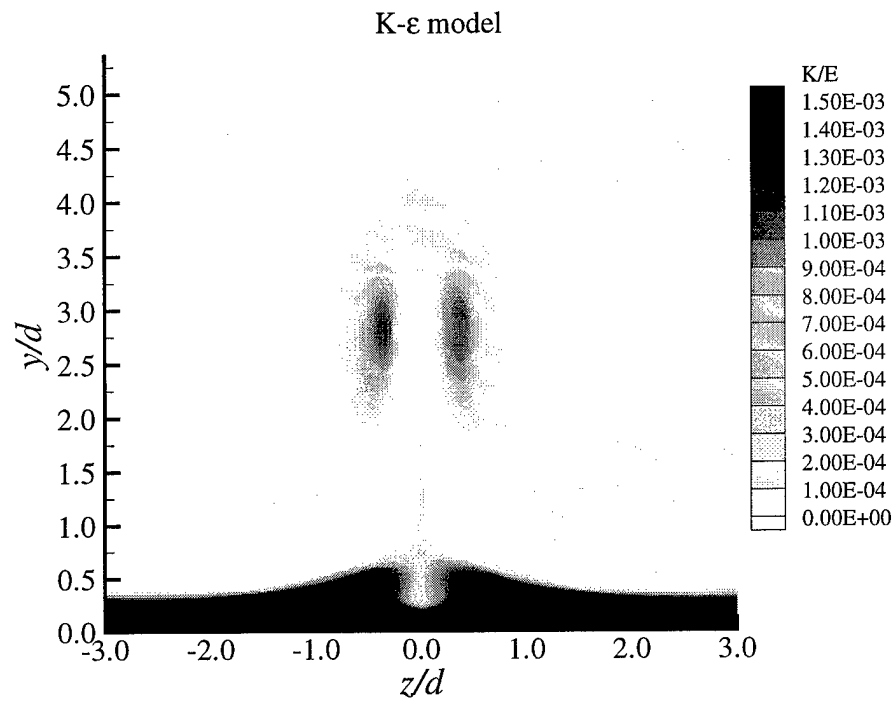


Figure 83. Comparison of turbulence model predictions for fraction of  $E$  comprised by  $K$  at station 20

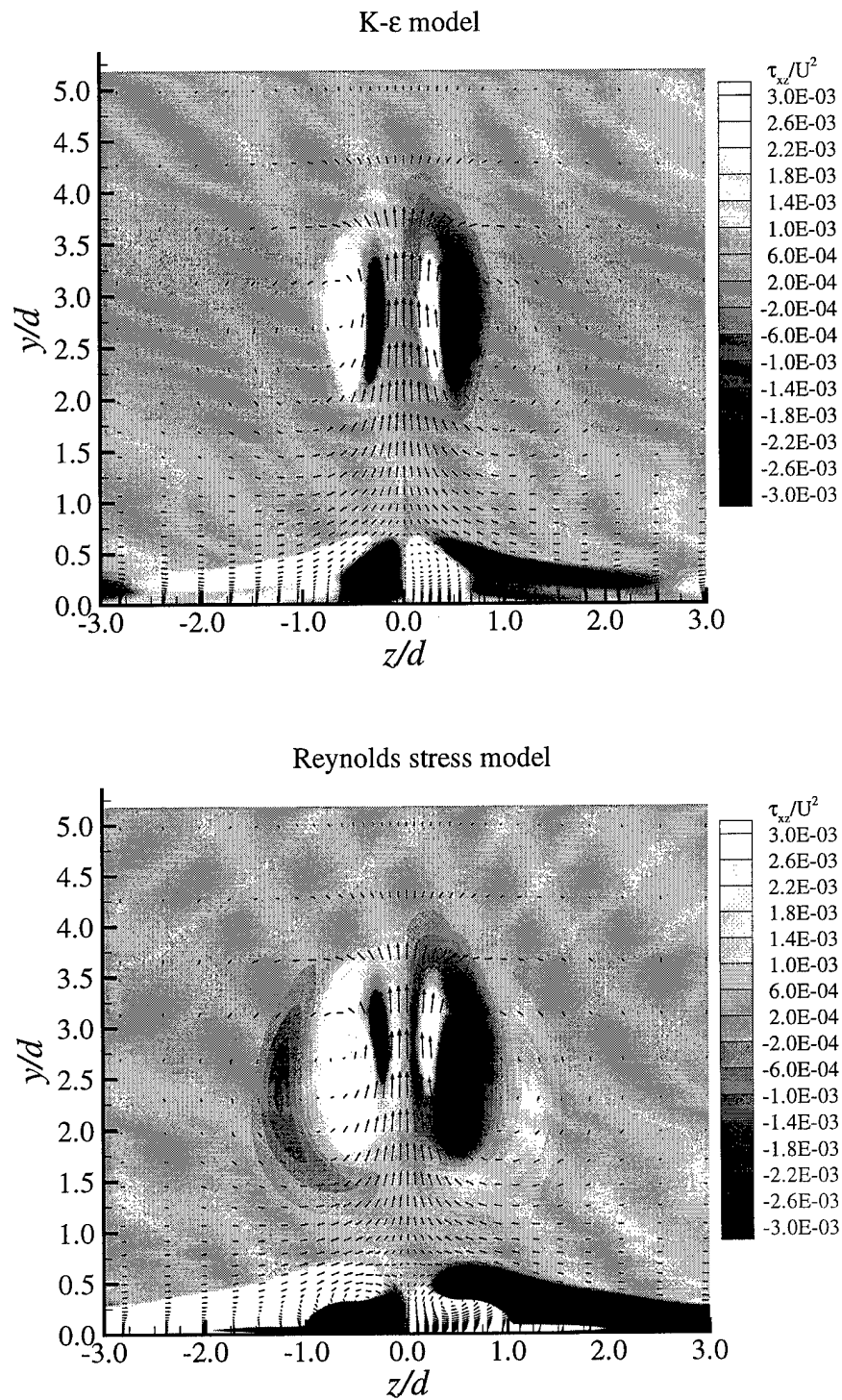


Figure 84. Comparison of turbulence model predictions of  $\tau_{xz}$  at station 20



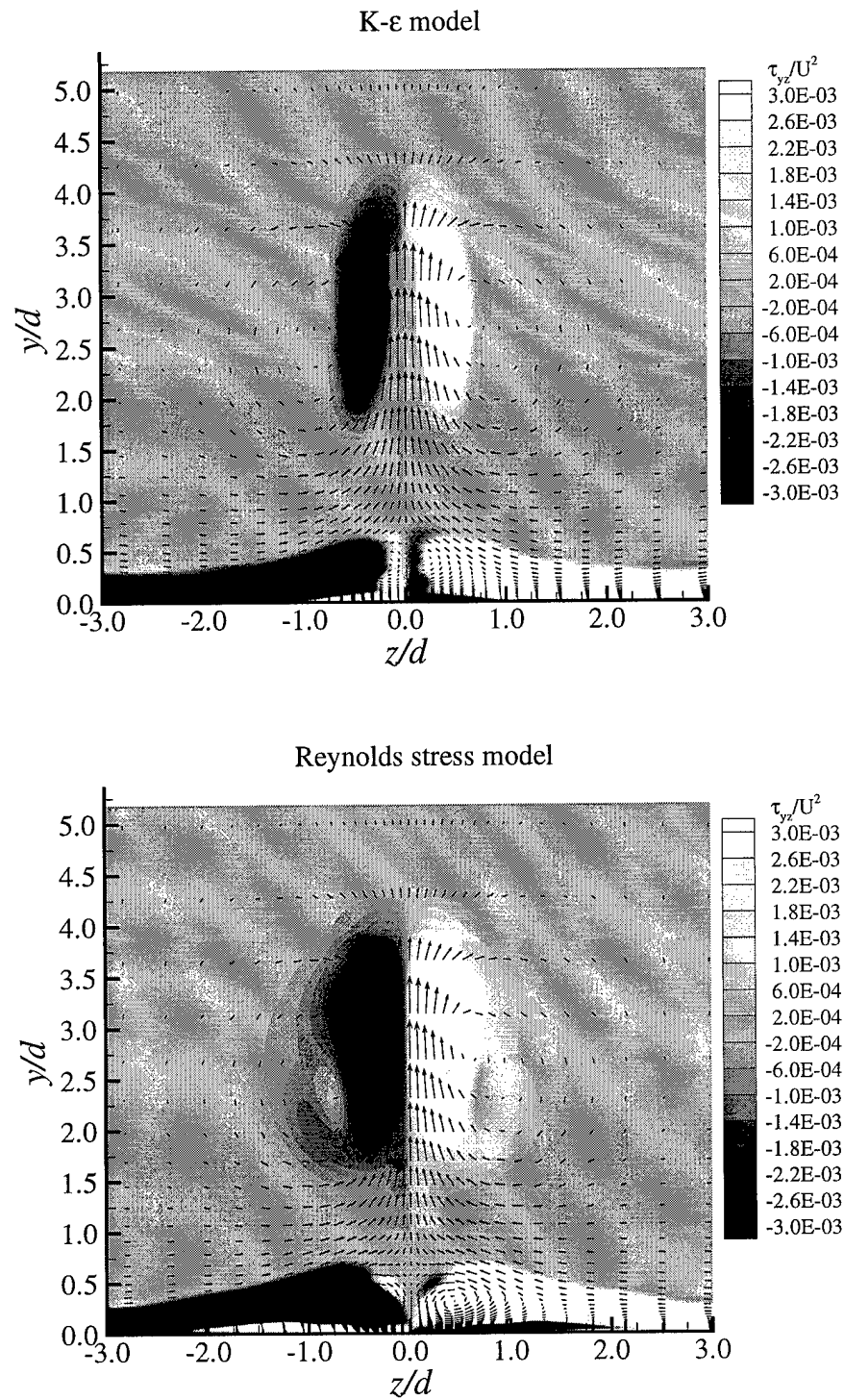


Figure 85. Comparison of turbulence model predictions of  $\tau_{yz}$  at station 20

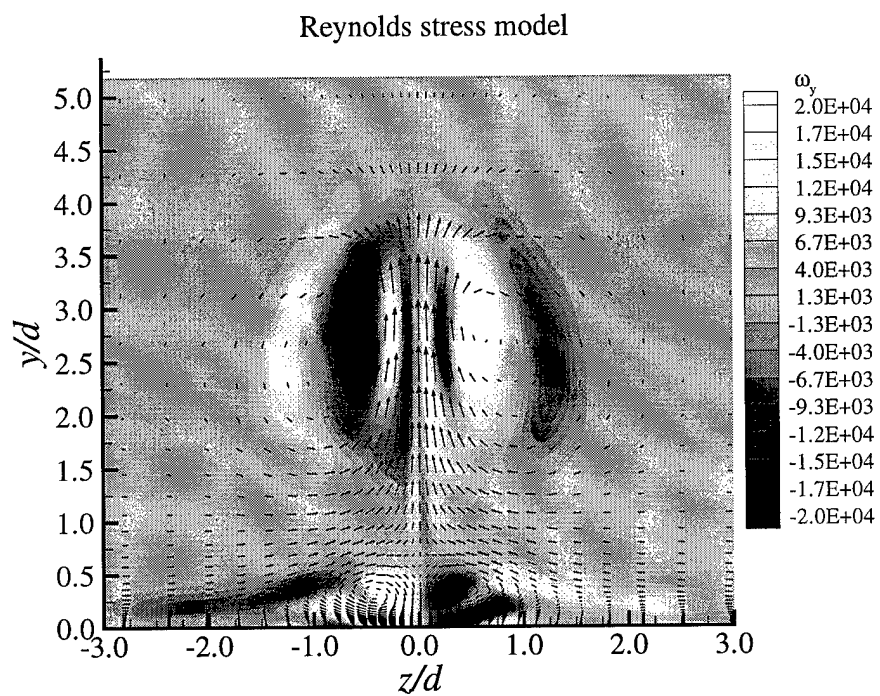
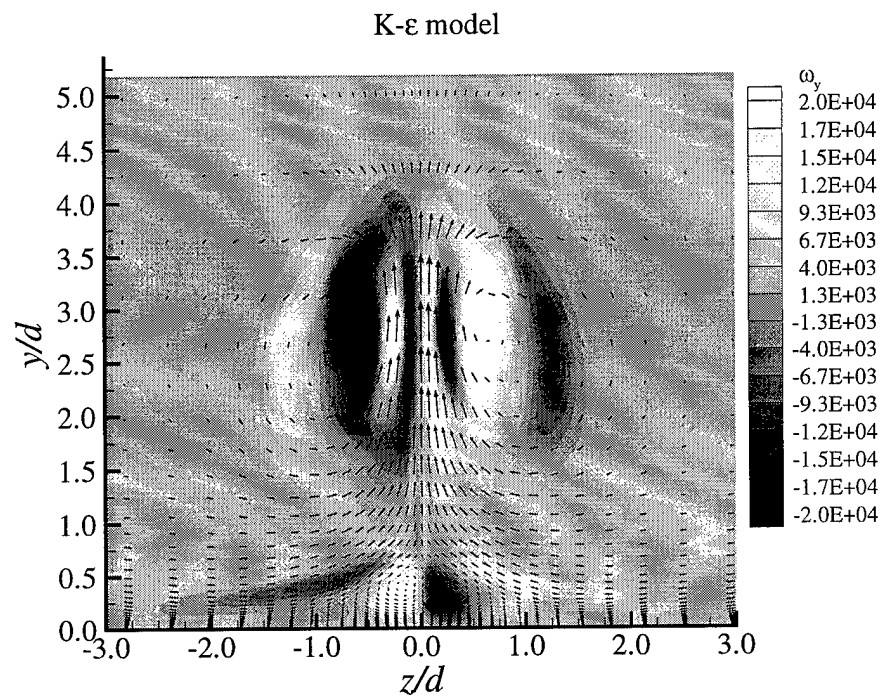


Figure 86. Comparison of turbulence model predictions of  $\omega_y$  at station 20

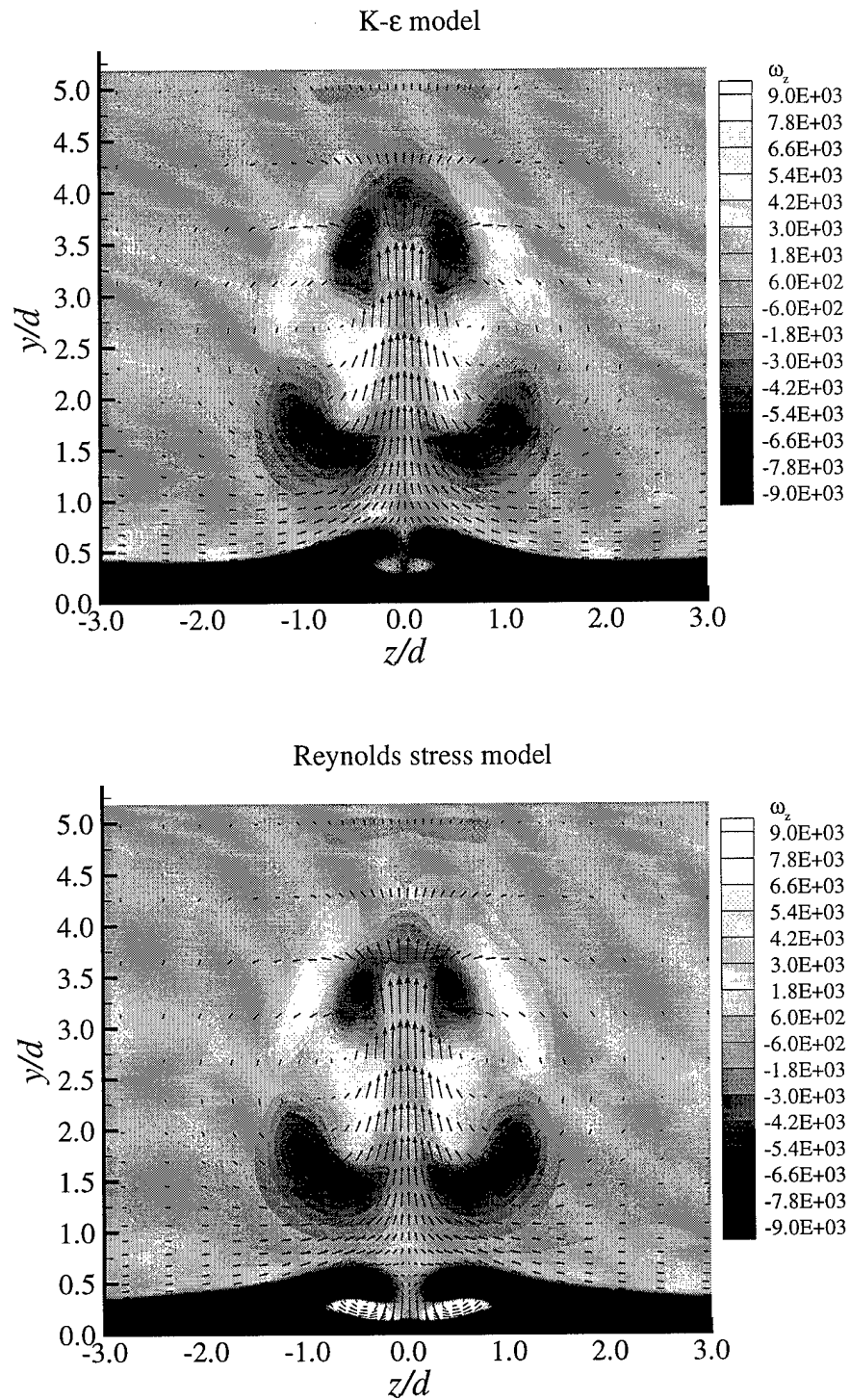


Figure 87. Comparison of turbulence model predictions of  $\omega_z$  at station 20

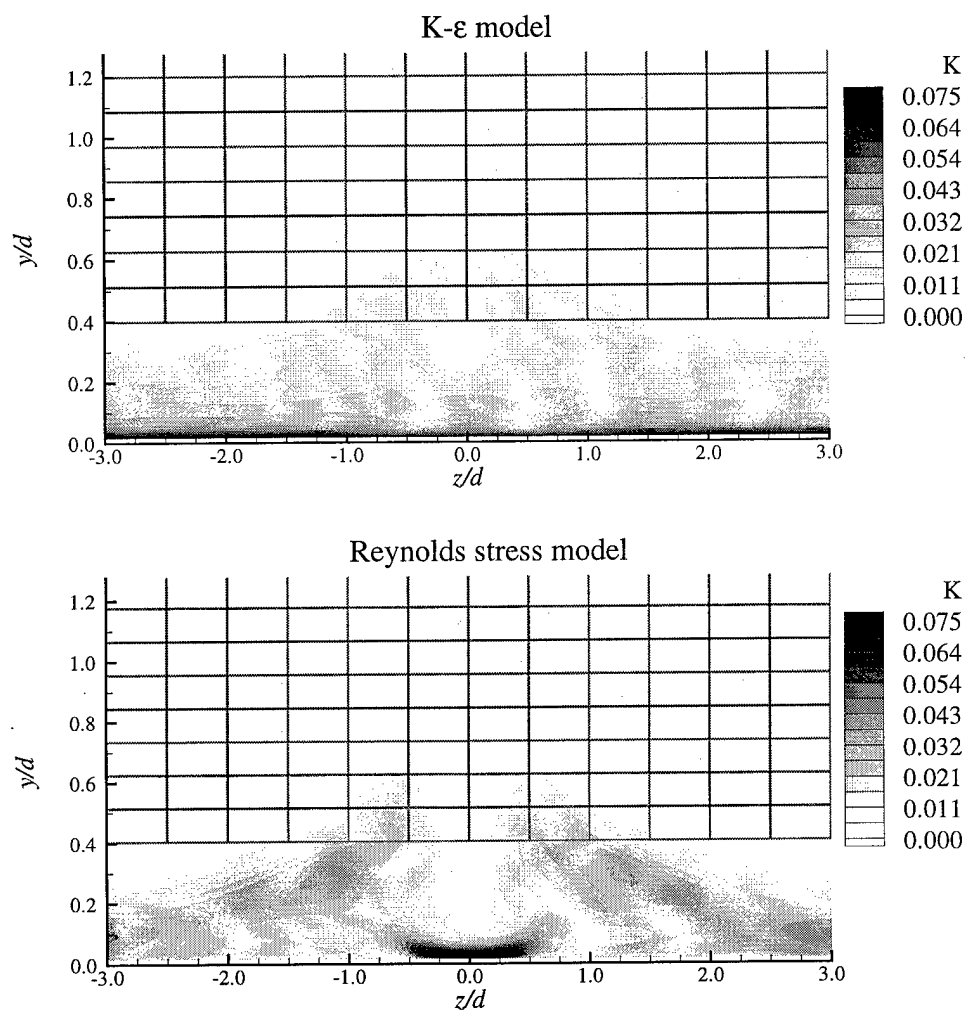


Figure 88. Comparison of turbulence model predictions of  $K$  in the boundary layer at station 20

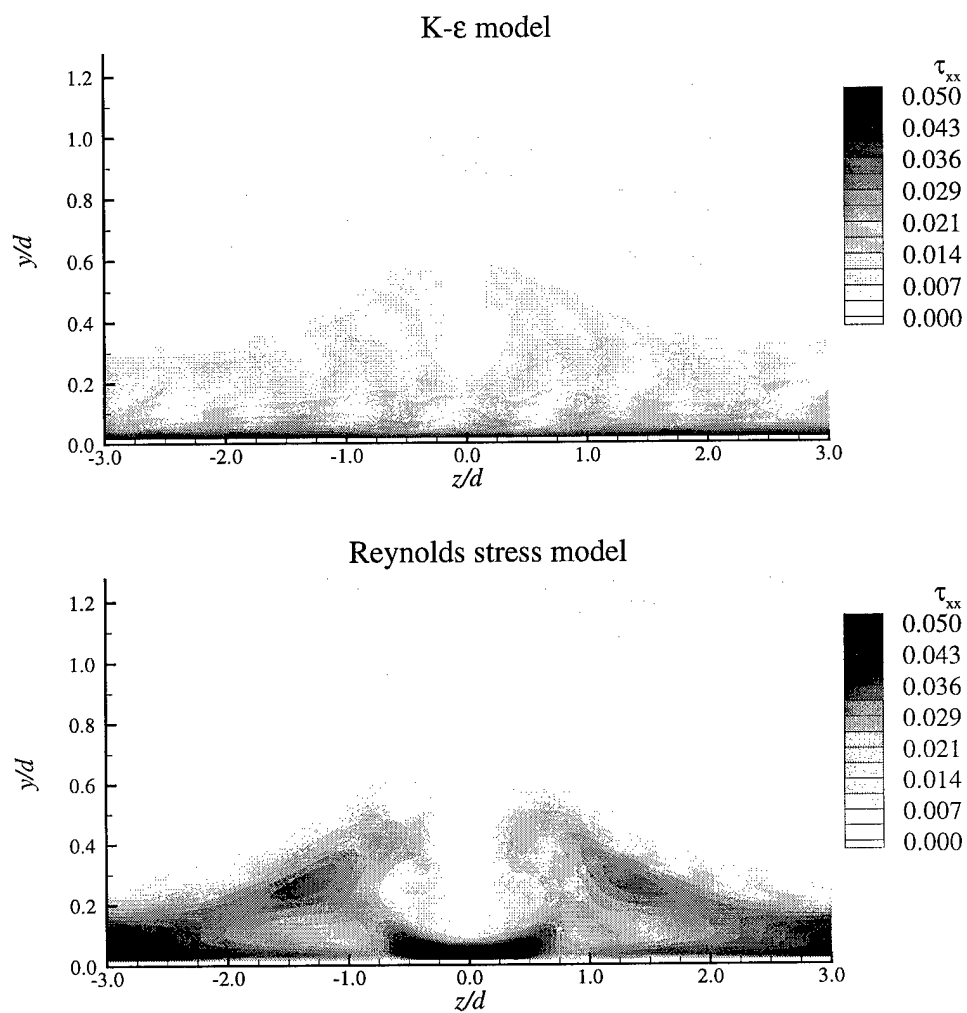


Figure 89. Comparison of turbulence model predictions of  $\tau_{xx}$  in the boundary layer at station 20

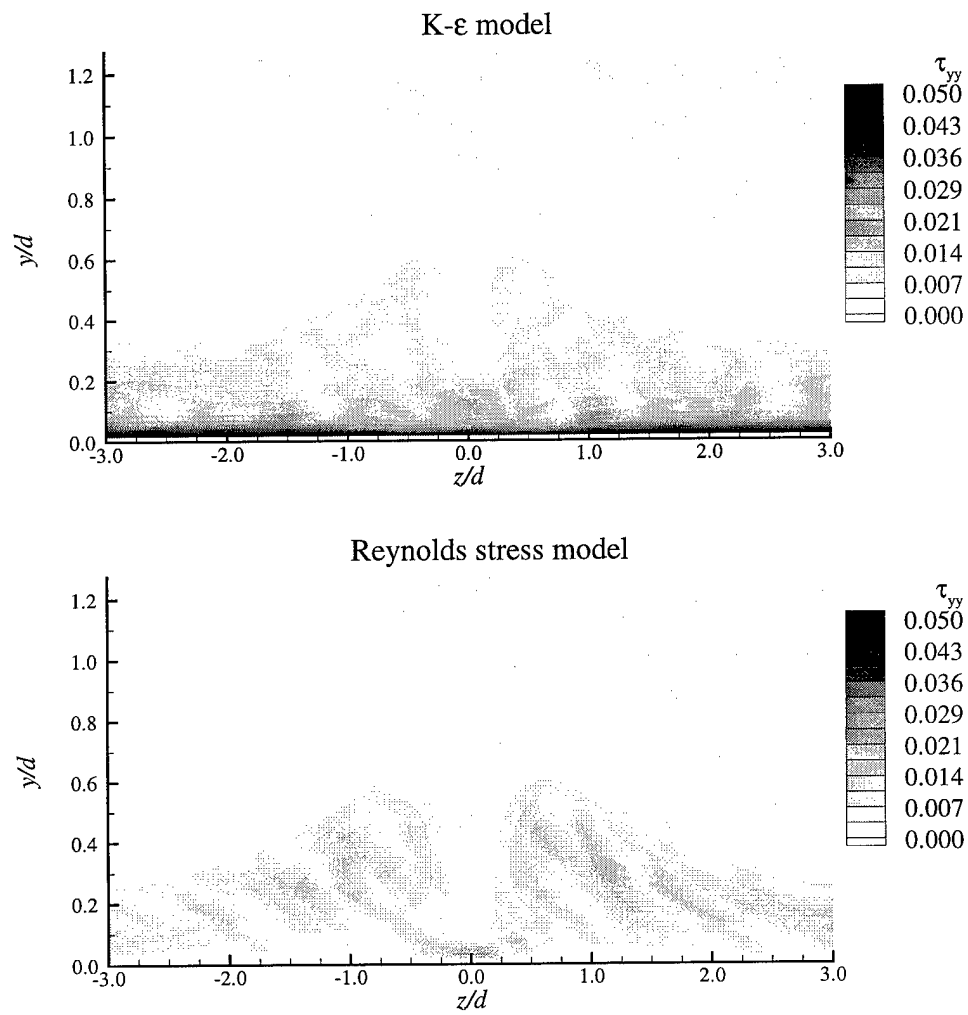


Figure 90. Comparison of turbulence model predictions of  $\tau_{yy}$  in the boundary layer at station 20

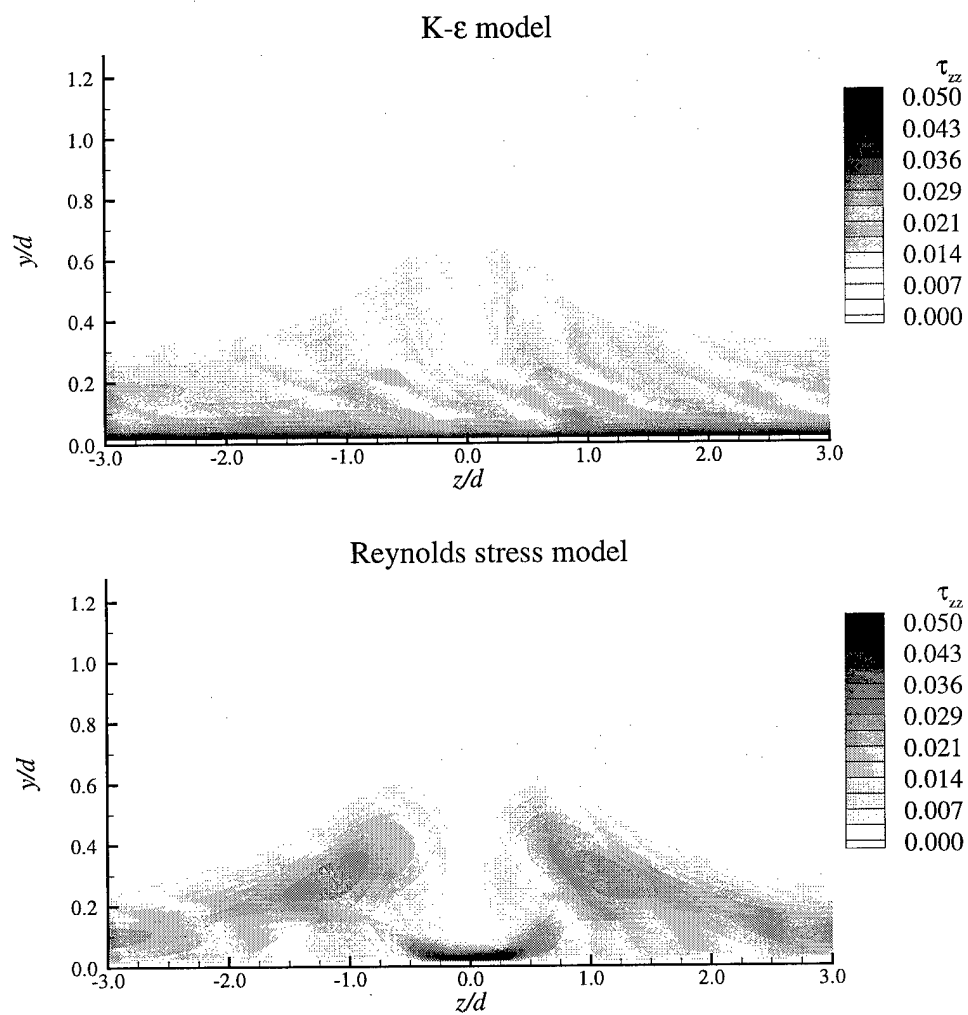


Figure 91. Comparison of turbulence model predictions of  $\tau_{zz}$  in the boundary layer at station 20

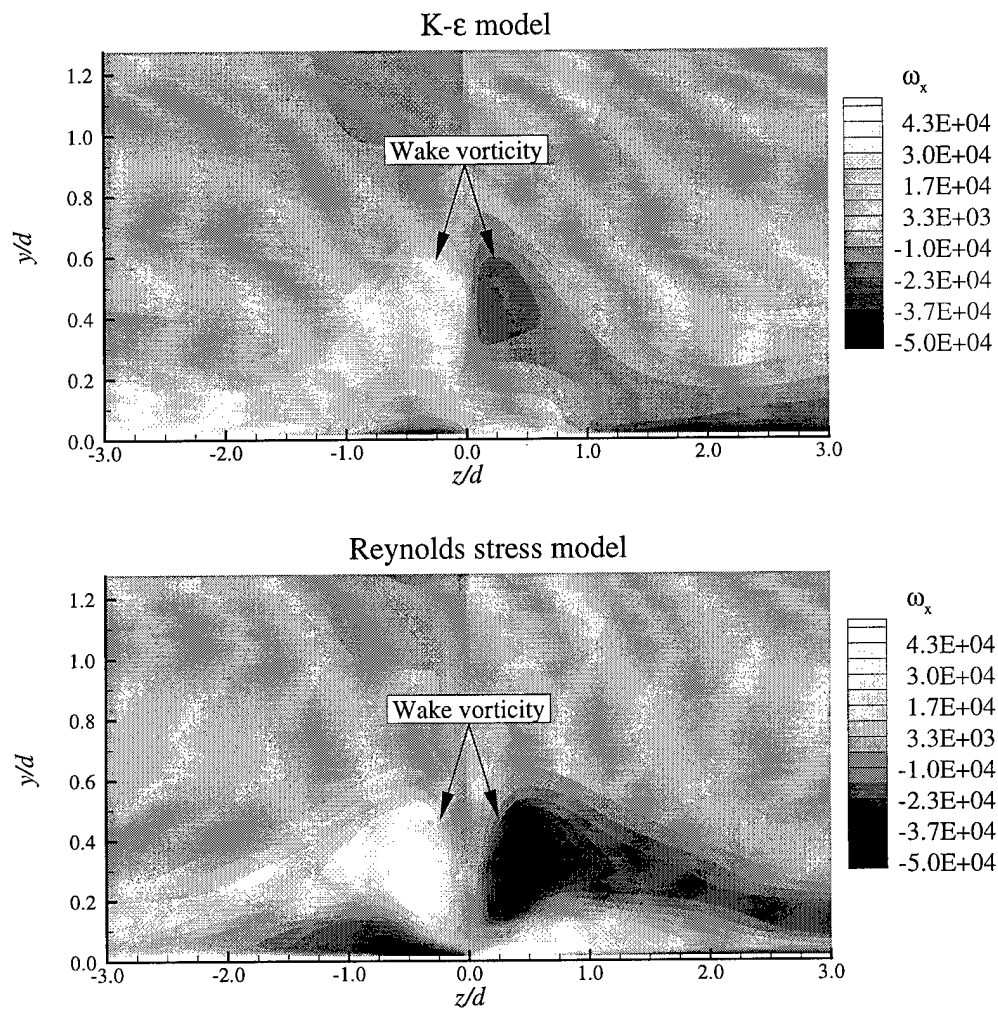


Figure 92. Comparison of turbulence model predictions of streamwise vorticity in the boundary layer at station 20



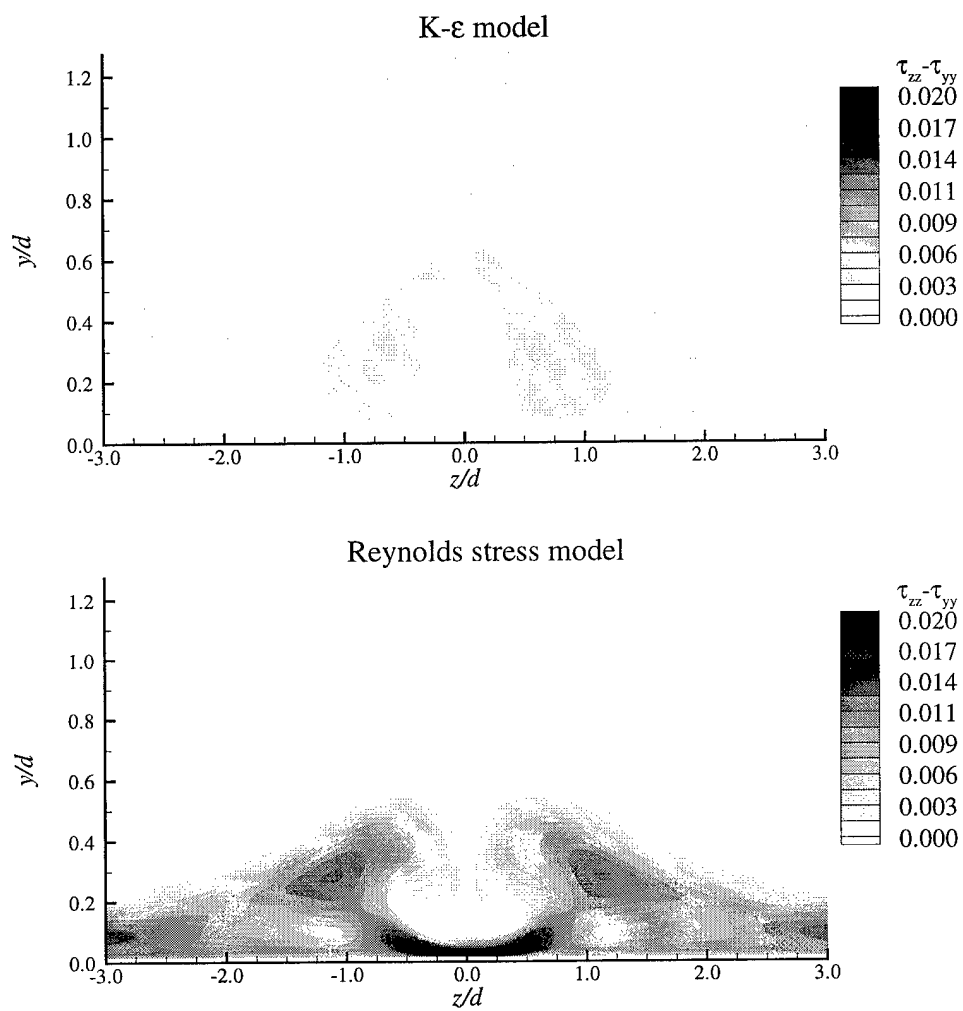


Figure 93. Homogenization of the axial Reynolds stresses in the boundary-layer

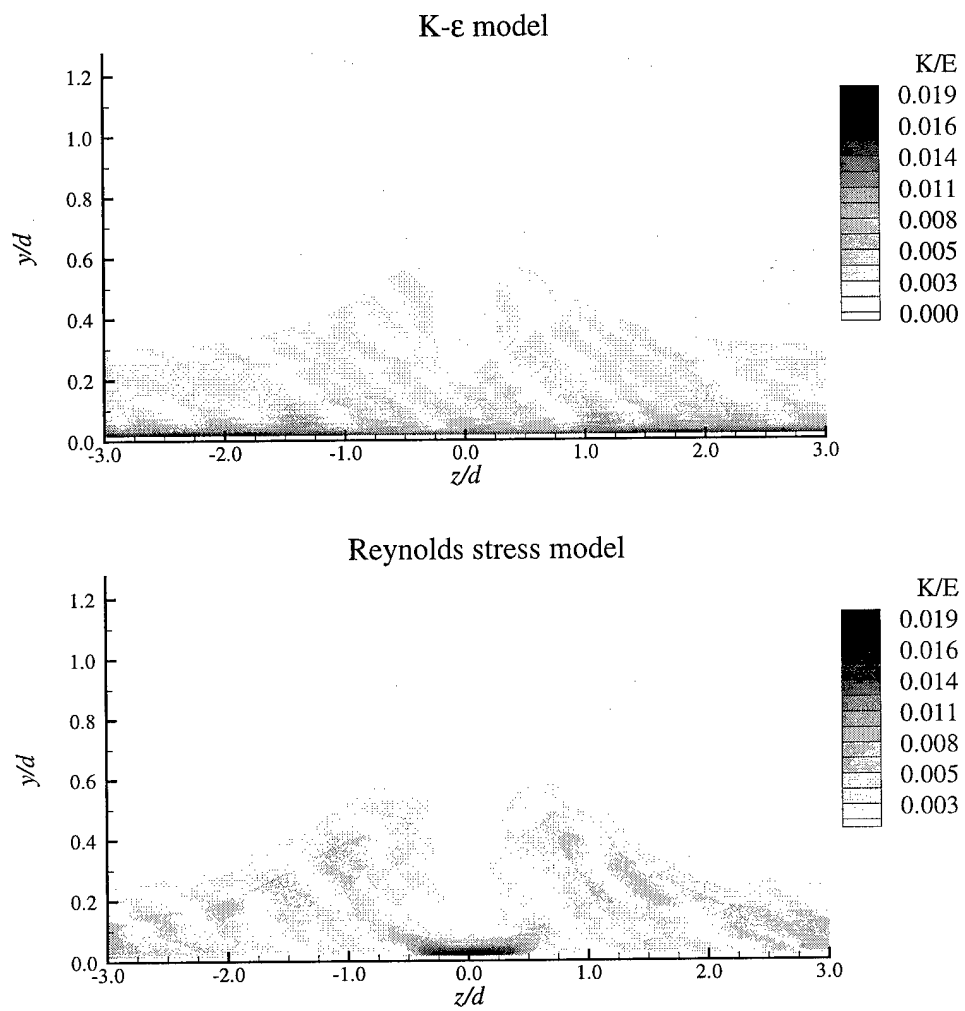


Figure 94. Comparison of turbulence model predictions of  $K/E$  in the boundary layer at station 20

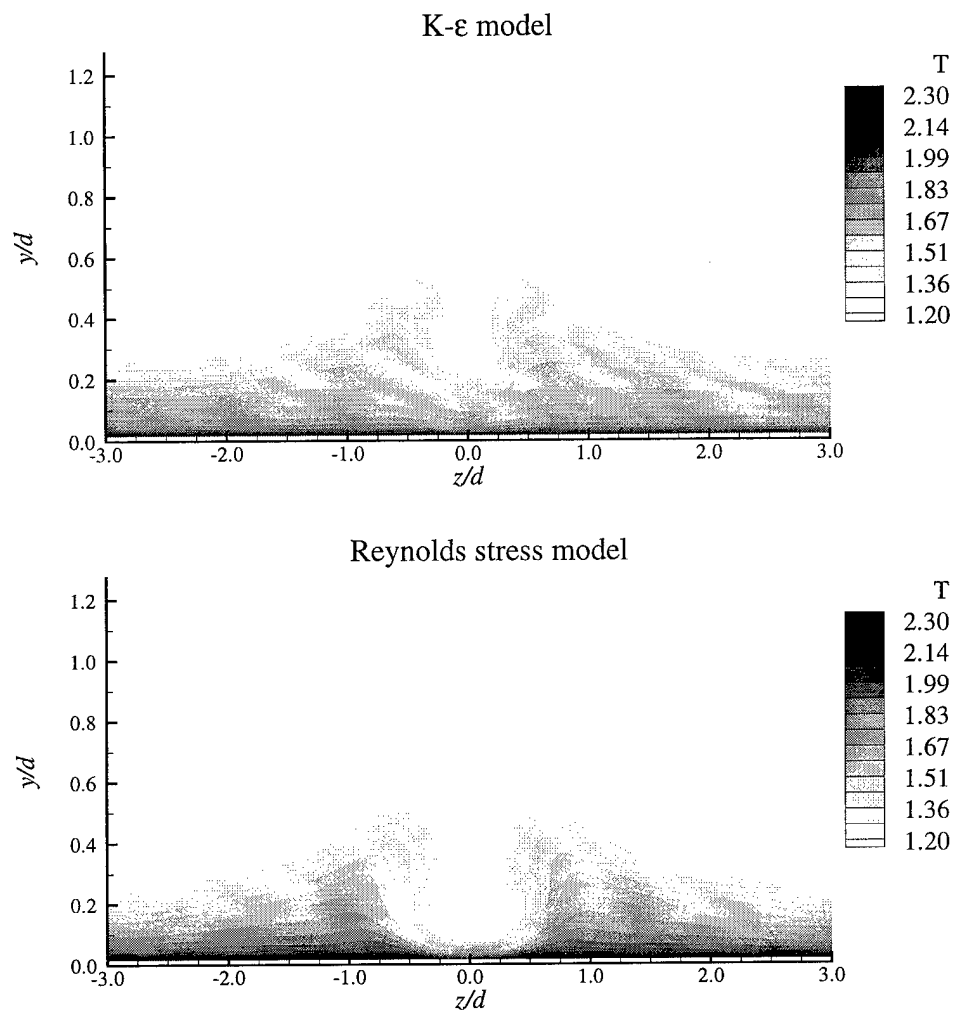


Figure 95. Comparison of turbulence model predictions of mean flow temperature in the boundary layer at station 20

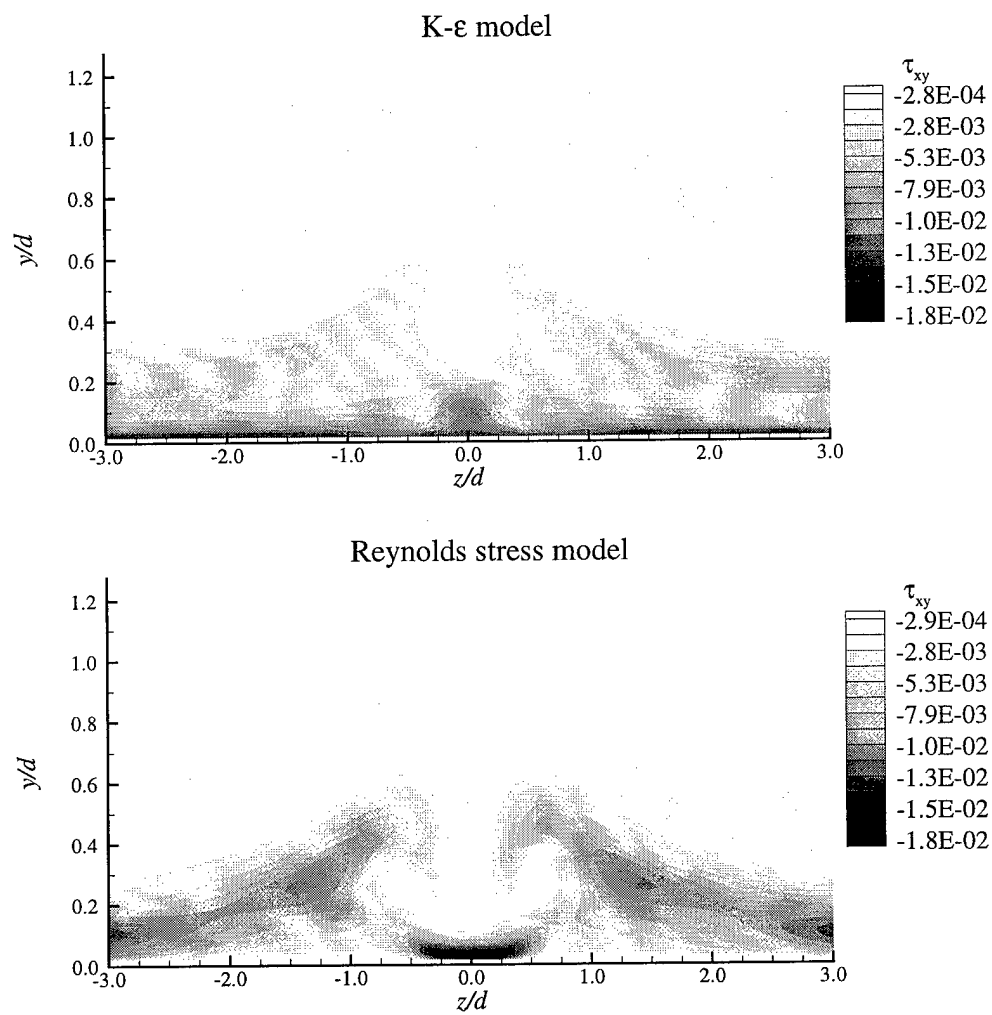


Figure 96. Comparison of turbulence model predictions of  $\tau_{xy}$  in the boundary layer at station 20

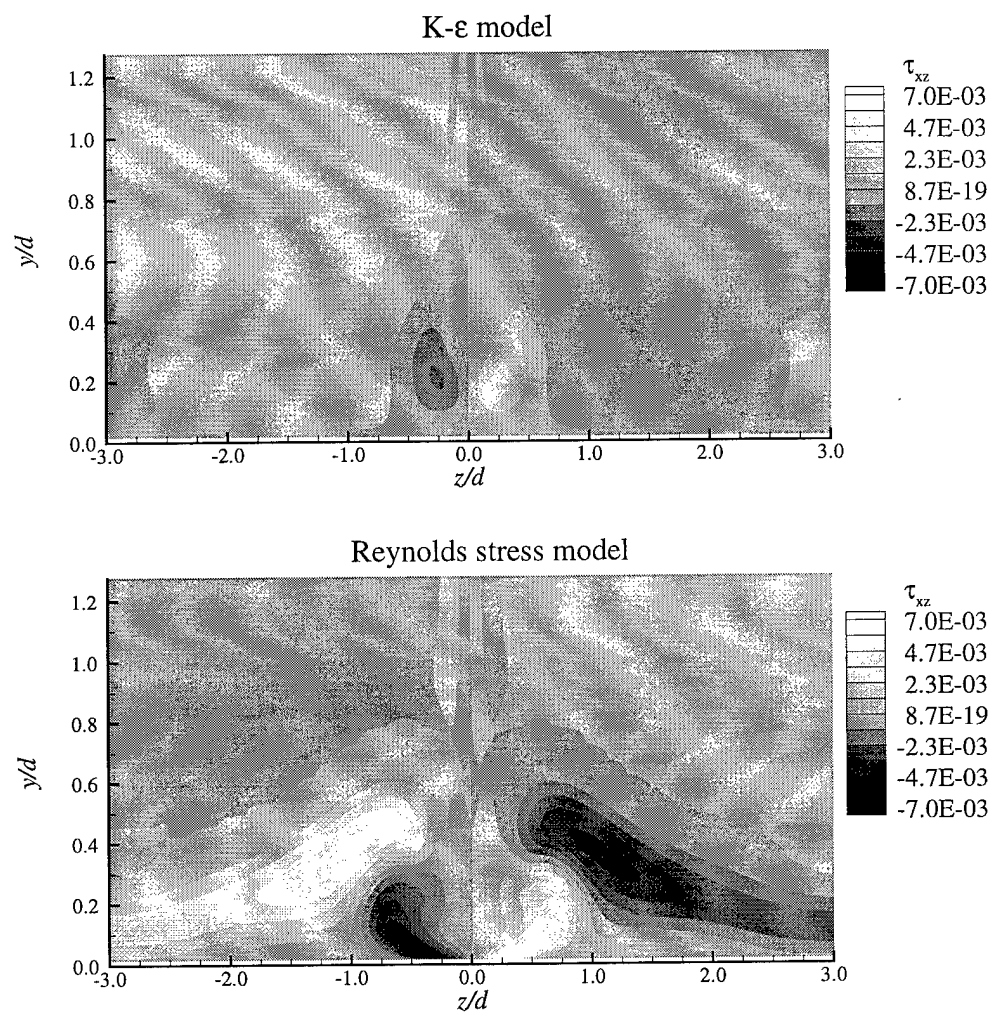


Figure 97. Comparison of turbulence model predictions of  $\tau_{xz}$  in the boundary layer at station 20

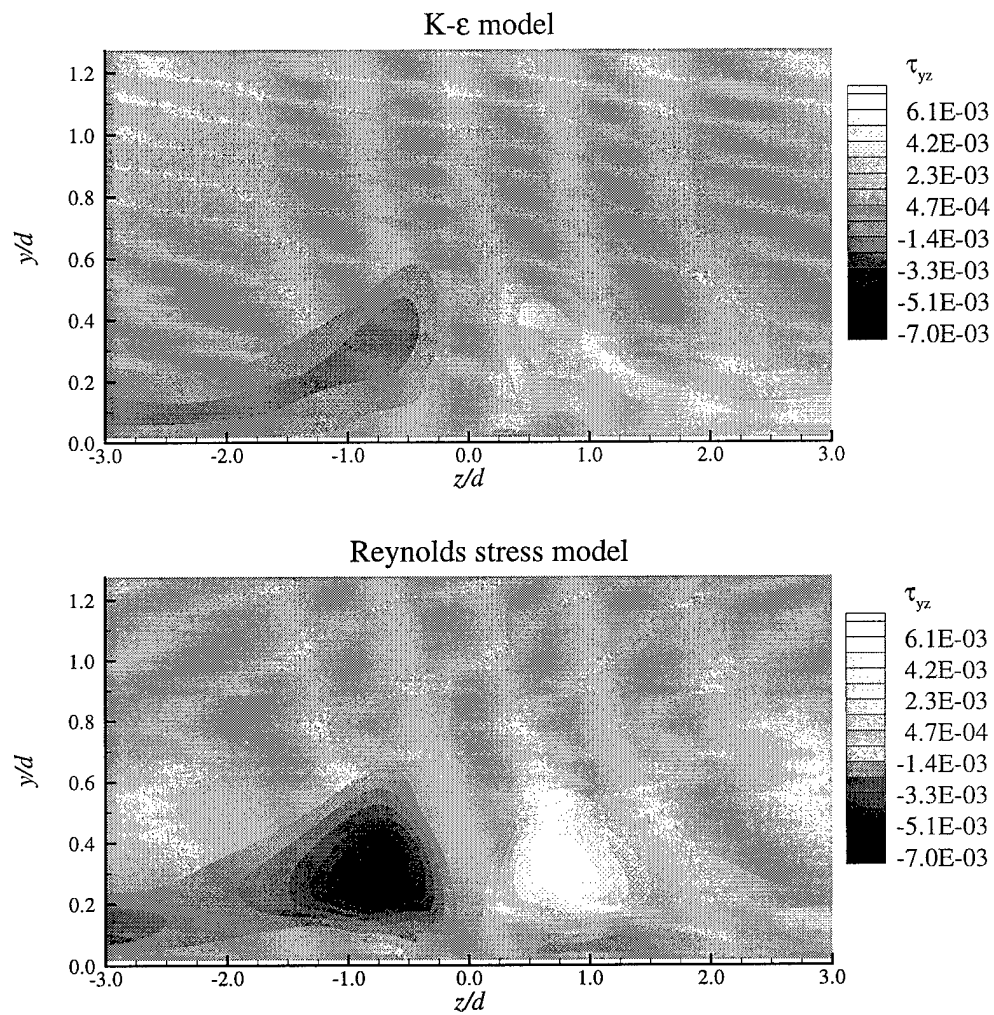


Figure 98. Comparison of turbulence model predictions of  $\tau_{yz}$  in the boundary layer at station 20

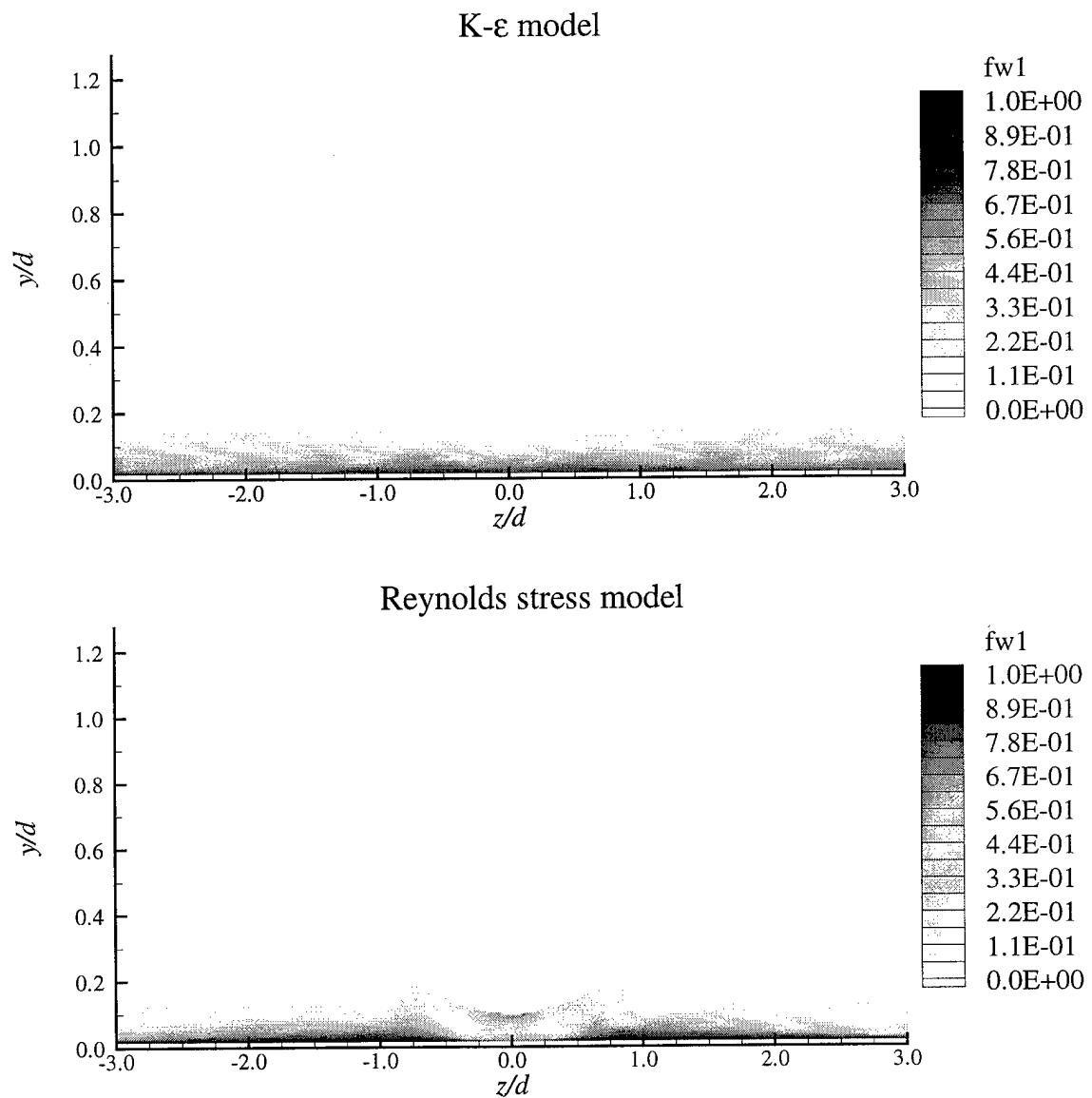


Figure 99. Magnitude of anisotropic wall damping function  $f_{w1}$  in the boundary layer

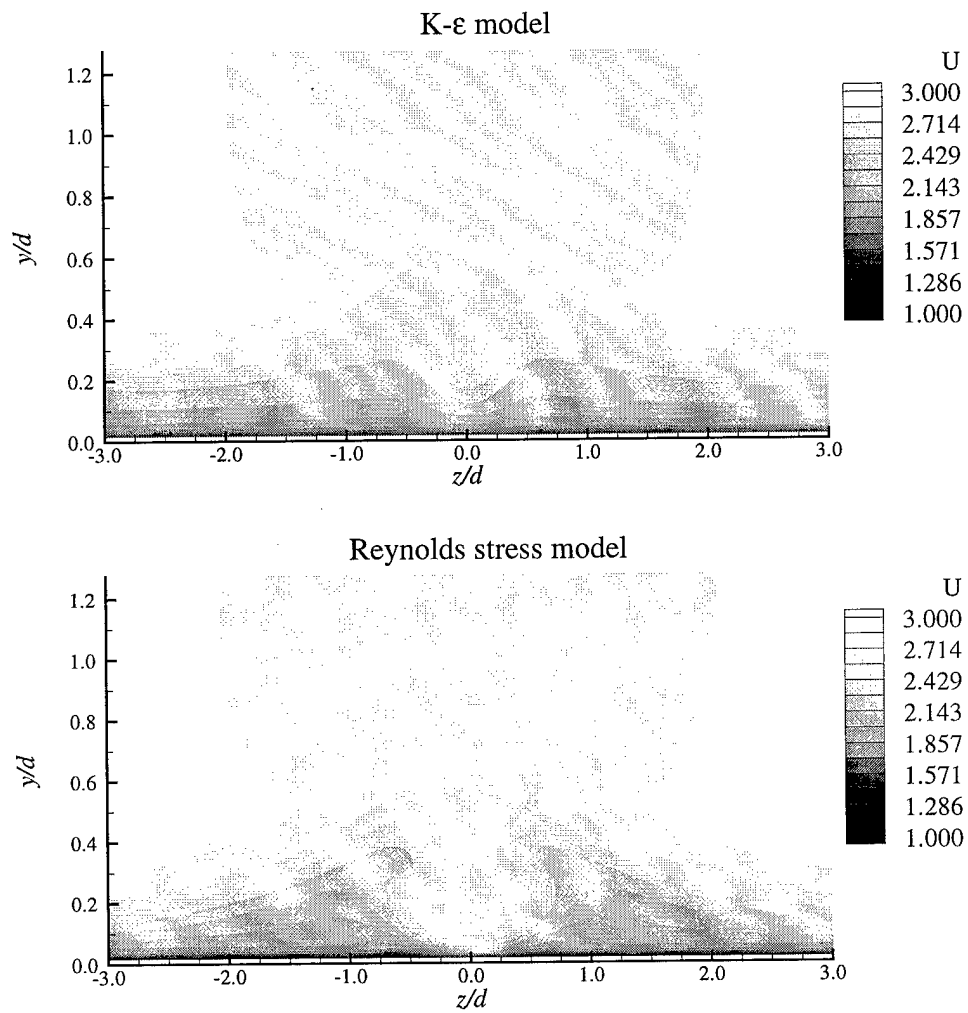


Figure 100. Comparison of turbulence model predictions of  $U$  component of velocity in the boundary layer at station 20



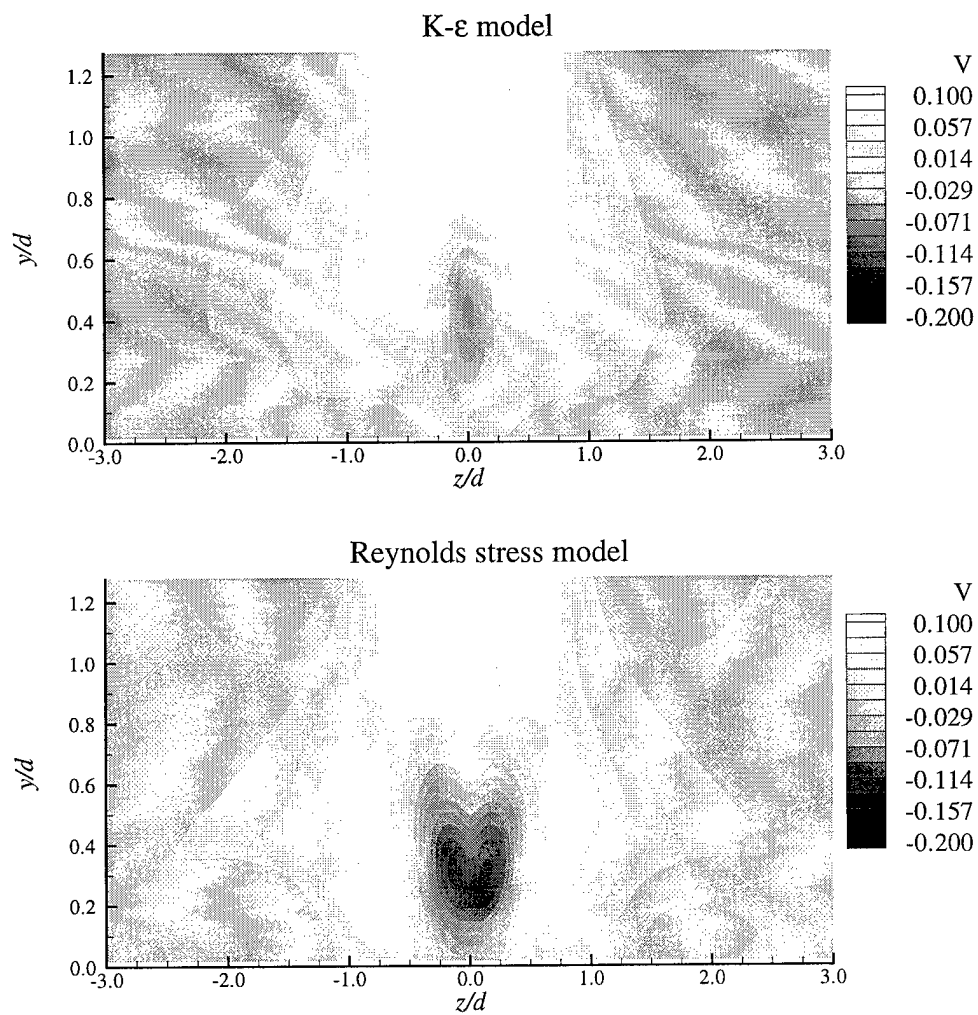


Figure 101. Comparison of turbulence model predictions of  $V$  component of velocity in the boundary layer at station 20

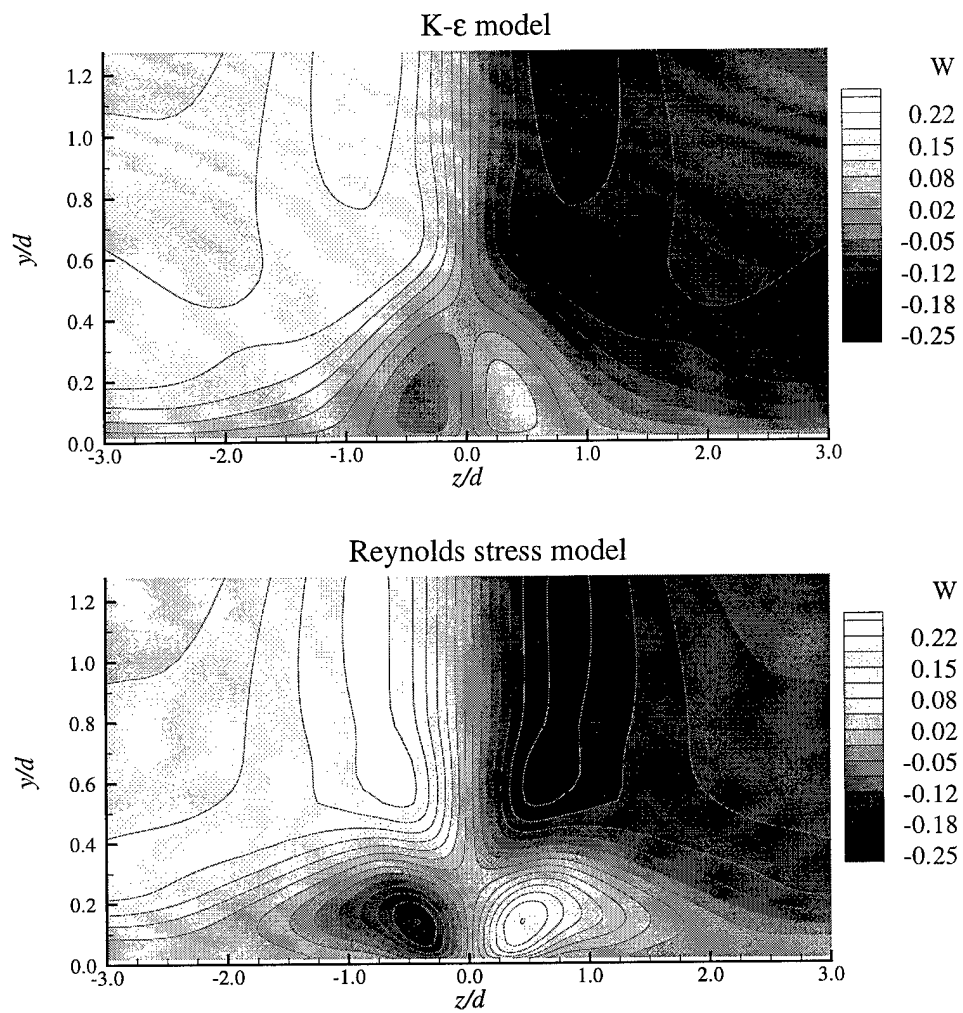


Figure 102. Comparison of turbulence model predictions of  $W$  component of velocity in the boundary layer at station 20

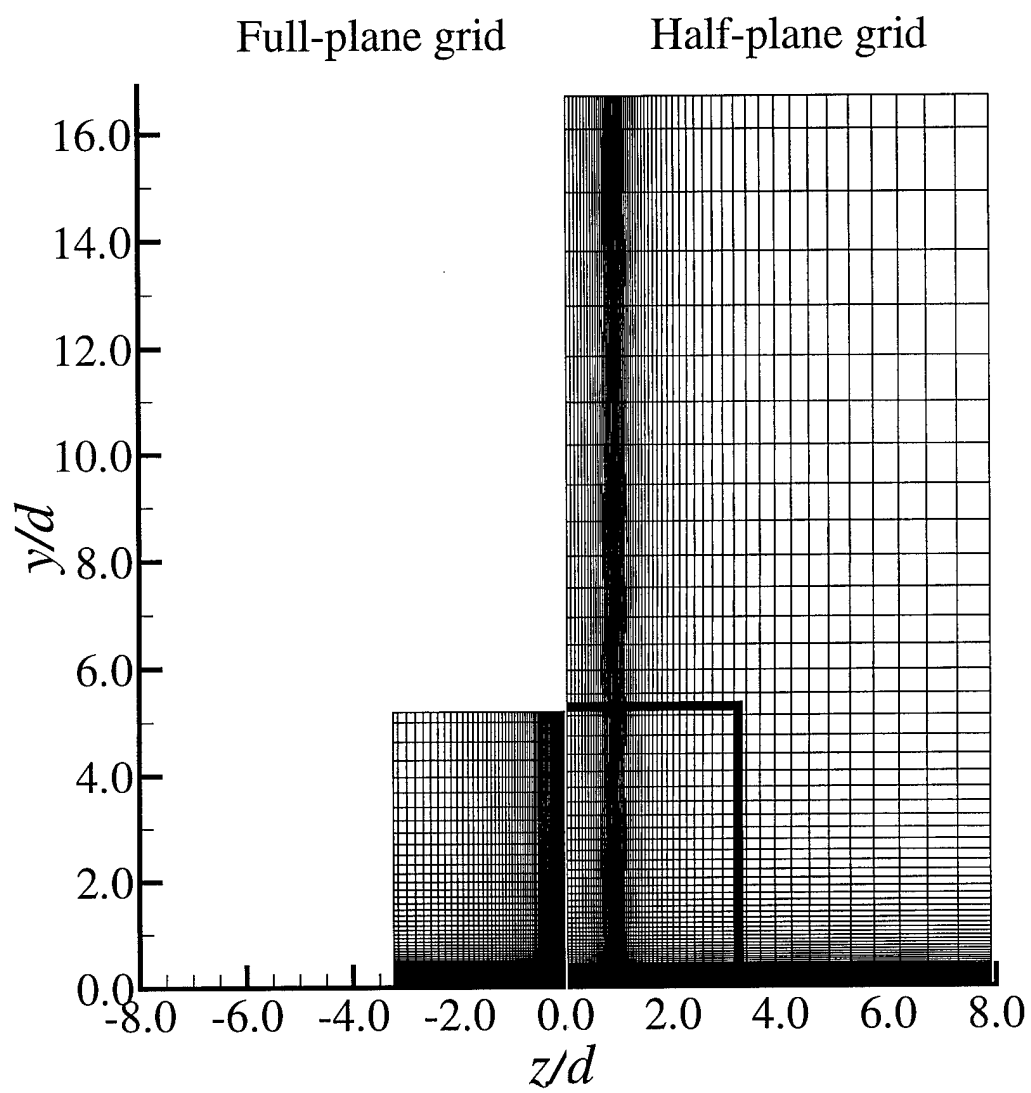


Figure 103. Comparison of cross-plane grid spacing

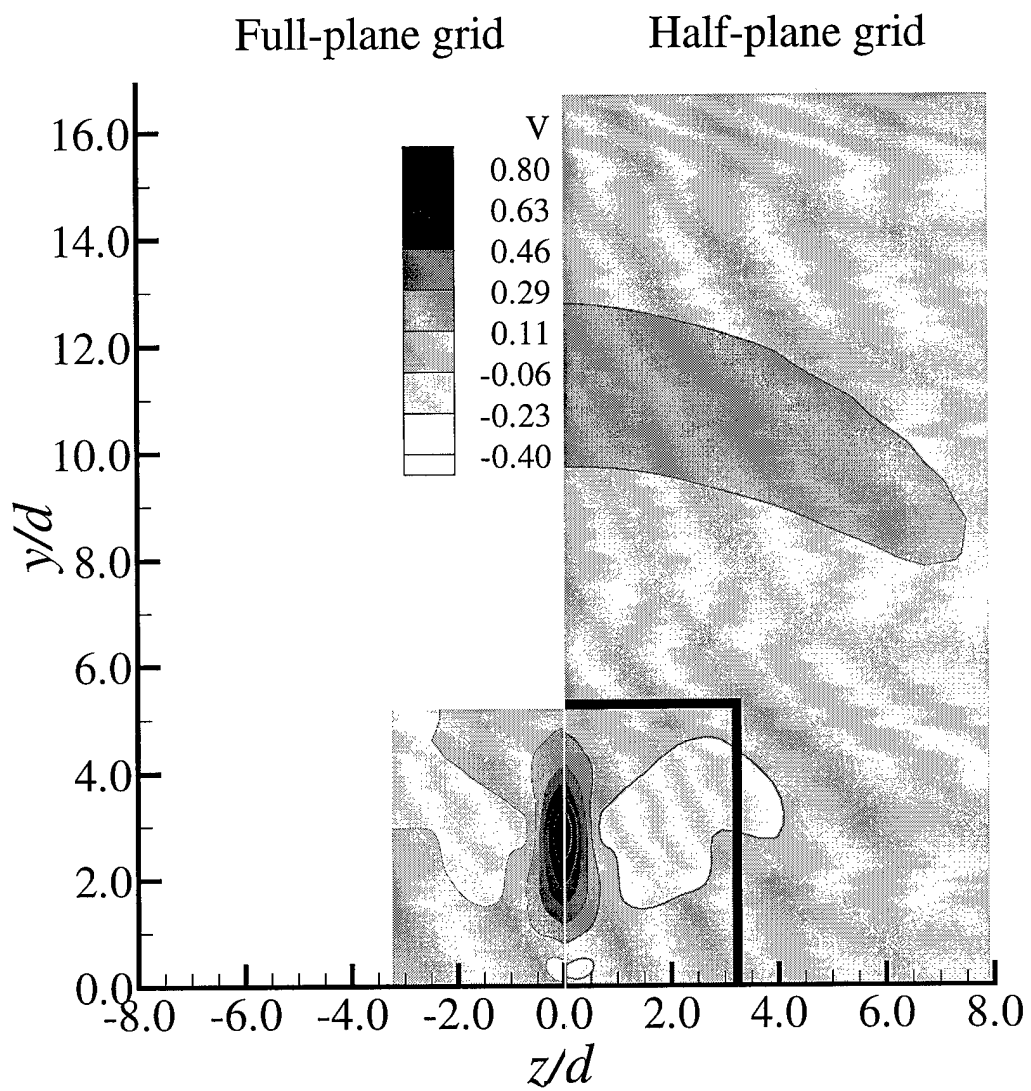


Figure 104. Symmetry boundary condition evaluation for the  $V$  component of velocity

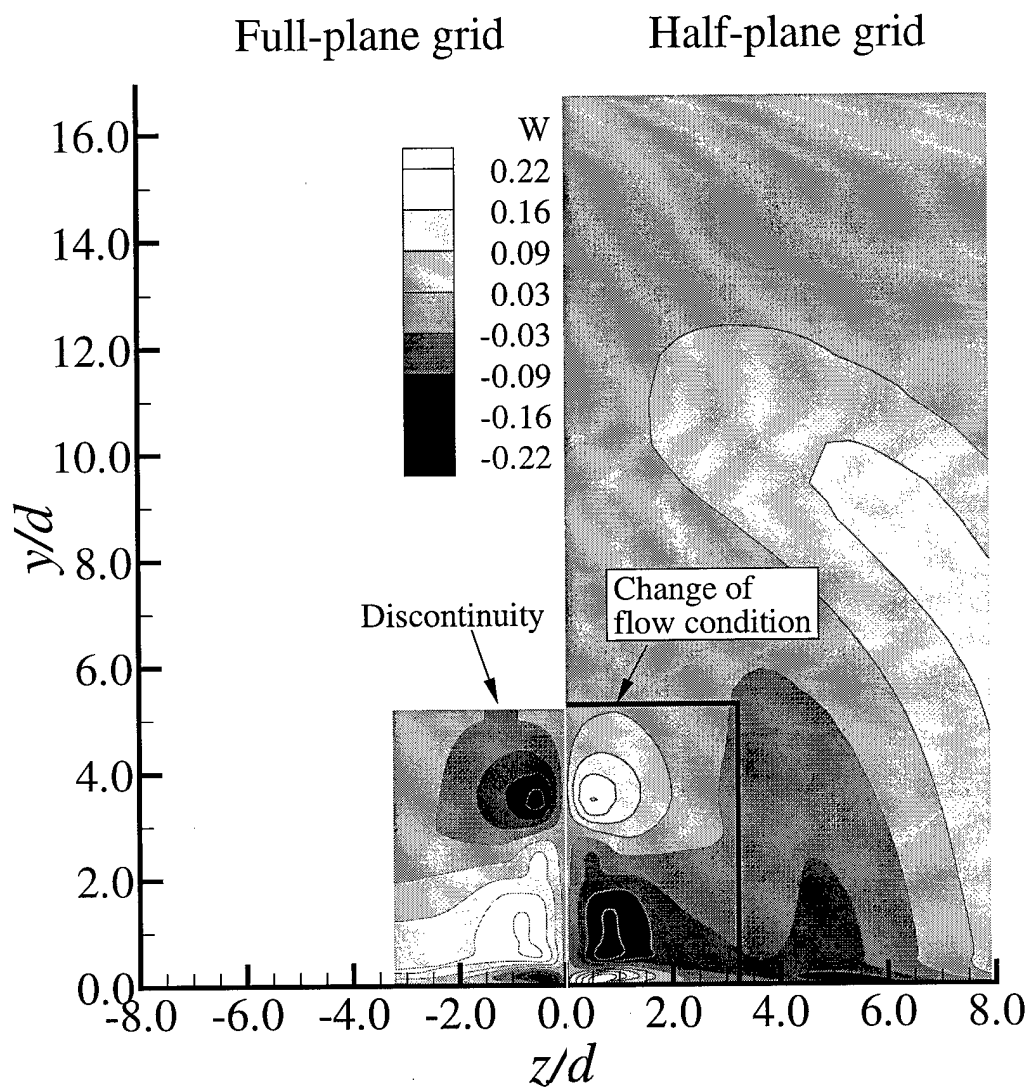


Figure 105. Symmetry boundary condition evaluation for the  $W$  component of velocity

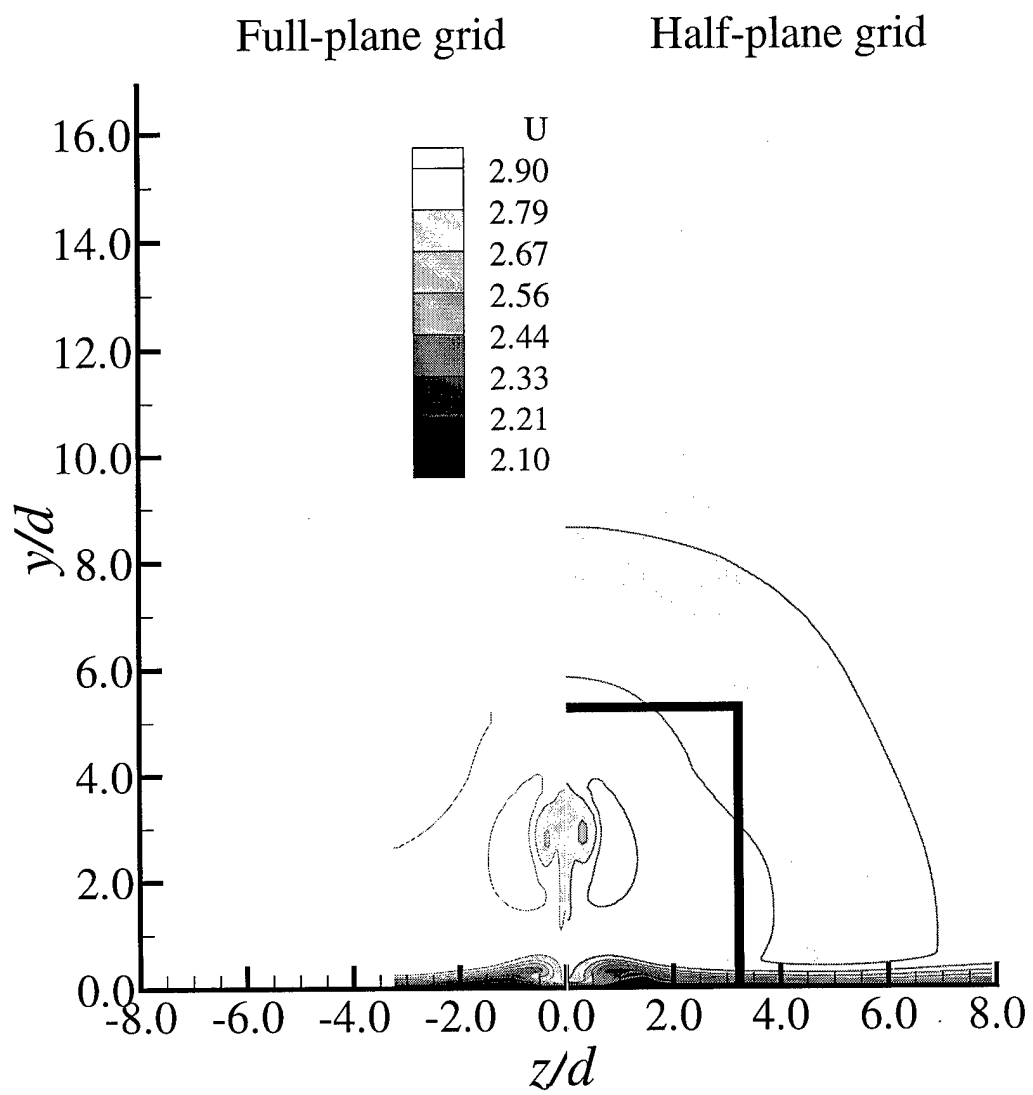


Figure 106. Symmetry boundary condition evaluation for the  $U$  component of velocity

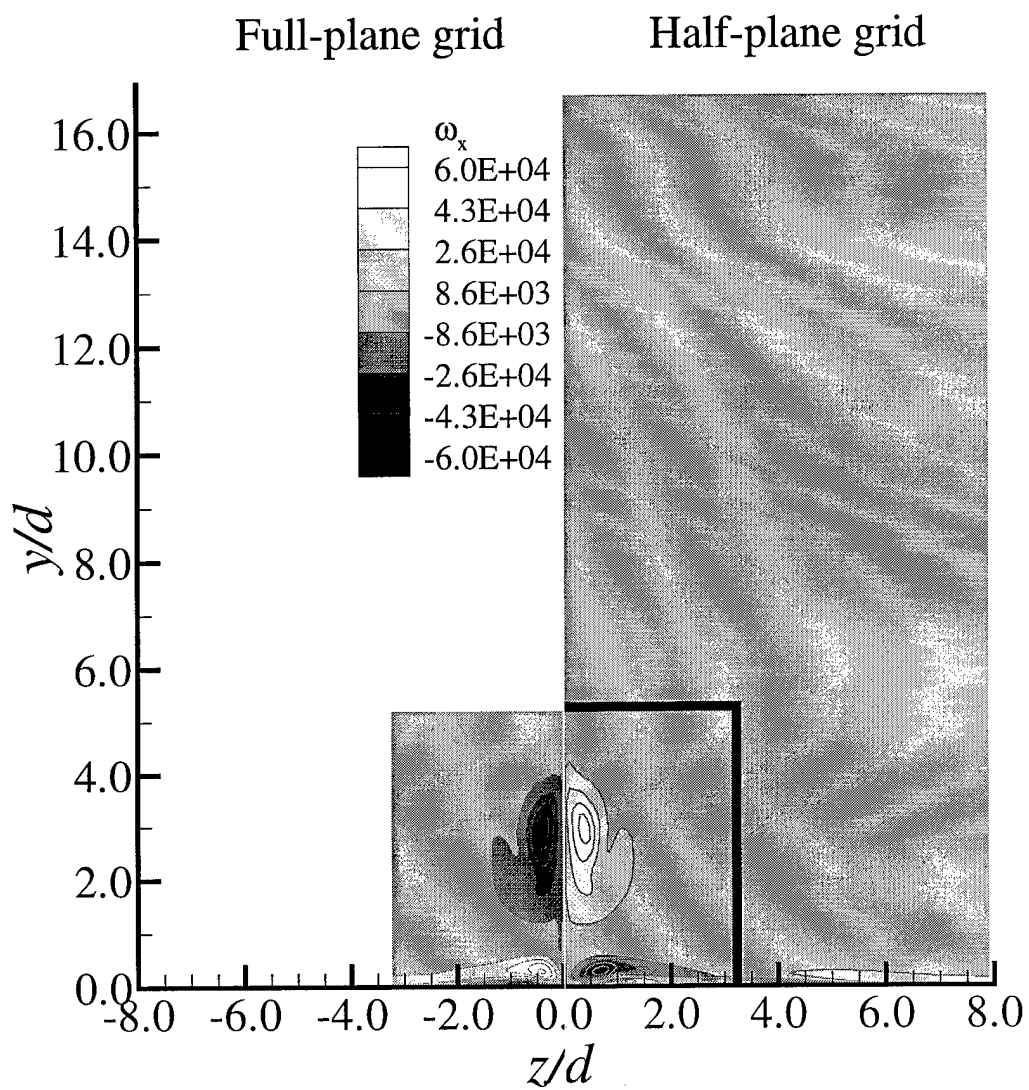


Figure 107. Symmetry boundary condition evaluation for  $\omega_x$

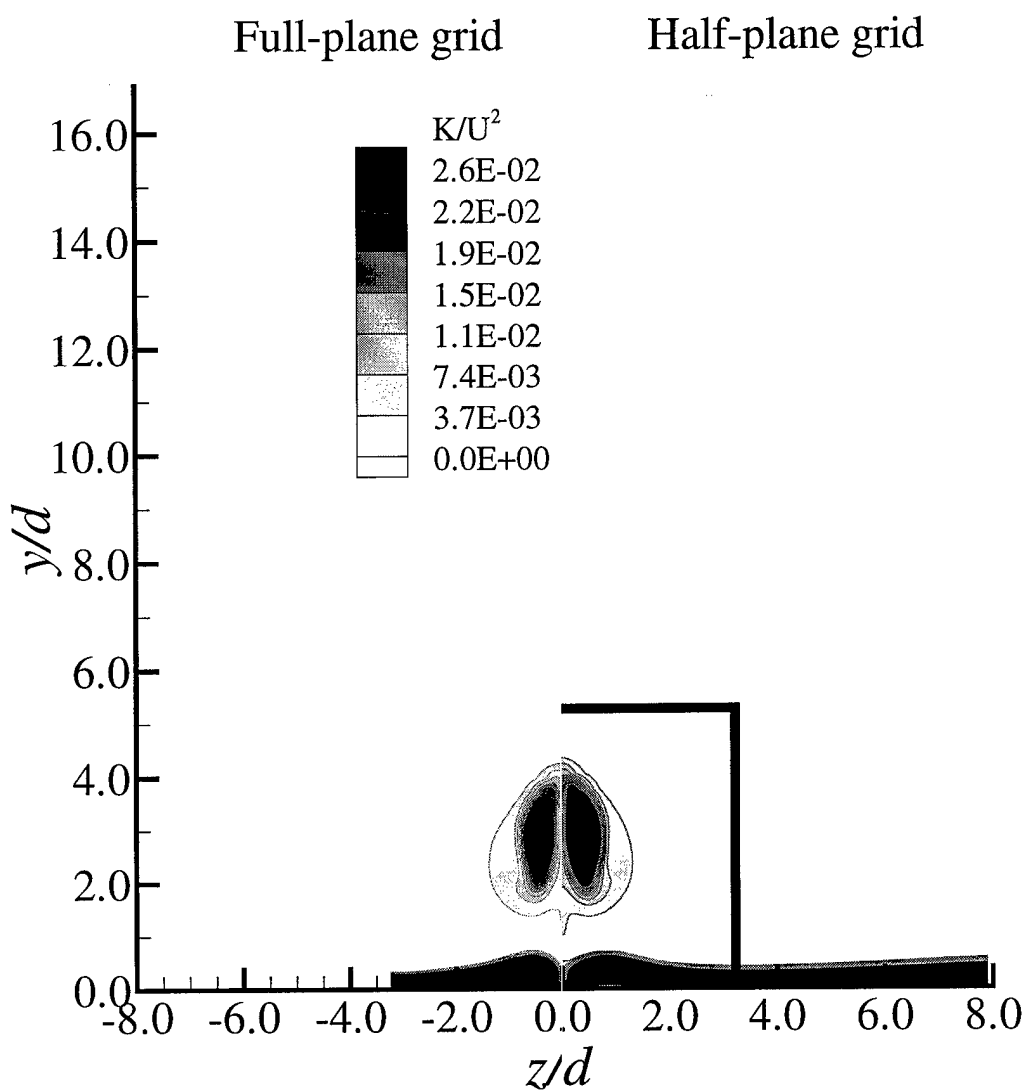


Figure 108. Symmetry boundary condition evaluation for  $K$



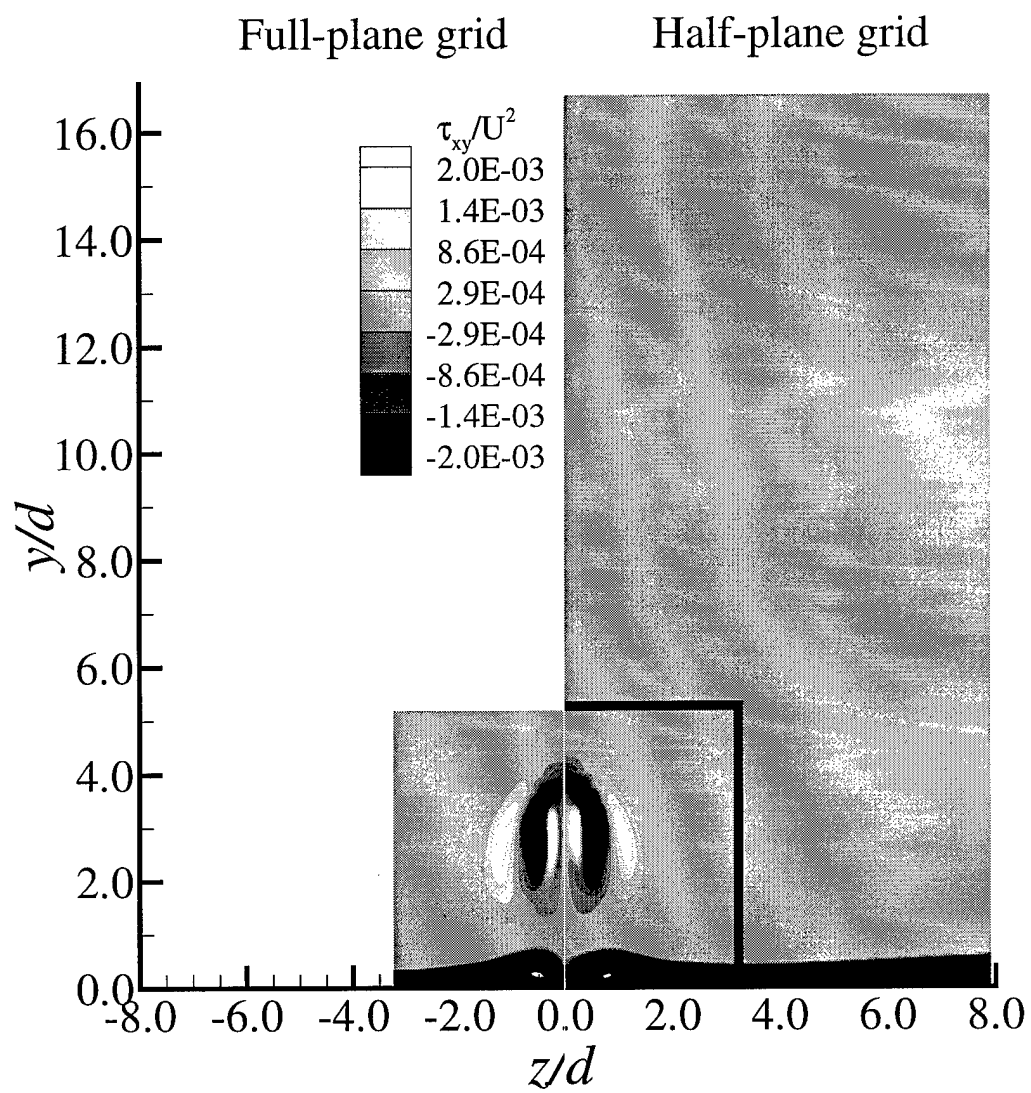


Figure 109. Symmetry boundary condition evaluation for  $\tau_{xy}$

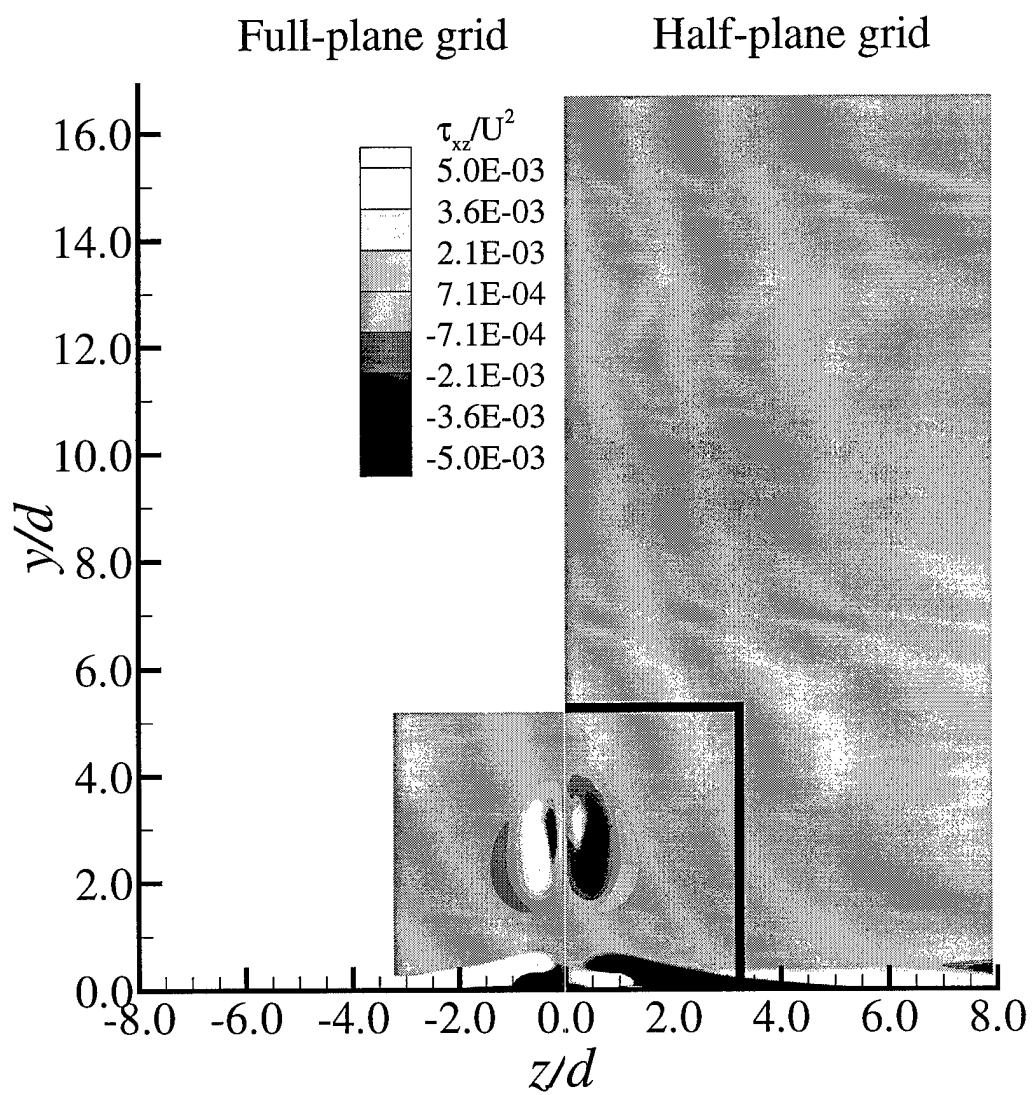


Figure 110. Symmetry boundary condition evaluation for  $\tau_{xz}$

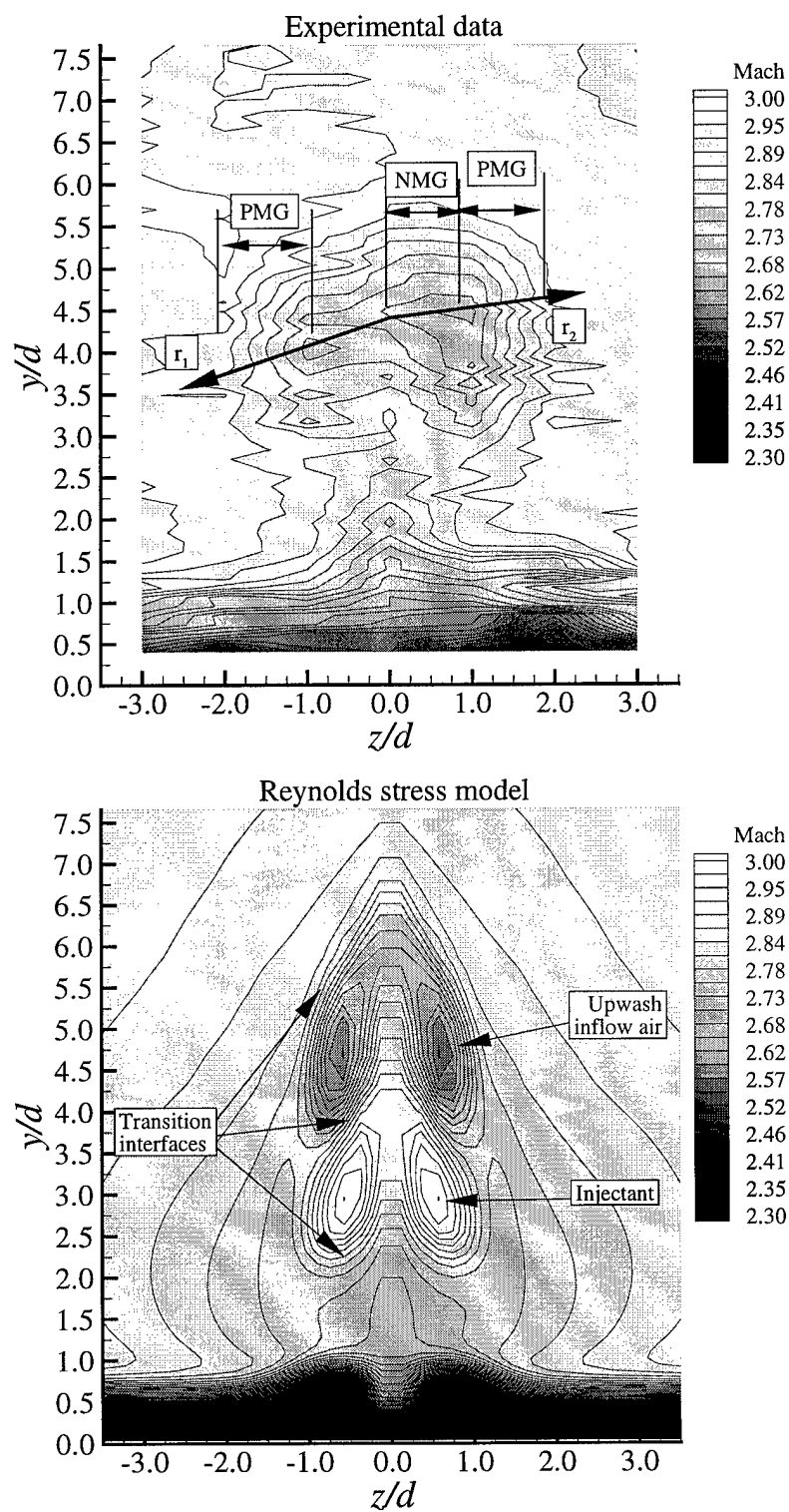


Figure 111. Comparison of experimental data and computational results of Mach number at station 40

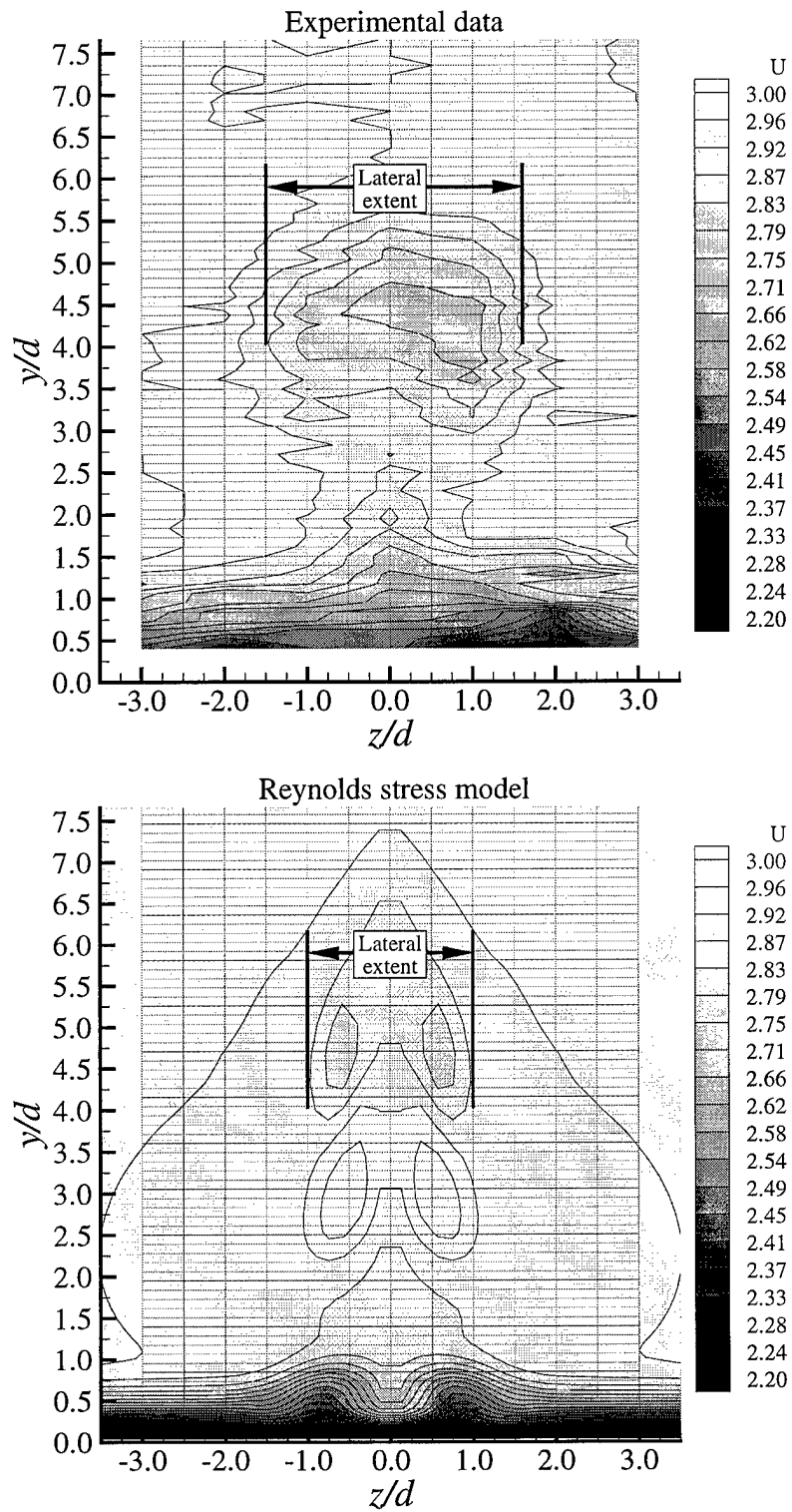


Figure 112. Comparison of experimental data and computational results of the  $U$  component of velocity at station 40

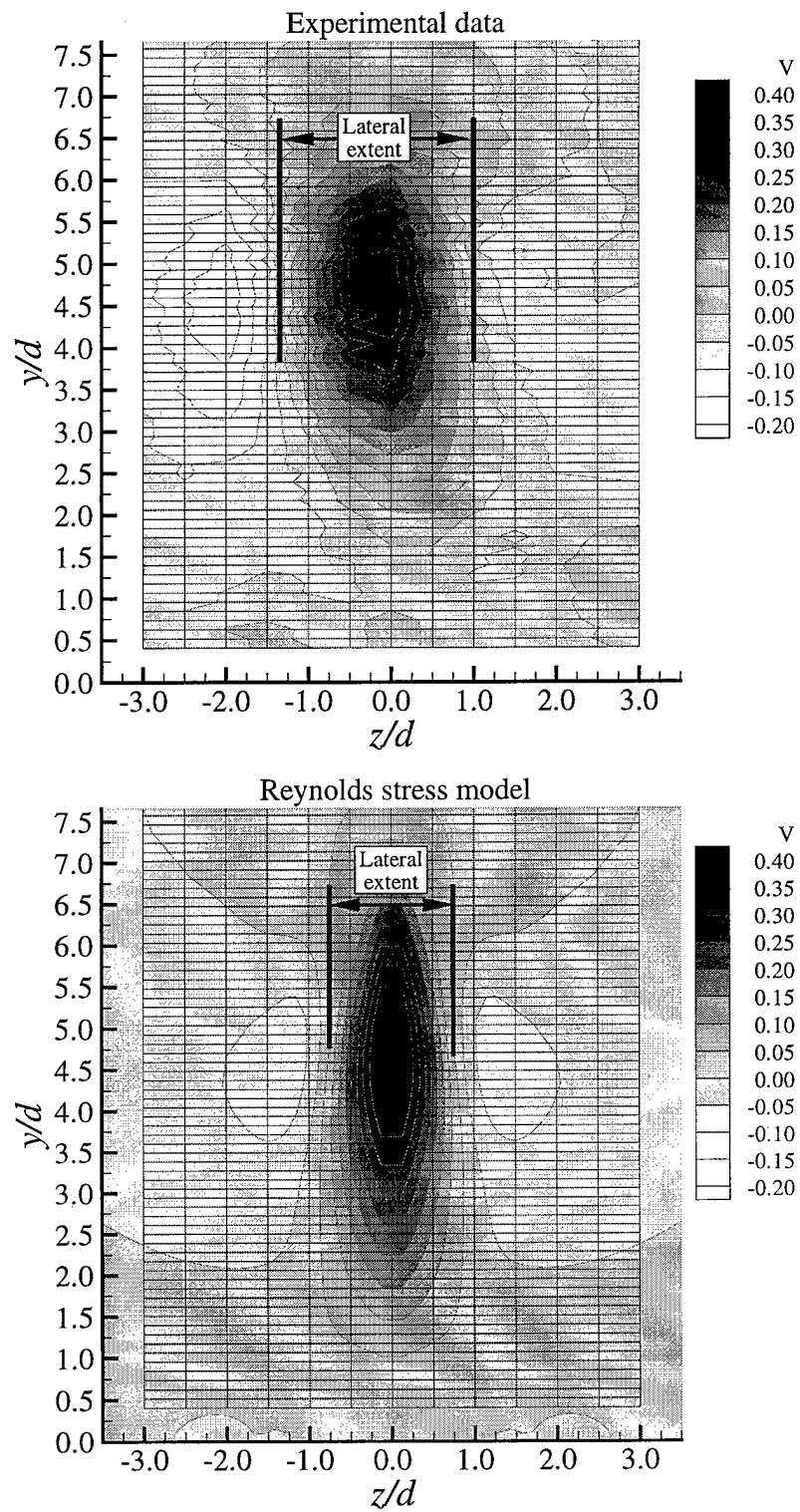


Figure 113. Comparison of experimental data and computational results of the  $V$  component of velocity at station 40

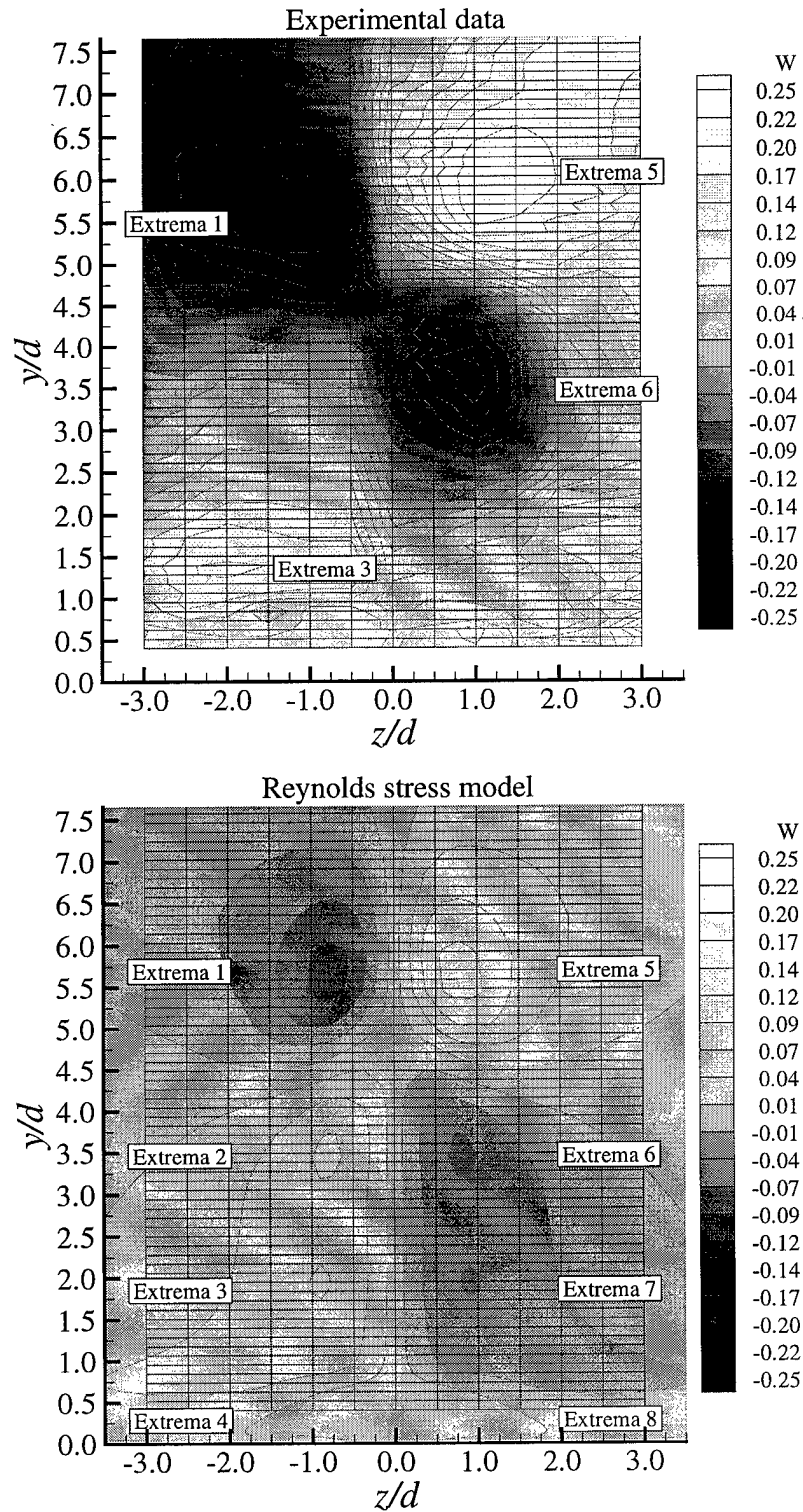


Figure 114. Comparison of experimental data and computational results of the  $W$  component of velocity at station 40

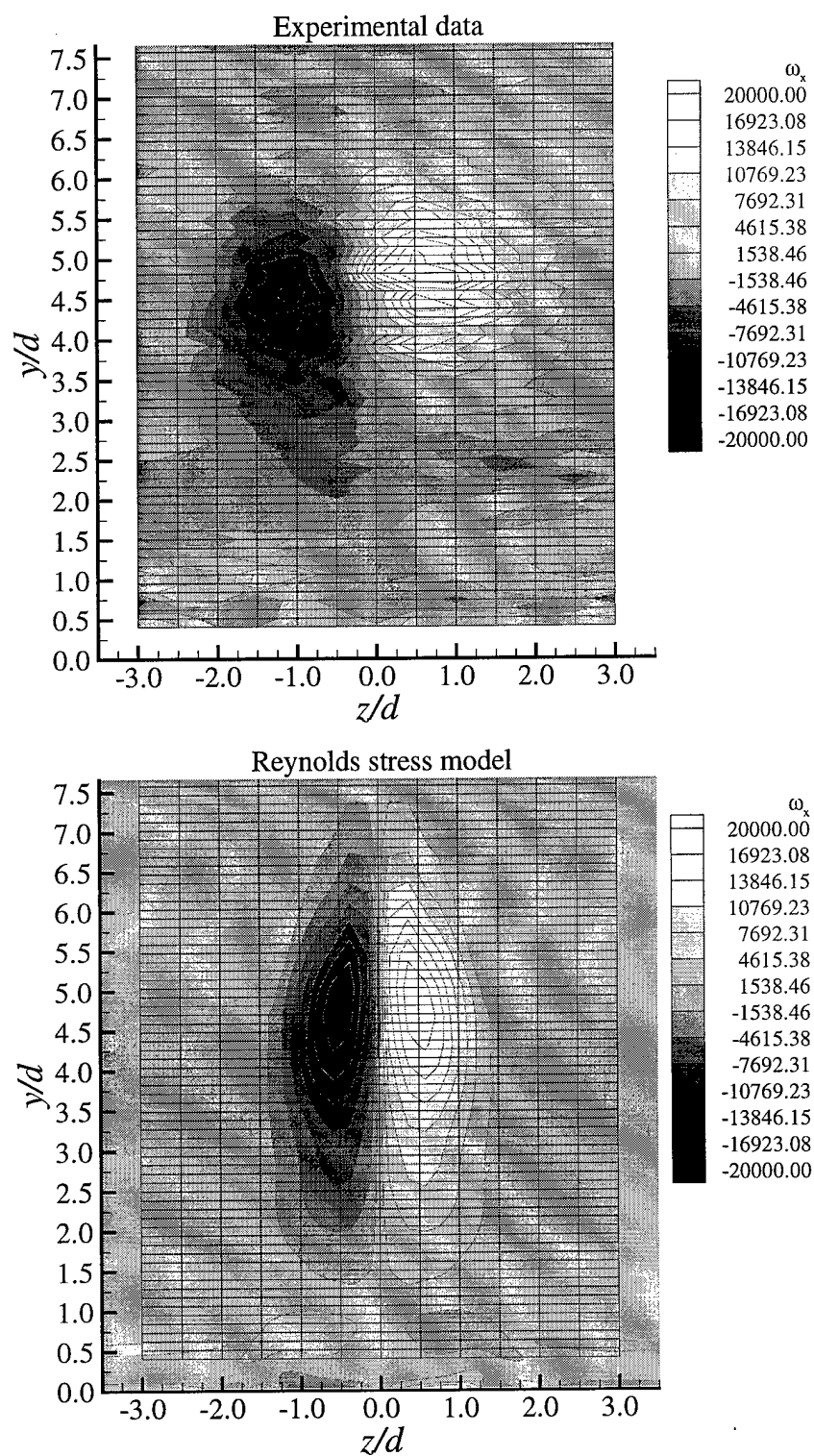


Figure 115. Comparison of experimental data and computational results for  $\omega_x$  at station 40

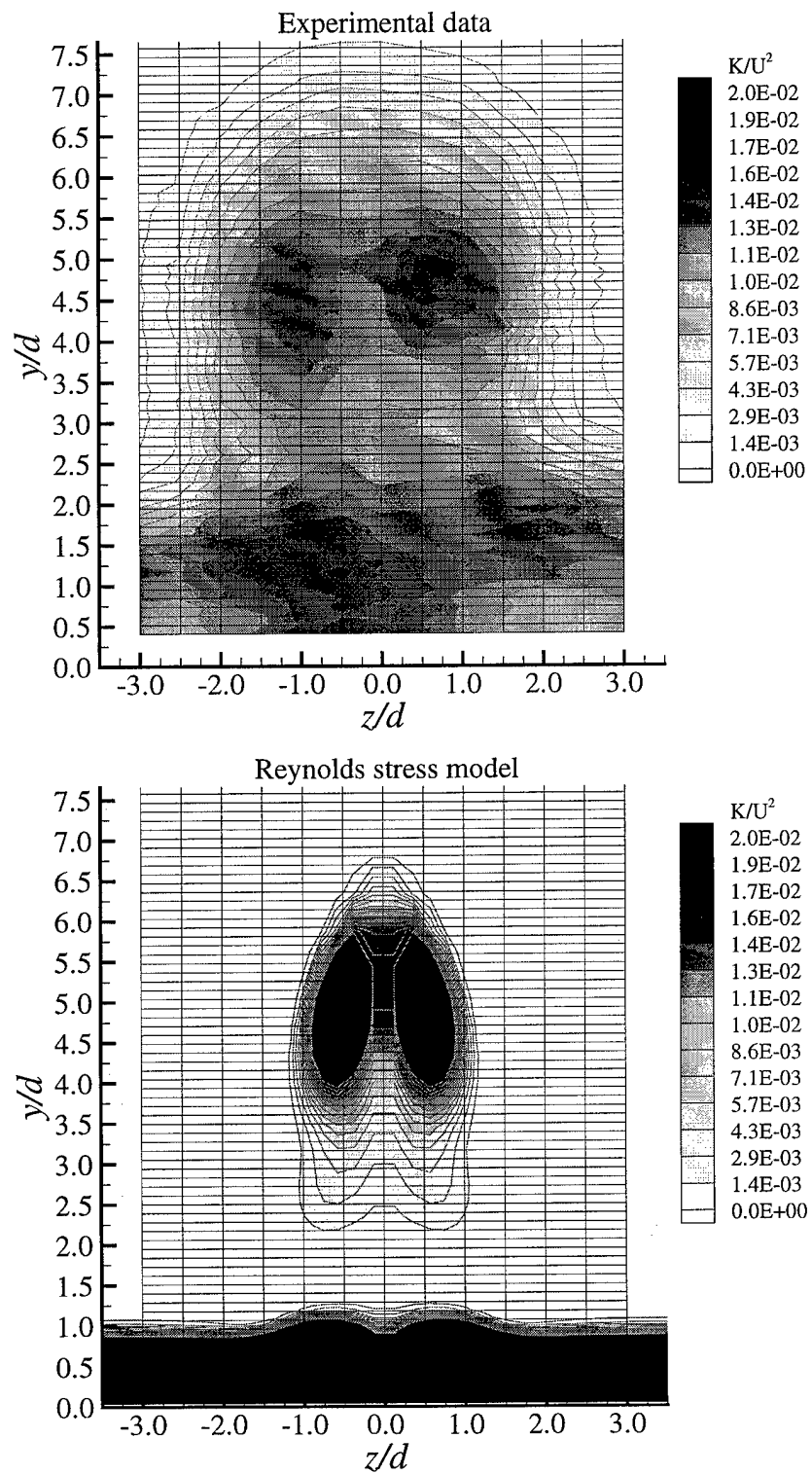


Figure 116. Comparison of experimental data and computational results for  $K$  at station 40



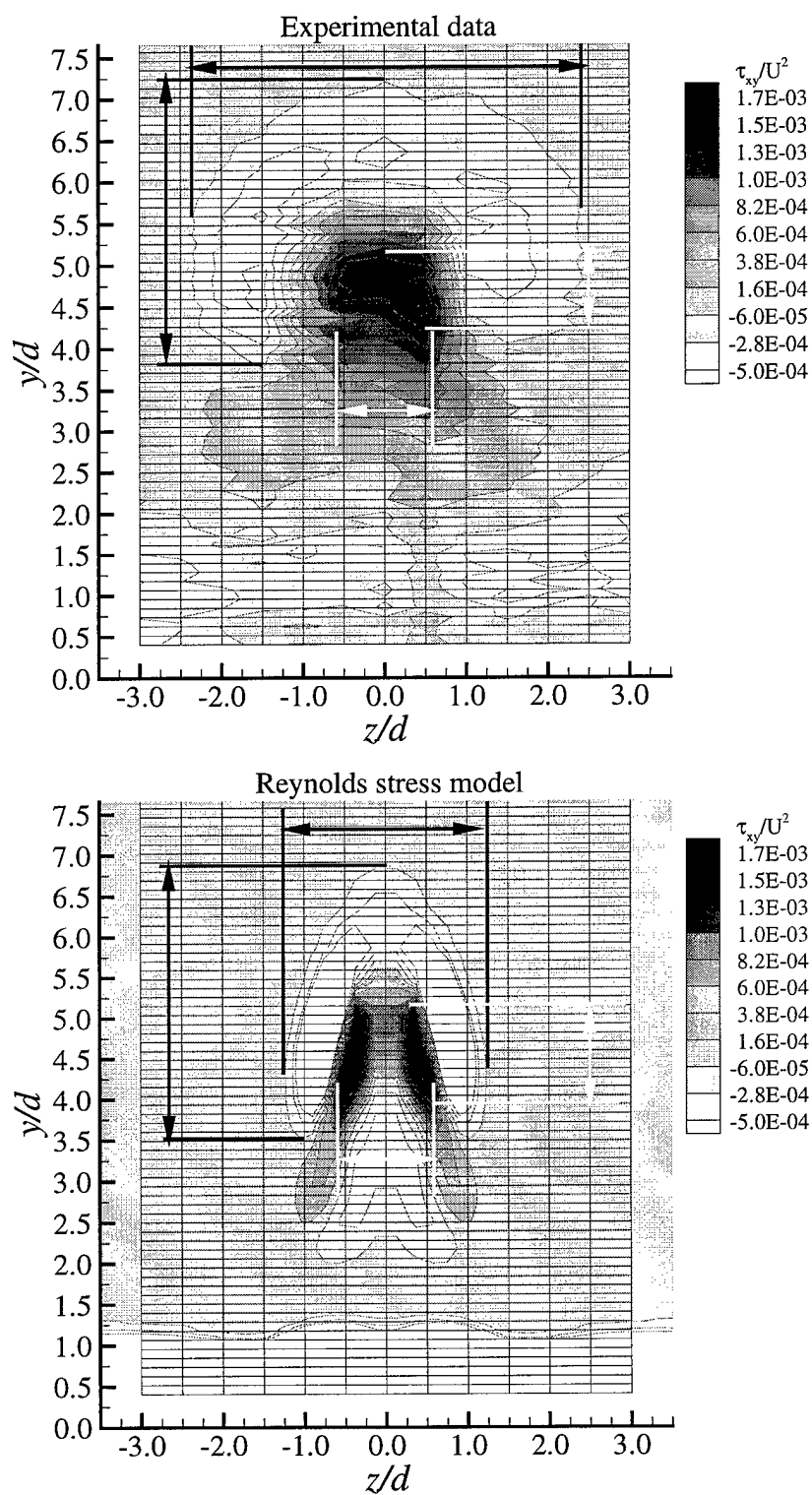


Figure 117. Comparison of experimental data and computational results for  $\tau_{xy}$  at station 40

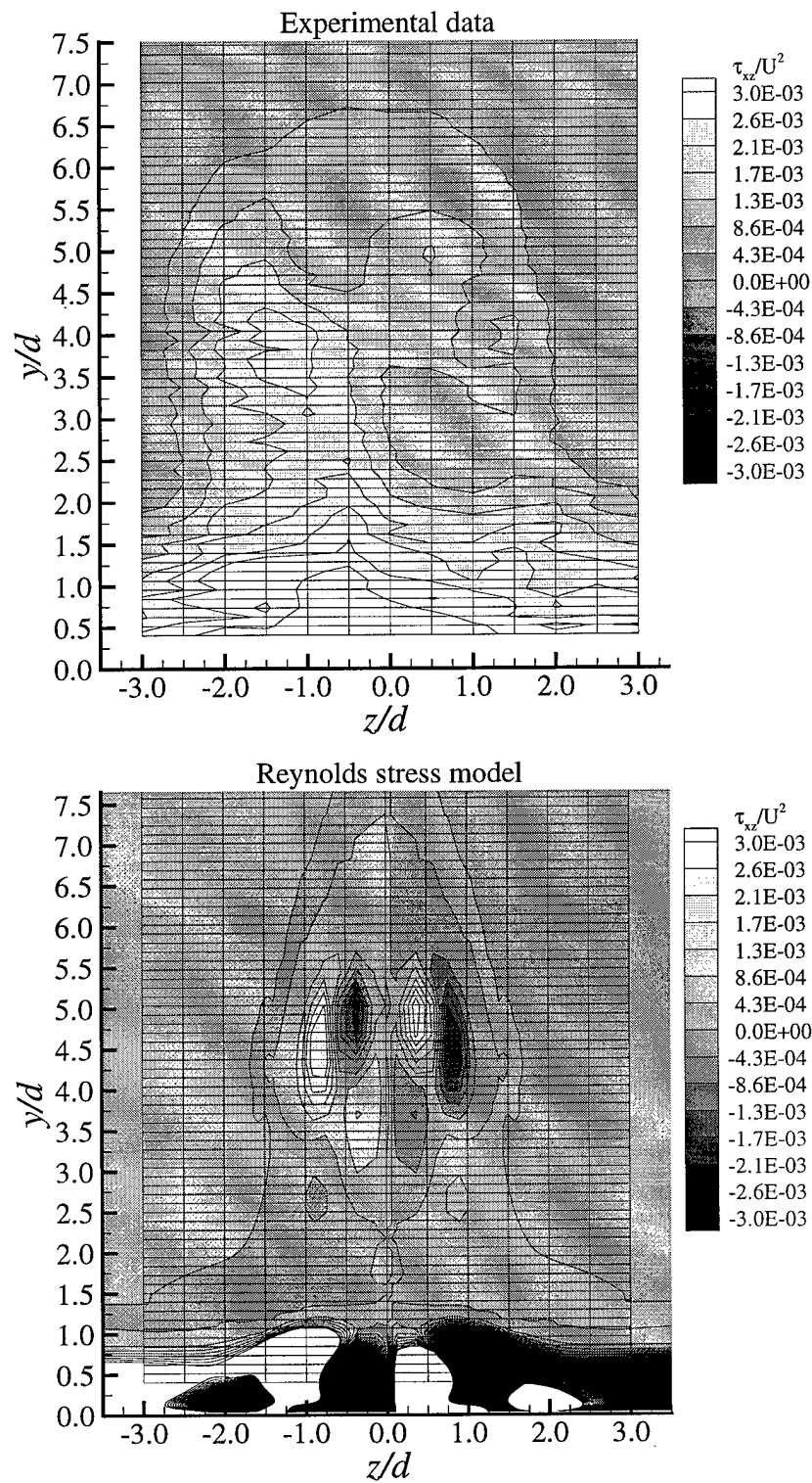


Figure 118. Comparison of experimental data and computational results for  $\tau_{xz}$  at station 40

# Reynolds stress model

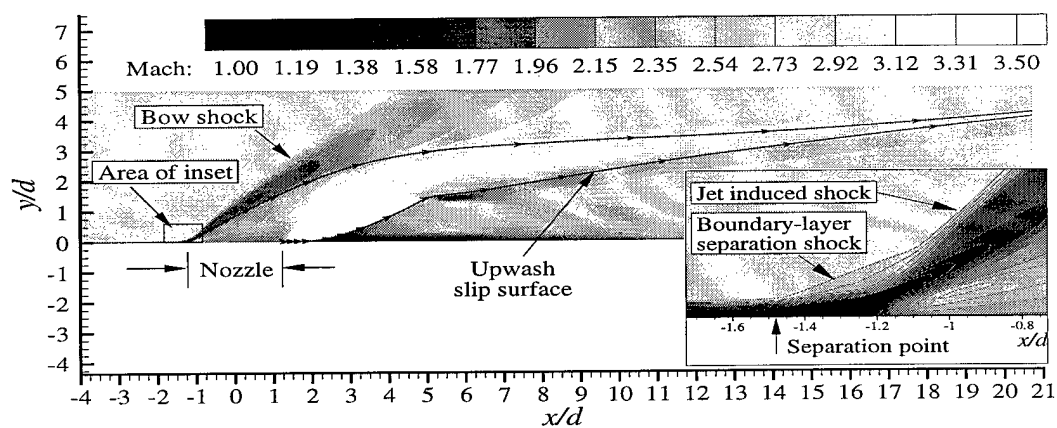


Figure 119. Mach contours at test section centerline

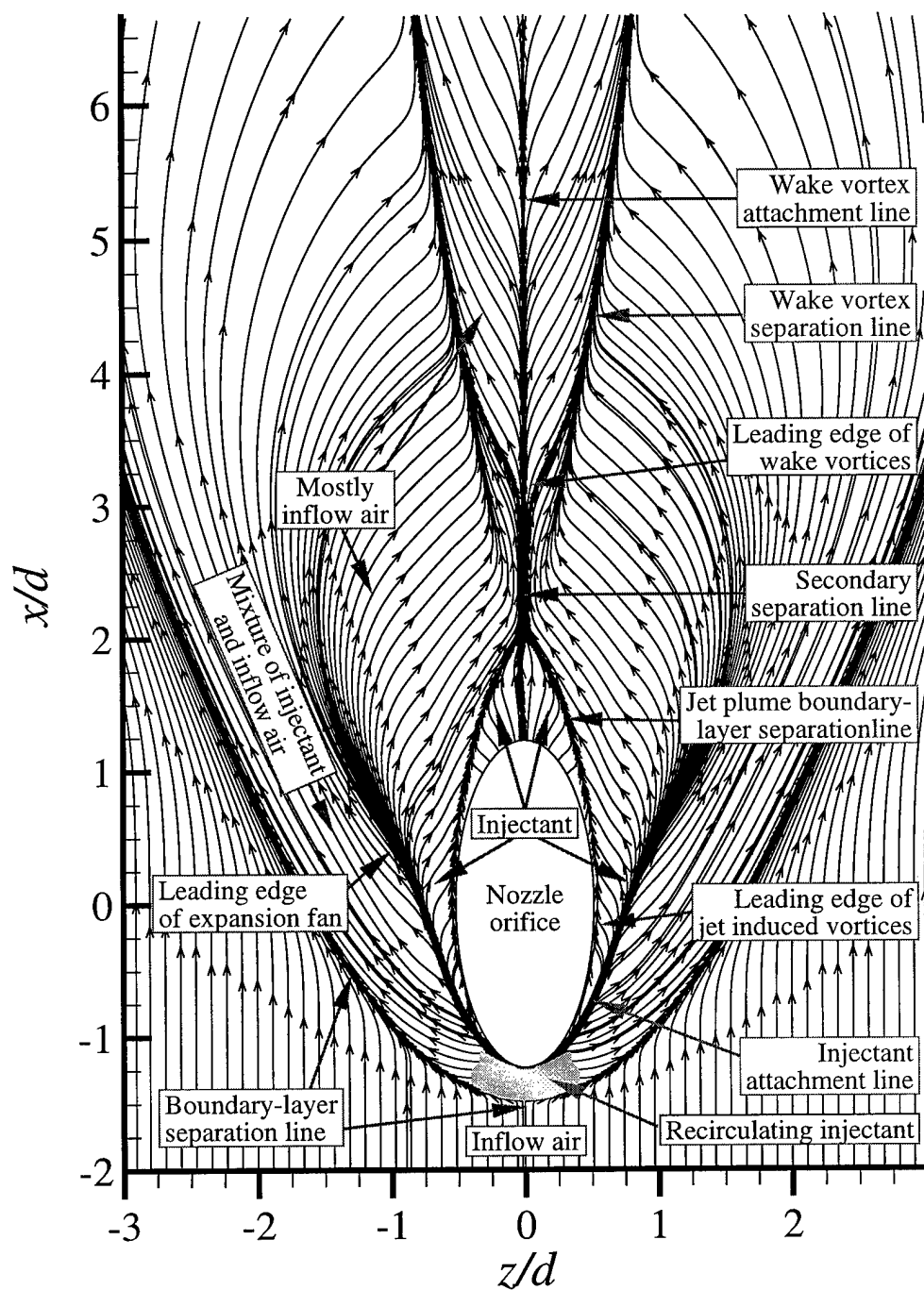


Figure 120. Near field numerical oil smear

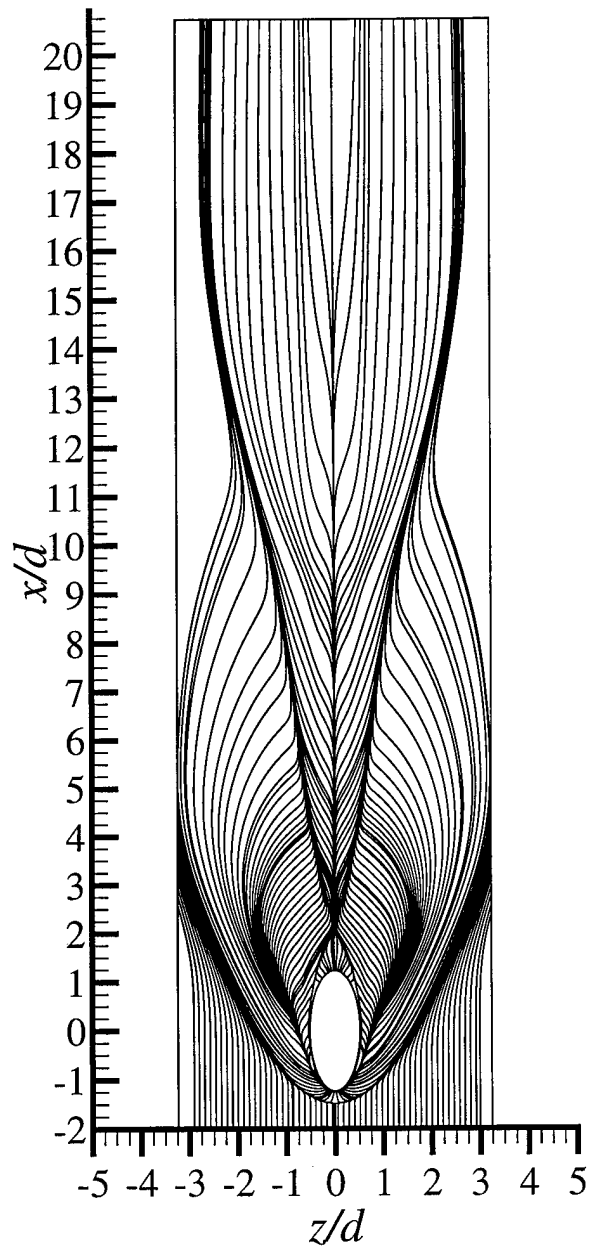


Figure 121. Far field numerical oil smear

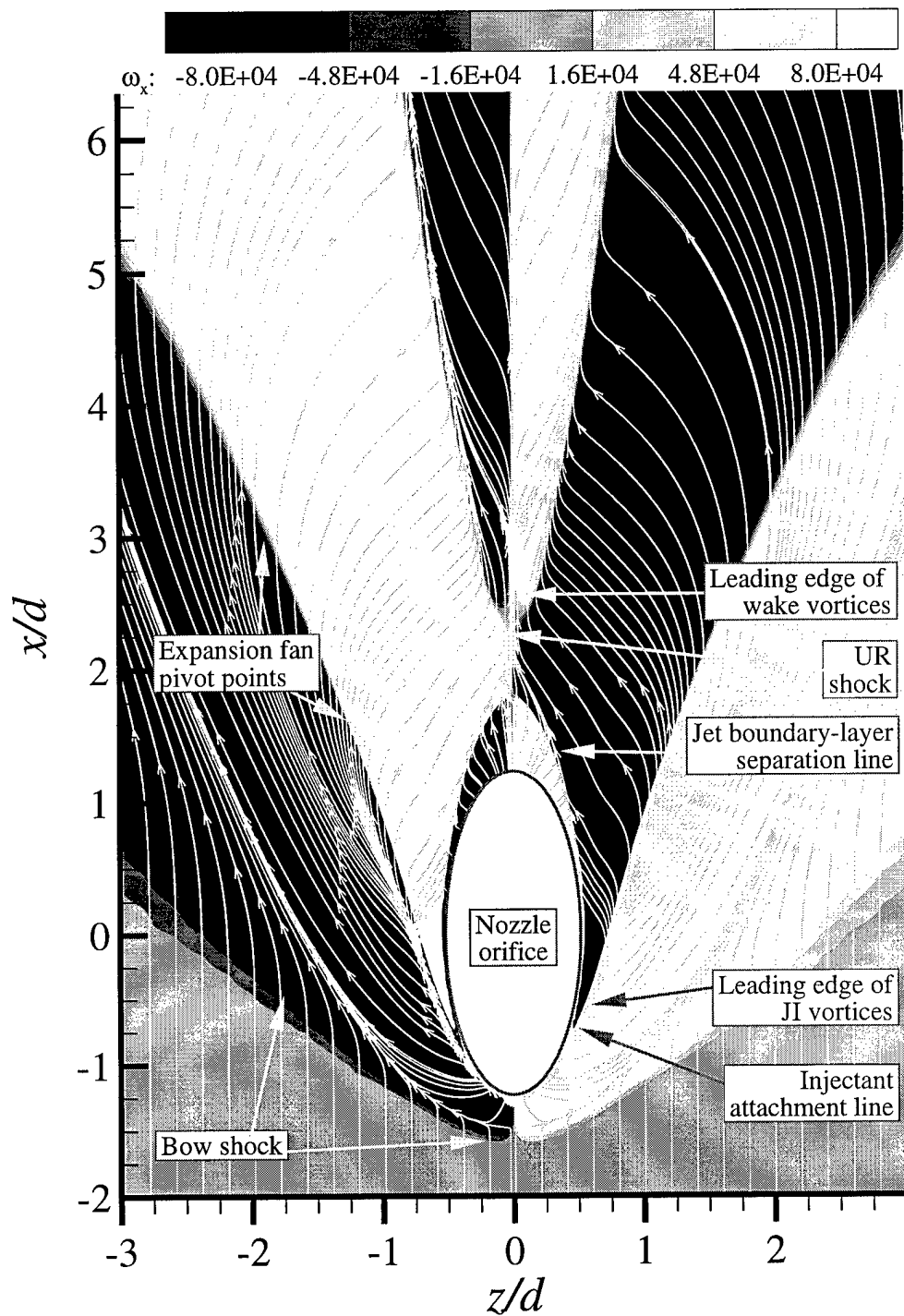


Figure 122.  $\omega_x$  contours at test section surface

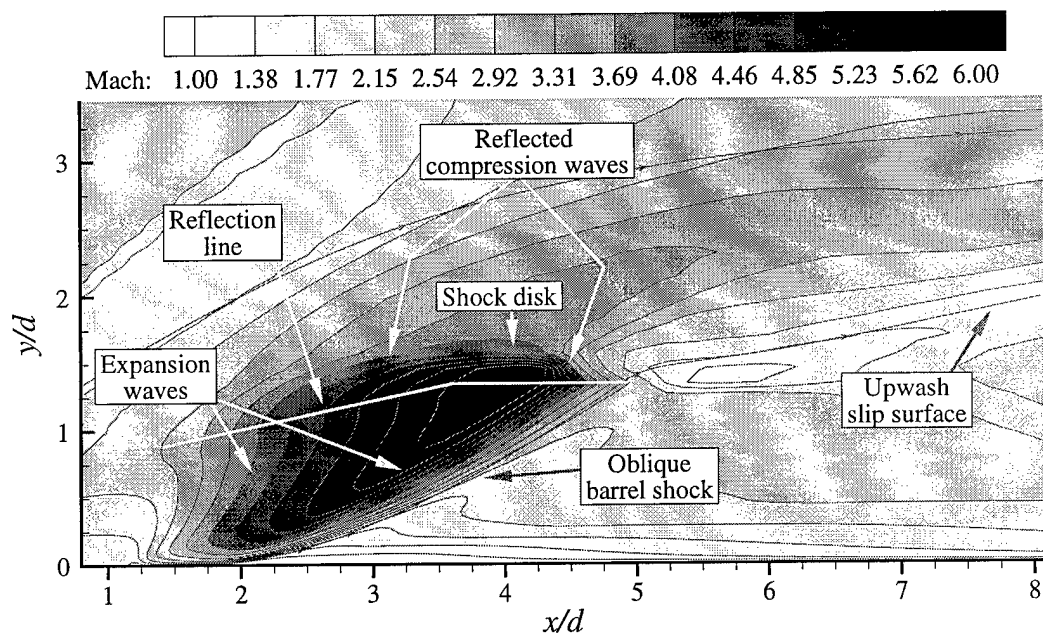


Figure 123. Expansion and shock structure in  $x - y$  plane ( $z/d = 0.0$ )

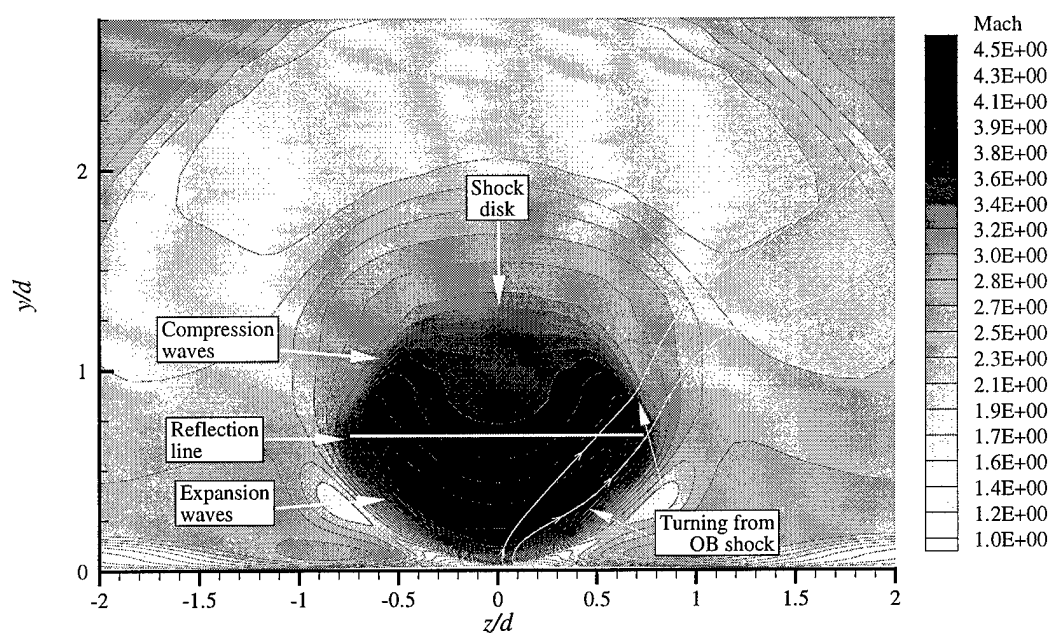


Figure 124. Expansion and shock structure in  $y - z$  plane ( $x/d = 2.00$ )



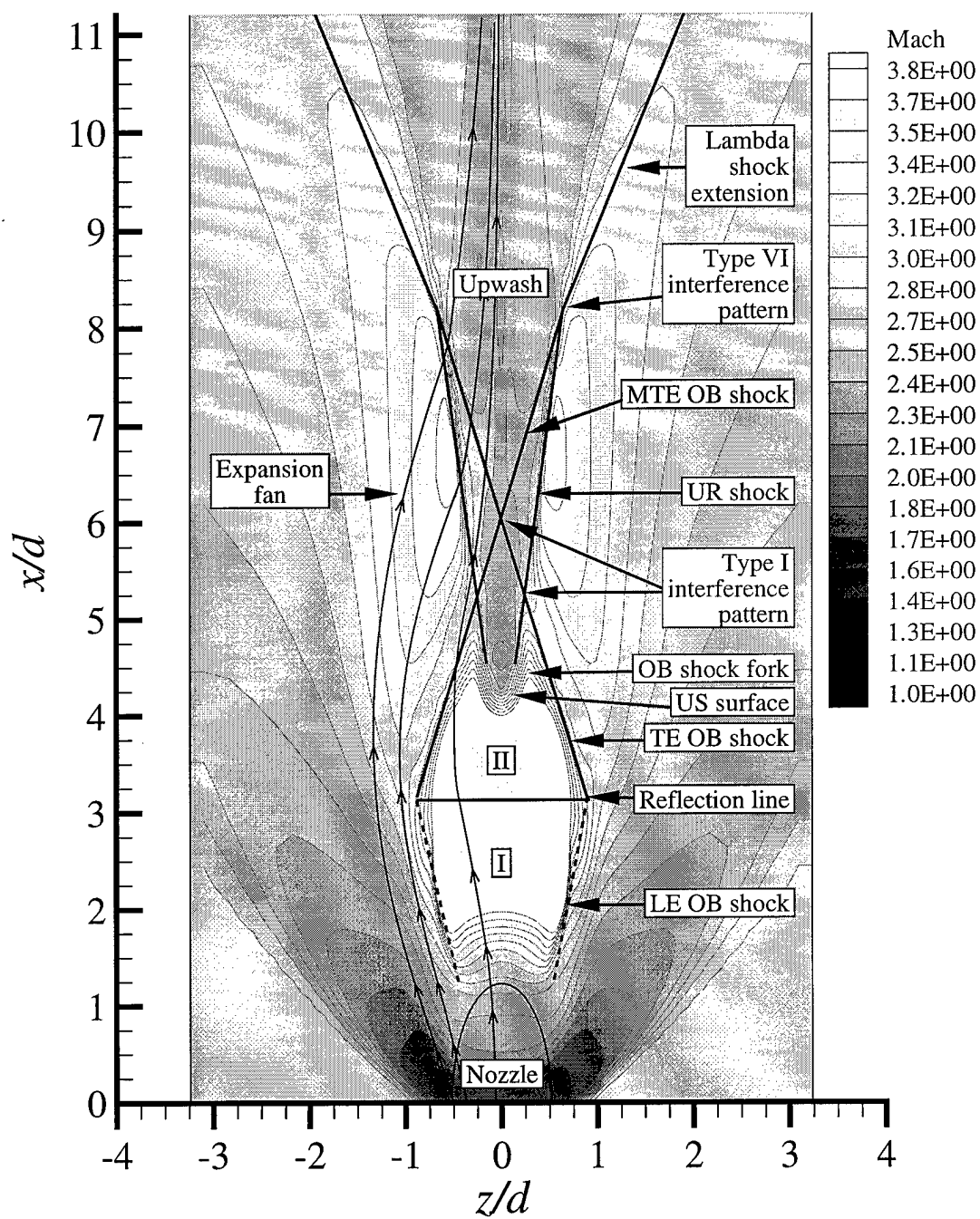


Figure 125. Expansion and shock structure in  $x - z$  plane ( $y/d = 0.91$ )

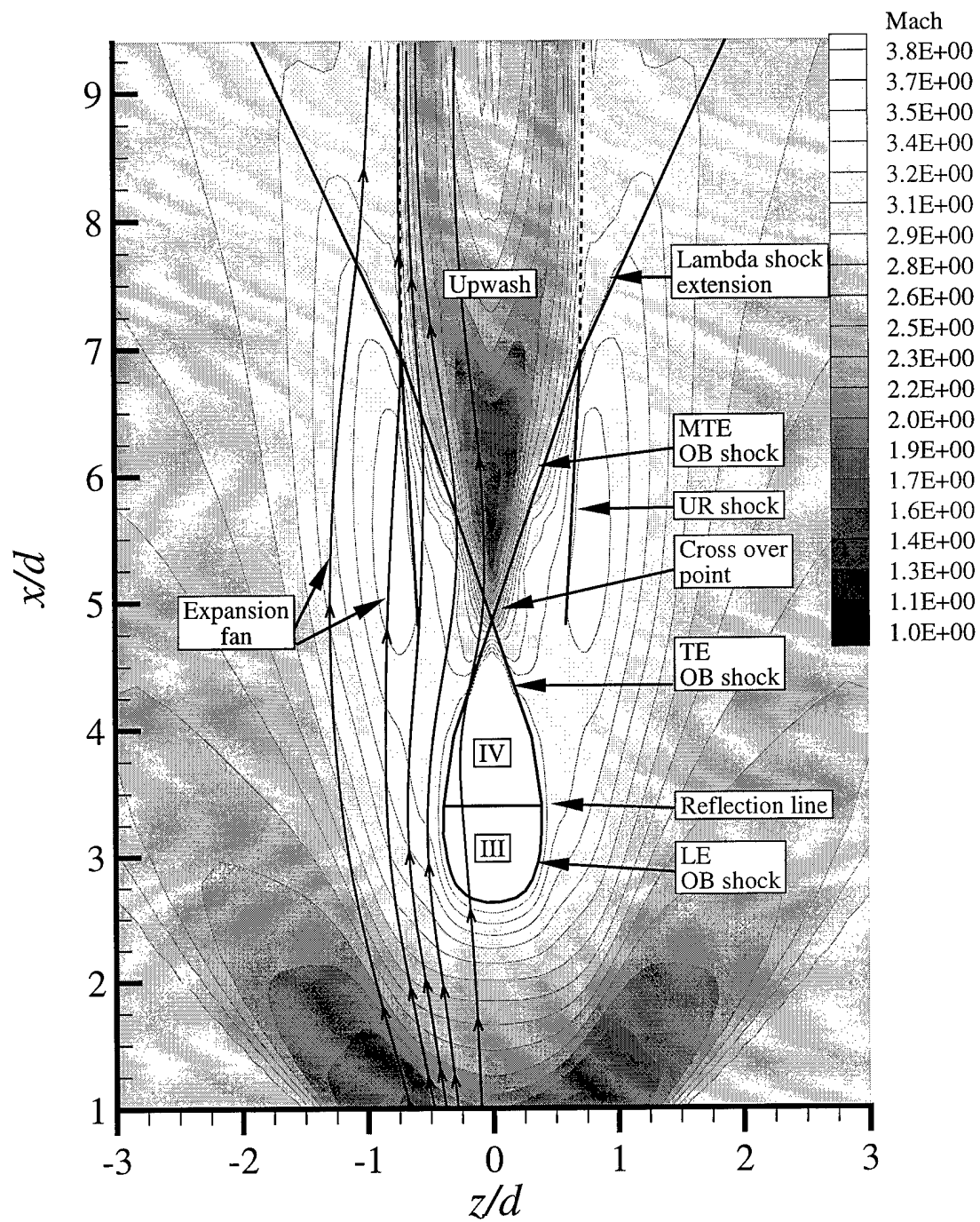


Figure 126. Expansion and shock structure in  $x - z$  plane ( $y/d = 1.45$ )

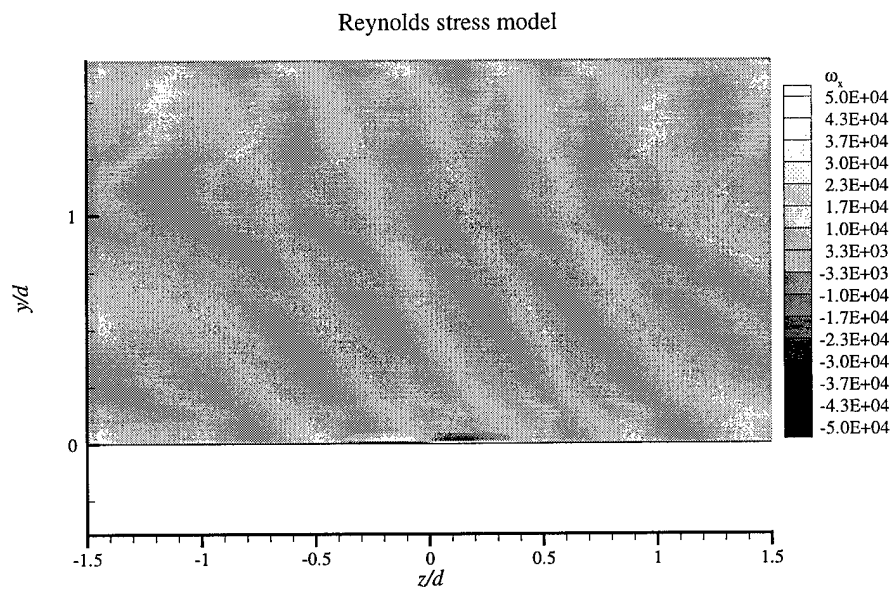
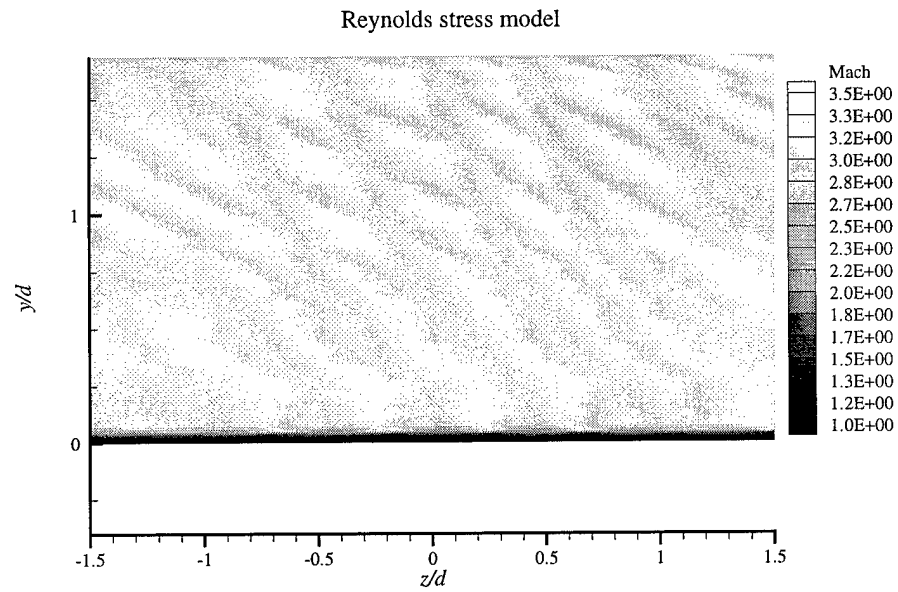


Figure 127. Mach and  $\omega_x$  contours at  $x/d = -1.50$

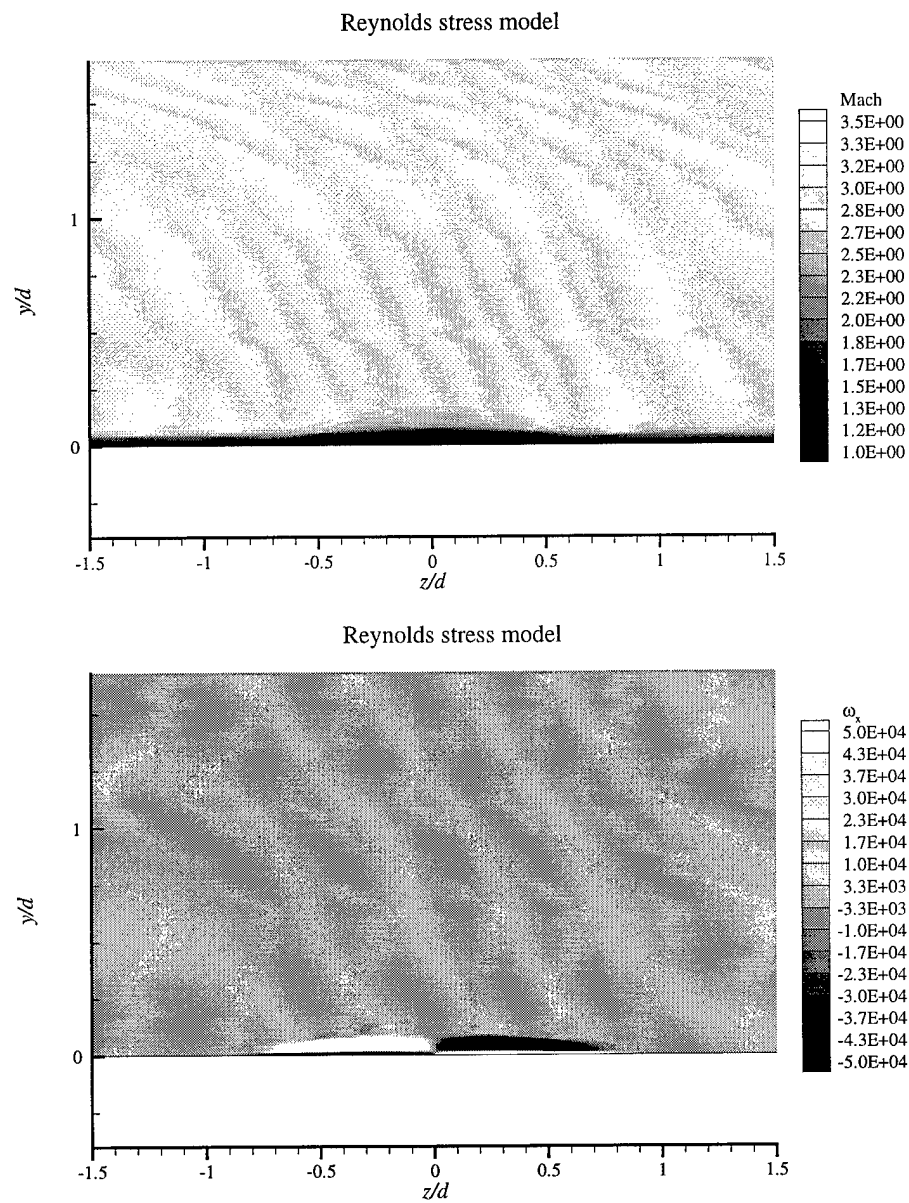


Figure 128. Mach and  $\omega_x$  contours at  $x/d = -1.25$

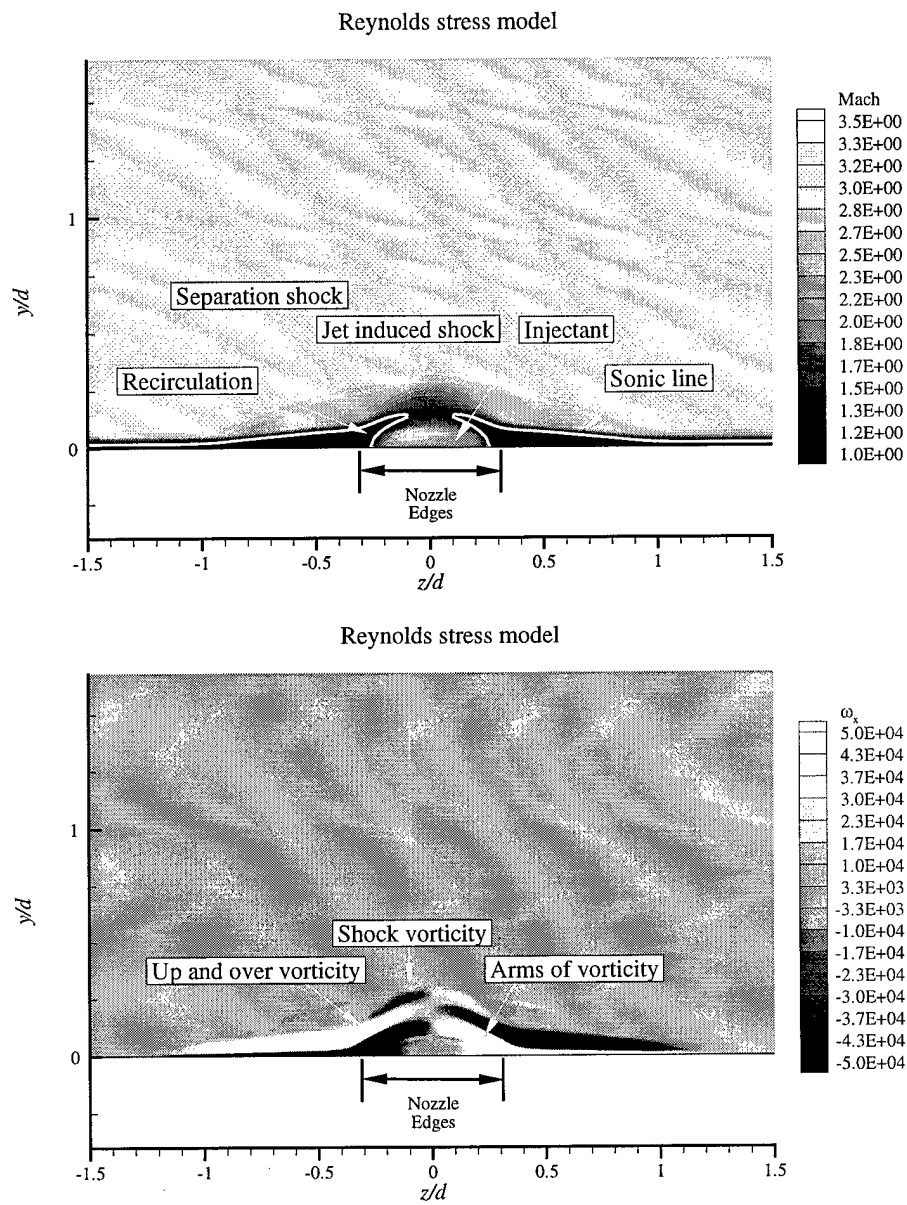
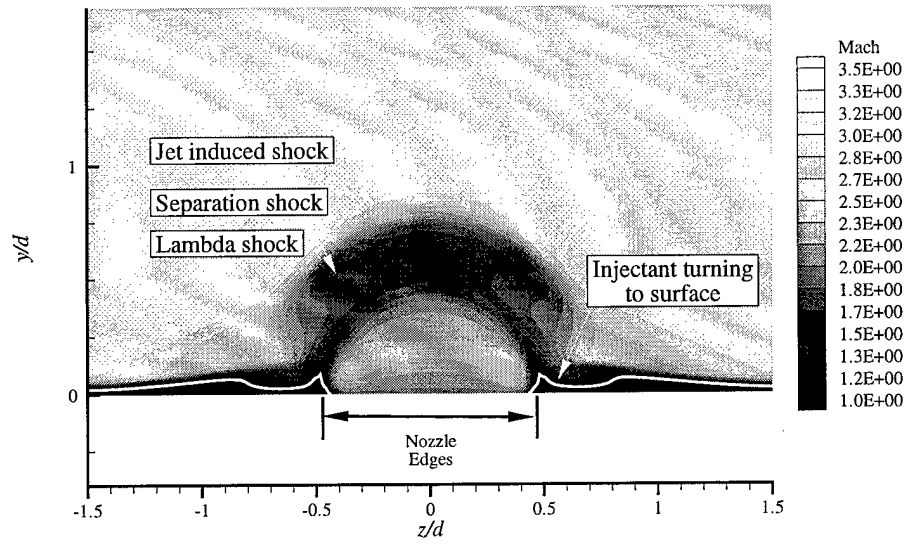


Figure 129. Mach and  $\omega_x$  contours at  $x/d = -1.00$

Reynolds stress model



Reynolds stress model

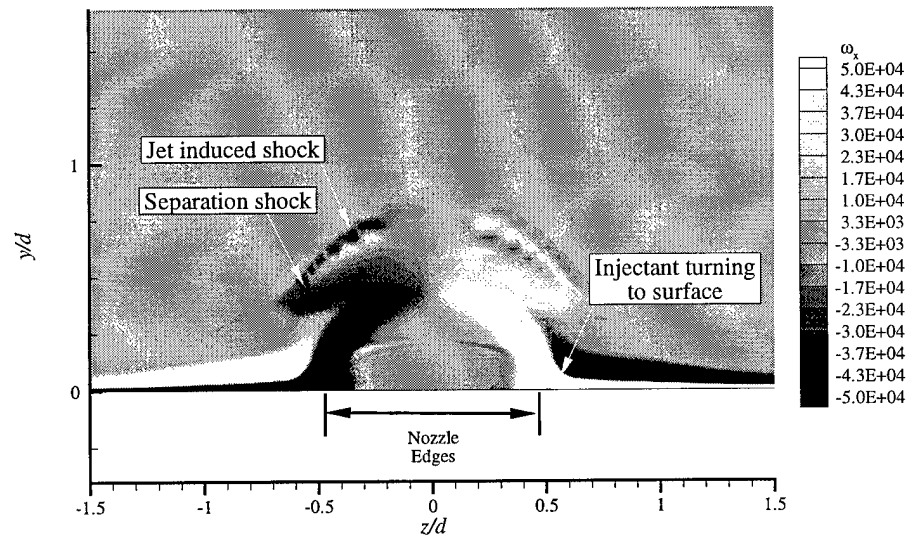


Figure 130. Mach and  $\omega_x$  contours at  $x/d = -0.50$

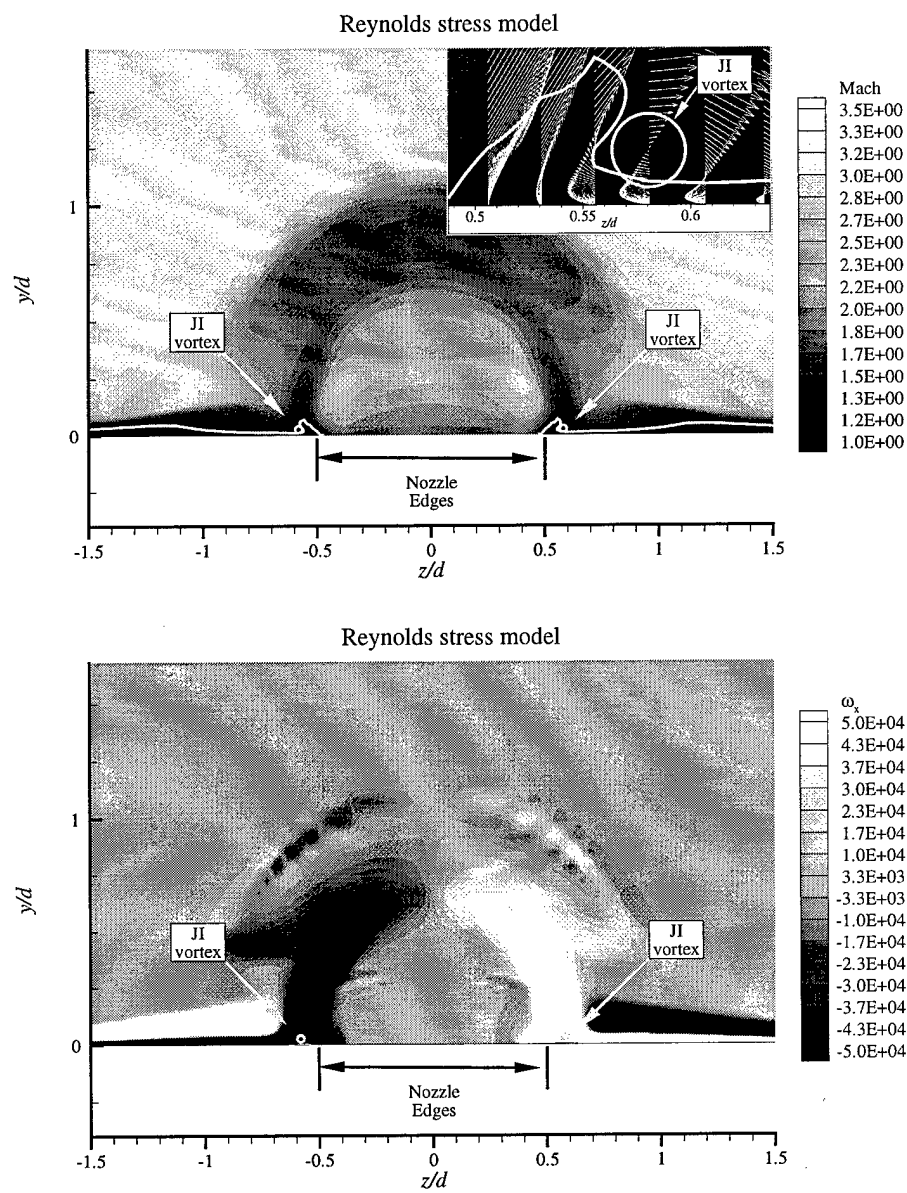


Figure 131. Mach and  $\omega_x$  contours at  $x/d = -0.25$

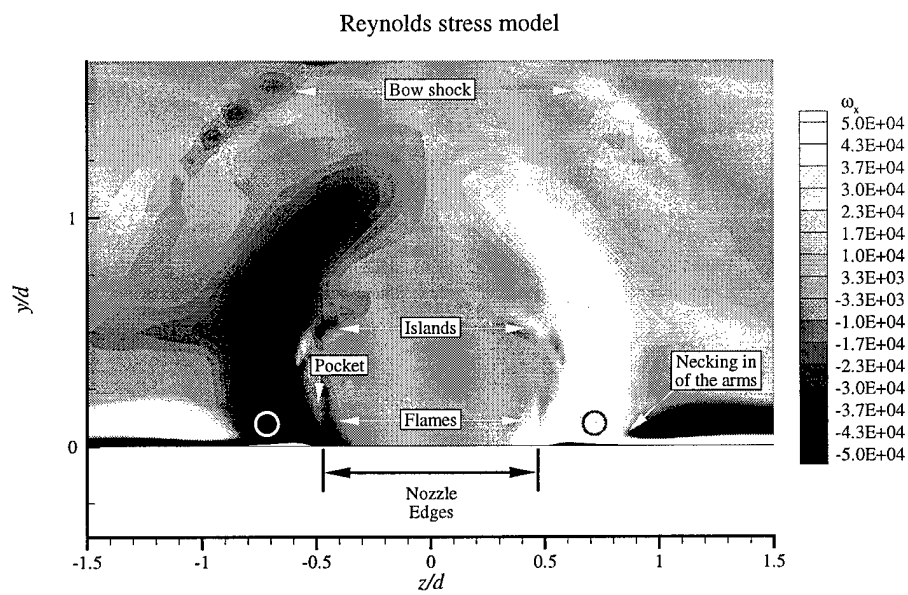
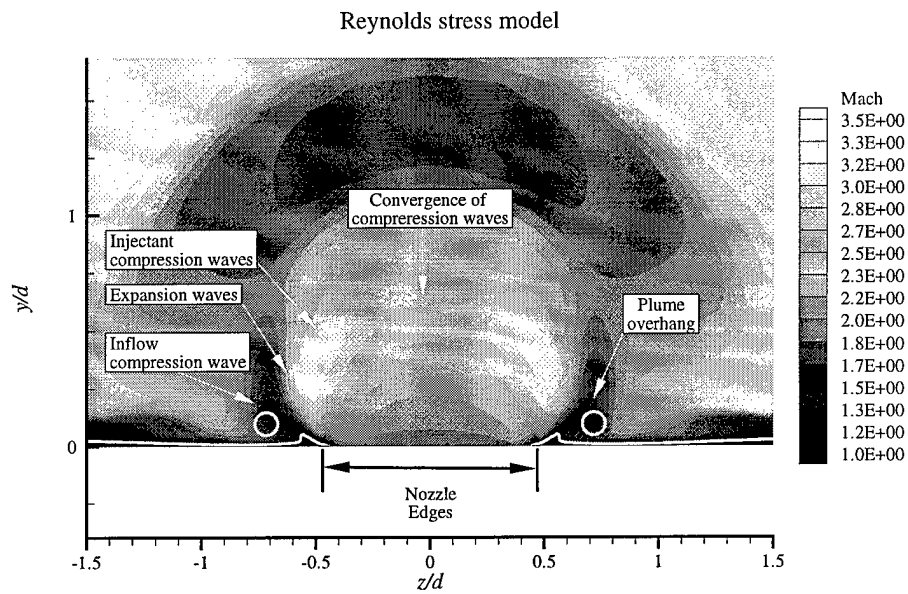
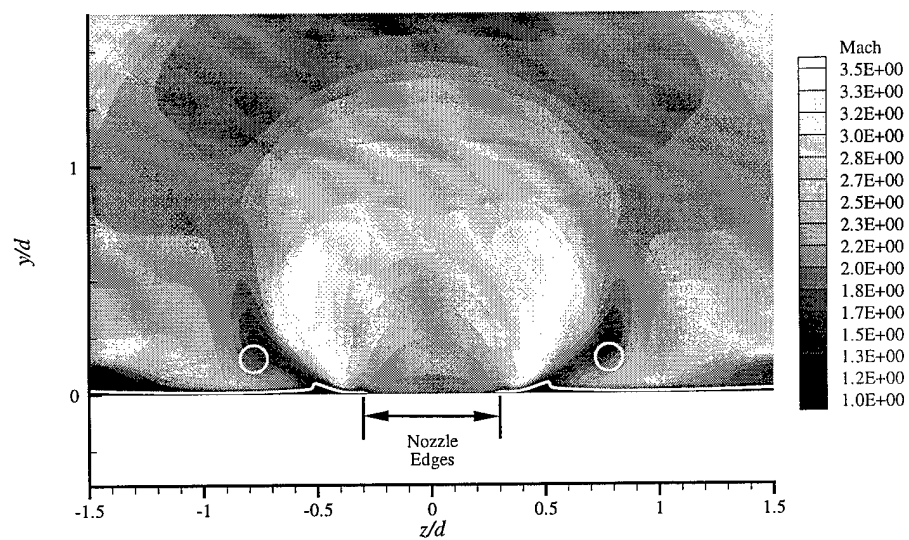


Figure 132. Mach and  $\omega_x$  contours at  $x/d = 0.50$



Reynolds stress model



Reynolds stress model

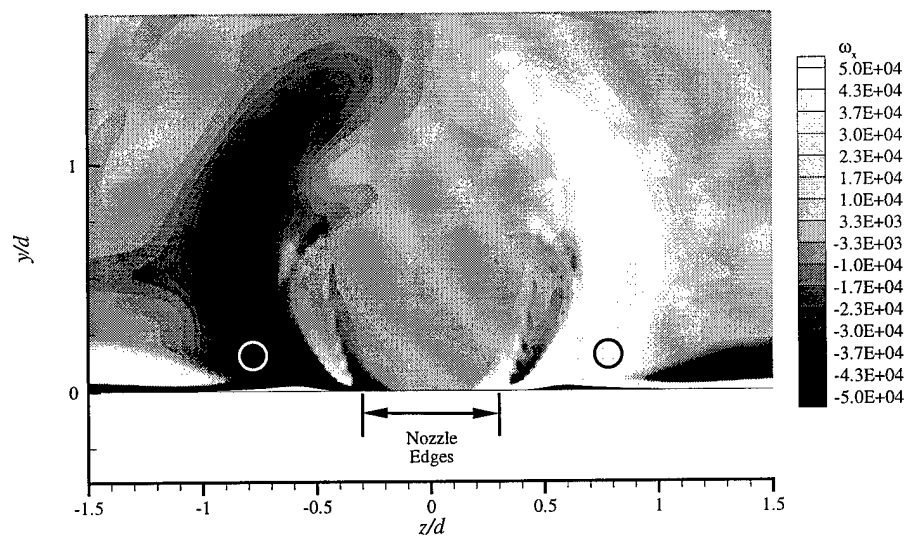


Figure 133. Mach and  $\omega_x$  contours at  $x/d = 1.00$

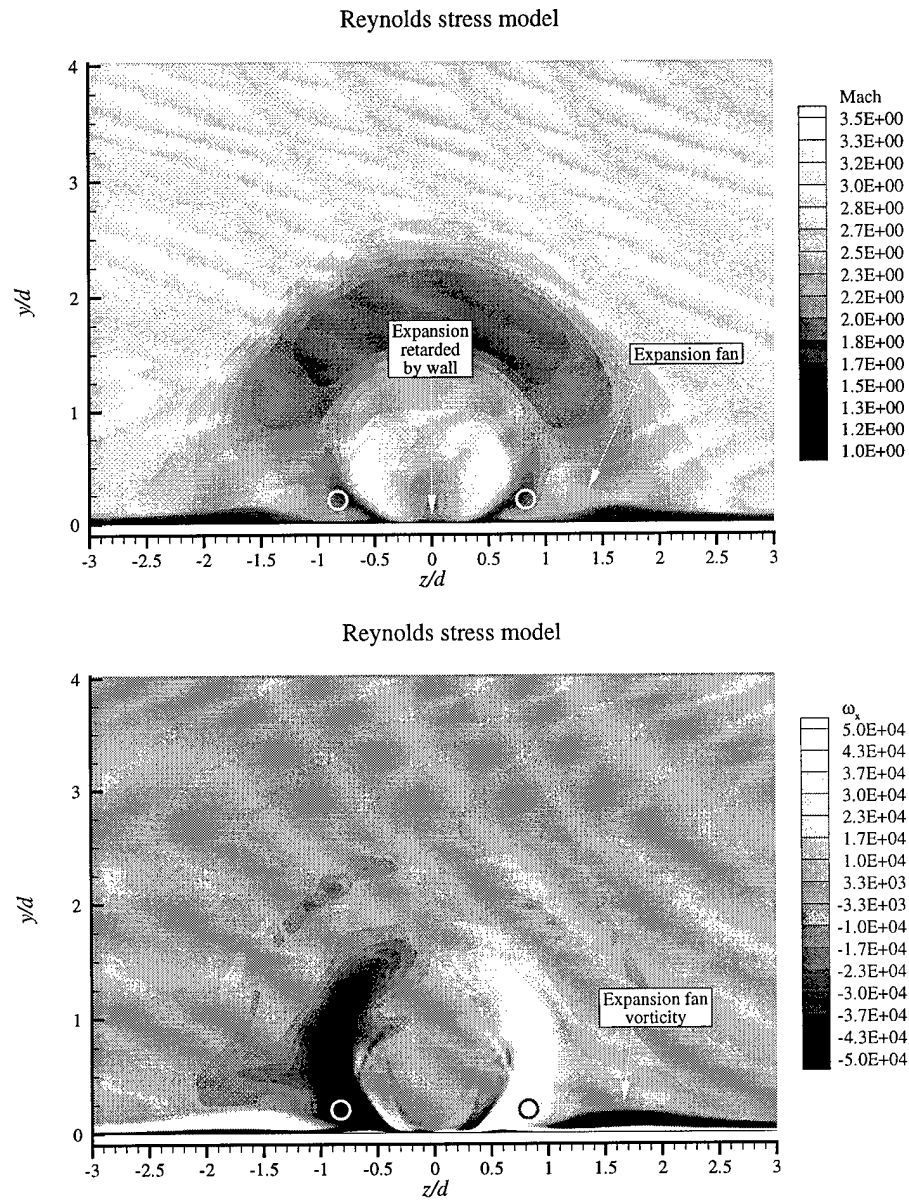
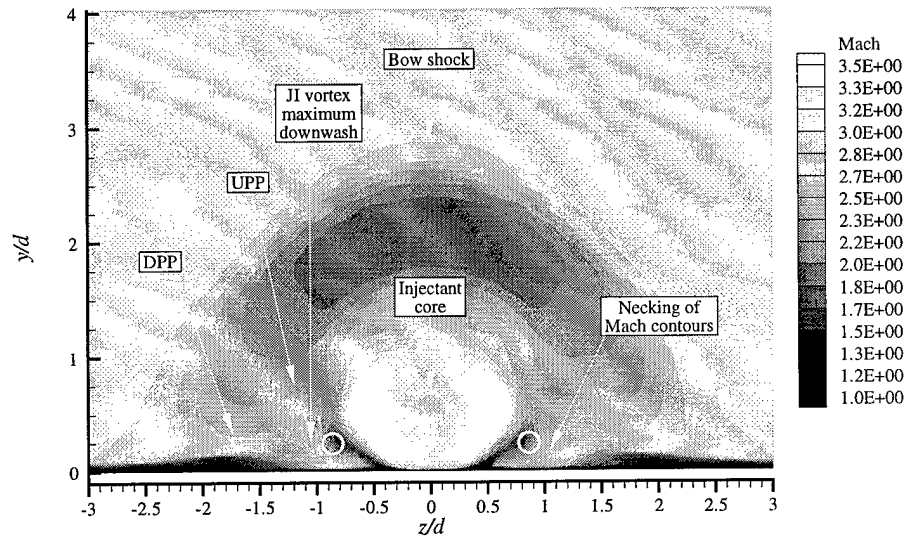


Figure 134. Mach and  $\omega_x$  contours at  $x/d = 1.25$

# Reynolds stress model



# Reynolds stress model

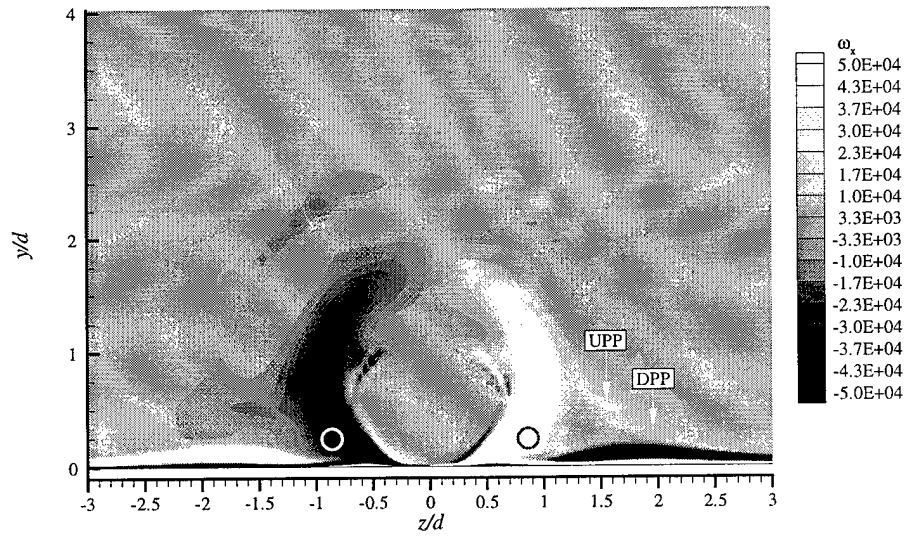


Figure 135. Mach and  $\omega_x$  contours at  $x/d = 1.50$

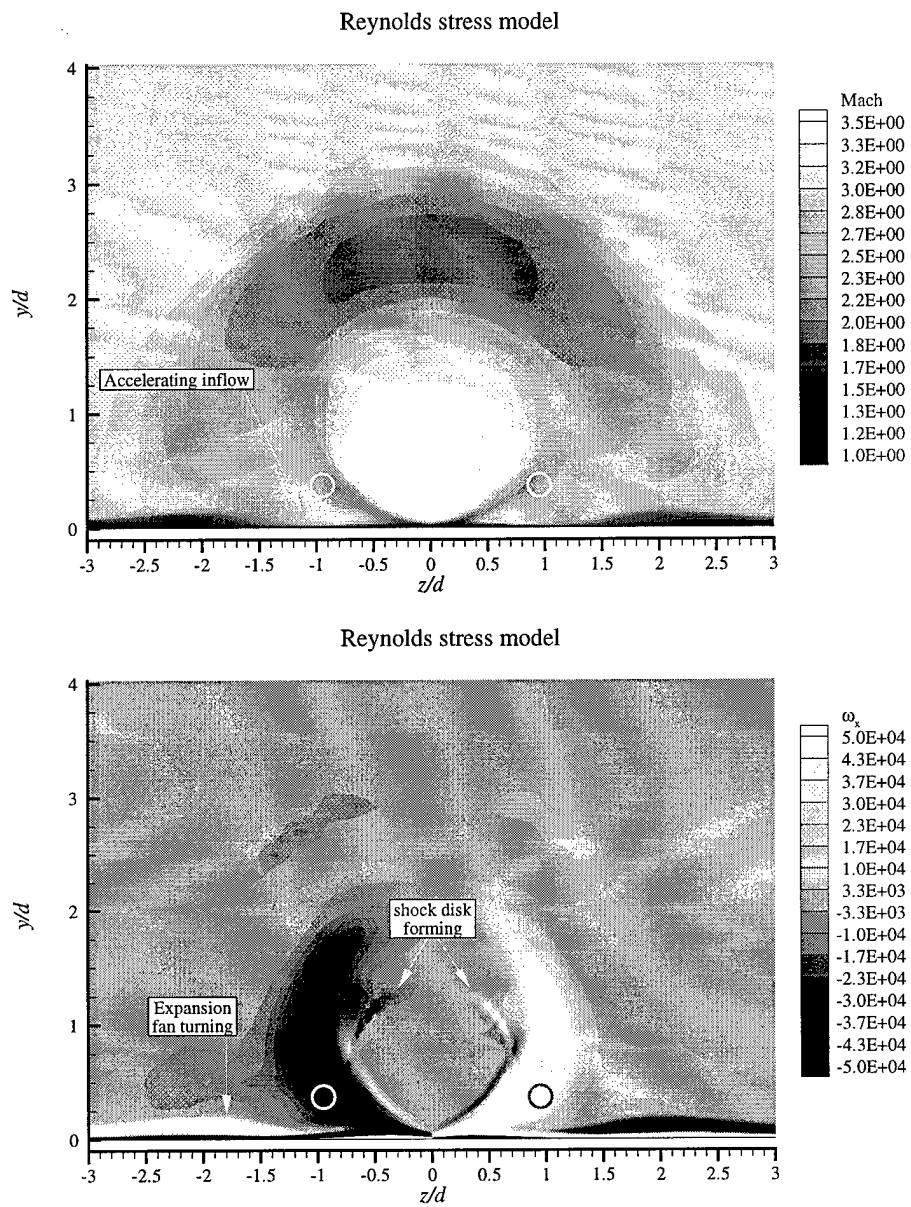


Figure 136. Mach and  $\omega_x$  contours at  $x/d = 2.00$

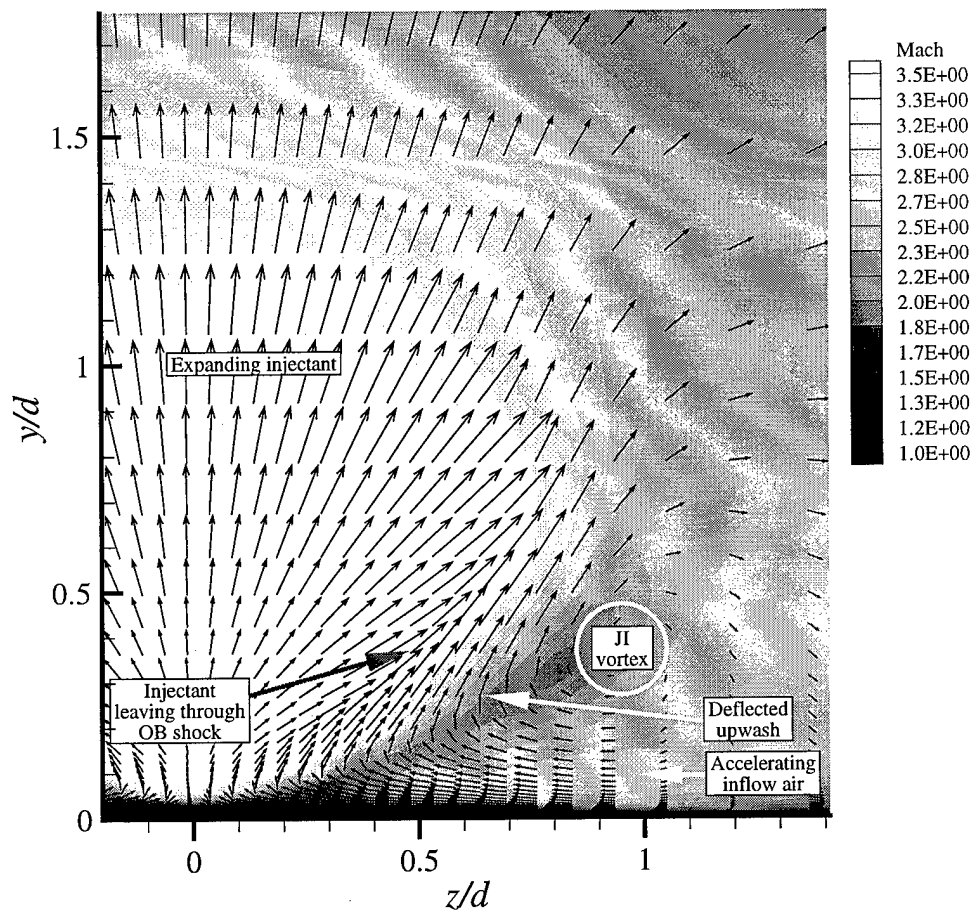


Figure 137. JI vortex sustenance mechanism at  $x/d = 2.00$

# Reynolds stress model

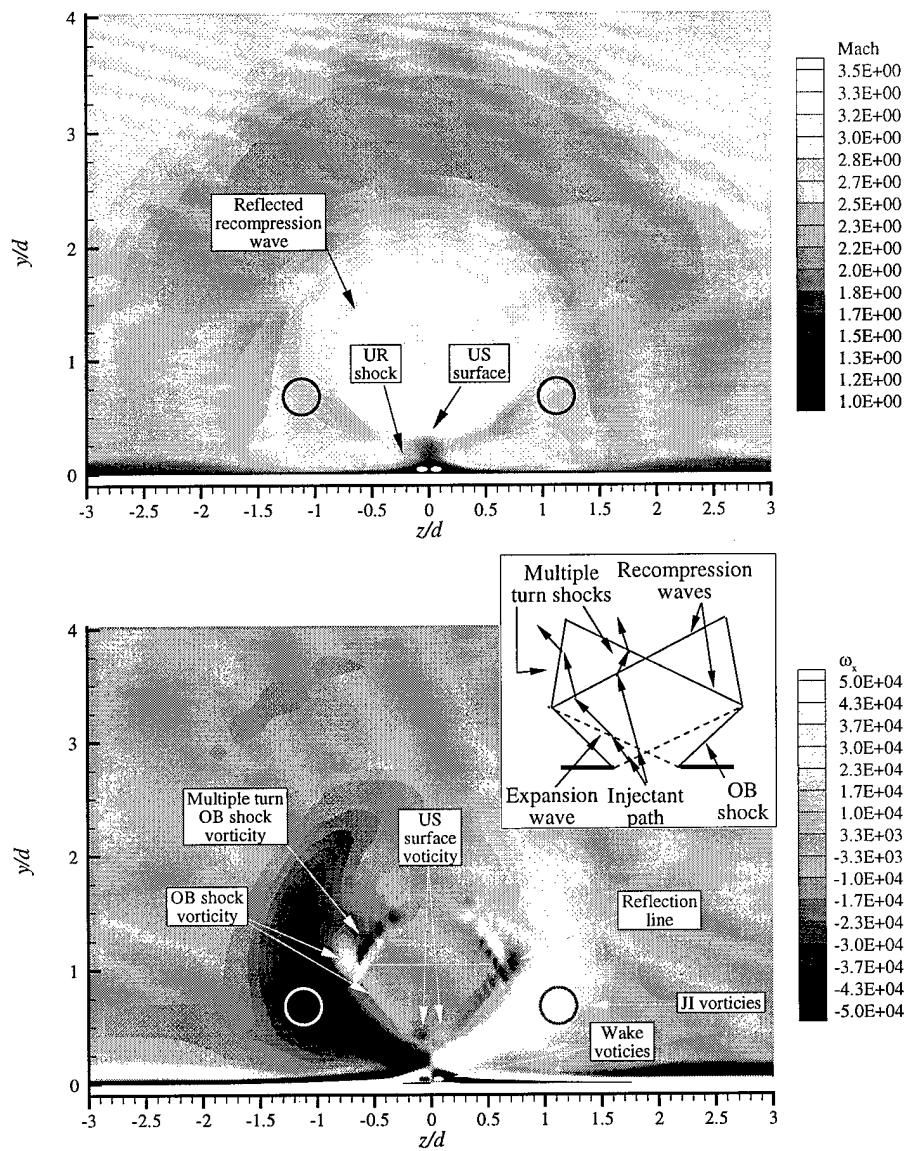


Figure 138. Mach and  $\omega_x$  contours at  $x/d = 3.00$

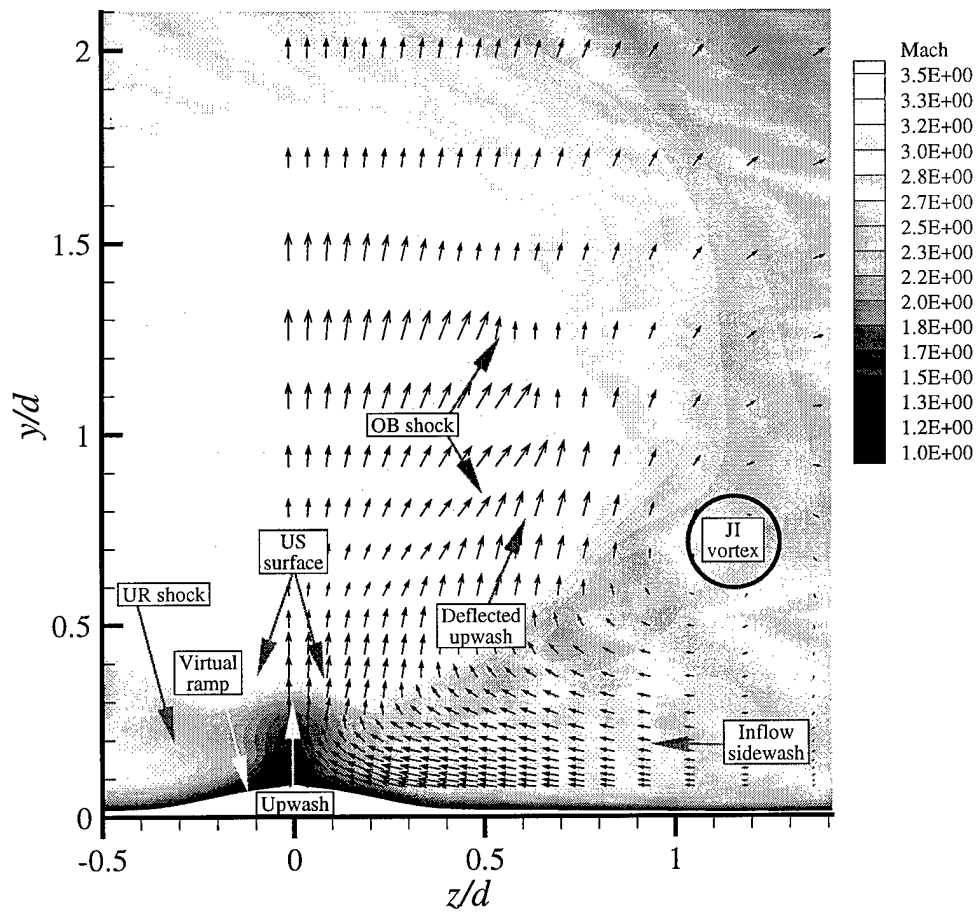
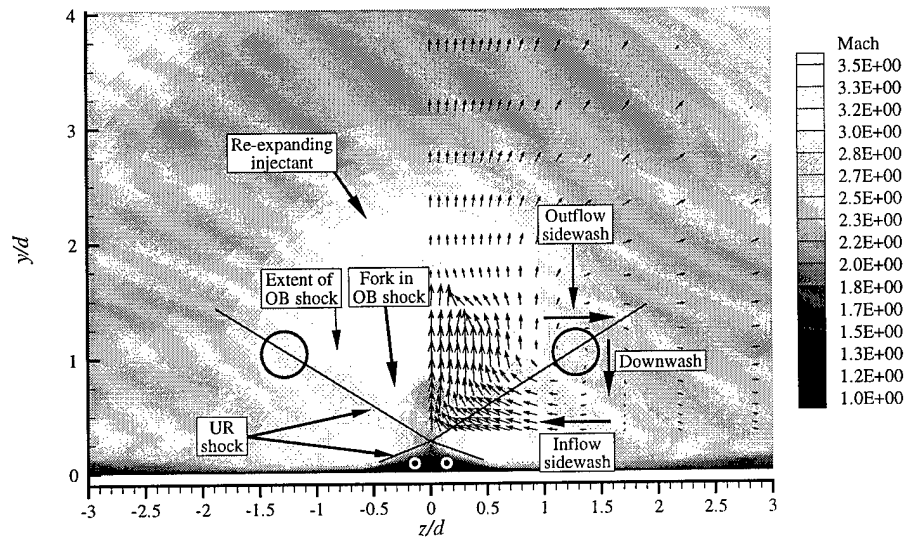


Figure 139. JI vortex sustenance mechanism at  $x/d = 3.00$

# Reynolds stress model



# Reynolds stress model

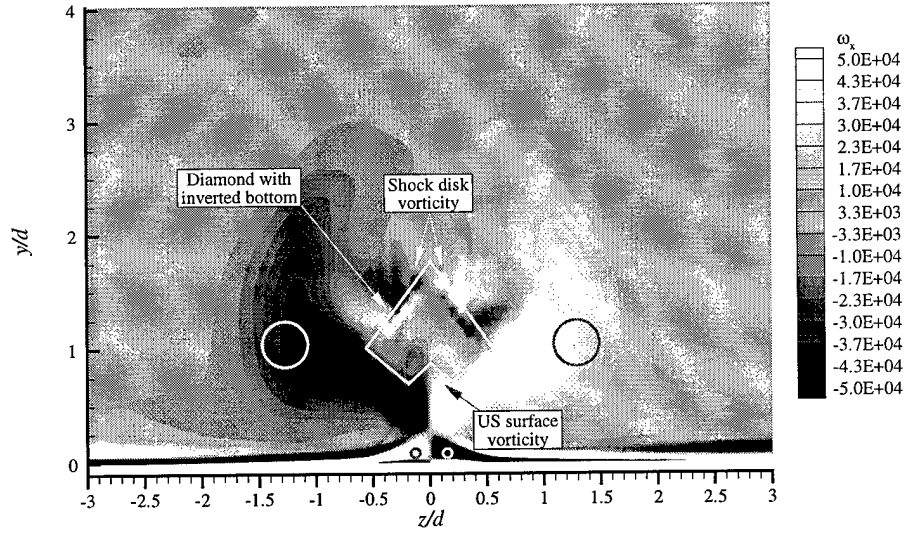


Figure 140. Mach and  $\omega_x$  contours at  $x/d = 4.00$



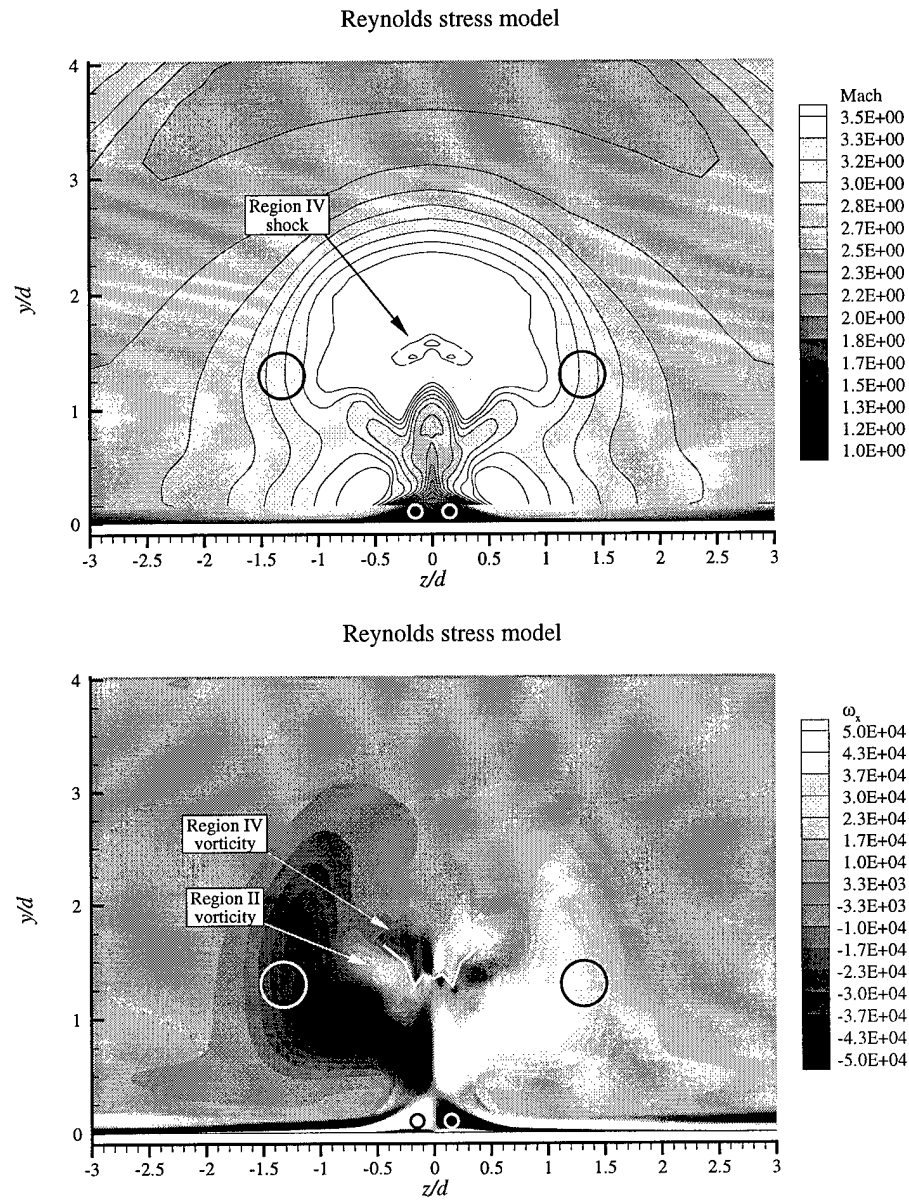


Figure 141. Mach and  $\omega_x$  contours at  $x/d = 4.50$

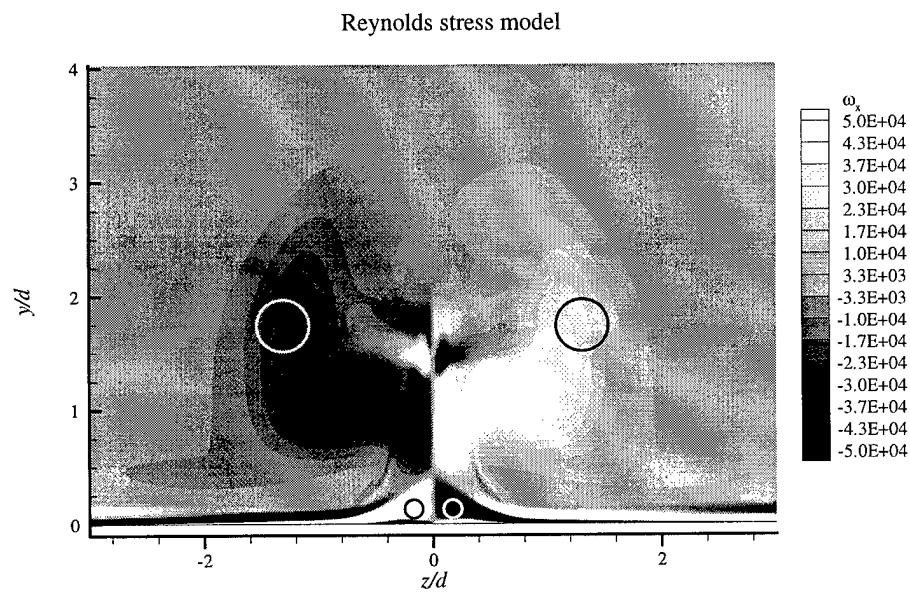
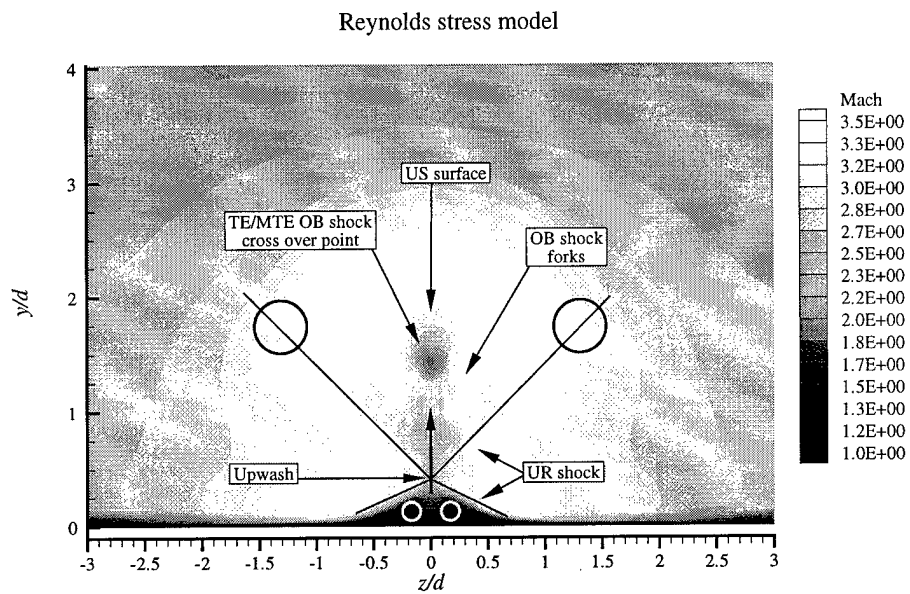


Figure 142. Mach and  $\omega_x$  contours at  $x/d = 5.00$

# Reynolds stress model

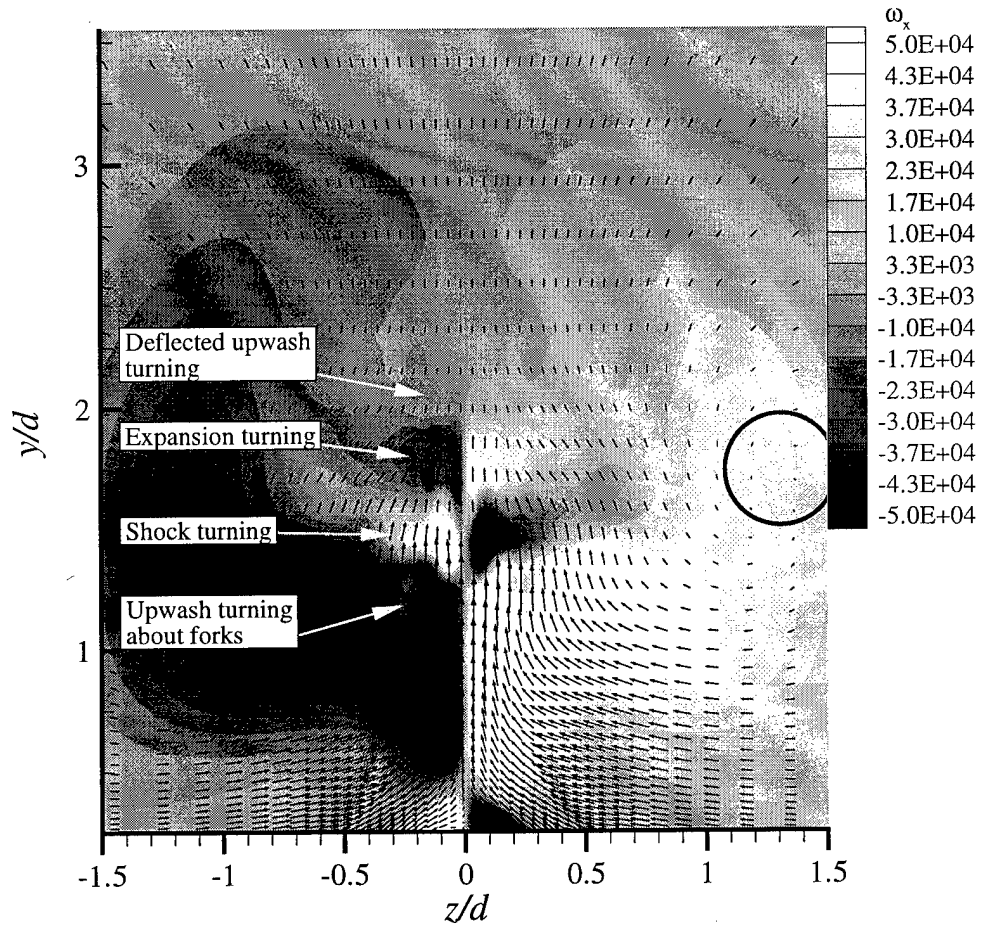


Figure 143. Enlarged view of  $\omega_x$  contours at  $x/d = 5.00$

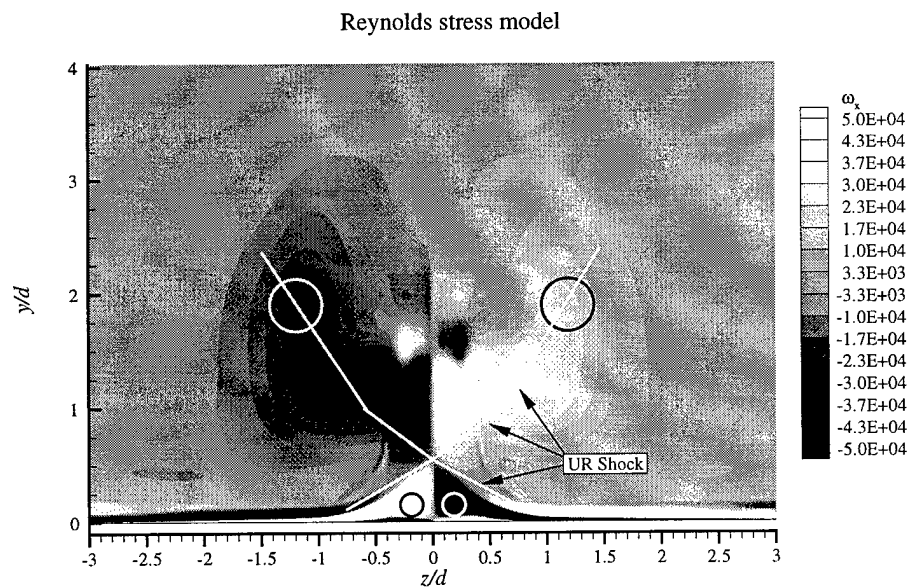
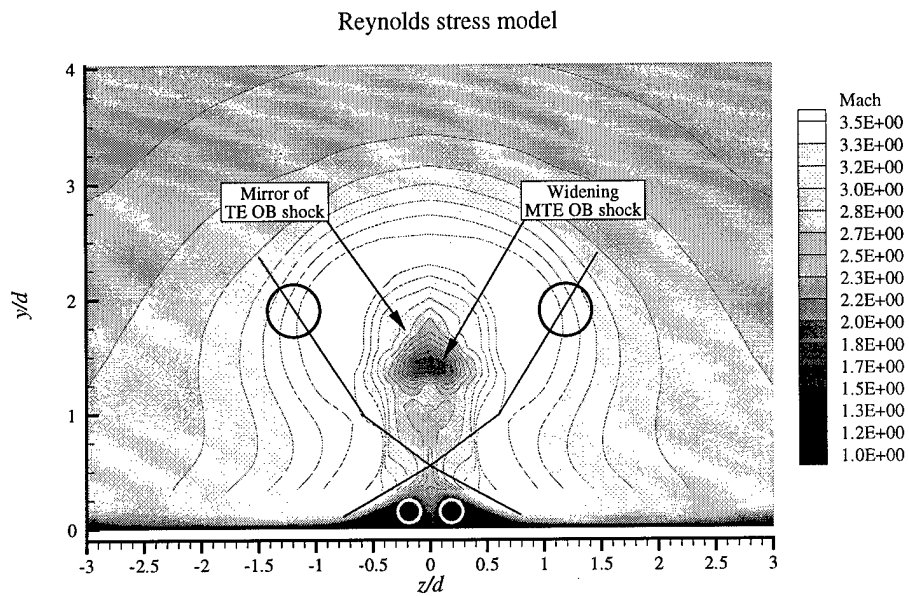
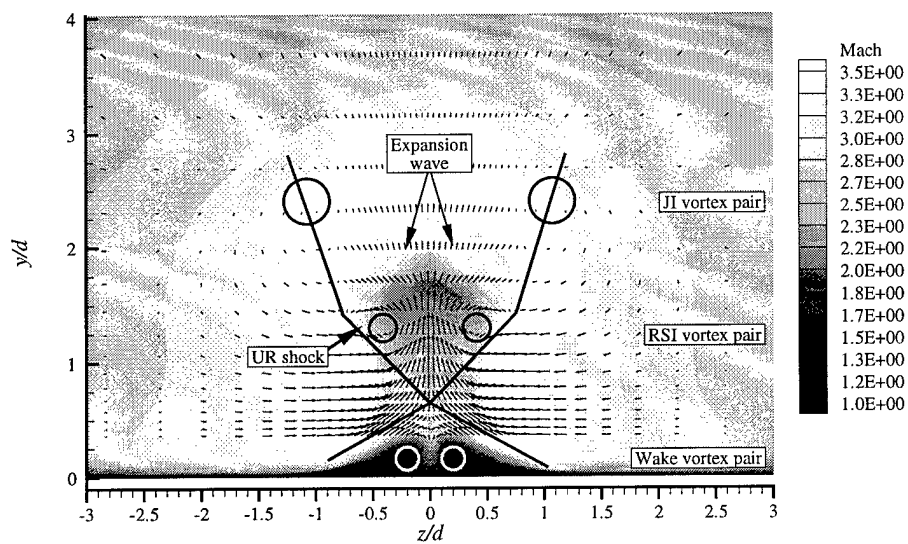


Figure 144. Mach and  $\omega_x$  contours at  $x/d = 6.00$

# Reynolds stress model



# Reynolds stress model

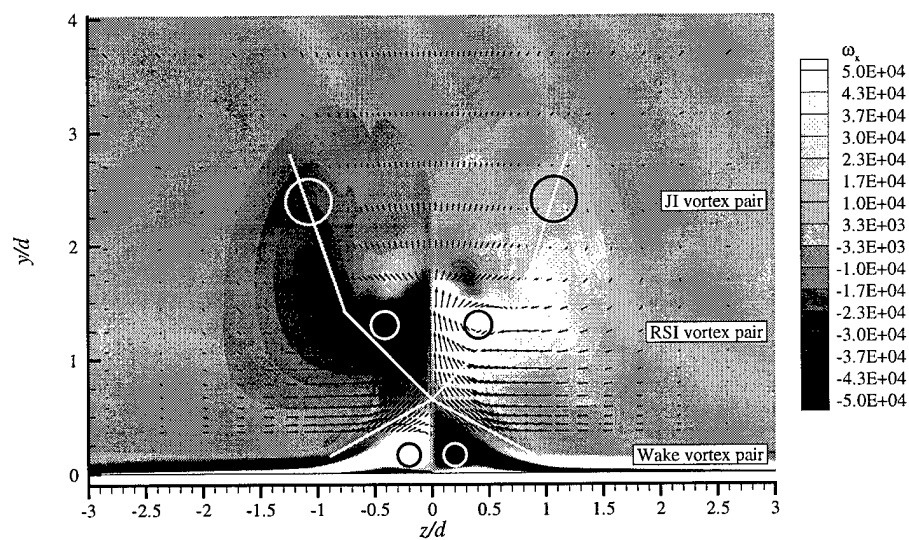


Figure 145. Mach and  $\omega_x$  contours at  $x/d = 7.00$

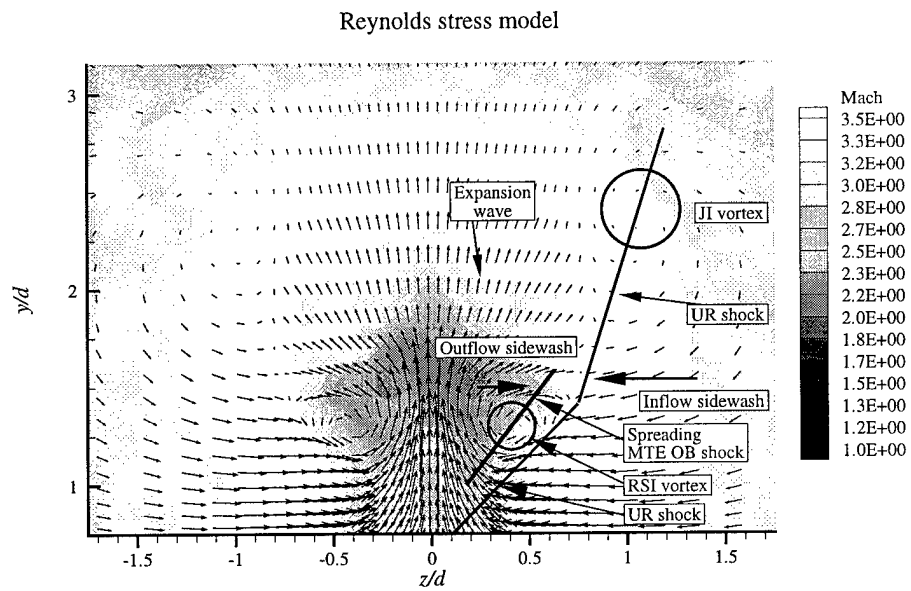
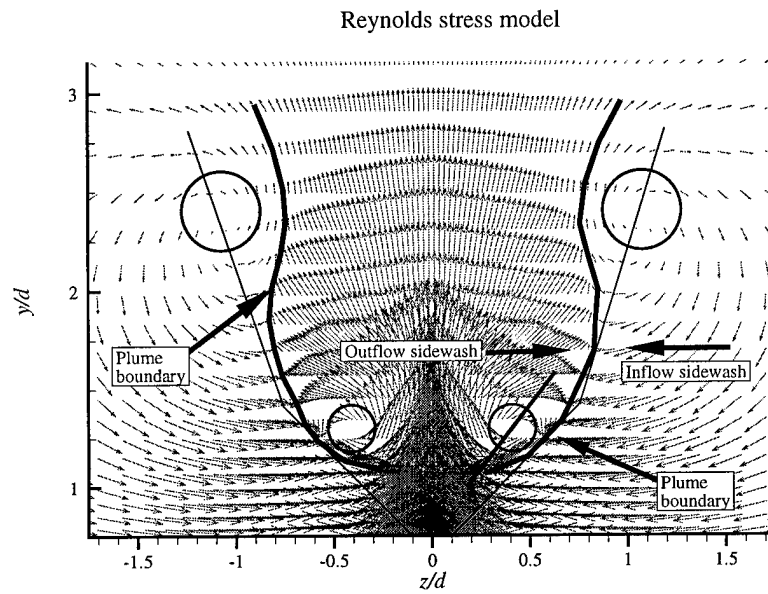


Figure 146. RSI vortex

Reynolds stress model

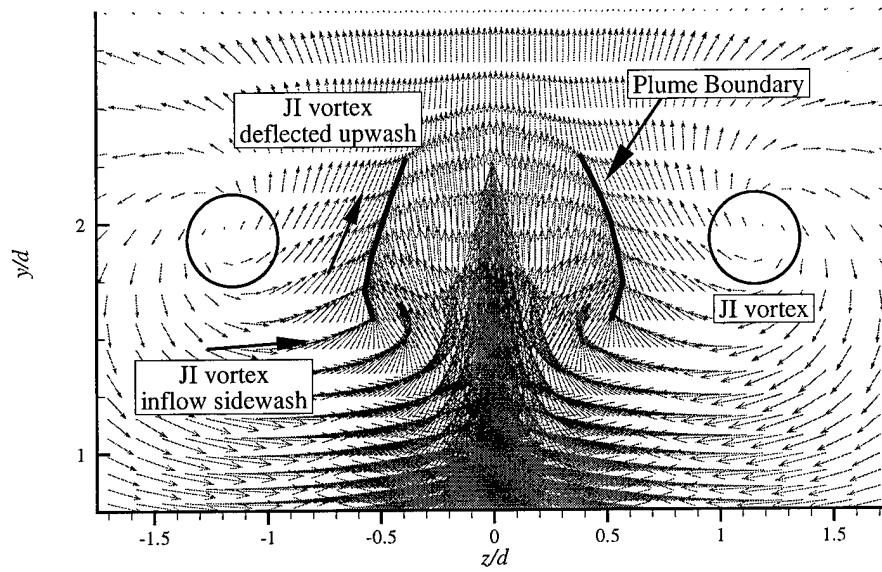


Figure 147. Plume boundary definition at  $x/d = 6.00$

Reynolds stress model

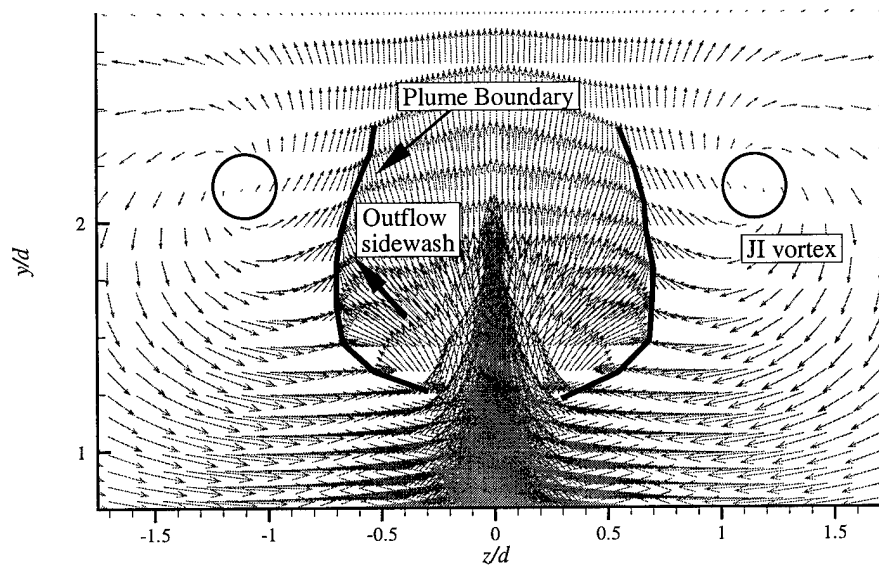


Figure 148. Plume boundary definition at  $x/d = 6.50$

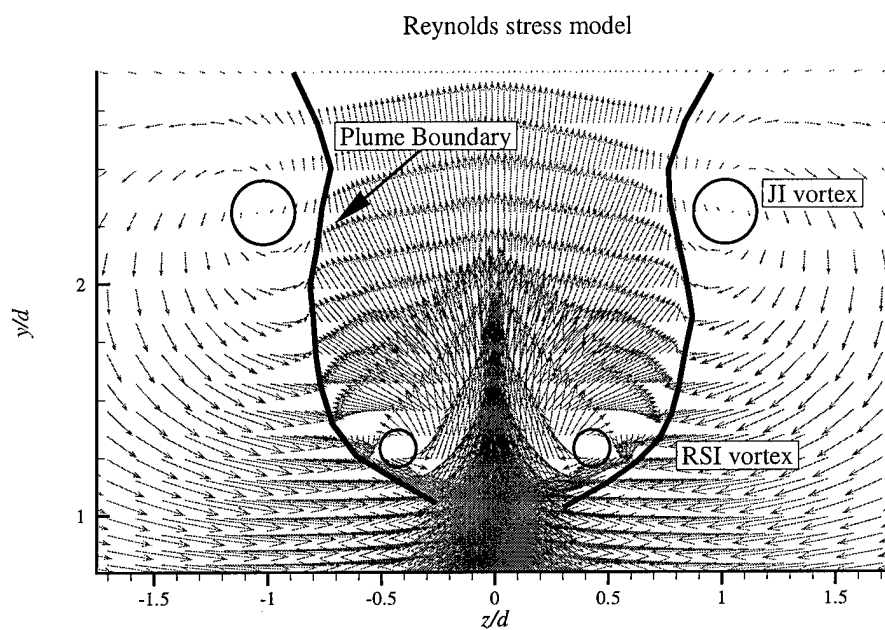


Figure 149. Plume boundary definition at  $x/d = 7.00$

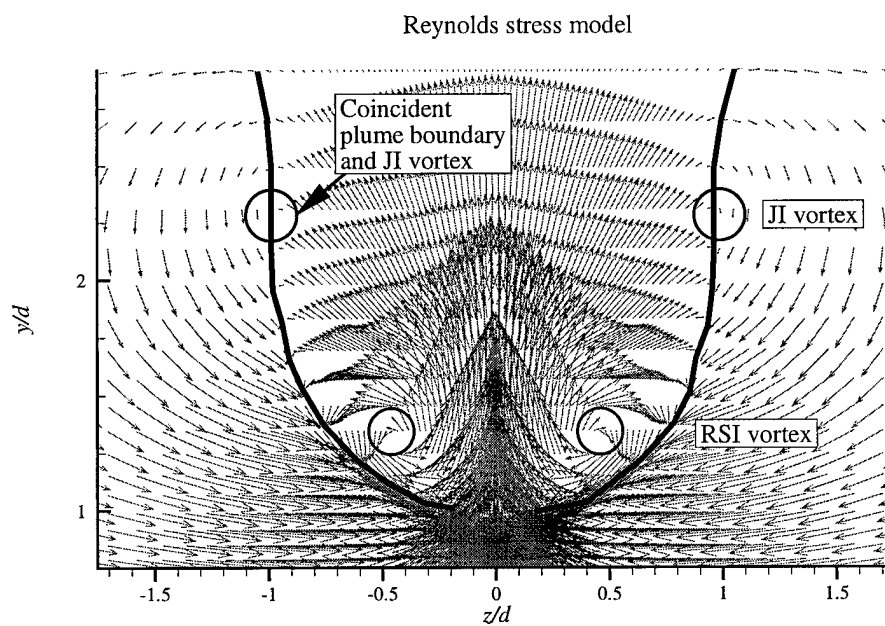


Figure 150. Plume boundary definition at  $x/d = 7.50$



Reynolds stress model

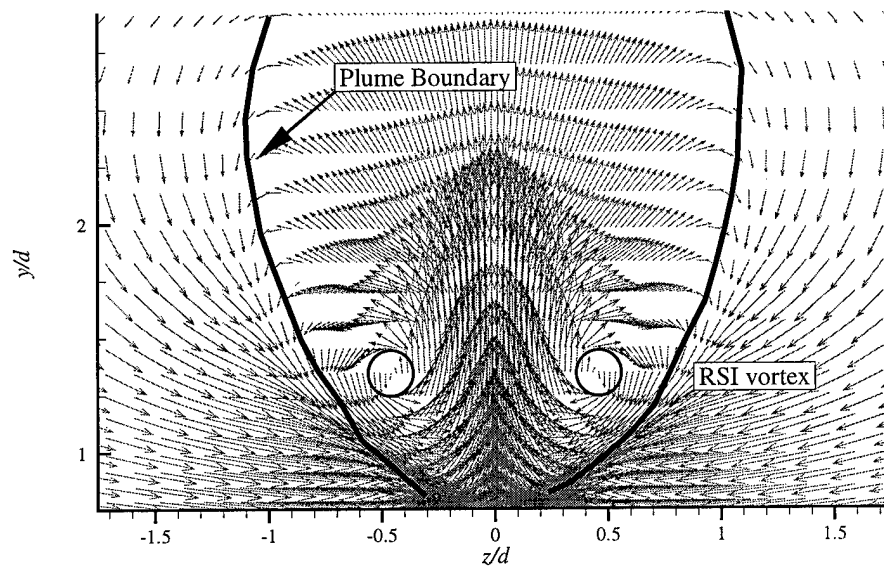


Figure 151. Plume boundary definition at  $x/d = 8.00$

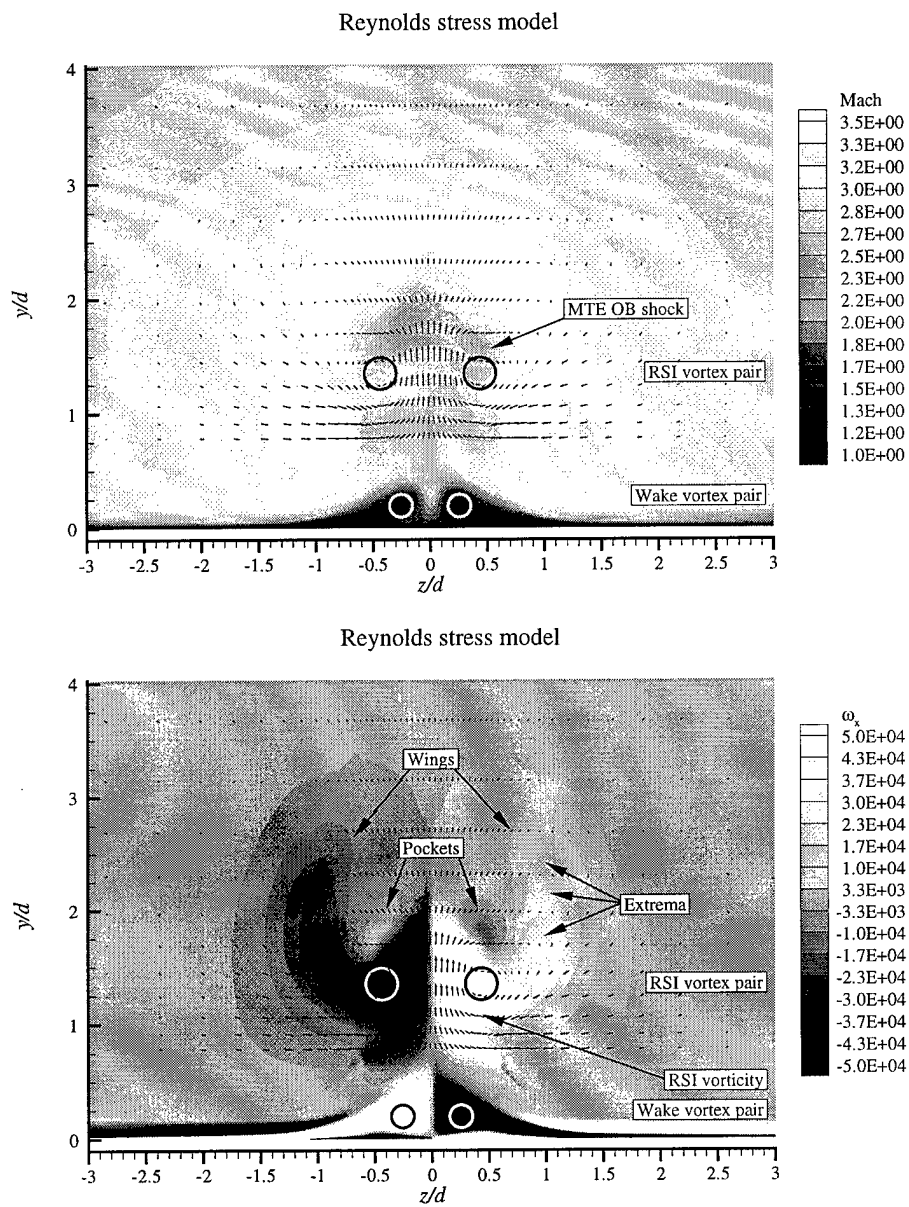


Figure 152. Mach and  $\omega_x$  contours at  $x/d = 8.00$

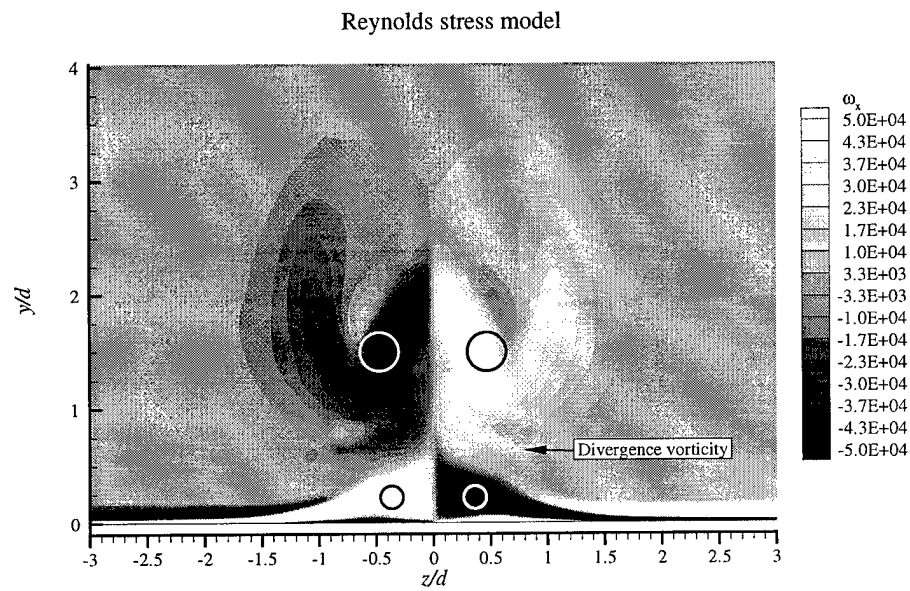
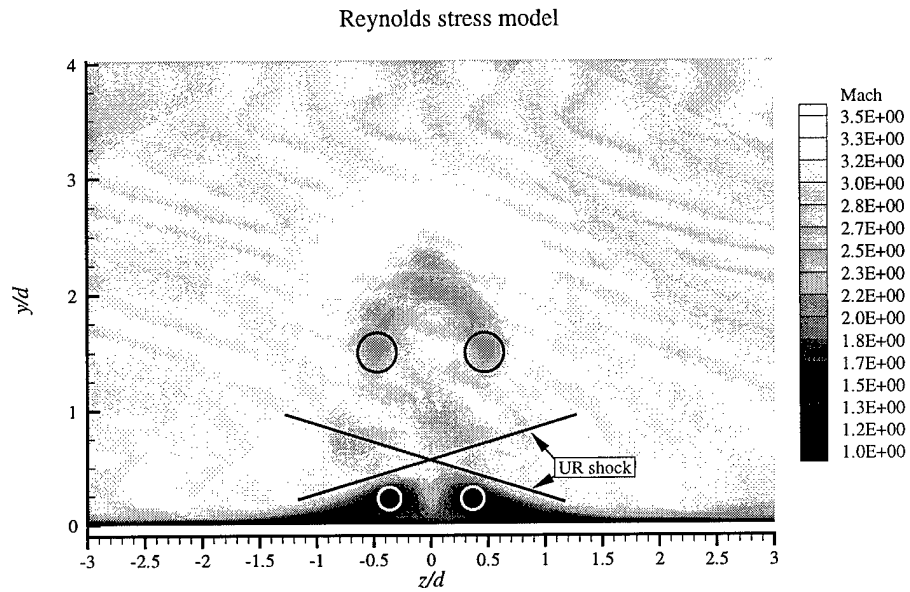


Figure 153. Mach and  $\omega_x$  contours at  $x/d = 9.50$

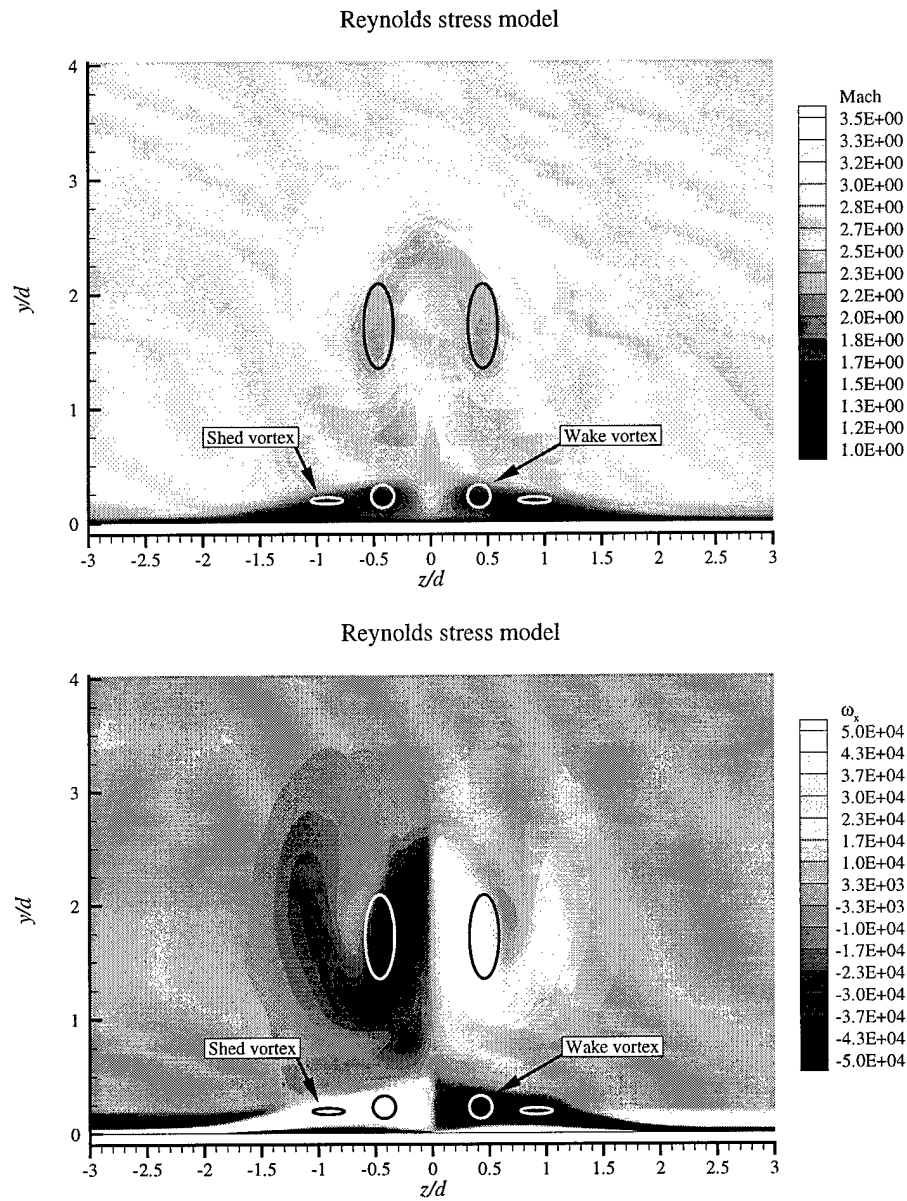


Figure 154. Mach and  $\omega_x$  contours at  $x/d = 10.50$

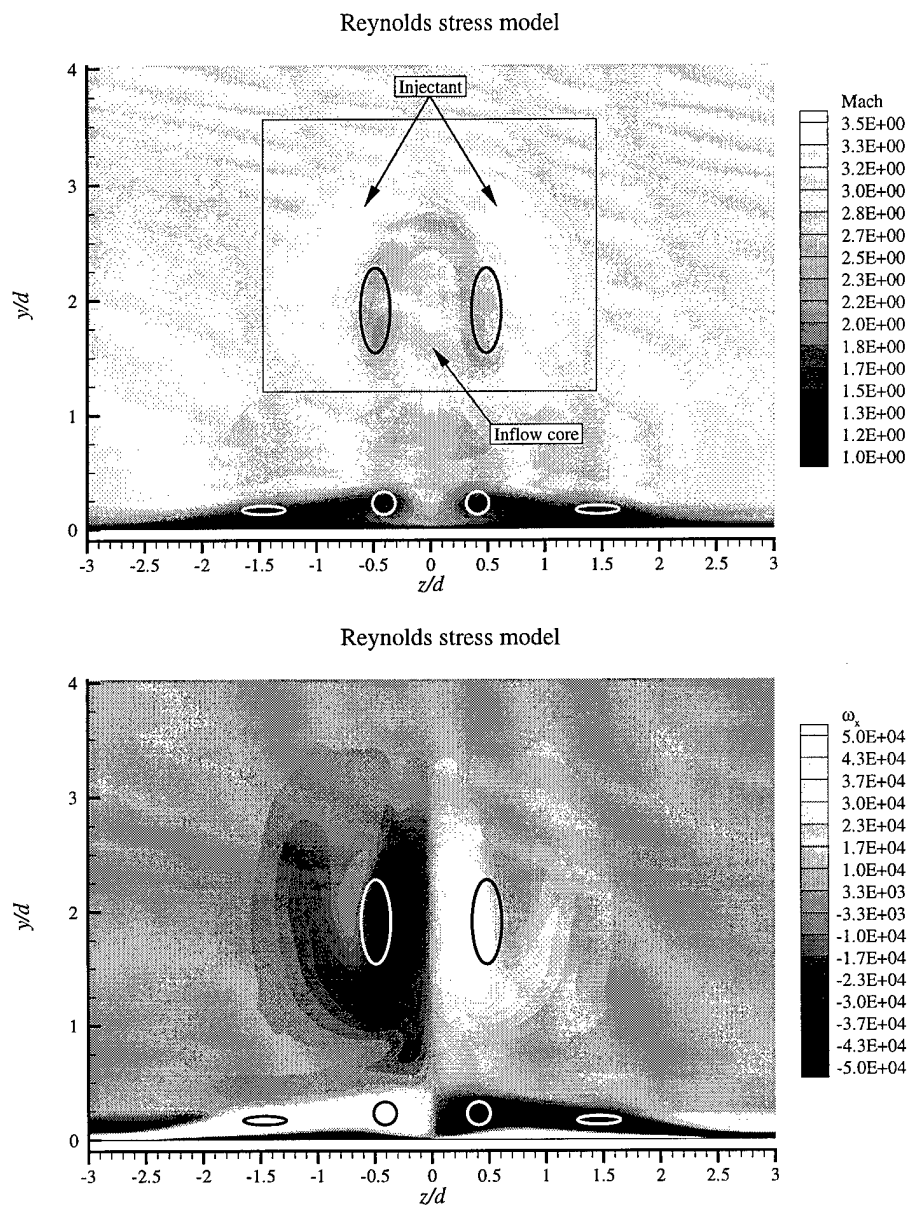


Figure 155. Mach and  $\omega_x$  contours at  $x/d = 12.50$

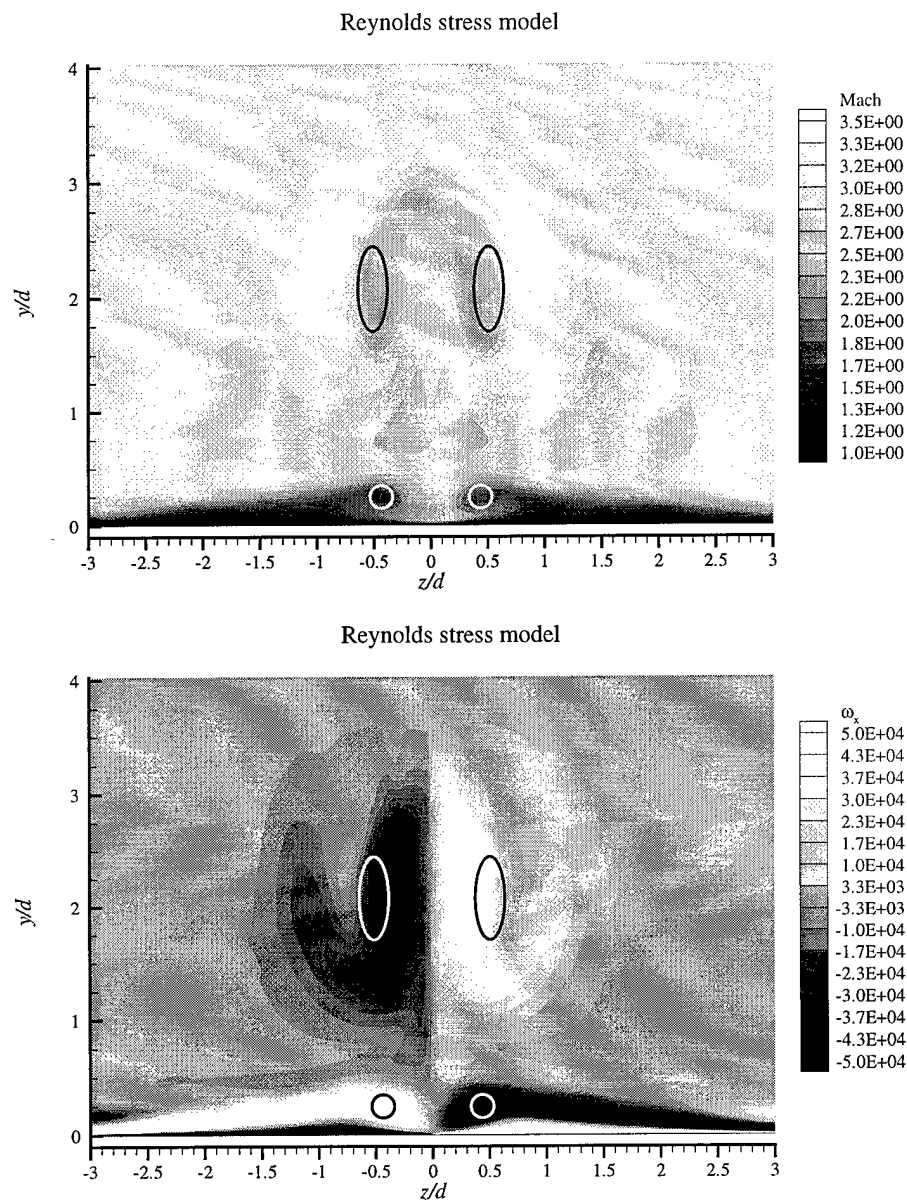


Figure 156. Mach and  $\omega_x$  contours at  $x/d = 14.50$

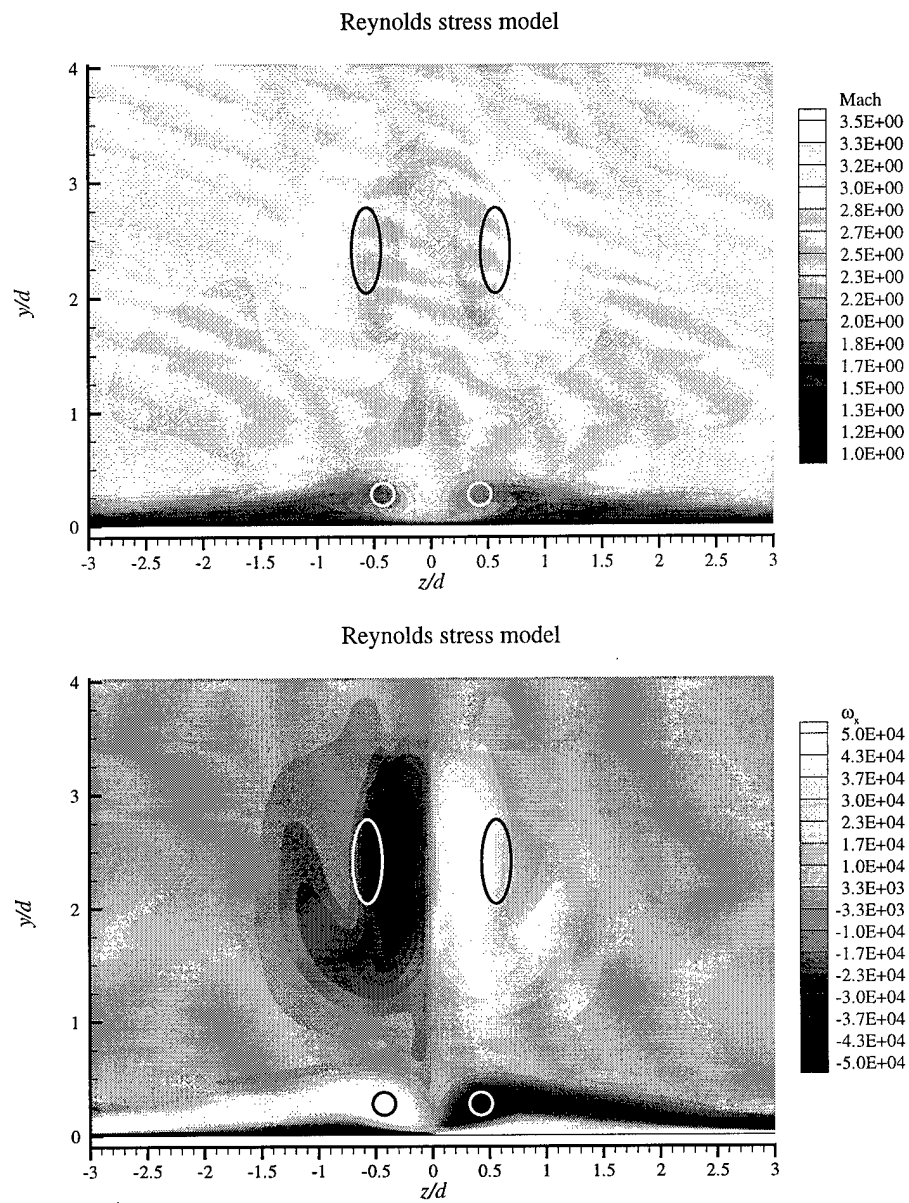


Figure 157. Mach and  $\omega_x$  contours at  $x/d = 16.50$

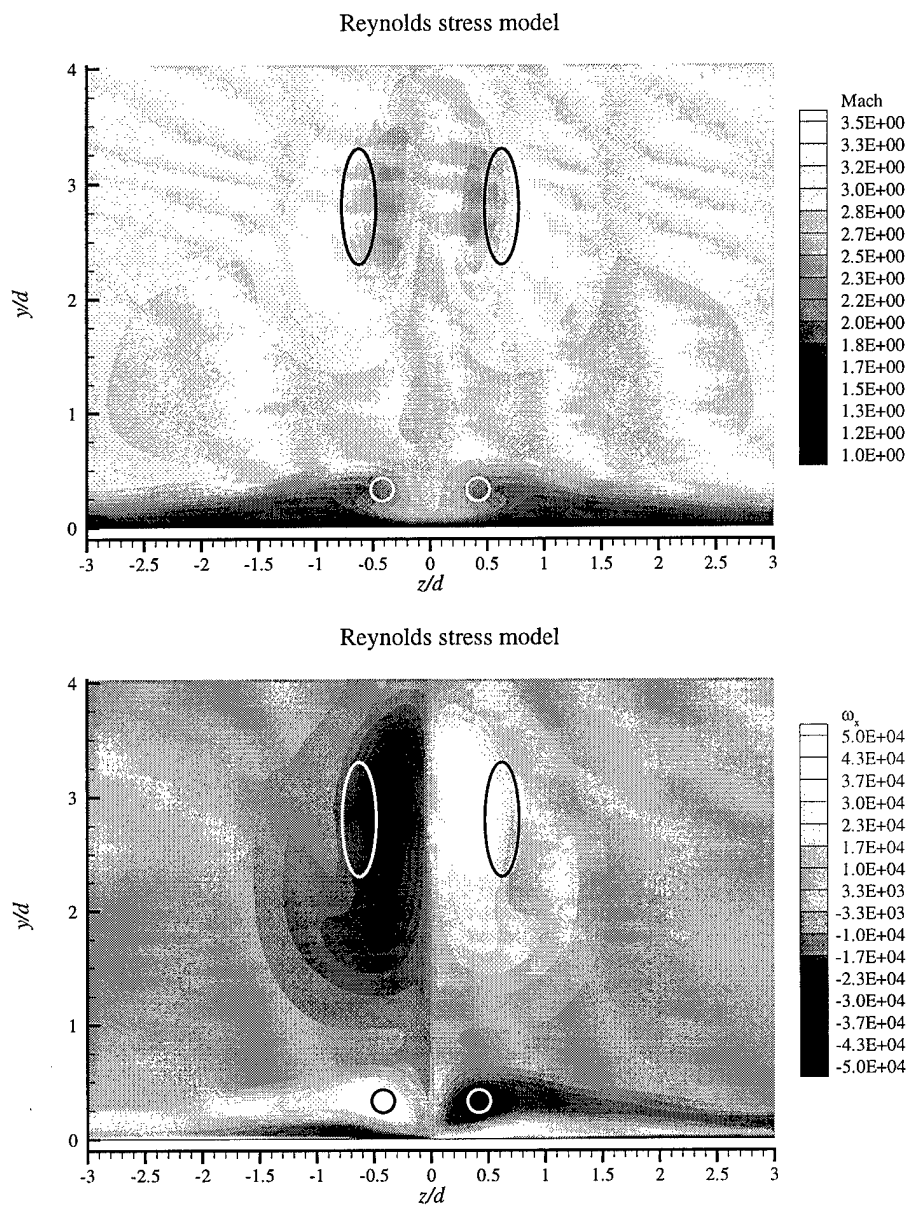


Figure 158. Mach and  $\omega_x$  contours at  $x/d = 20.00$



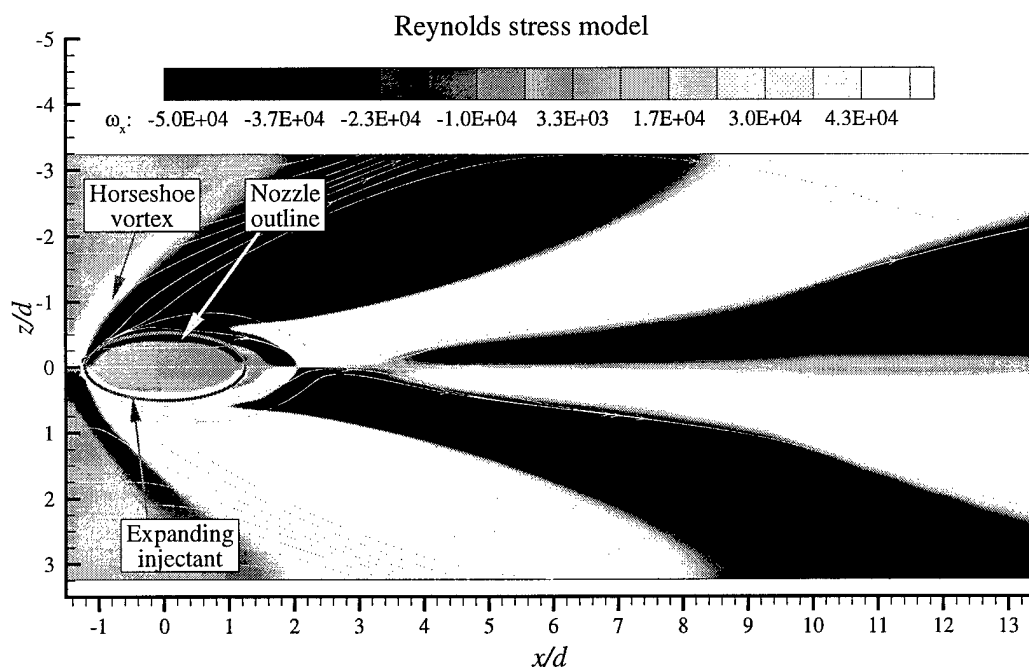
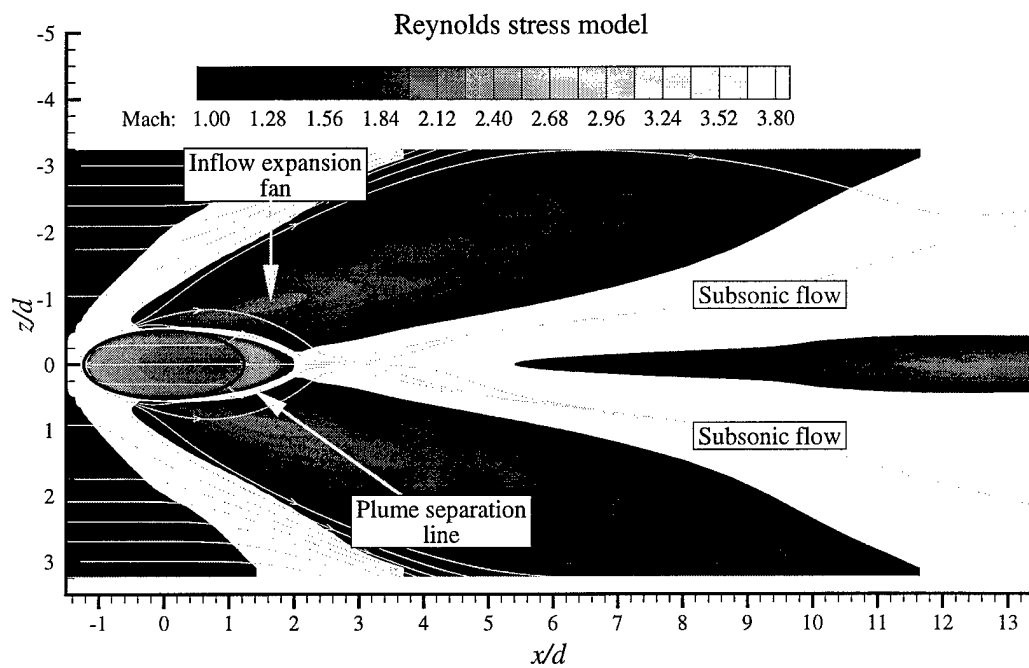


Figure 159. Mach and  $\omega_x$  contours at  $y/d = 0.022$

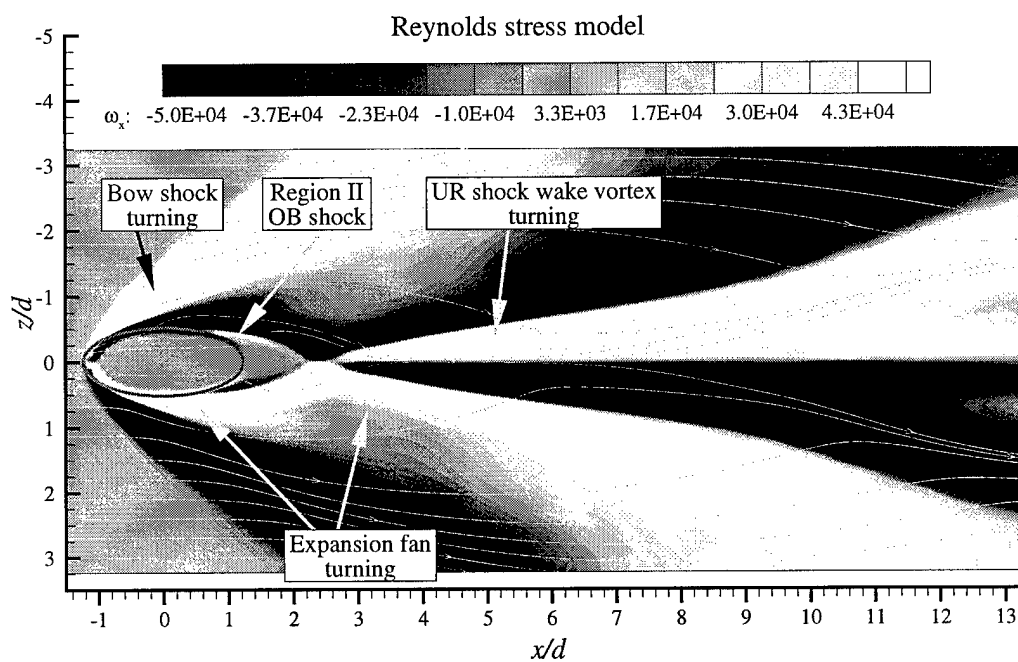
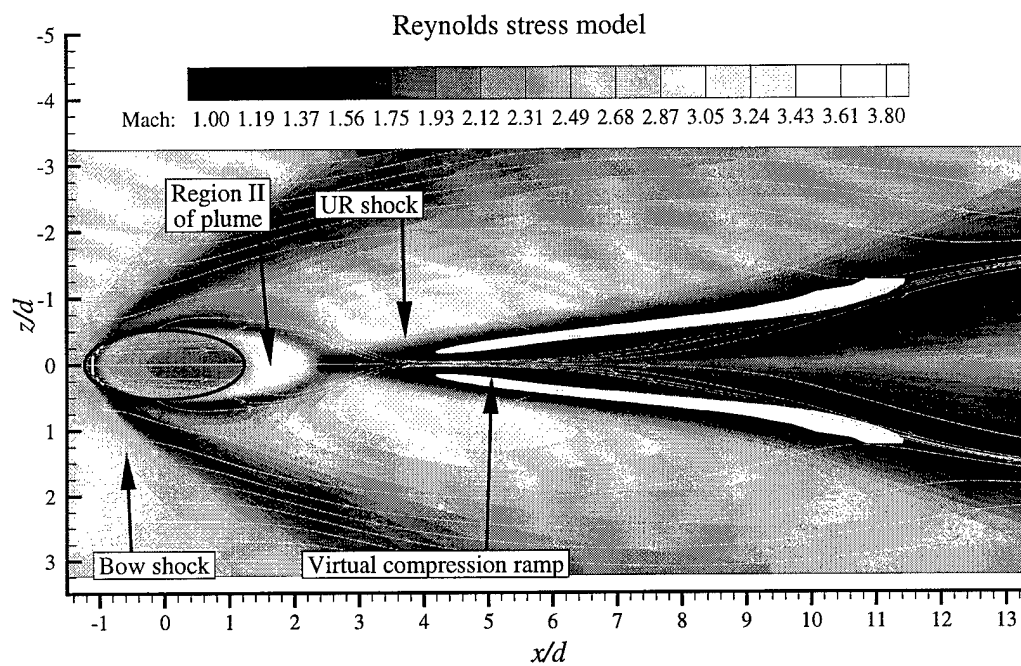


Figure 160. Mach and  $\omega_x$  contours at  $y/d = 0.100$

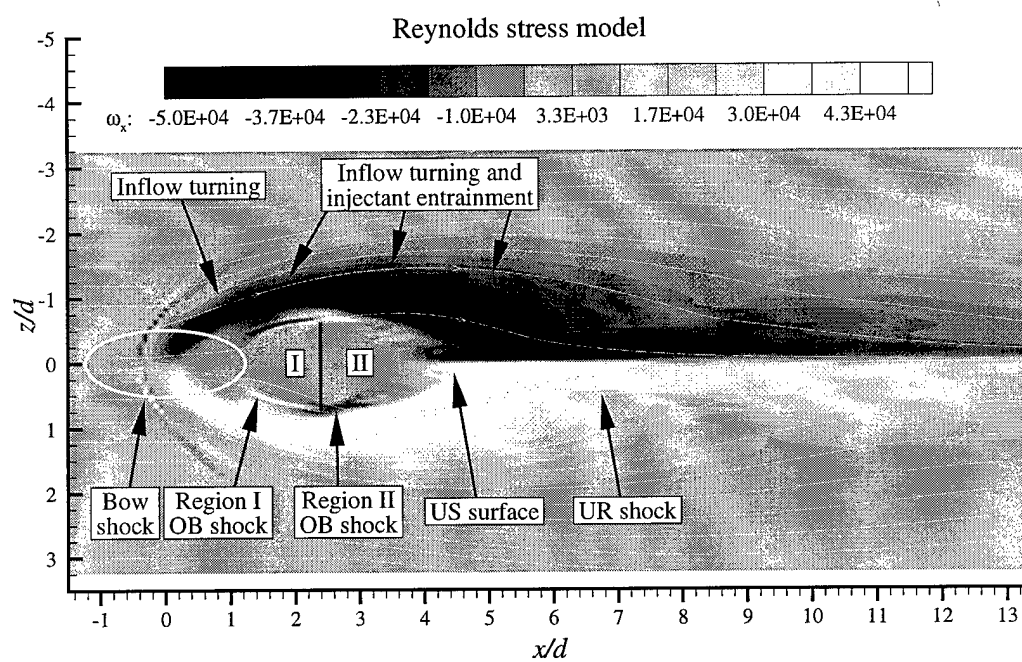


Figure 161.  $\omega_x$  contours at  $y/d = 0.910$

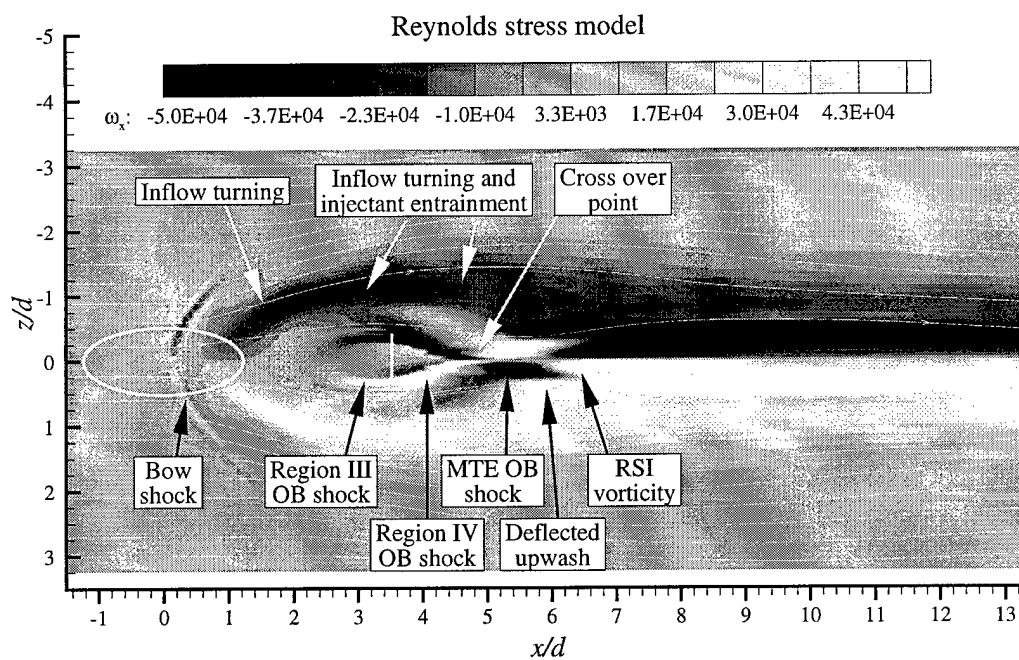


Figure 162.  $\omega_x$  contours at  $y/d = 1.49$

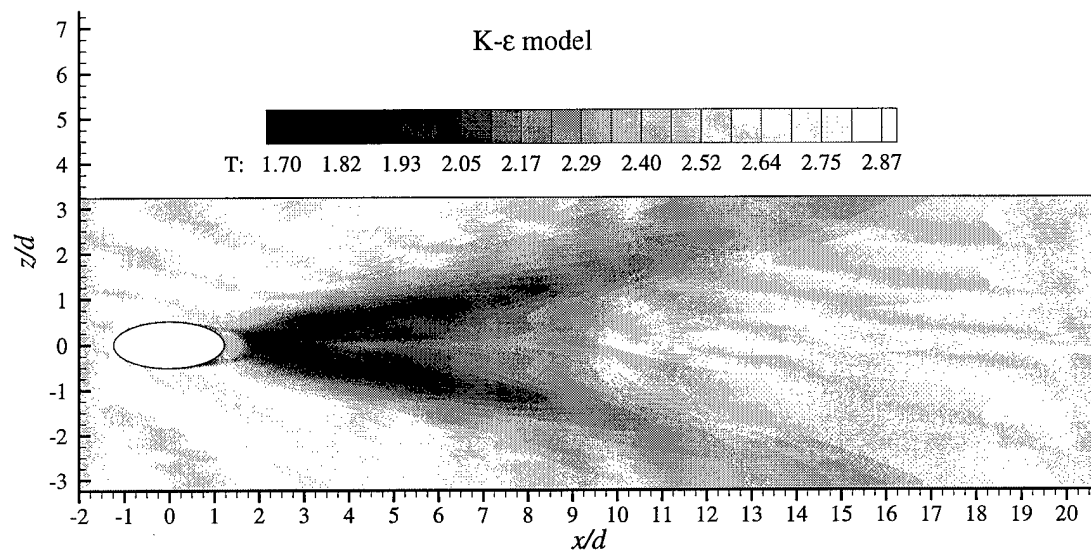


Figure 163. Surface temperature contours:  $K - \epsilon$  model

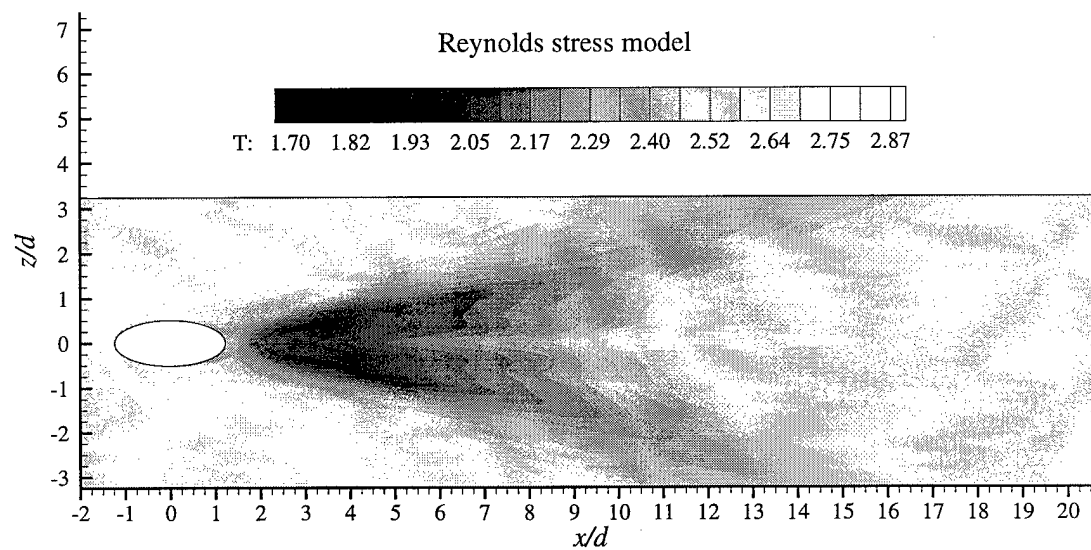


Figure 164. Surface temperature contours: RSTM

K- $\epsilon$  model

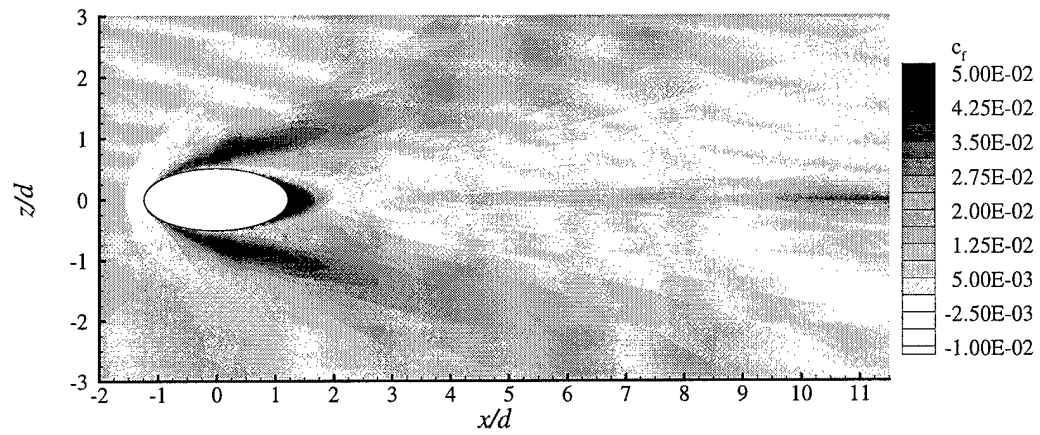


Figure 165.  $c_f$  contours:  $K - \epsilon$  model

Reynolds stress model

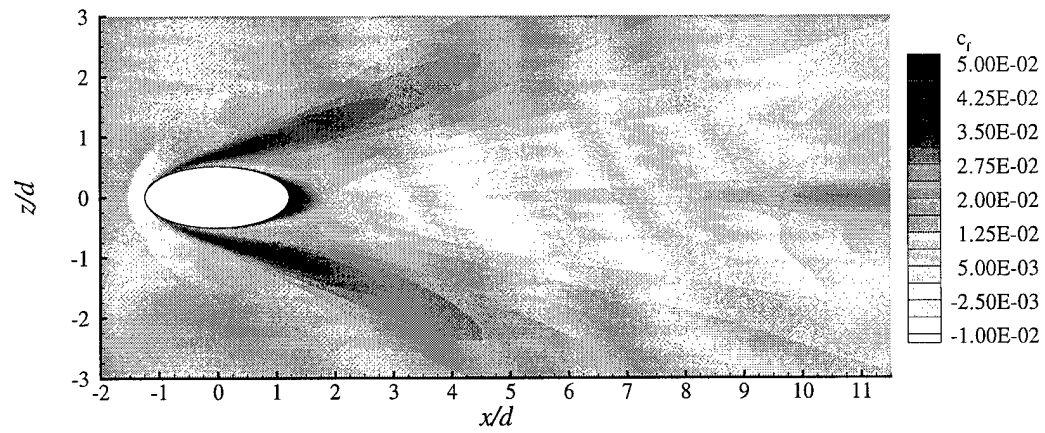


Figure 166.  $c_f$  contours: RSTM

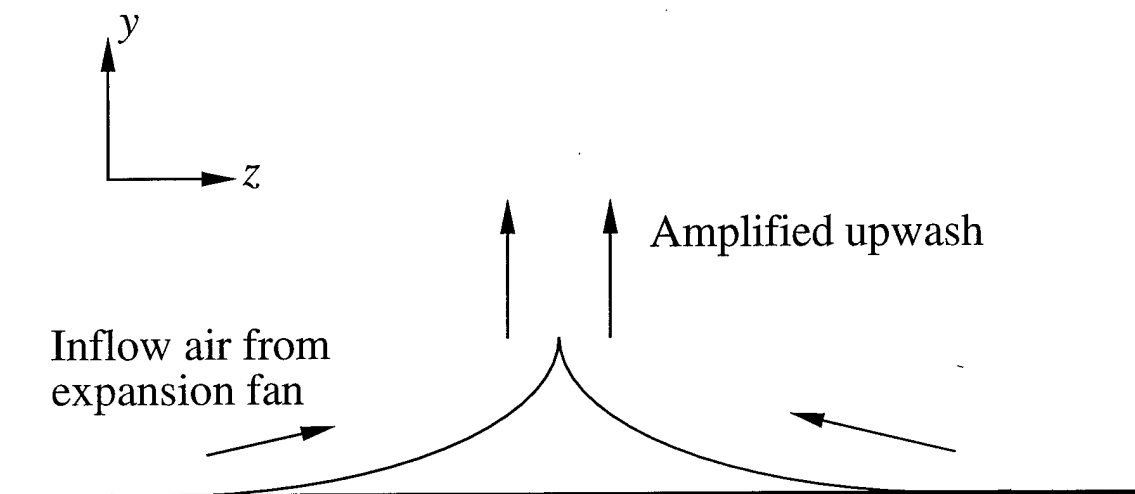


Figure 167. Upwash amplification device

## APPENDIX A - Time-Averaged Navier-Stokes Equations and the Favré-Averaged Reynolds-Stress Equation

This appendix presents a development of the compressible Reynolds-averaged Navier-Stokes equations and the Favré-averaged Navier-Stokes equations and some of the characteristics, advantages and disadvantages of each. Additionally, the Favré-averaged Reynolds-stress equations are developed.

### A.1 Navier-Stokes Equations

The compressible Navier-Stokes equations in conservative, differential form for a rectilinear coordinate system are given as:

$$\frac{\partial \rho}{\partial t} + \frac{\partial (\rho u_i)}{\partial x_i} = 0 \quad (235)$$

$$\frac{\partial (\rho u_i)}{\partial t} + \frac{\partial (\rho u_i u_j + p \delta_{ij})}{\partial x_j} - \frac{\partial \sigma_{ij}}{\partial x_j} = 0 \quad (236)$$

$$\frac{\partial (\rho E)}{\partial t} + \frac{\partial (\rho u_i H)}{\partial x_i} - \frac{\partial (u_j \sigma_{ij} - q_i)}{\partial x_i} = 0 \quad (237)$$

where

$$\sigma_{ij} = 2\mu S_{ij} + \lambda S_{kk} \delta_{ij} \quad (238)$$

$$S_{ij} = \frac{1}{2} \left( \frac{\partial u_i}{\partial x_j} + \frac{\partial u_j}{\partial x_i} \right) \quad (239)$$

and by Stokes hypothesis, the second bulk viscosity constant is given as

$$\lambda = -\frac{2}{3}\mu \quad (240)$$

and

$$E = e + \frac{1}{2} u_j u_j \quad (241)$$



$$H = E + \frac{p}{\rho} = h + \frac{1}{2}u_j u_j \quad (242)$$

$$q_i = -\kappa \frac{\partial T}{\partial x_i} \quad (243)$$

## A.2 Reynolds Averaged Navier-Stokes Equations

In 1895, Osborne Reynolds wrote *On the Dynamical Theory of Incompressible Viscous Fluids and the Determination of the Criterion* [64], in which he proposed a method of time averaging that bears his name. Reynolds-averaging allows the conservation equations to be separated into mean flow components and fluctuating components. When the instantaneous value of a characteristic flow variable,  $\phi_i$ , is Reynolds-averaged, it is decomposed as [109]

$$\phi_i = \bar{\phi}_i + \phi'_i \quad (244)$$

where the time averaged or mean flow value of  $\phi_i$  is given by

$$\bar{\phi}_i = \lim_{T \rightarrow \infty} \frac{1}{T} \int_t^{t+T} \phi_i(x_j, \tau) d\tau \quad (245)$$

with the fluctuating component  $\phi'$  found to be

$$\phi'_i = \phi_i - \bar{\phi}_i \quad (246)$$

It is easily seen that when Eq. 246 is time averaged,  $\overline{\phi'}$  vanishes [108].

Now consider the continuity equation given in Section A.1. After substituting in the mean and fluctuating components for all flow variables and expanding, Eq. 235 becomes

$$\frac{\partial (\bar{\rho} + \rho')}{\partial t} + \frac{\partial}{\partial x_i} (\bar{\rho} \bar{u}_i + \bar{\rho} u'_i + \rho' \bar{u}_i + \rho' u'_i) = 0 \quad (247)$$

After time averaging, the above equation reduces to

$$\frac{\partial (\bar{\rho})}{\partial t} + \frac{\partial}{\partial x_i} (\bar{\rho} \bar{u}_i + \overline{\rho' u'_i}) = 0 \quad (248)$$

Likewise, when the mean and fluctuating components for the flow variables are substituted into the momentum equation and expanded, Eq. 236 becomes

$$\begin{aligned} & \frac{\partial (\bar{\rho} \bar{u}_i + \bar{\rho} u'_i + \rho' \bar{u}_i + \rho' u'_i)}{\partial t} + \\ & \frac{\partial (\bar{\rho} \bar{u}_i \bar{u}_j + \bar{\rho} \bar{u}_i u'_j + \bar{\rho} u'_i \bar{u}_j + \bar{\rho} u'_i u'_j + \rho' \bar{u}_i \bar{u}_j + \bar{u}_i \rho' u'_j + \bar{u}_j \rho' u'_i + \rho' u'_i u'_j)}{\partial x_j} + \\ & \frac{\partial (\bar{p} + p')}{\partial x_j} - \frac{\partial (\bar{\sigma}_{ij} + \sigma'_{ij})}{\partial x_j} = 0 \end{aligned} \quad (249)$$

After time averaging, the above equation reduces to

$$\frac{\partial (\bar{\rho} \bar{u}_i + \rho' \bar{u}'_i)}{\partial t} + \frac{\partial (\bar{\rho} \bar{u}_i \bar{u}_j - \bar{\sigma}_{ij} - \tau_{ij}^T + \bar{p} \delta_{ij})}{\partial x_j} = 0 \quad (250)$$

where the Reynolds stress is given by

$$\tau_{ij}^T = - (\bar{\rho} u'_i u'_j + \bar{u}_i \bar{\rho}' u'_j + \bar{u}_j \bar{\rho}' u'_i + \bar{\rho}' u'_i u'_j) \quad (251)$$

A similar process is performed on the energy equation and the resultant Reynolds averaged form of the energy equation is

$$\frac{\partial (\bar{\rho} \bar{E} + \bar{\rho}' E')}{\partial t} + \frac{\partial (\bar{\rho} \bar{u}_i \bar{H})}{\partial x_i} - \frac{\partial (\bar{u}_j \bar{\sigma}_{ij} + \bar{u}'_j \bar{\sigma}'_{ij} - \bar{q}_i - q_i^T)}{\partial x_i} = 0 \quad (252)$$

where the turbulent heat flux is given by

$$q_i^T = \bar{\rho} u'_j \bar{H}' + \bar{u}_j \bar{\rho}' \bar{H}' + \bar{H} \bar{\rho}' u'_j + \bar{\rho}' u'_j \bar{H}' \quad (253)$$

Some comments about a few of the terms appearing in the Reynolds-averaged Navier-Stokes equations are in order. In the Reynolds-averaged Navier-Stokes equations,  $\bar{\rho}' u'_i$  appears in several places and is referred to as the apparent, or compressible mass. The components of the Reynolds stress tensor,  $\tau_{ij}^T$  given by Eq. 251 is composed of four terms. The first term is referred to as the incompressible turbulent shear stress and the other three terms are the compressible turbulent shear stresses. The turbulence heat transfer,  $q_i^T$ , given by Eq. 253, is also composed of four terms. In this

expression the first term is the incompressible turbulent heat transfer rate and the other three terms are compressible turbulent heat transfer rates. Also appearing in the Reynolds-averaged energy equation is an apparent energy term. All of the compressible or apparent terms are identically equal to zero for incompressible flows, i.e.  $\rho' = 0$ .

Comparison of the compressible Reynolds-averaged Navier-Stokes equations to the compressible Navier-Stokes equations reveals that the compressible terms in the compressible Reynolds-averaged Navier-Stokes equations do not have analogous terms in the laminar equations. These compressible terms make solution of the compressible Reynolds-averaged Navier-Stokes equations quite cumbersome and difficult to model, especially the apparent mass and unsteady terms. Consequently, models for the compressible Reynolds-averaged Navier-Stokes equations are seldom reported. However, when the compressible terms are negligible, e.g., incompressible flow, the Reynolds-averaged Navier-Stokes equations are similar in form to the laminar Navier-Stokes equations and are relatively easy to numerically solve once appropriate models are applied.

### A.2.1 Reynolds Averaged Navier-Stokes Equation Summary

#### Reynolds-averaged continuity equation

$$\frac{\partial (\bar{\rho})}{\partial t} + \frac{\partial (\bar{\rho} \bar{u}_i + \bar{\rho}' u'_i)}{\partial x_i} = 0 \quad (254)$$

#### Reynolds-averaged momentum equation

$$\frac{\partial (\bar{\rho} \bar{u}_i + \bar{\rho}' u'_i)}{\partial t} + \frac{\partial (\bar{\rho} \bar{u}_i \bar{u}_j - \bar{\sigma}_{ij} - \tau_{ij}^T + \bar{p} \delta_{ij})}{\partial x_j} = 0 \quad (255)$$

where

$$\tau_{ij}^T = - (\bar{\rho} u'_i u'_j + \bar{u}_i \bar{\rho}' u'_j + \bar{u}_j \bar{\rho}' u'_i + \bar{\rho}' u'_i u'_j) \quad (256)$$

#### Reynolds-averaged energy equation

$$\frac{\partial (\bar{\rho} \bar{E} + \bar{\rho}' E')}{\partial t} + \frac{\partial (\bar{\rho} \bar{u}_i \bar{H})}{\partial x_i} - \frac{\partial (\bar{u}_j \bar{\sigma}_{ij} + \bar{u}'_j \bar{\sigma}'_{ij} - \bar{q}_i - q_i^T)}{\partial x_i} = 0 \quad (257)$$

where

$$q_i^T = \overline{\bar{\rho} u_j' H'} + \bar{u}_j \overline{\rho' H'} + \bar{H} \overline{\rho' u_j'} + \overline{\rho' u_j' H'} \quad (258)$$

### A.3 Favré Averaged Navier-Stokes Equations

Favré suggested mass averaging the flow variables describing the flow field as another method to account for the turbulent fluctuations in the flow field and at the same time reduce the number of assumptions needed to model the turbulent quantities appearing in the compressible Navier-Stokes equations [19]. In Favré's method, the premise of replacing the flow quantities with a mean value plus a fluctuating component does not change, but the method by which the averaging process is executed does. Consider again the generic flow variable,  $\phi_i$ , and denote the Favré-averaged mean value component with a ' $\sim$ ' and the Favré-averaged fluctuating component by a '''. Thus, we have

$$\phi_i = \tilde{\phi}_i + \phi_i'' \quad (259)$$

In this decomposition the time averaged mean flow variable is defined as

$$\tilde{\phi}_i = \frac{\int_t^{t+T} \rho(x_j, \tau) \phi_i(x_j, \tau) d\tau}{\int_t^{t+T} \rho(x_j, \tau) d\tau} = \frac{\overline{\rho \phi_i}}{\bar{\rho}} \quad (260)$$

It is easily shown that time averaging eliminates the Favré averaged terms involving the product of the density and the fluctuating term, i.e.  $\overline{\rho \phi_i''} = 0$ . This can be seen by multiplying Eq. 259 by the density

$$\rho \phi_i = \rho \tilde{\phi}_i + \rho \phi_i'' \quad (261)$$

and then time averaging which results in

$$\overline{\rho \phi_i} = \overline{\rho \tilde{\phi}_i} + \overline{\rho \phi_i''} \quad (262)$$

$$\overline{\rho \phi_i} = \bar{\rho} \tilde{\phi}_i + \overline{\rho \phi_i''} \quad (263)$$

When combined with Eq. 260, the result is

$$\overline{\rho\phi_i} = \bar{\rho}\frac{\overline{\rho\phi_i}}{\bar{\rho}} + \overline{\rho\phi_i''} \quad (264)$$

or

$$\overline{\rho\phi_i''} = 0 \quad (265)$$

Unlike the time-averaged Reynolds-averaged fluctuating component,  $\overline{\phi'}$ , the time-averaged Favré-averaged fluctuating component,  $\overline{\phi''}$ , does not go to zero. This is clearly seen through the following exercise. Using the results just seen in Eq. 265 and substituting in the Reynolds decomposed form for  $\rho$  results in

$$\overline{\rho\phi_i''} = \overline{(\bar{\rho} + \rho')\phi_i''} = 0 \quad (266)$$

Upon performing the indicated multiplication and time averaging, the result is

$$\bar{\rho}\overline{\phi_i''} + \overline{\rho'\phi_i''} = 0 \quad (267)$$

or

$$\bar{\rho}\overline{\phi_i''} = -\overline{\rho'\phi_i''} \quad (268)$$

After dividing by  $\bar{\rho}$  one arrives at

$$\overline{\phi_i''} = -\frac{\overline{\rho'\phi_i''}}{\bar{\rho}} \quad (269)$$

which is not zero unless  $\rho'$  is zero, as is the case of an incompressible flow.

A relationship between the instantaneous Favré-averaged and Reynolds-averaged fluctuating variables can also be derived by setting Eqs. 259 and 244 equal to each other and time averaging as follows:

$$\overline{\phi_i} = \overline{\tilde{\phi}_i + \phi_i''} = \overline{\tilde{\phi}_i} + \overline{\phi_i''} \quad (270)$$

or

$$\tilde{\phi}_i + \overline{\phi_i''} = \bar{\phi}_i \quad (271)$$

solving for  $\overline{\phi_i''}$  results in

$$\overline{\phi_i''} = \bar{\phi}_i - \tilde{\phi}_i \quad (272)$$

Now, once again set Eqs. 259 and 244 equal to each other but do not time average. After solving for  $\phi_i''$  the result is

$$\phi_i'' = \phi_i' + (\bar{\phi}_i - \tilde{\phi}_i) \quad (273)$$

Substitution of Eq. 272 into the right-hand-side of the above equation results in

$$\phi_i'' = \phi_i' + \overline{\phi_i'} \quad (274)$$

Applying the definition of  $\overline{\phi_i''}$  given in Eq. 269 to the above expression results in

$$\phi_i'' = \phi_i' - \frac{\rho' \phi_i'}{\bar{\rho}} \quad (275)$$

Thus, it is seen that if the flow is incompressible,  $\rho' = 0$ , the Favré-averaged and Reynolds-averaged fluctuating components are equal to each other.

Finally, consider a correlation consisting of a Favré-averaged variable,  $\phi_i''$ , and a Reynolds-averaged variable,  $\gamma_i'$ , such that one has  $\overline{\phi_i'' \gamma_i'}$ . Substituting Eq. 275 in for  $\phi_i''$  results in

$$\overline{\phi_i'' \gamma_i'} = \overline{\phi_i' \gamma_i'} - \frac{\overline{\rho' \phi_i' \gamma_i'}}{\bar{\rho}} = \overline{\phi_i' \gamma_i'} \quad (276)$$

Returning to the task at hand, the compressible Navier-Stokes equations are mass averaged using a combination of Favré- and Reynolds-averaged flow properties, which are decomposed as follows:

$$u_i = \tilde{u}_i + u_i'' \quad e = \tilde{e} + e'' \quad (277)$$

$$\rho = \bar{\rho} + \rho' \quad p = \bar{p} + p' \quad (278)$$

$$\sigma_{ij} = \bar{\sigma}_{ij} + \sigma_{ij}' \quad q_i = \bar{q}_i + q_i' \quad (279)$$

$$h = \tilde{h} + h'' \quad (280)$$

Once again consider the continuity equation given in Section A.1. After substituting in the mean and fluctuating components for the flow variables, expanding the terms and time averaging, Eq.

235 becomes

$$\frac{\partial \bar{\rho}}{\partial t} + \frac{\partial (\bar{\rho} \tilde{u}_i + \overline{\rho u_i''})}{\partial x_i} = 0 \quad (281)$$

Now applying the property demonstrated in Eq. 265, the above equation reduces to

$$\frac{\partial \bar{\rho}}{\partial t} + \frac{\partial (\bar{\rho} \tilde{u}_i)}{\partial x_i} = 0 \quad (282)$$

which is identical in form to the laminar continuity equation.

Focusing next on the momentum equation, the Favré-averaged form is found by substituting the appropriate decomposed components into Eq. 236 and expanding. The result is the following expression

$$\begin{aligned} & \frac{\partial (\bar{\rho} \tilde{u}_i + \rho u_i'')}{\partial t} + \frac{\partial (\bar{\rho} \tilde{u}_i \tilde{u}_j + \tilde{u}_i \rho u_j'' + \tilde{u}_j \rho u_i'' + \rho u_i'' u_j'')}{\partial x_j} + \\ & \frac{\partial (\bar{p} + p')}{\partial x_i} - \frac{\partial (\bar{\sigma}_{ij} + \sigma'_{ij})}{\partial x_j} = 0 \end{aligned} \quad (283)$$

Applying the rules of time averaging, the above equation reduces to

$$\frac{\partial (\bar{\rho} \tilde{u}_i)}{\partial t} + \frac{\partial (\bar{\rho} \tilde{u}_i \tilde{u}_j)}{\partial x_j} + \frac{\partial \bar{p}}{\partial x_i} - \frac{\partial (\bar{\sigma}_{ij} - \overline{\rho u_i'' u_j''})}{\partial x_j} = 0 \quad (284)$$

Finally, the energy equation, Eq. 237, is modified. Once again, the appropriate decomposed expressions are substituted into Eq. 237 and expanded. The resulting expression is

$$\begin{aligned} & \frac{\partial (\bar{\rho} \tilde{e} + \rho e'' + \frac{1}{2} \bar{\rho} \tilde{u}_j \tilde{u}_j + \tilde{u}_j \rho u_j'' + \frac{1}{2} \rho u_j'' u_j'')}{\partial t} + \frac{\partial (\bar{\rho} \tilde{u}_i \tilde{h} + \tilde{u}_i \rho h'' + \tilde{h} \rho u_i'' + \rho u_i'' h'')}{\partial x_i} + \\ & \frac{\partial (\frac{1}{2} \bar{\rho} \tilde{u}_i \tilde{u}_j \tilde{u}_j + \tilde{u}_i \tilde{u}_j \rho u_j'' + \frac{1}{2} \bar{\rho} \tilde{u}_i u_j'' u_j'' + \frac{1}{2} \tilde{u}_j \tilde{u}_j \rho u_i'' + \rho \tilde{u}_j u_i'' u_j'' + \frac{1}{2} \rho u_i'' u_j'' u_j'')}{\partial x_i} - \\ & \frac{\partial (\tilde{u}_j \bar{\sigma}_{ij} + u_j'' \bar{\sigma}_{ij} + u_j'' \sigma'_{ij} + \tilde{u}_j \sigma'_{ij} - \bar{q}_i - q_i')}{\partial x_i} = 0 \end{aligned} \quad (285)$$

After the above equation is time averaged, the following expression is obtained:

$$\frac{\partial \left[ \bar{\rho} \left( \tilde{e} + \frac{1}{2} \tilde{u}_j \tilde{u}_j + \frac{1}{2} \overline{u_j'' u_j''} \right) \right]}{\partial t} + \frac{\partial \left[ \bar{\rho} \tilde{u}_i \left( \tilde{h} + \frac{1}{2} \tilde{u}_j \tilde{u}_j + \frac{1}{2} \overline{u_j'' u_j''} \right) \right]}{\partial x_i} + \frac{\partial \left( \overline{\bar{\rho} u_i'' h''} + \bar{\rho} \tilde{u}_j \overline{u_i'' u_j''} + \frac{1}{2} \overline{\bar{\rho} u_i'' u_j'' u_j''} \right)}{\partial x_i} - \frac{\partial \left( \tilde{u}_j \bar{\sigma}_{ij} + \overline{u_j'' \sigma_{ij}} + \overline{u_j'' \sigma_{ij}'} - \bar{q}_i \right)}{\partial x_i} = 0$$

It can be shown that

$$\overline{u_i'' h''} \approx \overline{u_i'' e''} = C_v \overline{u_i'' T''} \quad (286)$$

and by using Eq. 276 that

$$\overline{u_j'' \sigma_{ij}'} = \overline{u_j' \sigma_{ij}'} \quad (287)$$

Thus using the above relationship, the Favré-averaged energy equation can be written as

$$\frac{\partial (\bar{\rho} \tilde{E})}{\partial t} + \frac{\partial (\bar{\rho} \tilde{u}_i \tilde{H})}{\partial x_i} - \frac{\partial \left( \tilde{u}_j \bar{\sigma}_{ij} - \bar{q}_i + \overline{u_j'' \sigma_{ij}} + \overline{u_j' \sigma_{ij}'} - \bar{\rho} \overline{E'' u_i''} \right)}{\partial x_i} = 0 \quad (288)$$

where

$$K = \frac{1}{2} \overline{u_j'' u_j''} \quad (289)$$

$$\tilde{E} \equiv \tilde{e} + \frac{1}{2} \tilde{u}_j \tilde{u}_j + K \quad (290)$$

$$\tilde{H} \equiv \tilde{h} + \frac{1}{2} \tilde{u}_j \tilde{u}_j + K \quad (291)$$

$$\bar{\rho} \overline{E'' u_i''} = C_v \bar{\rho} \overline{u_i'' T''} + \bar{\rho} \tilde{u}_j \overline{u_i'' u_j''} + \frac{1}{2} \overline{\bar{\rho} u_i'' u_j'' u_j''} \quad (292)$$

The advantage of using Favré-averaging over Reynolds-averaging for a compressible flow is obvious when the Reynolds stress tensor obtained from each method is examined. Notice that the Reynolds stress tensor produced by the Favré-averaging process has three less terms than the tensor produced by the Reynolds-averaging process. In fact, the Favré-averaged term looks very much like the “incompressible” portion of the Reynolds-averaged term. The following exercise more formally shows the relationship between the Favré-averaged and the Reynolds-averaged terms.



Multiplying  $\overline{u_i'' u_j''}$  by  $\bar{\rho}$  and substituting Eq. 275 in for  $u_i''$  and  $u_j''$  results in

$$\bar{\rho} \overline{u_i'' u_j''} = \bar{\rho} \left( u_i' - \frac{\rho' u_i'}{\bar{\rho}} \right) \left( u_j' - \frac{\rho' u_j'}{\bar{\rho}} \right) \quad (293)$$

After performing the indicated multiplication, the result is

$$\bar{\rho} \overline{u_i'' u_j''} = \bar{\rho} \left( u_i' u_j' - u_j' \frac{\rho' u_i'}{\bar{\rho}} - u_i' \frac{\rho' u_j'}{\bar{\rho}} + \frac{\rho' u_i'}{\bar{\rho}} \frac{\rho' u_j'}{\bar{\rho}} \right) \quad (294)$$

Now, after applying the rules of time averaging, the above equation reduces to

$$\bar{\rho} \overline{u_i'' u_j''} = \bar{\rho} \overline{u_i' u_j'} + \bar{\rho} \frac{\overline{\rho' u_i'} \overline{\rho' u_j'}}{\bar{\rho}} \quad (295)$$

Note that if the second term on the right-hand-side of this equation is negligible, as one may expect of a fourth-order fluctuation term, the above relation reduces to

$$\bar{\rho} \overline{u_i'' u_j''} \approx \bar{\rho} \overline{u_i' u_j'} \quad (296)$$

Thus solving the Favré-averaged form of the governing equations incorporates the effects of  $\rho'$  into the solution. Justification for doing so lies in the Morkovin Hypothesis [54], which states that the effect of density fluctuations on turbulent flow may be neglected as long as the magnitude of the density fluctuations are small when compared to the mean flow density.

### A.3.1 Favré Averaged Navier-Stokes Equation Summary

Favré-averaged continuity equation

$$\frac{\partial \bar{\rho}}{\partial t} + \frac{\partial (\bar{\rho} \tilde{u}_i)}{\partial x_i} = 0 \quad (297)$$

Favré-averaged momentum equation

$$\frac{\partial (\bar{\rho} \tilde{u}_i)}{\partial t} + \frac{\partial (\bar{\rho} \tilde{u}_i \tilde{u}_j)}{\partial x_j} + \frac{\partial \bar{p}}{\partial x_i} - \frac{\partial (\bar{\sigma}_{ij} - \bar{\rho} \overline{u_i'' u_j''})}{\partial x_j} = 0 \quad (298)$$

Favré-averaged energy equation

$$\frac{\partial (\bar{\rho}\tilde{E})}{\partial t} + \frac{\partial (\bar{\rho}\tilde{u}_j\tilde{H})}{\partial x_j} - \frac{\partial (\tilde{u}_i\bar{\sigma}_{ij} - \bar{\rho}\tilde{u}_i\tau_{ij} - \bar{q}_j + \overline{u_i''\sigma_{ij}} + \bar{\rho}\overline{E''u_j''})}{\partial x_j} = 0 \quad (299)$$

where

$$K = \frac{1}{2}\overline{u_i''u_i''} \quad (300)$$

$$\tilde{E} \equiv \tilde{e} + \frac{1}{2}\tilde{u}_i\tilde{u}_i + K \quad (301)$$

$$\tilde{H} \equiv \tilde{h} + \frac{1}{2}\tilde{u}_i\tilde{u}_i + K \quad (302)$$

$$\overline{\rho E''u_j''} = \overline{u_j'\sigma_{ij}'} - \frac{1}{2}\overline{\rho u_j''u_i''u_i''} - C_p\overline{\rho u_j''T''} \quad (303)$$

#### A.4 Favré-Averaged Reynolds-Stress Equation

This section presents a development of the Favré-averaged Reynolds-Stress equations. The development of the Favré-averaged Reynolds-Stress equations begins by multiplying the  $i$  and  $j$  momentum equations given in Eq. 298 by  $u_j$  and  $u_i$  respectively. This results in

$$u_j \frac{\partial (\rho u_i)}{\partial t} + u_j \frac{\partial (\rho u_i u_k)}{\partial x_k} = -u_j \frac{\partial p}{\partial x_i} + u_j \frac{\partial \sigma_{ik}}{\partial x_k} \quad (304)$$

$$u_i \frac{\partial (\rho u_j)}{\partial t} + u_i \frac{\partial (\rho u_j u_k)}{\partial x_k} = -u_i \frac{\partial p}{\partial x_j} + u_i \frac{\partial \sigma_{jk}}{\partial x_k} \quad (305)$$

Adding the two equations, employing the product rule and taking advantage of the continuity equation, results in

$$\underbrace{\frac{\partial (\rho u_i u_j)}{\partial t}}_A + \underbrace{\frac{\partial (\rho u_i u_j u_k)}{\partial x_k}}_B = - \underbrace{u_i \frac{\partial p}{\partial x_j}}_C - \underbrace{u_j \frac{\partial p}{\partial x_i}}_D + \underbrace{u_i \frac{\partial \sigma_{jk}}{\partial x_k}}_E + \underbrace{u_j \frac{\partial \sigma_{ik}}{\partial x_k}}_F \quad (306)$$

Each individual term is Favré-averaged and then time averaged. Starting with the unsteady term, term A, the resultant Favré-averaged form is

$$A = \frac{\partial}{\partial t} (\rho \tilde{u}_i \tilde{u}_j + \rho \tilde{u}_i u_j'' + \rho u_i'' \tilde{u}_j + \rho u_i'' u_j'') \quad (307)$$

Applying the rules of time averaging to the above expression results in

$$A = \frac{\partial}{\partial t} (\bar{\rho} \tilde{u}_i \tilde{u}_j + \bar{\rho} \tau_{ij}) \quad (308)$$

Next, the convection term, term B, is Favré-averaged. The result is

$$B = \frac{\partial}{\partial x_k} \left( \begin{aligned} &\rho \tilde{u}_i \tilde{u}_j \tilde{u}_k + \tilde{u}_i \tilde{u}_k \rho u_j'' + \tilde{u}_j \tilde{u}_k \rho u_i'' + \tilde{u}_k \rho u_i'' u_j'' + \tilde{u}_i \tilde{u}_j \rho u_k'' \\ &+ \rho \tilde{u}_i u_j'' u_k'' + \tilde{u}_j \rho u_i'' u_k'' + \rho u_i'' u_j'' u_k'' \end{aligned} \right) \quad (309)$$

Applying the rules of time averaging to the above expression results in

$$B = \frac{\partial}{\partial x_k} \left( \bar{\rho} \tilde{u}_i \tilde{u}_j \tilde{u}_k + \bar{\rho} \tilde{u}_k \overline{u_i'' u_j''} + \bar{\rho} \tilde{u}_i \overline{u_j'' u_k''} + \bar{\rho} \tilde{u}_j \overline{u_i'' u_k''} + \overline{\rho u_i'' u_j'' u_k''} \right) \quad (310)$$

Rearranging the above expression and using the product rule to expand the third and fourth terms results in

$$\begin{aligned} B = & \frac{\partial}{\partial x_k} \left( \bar{\rho} \tilde{u}_i \tilde{u}_j \tilde{u}_k + \bar{\rho} \tilde{u}_k \overline{u_i'' u_j''} + \bar{\rho} \overline{u_i'' u_j'' u_k''} \right) \\ & + \bar{\rho} \tau_{jk} \frac{\partial \tilde{u}_i}{\partial x_k} + \tilde{u}_i \frac{\partial (\bar{\rho} \tau_{jk})}{\partial x_k} + \bar{\rho} \tau_{ik} \frac{\partial \tilde{u}_j}{\partial x_k} + \tilde{u}_j \frac{\partial (\bar{\rho} \tau_{ik})}{\partial x_k} \end{aligned} \quad (311)$$

Next, the velocity-pressure-gradient term, term C is Favré-averaged. The result is

$$C = \tilde{u}_i \frac{\partial \bar{p}}{\partial x_j} + \tilde{u}_i \frac{\partial p'}{\partial x_j} + u_i'' \frac{\partial \bar{p}}{\partial x_j} + u_i'' \frac{\partial p'}{\partial x_j} \quad (312)$$

Applying the rules of time averaging to the above expression results in

$$C = \tilde{u}_i \frac{\partial \bar{p}}{\partial x_j} + \overline{u_i'' \frac{\partial \bar{p}}{\partial x_j}} + \overline{u_i'' \frac{\partial p'}{\partial x_j}} \quad (313)$$

However, using the property illustrated by Eq. 276 and by using the product rule, the third term in the above expression may be written as

$$\overline{u_i'' \frac{\partial p'}{\partial x_j}} = \overline{u_i' \frac{\partial p'}{\partial x_j}} = \overline{\frac{\partial (u_i' p')}{\partial x_j}} - \overline{p' \frac{\partial u_i'}{\partial x_j}} \quad (314)$$

Finally, the velocity-pressure-gradient term is written as

$$C = \tilde{u}_i \frac{\partial \bar{p}}{\partial x_j} + \overline{u_i'' \frac{\partial \bar{p}}{\partial x_j}} + \overline{\frac{\partial (u_i' p')}{\partial x_j}} - \overline{p' \frac{\partial u_i'}{\partial x_j}} \quad (315)$$

Likewise, term D is written as

$$D = \tilde{u}_j \frac{\partial \bar{p}}{\partial x_i} + \overline{u_j'' \frac{\partial \bar{p}}{\partial x_i}} + \overline{\frac{\partial (u_j' p')}{\partial x_i}} - \overline{p' \frac{\partial u_j'}{\partial x_i}} \quad (316)$$

and similarly, terms E and F can be written as

$$E = \tilde{u}_i \frac{\partial \bar{\sigma}_{jk}}{\partial x_k} + \overline{u_i''} \frac{\partial \bar{\sigma}_{jk}}{\partial x_k} + \frac{\partial (\overline{u_i' \sigma_{jk}'})}{\partial x_k} - \overline{u_i' \frac{\partial \sigma_{jk}'}{\partial x_k}} \quad (317)$$

$$F = \tilde{u}_j \frac{\partial \bar{\sigma}_{ik}}{\partial x_k} + \overline{u_j''} \frac{\partial \bar{\sigma}_{ik}}{\partial x_k} + \frac{\partial (\overline{u_j' \sigma_{ik}'})}{\partial x_k} - \overline{u_j' \frac{\partial \sigma_{ik}'}{\partial x_k}} \quad (318)$$

Combining the Favré-averaged form of terms A-F results in

$$\begin{aligned} \frac{\partial}{\partial t} (\bar{\rho} \tilde{u}_i \tilde{u}_j + \bar{\rho} \tau_{ij}) = & -\frac{\partial}{\partial x_k} \left( \bar{\rho} \tilde{u}_i \tilde{u}_j \tilde{u}_k + \bar{\rho} \tilde{u}_k \overline{u_i'' u_j''} + \overline{\rho u_i'' u_j'' u_k''} \right) \\ & - \bar{\rho} \tau_{jk} \frac{\partial \tilde{u}_i}{\partial x_k} - \tilde{u}_i \frac{\partial (\bar{\rho} \tau_{jk})}{\partial x_k} - \bar{\rho} \tau_{ik} \frac{\partial \tilde{u}_j}{\partial x_k} - \tilde{u}_j \frac{\partial (\bar{\rho} \tau_{ik})}{\partial x_k} \\ & - \tilde{u}_i \frac{\partial \bar{p}}{\partial x_j} - \overline{u_i''} \frac{\partial \bar{p}}{\partial x_j} - \frac{\partial (\overline{u_i' p'})}{\partial x_j} + \overline{p' \frac{\partial u_i'}{\partial x_j}} \\ & - \tilde{u}_j \frac{\partial \bar{p}}{\partial x_i} - \overline{u_j''} \frac{\partial \bar{p}}{\partial x_i} - \frac{\partial (\overline{u_j' p'})}{\partial x_i} + \overline{p' \frac{\partial u_j'}{\partial x_i}} \\ & + \tilde{u}_i \frac{\partial \bar{\sigma}_{jk}}{\partial x_k} + \overline{u_i''} \frac{\partial \bar{\sigma}_{jk}}{\partial x_k} + \frac{\partial (\overline{u_i' \sigma_{jk}'})}{\partial x_k} - \overline{u_i' \frac{\partial \sigma_{jk}'}{\partial x_k}} \\ & + \tilde{u}_j \frac{\partial \bar{\sigma}_{ik}}{\partial x_k} + \overline{u_j''} \frac{\partial \bar{\sigma}_{ik}}{\partial x_k} + \frac{\partial (\overline{u_j' \sigma_{ik}'})}{\partial x_k} - \overline{u_j' \frac{\partial \sigma_{ik}'}{\partial x_k}} \end{aligned} \quad (319)$$

Now by subtracting the mean mechanical energy from the above equation, the Favré-averaged

Reynolds-stress equation is obtained. The resultant form is

$$\begin{aligned} \frac{\partial}{\partial t} (\bar{\rho} \tau_{ij}) = & -\frac{\partial}{\partial x_k} (\bar{\rho} \tilde{u}_k \tau_{ij}) - \bar{\rho} \tau_{jk} \frac{\partial \tilde{u}_i}{\partial x_k} - \bar{\rho} \tau_{ik} \frac{\partial \tilde{u}_j}{\partial x_k} \\ & + \overline{p' \frac{\partial u_i'}{\partial x_j}} + \overline{p' \frac{\partial u_j'}{\partial x_i}} + \frac{\partial}{\partial x_k} (\overline{u_i' p' \delta_{jk}} + \overline{u_j' p' \delta_{ik}}) \\ & + \overline{u_i''} \left( \frac{\partial \bar{\sigma}_{jk}}{\partial x_k} - \frac{\partial \bar{p}}{\partial x_j} \right) + \overline{u_j''} \left( \frac{\partial \bar{\sigma}_{ik}}{\partial x_k} - \frac{\partial \bar{p}}{\partial x_i} \right) \\ & + \frac{\partial}{\partial x_k} (\overline{u_j' \sigma_{ik}'} + \overline{u_i' \sigma_{jk}'} ) - \frac{\partial}{\partial x_k} (\overline{\rho u_i'' u_j'' u_k''}) \\ & - \overline{u_i' \frac{\partial \sigma_{jk}'}{\partial x_k}} - \overline{u_j' \frac{\partial \sigma_{ik}'}{\partial x_k}} \end{aligned} \quad (320)$$

or

$$\frac{\partial (\bar{\rho} \tau_{ij})}{\partial t} + \frac{\partial (\bar{\rho} \tilde{u}_k \tau_{ij})}{\partial x_k} = P_{ij} + \Pi_{ij} + M_{ij} + D_{ij}^t + D_{ij}^v - \epsilon_{ij} \quad (321)$$

In Eq. 321, the left-hand-side represents the unsteady transport and convection of the turbulent stresses. While, the right-hand-side of Eq. 321 represents the turbulent stress transport produced by the turbulent production,  $P_{ij}$ , the velocity-pressure-gradient correlation tensor,  $\Pi_{ij}$ , the mass flux variation,  $M_{ij}$ , turbulent diffusion,  $D_{ij}^t$ , and viscous diffusion,  $D_{ij}^v$ , and the viscous dissipation rate tensor,  $\epsilon_{ij}$  [22]. where the terms on the right-hand-side of Eq. 321 are given as

$$P_{ij} = -\bar{\rho}\tau_{ik}\frac{\partial\tilde{u}_j}{\partial x_k} - \bar{\rho}\tau_{jk}\frac{\partial\tilde{u}_i}{\partial x_k} \quad (322)$$

$$\Pi_{ij} = \left( \overline{p'\frac{\partial u'_i}{\partial x_j}} + \overline{p'\frac{\partial u'_j}{\partial x_i}} \right) - \frac{\partial \left( \overline{p'u'_i\delta_{jk}} + \overline{p'u'_j\delta_{ik}} \right)}{\partial x_k} \quad (323)$$

$$M_{ij} = \overline{u''_i} \left( \frac{\partial \bar{\sigma}_{jk}}{\partial x_k} - \frac{\partial \bar{p}}{\partial x_j} \right) + \overline{u''_j} \left( \frac{\partial \bar{\sigma}_{ik}}{\partial x_k} - \frac{\partial \bar{p}}{\partial x_i} \right) \quad (324)$$

$$D_{ij}^t = -\frac{\partial \left( \overline{\rho u''_i u''_j u''_k} \right)}{\partial x_k} \quad (325)$$

$$D_{ij}^v = \frac{\partial \left( \overline{\sigma'_{ik} u'_j} + \overline{\sigma'_{jk} u'_i} \right)}{\partial x_k} \quad (326)$$

$$\epsilon_{ij} = \overline{\sigma'_{ik} \frac{\partial u'_j}{\partial x_k}} + \overline{\sigma'_{jk} \frac{\partial u'_i}{\partial x_k}} \quad (327)$$

## APPENDIX B - Summary of Reynolds Stress Turbulence Model

### Closures

A summary of the second-order models presented in Chapter 4 are presented below along with the form of the Navier-Stokes equations needed to close the models.

#### B.1 Navier-Stokes Equations in a Second-Order Model

The Navier-Stokes equations presented below are simplified to account for Morkovin's hypothesis [54]. Thus, the mean flow equations which can be used by all of the second-order models are

$$\frac{\partial \bar{\rho}}{\partial t} + \frac{\partial (\bar{\rho} \tilde{u}_i)}{\partial x_i} = 0 \quad (328)$$

$$\frac{\partial (\bar{\rho} \tilde{u}_i)}{\partial t} + \frac{\partial (\bar{\rho} \tilde{u}_i \tilde{u}_j + \bar{\rho} \delta_{ij})}{\partial x_j} - \frac{\partial (\bar{\sigma}_{ij} + \bar{\rho} \tau_{ij})}{\partial x_j} = 0 \quad (329)$$

$$\frac{\partial (\bar{\rho} \tilde{E})}{\partial t} + \frac{\partial (\bar{\rho} \tilde{u}_j \tilde{H})}{\partial x_j} - \frac{\partial \left( -\bar{\rho} \tilde{u}_j \tau_{ij} + \kappa \frac{\partial \tilde{T}}{\partial x_j} + \bar{\rho} \overline{E'' u_j''} + \tilde{u}_i \bar{\sigma}_{ij} + \overline{u_i'' \sigma_{ij}} \right)}{\partial x_j} = 0$$

where

$$\tilde{E} \equiv \tilde{e} + \frac{1}{2} \tilde{u}_i \tilde{u}_i + K$$

$$\tilde{H} \equiv \tilde{h} + \frac{1}{2} \tilde{u}_i \tilde{u}_i + K$$

$$\overline{u_i''} = \frac{C_\mu f_\mu}{\bar{\rho} \sigma_\rho Pr_t} \frac{K^2}{\epsilon} \frac{\partial \bar{\rho}}{\partial x_j}$$

$$\bar{\rho} \overline{E'' u_j''} \equiv -\bar{\mu} \left( \frac{\partial K}{\partial x_j} + \frac{\partial \tau_{ij}}{\partial x_i} \right) + \frac{C_\mu f_\mu}{Pr_t} \bar{\rho} \frac{K^2}{\epsilon} \frac{\partial \tilde{T}}{\partial x_j} + \bar{\rho} C_s \frac{K}{\epsilon} \left( \frac{\partial K}{\partial x_j} + \frac{\partial \tau_{ij}}{\partial x_i} \right)$$

where  $C_\mu = 0.096$ ,  $\sigma_\rho = 0.5$ ,  $Pr_t = 0.9$  for air, and  $C_s$  is model dependent [94].

#### B.2 Second-Order Models

All of the second-order models use the following form of the Favré-averaged Reynolds-stress transport equations

$$\frac{\partial (\bar{\rho}\tau_{ij})}{\partial t} + \frac{\partial (\bar{\rho}\tilde{u}_i\tau_{ij})}{\partial x_k} - \frac{\partial D_{ij}^t}{\partial x_k} - \frac{\partial D_{ij}^v}{\partial x_k} = P_{ij} + M_{ij} - \epsilon_{ij} + \Pi_{ij} \quad (330)$$

where unless otherwise noted

$$P_{ij} = -\bar{\rho}\tau_{ik}\frac{\partial \tilde{u}_j}{\partial x_k} - \bar{\rho}\tau_{jk}\frac{\partial \tilde{u}_i}{\partial x_k} \quad (331)$$

$$D_{ij}^v = \bar{\mu} \left( \frac{\partial \tau_{ij}}{\partial x_k} + \frac{\partial \tau_{jk}}{\partial x_i} + \frac{\partial \tau_{ik}}{\partial x_j} \right) \quad (332)$$

$$D_{ij}^t = \bar{\rho}C_s \frac{K}{\epsilon} \left( \frac{\partial \tau_{ij}}{\partial x_k} + \frac{\partial \tau_{jk}}{\partial x_i} + \frac{\partial \tau_{ik}}{\partial x_j} \right) \quad (333)$$

and by Morkovin's hypothesis  $M_{ij}$  is assumed to be negligible [54].

Furthermore, all of the second-order models use the following form of the Favré-averaged dissipation-rate transport equation

$$\frac{\partial (\bar{\rho}\epsilon)}{\partial t} + \frac{\partial (\tilde{u}_k\bar{\rho}\epsilon)}{\partial x_k} - \frac{\partial D_\epsilon^\nu}{\partial x_k} - \frac{\partial D_\epsilon^t}{\partial x_k} = P_\epsilon - D_\epsilon + \Psi + \xi \quad (334)$$

where unless otherwise noted

$$D_\epsilon^\nu = \bar{\mu} \frac{\partial \epsilon}{\partial x_k} \quad (335)$$

$$D_\epsilon^t = C_\epsilon \bar{\rho} \frac{K}{\epsilon_s} \tau_{ik} \frac{\partial \epsilon}{\partial x_i} \quad (336)$$

## B.2.1 Launder, Reece, and Rodi Closure Summary

### Velocity-pressure-gradient correlation model

$$\Pi_{ij} \cong \phi_{ij,1} + \phi_{ij,2} + \phi_{ij}^w \quad (337)$$

$$\phi_{ij,1} = -C_1 \bar{\rho} \frac{\epsilon}{2K} \left( \tau_{ij} - \frac{2}{3} K \delta_{ij} \right) \quad (338)$$

$$\phi_{ij,2} = -\alpha_1 \left( P_{ij} - \frac{1}{3} P_{kk} \delta_{ij} \right) - \beta_1 \left( D_{ij} - \frac{1}{3} P_{kk} \delta_{ij} \right) \quad (339)$$

$$-2\gamma_1 \bar{\rho} K \left( S_{ij} - \frac{1}{3} S_{kk} \delta_{ij} \right)$$

$$\phi_{ij}^w = \left[ 0.125 \frac{\epsilon}{K} \left( \tau_{ij} - \frac{2}{3} K \delta_{ij} \right) + 0.015 (P_{ij} - D_{ij}) \right] \left( \frac{K^{\frac{3}{2}}}{\epsilon x_2} \right) \quad (340)$$

$$D_{ij} = -\bar{\rho} \tau_{ik} \frac{\partial \tilde{u}_k}{\partial x_j} - \bar{\rho} \tau_{jk} \frac{\partial \tilde{u}_k}{\partial x_i} \quad (341)$$

$$S_{ij} = \frac{1}{2} \left( \frac{\partial \tilde{u}_i}{\partial x_j} + \frac{\partial \tilde{u}_j}{\partial x_i} \right) \quad (342)$$

#### Dissipation rate tensor

$$\epsilon_{ij} = \frac{2}{3} \bar{\rho} \epsilon \delta_{ij} \quad (343)$$

#### Dissipation-rate transport equation model

$$D_\epsilon = C_{\epsilon_2} \bar{\rho} \frac{\epsilon^2}{K} \quad (344)$$

$$P_\epsilon = C_{\epsilon_1} \frac{\epsilon}{2K} P_{ii} \quad (345)$$

$$\Psi = 0 \quad (346)$$

$$\xi = 0 \quad (347)$$

#### Closure constants

$$\alpha_1 \equiv \frac{C_2 + 8}{11} \quad (348)$$

$$\beta_1 \equiv \frac{8C_2 - 2}{11} \quad (349)$$

$$\gamma_1 \equiv \frac{30C_2 - 2}{55} \quad (350)$$

$$C_1 = 3.0 \quad C_2 = 0.4 \quad C_s = 0.18 \quad (351)$$

$$C_\epsilon = 0.11, \quad C_{\epsilon_1} = 1.44, \quad C_{\epsilon_2} = 1.90 \quad (352)$$



### Wall boundary conditions

$$\tau_{ij} = 0 \quad (353)$$

$$\epsilon = \nu \frac{\partial^2 K}{\partial x_2^2} \quad (354)$$

## **B.2.2 Shima Closure Summary**

### Velocity-pressure-gradient correlation model

$$\Pi_{ij} \cong \phi_{ij,1} + \phi_{ij,2} + \phi_{ij}^w \quad (355)$$

$$\phi_{ij,1} = -C_1^* \bar{\rho} \frac{\epsilon}{2K} \left( \tau_{ij} - \frac{2}{3} K \delta_{ij} \right) \quad (356)$$

$$\begin{aligned} \phi_{ij,2} = & -\alpha_1 \left( P_{ij} - \frac{1}{3} P_{kk} \delta_{ij} \right) - \beta_1 \left( D_{ij} - \frac{1}{3} P_{kk} \delta_{ij} \right) \\ & - 2\gamma_1 \bar{\rho} K \left( S_{ij} - \frac{1}{3} S_{kk} \delta_{ij} \right) \end{aligned} \quad (357)$$

$$\phi_{ij}^w = f_{w1} \left[ \alpha \left( P_{ij} - \frac{2}{3} P_{kk} \delta_{ij} \right) + \beta \left( D_{ij} - \frac{2}{3} P_{kk} \delta_{ij} \right) + \gamma K S_{ij} \right] \quad (358)$$

$$C_1^* = C_1 \left[ 1 - \left( 1 - \frac{1}{C_1} \right) f_{w1} \right] \quad (359)$$

$$f_{w1} = \exp \left[ - \left( \frac{0.015 x_2 \sqrt{K}}{\bar{\nu}} \right)^4 \right] \quad (360)$$

$$D_{ij} = -\bar{\rho} \tau_{ik} \frac{\partial \tilde{u}_k}{\partial x_j} - \bar{\rho} \tau_{jk} \frac{\partial \tilde{u}_k}{\partial x_i} \quad (361)$$

$$S_{ij} = \frac{1}{2} \left( \frac{\partial \tilde{u}_i}{\partial x_j} + \frac{\partial \tilde{u}_j}{\partial x_i} \right) \quad (362)$$

### Dissipation rate tensor

$$\epsilon_{ij} = \frac{2}{3} \bar{\rho} \epsilon \delta_{ij} \quad (363)$$

### Dissipation-rate transport equation model

$$P_\epsilon + \Psi = C_{\epsilon_1} (1 + \sigma f_{w_1}) \frac{\epsilon}{2K} P_{ii} \quad (364)$$

$$D_\epsilon = C_{\epsilon_2} \bar{\rho} \frac{\epsilon \tilde{\epsilon}}{K} \quad (365)$$

$$\xi = \bar{\rho} f_{w_1} \left[ \left( \frac{7}{9} C_{\epsilon_2} - 2 \right) \frac{\epsilon \tilde{\epsilon}}{K} - \frac{\tilde{\epsilon}^2}{2K} \right] \quad (366)$$

$$\tilde{\epsilon} = \epsilon_s - 2\bar{\nu} \left( \frac{\partial \sqrt{K}}{\partial x_i} \right)^2 \quad (367)$$

$$\bar{\epsilon} = \epsilon - \bar{\nu} \frac{\partial^2 K}{\partial x_i^2} \quad (368)$$

### Closure constants

$$\alpha_1 \equiv \frac{C_2 + 8}{11} \quad (369)$$

$$\beta_1 \equiv \frac{8C_2 - 2}{11} \quad (370)$$

$$\gamma_1 \equiv \frac{30C_2 - 2}{55} \quad (371)$$

$$\alpha = 0.45, \quad \beta = 0.0, \quad \gamma = 0.08 \quad (372)$$

$$C_1 = 1.5, \quad C_2 = 0.4 \quad C_s = 0.18 \quad (373)$$

$$C_\epsilon = 0.11, \quad C_{\epsilon_1} = 1.35, \quad C_{\epsilon_2} = 1.8, \quad \sigma = 1 \quad (374)$$

### Wall boundary conditions

$$\tau_{ij} = 0 \quad (375)$$

$$\epsilon = \bar{\nu} \frac{\partial^2 K}{\partial x_2^2} \quad (376)$$

### B.2.3 Lai and So Closure Summary

#### Velocity-pressure-gradient correlation model

$$\Pi_{ij} \cong \phi_{ij,1} + \phi_{ij,2} + \phi_{ij}^w \quad (377)$$

$$\phi_{ij,1} = -C_1 \bar{\rho} \frac{\epsilon}{2K} \left( \tau_{ij} - \frac{2}{3} K \delta_{ij} \right) \quad (378)$$

$$\begin{aligned} \phi_{ij,2} = & -\alpha_1 \left( P_{ij} - \frac{1}{3} P_{kk} \delta_{ij} \right) - \beta_1 \left( D_{ij} - \frac{1}{3} P_{kk} \delta_{ij} \right) \\ & - 2\gamma_1 \bar{\rho} K \left( S_{ij} - \frac{1}{3} S_{kk} \delta_{ij} \right) \end{aligned} \quad (379)$$

$$\phi_{ij}^w = f_{w_1} \left[ \frac{C_1 \bar{\rho} \frac{\epsilon}{K} \left( \tau_{ij} - \frac{2}{3} K \delta_{ij} \right) - \bar{\rho} \frac{\epsilon}{K} (\tau_{ik} n_k n_j + \tau_{jk} n_k n_i)}{+\alpha^* \left( P_{ij} - \frac{1}{3} P_{kk} \delta_{ij} \right)} \right] \quad (380)$$

$$D_{ij} = -\bar{\rho} \tau_{ik} \frac{\partial \tilde{u}_k}{\partial x_j} - \bar{\rho} \tau_{jk} \frac{\partial \tilde{u}_k}{\partial x_i} \quad (381)$$

$$S_{ij} = \frac{1}{2} \left( \frac{\partial \tilde{u}_i}{\partial x_j} + \frac{\partial \tilde{u}_j}{\partial x_i} \right) \quad (382)$$

#### Dissipation rate tensor

$$\epsilon_{ij} = \frac{2}{3} \bar{\rho} \epsilon \delta_{ij} + \epsilon_{ij}^w \quad (383)$$

$$\epsilon_{ij}^w = f_{w_1} \left[ -\frac{2}{3} \bar{\rho} \epsilon \delta_{ij} + \bar{\rho} \frac{\epsilon}{K} \frac{(\tau_{ij} + \tau_{ik} n_k n_j + \tau_{jk} n_k n_i + n_i n_j \tau_{kl} n_k n_l)}{\left(1 + \frac{3}{2} \frac{\tau_{kl} n_k n_l}{K}\right)} \right] \quad (384)$$

$$f_{w_1} = \exp \left[ - \left( \frac{Re_t}{150} \right)^2 \right] \quad (385)$$

$$Re_t = \frac{K^2}{\bar{\nu} \epsilon} \quad (386)$$

#### Dissipation-rate transport equation model

$$D_\epsilon = C_{\epsilon_2} \bar{\rho} \frac{\epsilon \tilde{\epsilon}}{K} \quad (387)$$

$$P_\epsilon + \Psi = C_{\epsilon_1} (1 + \sigma f_{w_2}) \frac{\epsilon}{2K} P_{ii} \quad (388)$$

$$\xi = \bar{\rho} f_{w_2} \left[ \left( \frac{7}{9} C_{\epsilon_2} - 2 \right) \frac{\epsilon \tilde{\epsilon}}{K} - \frac{\epsilon^{*2}}{2K} \right] \quad (389)$$

$$\sigma = 1.0 - 0.6 \exp \left[ - \left( \frac{Re}{10^4} \right) \right] \quad (390)$$

$$\tilde{\epsilon} = \epsilon - 2\bar{\nu} \left( \frac{\partial \sqrt{K}}{\partial x_2} \right)^2 \quad (391)$$

$$f_{w_2} = \exp \left[ - \left( \frac{Re_t}{64} \right)^2 \right] \quad (392)$$

$$\epsilon^* = \epsilon - \frac{\bar{\nu} K}{x_2^2} \quad (393)$$

#### Closure constants

$$\alpha_1 \equiv \frac{C_2 + 8}{11} \quad (394)$$

$$\beta_1 \equiv \frac{8C_2 - 2}{11} \quad (395)$$

$$\gamma_1 \equiv \frac{30C_2 - 2}{55} \quad (396)$$

$$\alpha^* = 0.45 \quad C_1 = 3.0 \quad C_2 = 0.4 \quad C_s = 0.18 \quad (397)$$

$$C_\epsilon = 0.15, \quad C_{\epsilon_1} = 1.35, \quad C_{\epsilon_2} = 1.80 \quad (398)$$

#### Wall boundary conditions

$$\tau_{ij} = 0 \quad (399)$$

$$\epsilon = 2\bar{\nu} \left( \frac{\partial \sqrt{K}}{\partial x_2} \right)^2 \quad (400)$$

## B.2.4 Lai, So, Zhang, and Speziale Closure Summary

### Velocity-pressure-gradient correlation model

$$\Pi_{ij} \cong \phi_{ij,1} + \phi_{ij,2} + \phi_{ij}^w \quad (401)$$

$$\phi_{ij,1} = -C_1 \bar{\rho} \frac{\epsilon}{2K} \left( \tau_{ij} - \frac{2}{3} K \delta_{ij} \right) \quad (402)$$

$$\begin{aligned} \phi_{ij,2} = & -\alpha_1 \left( P_{ij} - \frac{1}{3} P_{kk} \delta_{ij} \right) - \beta_1 \left( D_{ij} - \frac{1}{3} P_{kk} \delta_{ij} \right) \\ & - 2\gamma_1 \bar{\rho} K \left( S_{ij} - \frac{1}{3} S_{kk} \delta_{ij} \right) \end{aligned} \quad (403)$$

$$\phi_{ij}^w = f_{w_1} \left[ C_1 \bar{\rho} \frac{\epsilon}{K} \left( \tau_{ij} - \frac{2}{3} K \delta_{ij} \right) - \bar{\rho} \frac{\epsilon}{K} (\tau_{ik} n_k n_j + \tau_{jk} n_k n_i) + \alpha^* \left( P_{ij} - \frac{1}{3} P_{kk} \delta_{ij} \right) \right] \quad (404)$$

$$D_{ij} = -\bar{\rho} \tau_{ik} \frac{\partial \tilde{u}_k}{\partial x_j} - \bar{\rho} \tau_{jk} \frac{\partial \tilde{u}_k}{\partial x_i} \quad (405)$$

$$S_{ij} = \frac{1}{2} \left( \frac{\partial \tilde{u}_i}{\partial x_j} + \frac{\partial \tilde{u}_j}{\partial x_i} \right) \quad (406)$$

$$f_{w_1} = \exp \left[ - \left( \frac{Re_t}{150} \right)^2 \right] \quad (407)$$

$$Re_t = \frac{K^2}{\bar{\nu} \epsilon} \quad (408)$$

### Dissipation rate tensor

$$\epsilon_{ij} = \frac{2}{3} \bar{\rho} \epsilon \delta_{ij} + \epsilon_{ij}^w \quad (409)$$

$$\epsilon_{ij}^w = f_{w_1} \left[ -\frac{2}{3} \bar{\rho} \epsilon \delta_{ij} + \bar{\rho} \frac{\epsilon}{K} \frac{(\tau_{ij} + \tau_{ik} n_k n_j + \tau_{jk} n_k n_i + n_i n_j \tau_{kl} n_k n_l)}{(1 + \frac{3}{2} \frac{\tau_{kl} n_k n_l}{K})} \right] \quad (410)$$

### Dissipation-rate transport equation model

$$D_\epsilon = C_{\epsilon_2} \bar{\rho} \frac{\epsilon \tilde{\epsilon}}{K} \quad (411)$$

$$P_\epsilon + \Psi = C_{\epsilon_1} (1 + \sigma f_{w_2}) \frac{\epsilon}{2K} P_{ii} \quad (412)$$

$$\xi = \bar{\rho} f_{w_2} \left[ -2 \frac{\epsilon \tilde{\epsilon}}{K} + 3 \frac{\epsilon^{*2}}{2K} \right] \quad (413)$$

$$\sigma = 1.0 - 1.5 \exp \left[ - \left( \frac{Re}{10^4} \right) \right] \quad (414)$$

$$\tilde{\epsilon} = \epsilon - 2\bar{\nu} \left( \frac{\partial \sqrt{K}}{\partial x_2} \right)^2 \quad (415)$$

$$f_{w_2} = \exp \left[ - \left( \frac{Re_t}{64} \right)^2 \right] \quad (416)$$

$$\epsilon^* = \epsilon - \frac{\bar{\nu} K}{x_2^2} \quad (417)$$

#### Closure constants

$$\alpha_1 \equiv \frac{C_2 + 8}{11} \quad (418)$$

$$\beta_1 \equiv \frac{8C_2 - 2}{11} \quad (419)$$

$$\gamma_1 \equiv \frac{30C_2 - 2}{55} \quad (420)$$

$$\alpha^* = 0.45 \quad C_1 = 3.0 \quad C_2 = 0.4 \quad C_s = 0.18 \quad (421)$$

$$C_\epsilon = 0.15, \quad C_{\epsilon_1} = 1.35, \quad C_{\epsilon_2} = 1.80 \quad (422)$$

#### Wall boundary conditions

$$\tau_{ij} = 0 \quad (423)$$

$$\epsilon = 2\bar{\nu} \left( \frac{\partial \sqrt{K}}{\partial x_2} \right)^2 \quad (424)$$

## B.2.5 Zhang, So, Gatski, and Speziale Closure Summary

### Velocity-pressure-gradient correlation model

$$\Pi_{ij} \cong \phi_{ij,1} + \phi_{ij,2} + \phi_{ij}^w + \phi_{ij}^R \quad (425)$$

$$\phi_{ij,1} = -C_1 \bar{\rho} \frac{\epsilon}{2K} \left( \tau_{ij} - \frac{2}{3} K \delta_{ij} \right) \quad (426)$$

$$\begin{aligned} \phi_{ij,2} = & -\alpha_1 \left( P_{ij} - \frac{1}{3} P_{kk} \delta_{ij} \right) - \beta_1 \left( D_{ij} - \frac{1}{3} P_{kk} \delta_{ij} \right) \\ & - 2\gamma_1 \bar{\rho} K \left( S_{ij} - \frac{1}{3} S_{kk} \delta_{ij} \right) \end{aligned} \quad (427)$$

$$\phi_{ij}^w = f_{w_1} \left[ C_1 \bar{\rho} \frac{\epsilon}{K} \left( \tau_{ij} - \frac{2}{3} K \delta_{ij} \right) - \bar{\rho} \frac{\epsilon}{K} (\tau_{ik} n_k n_j + \tau_{jk} n_k n_i) + \alpha^* \left( P_{ij} - \frac{1}{3} P_{kk} \delta_{ij} \right) \right] \quad (428)$$

$$\phi_{ij}^R = 2C_w \bar{\rho} K \left( S_{ij} - \frac{1}{3} S_{kk} \delta_{ij} \right) \frac{K^{\frac{2}{3}}}{\epsilon x_2} \quad (429)$$

$$D_{ij} = -\bar{\rho} \tau_{ik} \frac{\partial \tilde{u}_k}{\partial x_j} - \bar{\rho} \tau_{jk} \frac{\partial \tilde{u}_k}{\partial x_i} \quad (430)$$

$$S_{ij} = \frac{1}{2} \left( \frac{\partial \tilde{u}_i}{\partial x_j} + \frac{\partial \tilde{u}_j}{\partial x_i} \right) \quad (431)$$

$$f_{w_1} = \exp \left[ - \left( \frac{Re_t}{150} \right)^2 \right] \quad (432)$$

$$Re_t = \frac{K^2}{\bar{\nu} \epsilon} \quad (433)$$

$$\begin{aligned} C_w &= (C_w)_{in} - (5.8 \times 10^{-4}) M_\infty \quad \text{for } M_\infty > 2.5 \\ C_w &= (C_w)_{in} \quad \text{for } M_\infty < 2.5 \end{aligned} \quad (434)$$

$$\begin{aligned} (C_w)_{in} &= 4.14 \times 10^{-3} + 3 \times 10^{-3} (\log Re_\theta) \quad \text{for } Re_\theta \leq 5.500 \\ (C_w)_{in} &= 0.0153 \quad \text{for } Re_\theta > 5.500 \end{aligned} \quad (435)$$

### Dissipation rate tensor

$$\epsilon_{ij} = \frac{2}{3}\bar{\rho}\epsilon\delta_{ij} + \epsilon_{ij}^w \quad (436)$$

$$\epsilon_{ij}^w = f_{w_1} \left[ -\frac{2}{3}\bar{\rho}\epsilon\delta_{ij} + \bar{\rho}\frac{\epsilon}{K} \frac{(\tau_{ij} + \tau_{ik}n_kn_j + \tau_{jk}n_kn_i + n_in_j\tau_{kl}n_kn_l)}{(1 + \frac{3}{2}\frac{\tau_{kl}n_kn_l}{K})} \right] \quad (437)$$

### Dissipation-rate transport equation model

$$D_\epsilon = C_{\epsilon_2}\bar{\rho}\frac{\epsilon\tilde{\epsilon}}{K} \quad (438)$$

$$P_\epsilon + \Psi = C_{\epsilon_1}(1 + \sigma f_{w_2})\frac{\epsilon}{2K}P_{ii} \quad (439)$$

$$\xi = f_{w_2}\bar{\rho}\left(-2\frac{\epsilon\tilde{\epsilon}}{K} + 1.5\frac{\bar{\epsilon}}{K}\right) \quad (440)$$

$$\sigma = 1.0 \quad (441)$$

$$\tilde{\epsilon} = \epsilon - 2\bar{\nu}\left(\frac{\partial K^{1/2}}{\partial x_2}\right)^2 \quad (442)$$

$$f_{w_2} = \exp\left[-\left(\frac{Re_t}{40}\right)^2\right] \quad (443)$$

$$\bar{\epsilon} = \epsilon - 2\bar{\nu}\frac{K}{x_2^2} \quad (444)$$

### Closure constants

$$\alpha_1 \equiv \frac{C_2 + 8}{11} \quad (445)$$

$$\beta_1 \equiv \frac{8C_2 - 2}{11} \quad (446)$$

$$\gamma_1 \equiv \frac{30C_2 - 2}{55} \quad (447)$$

$$\alpha^* = 0.45 \quad C_1 = 3.0 \quad C_2 = 0.4 \quad C_s = 0.18 \quad (448)$$



$$C_\epsilon = 0.1, \quad C_{\epsilon_1} = 1.5, \quad C_{\epsilon_2} = 1.83 \quad (449)$$

Wall boundary conditions

$$\tau_{ij} = 0 \quad (450)$$

$$\epsilon = 2\bar{\nu} \left( \frac{\partial \sqrt{K}}{\partial x_2} \right)^2 \quad (451)$$

## APPENDIX C - Metric Development

Discretization of the domain into a structured grid of finite-volume cells with constant fluid properties over the cell volume permits application of Eq. 126 to the individual cells. Upon performing the volume integration for an individual cell, Eq. 126 is expressed as:

$$\frac{\partial}{\partial t} [(\mathbf{Q}Vol)_{i,j,k}] + \oint_{S_{i,j,k}} (\vec{\mathbf{F}} - \vec{\mathbf{F}}_v) \cdot \vec{n} dS = (\mathbf{S}Vol)_{i,j,k} \quad (452)$$

where the  $i$ ,  $j$ , and  $k$  subscripts are coordinate indices for the cell centers. Since a structured grid approach is used for this formulation, the indices range from 1 to the maximum cell index;  $I_{max}$ ,  $J_{max}$  or  $K_{max}$ , in each coordinate direction.

Applying the geometric constraints given by Eqs. 127 - 141 to individual cells results in

$$\oint_{S_{i,j,k}} \vec{n} dS = 0 \quad (453)$$

$$\int_{Vol_{i,j,k}} dVol = Vol_{i,j,k} \quad (454)$$

where

$$\sum_{i=1}^{I_{max}} \sum_{j=1}^{J_{max}} \sum_{k=1}^{K_{max}} Vol_{i,j,k} = Vol \quad (455)$$

Equations 453 and 454 require the volume of any cell identified by its  $i$ ,  $j$  and  $k$  index by finite and have a closed surface area. Additionally, Eq. 455 requires the sum of the individual cell volumes given by Eq. 141, equal the volume of the domain given by Eq. 128. These conditions are easily satisfied in finite-volume discretization schemes when the surface area and cell volume calculation method described in Vinokur [106], and Kordulla and Vinokur [37] are used. This method allows a great deal of flexibility in cell dimensions since planar cell faces are not required when this method is used.

Consider the six-sided cell with eight arbitrary corner points shown in Figure 168a for which

the surface area vectors and cell volume must be evaluated. This figure represents the transformation of a cell in physical space to computational space. The cell centroid is located at node  $i, j, k$  with vertices at points 1, 2, 3, 4, 5, 6, 7 and 8. The sides of the cell are not necessarily planar. Non-planar cell sides are a potential source of geometric error that need not be incurred. Reference [37] provides an excellent discussion of how a cell with non-planar sides is easily and accurately evaluated by dividing each cell face into two planar triangles and the volume into six tetrahedra.

Let the surface area vectors in the positive  $\xi$ ,  $\eta$  and  $\zeta$  and directions be denoted by  $\vec{S}^\xi$ ,  $\vec{S}^\eta$  and  $\vec{S}^\zeta$  respectively. Additionally, transformation vectors from physical space to computational space are defined as follows, where subscripts denote partial differentiation:

$$\vec{r}_\xi = x_{\xi\eta}\hat{\mathbf{i}} + y_{\xi\eta}\hat{\mathbf{j}} + z_{\xi\eta}\hat{\mathbf{k}} \quad (456)$$

$$\vec{r}_\eta = x_\eta\hat{\mathbf{i}} + y_\eta\hat{\mathbf{j}} + z_\eta\hat{\mathbf{k}} \quad (457)$$

$$\vec{r}_\zeta = x_\zeta\hat{\mathbf{i}} + y_\zeta\hat{\mathbf{j}} + z_\zeta\hat{\mathbf{k}} \quad (458)$$

Using the transformation vectors, Reference [106] expresses the surface area vector in the positive direction and the transformation metrics as follows:

$$\begin{aligned} \vec{S}^\xi &= \vec{S}_{1234} = \frac{1}{2} [\vec{r}_\eta \times \vec{r}_\zeta] \\ &= \frac{1}{2} [(\vec{r}_4 - \vec{r}_2) \times (\vec{r}_3 - \vec{r}_1)] \\ &= \frac{1}{2} [\vec{r}_{42} \times \vec{r}_{31}] \\ &= \left[ (y_\eta z_\zeta - y_\zeta z_\eta) \hat{\mathbf{i}} + (x_\zeta z_\eta - x_\eta z_\zeta) \hat{\mathbf{j}} + (x_\eta y_\zeta - x_\zeta y_\eta) \hat{\mathbf{k}} \right] \end{aligned}$$

With the transformation identities found in Reference [3], the surface area vector can be expressed as

$$\vec{S}^\xi = \frac{\xi_x}{J} \hat{\mathbf{i}} + \frac{\xi_y}{J} \hat{\mathbf{j}} + \frac{\xi_z}{J} \hat{\mathbf{k}} \quad (459)$$

or

$$\vec{S}^\xi = S_x^\xi \hat{\mathbf{i}} + S_y^\xi \hat{\mathbf{j}} + S_z^\xi \hat{\mathbf{k}} \quad (460)$$

where  $J$  is defined as the Jacobian of transformation in Reference [3] where it is shown that the cell  $Vol = \frac{1}{J}$ . Furthermore,  $\xi_x$ ,  $\xi_y$  and  $\xi_z$  are transformation metrics, and  $S_x^\xi$ ,  $S_y^\xi$  and  $S_z^\xi$  are the components of the surface area vector in physical space. Thus, the transformation metrics are projections of the cell surface area in physical space into computational space, scaled by the transformation Jacobian.

The surface area vectors for the  $\eta$  and  $\zeta$  directions are given as follows [106]:

$$\begin{aligned}\vec{S}^\eta &= \vec{S}_{1265} = \frac{1}{2} [\vec{r}_\zeta \times \vec{r}_\xi] \\ &= \frac{1}{2} [(\vec{r}_6 - \vec{r}_1) \times (\vec{r}_5 - \vec{r}_2)] \\ &= \frac{1}{2} [\vec{r}_{61} \times \vec{r}_{52}] \\ &= [(y_\zeta z_\xi - y_\xi z_\zeta) \hat{i} + (x_\xi z_\zeta - x_\zeta z_\xi) \hat{j} + (x_\zeta y_\xi - x_\xi y_\zeta) \hat{k}]\end{aligned}$$

thus

$$\vec{S}^\eta = \frac{\eta_x}{J} \hat{i} + \frac{\eta_y}{J} \hat{j} + \frac{\eta_z}{J} \hat{k} \quad (461)$$

and

$$\vec{S}^\eta = S_x^\eta \hat{i} + S_y^\eta \hat{j} + S_z^\eta \hat{k} \quad (462)$$

Also

$$\begin{aligned}\vec{S}^\zeta &= \vec{S}_{1584} = \frac{1}{2} [\vec{r}_\xi \times \vec{r}_\eta] \\ &= \frac{1}{2} [(\vec{r}_8 - \vec{r}_1) \times (\vec{r}_4 - \vec{r}_5)] \\ &= \frac{1}{2} [\vec{r}_{81} \times \vec{r}_{45}] \\ &= [(y_\xi z_\eta - y_\eta z_\xi) \hat{i} + (x_\eta z_\xi - x_\xi z_\eta) \hat{j} + (x_\xi y_\eta - x_\eta y_\xi) \hat{k}]\end{aligned} \quad (463)$$

thus

$$\vec{S}^\zeta = \frac{\zeta_x}{J} \hat{i} + \frac{\zeta_y}{J} \hat{j} + \frac{\zeta_z}{J} \hat{k} \quad (464)$$

and

$$\vec{S}^\zeta = S_x^\zeta \hat{i} + S_y^\zeta \hat{j} + S_z^\zeta \hat{k} \quad (465)$$

In addition to the surface area vectors, the volume of the cell is required to evaluate Eq.

452. Kordulla and Vinokur [37] recommend the following triple scalar product relationship for computation of the cell volume:

$$Vol = \vec{r}_\xi \cdot \vec{r}_\eta \times \vec{r}_\zeta \quad (466)$$

$$Vol = x_\xi (y_\eta z_\zeta - y_\zeta z_\eta) - y_\xi (x_\eta z_\zeta - x_\zeta z_\eta) + z_\xi (x_\eta y_\zeta - x_\zeta y_\eta) \quad (467)$$

Thus, the volume can be expressed as [37]

$$\begin{aligned} Vol &= J^{-1} \\ &= \frac{1}{3} (\vec{r}_7 - \vec{r}_1) \cdot \left\{ [(\vec{r}_6 - \vec{r}_1) \times (\vec{r}_5 - \vec{r}_2)] + [(\vec{r}_8 - \vec{r}_1) \times (\vec{r}_4 - \vec{r}_5)] \right. \\ &\quad \left. + [(\vec{r}_4 - \vec{r}_2) \times (\vec{r}_3 - \vec{r}_1)] \right\} \\ &= \frac{1}{3} (\vec{r}_{71}) \cdot \{ [\vec{r}_{61} \times \vec{r}_{52}] + [\vec{r}_{81} \times \vec{r}_{45}] + [\vec{r}_{42} \times \vec{r}_{31}] \} \end{aligned} \quad (468)$$

or simply as

$$Vol = J^{-1} = \frac{1}{3} (\vec{r}_{71}) \cdot (\vec{S}_{1265} + \vec{S}_{1584} + \vec{S}_{1234}) \quad (469)$$

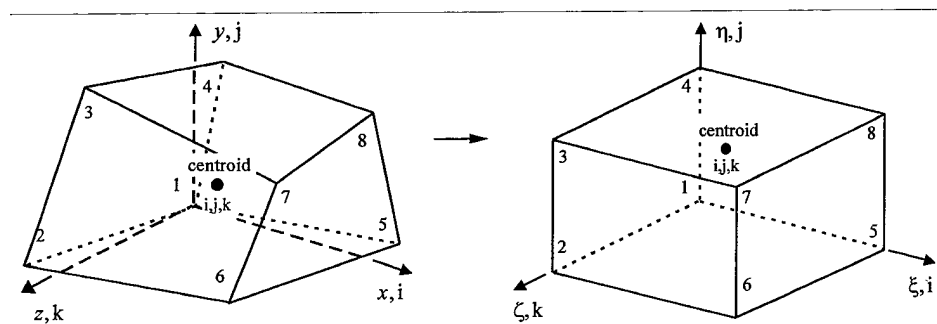


Figure 168. Transformation from Physical Space to Computational Space

## APPENDIX D - Diagonalization Matrices

The Jacobian matrices, A, B and C, for the RSTM may be written in a single form, with

$m = (\xi, \eta, \zeta)$  as [56]:

$$\frac{\partial \hat{F}}{\partial \hat{Q}} = |\nabla m| \left[ \begin{array}{cccc} 0 & \hat{m}_x & \hat{m}_y & \hat{m}_z \\ \hat{m}_x \Phi - \tilde{u} \tilde{U} & \tilde{U} - \hat{m}_x (\gamma - 2) \tilde{u} & \hat{m}_y \tilde{u} - \hat{m}_x (\gamma - 1) \tilde{v} & \hat{m}_z \tilde{u} - \hat{m}_x (\gamma - 1) \tilde{w} \\ \hat{m}_y \Phi - \tilde{v} \tilde{U} & \hat{m}_x \tilde{v} - \hat{m}_y (\gamma - 1) \tilde{u} & \tilde{U} - \hat{m}_y (\gamma - 2) \tilde{v} & \hat{m}_z \tilde{v} - \hat{m}_y (\gamma - 1) \tilde{w} \\ \hat{m}_z \Phi - \tilde{w} \tilde{U} & \hat{m}_x \tilde{w} - \hat{m}_z (\gamma - 1) \tilde{u} & \hat{m}_y \tilde{w} - \hat{m}_z (\gamma - 1) \tilde{v} & \tilde{U} - \hat{m}_z (\gamma - 2) \tilde{w} \\ \tilde{U} \Phi - \tilde{U} \tilde{H} & \hat{m}_x \tilde{H} - (\gamma - 1) \tilde{u} \tilde{U} & \hat{m}_y \tilde{H} - (\gamma - 1) \tilde{v} \tilde{U} & \hat{m}_z \tilde{H} - (\gamma - 1) \tilde{w} \tilde{U} \\ -\tilde{U} \tau_{xx} & \hat{m}_x \tau_{xx} & \hat{m}_y \tau_{xx} & \hat{m}_z \tau_{xx} \\ -\tilde{U} \tau_{yy} & \hat{m}_x \tau_{yy} & \hat{m}_y \tau_{yy} & \hat{m}_z \tau_{yy} \\ -\tilde{U} \tau_{zz} & \hat{m}_x \tau_{zz} & \hat{m}_y \tau_{zz} & \hat{m}_z \tau_{zz} \\ -\tilde{U} \tau_{xy} & \hat{m}_x \tau_{xy} & \hat{m}_y \tau_{xy} & \hat{m}_z \tau_{xy} \\ -\tilde{U} \tau_{xz} & \hat{m}_x \tau_{xz} & \hat{m}_y \tau_{xz} & \hat{m}_z \tau_{xz} \\ -\tilde{U} \tau_{yz} & \hat{m}_x \tau_{yz} & \hat{m}_y \tau_{yz} & \hat{m}_z \tau_{yz} \\ -\tilde{U} \epsilon & \hat{m}_x \epsilon & \hat{m}_y \epsilon & \hat{m}_z \epsilon \end{array} \right] \\ \left[ \begin{array}{cccc} 0 & 0 & 0 & 0 \\ \hat{m}_x (\gamma - 1) & -\hat{m}_x \frac{(\gamma-1)}{2} & -\hat{m}_x \frac{(\gamma-1)}{2} & -\hat{m}_x \frac{(\gamma-1)}{2} \\ \hat{m}_y (\gamma - 1) & -\hat{m}_y \frac{(\gamma-1)}{2} & -\hat{m}_y \frac{(\gamma-1)}{2} & -\hat{m}_y \frac{(\gamma-1)}{2} \\ \hat{m}_z (\gamma - 1) & -\hat{m}_z \frac{(\gamma-1)}{2} & -\hat{m}_z \frac{(\gamma-1)}{2} & -\hat{m}_z \frac{(\gamma-1)}{2} \\ \gamma \tilde{U} & -(\gamma - 1) \frac{\tilde{U}}{2} & -(\gamma - 1) \frac{\tilde{U}}{2} & -(\gamma - 1) \frac{\tilde{U}}{2} \\ 0 & \tilde{U} & 0 & 0 \\ 0 & 0 & \tilde{U} & 0 \\ 0 & 0 & 0 & \tilde{U} \\ 0 & 0 & 0 & 0 \\ 0 & 0 & 0 & 0 \\ 0 & 0 & 0 & 0 \\ 0 & 0 & 0 & 0 \\ 0 & 0 & 0 & 0 \\ 0 & 0 & 0 & 0 \end{array} \right] \quad (470)$$

where

$$\tilde{U} = \hat{m}_x \tilde{u} + \hat{m}_y \tilde{v} + \hat{m}_z \tilde{w} \quad (471)$$

$$\Phi = \frac{1}{2} (\gamma - 1) \tilde{q}^2 \quad (472)$$

$$\tilde{q}^2 = \tilde{u}^2 + \tilde{v}^2 + \tilde{w}^2 \quad (473)$$

The Jacobian matrix may be written as  $\frac{\partial \hat{F}}{\partial \hat{Q}} = T \Lambda T^{-1}$ . The symmetry matrix,  $T$ , is given as [56]:

$$T = \begin{bmatrix} 1 & 0 & 0 & 1 & 1 & 0 & 0 & 0 & 0 & 0 & 0 & 0 \\ \tilde{u} & \hat{l}_x & \hat{j}_x & \tilde{u} + \hat{m}_x \tilde{a} & \tilde{u} - \hat{m}_x \tilde{a} & 0 & 0 & 0 & 0 & 0 & 0 & 0 \\ \tilde{v} & \hat{l}_y & \hat{j}_y & \tilde{v} + \hat{m}_y \tilde{a} & \tilde{v} - \hat{m}_y \tilde{a} & 0 & 0 & 0 & 0 & 0 & 0 & 0 \\ \tilde{w} & \hat{l}_z & \hat{j}_z & \tilde{w} + \hat{m}_z \tilde{a} & \tilde{w} - \hat{m}_z \tilde{a} & 0 & 0 & 0 & 0 & 0 & 0 & 0 \\ \frac{\tilde{q}^2}{2} + K & \tilde{V} & \tilde{W} & \tilde{H} + \tilde{U} \tilde{a} & \tilde{H} - \tilde{U} \tilde{a} & 1/2 & 1/2 & 1/2 & 0 & 0 & 0 & 0 \\ \tau_{xx} & 0 & \tau_{xx} & \tau_{xx} & 0 & 1 & 0 & 0 & 0 & 0 & 0 & 0 \\ \tau_{yy} & 0 & \tau_{yy} & \tau_{yy} & 0 & 0 & 1 & 0 & 0 & 0 & 0 & 0 \\ \tau_{zz} & 0 & \tau_{zz} & \tau_{zz} & 0 & 0 & 0 & 1 & 0 & 0 & 0 & 0 \\ \tau_{xy} & 0 & \tau_{xy} & \tau_{xy} & 0 & 0 & 0 & 0 & 1 & 0 & 0 & 0 \\ \tau_{xz} & 0 & \tau_{xz} & \tau_{xz} & 0 & 0 & 0 & 0 & 0 & 1 & 0 & 0 \\ \tau_{yz} & 0 & \tau_{yz} & \tau_{yz} & 0 & 0 & 0 & 0 & 0 & 0 & 1 & 0 \\ \epsilon & 0 & 0 & \epsilon & \epsilon & 0 & 0 & 0 & 0 & 0 & 0 & 1 \end{bmatrix} \quad (474)$$

where

$$\tilde{V} = \hat{l}_x \tilde{u} + \hat{l}_y \tilde{v} + \hat{l}_z \tilde{w} \quad (475)$$

$$\tilde{W} = \hat{j}_x \tilde{u} + \hat{j}_y \tilde{v} + \hat{j}_z \tilde{w} \quad (476)$$

The inverse of the symmetry matrix,  $T^{-1}$ , is given as [56]:

$$T^{-1} = \begin{bmatrix} 1 - \Upsilon \tilde{q}^2/2 & \Upsilon \tilde{u} & \Upsilon \tilde{v} \\ -\tilde{V} & \hat{l}_x & \hat{l}_y \\ -\tilde{W} & \hat{j}_x & \hat{j}_y \\ \Upsilon \tilde{q}^2/4 - \tilde{U}/2\tilde{a} & \hat{m}_x/2\tilde{a} - \Upsilon \tilde{u} \tilde{q}^2/2 & \hat{m}_y/2\tilde{a} - \Upsilon \tilde{v} \tilde{q}^2/2 \\ \Upsilon \tilde{q}^2/4 + \tilde{U}/2\tilde{a} & -\hat{m}_x/2\tilde{a} - \Upsilon \tilde{u} \tilde{q}^2/2 & -\hat{m}_y/2\tilde{a} - \Upsilon \tilde{v} \tilde{q}^2/2 \\ -\tau_{xx} & 0 & 0 \\ -\tau_{yy} & 0 & 0 \\ -\tau_{zz} & 0 & 0 \\ -\tau_{xy} & 0 & 0 \\ -\tau_{xz} & 0 & 0 \\ -\tau_{yz} & 0 & 0 \\ -\epsilon & 0 & 0 \\ \Upsilon \tilde{w} & -\Upsilon & \Upsilon/2 & \Upsilon/2 & \Upsilon/2 & 0 & 0 & 0 & 0 \\ \hat{l}_z & 0 & 0 & 0 & 0 & 0 & 0 & 0 & 0 \\ \hat{j}_z & 0 & 0 & 0 & 0 & 0 & 0 & 0 & 0 \\ \hat{m}_z/2\tilde{a} - \Upsilon \tilde{w} \tilde{q}^2/2 & \Upsilon/2 & -\Upsilon/4 & -\Upsilon/4 & -\Upsilon/4 & 0 & 0 & 0 & 0 \\ -\hat{m}_z/2\tilde{a} - \Upsilon \tilde{w} \tilde{q}^2/2 & \Upsilon/2 & -\Upsilon/4 & -\Upsilon/4 & -\Upsilon/4 & 0 & 0 & 0 & 0 \\ 0 & 0 & 1 & 0 & 0 & 0 & 0 & 0 & 0 \\ 0 & 0 & 0 & 1 & 0 & 0 & 0 & 0 & 0 \\ 0 & 0 & 0 & 0 & 1 & 0 & 0 & 0 & 0 \\ 0 & 0 & 0 & 0 & 0 & 1 & 0 & 0 & 0 \\ 0 & 0 & 0 & 0 & 0 & 0 & 1 & 0 & 0 \\ 0 & 0 & 0 & 0 & 0 & 0 & 0 & 1 & 0 \\ 0 & 0 & 0 & 0 & 0 & 0 & 0 & 0 & 1 \end{bmatrix} \quad (477)$$



where

$$\Upsilon = (\gamma - 1) \tilde{a} \quad (478)$$

The vectors  $\hat{l}$  and  $\hat{j}$  are non-unique, mutually orthogonal to  $\hat{m}$ , and tangent vectors in the plane of the cell interface.

## APPENDIX E - Boundary Conditions

The finite-volume method used by ISAAC requires a six-sided computational domain for both two- and three-dimensional simulations. A typical six-sided computational domain is shown in Figure 169. For the simulations conducted for this research, side one corresponds to the solid surface of the flat plate or test section. Side two is the inflow plane, and side three is the outflow plane. Depending of the configuration being simulated, sides four, five and six are either the top of the wind tunnel and the two side walls or they may be additional planes through which allow flow passage.

### E.1 Inflow Boundary Conditions

The flow upstream of the inflow plane is supersonic for all of the configurations investigated during this research. Thus, the leading edge of the flat plate is taken to be the beginning of the computational domain and all mean flow variables are assigned freestream values. Inflow turbulence quantities for both models are based upon the turbulence intensity of the undisturbed flow. Turbulence intensity is defined as  $TI \equiv \sqrt{2/3K_\infty}/u_\infty$  and the value of  $TI$  is usually a well documented characteristic of a particular wind tunnel test section. For the  $K - \epsilon$  model,  $K_\infty$  is computed directly from the definition of  $TI$  such that  $K_\infty = \frac{3}{2}(TIu_\infty)^2$ . For the RSTM,  $\tau_{xx}$ ,  $\tau_{yy}$  and  $\tau_{zz}$  are determined by assuming the freestream turbulence is homogeneous and isotropic. Thus, from the definition  $K \equiv (\tau_{xx} + \tau_{yy} + \tau_{zz})/2$  one arrives at  $\tau_{xx_\infty} = \tau_{yy_\infty} = \tau_{zz_\infty} = 2/3K_\infty$  and  $\tau_{xy_\infty} = \tau_{xz_\infty} = \tau_{yz_\infty} = 0$ . The freestream dissipation-rate for both turbulence models is commonly found by setting  $\mu_{t_\infty} = \mu_\infty$  in Eq. 37 such that  $\epsilon_\infty = \rho_\infty K_\infty^2 / \mu_\infty$  [23, 65].

### E.2 Wall, Tangency, Symmetry and Extrapolation Boundary Conditions

At the test section surface, the no-slip condition,  $u = v = w = 0$ , is invoked, along with  $\partial p / \partial n = 0$ . For an adiabatic wall,  $\partial T / \partial n = 0$ , is enforced for temperature, or a specified constant temperature for the wall may be used if the wall is heated or cooled. The homogeneous condition applies to the Reynolds stresses at the wall such that  $K = \tau_{ij} = 0$ . To maintain asymptotic

consistency of the dissipation-rate equation at the wall,  $\epsilon = 2\bar{\nu} \left( \partial \sqrt{K} / \partial y \right)^2$  is used as the boundary condition for the dissipation-rate equation [56].

When all four walls of the test section are included in the computational domain, the viscous no-slip boundary condition should be applied at each wall. However, proper modeling of a viscous boundary layer requires a substantial number of nodes near each solid surface to accurately capture the boundary layer structure. However, if the main reason for modeling a wall is to capture the reflected shock structure, a tangency boundary condition is an alternative which will reduce the number of cells required at a solid surface. Thus, in the interest of minimizing the number of nodes needed to model the test section, the viscous no-slip boundary condition is only enforced on the lower wall and the tangency boundary condition is used at all other solid surfaces.

Abbett's method [1] is used to enforce tangency of the velocity components at solid surfaces in ISAAC. Abbett's method requires the dot product of the velocity vector and a unit vector normal to the solid surface be zero. The boundary conditions imposed on the other variables when tangency is used are as follows:  $\partial T / \partial n = 0$  for temperature and zero gradient at the wall for pressure and the turbulent variables such that  $\partial p / \partial n = 0$ ,  $\partial \epsilon / \partial n = 0$  and  $\partial K / \partial n = 0$  or  $\partial \tau_{ij} / \partial n = 0$ .

When symmetry across the line  $z/d = 0.0$  is required, the values one cell into the domain normal to the  $x - y$  plane is used as value of the ghost cell. This procedure is used for each of the conserved variables with the exception of  $w$ ,  $\tau_{xz}$ , and  $\tau_{yz}$ . For these variables, the additive inverse is reflected across the boundary.

Finally, a first-order extrapolation from the interior is used as the boundary condition at any surface considered an outflow plane.

### E.3 Jet Boundary Conditions

A discontinuity is present between the jet exit and the surrounding flowfield when uniform mean flow properties are used for the exit properties of the jet. During the initial phase of this

research, this discontinuity often lead to unstable behavior in the algorithm. Therefore, a blending algorithm which simulates the boundary layer over the interior of the nozzle is used to smooth transition between the injectant mean flow properties and the surrounding flowfield properties for both the two- and three-dimensional simulations.

### E.3.1 Two-Dimensional Jet

For the two-dimensional slots and rectangular jets, a laminar Couette flow (see White [108]) boundary layer is simulated as the outflow velocity over the jet. The additional constraint of constant total enthalpy or constant total temperature is imposed to simulate adiabatic expansion within the nozzle. The input data required by ISAAC to model these jet outflow conditions are as follows:

$$PJET = \frac{p_{inj}}{p_{\infty}} \quad (479)$$

$$TJET = \frac{T_{inj}}{T_{\infty}} \quad (480)$$

$$UJET = \frac{u_{inj}}{a_{\infty}} \quad (481)$$

$$VJET = \frac{v_{inj}}{a_{\infty}} \quad (482)$$

$$WJET = \frac{w_{inj}}{a_{\infty}} \quad (483)$$

$$NCELLS \quad (484)$$

where the subscript *inj* denotes local jet conditions and  $\infty$  denotes freestream conditions and *NCELLS* is the number of cells at each edge of the nozzle used to simulate the boundary layer.

Prior to computing the velocity profile, the total temperature of the injectant,  $T_{0_{inj}}$ , and the incremental values of the injectant Mach number must be determined. Thus,  $T_{0_{inj}}$  is computed from the following equation [4]

$$T_{0_{inj}} = T_{inj} \left( 1 + \frac{\gamma - 1}{2} M_{inj}^2 \right) \quad (485)$$

where  $T_{inj}$  and  $M_{inj}$  are computed from input values using the following expressions

$$T_{inj} = T_{\infty} * TJET \quad (486)$$

$$M_{inj} = \sqrt{\frac{UJET^2 + VJET^2 + WJET^2}{TJET}} \quad (487)$$

Linear increments for the Mach number at an edge of the nozzle are given by

$$M_{inj_{inc}} = \frac{M_{inj}}{\sum_{i=1}^{NCELLS} \Delta x_i} \Delta x_{inc} \quad (488)$$

where  $inc$  denotes an incremental value,  $\Delta x_i$  is the distance between any two cells and  $\Delta x_{inc}$  is the distance between the edge of the jet and the current location within the jet. This is simply a linear profile for Mach number which assumes the Mach number at the edge of the nozzle is zero.

Now, assuming constant total temperature and a linear velocity profile, the injectant temperature at any location between the edge of the nozzle and the nozzle interior is given as

$$T_{inj_{inc}} = \frac{T_{0_{inj}}}{1 + \frac{\gamma - 1}{2} M_{inj_{inc}}^2} \quad (489)$$

Thus, the individual velocity components over this same interval are computed as

$$UJET_{inc} = \sqrt{(U_{fraction} M_{inj_{inc}})^2 T_{inj_{inc}}} \quad (490)$$

$$VJET_{inc} = \sqrt{(V_{fraction} M_{inj_{inc}})^2 T_{inj_{inc}}} \quad (491)$$

$$WJET_{inc} = \sqrt{(W_{fraction} M_{inj_{inc}})^2 T_{inj_{inc}}} \quad (492)$$

where the subscript *fraction* denotes the fraction of  $M_{inj}$  comprised by each velocity component.

The fraction for each component is given by

$$U_{fraction} = \frac{\sqrt{UJET^2 / TJET}}{M_{inj}} \quad (493)$$

$$V_{fraction} = \frac{\sqrt{VJET^2/TJET}}{M_{inj}} \quad (494)$$

$$W_{fraction} = \frac{\sqrt{WJET^2/TJET}}{M_{inj}} \quad (495)$$

Theoretically, the pressure across the jet exit plane should be constant [108]. However, enforcing the pressure profile as a step function across the edge of the jet and the solid surface of the plate results in numerical instability when large pressure ratios are used. This algorithm is particularly sensitive to this pressure jump at corners of the rectangular nozzles. Thus, to lessen the sudden discontinuity at the interface, a linear progression similar to the one performed for  $M_{inj}$  is performed with  $p_{wall}$  and  $PJET$  to smooth the transition between the two pressure boundary conditions.

Uniform mean flow boundary conditions specified by  $PJET$ ,  $UJET$ ,  $VJET$ ,  $WJET$  and  $TJET$  are used at all other locations within the outflow plane of the nozzle.

Since the flowfields evaluated in this study have either sonic or supersonic conditions at the exit plane of the nozzle, turbulence levels for  $K$ ,  $\tau_{ij}$  and  $\epsilon$  should be specified along this boundary. However, this information is generally not available for computational efforts. Therefore, in a manner similar to that used by Rizzetta [65], uniform boundary conditions of  $\partial K/\partial n = \partial \tau_{ij}/\partial n = \partial \epsilon/\partial n = 0$  are used for the turbulence variables at all locations over the outflow plane of the nozzle. The acceptability of the numerical results based on these conditions must be evaluated by comparison of the numerical results with the experimental data.

### E.3.2 Three-Dimensional Jet

For three-dimensional elliptic or circular nozzles, a truncated tanh function is used to simulate a velocity boundary layer profile for the outflow over the nozzle. Once again, the additional constraint of constant total enthalpy or constant total temperature is imposed to simulate adiabatic expansion within the nozzle. The input data required by ISAAC to model this jet outflow condition

is as follows:

$$PJET = \frac{p_{inj}}{p_{\infty}} \quad (496)$$

$$TJET = \frac{T_{inj}}{T_{\infty}} \quad (497)$$

$$UJET = \frac{u_{inj}}{a_{\infty}} \quad (498)$$

$$VJET = \frac{v_{inj}}{a_{\infty}} \quad (499)$$

$$WJET = \frac{w_{inj}}{a_{\infty}} \quad (500)$$

$$SEMMJR \quad (501)$$

$$SEMMNR \quad (502)$$

$$DELTA RO \quad (503)$$

where the subscript *inj* denotes local jet conditions,  $\infty$  denotes freestream conditions, *SEMMJR* and *SEMMNR* are the semimajor and semiminor axes of the nozzle exit and *DELTA RO* is the radial width of the region within the nozzle exit used to simulate the boundary layer.

When the conic jet boundary condition is used, one of three types of boundary conditions are applied to cells at the test section surface. The type of boundary condition applied is determined by the radial distance of the cell centroid from the center of the nozzle outflow plane. The application of a particular type of boundary condition to a cell is given by the following criteria:

$$\text{Boundary condition applied} = \begin{cases} \text{mean flow nozzle conditions} & \text{if } r_{act} - r_{edge} < 0 \\ \text{viscous wall conditions} & \text{if } r_{act} - r_{edge} > DELTA RO \\ \text{simulated boundary layer} & \text{if } 0 \leq r_{act} - r_{edge} \leq DELTA RO \end{cases} \quad (504)$$

where, as shown in Figure 170,  $r_{act}$  is the distance of the current cell centroid from  $r_0$  and  $r_{edge}$  is the distance of the edge of the nozzle from  $r_0$  along the same ray as  $r_{act}$ .

If the current cell requires the simulated boundary condition, the algorithm outlined below is applied. Prior to computing the velocity profile, the total temperature of the injectant,  $T_{0_{inj}}$ , the Mach number of the injectant,  $M_{inj}$ , and the fraction of the Mach number comprised of by each component of velocity are determined. Thus,  $T_{0_{inj}}$  is computed from the following equation [4]

$$T_{0_{inj}} = T_{inj} \left( 1 + \frac{\gamma - 1}{2} M_{inj}^2 \right) \quad (505)$$

where  $T_{inj}$  and  $M_{inj}$  are computed from input values using the following expressions

$$T_{inj} = T_{\infty} * TJET \quad (506)$$

$$M_{inj} = \sqrt{\frac{UJET^2 + VJET^2 + WJET^2}{TJET}} \quad (507)$$

The velocity fractions are computed as

$$U_{fraction} = \frac{\sqrt{UJET^2/TJET}}{M_{inj}} \quad (508)$$

$$V_{fraction} = \frac{\sqrt{VJET^2/TJET}}{M_{inj}} \quad (509)$$

$$W_{fraction} = \frac{\sqrt{WJET^2/TJET}}{M_{inj}} \quad (510)$$

The incremental values of the Mach number within the simulated boundary layer are computed from

$$M_{inj_{inc}} = \tanh \left( \frac{2(r_{act} - r_{edge})}{DELTA RO} \right) M_{inj} \quad (511)$$

This function varies between 0 and  $M_{inj}$  and provides a smooth, continuous transition from the test section surface to the interior of the nozzle. Now, assuming constant total temperature, the injectant temperature at any location within the simulated boundary layer is given as

$$T_{inj_{inc}} = \frac{T_{0_{inj}}}{1 + \frac{\gamma - 1}{2} M_{inj_{inc}}^2} \quad (512)$$



and the individual velocity components over this same interval are computed as

$$UJET_{inc} = \sqrt{(U_{fraction} M_{inj_{inc}})^2 T_{inj_{inc}}} \quad (513)$$

$$VJET_{inc} = \sqrt{(V_{fraction} M_{inj_{inc}})^2 T_{inj_{inc}}} \quad (514)$$

$$WJET_{inc} = \sqrt{(W_{fraction} M_{inj_{inc}})^2 T_{inj_{inc}}} \quad (515)$$

As stated in the previous section, the pressure across the jet exit plane should be constant [108]. However, enforcing the pressure profile as a step function across the edge of the jet and the solid surface of the plate can result in numerical instability when large pressure ratios are used. Thus, to lessen the sudden discontinuity at the interface, a similar function to the one performed for  $M_{inj}$  is performed with  $p_{wall}$  and is given as

$$P_{inj_{inc}} = \tanh\left(\frac{2(r_{act} - r_{edge})}{DELTA_{RO}}\right) (PJET - 1) + 1 \quad (516)$$

This function varies between 1 at the nozzle edges to  $PJET$  at the nozzle interior.

Uniform mean flow boundary conditions specified by  $PJET$ ,  $UJET$ ,  $VJET$ ,  $WJET$  and  $TJET$  are used at all other locations within the outflow plane of the nozzle.

Since the flowfields evaluated in this study have either sonic or supersonic conditions at the exit plane of the nozzle, turbulence levels for  $K$ ,  $\tau_{ij}$  and  $\epsilon$  should be specified along this boundary. However, this information is generally not available for computational efforts. Therefore, in a manner similar to that used by Rizzetta [65], uniform boundary conditions of  $\partial K / \partial n = \partial \tau_{ij} / \partial n = \partial \epsilon / \partial n = 0$  are used for the turbulence variables at all locations over the outflow plane of the nozzle. The acceptability of the numerical results based on these conditions must be evaluated by comparison of the numerical results with the experimental data.

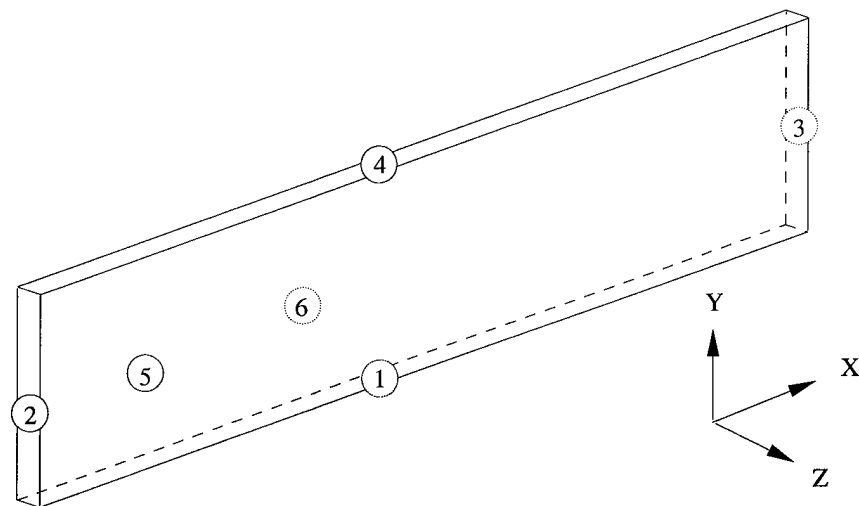


Figure 169. Typical computational box

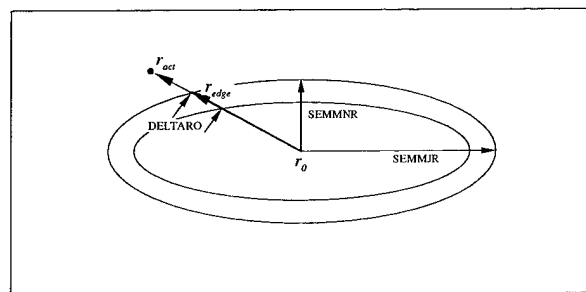


Figure 170. Three-dimensional conic jet boundary condition

## APPENDIX F - Convergence Criteria

This appendix addresses the criteria used to determine temporal convergence of the simulations and presents the data used to evaluate grid convergence. All of the analyses presented in this appendix are based on the ZSGS  $K - \epsilon$  model.

### F.1 Temporal Convergence Criteria

Temporal convergence of a simulation is assessed through an evaluation of the residual error of a simulation; cyclic minimum in the residual is used as the basis for temporal convergence in this study. The residual error and the surface static pressure ratio ( $p_{wall}/p_{\infty}$ ) from a simulation of the Aso et al. configuration with  $p_{inj}/p_{\infty} = 10.29$  is shown in Figures 171 and 172 respectively. The quantities shown in these two figures are typical of the representations of the residual and pressure ratio results from the simulations performed in this study.

The plot of the equation residuals show that convergence to a minimum value is not a smooth process with this turbulence model. This is especially true of the dissipation-rate equation,  $\epsilon$ . The stiff nature of the turbulence equations makes convergence of the residuals to machine zero unlikely and the best that is likely to occur, is reduction of three to four orders of magnitude and then asymptotic convergence to a cyclic minimum [57, 66]. A cyclic minimum is observed in Figure 171 for all of the variables after 10,000 iterations.

Periodic evaluation of a surface quantity, such as  $p_{wall}/p_{\infty}$ , for convergence after a period of iterations is suggested by Rizzetta [66] as a possible alternative to residual evaluation. Plots of the surface static pressure ratio after various iteration intervals are shown in Figure 172 for this simulation. These pressure plots indicate there is little change in the solution beyond 10,000 iterations.

Evaluation of a surface quantity with ISAAC is not particularly difficult in a two-dimensional simulation. However, in three-dimensional simulations, it becomes increasingly difficult with

ISAAC to evaluate any particular spatial quantity for convergence as the size of the domain increases. Fortunately, the cyclic minimum observed in Figure 171 appears to be a satisfactory measure of convergence. It is seen in Figures 171 and 172 that the cyclic minimum and the point where the solution in Figure 172 became relatively constant, corresponds to the same number of iterations. Thus, convergence to a cyclic minimum is used as the temporal convergence criteria in this study.

## **E2 Spatial Convergence Studies**

The results of the spatial convergence studies conducted to arrive at the grids used during this research are presented in the following sections.

### **E2.1 Aso et al./Spaid and Zukoski Configuration**

The Aso et al. [6] configuration discussed in Section 6.2 served as the basis for the grid sensitivity study for the first part of the two-dimensional slot injection analysis and validation phase. The convergence analysis used the freestream inflow conditions list in Table 2 with a static pressure ratio of  $p_{inj}/p_{\infty} = 10.29$ . This pressure ratio was used for the grid study because it had the most complete and thermodynamically consistent data listed by Aso et al.

A two step method was used to determine the final dimensions ( $i \times j$ ) of the sonic injection grid. First, three algebraic, nonuniform, Cartesian meshes with origin at the leading edge of the plate and nondimensionalized by the length  $l$  were generated using GRIDGEN Version 9 [95]. Using these grids, the requirement for  $j$  was determined by examining the static surface pressure profiles of steady state solutions for grid dimensions of  $253 \times 81$ ,  $253 \times 121$ , and  $253 \times 161$ . The pressure profiles computed with these three grids are seen in Figure 173. It was evident that grid convergence in the normal direction was obtained with the two finest meshes; thus,  $j = 121$  was used for the remainder of the grid study. Second, three additional grids were generated so the streamwise grid requirements could be determined. This was done by examining the static surface pressure profiles

for grid dimensions of  $253 \times 121$ ,  $337 \times 121$ , and  $439 \times 121$ . The pressure profiles computed with these three grids are seen in Figure 174. Here again, it was evident that grid convergence in the streamwise direction was obtained on the two finest grids. Thus,  $i = 337$  was specified in the final construction of the grid used for the sonic injection simulations discussed in Section 6.2.

The final computational grid consisted of  $337 \times 121$  nodes in the  $x$  and  $y$  directions, respectively with the nodes representing cell vertices (Figure 175). The minimum of  $\Delta x$  occurred across the nozzle, where 44 uniformly spaced nodes were used. Streamwise node spacing was increased away from the slot according to the one-dimensional *tanh* stretching function of Vinokur [105]. There were 201 nodes upstream of the jet and 94 nodes downstream of the jet. At the leading edge of the domain, the mesh step was  $\Delta x/l = 0.01$  and  $\Delta x/l = 0.00987$  at the trailing edge of the domain. In the normal direction, *tanh* stretching was used to insure a smooth distribution of the nodes through the boundary layer and out into the freestream. Since low-Reynolds number terms in the turbulence models were sensitive to grid spacing at solid boundaries,  $\Delta y$  was chosen at the surface such that  $y^+ < 1.0$  at the first mesh point above the plate for all grid distributions evaluated. It was found that  $\Delta y/l = 0.00001$  satisfied this requirement for all cases examined.

## **E2.2 Tucker Configuration**

The grid dimensions used for the supersonic injection simulations discussed in Section 6.3 were determined with a method similar to that used to arrive at the dimensions of the sonic injection grid. Once again a two step method was used to arrive at the final grid dimensions ( $i \times j$ ). First, the requirements for  $j$  were determined by examining the static pressure profiles of steady state solutions at the test section surface for grid dimensions of  $341 \times 61$ ,  $341 \times 91$ , and  $341 \times 121$ . The pressure profiles computed with these three grids are seen in Figure 176 and it was evident that grid convergence in the normal direction was obtained with the two finest meshes; thus,  $j = 121$  was used for the remainder of the grid study. Second, streamwise grid requirements were determined by

examining the static pressure profiles at the test section surface for grid dimensions of  $171 \times 121$ ,  $257 \times 121$ , and  $341 \times 121$ . The pressure profiles computed with these three grids are seen in Figure 177 and again, it was evident that grid convergence in the streamwise direction was obtained on the two finest grids. Thus,  $i = 341$  was specified in the final construction of the grid used for both physical configurations.

The computational grid used in the numerical simulations in Section 6.3 of Tucker's configuration is shown in Figure 178. This grid has the streamwise cells swept back to better capture the boundary-layer separation and jet induced shocks, and consists of  $341 \times 121$  nodes in the  $x$  and  $y$  directions respectively. The minimum values of  $\Delta x/l$  is 0.005 ( $l = 1\text{cm}$ ) and occurs across the slot, where 41 uniformly spaced nodes are used. The reference length of one  $\text{cm}$  was used so that the nondimensional grid dimensions would have a one-to-one correspondence to the dimensional lengths of the experimental apparatus used by Tucker [100]. Streamwise node spacing is increased away from the slot boundaries according to the one-dimensional  $\tanh$  stretching function of Vinokur [105]. There are 101 nodes upstream of the slot and 201 nodes downstream of the slot. At the leading edge of the domain, the streamwise node spacing is  $\Delta x/l = 0.1$  and decreases to 0.025 at the trailing edge of the domain. In the normal direction,  $\tanh$  stretching is used to insure a smooth distribution of the nodes through the boundary layer and up into the freestream. Low-Reynolds number terms in the turbulence models, which are sensitive to node spacing at solid boundaries, require  $y^+ < 1.0$  at the first mesh point above the plate;  $\Delta y/l = 0.00005$  at the surface is used, and satisfies this constraint on  $y^+$ .

### **F2.3 McCann and Bowersox Configuration**

A two-dimensional mesh study and a three-dimensional mesh study was conducted to arrive at the three-dimensional grid used in simulations discussed in Chapter 6. This two phase approach was used to reduce the resources required to arrive at the final grid configuration. The grid dimensions in

the  $x - y$  plane were determined with a two-dimensional analysis similar to the analyses performed for the two previous configurations.

It was assumed that grid dimensions and spacing in the  $x - y$  plane of the three-dimensional grid could be sufficiently resolved with a mesh study of a two-dimensional flowfield simulation of the  $x - y$  plane. This assumption is based on the absence of three-dimensional relaxation of the shocks and recirculation in two-dimensional flowfields; the strength of the shocks and the size of the recirculation regions should be more severe in a two-dimensional flowfield. Once the  $x - y$  plane grid dimensions and mesh spacing was determined, the  $y - z$  dimensions and mesh spacing was determined from an analysis of three three-dimensional grids.

#### ***F2.3.1 Two-Dimensional Grid***

The domain of the two-dimensional grid used for the mesh study had to model the test section from  $x/d = -5.0$  to  $x/d = 41.0$  in the streamwise direction and from  $y/d = 0.0$  to  $y/d = 16.44$  in the normal direction. This domain was needed so that the flowfield at  $x/d = 40.0$  and the reflected shocks off of the upper wall of the test section were captured.

Coarse, medium and fine grids with  $i \times j$  dimensions of  $181 \times 61$ ,  $339 \times 121$  and  $508 \times 181$  respectively, were evaluated for spatial convergence for the variables  $\rho$ ,  $U$ ,  $V$ ,  $p$ ,  $T$  and  $K$ . Contours plots of these variables for each of the simulations are seen in Figures 179 - 184. There were clear differences between the results of the coarse grid and the medium grid for each of the variables examined. While there were also some differences between the results of the medium grid and the fine grid, they were significantly smaller than the results of the previous comparison. It was reasonably evident that grid convergence in the  $x - y$  plane had been obtained with the two finest grids and in light of the limited resources available for the full three-dimensional simulations, the dimensions and spacing of the medium grid were used for the  $x - y$  plane.

### F2.3.2 Three-Dimensional Grid

The dimensions and spacing of the  $y - z$  plane were also determined through a comparison of simulation results from coarse, medium and fine grids the variables  $\rho$ ,  $U$ ,  $V$ ,  $p$ ,  $T$  and  $K$ . The  $i \times j \times k$  dimensions of the grids were  $261 \times 121 \times 31$ ,  $261 \times 121 \times 61$  and  $261 \times 121 \times 91$  respectively for the coarse, medium and fine grids. Each of these grids modeled half of the test section and used the boundary conditions and inflow parameters listed in Tables 7, 8 and 11 and the domain of each grid was  $x/d = -7.0$  to  $x/d = 10.0$ ,  $y/d = 0.0$  to  $y/d = 16.44$  and  $z/d = 0.0$  to  $z/d = 8.22$ . The streamwise domain was limited to  $x/d = 8.0$  to reduce the computational resources and run time required to perform the simulations. The streamwise spacing up to  $x/d = 8.0$  uses the spacing which was determined to be grid convergent in the previous section. This location ( $x/d = 8.0$ ) was selected as the streamwise limit because experimental data and the two-dimensional simulation results implied that the structure of the flowfield did not undergo drastic changes beyond this point. Thus, it was assumed that if the solution was grid converged in the  $y - z$  plane at this streamwise location, extensions of the grid to other downstream locations would also be grid converged in the  $y - z$  plane.

The results of the simulations with each of the three grids at  $x/d = 8.0$  are seen in Figures 185 - 191. As with the two-dimensional simulations, there were clear differences between the results of the coarse grid and the medium grid for each of the variables examined. And again, while there were also some differences between the results of the medium grid and the fine grid, they were significantly smaller than the results of the previous comparison. The only exception to this trend was seen in the contours for  $K$ . Thus, it was reasonably evident that grid convergence in the  $y - z$  plane had been obtained with the two finest grids and in light of the limited resources available for the full three-dimensional simulations and the run-time requirements of the RSTM, the dimensions and spacing of the medium grid were used for the  $y - z$  plane.



### F2.3.3 Half-Plane Grid

The half-plane grid shown in Figure 192, has streamwise dimensions and mesh spacing as determined in the two-dimensional study and dimensions and spacing in the  $y - z$  plane as determined in the three-dimensional study. This grid has  $i \times j \times k$  dimensions of  $339 \times 121 \times 61$  and in the streamwise direction, 92 evenly spaced nodes are used to simulate the outflow plane of the nozzle and 21 nodes are used to simulate the nozzle outflow in the cross flow direction. The flowfield upstream of the nozzle is simulated with 78 nodes and the remaining 170 are used to simulate the flow downstream of the nozzle. One dimensional tanh stretching is used in all regions which are not evenly spaced and the stretching always starts at a solid surface or from a region of evenly spaced nodes.

Experimental data shows that the primary structures of the flowfield drift away from the centerline downstream of  $x/d = 8.0$ . Thus, in an effort to more fully capture these structures, the concentration of the cell spacing is shifted from the test section centerline to a region  $1d$  from the line  $z/d = 0.0$ . Since this is a structured grid, the dimensions and spacing in the  $x - z$  plane are determined by the other two planes. The cell spacing of the grid is summarized in Table 12.

Table 12. Half-plane grid mesh spacing

Region	Spacing (cm)
$\Delta x_1$	$2.00 \times 10^{-2}$
$\Delta x_2$	$1.00 \times 10^{-2}$
$\Delta x_3$	$2.78 \times 10^{-1}$
$\Delta y_1$	$1.00 \times 10^{-3}$
$\Delta y_2$	$4.67 \times 10^{-1}$
$\Delta z_1$	$1.00 \times 10^{-2}$
$\Delta z_2$	$2.78 \times 10^{-1}$
$\Delta z_3$	$1.00 \times 10^{-2}$
$\Delta z_4$	$1.06 \times 10^{-1}$
$\Delta z_5$	$2.81 \times 10^{-1}$

#### ***F2.3.4 Full-Plane Grid***

The full-plane grid shown in Figure 193, has truncated streamwise dimensions and mesh spacing as determined in the two-dimensional study and dimensions and truncated spacing in the  $y - z$  plane as determined in the three-dimensional study. Among the objective of the simulations conducted with this grid is to determine the asymmetric properties of the flowfield, thus the flowfield on both sides of nozzle must to be modeled. However, the computational resources and run-times required to model the entire test section are unreasonable. Thus, a smaller region of the flowfield is simulated with a grid which has the following domain  $x/d = -5$  to  $21$ ,  $y/d = 0.0$  to  $5.2$  and  $z/d = -3.25$  to  $3.25$ . The dimensions and mesh spacing over these intervals are determined from the two- and three-dimensional mesh studies for the same intervals. These intervals are mirrored across  $z/d = 0.0$  to complete the grid. As with the half-plane grid, an effort is made to more fully capture the spreading structures downstream of  $x/d = 8.0$ . For this grid the changes to the lateral spacing downstream of  $x/d = 8.0$  is simply stretched with the tanh function as the distance from  $z/d = 0.0$  increases. The cell spacing of the grid is summarized in Table 13.

This grid has  $i \times j \times k$  dimensions of  $275 \times 106 \times 102$  and in the streamwise direction, 92 evenly spaced nodes are used to simulate the outflow plane of the nozzle and 43 nodes are used to simulate the nozzle outflow in the cross flow direction. The flowfield upstream of the nozzle is simulated with 49 nodes and the remaining 135 are used to simulate the flow downstream of the nozzle. One dimensional tanh stretching is used in all regions which are not evenly spaced and the stretching always starts at a solid surface or from a region of evenly spaced nodes.

Table 13. Full-plane grid mesh spacing

Region	Spacing ( <i>cm</i> )
$\Delta x_1$	$2.00 \times 10^{-2}$
$\Delta x_2$	$1.00 \times 10^{-2}$
$\Delta x_3$	$1.40 \times 10^{-1}$
$\Delta y_1$	$1.00 \times 10^{-3}$
$\Delta y_2$	$1.48 \times 10^{-1}$
$\Delta z_1$	$1.00 \times 10^{-2}$
$\Delta z_2$	$1.10 \times 10^{-1}$
$\Delta z_3$	$1.00 \times 10^{-2}$
$\Delta z_4$	$6.56 \times 10^{-2}$

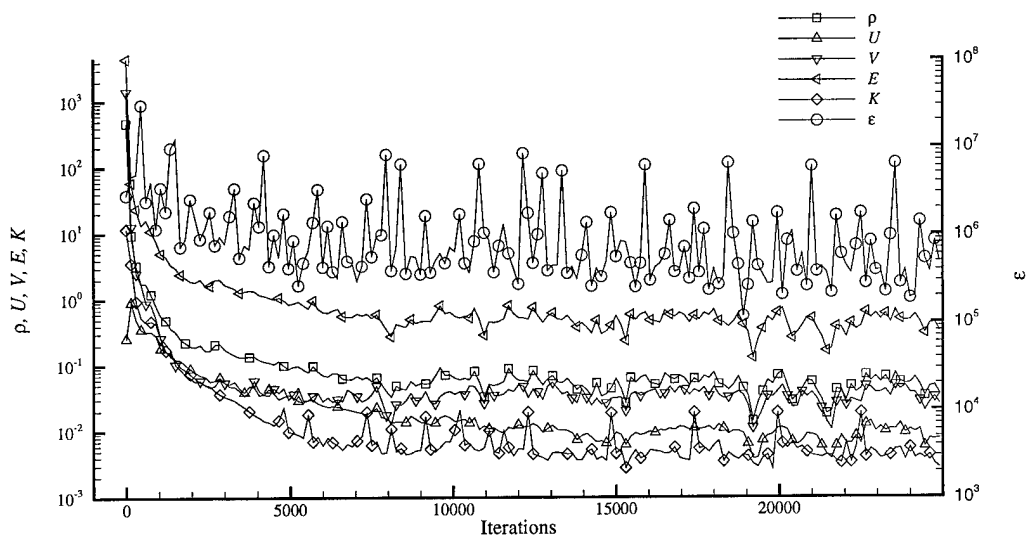


Figure 171. Residual results for Aso et al. configuration ( $p_{inj}/p_{\infty} = 10.29$ )

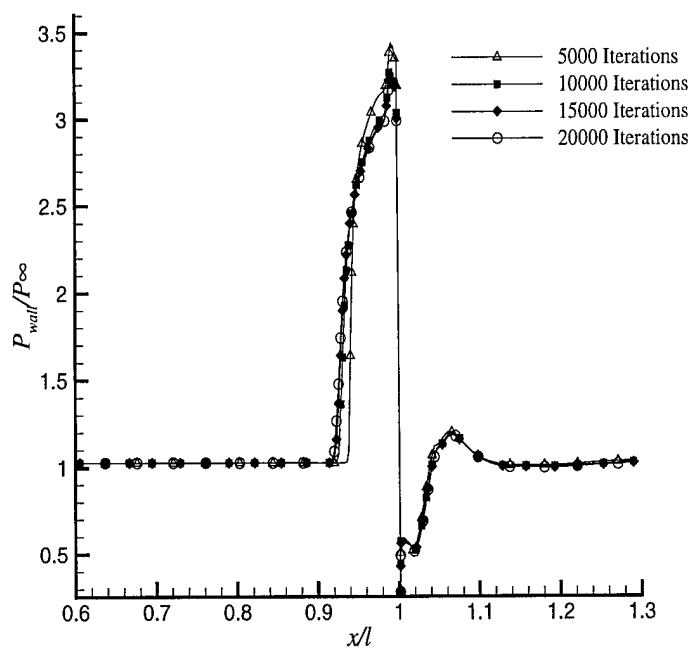


Figure 172. Surface static pressure ratio results for various iteration levels (Aso et al. configuration with  $p_{inj}/p_{\infty} = 10.29$ )

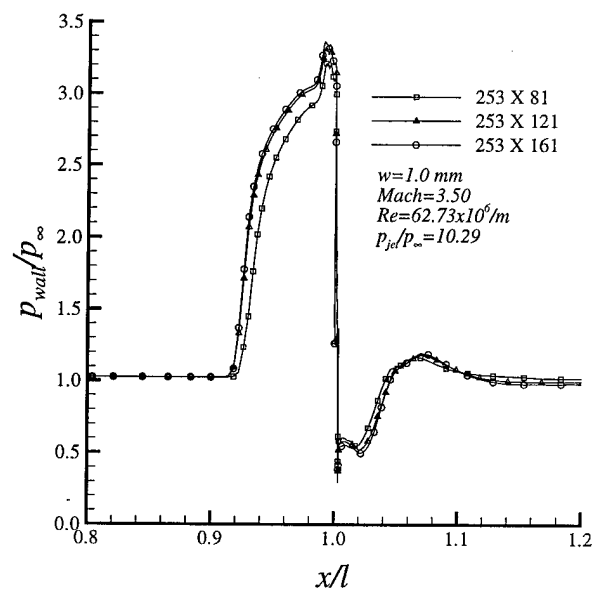


Figure 173. Sonic injection configuration normal direction grid refinement results

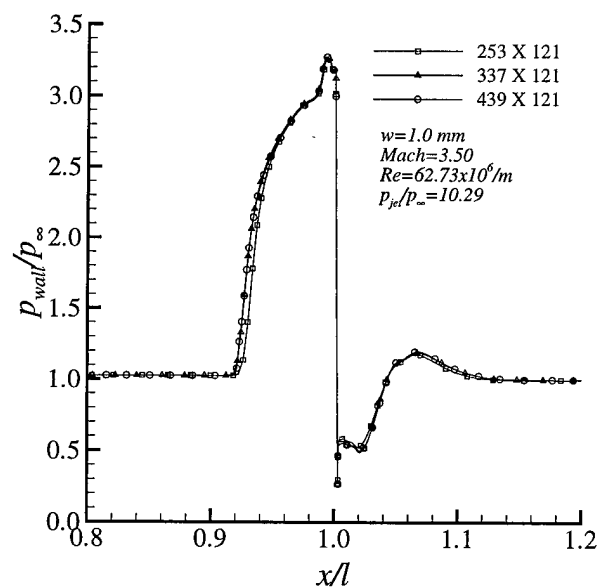


Figure 174. Sonic injection configuration streamwise direction grid refinement results

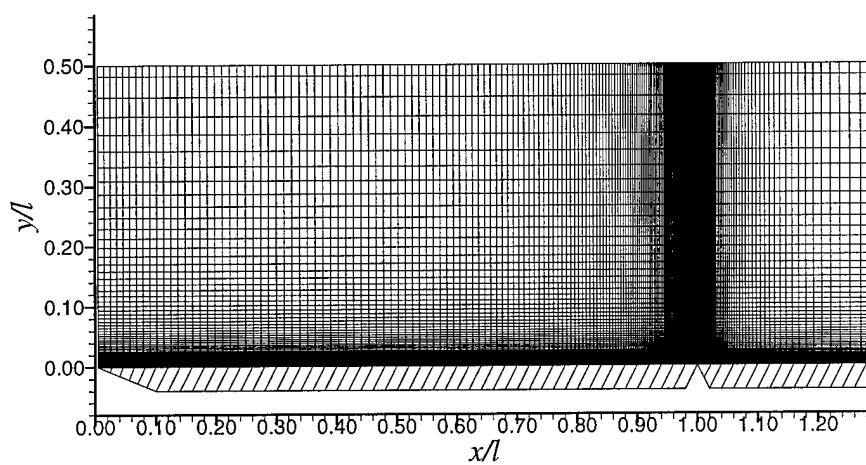


Figure 175. Two-dimensional computational grid used for Aso et al. and Spaid and Zukoski configurations

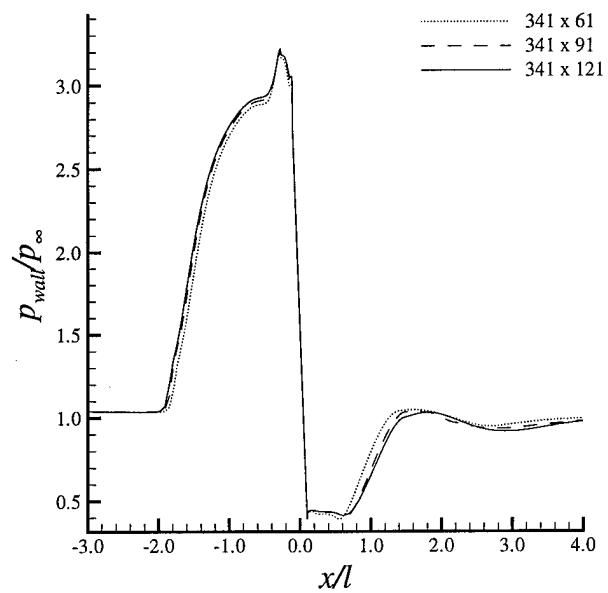


Figure 176. Supersonic injection configuration normal direction grid refinement results

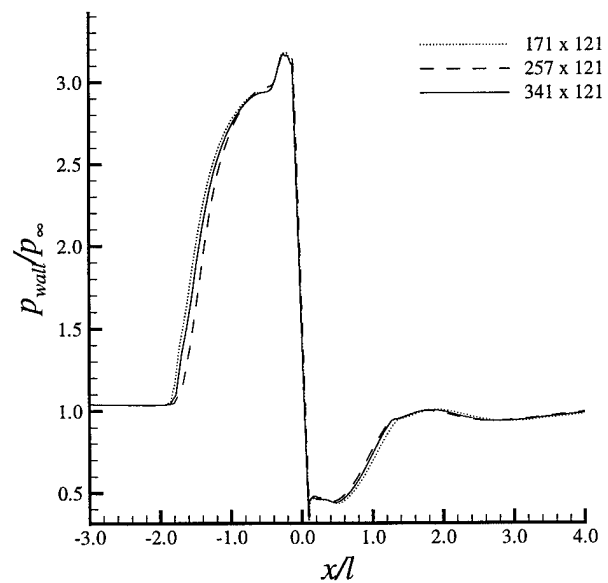


Figure 177. Supersonic injection configuration streamwise direction grid refinement results

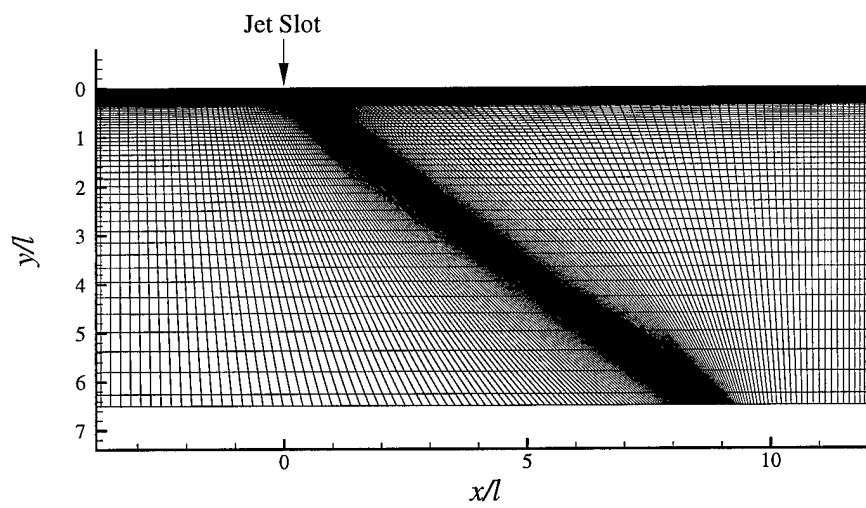


Figure 178. Tucker configuration computational grid



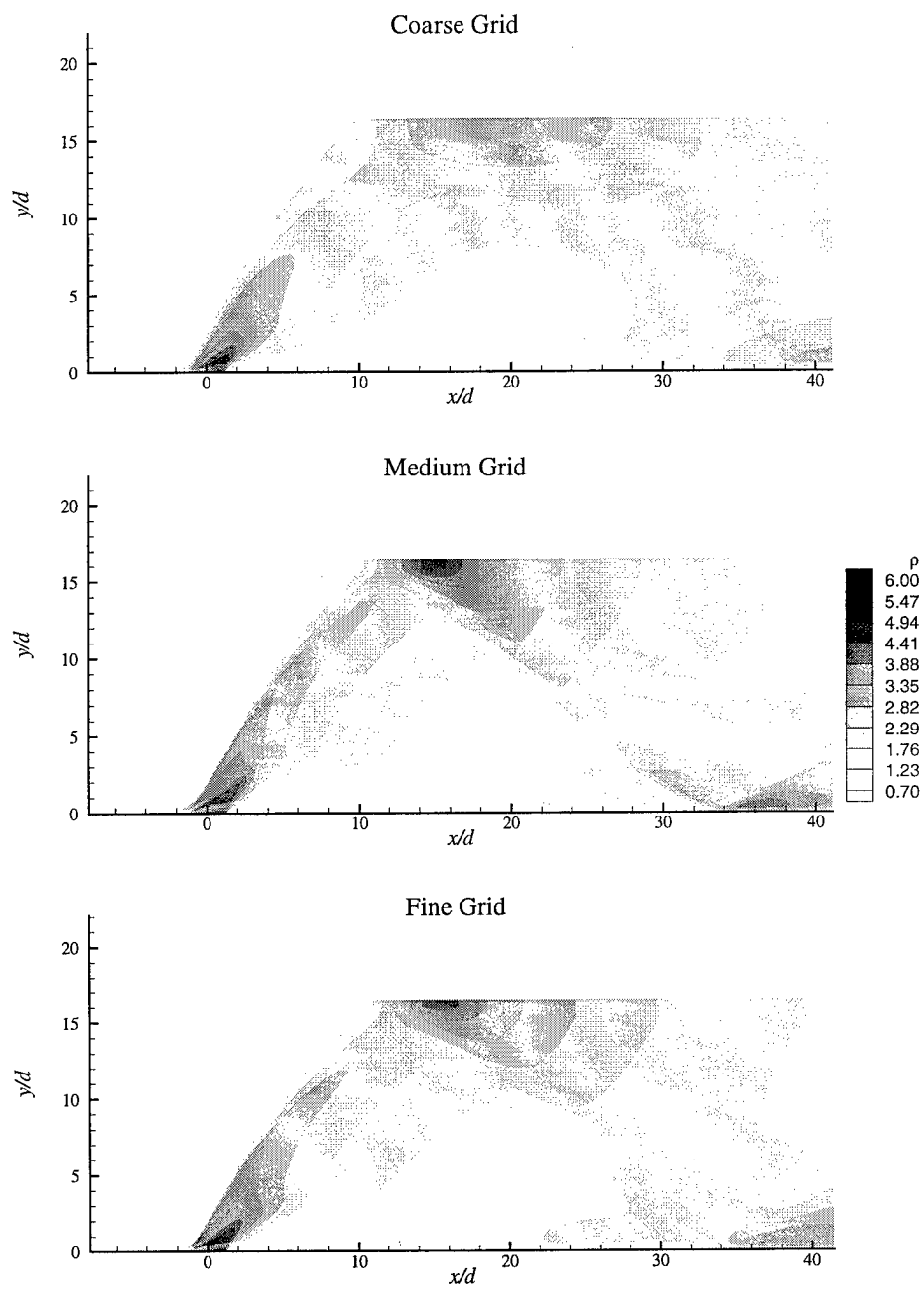


Figure 179. Two-dimensional mesh study results for  $\rho$

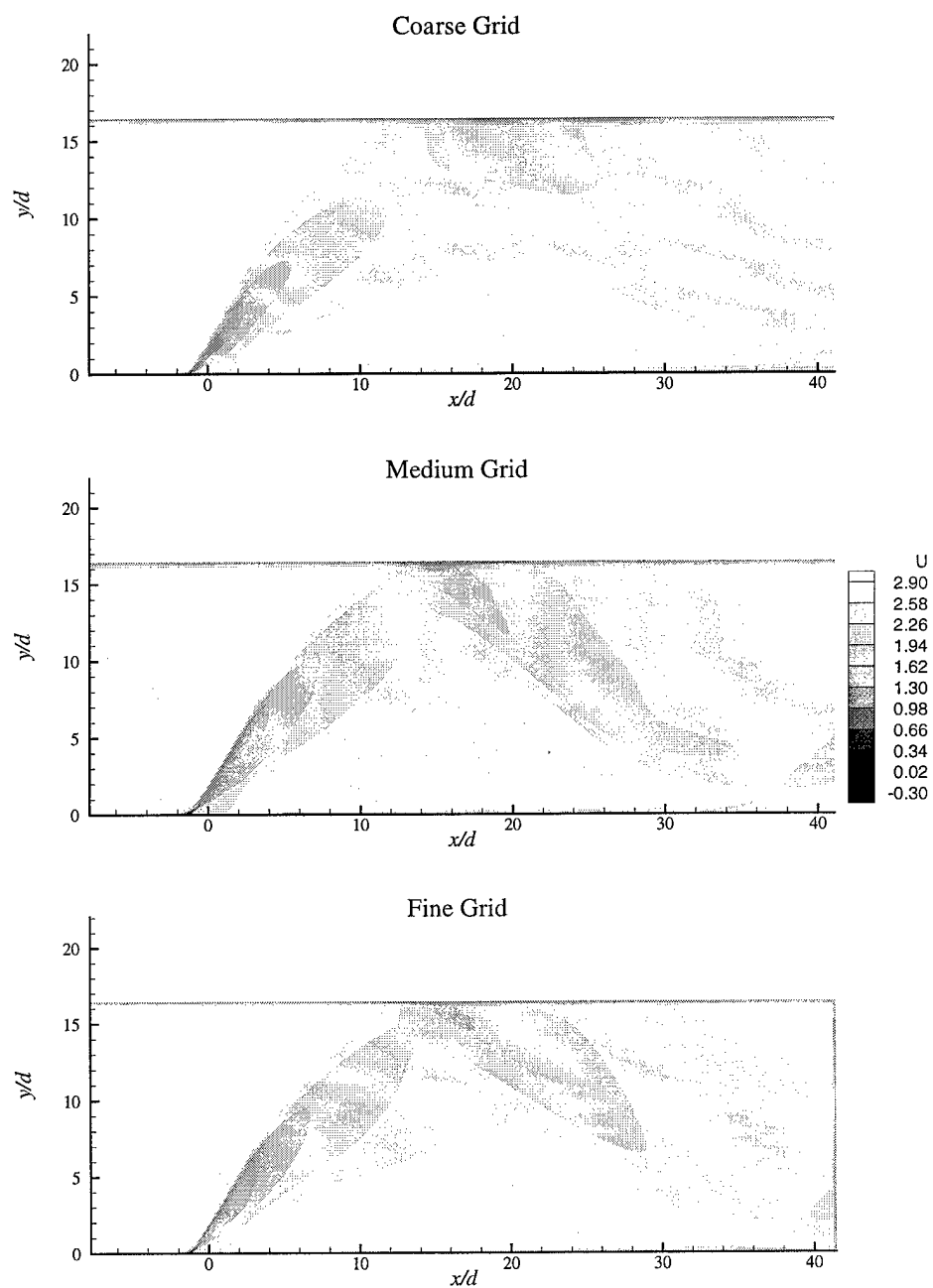


Figure 180. Two-dimensional mesh study results for the  $U$  component of velocity

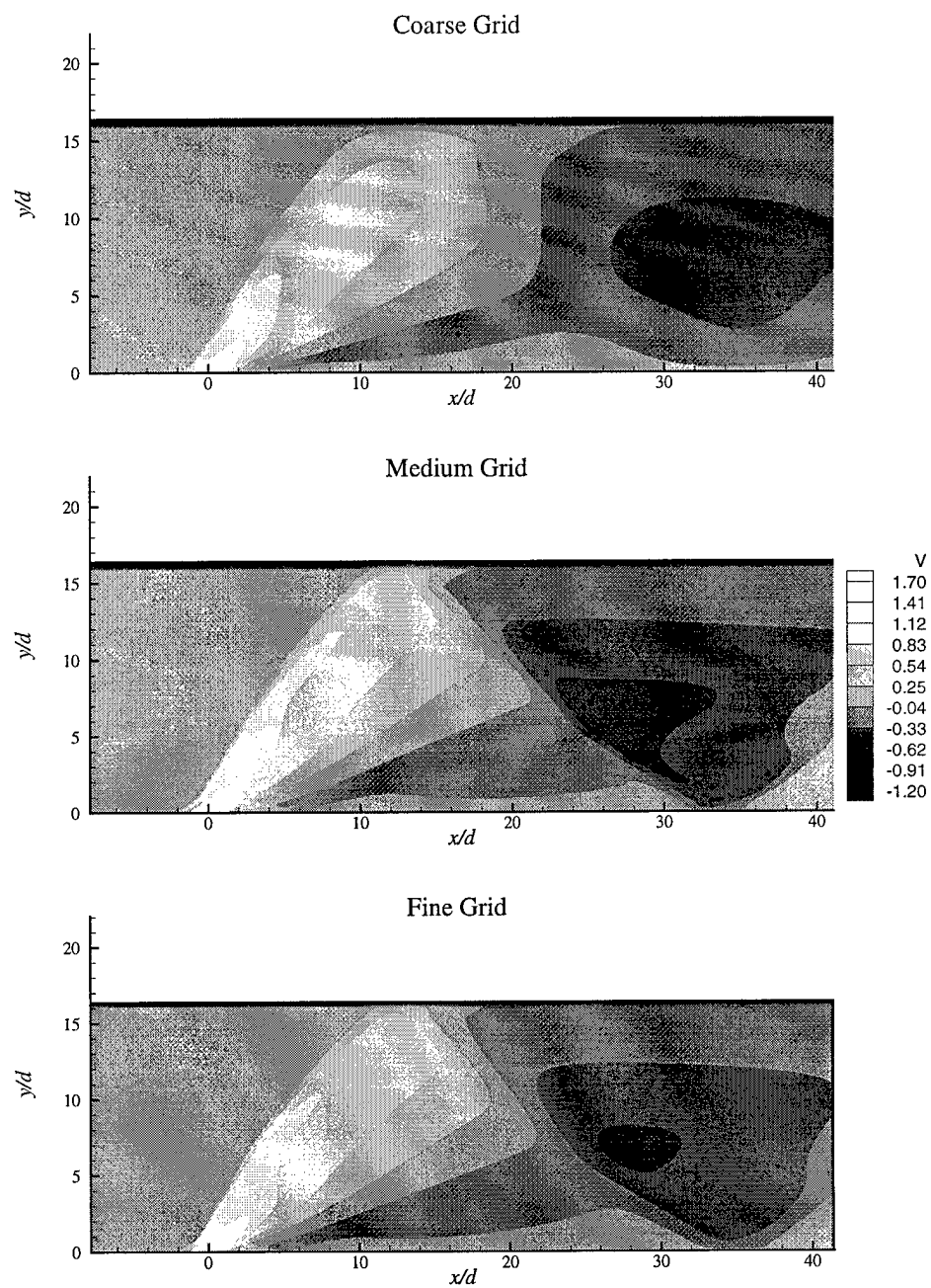


Figure 181. Two-dimensional mesh study results for the  $V$  component of velocity

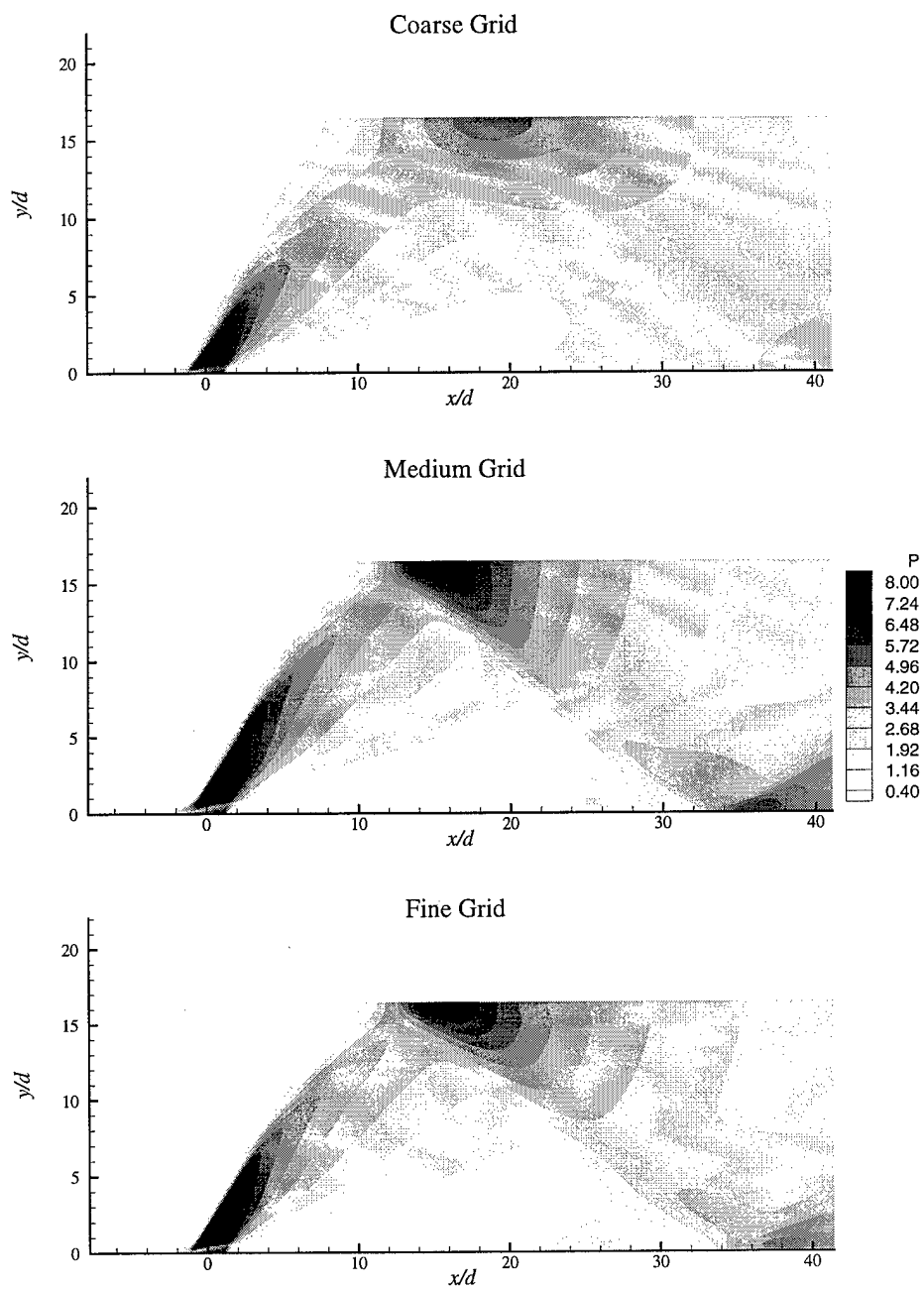


Figure 182. Two-dimensional mesh study results for  $p$

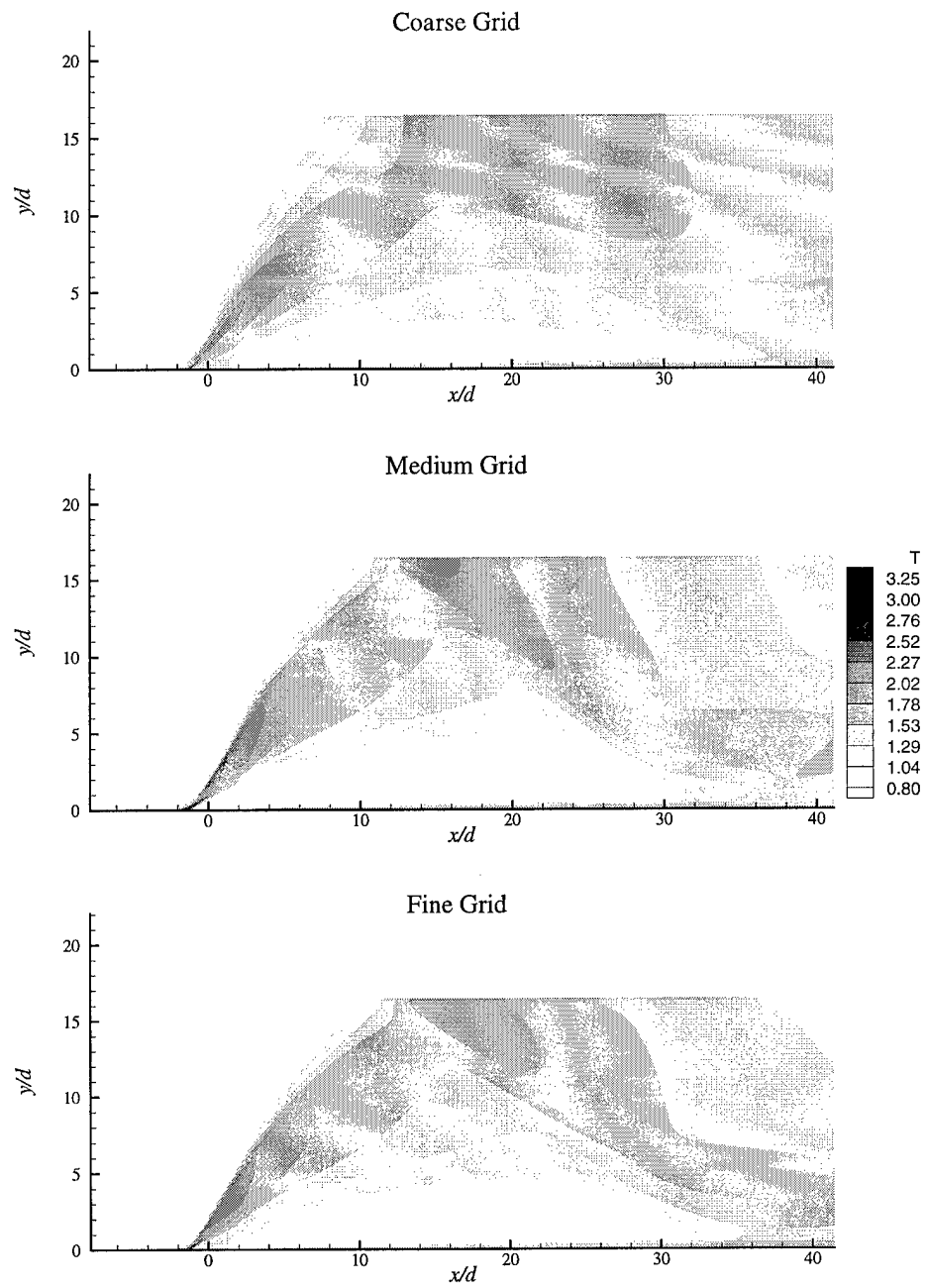


Figure 183. Two-dimensional mesh study results for  $T$

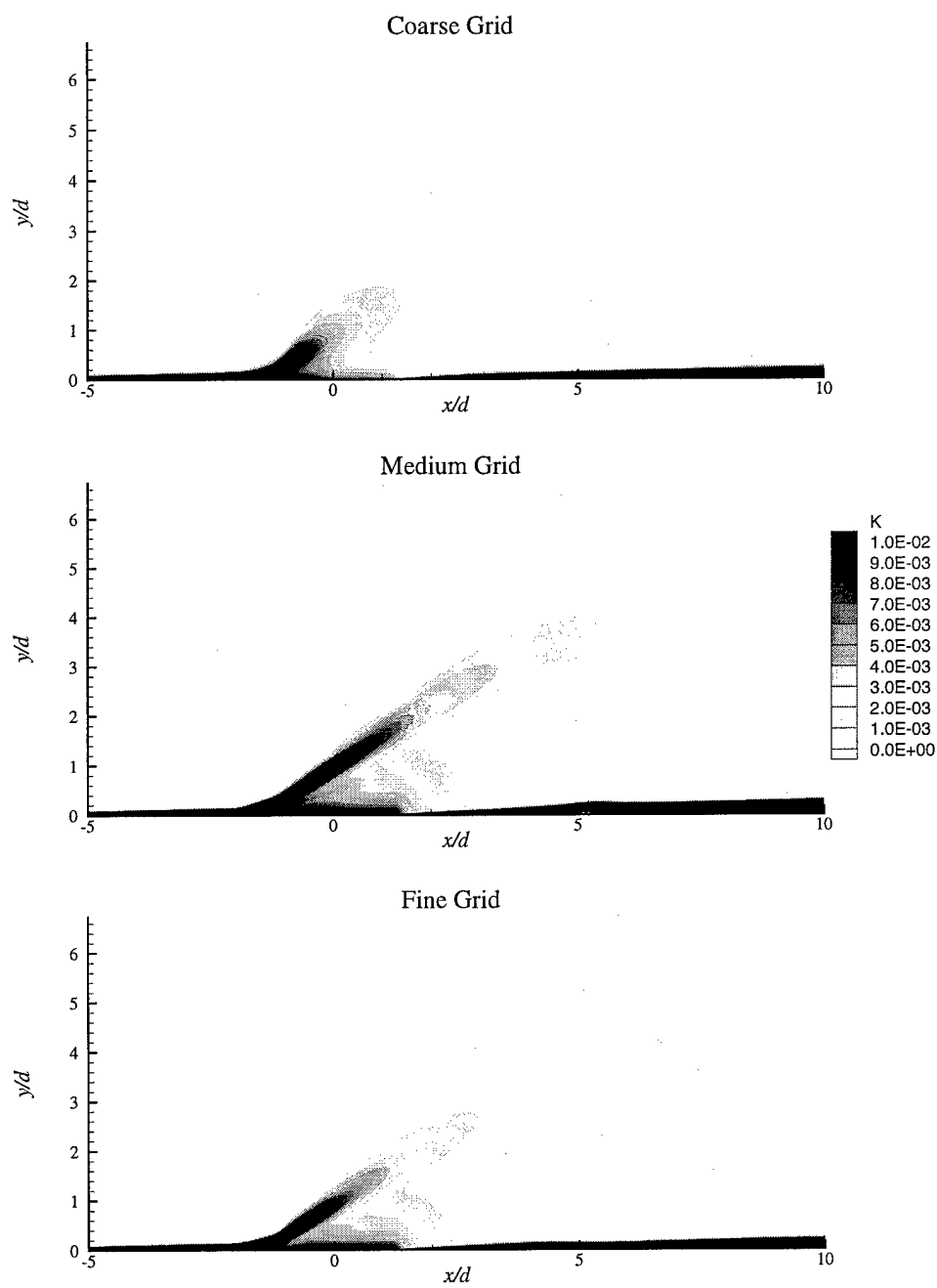


Figure 184. Two-dimensional mesh study results for  $K$

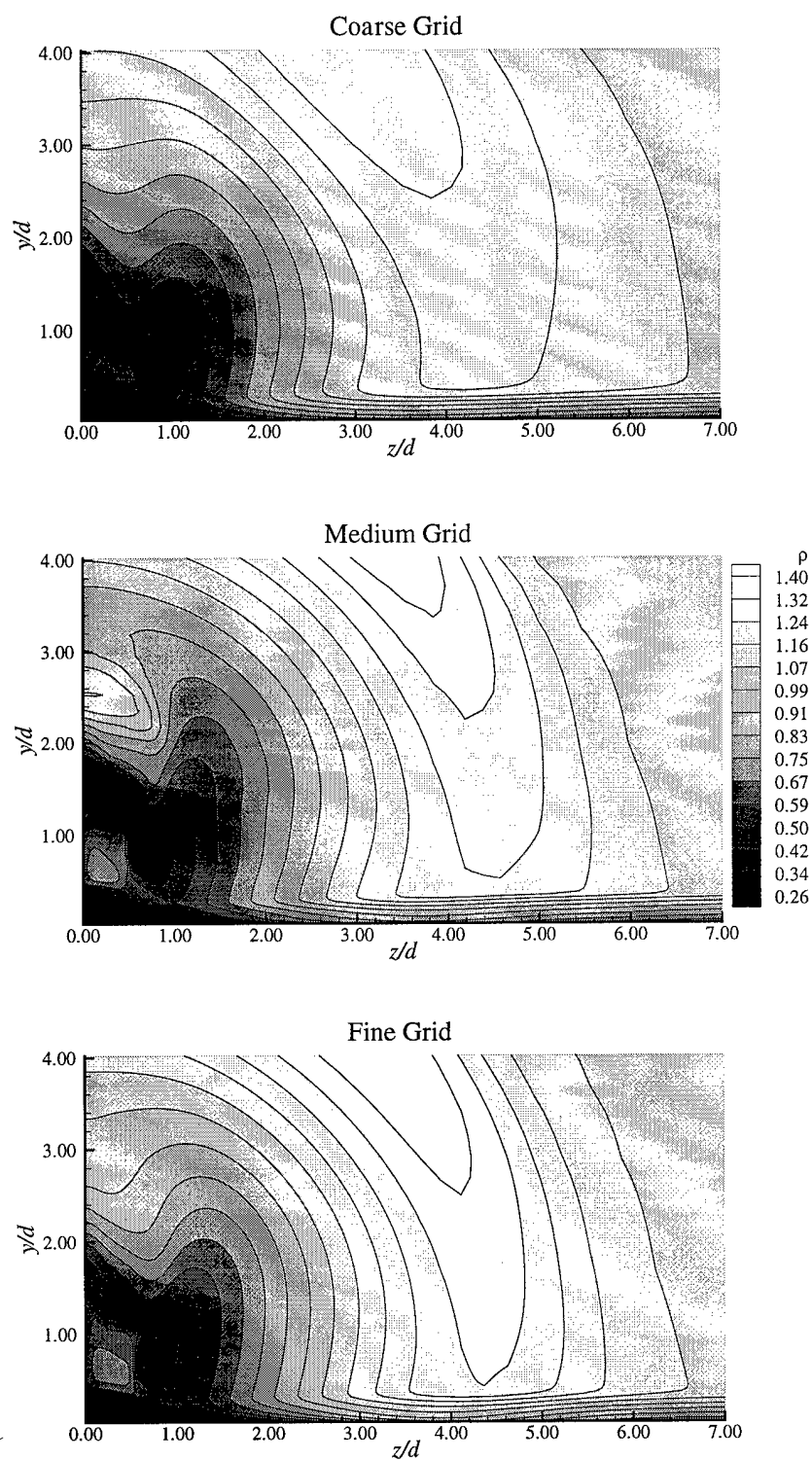


Figure 185. Three-dimensional mesh study results for  $\rho$  at  $x/d = 8.0$

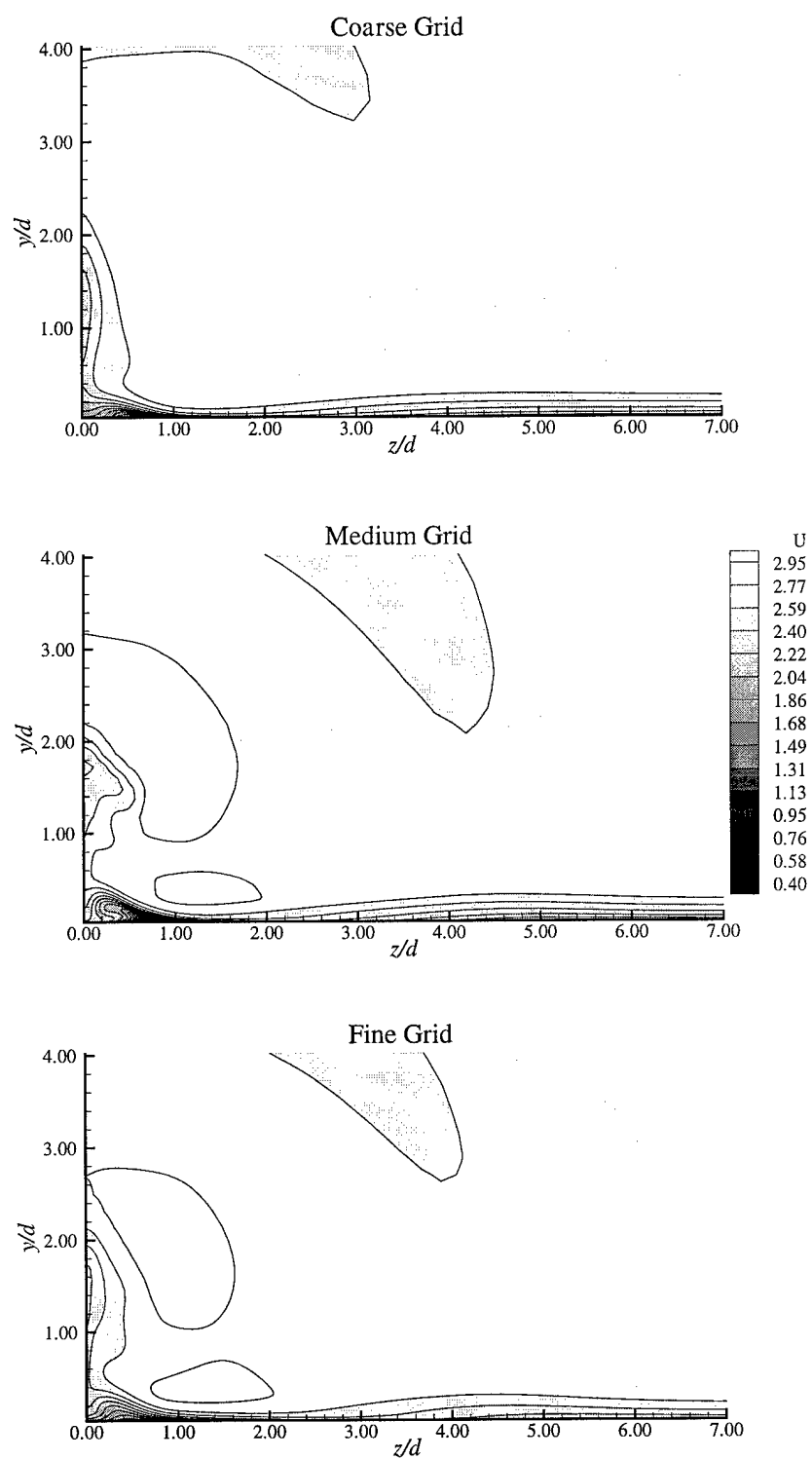


Figure 186. Three-dimensional mesh study results for the  $U$  component of velocity at  $x/d = 8.0$



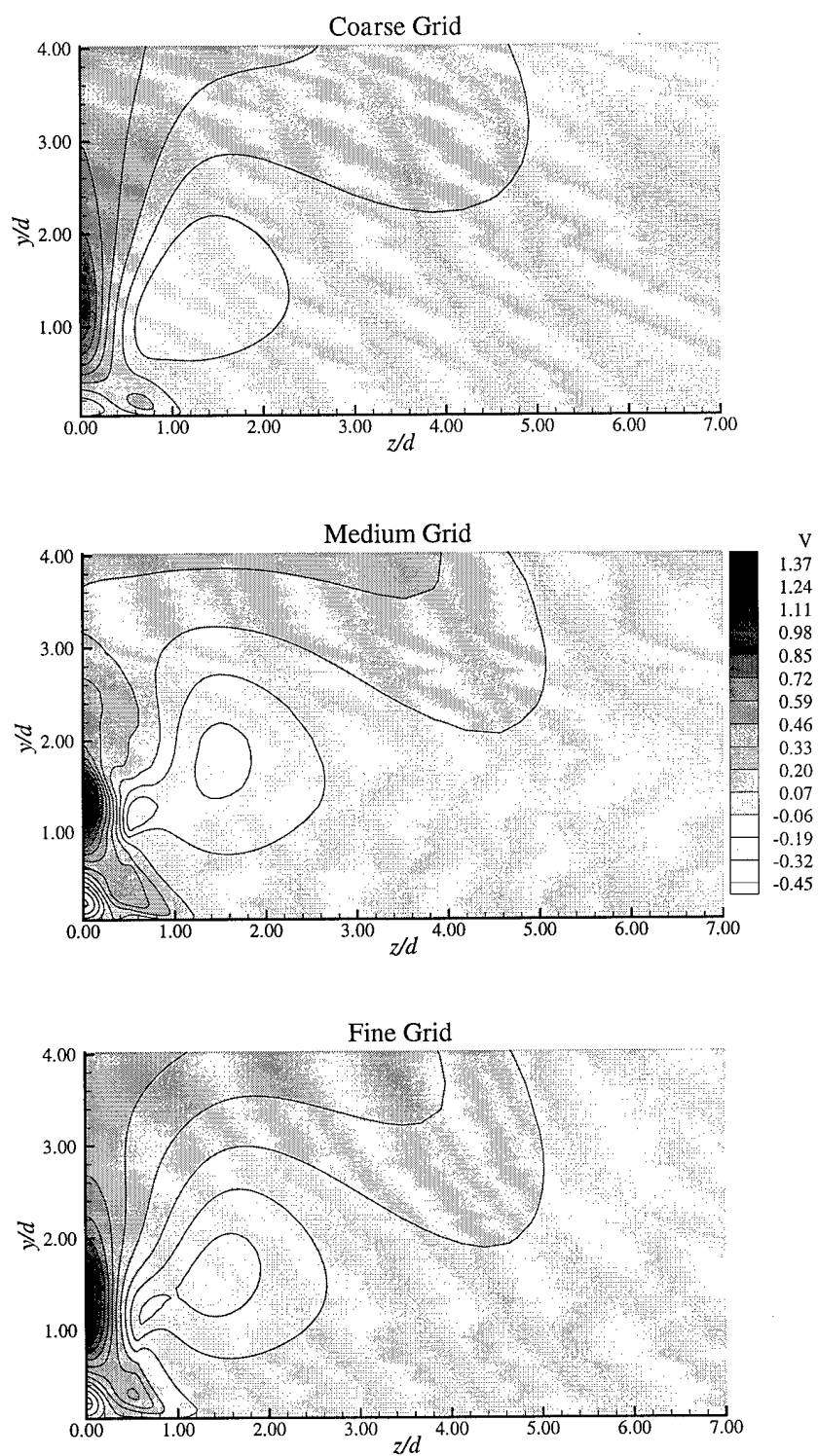


Figure 187. Three-dimensional mesh study results for the  $V$  component of velocity at  $x/d = 8.0$

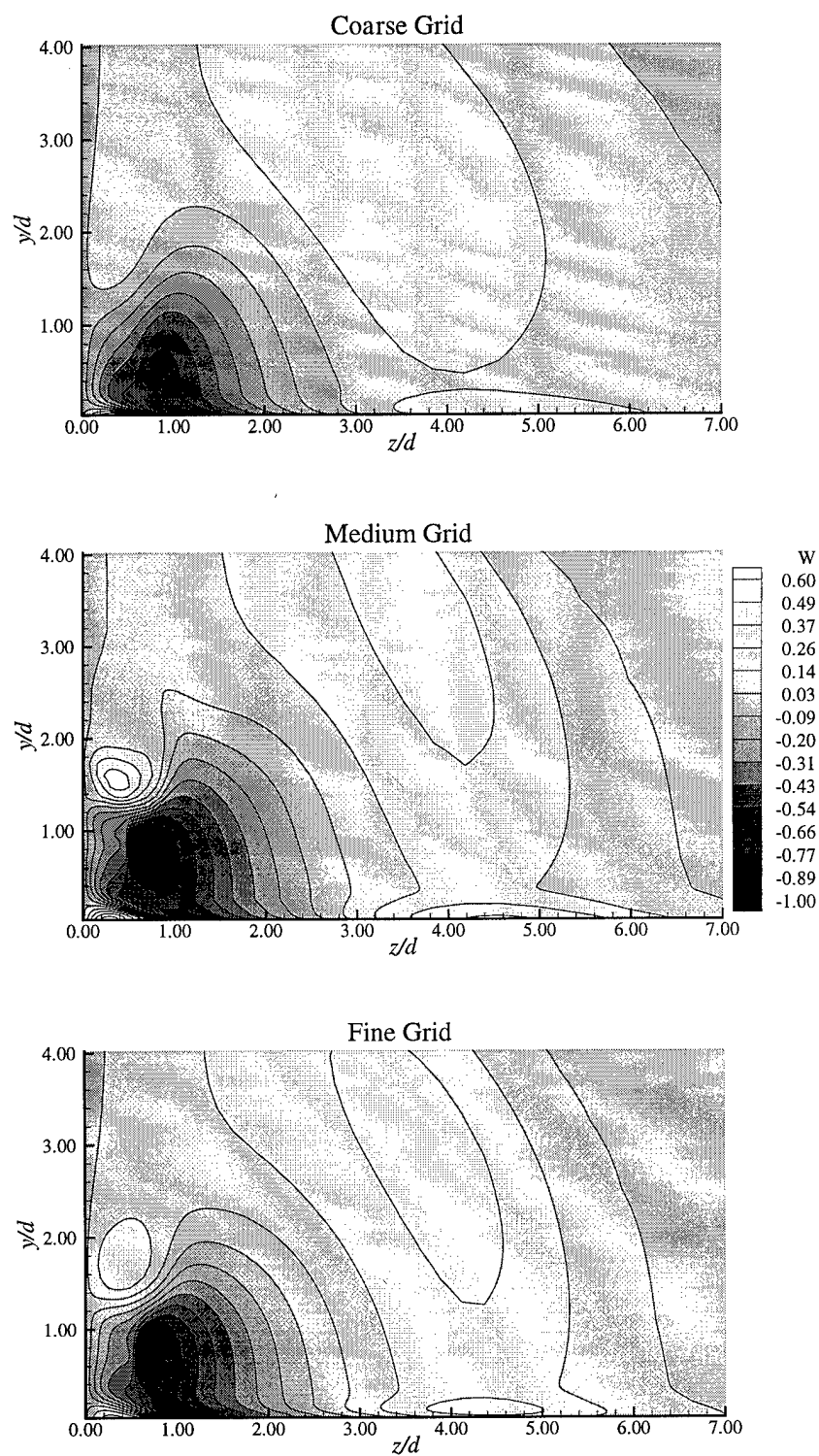


Figure 188. Three-dimensional mesh study results for the  $W$  component of velocity at  $x/d = 8.0$

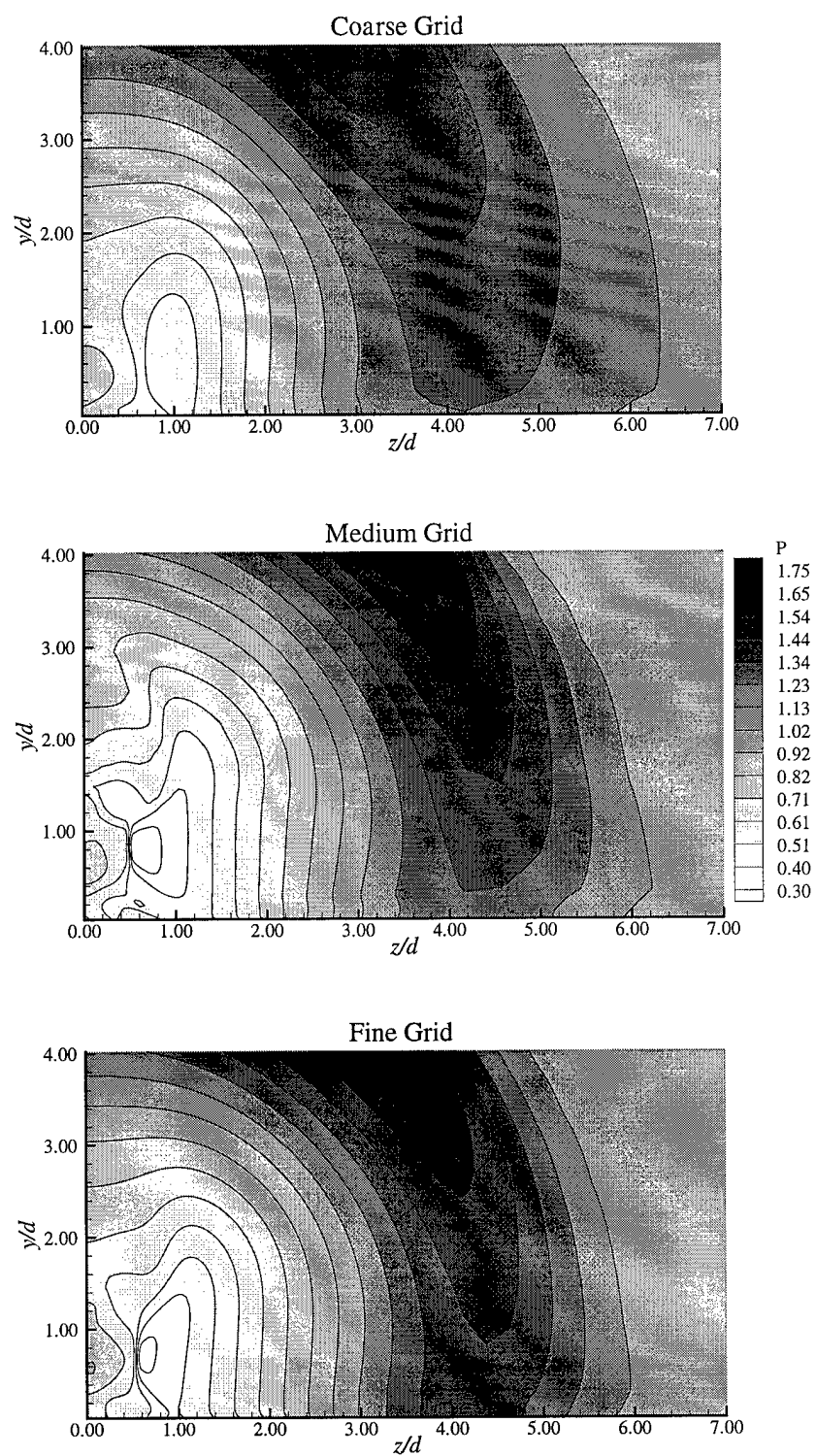


Figure 189. Three-dimensional mesh study results for  $p$  at  $x/d = 8.0$

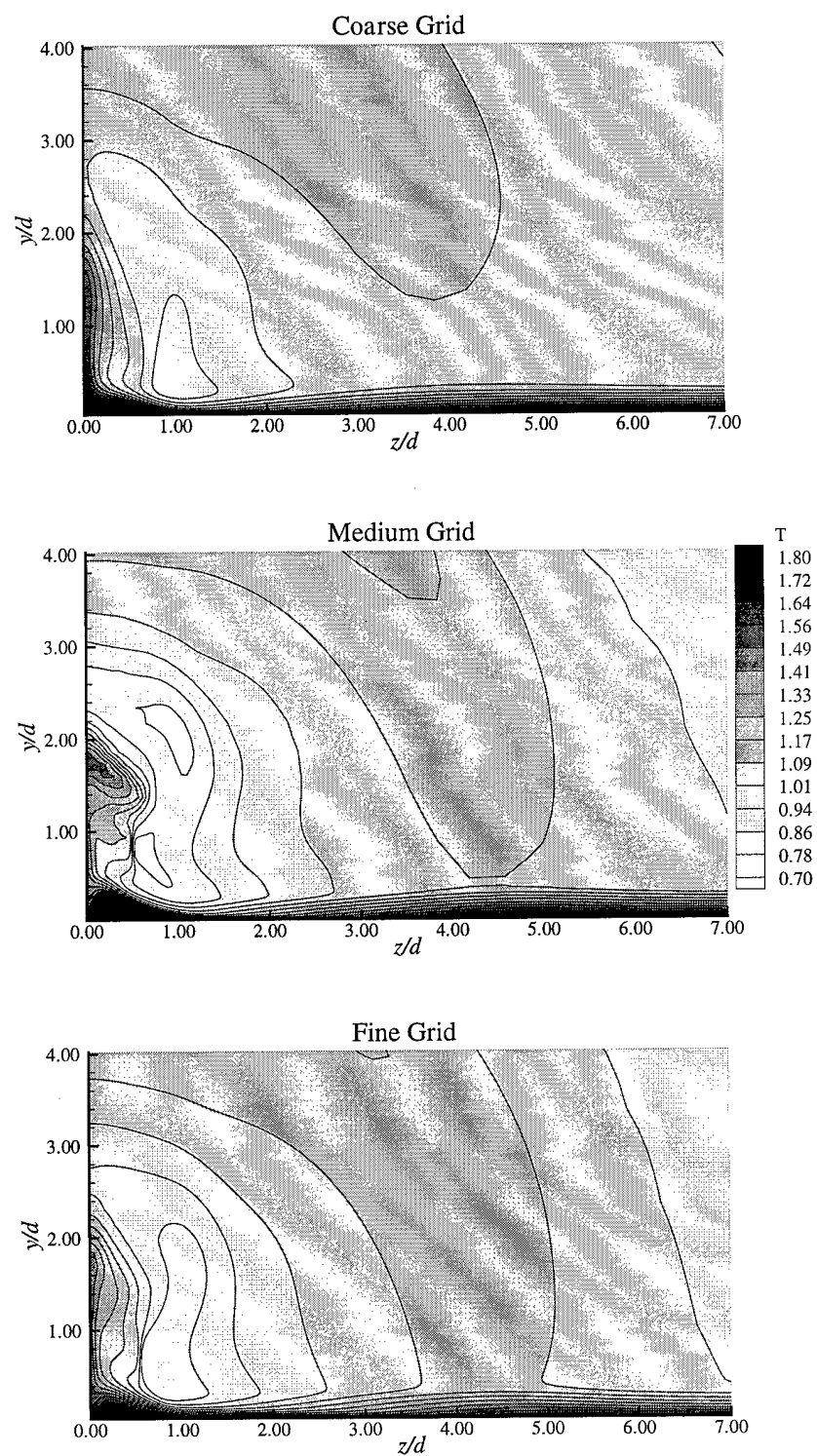


Figure 190. Three-dimensional mesh study results for  $T$  at  $x/d = 8.0$

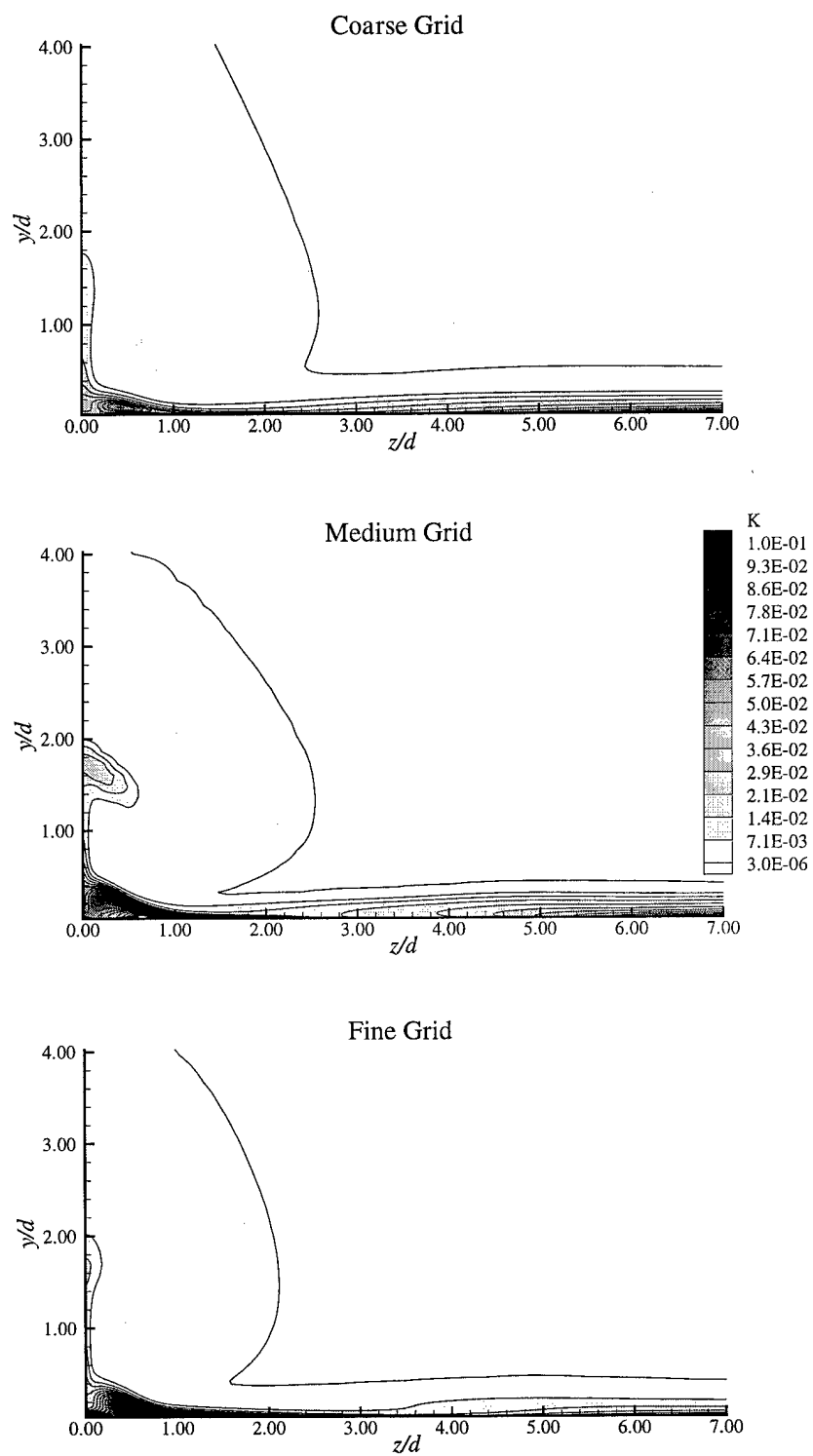


Figure 191. Three-dimensional mesh study results for  $K$  at  $x/d = 8.0$

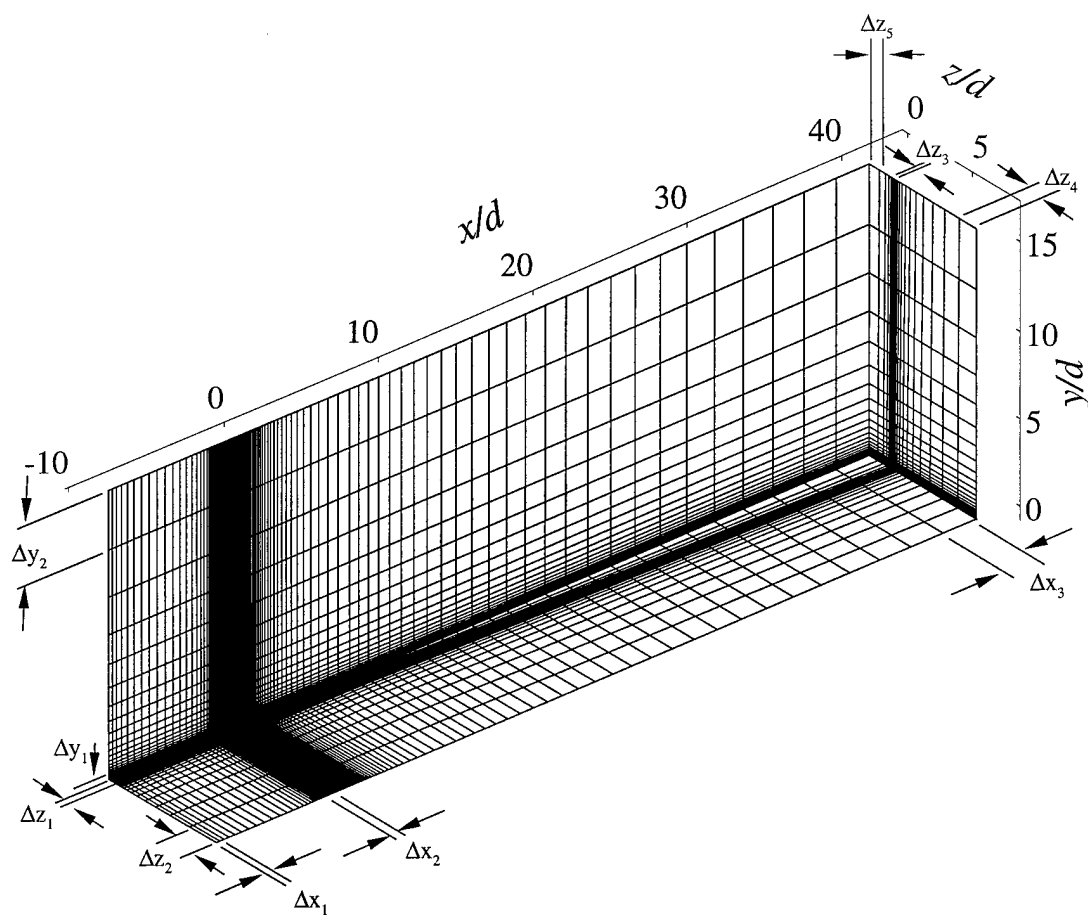


Figure 192. Half-plane grid (339 x 121 x 61)

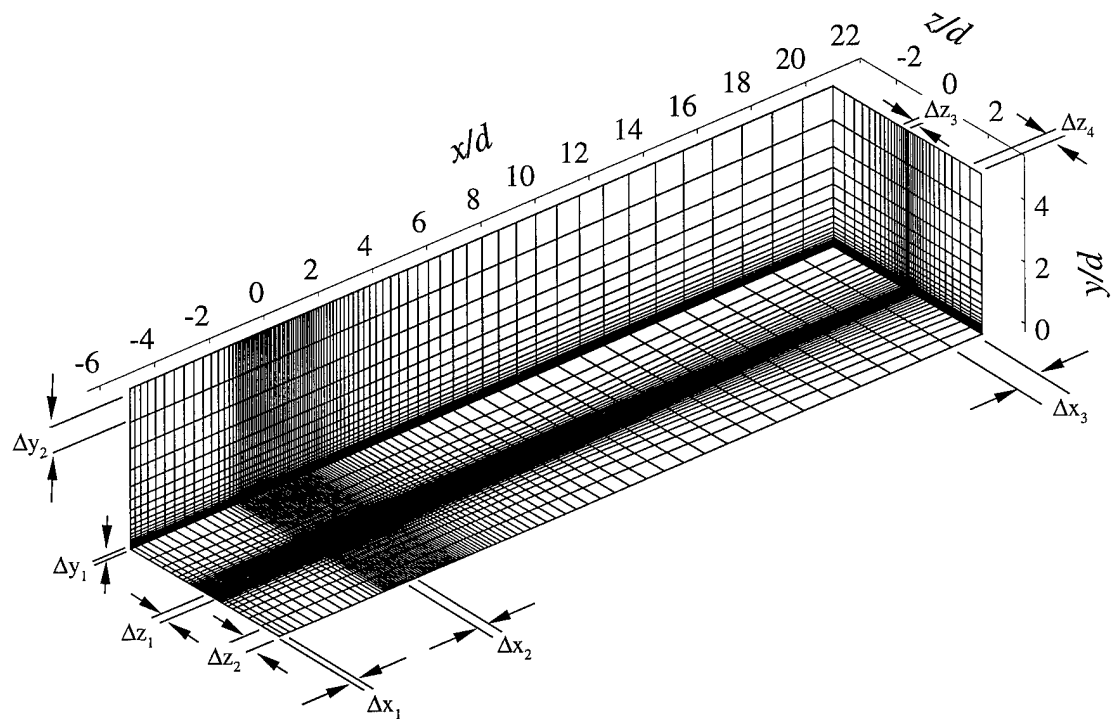


Figure 193. Full-plane grid (275 x 105 x 101)

## APPENDIX G - Higher Pressure Ratio Simulation Results

In Chapter 7 the asymmetric behavior of the experimental data for the McCann and Bowersox [52] configuration did not appear in the numerical results. In an effort to further determine the cause of the asymmetries in the experimental data, an RSTM simulation was performed with the pressure of the injectant twice the value used in the experiments. This simulation was performed with the full-plane grid and used the inflow conditions and boundary conditions listed in Tables 7, 8 and 10. The only exception to these values was  $p_{inj}$ . For this simulation,  $p_{inj} = 134.7$  kPa was used, which resulted in a pressure ratio of 21.0 rather than 10.5.

The numerical results of this simulation indicate that the increase in pressure has no effect on the symmetry of the computed solution. The results from this simulation with  $p_{inj}/p_{\infty} = 21.0$  are shown in Figures 194 - 203. These contour plots in these figures show that these results are just as symmetric as the results seen in Chapter 7 when  $p_{inj}/p_{\infty} = 10.5$ . Thus, the asymmetric behavior seen in the experimental data is still not seen in the numerical results, even at this higher pressure ratio.



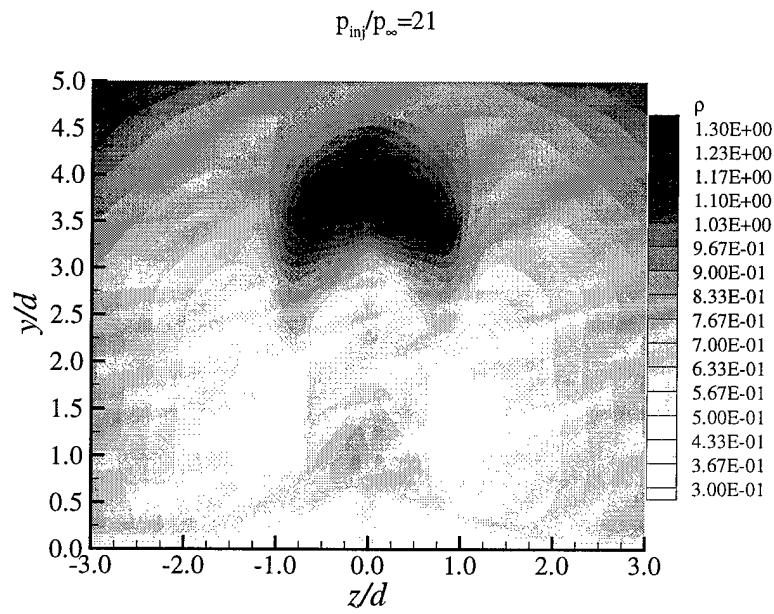


Figure 194. Comparison of  $\rho$  at higher pressure ratio ( $x/d = 10.0$ )

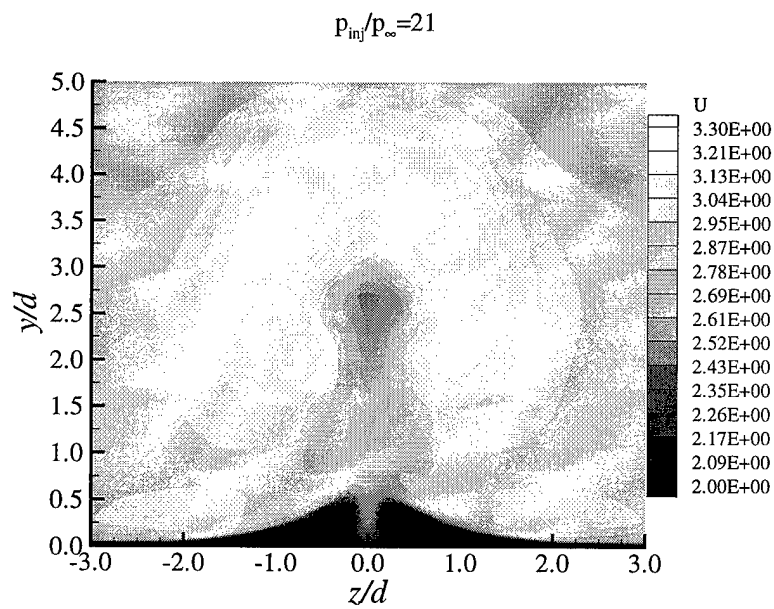


Figure 195. Comparison of the  $U$  component of velocity at higher pressure ratio ( $x/d = 10.0$ )

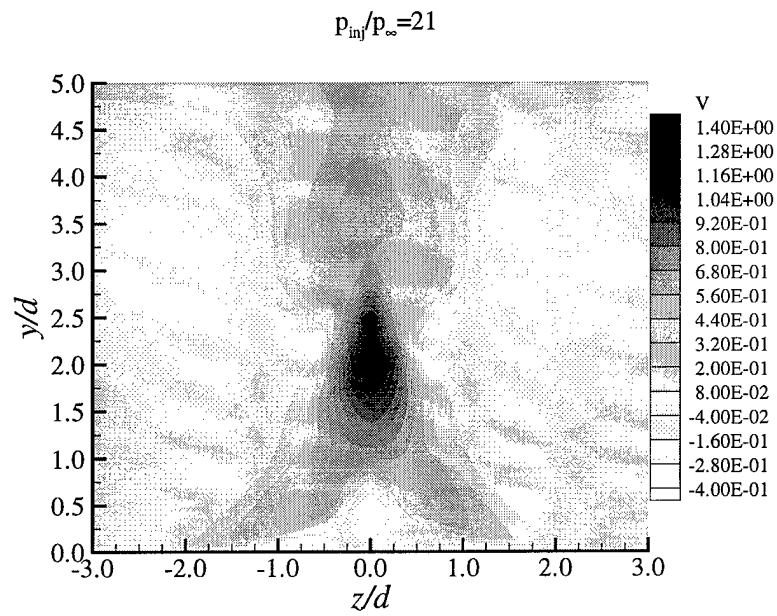


Figure 196. Comparison of the  $V$  component of velocity at higher pressure ratio ( $x/d = 10.0$ )

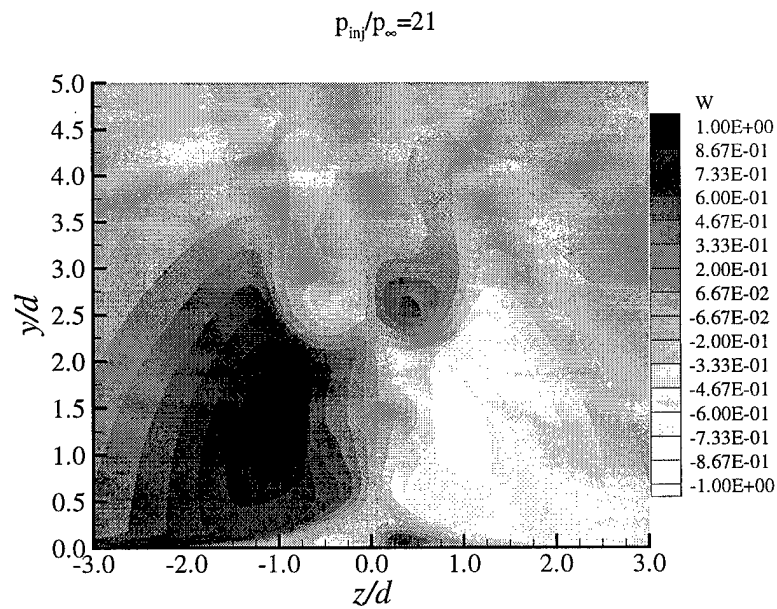


Figure 197. Comparison of the  $W$  component of velocity at higher pressure ratio ( $x/d = 10.0$ )

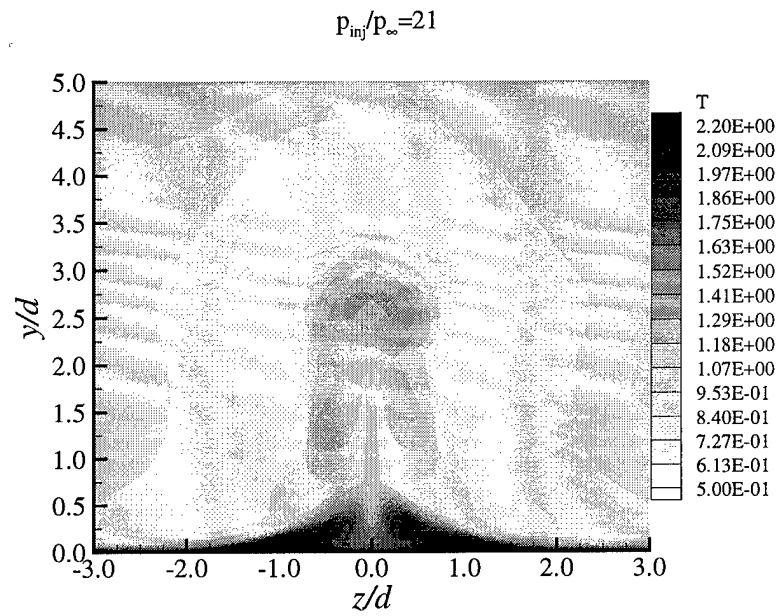


Figure 198. Comparison of  $T$  at higher pressure ratio ( $x/d = 10.0$ )

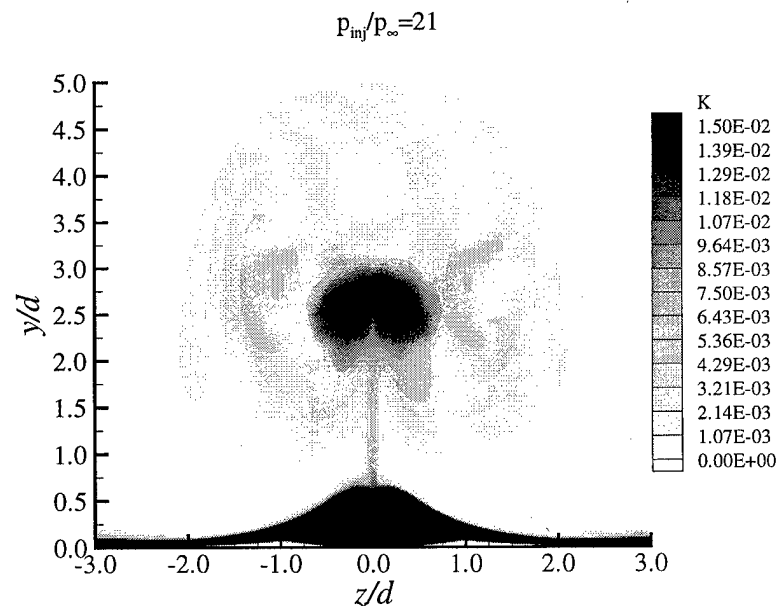


Figure 199. Comparison of  $K$  at higher pressure ratio ( $x/d = 10.0$ )

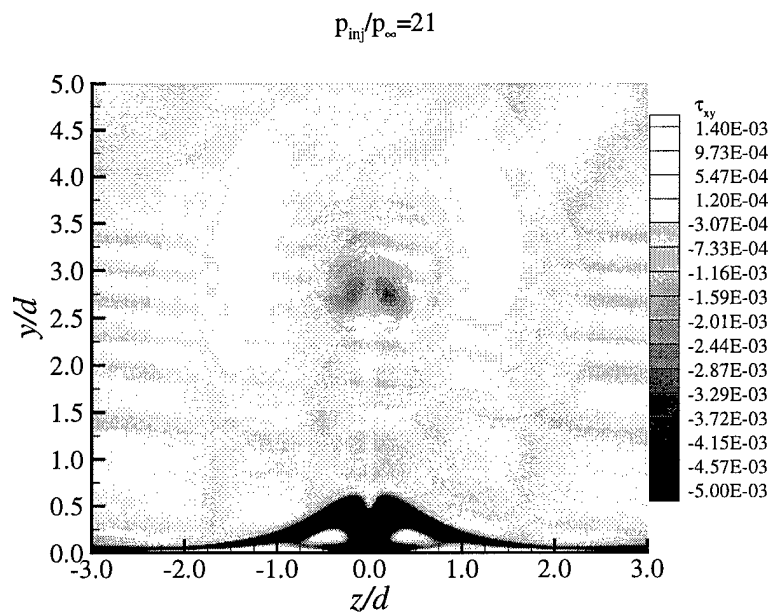


Figure 200. Comparison of  $\tau_{xy}$  at higher pressure ratio ( $x/d = 10.0$ )

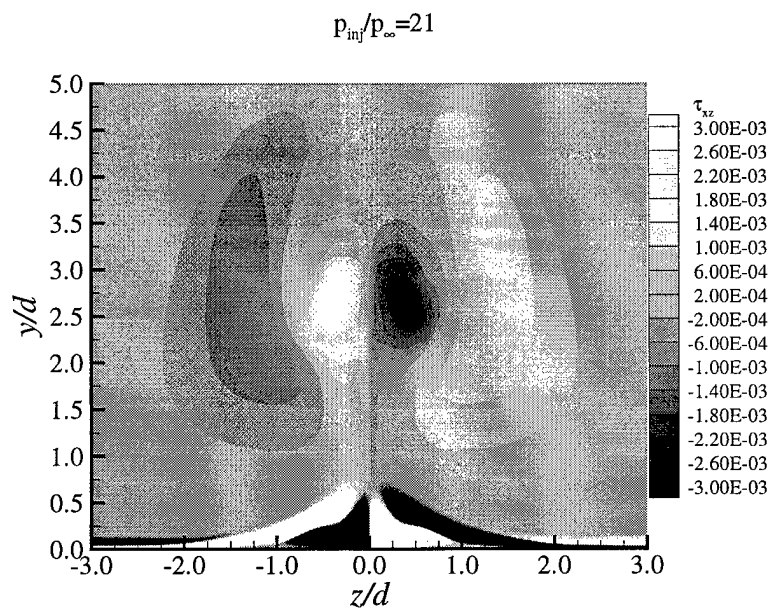


Figure 201. Comparison of  $\tau_{xz}$  at higher pressure ratio ( $x/d = 10.0$ )

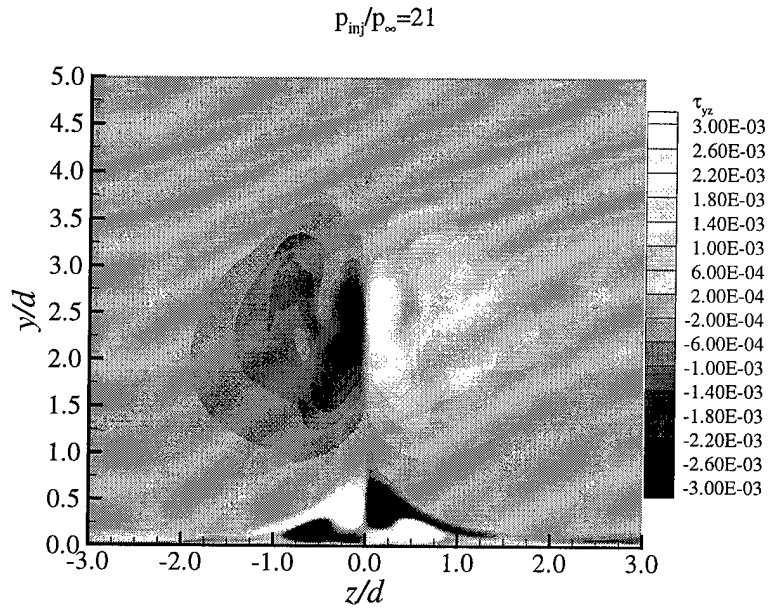


Figure 202. Comparison of  $\tau_{yz}$  at higher pressure ratio ( $x/d = 10.0$ )

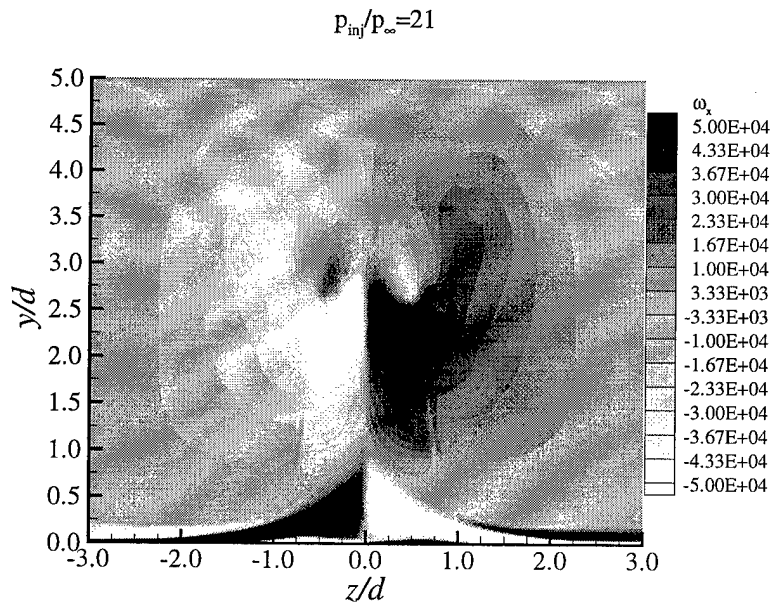


Figure 203. Comparison of  $\omega_x$  at higher pressure ratio ( $x/d = 10.0$ )

## APPENDIX H - Run Time Summary

This appendix contains a summary of the system performance data for each of the simulations presented in this document. Also found in this appendix are the CFL numbers of each simulation.

All of the two-dimensional simulations were performed with AFIT's DEC Alpha computers. These computers were equipped with the EV5 chip set and operated at a clock speed of 250MHz. The three-dimensional simulations were performed on the Cray J916 located at the Aeronautical Systems Command Major Shared Resource Center, Wright-Patterson AFB, OH. Typical values for the CPU time/grid point/iteration of these two computer systems are summarized in Table 14.

Table 14. System performance data

Model	DEC Alpha	Cray J916
$K - \epsilon$	$92\mu s$	$19\mu s$
RSTM	$157\mu s$	$32\mu s$

The following tables present a summary of system performance data for each of the simulations reported in this document. The experimental configuration of each table corresponds to is given in the table heading. The case numbers listed in the tables are the numbers used to identify the data files during the research phases of this study. The "restart file" is a data file used to initialize the flowfield of the simulation. For the  $K - \epsilon$  model simulations, this file is the flowfield data from a solution at a lower pressure ratio and for the RSTM simulations, this file consists of flowfield data from the  $K - \epsilon$  model simulation at the current pressure ratio.

The ISAAC algorithm permits initial and final CFL numbers as inputs. The initial CFL number is the CFL number the algorithm begins the iteration process with. Over the period of "ramped iterations" the CFL number is increased until it reaches the final CFL number. Once the final CFL number is reached, that value is used until the iteration process is completed.

The ISAAC algorithm also permits grid sequencing to accelerate convergence of the solution. A single level of grid sequencing is used with the  $K - \epsilon$  model during the three-dimensional simulations. This solution is interpolated up to the next higher level grid and used as the restart file to initialize the  $K - \epsilon$  and RSTM simulations.

The run time data provided for the two-dimensional solutions represents a significant learning curve in grid management and convergence properties of the ISAAC algorithm.. During the two-dimensional simulations, grid sequencing was not used and the algorithm was allowed to run beyond the point where the solution had converged. Thus, the run times reported for the two-dimensional cases are not necessarily the minimum run time which could have been realized with this algorithm. It is certainly possible that reduced run times for the two-dimensional computation with the RSTM could have been achieved with proper use of the grid sequencing option.

The run time data provided for the three-dimensional computations incorporates grid sequencing and an initial solution of the flowfield based on the  $K - \epsilon$  model.

Table 15. Aso et al. run time data

Case number	$p_{inj}/p_{\infty}$	Restart file	Grid size	Total # of iterations	Run time ( $s \times 10^{-3}$ )	Model
KeGw27-2a	4.86	None	$337 \times 121$	10,000	194	$K - \epsilon$
KeGw27-3a	10.29	KeGw27-2a	$337 \times 121$	10,000	194	$K - \epsilon$
KeGw27-4b	17.72	KeGw27-3a	$337 \times 121$	12,000	233	$K - \epsilon$
KeGw27-5a	25.15	KeGw27-4b	$337 \times 121$	12,000	233	$K - \epsilon$
RseGw27-2a	4.86	KeGw27-2a	$337 \times 121$	18,000	600	RSTM
RseGw27-3f	10.29	KeGw27-3a	$337 \times 121$	18,000	600	RSTM
RseGw27-4b	17.72	KeGw27-4b	$337 \times 121$	20,000	663	RSTM
RseGw27-5b	25.15	KeGw27-5a	$337 \times 121$	20,000	663	RSTM

Table 16. Aso et al. CFL data

Case number	Initial CFL	Final CFL	Ramped iterations	Model
KeGw27-2a	1	5	2,000	$K - \epsilon$
KeGw27-3a	1	5	2,000	$K - \epsilon$
KeGw27-4a	1	3	4,000	$K - \epsilon$
KeGw27-5a	1	3	5,000	$K - \epsilon$
RseGw27-2a	0.1	0.4	6,000	RSTM
RseGw27-3f	0.1	0.4	6,000	RSTM
RseGw27-4b	0.1	0.4	6,000	RSTM
RseGw27-5b	0.1	0.4	6,000	RSTM

Table 17. Spaid and Zukoski run time data

Case number	$p_{inj}/p_{\infty}$	Restart file	Grid size	Total # of iterations	Run time ( $s \times 10^{-3}$ )	Model
KeGw27-13b	8.743	None	$337 \times 121$	17,000	330	$K - \epsilon$
KeGw27-14a	17.117	KeGw27-13b	$337 \times 121$	12,000	233	$K - \epsilon$
KeGw27-15a	42.69	KeGw27-14a	$337 \times 121$	17,000	330	$K - \epsilon$
KeGw27-16a	63.50	KeGw27-15a	$337 \times 121$	20,000	388	$K - \epsilon$
RseGw27-13b	8.743	KeGw27-13b	$337 \times 121$	20,000	663	RSTM
RseGw27-14b	17.117	KeGw27-14a	$337 \times 121$	20,000	663	RSTM
RseGw27-15b	42.69	KeGw27-15a	$337 \times 121$	20,000	663	RSTM
RseGw27-16b	63.50	KeGw27-16a	$337 \times 121$	20,000	663	RSTM

Table 18. Spaid and Zukoski CFL data

Case number	Initial CFL	Final CFL	Ramped iterations	Model
KeGw27-13b	1	4	2,000	$K - \epsilon$
KeGw27-14a	1	4	2,000	$K - \epsilon$
KeGw27-15a	1	4	2,000	$K - \epsilon$
KeGw27-16a	1	4	2,000	$K - \epsilon$
RseGw27-13b	0.1	0.5	4,000	RSTM
RseGw27-14b	0.1	0.5	4,000	RSTM
RseGw27-15b	0.1	0.5	4,000	RSTM
RseGw27-16b	0.1	0.5	4,000	RSTM



Table 19. Tucker run time data

Case number	Injection type	Restart file	Grid size	Total # of iterations	Run time (s $\times 10^{-3}$ )	Model
KeTu9-2a	Cooled	None	$343 \times 121$	20,000	395	$K - \epsilon$
KeTu9-2heat	Heated	KeTu9-2a	$343 \times 121$	20,000	395	$K - \epsilon$
RseTu9-2a	Cooled	KeTu9-2a	$343 \times 121$	20,000	675	RSTM
RseTu9-2heat	Heated	KeTu9-2heat	$343 \times 121$	20,000	675	RSTM

Table 20. Tucker CFL data

Case number	Initial CFL	Final CFL	Ramped iterations	Model
KeTu9-2a	1	3	2,000	$K - \epsilon$
KeTu9-2heat	1	3	2,000	$K - \epsilon$
RseTu9-2a	0.1	0.5	2,000	RSTM
RseTu9-2heat	0.1	0.5	2,000	RSTM

Table 21. McCann and Bowersox run time data

Case number	Restart file	Grid	Grid size	Total # of iterations	Run time (s $\times 10^{-3}$ )	Model
KeGMR14-1a	None	Half-plane	$169 \times 61 \times 31$	8,000	56	$K - \epsilon$
KeGMR14-2a	KeGMR14-1a	Half-plane	$339 \times 121 \times 61$	8,000	407	$K - \epsilon$
RseGMR14-2a	KeGMR14-1a	Half-plane	$339 \times 121 \times 61$	8,000	684	RSTM
KeGMR17-1a	None	Full-plane	$137 \times 53 \times 51$	8,000	106	$K - \epsilon$
KeGMR17-2a	KeGMR17-1a	Full-plane	$275 \times 105 \times 101$	8,000	470	$K - \epsilon$
RseGMR17-2a	KeGMR17-1a	Full-plane	$275 \times 105 \times 101$	8,000	790	RSTM

Table 22. McCann and Bowersox CFL data and memory requirements

Case number	Initial CFL	Final CFL	Ramped iterations	Memory requirements (MW)	Model
KeGMR14-1a	0.01	0.5	8,000	80	$K - \epsilon$
KeGMR14-2a	0.01	0.5	6,000	170	$K - \epsilon$
RseGMR14-2a	0.01	0.5	6,000	256	RSTM
KeGMR17-1a	0.01	0.5	6,000	80	$K - \epsilon$
KeGMR17-2a	0.01	0.5	6,000	170	$K - \epsilon$
RseGMR17-2a	0.01	0.5	6,000	256	RSTM

## Vita

Captain Clarence F. Chenault was born on June 22, 1961, in San Antonio, Texas. He graduated from MacArthur High School in San Antonio, Texas in 1980. He enlisted in the U.S. Air Force as an Airman First Class in 1981 and served his first tour of duty as a computer technician at Rhein Main AFB, W. Germany. In 1985 he was reassigned to Keesler AFB, MS. where he taught digital electronic principles until 1987, when he was selected by AFIT/CI to attend the University of Missouri-Rolla and graduated with a Bachelor of Science degree in Aerospace Engineering in 1990. Upon completion of Officer Training School, Captain Chenault was assigned as the project officer for the Small ICBM Laser Ordnance Firing System at Norton AFB, CA. He entered the AFIT School of Engineering in June of 1992 and upon graduation was assigned to the Special Projects Branch of the Advanced Propulsion and Power Directorate of the Wright Laboratory, Wright-Patterson AFB OH. Captain Chenault was recalled to AFIT in June of 1994 to pursue a Ph.D. in computational fluid dynamics. Upon graduation he will be assigned to the Aeromechanics Integration Branch of the Aeromechanics Division which is part of the Air Vehicles Directorate of the Air Force Research Laboratory.

REPORT DOCUMENTATION PAGE			Form Approved OMB No. 0704-0188	
Public reporting burden for this collection of information is estimated to average 1 hour per response, including the time for reviewing instructions, searching existing data sources, gathering and maintaining the data needed, and completing and reviewing the collection of information. Send comments regarding this burden estimate or any other aspect of this collection of information, including suggestions for reducing this burden, to Washington Headquarters Services, Directorate for Information Operations and Reports, 1215 Jefferson Davis Highway, Suite 1204, Arlington, VA 22202-4302, and to the Office of Management and Budget, Paperwork Reduction Project (0704-0188), Washington, DC 20503.				
1. AGENCY USE ONLY (Leave blank)	2. REPORT DATE March 1998	3. REPORT TYPE AND DATES COVERED Dissertation		
4. TITLE AND SUBTITLE Analysis of Turbulence Models as Applied to Two- and Three-Dimensional Injection Flows		5. FUNDING NUMBERS		
6. AUTHOR(S)  Captain Clarence F. Chenault				
7. PERFORMING ORGANIZATION NAME(S) AND ADDRESS(ES)  Air Force Institute of Technology, WPAFB OH 45433-7655		8. PERFORMING ORGANIZATION REPORT NUMBER AFIT/DS/ENY/98M-01		
9. SPONSORING/MONITORING AGENCY NAME(S) AND ADDRESS(ES)  Dr. Miguel Visbal 2645 5th St., Suite 6 Wright-Patterson AFB, OH 45433-7912 937-255-4305		10. SPONSORING/MONITORING AGENCY REPORT NUMBER		
11. SUPPLEMENTARY NOTES  Dissertation advisor Dr. Philip S. Beran				
12a. DISTRIBUTION / AVAILABILITY STATEMENT  Approved For Public Release; Distribution Unlimited			12b. DISTRIBUTION CODE	
13. ABSTRACT (Maximum 200 words)  A steady-state solution of the full, three-dimensional Favre-averaged Navier-Stokes equations, coupled with a second-order Reynolds stress turbulence model (RSTM) and an eddy-viscosity model were used to numerically simulate oblique injection into supersonic flow. Numerical results were compared to experimental data and the turbulence models were evaluated for accurate prediction of thermo-mechanical mean flow variables, Reynolds stresses, flowfield shock structure and boundary layer phenomena. The RSTM simulation resulted in physically consistent and accurate predictions for the mean flow and turbulent quantities. Simulations with the eddy viscosity model resulted in non-physical and inconsistent turbulence predictions. RSTM simulations were used to categorize the regions of the barrel shock and identify the shock/expansion mechanisms which generate vortical motion in and around the jet plume. Two distinct vortex pairs associated with plume expansion and injectant mixing were identified. These were the recompression shock induced vortices located within the plume and jet induced vortices located outside of the plume.				
14. SUBJECT TERMS  Turbulence, Second-order, Reynolds Stress, $K - \epsilon$ , Computational Fluid Dynamics, Supersonic injection, Two-Dimension, Three-Dimension, Mixing, Plume structure			15. NUMBER OF PAGES 471	
			16. PRICE CODE	
17. SECURITY CLASSIFICATION OF REPORT UNCLASSIFIED	18. SECURITY CLASSIFICATION OF THIS PAGE UNCLASSIFIED	19. SECURITY CLASSIFICATION OF ABSTRACT UNCLASSIFIED	20. LIMITATION OF ABSTRACT  UL	